The University of Technology, Sydney

Faculty of Engineering

A Numerical Study of a Rotary Valve Internal Combustion Engine

Glenn Horrocks

A dissertation submitted in fulfilment of the requirements for the degree of Doctor of Philosophy

11 October 2001

Supervisor: Prof. John Reizes
Co-Supervisor: Dr. Guang Hong

Confidential

This thesis is subject to a Research Agreement between

The University of Technology, Sydney
and
Bishop Innovation Limited.

Under the terms of this Agreement:

1. This thesis is confidential until 1 October 2004;
2. UTS is obliged to ensure that the examiners of this thesis undertake to keep the information confidential; and
3. UTS is obliged to ensure that this publication is secure and is not released into the public domain until 1 October 2004.

Tony Wallis
Manager BRV Technology,
Bishop Innovation Limited

Contents

List of Figures

List of Tables

Nomenclature

$\bar{R}$	Universal gas constant, see equation (2.6)
$\mathbf{B}$	Fluid body force, see equation (2.2)
$\mathbf{U}$	Local fluid velocity, see equation (2.1)
ϵ	Turbulent dissipation, see equation (2.35)
Γ	Scalar diffusion coefficient, see equation (2.8)
γ	Gas constant, or the ratio of specific heats, ($\gamma = C_p/C_v$), see equation (4.6)
λ	Fluid thermal conductivity, see equation (2.5)
$\mathbb{T}$	Fluid stress tensor, see equation (2.3)
$\mathbb{T}_t$	Turbulent stress tensor, see equation (2.23)
μ	Fluid molecular viscosity, see equation (2.3)
μ_t	Turbulent viscosity, see equation (2.37)
Φ	Scalar, see equation (2.8)
ρ	Fluid density, see equation (2.1)
°CA	Degrees crank angle. 0 °CA is defined as TDC at the start of the intake stroke, page 3
ζ	Fluid bulk viscosity, see equation (2.3)
A_e	Valve effective area, see equation (4.17)
C_D	Valve discharge coefficient, see equation (4.16)
C_p	Specific heat of gas at constant pressure, see equation (2.7)
H	Fluid total enthalpy, see equation (2.4)
h	Fluid static enthalpy, see equation (2.5)
H^+	Non-dimensional enthalpy near a wall, see equation (3.32)

H_t Turbulent mean total enthaply, see equation (2.24)

k Turbulent kinetic energy, see equation (2.25)

p Fluid pressure, see equation (2.3)

S Scalar source term, see equation (2.8)

T Fluid temperature, see equation (2.5)

t Time, see equation (2.1)

u^+ Non-dimensional velocity parallel to a wall, see equation (3.24)

W Molecular mass, see equation (2.6)

y^+ Non-dimensional distance to the wall in a turbulent boundary layer, see equation (3.25)

BMEP Brake mean effective pressure, see equation (1.3)

CFL Courant-Friedrichs-Lewy stability criterion, see equation (5.10)

CR Cross tumble ratio, see equation (4.4)

IMEP Indicated mean effective pressure, see equation (1.1)

MPV Mean piston velocity, see equation (8.3)

SQ Squish ratio, see equation (4.2)

SR Swirl ratio, see equation (4.5)

TR Tumble ratio, see equation (4.3)

BDC Bottom Dead Centre, that is the crank location which gives the maximum cylinder volume, page 3

BRV Bishop Rotary Valve, page 25

BSR Bore to stroke ratio, page 378

CFD Computational fluid dynamics, page 28

DNS Direct numerical simulation, page 33

EVC Exhaust valve close point. Usually expressed in °CA after TDC, page 4

EVO Exhaust valve open point. Usually expressed in °CA before BDC, page 4

IVC Inlet valve close point. Usually expressed in °CA after BDC, page 4

IVO Inlet valve open point. Usually expressed in °CA before TDC, page 4

LES Large eddy simulation, page 42

MOC Method of characteristics, page 84

RSM Reynolds stress turbulence model, page 37

TDC Top Dead Centre. Defined as the crank location which gives the minimum cylinder volume, page 3

Certificate of Authorship and Originality

I certify that the work in this thesis has not previously been submitted for a degree nor has it been submitted as part of requirements for a degree except as fully acknowledged within the text.

I also certify that the thesis has been written by me. Any help that I have received in my research work and the preparation of the thesis itself has been acknowledged. In addition, I certify that all information sources and literature used are indicated in the thesis.

Signature of Candidate

Acknowledgements

The author wishes to thank the members of the Bishop Rotary Valve engine team for access to engine design data and experimental results, and fruitful discussions about the engine during the course of this project. Thanks to Hamish Reid and Geoff Donohoo for assistance with solid modelling and valve geometries; Mark Profaca, Andrew Edwards and Mark Boxsell for performing much of the experimental work used in this thesis; and Andrew Thomas and Tony Wallis for their guidance and the wide ranging discussions about the engine. Figures 7.1 and 7.2 were provided by Mark Profaca.

Above all, the author wishes to thank his supervisor, Professor John Reizes, for his support, experience and direction during the course of this project. His enthusiastic supervision of this project is gratefully acknowledged.

The author would also like to express his appreciation for the contribution of Dr. Guang Hong, project co-supervisor, Merryn Mathie who assisted with proof-reading of the text, and the information technology staff of UTS who made provisions for the computationally intensive work presented here to be performed.

Abstract

A Computational Fluid Dynamics (CFD) simulation of the Bishop Rotary Valve (BRV) engine is developed. The simulation used an existing commercial CFD code, CFX 4.3, with a number of new routines written to allow it to simulate the conditions and motions involved in an internal combustion engine. The code is extensively validated using results from other researchers, and several new validations are performed to directly validate the code for simulating internal combustion engine flows.

Firstly, tumble vortex breakdown during the compression stroke of a square piston model engine is modelled. The results of the simulation are validated against published high quality experimental data. Both two- and three-dimensional models are tested, using the k-ϵ and Reynolds stress turbulence models. The Reynolds stress turbulence model simulations successfully predicted the tumble break down process during the compression stroke. A simple three-dimensional Large Eddy Simulation model is also presented.

The numerical simulation is then applied to the BRV engine. An in-cylinder flow field not previously described is discovered, created by the unique combustion chamber shape of the BRV engine. The flow field is not adequately described by the traditional descriptions of engine flows, being squish, swirl and tumble. The new flow structure is named "dual cross tumble", and is characterised by two counter-rotating vortices in the cross tumble plane on either side of the inlet air jet.

Analysis of the dual tumble structure indicates that it is most beneficial in high bore to stroke ratio engines. This flow structure has been predicted or visualised by a small number of previous researchers, however no published research has recognised its significance or potential benefits. The validated code is then used to predict the effect of modifying the valve cross sectional area, the effect of the inlet manifold wave, the effect of heat transfer from the inlet manifold walls, the effect of bore to stroke ratio, and the effect of engine speed.

This work presents a numerical simulation of a new rotary valve engine technology. This opens up a whole new area of engine aerodynamics research as no detailed examination of the flows in a rotary valve engine have been presented previously. In the process, it discovers a new compression stroke turbulence generation mechanism, "dual cross tumble", which offers the potential of performance levels not possible using poppet valve engines.

Chapter 1

Introduction

The reciprocating internal combustion engine is one of the most common sources of mechanical power in the modern world. Its uses range from transportation such as land vehicles, boats and ships, or aircraft; through to electrical power generation. There are many different types of reciprocating internal combustion engine designs, however the four-stroke spark ignition engine cycle is the one of primary interest in this work.

The operating principle of a four stroke spark ignition engine will now be described.

1.1 Fundamental Principles

A diagrammatic representation of a four stroke reciprocating internal combustion engine is shown in figure 1.1. The engine uses a crankshaft and connecting rod (or "conrod") to generate a reciprocating motion in the piston. This motion compresses and expands the gas above the piston, in the region called the combustion chamber. The cylinder head has inlet and exhaust valves to allow gas transfer to take place, and a spark plug to ignite the charge.

The name "four stroke cycle" comes from the four major processes performed by the engine. The four strokes are:

The induction stroke. The inlet valve is open, and the exhaust valve is shut. The piston travels from the top of its stroke to the bottom, drawing in fresh air/fuel mixture from the inlet manifold.

The compression stroke. Both valves are closed. The piston travels from the bottom of its stroke to the top, compressing the air/fuel mixture trapped in

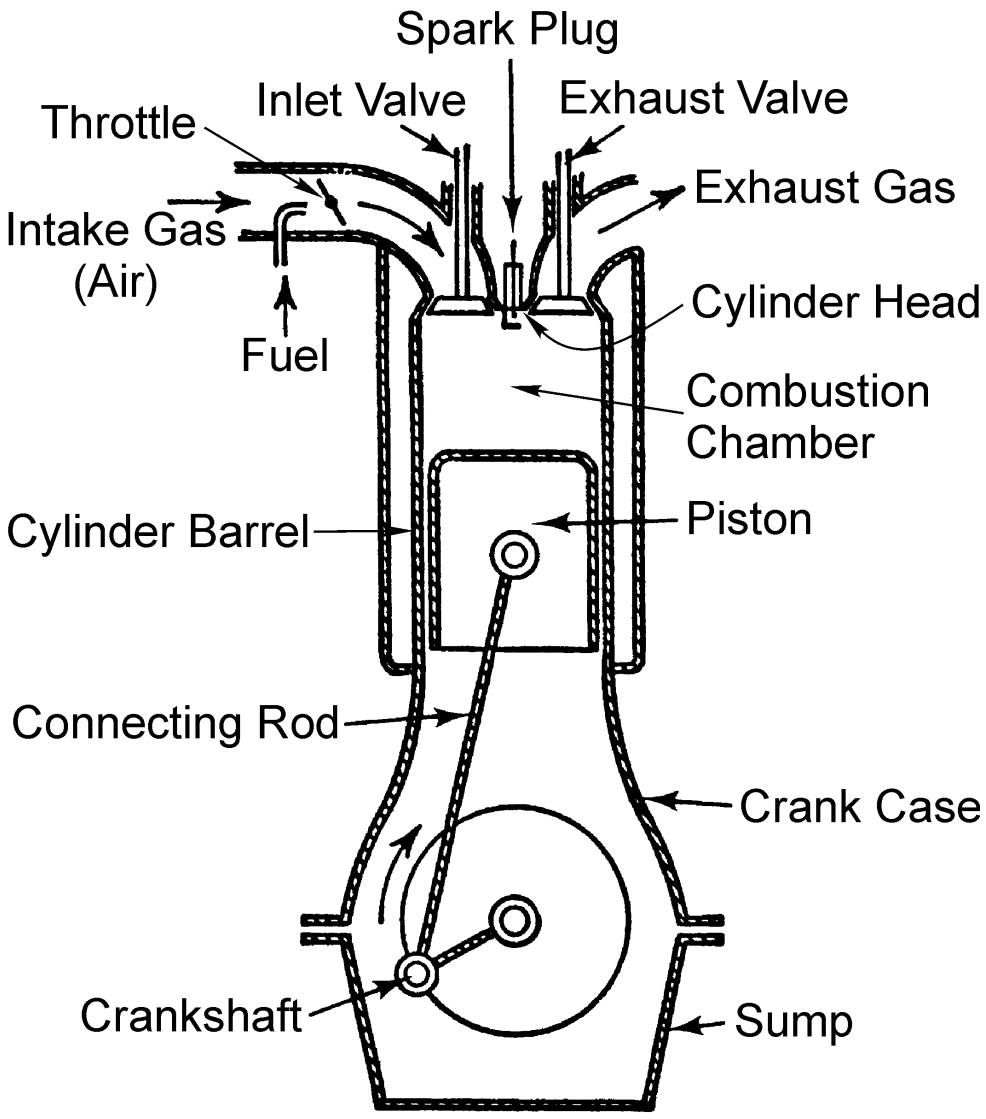

Figure 1.1: Diagrammatic representation of a four stroke, spark ignition, reciprocating, internal combustion engine. Adapted from Stone [263].

the combustion chamber. Near the top of the stroke the spark plug is fired and the mixture is ignited.

The expansion stroke. Both valves are closed. The piston travels from the top of its stroke to the bottom, pushed by the high pressure of the burnt gases. It is during this stroke that the vast majority of the power is applied to the crank.

The exhaust stroke. The exhaust valve is open, the inlet valve is shut. The piston travels from the bottom of its stroke to the top, pushing the burnt gas (exhaust) out the exhaust valve and into the exhaust manifold.

1.1.1 Terminology

The following list is terminology in common use in reciprocating internal combustion engine design:

IC engine. The reciprocating internal combustion engine is often referred to as merely the internal combustion engine, or IC engine. Strictly speaking, this category also includes gas turbines, however the term "IC engine" is commonly used to mean reciprocating internal combustion engine.

Bottom dead centre. This refers to the end of the intake and expansion strokes, when the piston is at the "bottom" of its motion. Bottom dead centre refers to when the combustion chamber is at its largest volume. It is abbreviated as BDC.

Top dead centre. This refers to the end of the compression and exhaust strokes, when the piston is at the "top" of its motion. Top dead centre refers to when the combustion chamber is at its smallest volume. It is abbreviated as TDC.

Degrees crank angle. This refers to the position of the crank during the two revolution engine cycle. Definitions of the zero point for crank angle vary between authors, however in the current work zero will be defined at TDC of the intake stroke. As the four stroke engine cycle covers two revolutions, crank angle increases from 0° to 720° and then repeats. It is abbreviated as $^\circ$CA.

Volumetric efficiency. This refers to the quantity of intake manifold air ingested during the intake stroke. It is expressed as a ratio of the mass of air ingested

divided by the mass of air that would exist in the cylinder at BDC at a reference temperature and pressure.

Compression ratio. This refers to the amount of compression performed during the compression stroke, and conversely the amount of expansion done during the expansion stroke. It is expressed as a ratio of the volume of the combustion chamber at BDC divided by the volume at TDC.

The fundamental process of a four stroke engine, described above, is only an overall description of the processes in a modern engine. As development of the IC engine progressed, it was found that small modifications to the ideal cycle can improve performance. Some of these modifications relevant to the work presented here are:

Spark advance. It has been found that igniting the spark a short time before the end of the compression stroke improves performance, and is called spark advance. The amount of spark advance is specified by the °CA before TDC of the compression stroke where ignition occurs.

Valve overlap. In modern high speed engines it is possible to increase performance by keeping the exhaust valve open after TDC of the exhaust stroke, and opening the inlet valve before TDC. This is called "valve overlap", and in a suitably designed engine allows the incoming inlet gas to blow additional exhaust gas out of the combustion chamber. This effect is called "scavenging". The amount of valve overlap is measured by the °CA before and after TDC at which the valves open or shut. The inlet valve open point is abbreviated IVO, and the exhaust valve close point is abbreviated EVC.

Inlet valve close. Similarly, performance can be increased if the inlet valve is shut after BDC of the intake stroke. The amount of inlet valve close delay is the °CA after BDC at which the inlet valve shuts, and is commonly abbreviated as IVC.

Exhaust valve open. Additionally, performance can be increased if the exhaust valve is opened before BDC of the exhaust stroke. The amount of exhaust valve open advance is the °CA before BDC at which the exhaust valve opens, and is commonly abbreviated EVO.

The valve opening and closing points are moved away from TDC and BDC to take advantage of the pressure waves which form in the inlet and exhaust manifolds. This is discussed in chapter 4.

A standard method of normalising engine performance is using the indicated mean effective pressure, or *IMEP*. It is defined as the area enclosed in an engine's pressure versus volume curve, normalised against the swept volume and speed of the engine. The *IMEP* is given by

$$IMEP = \frac{P_{indicated}}{V_{swept} N^*}, \tag{1.1}$$

where $P_{indicated}$ is the power produced by the cylinder gas on the piston. The indicated power, $P_{indicated}$, is determined by the area enclosed by the pressure versus volume diagram for the engine. The swept volume of the engine is V_{swept} and N^* is the number of engine cycles per second. For four stroke engines, $N^* = \frac{n}{2}$, where n is the engine crankshaft speed. The *IMEP* is a measure of the aerodynamic output of the engine, that is, it includes the effects of gas exchange and combustion, with the effects of engine capacity and speed removed. It can be used as a comparison of the aerodynamic performance of engines with different capacities and speeds. The *IMEP* is usually calculated from the cylinder pressure versus volume diagram using

$$IMEP = \frac{\int_{cycle} p_{cyl}\, dV_{cyl}}{V_{swept}}, \tag{1.2}$$

where p_{cyl} is the instantaneous cylinder pressure and V_{cyl} is the instantaneous cylinder volume. The integral is evaluated over a full cycle of the engine.

If the indicated power ($P_{indicated}$) is replaced with the power measured at the output shaft of the engine, we get a measure of the performance of the entire engine, again normalised against capacity and speed. This is denoted as brake mean effective pressure, or *BMEP*. It is defined as

$$BMEP = \frac{P_{brake}}{V_{swept} N^*}, \tag{1.3}$$

where P_{brake} is the power output of the engine at the crankshaft. Engine losses are included in the *BMEP* calculation, such as lubricant pumping power (if the lubricant pump is powered by the crankshaft) and engine friction. The *IMEP* and *BMEP* parameters will be used extensively in this thesis to compare engine performance.

1.2 The Modern High Performance Poppet Valve Engine

Poppet valve engine design has also evolved significantly from the early days of the internal combustion engine. An analysis of the history of this development is

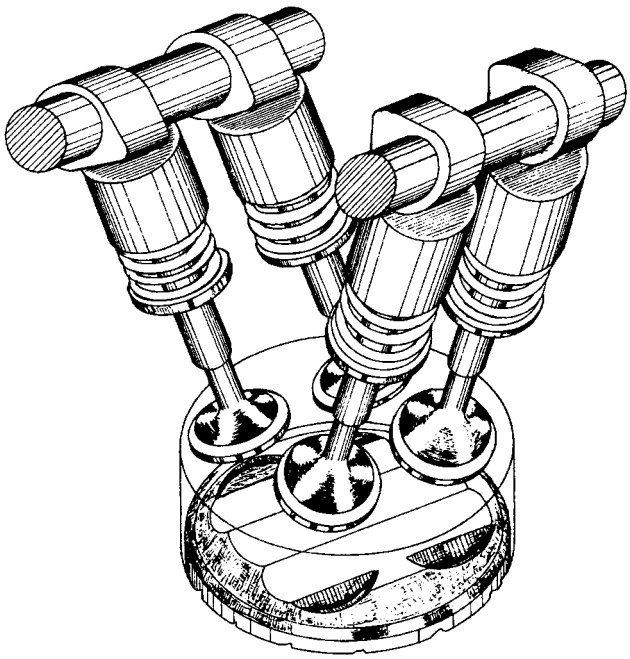

Figure 1.2: Schematic diagram of a four valve pentroof combustion chamber. Reproduced from Heisler [132].

beyond the scope of the current work, and is extensively covered in other works. The reader is referred to Clutton [69], Heisler [132], Stone [263], Ricardo [236] or Taylor [271, 272] for more information of the development of the poppet valve engine.

The state of the art in modern performance engine design is the "pentroof" combustion chamber shape, shown in figure 1.2. It has become almost universally accepted in poppet valve engine design for modern high performance applications. It is also known as the "cross flow head". It usually has four valves, with two inlet valves and two exhaust valves. The valves can be actuated either by a single camshaft using rocker arms, or two camshafts acting directly on the valves as shown in figure 1.2.

This design has been shown to have a good compromise between high volumetric efficiency, good combustion characteristics and a geometry able to achieve high compression ratios. An example of the application of this type of combustion chamber in a high performance production car engine is shown in figure 1.3, showing the Rover K series engine. This engine has been used in Rover vehicles since the early 1990s, and is also being produced by other manufacturers, including Lotus and Kia.

The pentroof combustion chamber is the benchmark poppet valve engine design against which the rotary valve engine will be compared.

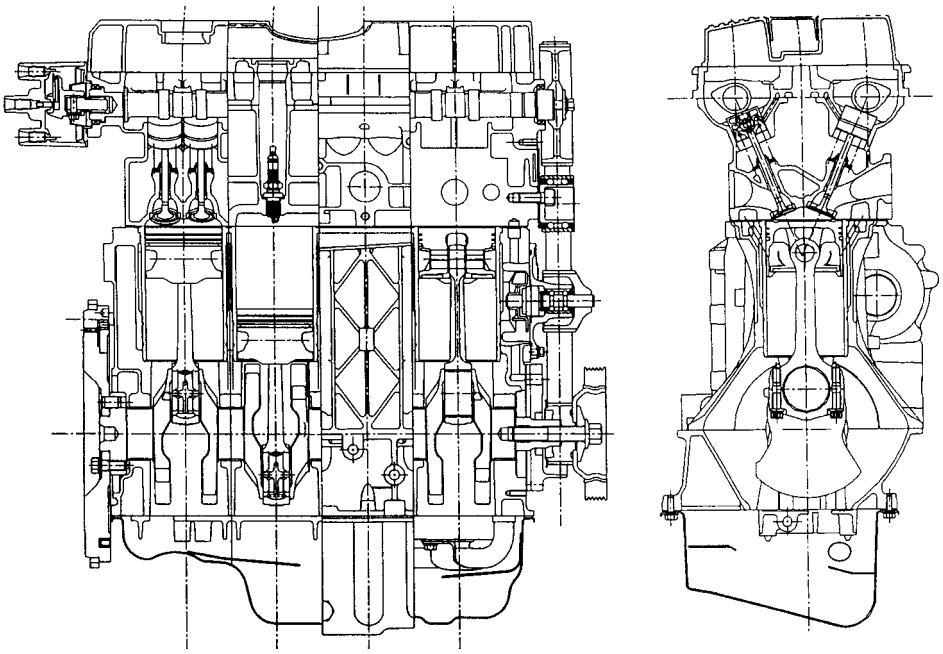

Figure 1.3: Longitudinal and transverse sections of the four cylinder, in-line Rover K series engine. The pentroof combustion chamber is shown in the cross section. Reproduced from Stone [263].

1.3 Rotary Valve Engine Fundamentals

It has been known since the earliest days of the internal combustion engine that using a rotary valve system for the gas exchange processes in an internal combustion engine has a number of advantages over traditional poppet valve mechanisms. These advantages were listed by Hunter in 1946 [147], and most of his comments are still valid for modern internal combustion engines, over 50 years after its publication:

Elimination of reciprocating valve motion. This can lead to smoother running and a reduction in operating noise. Additionally, the forces required to impart the reciprocating motion to the valves can be a limiting factor on the maximum speed of an engine, so its elimination may allow higher engine speeds and thus higher specific power outputs. A further and related advantage is due to the elimination of the cam and rocker arm mechanism. The rocker arms must be heavily loaded onto the camshaft so they can operate at high engine speeds, but this causes a power loss through friction. A rotary valve engine eliminates this mechanism, giving the potential of reducing engine power losses through friction.

Improved combustion chamber shapes. The valves in a poppet valve engine take up the majority of the area available on the cylinder head, and restrictions such as valve/piston clearance and inlet valve/exhaust valve interference place limitations on the possible design of the combustion chamber. Thus poppet valve combustion chamber design is a compromise between achieving an adequate compression ratio, component interference, maintaining good air flow through the valves and good combustion chamber design. Rotary valve systems avoid these restrictions as they do not require any object to protrude into the combustion chamber. This allows the opportunity for improved combustion chamber shapes.

Superior breathing characteristics. Rotary valve engines can have more streamlined ports than equivalent poppet valve engines as the flow is not obstructed by the valve head. Further, for a given cylinder bore a rotary valve port can have a larger cross section than the equivalent poppet valve engine. These effects combine to allow higher volumetric efficiencies. If engine breathing is the limiting factor on engine speed this will also allow an increase in maximum engine speed which will increase the power of an engine.

No exhaust valve exposed in the combustion chamber. As the exhaust valve in a poppet valve engine has a poor heat path to the engine coolant, it becomes a "hot spot" which can be the source of pre-ignition. Pre-ignition is a major performance limiting factor. Most rotary valve engine designs have no exhaust valve present in the combustion chamber during the compression or expansion strokes, eliminating this "hot spot". This allows the engine to run either a higher compression ratio or on lower grade fuel than an equivalent poppet valve engine. Potentially this can allow an increase in power and a reduction in fuel consumption.

Fewer parts. Rotary valve engines can have fewer parts than poppet valve engines. This can lead to manufacturing and maintenance cost reductions, however this is negated somewhat by the fact that the individual parts in a rotary valve engine can be quite complicated. Additionally, with the enormous scale of production of poppet valve engines it is unlikely that rotary valve engines will be cheaper to produce than poppet valve engines for some time.

Despite these advantages, no rotary valve engine has been able to make a significant commercial impact on poppet valve engines. No rotary valve engine design is commercially available at the time of writing. Numerous attempts at making a

usable rotary valve four stroke engine have been made and many patents issued, however only a small number of these designs have made it onto the market, and none have been commercially successful.

The reason for this lack of success lies in the disadvantages present in the rotary valve engine design—or better described as "challenges" for engine designers to overcome. Important issues include:

- The sealing of the valve rotor against the cylinder head under the combustion pressure,
- Lubrication of the rotor, and
- Friction losses of the rotor.

The methods used to overcome these issues by the various rotary valve engine designs have been many and varied. A brief history of the development of rotary valve engines will now be presented, leading to the Bishop Rotary Valve engine project and the current author's work; which is an attempt to revive the rotary valve engine as a leading internal combustion engine design.

1.4 History of the Rotary Valve Engine

Hundreds of patents exist describing rotary valve systems for internal combustion engines. Patents exist dating from 1911 [191] through to the current day, and so cover almost the entire development of the internal combustion engine. This demonstrates the wide range of people and considerable effort that has been applied to develop a successful rotary valve engine design.

The important rotary valve engine designs will now be discussed, as a background to the current rotary valve engine project.

1.4.1 Early History

In the early period of internal combustion engine development before 1950, the poppet valve was far from optimised, and significant advances in performance were being made from year to year. This also means that there were many opportunities for alternative valve systems to surpass the poppet valve. It was a time when engine development could be done by enthusiastic amateurs, using their own ideas and funding. In this environment many rotary valve engine designs were developed, most of which failed and quickly faded into obscurity.

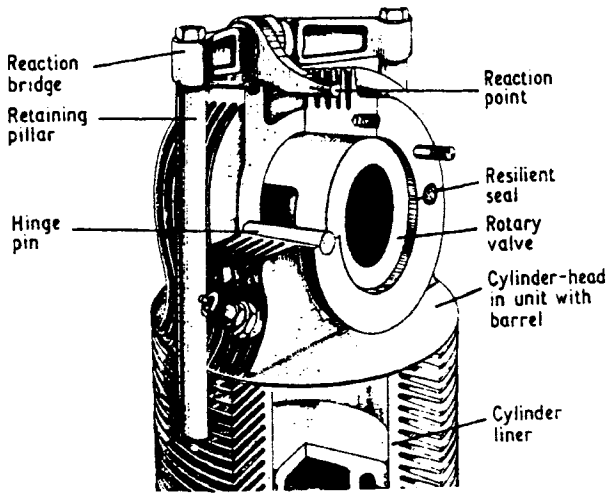

Figure 1.4: Schematic diagram of the Cross Rotary Valve engine. Reproduced from Baker and Cross [31].

As has been previously mentioned, the main problems with rotary valve engines uncovered by early designs are sealing of the valve/head interface against combustion pressure; high lubricant consumption and high engine losses caused by friction of the valve rotor [147]. These problems are interlinked, and a poor solution to one problem would cause another problem to flare up. Hunter [147] describes most of the developments during this early period, and the most significant designs are outlined below.

Unless stated otherwise, the following descriptions of the rotary valve engines developed by Cross, Aspin, Itala and Junkers are based on Hunter [147].

The Cross Rotary Valve

Roland Cross was a prolific designer of rotary valve engines. He, and the company he founded, designed many rotary valve engines over a period of 60 years. His worked commenced in 1922, when he developed a basic layout for a rotary valve engine which, superficially, is remarkably similar to the design considered by the current author. His design (see figure 1.4) uses a valve rotating about an axis parallel to the crankshaft, and driven at half crankshaft speed. The valve is accurately located in the head by close tolerances which require accurate manufacturing of the rotor and cylinder head. The top section of the head had a stirrup system designed to apply a carefully balanced force downwards on the valve such that it withstands the combustion pressure, without excessive force that would cause a friction loss. The

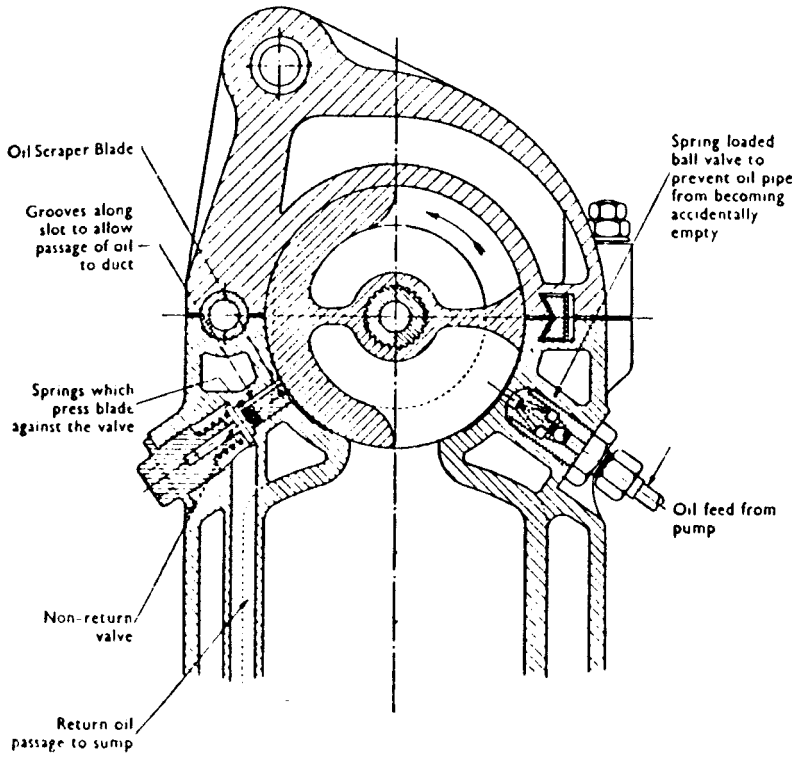

Figure 1.5: The lubrication system used in the Cross Rotary Valve engine. Reproduced from Hunter [147].

basic design was patented in 1932 [76], 1935 [77], and the stirrup system in 1944 [78].

Early designs, such as that shown in figure 1.4 had a high level of friction in driving the valve system so an ingenious lubrication system was developed, shown in figure 1.5. The lubricant was applied as a thin film directly onto the valve as it rotated away from the combustion zone. This film of oil travelled over the top surface of the valve, thus reducing friction against the head as it pressed down on the valve. If this film was allowed to remain on the valve it would then enter the combustion chamber, resulting in excessively high oil consumption. To reduce the quantity of oil wasted a "scraper" was developed which removed all but the finest film of oil from the valve surface just before it was exposed to the combustion gases. A non-return valve was placed behind the scraper to stop the vacuum in the inlet manifold during part throttle operation sucking oil back into the manifold from the oil drain. Cross claimed this system was very successful, and produced an oil consumption comparable to that of a poppet valve engine, whilst keeping engine friction to levels typical of a poppet valve engine.

A further significant development of the work of Cross was his development of a sealing system for his valve. It was known from the many previous attempts at rotary valves that a sealing system was required to prevent leakage of the combustion pressure during the expansion stroke. This was achieved in the early Cross engine through a sealing lip on the cylinder head. The lip is a section of the cylinder head that was slightly raised above the surrounding housing, and designed to have a small amount of resilience. Combustion pressure pushes against the lip, flexing it slightly so it pushes up against the valve, thereby sealing the space between the cylinder head and the valve. The head and valve were machined to tight tolerances so the deflection required by the lip would be small.

Water cooled valves with internal cooling channels in the rotor were developed, however it was found that they were only required for large engines. Most motorcycle and automobile sized engines did not require internal cooling passages.

The Cross Manufacturing Company was established to further the development of the engine, however, the second world war caused the project to lapse as the company focussed on the more immediate demands of supplying the Allied forces with internal combustion engine components. After the war the design was worked on occasionally, but no significant advances were achieved. Roland Cross died in 1970, and management of the company was placed in the charge of Roland's son, Michael Cross [74].

During the 1970s the Cross Manufacturing Company formed a joint research project with Esso Research to revive the rotary valve engine project. They developed a four cylinder, 1.6 L engine in a four cylinder radial layout, as may be seen in figure 1.6. The engine used the Cross rotary valve system. Other developments on this engine include a crankshaft with an eccentric to provide the reciprocating piston motion rather than a crankshaft and conrod, and the use of a separate sealing element rather than the flexible sealing lip design. These advances were patented in 1976 [75].

It was reported to be quite successful when compared to poppet valve engines of its day [245, 31, 72, 74], for instance figure 1.7 shows the engine to generate power equivalent to a leading poppet valve engine of the day, yet have considerably superior fuel consumption. This test was performed with the poppet valve engine fuelled by 100 octane number fuel and the rotary valve engine running on 66 octane number fuel, showing that this engine clearly has the ability to run on far lower octane fuel.

Despite its promise, the designers' hopes for the engine faded, and it never became a commercial success. The company abandoned the project during the 1980s.

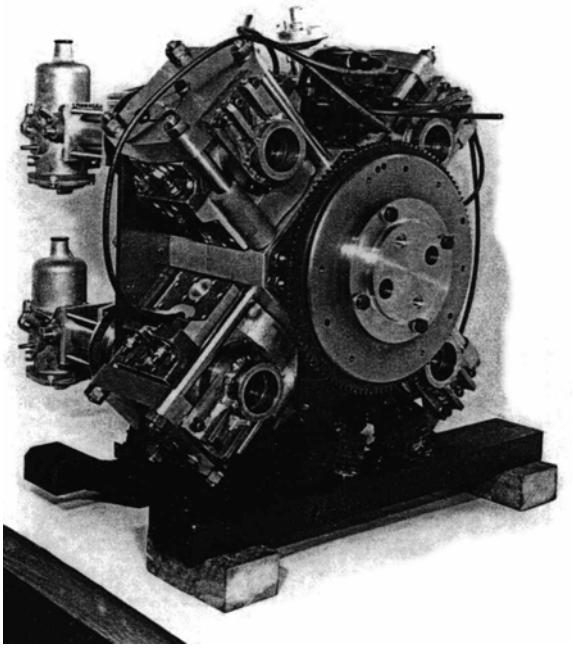

Figure 1.6: The 1.6 L, radial four cylinder Cross Rotary Valve engine. Reproduced from Scott [245].

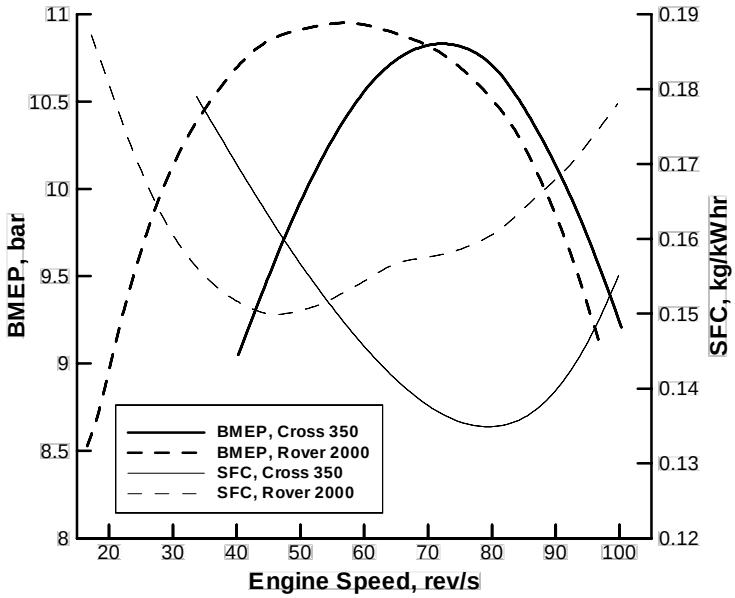

Figure 1.7: Comparison of the Cross 350 Single Cylinder Rotary Valve engine running on 66 octane number fuel, and a Rover 2000 poppet valve engine running on 100 octane number fuel. Reproduced from Scott [245].

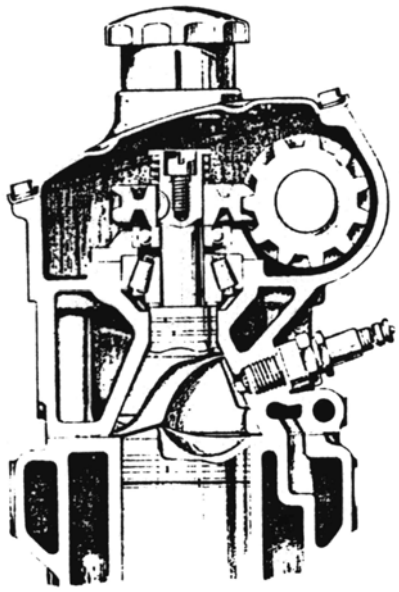

Figure 1.8: The Aspin rotary valve engine. This adaptation is a water-cooled multi-cylinder engine. Reproduced from Hunter [147].

Michael Cross, manager of the Cross Manufacturing Company at the time, commented about the perceived lack of need of the design by automobile manufacturers, and stated,

> "Technically, the design is sound, but I'm not as sure about its commercial potential." [212]

This demonstrates that sometimes good engineering designs fail, through commercial factors such as the cost of re-tooling for manufacture, or even just the human reluctance to depart too far from traditional designs—even if the new design promises improvements beyond those possible in the original design. The Cross Manufacturing Company is now a manufacturer of high-quality piston rings and related components for high performance racing and aero engines [9, 74, 73]. The technology used to manufacture the piston rings was originally developed to produce sealing elements for the rotary valve engine [212, 74, 73].

The Aspin Engine

An innovative design of rotary valve engine was developed by F. M. Aspin, with reports of the first prototype engine being published in 1937 [147]. It used a rotary valve rotating about an axis perpendicular to the crankshaft axis, as shown in figure

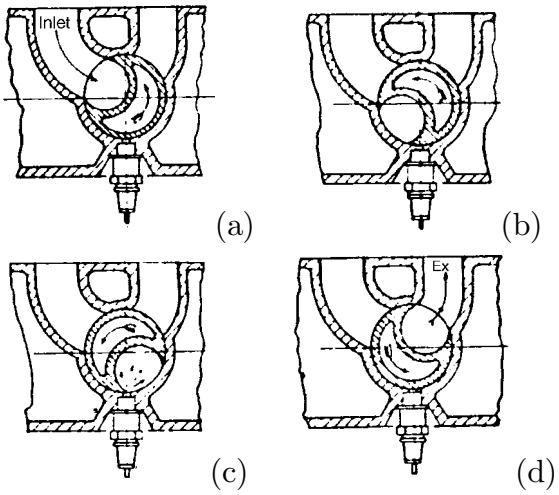

Figure 1.9: Position of the Aspin rotary valve combustion chamber during a four-stroke cycle. Reproduced from Hunter [147]. (a) – intake stroke; (b) – compression stroke; (c) – combustion and expansion stroke; and (d) – exhaust stroke.

1.8. The engine was also known as a "rotary combustion chamber" engine as the rotor included a large proportion of the combustion chamber at TDC, and thus the combustion chamber rotated with the valve.

Early designs of the Aspin Engine had the spark plug mounted along the axis of the rotor, however problems were found in keeping the spark plug cool. A radical solution was eventually adopted for this problem—by putting the spark plug in the head, in such a way that the spark plug was only exposed to the gases near the time of spark ignition, and was otherwise hidden behind the rotor [147]. The concept behind this design is shown for a four stroke cycle by figure 1.9.

The hidden spark plug concept is an interesting fundamental change to internal combustion engine design. The spark plug is often at high temperature, so it can be the cause of pre-ignition. This is similar to the hot exhaust valve causing pre-ignition for poppet valve engines, mentioned in section 1.3. This reduced tendency to pre-ignite also allows the combustion of leaner mixtures, and Aspin reports [147] that his engine runs efficiently and reliably at air-to-fuel ratios of $22:1$, whilst the best poppet valve engines of the day could only run to $16:1$.

The lubrication, sealing and drive systems of the valve also underwent significant development. Early designs had no specific sealing system but used the combustion pressure to press the tapered rotor up into the housing. This was found to cause a large amount of friction, and so was replaced by a system in which the majority of the combustion pressure load was taken by a thrust bearing, with sealing and lubrication being performed by a series of grooves on the periphery of the valve.

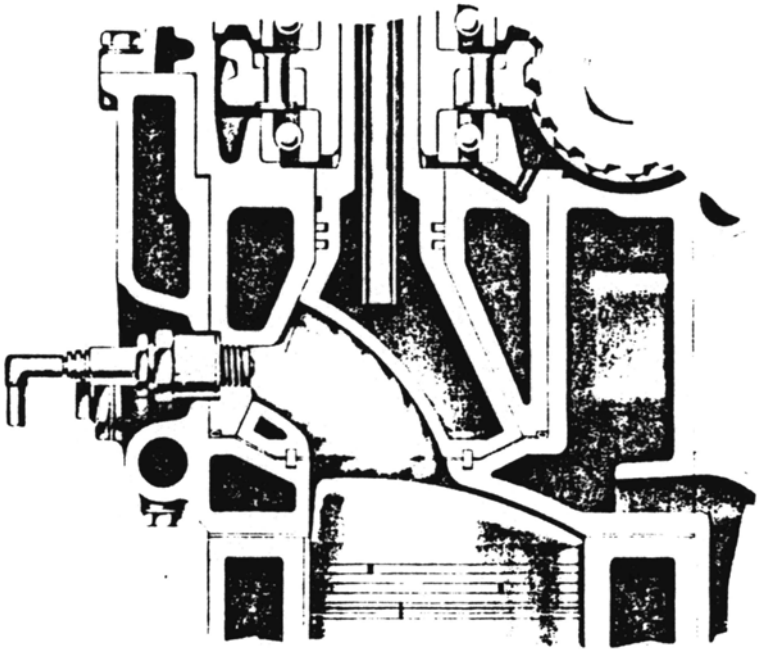

Figure 1.10: The Aspin rotary valve engine from the late 1940s. The sealing elements are visible on either side of the valve/cylinder head interface. Reproduced from Hunter [147].

This system was superseded in the mid 1940s, where sealing elements (effectively modified piston rings) were used, as shown in figure 1.10. The sealing elements are visible on either side of the valve/cylinder head interface.

Hunter [147] suggests that this engine produced impressive performance when compared with traditional poppet valve engines of its day. A US patent was issued for the design in 1946 [26], and a further patent issued many years later in 1977 [27]. However, no references can be found to suggest this engine progressed beyond the development stage. It appears that this design disappeared into the pages of history, as did so many rotary valve engine designs before it.

The Itala Automobiles Rotary Valve Engine

The only rotary valve engine ever to compete on the Grand Prix circuit was designed by the Itala Automobiles company, and it raced during the 1913 season. Details of the engine or the race have been very hard to find, so the following is the author's best assessment from the available evidence as to what transpired.

The 1913 Grand Prix season consisted of five races, with four events being in Europe and one in the USA. Itala entered a team in only one race—the third event

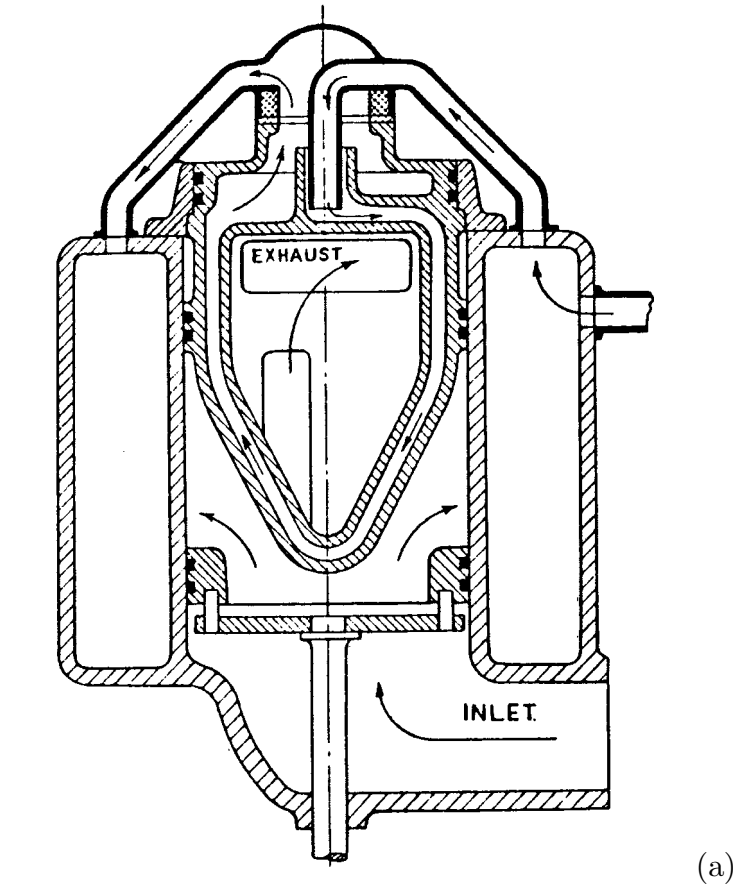

(a)

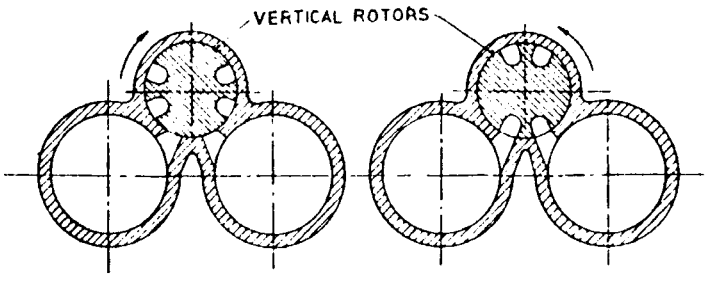

(b)

Figure 1.11: The Itala Rotary valve and engine layout, reproduced from Hunter [147]. (a) – Cross section through the valve, showing coolant flow; and (b) – Layout of engine with one rotor shared between two cylinders.

in the season, the Grand Prix de l'ACF, held in Amiens, France on 12 June 1913. It was a gruelling race of 916 km, and was probably held on public roads as very few dedicated race tracks existed at this time. Two drivers died during the event which indicates the high levels of risk in early automobile racing—one died during pre-race testing and the second died when his Peugeot crashed into a cart [10]. The Grand Prix formula rules for vehicle and engine design at the time were very flexible, as the only regulation enforced on cars was that they had to have a minimum mass of 800 kg, and a maximum fuel consumption of 20 L/100 km.

Itala entered a team of three cars in this race, which Clutton [69] reports used rotary valve engines. Clutton describes the Itala engine design to be a four cylinder engine in an in-line configuration, each cylinder having a bore of 125 mm and a stroke of 170 mm giving a total capacity of 8.3 L. The design philosophy of the engine was that a large, lightly loaded engine was the best approach to the fuel consumption regulation. Accordingly, the engine had a maximum speed of only 1400 rpm, whereas the engines it was competing against ran at up to 3000 rpm.

The valve designed for production car use is described in some detail by Hunter [147], and the current author assumes that the Grand Prix engine used a similar design. Figure 1.11b shows the basic layout of the valve in the engine, in which one valve was used to serve two adjacent cylinders. The axis of rotation of the valve is parallel to the axis of the piston motion. Figure 1.11a shows some of the internal detail of the valve, including elegant internal cooling channels and sealing elements—design features many years ahead of their time.

The car was not very successful, either as a racing car nor commercially as a production car. All three cars entered in the Grand Prix failed to finish, with one car withdrawing on the first lap due to engine failure, and the remaining two cars withdrawing half-way through the race due to suspension failures [10].

Technically the engine appears to have worked well, with power and smoothness as good as, or better than, poppet valve engines of the time. However, Hunter [147] blames the commercial failure of this design on the complex nature of the valve. The design would have been expensive to produce with manufacturing technology of the time due to its complicated internal cooling channels, and its requirement for accurate machining for the outer surfaces of the valve. It would have required highly skilled mechanics to install and maintain the system. This put the design at a considerable commercial disadvantage relative to its competitors, and the rotary valve engine was abandoned by the Itala company a short time later.

The Junkers Rotary Disk Valve Torpedo Engine

An interesting development in the history of rotary valve engines is an engine developed by the German Junkers Company during World War II to propel torpedoes. The engine, model name "JUMO KM8" used a rotary valve system in response to the unusual operating environment found in torpedoes. Hunter [147] reports that the engine was discovered by the Allied forces after the German surrender and a prototype engine was examined by British and American intelligence officers. A description of the engine was also supplied by an engineer who worked on the project.

The engine was developed to achieve the following specifications (amongst others) defined by the German Navy:

1. Engine power greater than 275 hp at 3650 rpm;
2. Minimum weight;
3. Engine had to run entirely autonomously, and quickly reach operating speed when started;
4. The engine was run breathing a mixture of exhaust gas, oxygen and fuel;
5. The operating life of the engine was only a few hours; and
6. Engine was to fit into a torpedo shell, specified at 530 mm internal diameter.

The engine designed by Junkers for these specifications had a capacity of 4.3 L and was supercharged. A disk valve was decided as the best way to reduce engine size to fit into the specified diameter, as the valve system only required a height above the cylinder of 45 mm. These compact dimensions are shown in figure 1.12. The engine was subject to high rates of wear, however, as the engine was designed for an operating life of only a few hours this was acceptable.

Disk valves are not often used in general or automotive applications due to the high wear, high friction and high valve operating temperature inherent in the design.

Post-war Allied testing of the engine design confirmed it reached the design specification, and further testing showed it to be a quite satisfactory engine when run on a more normal air and fuel mix. Whether the Germans used the engine in combat is unclear. Regardless of its promise, no further work on the design was performed.

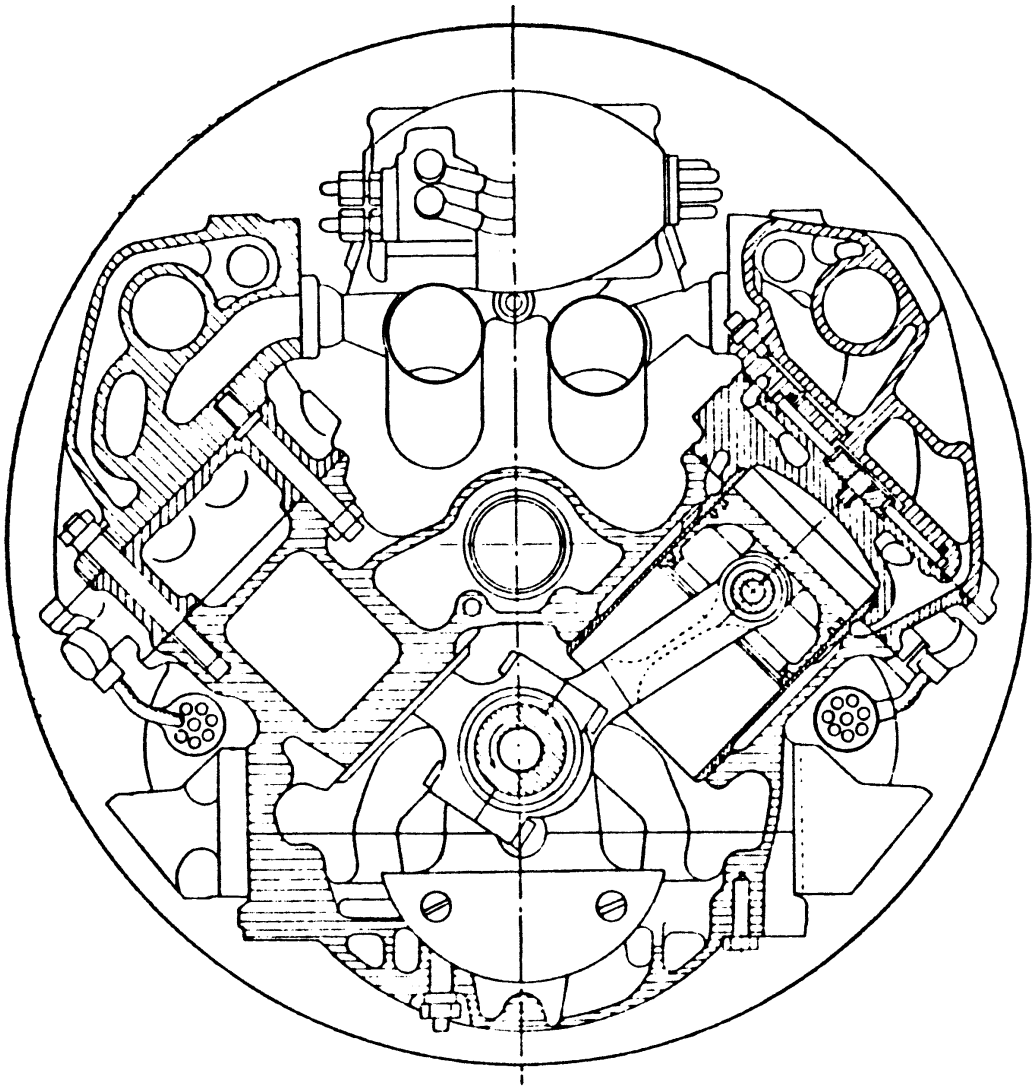

Figure 1.12: Cross section of the Junkers JUMO KM8 disk valve torpedo engine, shown inside the specified torpedo internal diameter. Reproduced from Hunter [147].

1.4.2 Modern Developments in Rotary Valve Engines

Engine research after the 1950s had developed to the point where it required large investments of money and resources to even attempt developing a new engine technology. This has made it very difficult for an inventive individual to perform engine development work. Engine development is now almost entirely done by large commercial organisations.

It is known that some of the modern major engine manufacturers have attempted rotary valve engine projects. Few have released any information publicly, and none has progressed to commercial release. A search of the patent literature on rotary valve engines uncovered a number of patents, for instance a US Patent lodged by Honda in 1983 [25]; a European patent lodged by Lotus in 1989 [180] and a US Patent lodged by Jaguar in 1989 [221] and 1990 [222]. Some papers on rotary valve engine research performed by major automobile manufacturers have also been published, for instance the Honda system is described by Hogan [123], or a system designed with the backing of Mitsubishi by Muroki et al [197].

A number of other companies have taken patents in rotary valve technology, such as two US patents granted to Dana Corporation in 1977 [121, 120], or a US patent granted to Tetrahedron Associates, California in 1975 [306]. Gabelish et al [105] reports on rotary valve engine research by the company G. V. Technology. Many patents on rotary valves have also been issued to individuals, such as Franz [101].

None of the systems mentioned above appear to have significantly progressed rotary valve engine development, and certainly none have progressed to commercial release. Two designs which will be analysed in more detail are firstly the rotary valve Formula One engine developed by MGN in the mid 1980's, and secondly a rotary valve engine project currently being developed by a firm called Coates International. Finally, a few less significant studies will be analysed. This will set the background for the current Bishop Rotary Valve engine development project, of which the current work is a part.

MGN Rotary Valve Engine for Formula One Racing

A recent attempt at the application of rotary valves to Formula One cars was the rotary valve engine manufactured by MGN, developed by the prolific inventor, Guy Negre. It never raced, however it was seriously investigated by a number of Formula One teams and the project progressed far enough for MGN to make a prototype Formula One car [56]. Due to the secrecy surrounding any modern Formula One

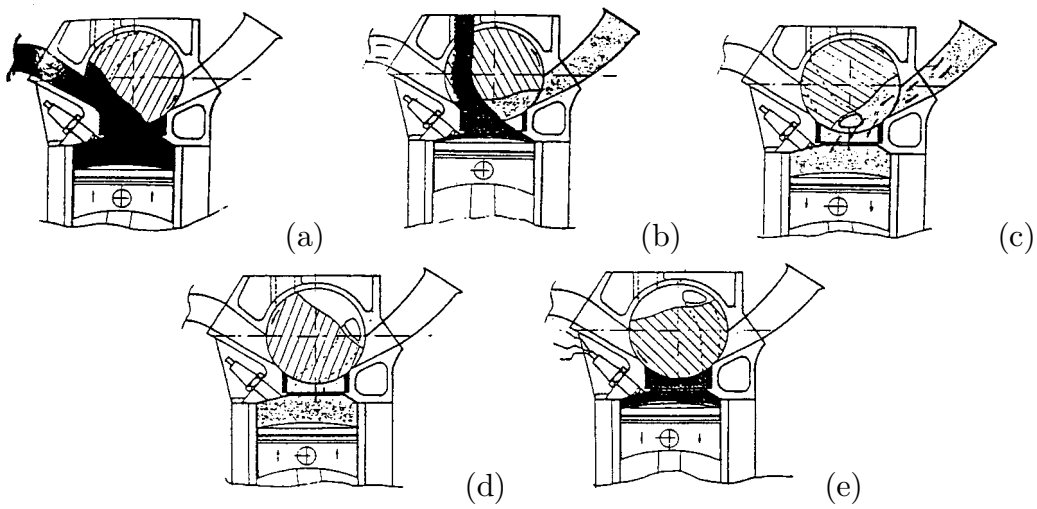

Figure 1.13: Operating principle of the MGN rotary valve engine, from Camus [54]. (a) – Exhaust stroke; (b) – TDC, exhaust continues through a secondary manifold, intake flow is commencing; (c) – Intake stroke; (d) – Compression stroke; and (e) – Combustion.

technical development the details of the engine were never released publicly, however the basic principle of the engine is shown in figure 1.13. The engine used an unusual W12 configuration, and one rotor was used down an entire bank of pistons. Inlet and exhaust valves were performed by notches in the rotor aligning with ports in the head and the combustion chamber.

The manufacturer, of course, claimed that the engine produced superior performance to poppet valve engines [54, 55]. However the engine had three fundamental flaws which the manufacturers were unable to overcome.

The first problem was the lubricating oil consumption of the engine was so high that anecdotal comments suggest that the car released clouds of smoke from burning oil when accelerating out of corners. Lubrication oil consumption of this magnitude is unacceptable in modern engines. This problem is the same as that faced by Cross in the early development of his valve, and whether a similar "scraper" system as was developed by Cross (see figure 1.5) would have been successful here is a matter for speculation.

The second flaw is due to design of the notches in the valve and the shape of the combustion chamber. The valve design allows gas to flow directly from the intake manifold to the exhaust manifold during scavenge, and does not force it to pass through the main area of the cylinder at all. Hence the engine would scavenge exhaust gases from the cylinder poorly. Also, an excessive quantity of intake air/fuel mixture would travel directly from the intake manifold to the exhaust manifold,

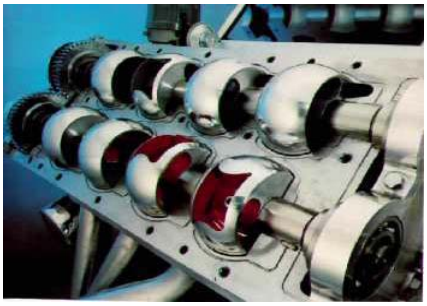

Figure 1.14: The Coates Spherical Rotary Valve engine head, from [1].

bypassing the cylinder entirely. This would increase fuel consumption and reduce trapped charge quality.

The third flaw is a further result of the notches on the valve. A pocket of exhaust gas would be trapped in the notch at the end of the exhaust stroke, and would be transported to the inlet manifold, polluting the incoming charge for the next stroke. This would further reduce intake charge quality.

MGN was obviously aware of these problems as they developed a design in which a secondary exhaust system was used to assist scavenge flow. This system is described in a US patent granted in 1988 [206]. This would have reduced the impact of the second flaw mentioned above. However, as no further development on the racing engine appears to have been made, it seems this project was abandoned and disappeared like so many others.

Coates Rotary Valve Engine

George Coates developed a rotary valve engine and claimed it produced promising results [1, 212]. The engine uses two spherical rotary valves per cylinder, one for exhaust and one for inlet. The spherical shape was chosen as it allows a simple sealing system for the rotors. It appears that the sealing is achieved using ceramic-carbon seals pre-loaded against the valve by a wave spring. The valve is located using a similar bushing material such that it does contact the inside of the cylinder head and does not require a lubricating film. Figure 1.14 shows the cylinder head of the Coates Spherical Rotary Valve engine, showing the valves. This design is explained in the seven patents granted to Coates, with the design shown in figure 1.14 being the most recent embodiment, covered in a 1994 US patent [70].

The 1994 patent [70] shows the port areas available for intake and exhaust flows to have a very small throat area at the entrance to the valve. This is caused by the requirement to fit two separate valve windows per cylinder. This means it is likely

the engine would have "breathing" problems at high engine speeds caused by the small size of the intake and exhaust throats.

Despite this apparent problem with the design, the manufacturer claims an enormous performance increase over a poppet valve engine [1]. They claim that in a comparison with a 5.0 L Ford Lincoln engine, the Ford engine resulted in a steady state flow of $180\,\mathrm{ft}^3\,\mathrm{min}^{-1}$ at 28 inches H_2O test pressure, against a flow of $319\,\mathrm{ft}^3\,\mathrm{min}^{-1}$ at the same conditions for the Coates Spherical Rotary Valve head. When tested on the dynamometer they claim the Ford engine produced 260 hp and 249 ft lb at 5500 rpm. When the Ford engine was subjected to the same test with the cylinder head replaced with the Coates Spherical Rotary Valve system they claim the engine produced 475 hp and 454 ft lb at the same conditions.

The magnitude of the performance increase claimed seems impossible. Production car engines have major performance compromises due to competing requirements for engine longevity, low cost and emissions regulations, but not of the magnitudes claimed here. Additionally, no reputable independent confirmation of these results could be found in the literature. A search of the scholarly journals found no publications from the inventor.

The company's web site makes the claim that the system will shortly go into production [1], and that "by the time you read this, retrofit kits should be available for the popular Ford and Chevy V-8". These quotes were written over two years ago, and there is no sign of this system being sold commercially.

The claims made by this manufacturer must be viewed with scepticism until more reliable evidence is produced. This scepticism appears well justified as the USA Securities and Exchange Commission filed a complaint against the company in April 2000, alleging the company fraudulently raised $6.5million from almost 400 share holders and had, amongst other allegations:

> "misrepresented the capabilities of the Coates engine; omitted to disclose negative results of independent tests on the engine; falsely claimed that [Coates International Limited] had sold licenses and received orders and other commercial opportunities." [7]

Coates is reported to have not admitted or denied the claims, but did submit to a Securities and Exchange Commission demand for a receiver to be appointed.

The USA Securities and Exchange Commission report continues by saying that Coates International have entered into an agreement with a Canadian company specialising in cogeneration engines, that is, engines to provide shaft power and heat

from the exhaust system simultaneously. They plan to have their first cogeneration plant running in April 2000 [7]. No report of this taking place could be found.

Other Less Significant Developments

A recent analysis of rotary valves for internal combustion engines is reported by Storer and Nelson [265]. They used a rotary valve on a G-Kart Racing engine, as it is a small, inexpensive class of racing vehicle ideal for testing new ideas. They performed some elementary computational modelling and a simple analysis of the concept and concluded the rotary valve has the potential to increase volumetric efficiency and reduce friction losses compared to poppet valve engines, and they believed the sealing problems could be overcome. They had not built a prototype engine at the time of publication, and no further publications could be found by the authors regarding rotary valve engines, so it is unlikely the project progressed beyond the concept stage.

A publication describing the design of a rotary valve internal combustion engine was published by Muroki et al [197], as mentioned previously. They did experiments to establish the torque required to drive the valve and performed three-dimensional numerical simulations to establish the flow during the inlet stroke. They calculate that the rotary valve required 40% less torque to drive than a poppet valve, and almost eliminated the periodic nature of the torque over the engine cycle in the poppet valve engine. The intake stroke simulations were not compared with a poppet valve engine, so it is not clear whether their system would have superior aerodynamics to a poppet valve engine. They did not construct a working rotary valve engine, and so could not perform an experimental validation of their results. Again, it is unlikely this project progressed beyond the concept phase.

1.4.3 The Bishop Rotary Valve Engine

The Bishop Rotary Valve (BRV) engine, of which the current work is a part, is an attempt to revive interest in rotary valve engines. The project began with a patent granted to Arthur Bishop in 1989 [42]. The fundamental advance made in this patent was the invention of a rotary valve incorporating both the inlet and exhaust ports in the same valve, and rotating with clearance in its housing. The combustion pressure was sealed using sealing elements around the valve window. However, no seal between the inlet and exhaust ports in the valve was used, instead the small radial clearance between rotor and housing provided an adequate seal due to the small pressure difference. The rotor does not require pre-loading, so friction losses

are substantially reduced over previous rotary valve designs.

Further patents primarily dealing with the valve sealing and lubrication systems have been granted as the project has progressed, including a number of patents covering improved sealing mechanisms by Wallis and Thomas [295] and Wallis [292, 294], and a modified lubrication system designed for the new sealing systems by Wallis [293]. Details of these developments are beyond the scope of the current work, however they have progressed the BRV engine to a stage where the seals, lubrication, heat and friction issues have been adequately dealt with, and the engine is producing some very encouraging results on the dynamometer.

As has been noticed by a number of rotary valve engine designers previously, rotary valve engines should have the greatest advantage over poppet valve engines in high performance engine applications. In high performance engines, complicating issues such as emissions control, manufacturing costs, maintenance costs and engine wear are of less significance. The fundamental issue in deciding whether the design is superior is the engine power produced. Of course, many other factors such as fuel consumption, oil consumption, reliability, weight and size must still be satisfactorily addressed, but the primary parameter to be considered is engine power. The high performance engine community is also more willing to accept new technologies than the normal production car community.

These issues were foreseen early in the BRV engine project, so the engine was initially aimed at the high performance engine market.

Many developments have occurred in the BRV project before and during the course of the current project. Many of these developments are beyond the scope of this work, and most are confidential and so cannot be discussed in this work. However, the BRV engine has developed to a stage where it is very close to being commercialised.

With the BRV engine almost developed to a stage where it is a viable commercial product, a study of the air flows in a rotary valve engine is required. This has not been required up until now as no previous rotary valve engine had overcome fundamental problems with sealing, lubrication, friction or commercialisation. Therefore the current work opens up an exciting new field of engine aerodynamics research.

Conversely, the aerodynamics of traditional poppet valve engines has been extensively studied, this will be discussed in chapter 4. Analysis has matured to a stage where the possible improvements in poppet valve engine performance remaining to be found are small.

This study is an exciting work in a field which has not been previously analysed in any depth. It opens up a fundamentally new field of engine design, by giving

the engine designer freedom not possible in poppet valve engines. It offers an opportunity to find engine performance which surpasses even the best poppet valve engines of our time.

1.5 Outline of The Current Work

The aim of the current work is to analyse the aerodynamics of the BRV engine. This will be performed through the use of computational models of the fluid flows in the engine, using a technique called computational fluid dynamics (CFD). The specific objectives of this work are 1) to develop a numerical model capable of modelling a rotary valve internal combustion engine; 2) to validate the model as being sufficiently accurate to be a design tool; 3) to use the results of the model to provide insight into the aerodynamic processes of the engine; 4) to use the results of the model to analyse phenomena which are not possible or practical to analyse by traditional experimental means; 5) to provide numerical simulation data to complement experimental data to assist engine design; and 6) to perform "computational experiments", in which the performance of proposed engine designs are tested computationally before any experimental work is performed.

In chapter 2 the mathematical models used for this work will be presented. These mathematical models are solved using numerical techniques described in chapter 3.

Chapter 4 will then review the existing literature on computational modelling of engine flows. Chapter 5 will validate the computational model through the use of existing published validations, and a new validation of one-dimensional shock wave flow to validate some aspects of the code relevant to modelling flows in engine manifolds. Chapter 6 performs a detailed validation of the ability of the computational model to predict flows occurring in the intake and compression strokes of a model square piston engine. The work presented in this chapter also uncovers some fundamental behaviour of the flow during the compression stroke.

Chapters 7 and 8 will apply the validated computational model to the BRV engine. Chapter 7 describes some preliminary work, which discovers that the fundamental flow process occurring in the BRV engine has not been previously described, and has been called "dual cross tumble". This chapter shows dual cross tumble has the potential to be superior to the existing engine flow processes. Chapter 8 performs a parametric study of the dual cross tumble flow with a number of engine design variables.

Finally, in chapter 9 the work is summarised and main conclusions reached.

Chapter 2

Mathematical Models

The mathematical model used for simulating the motion of air in the BRV engine in this work is the fully compressible, transient Reynolds Averaged Navier Stokes equations. A commercial computational fluid dynamics (CFD) code, CFX-4.3 supplied by AEA Technologies, was used to perform the simulations; and this mathematical model is included as a standard part of the CFX-4.3 code. Therefore only a brief outline of the mathematical models used will be presented here as the code has already been described in the user manual of the code [13]. Detailed derivations of the Reynolds averaged Navier Stokes equations have also been published extensively, the interested reader is referred to Fletcher [98], Versteeg and Malalasekera [284] or Anderson [154].

The numerical methods used to solve these equations will be discussed in chapter 3, and the accuracy of these models in predicting flows in the BRV engine is assessed in chapter 5.

2.1 Notation

The following notation system will be used in this chapter:

- A scalar quantity will be denoted by italic type, for example pressure, p.
- A vector quantity will be denoted in bold type, for example velocity, $\mathbf{U}$. A vector is made up of scalar components, such as $\mathbf{U} = (\mathrm{h}, v, \mathrm{C}) = \mathrm{h}_i$ where h, v and C are the scalar velocity components of $\mathbf{U}$; or h_i is the tensor notation of $\mathbf{U}$.
- A tensor quantity will be denoted in upper case outline, such as stress tensor, $\mathbb{S}$. In tensor form this is defined as $\mathbb{S} = s_{ij}$.

- A tensor product will be shown as $\mathbf{A} \otimes \mathbf{B}$, and defined as $(\mathbf{A} \otimes \mathbf{B})_{ij} = a_i b_j$.
- The transpose of a rank two tensor $\mathbb{S}$ is shown as $\mathbb{S}^T$. If $\mathbb{S} = s_{ij}$ then $\mathbb{S}^T = s_{ji}$.
- The divergence of a vector is shown as $\nabla \cdot \mathbf{V}$, and is defined as $(\nabla \cdot \mathbf{V}) = \frac{\partial v_i}{\partial x_i}$.
- The divergence of a rank two tensor $\mathbb{S} = s_{ij}$ is shown as $\nabla \cdot \mathbb{S}$, and defined as $(\nabla \cdot \mathbb{S})_i = \frac{\partial s_{ji}}{\partial x_j}$.
- The contraction of the tensor, $\mathbb{S}$, with a vector, $\mathbf{V}$, is shown as $\mathbb{S} \cdot \mathbf{V}$ and defined as $(\mathbb{S} \cdot \mathbf{V})_i = s_{ij} v_j$.

2.2 Conservation Equations

The conservation equations represent the conservation of mass, momentum and energy, and form the basic partial differential equations describing transient compressible fluid flow. An equation of state is required in order to provide a relationship between the fluid properties. A final equation is needed to describe the motion of passive scalars. Passive scalars do not affect the flow field, but can be used to track the motion of the gas through the flow. Passive scalars were used in this work to track the inlet gas/exhaust gas exchange process.

2.2.1 Continuity

Conservation of mass is expressed as

$$\frac{\partial \mathrm{m}}{\partial \mathrm{t}} + \nabla \cdot (\mathrm{m}\mathbf{U}) = 0 \tag{2.1}$$

in which m is the fluid density, t is the simulation time, and $\mathbf{U}$ is the fluid velocity vector.

2.2.2 Momentum

Conservation of momentum is expressed as

$$\frac{\partial \mathrm{m}\mathbf{U}}{\partial \mathrm{t}} + \nabla \cdot (\mathrm{m}\mathbf{U} \otimes \mathbf{U}) = \mathbf{B} + \nabla \cdot \mathbb{T} \tag{2.2}$$

in which $\mathbf{B}$ is the body force per unit volume acting on the fluid. The stress tensor, $\mathbb{T}$, is defined by

$$\mathbb{T} = -p\boldsymbol{\delta} + \left(\zeta - \frac{2}{3}\mu\right) \nabla \cdot \mathbf{U}\boldsymbol{\delta} + \mu \left(\nabla \mathbf{U} + (\nabla \mathbf{U})^T\right), \tag{2.3}$$

where p is the pressure, $\boldsymbol{\delta}$ is the Kronecker delta, ζ is the bulk viscosity and μ is the molecular viscosity.

Equation 2.2 is often referred to as the Navier-Stokes equation.

A number of terms have been left out of this equation, for example terms dealing with variable viscosity and non-Newtonian fluids have been neglected. Flows found in internal combustion engines have moderate to high Reynolds numbers, so are highly turbulent. In highly turbulent flows the effect of molecular viscosity on the stress tensor is small compared to the effect of the turbulent motions [298]. Therefore, even though the molecular viscosity varies over a factor of about four in the range of temperatures typical of an internal combustion engine [148], the variations in laminar viscosity due to temperature have a negligible effect on the resulting flow as the molecular viscosity is very small compared to the effective turbulent viscosity (equation 2.37). Thus for this work it has been assumed that molecular viscosity is constant.

2.2.3 Energy

Conservation of energy is expressed as

$$\frac{\partial \mathrm{nb}}{\partial \mathrm{t}} + \nabla \cdot B\mathrm{hU b}\ ) - \nabla \cdot B9\nabla T) = \frac{\partial p}{\partial \mathrm{t}} \tag{2.4}$$

where b is total enthalpy, given in terms of the static (thermodynamic) enthalpy h by

$$\mathrm{b}\ = h + \frac{1}{2}\mathbf{U}^2, \tag{2.5}$$

and 9 is the thermal conductivity and T is the temperature.

Again, a number of terms have not been included. Specifically, heating due to viscous dissipation has been assumed to be negligible as the heat dissipated from gas motions is negligibly small in engine flows. Thermal conductivity has also been assumed constant. The reason for this is similar to the reason for the assumption of constant molecular viscosity, that is, the turbulent enhancement of heat transfer will far exceed the heat transfer from pure conduction, so variations in the small amount of pure conduction will have an insignificant effect on the total heat transfer.

2.2.4 Equation of State

To close this system of equations, two relations must be introduced. Firstly there is the equation of state, which for a perfect gas is

$$\mathrm{m}= \frac{pW}{\bar{R}T}, \tag{2.6}$$

where $\bar{R}$ is the universal gas constant, $E314510\,\mathrm{J\,m}\mathit{l}^{-1}\,\mathrm{K}^{-1}$ and W is the molecular mass of the gas. For air this is $2E97\,\mathrm{kg\,km}\mathit{l}^{-1}$.

Secondly there is the constitutive equation,

$$h = C_p T \tag{2.7}$$

in which C_p is the constant pressure specific heat of air. C_p is a weak function of temperature, and varies by around 20% over the temperature range found in an internal combustion engine [148]. Modifying the value of C_p was found not to have a significant effect on results, so C_p was assumed constant.

2.2.5 Passive Scalars

A passive scalar equation was used to track the motion of the intake gas/exhaust gas interface. The motion of a scalar, Φ, is given by

$$\frac{\partial \rho \Phi}{\partial t} + \nabla \cdot \rho(\mathbf{U}\Phi - \Gamma \nabla \Phi) = S \tag{2.8}$$

in which Γ is the diffusion coefficient, and S is the source term.

2.3 Turbulence

The nature of fluid turbulence and its modelling is one of the great unsolved problems of modern science. Research in this area is extensive, and only issues relevant to internal combustion engines will be discussed here. The aim of the discussion below is to allow the reader to understand which model was chosen for the current work and the justification for its choice. The reader is referred to Wilcox [298], Rodi [239] or Warsi [296] for a more complete derivation and discussion of turbulence modelling.

The Navier Stokes and energy equations are thought to define fluid flows at all Reynolds numbers. However, at Reynolds numbers encountered in most engineering flows the flow becomes extremely complex and time-dependant. Many authors have presented a description of the physics of turbulence [298, 239, 296], however a summary will now be described.

Turbulence is an essentially random, small scale motion of fluid in both space and time. The motions do show statistical trends, and hence it is important for any fluid simulation to correctly reproduce these trends. A useful definition of turbulence has been stated by Hinze:

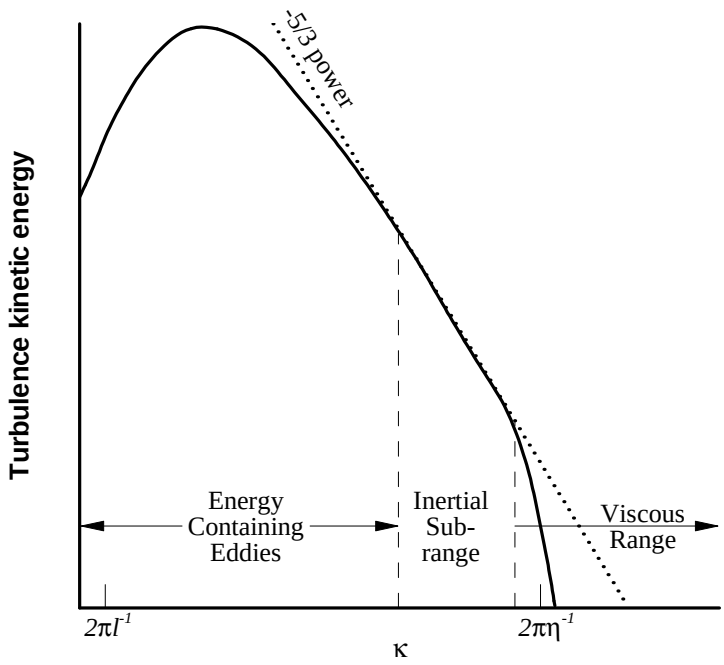

Figure 2.1: Typical energy spectrum for a turbulent flow, shown on log-log scales. Adapted from Wilcox [298].

> "Turbulent fluid motion is an irregular condition of flow in which the various quantities show a random variation with time and space coordinates, so that statistically distinct average values can be discerned." [138]

A useful way to analyse turbulence is to typify the size of a turbulent eddy by the concept of a wave number, κ. This is defined as $\kappa = 2\pi \mathrm{l}\, l_w$, where l_w is the wave length of the eddy. The energy contained in eddies over the range of turbulent length scales for a typical turbulent flow is shown in figure 2.1. The length scale typical of the larger turbulent eddies is often taken as the integral length scale, l. The length scale typical of the smallest eddies is the Kolmogorov length scale, η.

It can be seen that the majority of the energy in the turbulence exists in the larger length scales near the integral length scale. The energy present at the Kolmogorov length scales is substantially smaller. For sizes smaller than the Kolmogorov length scale the energy rapidly decreases due to viscous action.

Between these two regions is a region known as the inertial sub-range, where the energy profile follows the well known $-5\mathrm{l}\,3$ law. This relationship was devel-

oped by Kolmogorov through dimensional analysis, and can be written as $7\ B\kappa) = C_K \epsilon^{2/3} \kappa^{-5/3}$, in which C_K is the Kolmogorov constant and ϵ is the dissipation rate.

One possible method of simulating turbulence is to resolve all fluid motions to the Kolmogorov length scale. This technique is called Direct Numerical Simulation (DNS).

2.3.1 Direct Numerical Simulation

To perform DNS, a numerical system fine and accurate enough to resolve all flow time and length scales must be used. Thus the numerical simulation must be able to accurately resolve structures as small as the Kolmogorov length scale. This method requires no turbulence model as the fluid motion is described by equations 2.1, 2.2, 2.4 and 2.8; and all fluid motions are resolved.

In practice, however this technique is limited to low Reynolds numbers as the Kolmogorov length scale for high Reynolds number flows is very small, typically a fraction of a millimetre. This means huge mesh numbers are required for adequate resolution. DNS also requires the use of accurate but often unstable high order spatial and temporal differencing schemes, which are difficult to apply to complicated geometries.

To date the only applications of DNS has been on very simple geometries, such as simple channel flows at low turbulent Reynolds numbers [161] or jet flows [298]. There have been no documented use of DNS models on internal combustion engine flows. It is unlikely that a DNS model of an engine can be performed until computer technology improves by several orders of magnitude.

To overcome this problem, various turbulence models have been developed to eliminate the requirement to resolve flows at the Kolmogorov length scale. The most widely used method is to average the flow such that the turbulent fluctuations are "averaged out", leaving only an average flow with no turbulent components requiring resolution. One such technique, called Reynolds averaging, will now be discussed.

2.3.2 Reynolds Averaged Equations

The turbulence models used in this work are based on Reynolds averaging [235], where it is assumed that it is possible to split the range of flow time and length scale fluctuations into "averaged" and "instantaneous fluctuation" components. The "averaged" component is what the model will directly simulate. The "instantaneous fluctuation" portion of the flow is assumed to affect the "averaged" portion only

through its effect on the stress tensor and thermal conductivity, and hence its effect can be modelled.

Reynolds averaging defines the average values by integrals or summations. If the instantaneous variable which we wish to average is a function of both space and time, for instance $f(\mathbf{X}, \mathrm{t})$, we have three main forms of Reynolds averaging. These are [298]:

Time averaging is appropriate for stationary turbulence. This is a flow that, on the average, does not vary with time. The time average value, $\overline{f_T}$, is defined as

$$\overline{f_T(\mathbf{X})} = \lim_{T\to\infty} \frac{1}{T} \int_t^{t+T} f(\mathbf{X}, \mathrm{t})\, d\mathrm{t}; \tag{2.9}$$

Spatial averaging is appropriate for homogenous turbulence. This is turbulence that is uniform in all directions. The spatial average value, $\overline{f_V}$, is defined as

$$\overline{f_V(\mathbf{X})} = \lim_{V\to\infty} \frac{1}{\mathrm{p}} \iiint_V f(\mathbf{X}, \mathrm{t})\, d\mathrm{p}\ ; \text{ and} \tag{2.10}$$

Ensemble averaging is appropriate for general turbulence. This occurs when the flow varies in both time and space. As an idealised example, if an experiment is performed N times, with each experiment varying by an infinitesimal perturbation in initial or boundary condition; the ensemble average is defined as the average of N realisations of the flow. If $f_n(\mathbf{X}, \mathrm{t})$ is the value of the variable $f(\mathbf{X}, \mathrm{t})$ in the nth realisation, the ensemble average, $\overline{f_E}$, is defined as

$$\overline{f_E(\mathbf{X}, \mathrm{t})} = \lim_{N\to\infty} \frac{1}{N} \sum_{n=1}^{N} f_n(\mathbf{X}, \mathrm{t})\,. \tag{2.11}$$

Other methods of Reynolds averaging exist, but are not relevant here. The limits expressed in equations 2.9 to 2.11 require infinite time, volume or realisations. This is not possible to perform, so is replaced with

$$\overline{f_T(\mathbf{X}, \mathrm{t})} = \frac{1}{T} \int_{t-\frac{T}{2}}^{t+\frac{T}{2}} f(\mathbf{X}, \mathrm{t})\, d\mathrm{t}; \tag{2.12}$$

$$\overline{f_V(\mathbf{X}, \mathrm{t})} = \frac{1}{\mathrm{p}} \iiint_V f(\mathbf{X}, \mathrm{t})\, d\mathrm{p}\ ; \text{ and} \tag{2.13}$$

$$\overline{f_E(\mathbf{X}, \mathrm{t})} = \frac{1}{N} \sum_{n=1}^{N} f_n(\mathbf{X}, \mathrm{t})\,. \tag{2.14}$$

The modified definition in equation 2.12 approximates the infinite time average of equation 2.9 if T is an averaging time which is long compared to the period of

the turbulent fluctuations, but small compared to the period of the average flow fluctuations. Similarly, the modified definition in equation 2.13 approximates the infinite volume average of equation 2.10 if p is an averaging volume which is large compared to the size of the turbulent fluctuations, but small compared to the size of the average flow fluctuations. Finally, the modified definition in equation 2.14 approximates the infinite time average of equation 2.11 if N is large enough to gain a statistically significant average for the variable.

After the average value has been determined by any of the above methods, the instantaneous variable, $f(\mathbf{x},t)$ can be split into an average value, $\overline{f(\mathbf{x},t)}$, and an instantaneous fluctuation, $f'(\mathbf{x},t)$, by

$$f(\mathbf{x},t) = \overline{f(\mathbf{x},t)} + f'(\mathbf{x},t)\,. \tag{2.15}$$

For compressible flows the Reynolds averaged equations become complex with additional terms appearing due to density fluctuations. Fauve averaging is a modification to Reynolds averaging which uses a density weighting in the averaging process, significantly reducing the complexity of the final equations for compressible flows [298].

Fauve averaging is similar to Reynolds averaging (equation 2.15) in that the instantaneously fluctuating variable, $f(\mathbf{x},t)$, is also split into an average and an instantaneous fluctuation component, namely,

$$f(\mathbf{x},t) = \widetilde{f(\mathbf{x},t)} + f''(\mathbf{x},t) \tag{2.16}$$

and the Fauve averaged quantity is $\widetilde{f(\mathbf{x},t)}$. The wavy overbar, $\widetilde{\ }$, denotes a Fauve averaged quantity, and the variable with a double dash, $f''(\mathbf{x},t)$, is the instantaneous fluctuation after the Fauve averaged component is removed. The following analysis will be based on time averaging, however the choice of averaging technique does not change the following derivation. The "T" subscript indicating time averaging will now be dropped for simplicity.

The Fauve time averaged component, $\widetilde{f(\mathbf{x},t)}$, is defined as

$$\widetilde{f(\mathbf{x},t)} = \frac{1}{T}\int_{t-\frac{T}{2}}^{t+\frac{T}{2}} f(\mathbf{x},t)\;dt. \tag{2.17}$$

The variables to be averaged are defined by the following system,

$$\begin{aligned} \mathbf{U} &= \widetilde{\mathbf{U}} + \mathbf{U}'', \\ \mathrm{m} &= \overline{\mathrm{m}} + \acute{\mathrm{m}}, \\ p &= \overline{p} + p', \\ T &= \widetilde{T} + T'', \\ h &= \widetilde{h} + h'' \text{ and} \\ \Phi &= \widetilde{\Phi} + \Phi''. \end{aligned} \tag{2.18}$$

We can then re-cast the equations describing the fluid motion, equations 2.1, 2.2, 2.4 and 2.8 into Fauve averaged form. This yields, after some simplification;

$$\frac{\partial \overline{\mathrm{m}}}{\partial \mathrm{t}} + \nabla \cdot \left(\overline{\mathrm{m}} \widetilde{\mathbf{U}} \right) = 0, \tag{2.19}$$

$$\frac{\partial \overline{\mathrm{m}} \widetilde{\mathbf{U}}}{\partial \mathrm{t}} + \nabla \cdot \left(\overline{\mathrm{m}} \widetilde{\mathbf{U}} \otimes \widetilde{\mathbf{U}} \right) = \mathbf{B} + \nabla \cdot \left(\mathbb{T}_t - \overline{\mathrm{m}} \overline{\mathbf{U}'' \otimes \mathbf{U}''} \right), \tag{2.20}$$

$$\frac{\partial \overline{\mathrm{m}} \mathrm{b}_{\,t}}{\partial \mathrm{t}} + \nabla \cdot \left(\overline{\mathrm{m}} \widetilde{\mathbf{U}} \mathrm{b}_{\,t} + \overline{\mathrm{m}} \overline{\mathbf{U}'' h''} - 9 \nabla \widetilde{T} \right) = \frac{\partial \overline{p}}{\partial \mathrm{t}}, \text{ and} \tag{2.21}$$

$$\frac{\partial \overline{\mathrm{m}} \widetilde{\Phi}}{\partial \mathrm{t}} + \nabla \cdot \left(\overline{\mathrm{m}} \widetilde{\mathbf{U}} \widetilde{\Phi} + \overline{\mathrm{m}} \overline{\mathbf{U}'' \Phi''} - \Gamma \nabla \widetilde{\Phi} \right) = S; \tag{2.22}$$

in which the stress tensor in a turbulent flow, $\mathbb{T}_t$, is now

$$\mathbb{T}_t = -\overline{p} \boldsymbol{\delta} + \left(\zeta - \frac{2}{3} \mu \right) \nabla \cdot \widetilde{\mathbf{U}} \boldsymbol{\delta} + \mu \left(\nabla \widetilde{\mathbf{U}} + \left(\nabla \widetilde{\mathbf{U}} \right)^T \right), \tag{2.23}$$

and the mean total enthalpy in a turbulent flow, $\mathrm{b}_{\,t}$, is given by

$$\mathrm{b}_{\,t} = \widetilde{h} + \frac{1}{2} \left(\widetilde{\mathbf{U}} \cdot \widetilde{\mathbf{U}} \right) + k. \tag{2.24}$$

Equation 2.24 introduces a new term, k, which is defined as the kinetic energy of the turbulent fluctuations,

$$k = \frac{1}{2} \left(\mathbf{U}'' \cdot \mathbf{U}'' \right). \tag{2.25}$$

The main differences between the non-averaged Navier Stokes equations 2.1, 2.2 and 2.4; and their Fauve averaged counterparts, equations 2.19, 2.20 and 2.21; are the inclusion of the term $\overline{\mathrm{m}} \overline{\mathbf{U}'' \otimes \mathbf{U}''}$ in the momentum equation and the appearance of the term $\overline{\mathrm{m}} \overline{\mathbf{U}'' h''}$ in the energy equation. These terms are known as the Reynolds stress and Reynolds flux respectively. The various turbulences models are variations on techniques for evaluating these terms.

Some additional turbulence terms in the energy equation have been neglected, this is discussed further in the following sections.

2.3.3 Reynolds Stress Models

In Reynolds stress turbulence models (RSM), equations are solved for the individual components of the Reynolds stresses. The model discussed here is closely related to the model proposed by Launder, Reece and Rodi [173].

The momentum transport equation used in this model is

$$\frac{\partial \overline{\rho}\widetilde{\mathbf{U}}}{\partial t} + \nabla \cdot \left(\overline{\rho}\widetilde{\mathbf{U}} \otimes \widetilde{\mathbf{U}}\right) - \nabla \cdot \left(\mu \nabla \widetilde{\mathbf{U}}\right) = -\nabla p_n - \nabla \cdot \left(\overline{\rho}\overline{\mathbf{U}'' \otimes \mathbf{U}''}\right) + \mathbf{B}, \tag{2.26}$$

in which p_n is the modified pressure, which this time is defined as

$$p_n = \overline{p} + \left(\frac{2}{3}\mu - \zeta\right) \nabla \cdot \widetilde{\mathbf{U}} - \overline{\rho}\mathbb{S}, \tag{2.27}$$

in which $\mathbb{S}$ is the pressure-strain correlation, defined in equation 2.30.

The Reynolds stresses, $\overline{\mathbf{U}'' \otimes \mathbf{U}''}$, are assumed to satisfy the following equation

$$\frac{\partial \overline{\rho}\,\overline{\mathbf{U}'' \otimes \mathbf{U}''}}{\partial t} + \nabla \cdot \left(\overline{\rho}\overline{\mathbf{U}'' \otimes \mathbf{U}''} \otimes \widetilde{\mathbf{U}}\right) - \nabla \cdot \left(\overline{\rho}\frac{C_S}{\sigma_{DS}}\frac{k}{\epsilon}\,\overline{\mathbf{U}'' \otimes \mathbf{U}''}\left(\nabla\,\overline{\mathbf{U}'' \otimes \mathbf{U}''}\right)^T\right) = \mathbb{P} + \mathbb{G} + \mathbb{S} - \frac{2}{3}\overline{\rho}\epsilon\mathbf{I}, \tag{2.28}$$

where $\mathbb{P}$ is the shear stress production tensor,

$$\mathbb{P} = -\overline{\rho}\left(\overline{\mathbf{U}'' \otimes \mathbf{U}''}\left(\nabla\widetilde{\mathbf{U}}\right)^T + \left(\nabla\widetilde{\mathbf{U}}\right)\overline{\mathbf{U}'' \otimes \mathbf{U}''}\right); \tag{2.29}$$

and $\mathbb{S}$ is the pressure-strain correlation,

$$\mathbb{S} = \mathbb{S}_1 + \mathbb{S}_2 + \mathbb{S}_3. \tag{2.30}$$

The components which make up $\mathbb{S}$ are

$$\mathbb{S}_1 = -\overline{\rho}C_{1S}\frac{\epsilon}{k}\left(\overline{\mathbf{U}'' \otimes \mathbf{U}''} - \frac{2}{3}k\boldsymbol{\delta}\right), \tag{2.31}$$

$$\mathbb{S}_2 = -C_{2S}\left(\mathbb{P} - \frac{2}{3}P\boldsymbol{\delta}\right) \text{ and} \tag{2.32}$$

$$\mathbb{S}_3 = -C_{3S}\left(\mathbb{G} - \frac{2}{3}G\boldsymbol{\delta}\right). \tag{2.33}$$

The term $\mathbb{G}$ in equations 2.28 and 2.33 is the buoyancy stress production tensor, and G is the buoyancy production of turbulent energy; both of which are assumed to be negligibly small, so $\mathbb{G} = G = 0$. The shear production of turbulent energy, P, is

$$P = -\overline{\rho}\overline{\mathbf{U}'' \otimes \mathbf{U}''} \cdot \nabla\widetilde{\mathbf{U}}. \tag{2.34}$$

Constant	Value
C_1	1.44
C_2	1.92
C_3	0
C_μ	0.09
σ_{DS}	1.0
σ_ϵ	1.375
σ_H	0.9
σ_Φ	0.9
C_{1S}	1.8
C_{2S}	0.6
C_{3S}	0.5
C_1	0.5
C_2	0.3
C_3	0.5
C_S	0.22

Table 2.1: Constants used in the Reynolds Stress turbulence model.

To close these equations, the rate of turbulent dissipation is required. Turbulent dissipation is defined as

$$\epsilon = 5\,\overline{\frac{\partial \mathrm{h}_i''}{\partial x_j}\frac{\partial \mathrm{h}_i''}{\partial x_j}}, \tag{2.35}$$

and its behaviour is assumed to be described by

$$\frac{\partial \overline{\mathrm{n}}\overline{\epsilon}}{\partial \mathrm{t}} + \nabla\cdot\left(\overline{\mathrm{n}}\widetilde{\mathbf{U}}\boldsymbol{\epsilon}\right) - \nabla\cdot\left(\overline{\mathrm{n}}\frac{C_S}{\sigma_\varepsilon}\frac{k}{\epsilon}\,\overline{\mathbf{U}''\otimes\mathbf{U}''}\,\nabla\epsilon\right) = C_1\frac{\epsilon}{k}\,\mathit{BP} + C_3\,\max\mathit{BG},0)) - C_2\overline{\mathrm{n}}\frac{\epsilon^2}{k}. \tag{2.36}$$

Note that k is calculated directly from the Reynolds stresses, using equation 2.25. The constants used in this model are listed in table 2.1.

For the sake of simplicity and to comply with commonly used nomenclature, the Reynolds stresses, $\overline{\mathbf{U}''\otimes\mathbf{U}''}$, will be written in short-hand form in the following chapters. The normal Reynolds stress in the 0 direction will be shown as $\overline{\mathrm{h}\mathrm{h}}$, in the s direction and $\overline{vv}$ and in the Z direction $\overline{\mathrm{C}\mathrm{C}}$. The off diagonal Reynolds stresses will be denoted as $\overline{\mathrm{h}v}$, $\overline{v\mathrm{C}}$ and $\overline{\mathrm{h}\mathrm{C}}$.

It can be seen in equation 2.28, that in attempting to derive an equation to describe the Reynolds stresses, a number of new terms appeared which are not determined. This means that the model is not "closed", meaning all terms are defined and the equations can be solved. This problem of "closure" is in fact general—it is well known [298, 239, 296] that it is not possible to derive an exact expression to describe turbulence. This means that one has to resort to closure

coefficients and approximations, such as those in table 2.1, to close the system of equations and make a solution possible.

The current author used the Reynolds stress turbulence model for simulations of the compression stroke of a model square piston engine in chapter 6. The Reynolds stress turbulence model has only been used by a small number of researchers for engine simulations [176, 175, 302, 92, 184]. The reason for this low usage is due to the high computational cost involved in this model, as in three-dimensions it requires an additional seven equations to be solved. It can also prove numerically unstable in the distorted grids typical of internal combustion engines.

To avoid these problems, most researchers use a simpler turbulence model, known as the k-ϵ turbulence model.

2.3.4 The k-ϵ Turbulence Model

The k-ϵ turbulence model assumes that the Reynolds stresses can be linearly related to the mean velocity gradients in a manner analogous to the relationship between the stress and strain tensors in laminar flow. Similarly, the Reynolds stresses are also assumed to linearly affect the conduction term in the heat equation and scalar equation. This is done by assuming that the turbulence can be characterised by two parameters; k, which represents the kinetic energy of the non-resolved turbulent motions, defined in equation 2.25; and ϵ, which represents the turbulent dissipation rate, defined in equation 2.35.

The turbulence is assumed to increase the fluid viscosity, so the term μ_t is defined as the contribution to the total turbulence from the turbulent motions. It is often called the "eddy viscosity" or "turbulent viscosity". It is defined by

$$\mu_t = C_\mu \overline{\mathrm{m}} \frac{k^2}{\epsilon}, \tag{2.37}$$

where C_μ is an empirical closure coefficient, with the value of C_μ used here shown in table 2.2. The effective viscosity, μ_{eff}, now acting on the fluid is the sum of molecular and turbulent viscosity components,

$$\mu_{\mathit{eff}} = \mu + \mu_t. \tag{2.38}$$

The Fauve averaged continuity (equation 2.19), momentum (equation 2.20), energy (equation 2.21) and scalar transport (equation 2.22) equations are modelled as

$$\frac{\partial \overline{\mathrm{m}}}{\partial \mathrm{t}} + \nabla \cdot \left(\overline{\mathrm{m}} \widetilde{\mathbf{U}} \right) = 0, \tag{2.39}$$

$$\frac{\partial \overline{\rho}\widetilde{\mathbf{U}}}{\partial t} + \nabla \cdot \left(\overline{\rho}\widetilde{\mathbf{U}} \otimes \widetilde{\mathbf{U}}\right) - \nabla \cdot \left(\mu_{eff} \nabla \widetilde{\mathbf{U}}\right) = -\nabla p_m + \nabla \cdot \left(\mu_{eff}\left(\nabla \widetilde{\mathbf{U}} + \left(\nabla \widetilde{\mathbf{U}}\right)^T\right)\right) + \mathbf{B} \text{ and} \tag{2.40}$$

$$\frac{\partial \overline{\rho} b_t}{\partial t} + \nabla \cdot \left(\overline{\rho}\widetilde{\mathbf{U}} b_t - \left(\frac{9}{C_p} + \frac{\mu_t}{\sigma_H}\right) \nabla b_t\right) = \frac{\partial \overline{p}}{\partial t}; \tag{2.41}$$

$$\frac{\partial \overline{\rho}\widetilde{\Phi}}{\partial t} + \nabla \cdot \left(\overline{\rho}\widetilde{\mathbf{U}}\widetilde{\Phi} - \left(\Gamma + \frac{\mu_t}{\sigma_\Phi}\right) \nabla \widetilde{\Phi}\right) = S; \tag{2.42}$$

where p_m is a modified pressure, given by

$$p_m = \overline{p} + \frac{2}{3}\overline{\rho}k + \left(\frac{2}{3}\mu_{eff} - \zeta\right) \nabla \cdot \widetilde{\mathbf{U}}. \tag{2.43}$$

The energy equation now has an additional term, $\frac{\mu_t}{\sigma_H}$. This term is the turbulent thermal diffusivity term, and represents the enhancement of thermal diffusivity due to the turbulent motion. The constant σ_H is the turbulent Prandtl number for enthalpy, and is a further model constant. Similarly the scalar equation also contains an additional term, $\frac{\mu_t}{\sigma_\Phi}$, which represents the enhancement to scalar mixing due to the turbulent motion. The values of σ_H and σ_Φ used here are shown in table 2.2.

Conservation equations for k and ϵ have also been developed, which add two additional partial differential equations to the system of equations. Hence this model is known as a two-equation turbulence model. The turbulent energy, k, and turbulent dissipation, ϵ, are assumed to be described by

$$\frac{\partial \overline{\rho}k}{\partial t} + \nabla \cdot \left(\overline{\rho}\widetilde{\mathbf{U}}k\right) - \nabla \cdot \left(\left(\mu + \frac{\mu_T}{\sigma_k}\right) \nabla k\right) = P + G - \overline{\rho}\varepsilon, \text{ and} \tag{2.44}$$

$$\frac{\partial \overline{\rho}\varepsilon}{\partial t} + \nabla \cdot \left(\overline{\rho}\widetilde{\mathbf{U}}\varepsilon\right) - \nabla \cdot \left(\left(\mu + \frac{\mu_T}{\sigma_\epsilon}\right) \nabla \varepsilon\right) = C_1 \frac{\varepsilon}{k}\left(P + C_3 \max\left(G, 0\right)\right) - C_2 \overline{\rho}\frac{\varepsilon^2}{k}. \tag{2.45}$$

These equations introduce a number of new model constants, σ_k, σ_ϵ, C_1, C_2 and C_3. See table 2.2 for the values used in this work.

Also introduced are a number of extra terms. The turbulent shear production rate, P, is defined by

$$P = \mu_{eff} \nabla \widetilde{\mathbf{U}} \cdot \left(\nabla \widetilde{\mathbf{U}} + \left(\nabla \widetilde{\mathbf{U}}\right)^T\right) - \frac{2}{3} \nabla \cdot \widetilde{\mathbf{U}} \left(\mu_{eff} \nabla \cdot \widetilde{\mathbf{U}} + \overline{\rho}k\right) \tag{2.46}$$

and G is the turbulent production due to body forces, taken as

$$G = G_{buoy} + G_1 + G_2. \tag{2.47}$$

The turbulence production due to buoyancy body forces is represented by G_{buoy}, and is assumed to be negligible in the high Reynolds number flows typical of an IC

Constant	Value
C_1	1.44
C_2	1.92
C_3	0
C_μ	0.09
σ_k	1.0
σ_ϵ	1.217
σ_H	0.9
σ_Φ	0.9

Table 2.2: Constants used in the k-ϵ turbulence model.

engine. The remaining two terms, G_1 and G_2, are the turbulent production terms due to fluid compression, defined as

$$G_1 = -\frac{\mu_T}{\sigma_\rho}\frac{1}{\overline{\rho}^2}\nabla\overline{\rho}\cdot\nabla\overline{p} \text{ and} \tag{2.48}$$

$$G_2 = -\frac{9}{55}\overline{\rho}k\nabla\cdot\widetilde{\mathbf{U}}. \tag{2.49}$$

The values listed in table 2.2 are widely accepted values [13, 298]. The values chosen are based on empirical "tuning" of the constants against experimental data. The flows used to tune these constants are generally simple flows designed to focus on certain aspects of flow behaviour, such as free shear layer or flat plate boundary layer flow.

The k-ϵ turbulence model is by far the most widely used turbulence model for engine flows, and in engineering in general. It has been used by the current author for the majority of the simulations performed in this work.

Many researchers have analysed the accuracy of the k-ϵ turbulence model for engine simulations, and a number of minor modifications have been suggested to improve its accuracy in engine configurations [204, 205, 126, 15, 28]. Most of these modifications are in the closure constants or boundary condition treatment. None of these model variations have been widely used, and the majority of researchers use the unmodified k-ϵ model.

The only variation on the k-ϵ model which has become widely accepted is known as the RNG k-ϵ model, which essentially only varies from the model described above in that it uses a modified ϵ equation and different closure constants. There are a few examples of the use of the RNG k-ϵ model for engine flows [249, 125], however it has not been established that it is more accurate than the k-ϵ model for IC engine flows.

The third and final main approach to modelling turbulent flows is where part of the turbulent energy spectrum is modelled. This approach is called large eddy simulation (LES), and can be considered intermediate between a Reynolds averaged approach and a DNS approach.

2.3.5 Large Eddy Simulation

LES is similar to the Reynolds averaged approach in that the instantaneously fluctuating variable is still decomposed into a component which the simulation directly simulates (or "resolves"), and a turbulent fluctuating component which is only modelled (or "non resolved"). The difference between Reynolds averaging and LES is twofold. Firstly, the split between resolved and non-resolved components occurs in the middle of the turbulent spectrum rather than far above it. This means that the larger scale turbulent motions are resolved, and only the smaller turbulence scales are modelled. It also means that there is no requirement for a clear separation between turbulence length or time scales. Secondly, the mean component is determined using a filtering function rather than an averaging function.

The aim of this type of model is to directly simulate the larger turbulent eddies as they have a complex interaction with the bulk flow. The small scale eddies are still modelled, but as they have a much simpler interaction with the resolved flow a simple model can be used to describe their effects. This simplicity is due firstly to the smaller eddies only contributing a small amount to the Reynolds stress, so errors in predicting their effects on the Reynolds stress are less significant than those of the larger eddies; and secondly, the smaller eddies are nearly isotropic, making them far easier to model than the anisotropic larger eddies. Ideally the split should be made in the inertial sub-range of the turbulence spectrum (see figure 2.1).

The derivation of the filtered Navier Stokes equations for LES is similar to that of the Reynolds averaged equations, but the different properties of a filtering function compared to an averaging function means that it exhibits a number of unique properties. Many different filtering functions have been proposed, including simple volume averaged box filters, Fourier cutoff filters and Gaussian filters. The details of these filters and the derivation of the LES equations is beyond the scope of this work, the reader is referred to Wilcox [298] or Haworth [128] for further details.

Some other important properties of LES models are:

- A LES model will converge to an exact solution of the unfiltered Navier Stokes equations as the mesh size and time step is decreased. This is a fundamental

difference to the Reynolds averaged simulation, which will converge to an exact solution of the averaged Navier Stokes equations [128];

- LES still suffers from the closure problem, however fewer closure constants and other empiricisms are required in LES than in Reynolds averaged simulations [298];
- LES requires a finer grid than Reynolds averaged based simulations, however not as fine as is required in DNS. Computing power has recently developed to a level sufficient to allow simple LES simulations of engine flows [128]; and
- Reynolds averaged simulations only require the averaged flow conditions and turbulence parameters to be specified initially and at the boundaries. These parameters are easily measured experimentally. LES requires a representation of the initial flow and a time accurate history of the flow from the boundaries. This is difficult to measure experimentally.

These points mean that LES shows promise to provide superior accuracy compared to Reynolds averaged simulations, however there are a number of problems that must be overcome before it can be performed accurately. Due to these difficulties, LES has only recently been applied to engine turbulence modelling, and will be discussed in chapter 4.5.4. A preliminary study of a simple LES model is presented in the current work applied to the model square piston engine in chapter 6.

This chapter has described the equations used to describe the flow of fluid in an engine. As the flow of air in an engine is turbulent, three main methods of modelling the turbulence have been described. In summary, these are:

1. The Reynolds Stress turbulence model (RSM), where equations are solved for each of the six components of the turbulent Reynolds stress tensor directly, and an additional equation for dissipation;
2. The k-ϵ turbulence model where the turbulence is assumed to cause an increase in the viscosity and conductivity of the fluid. This model is considerably simpler than the RSM model and only uses two equations; and
3. Large Eddy Simulation (LES), where the larger turbulent eddies are directly simulated, and only the smaller eddies (which have a simpler relationship to the mean flow) and modelled.

Analytical solutions exist only for the most simple of flows, so to obtain a solution to these equations when describing a complicated flow such as in an engine, numerical methods must be used. The numerical methods used in this work are described in chapter 3.

Chapter 3

Numerical Methods

The mathematical models discussed in chapter 2 define the general equations for which we wish to find a solution. In general it is not possible to derive analytical solutions to these equations, so other methods must be found. Numerical methods are generally used in these circumstances. The fundamental numerical method used in this work is:

- The geometry is discretised into many small volumes (the "mesh" or "grid");
- The conservation equations are integrated over the discretised volumes;
- The modified conservation equations are approximated by finite difference equations; and
- The finite difference equations are solved using an iterative solver.

As the CFX-4.3 commercial CFD code was used to simulate the fluid flows, only a brief outline of the numerical models used will be presented here, adapted from the user manual of the code [13]. For a more complete derivation of these equations the reader is referred to Versteeg and Malalasekera [284], Ferziger and Perić [96], Patankar [224] or Fletcher [98, 99].

This chapter also describes the method used to create the numerical model of the BRV engine. As part of the development of this model, a new sliding boundary condition was developed by the current author to allow the motion of the valve to be simulated. To the current author's knowledge, this is the first time this type of boundary condition has been implemented on the CFX-4.3 code.

The method used to process the geometry for the simulation is also described.

3.1 SIMPLEC Algorithm

The fundamental solution procedure is the SIMPLEC algorithm. SIMPLEC is a close derivative of the SIMPLE algorithm of Patankar and Spalding [225]. SIMPLEC is a method of iterating towards a solution of the Navier Stokes equations by solving for the three velocity components sequentially, then the pressure (as a pressure correction), then the enthalpy, turbulence and scalar equations. This results in less computer memory usage than if the entire solution was achieved simultaneously. Further details on the SIMPLEC algorithm can be found in the CFX user manual [13], or the many published works in this area [96, 270, 284, 98, 99].

Body fitted coordinates are used to allow the geometry to model complex three-dimensional shapes. Applying the "staggered grid" implementation suggested by Patankar and Spalding [225] is difficult in body fitted coordinates, so cell-centred variable storage is used. To overcome the spatial pressure oscillations that can occur with cell-centred variables, the interpolation scheme of Rhie and Chow was used [13].

To allow meshing of complicated geometries a multi-block structured grid was used. This allows the geometry to be split into a number of simpler sub-domains with "inter-block" boundaries between the sub-domains. Inter-block boundary conditions are boundary conditions applied between the sub-domains to allow transfer of flow information between the blocks, thus allowing the blocks to behave if they were joined. Again, further details can be found in the CFX user manual [13], or the many published works in this area [96, 270, 284, 98, 99].

3.1.1 Body Fitted Coordinates

To allow the grid to model complicated geometries a body fitted coordinate transformation is applied. This transformation generates two coordinate systems, being computational space and physical space. Computational space is rectilinear, with all node spacings being unity. Physical space is the computational space grid transformed to fit the physical geometry of the model, with a non-orthogonal grid and arbitrary node spacing. The equations describing the flow are discretised in computational space, and are modified to take into account the effect of the computational space to physical space coordinates. This transformation is shown conceptually in figure 3.1.

A ring of "dummy nodes" are added around the block in computational space, as shown in figure 3.1. These extra nodes are used to transfer data between blocks at inter-block boundaries. Details of the body fitted coordinates transformation are

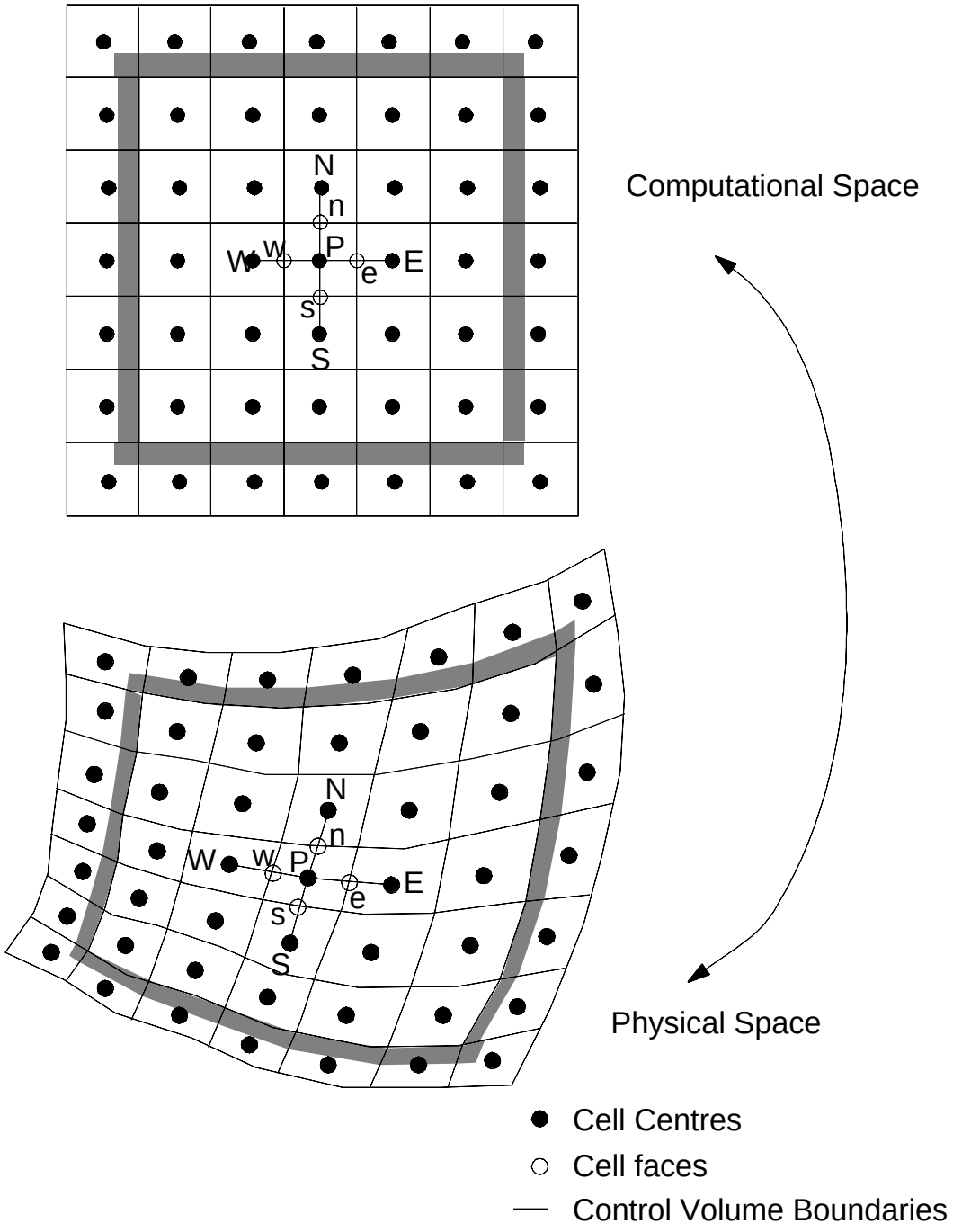

Figure 3.1: Grid structure in computational space and physical space, reproduced from [3].

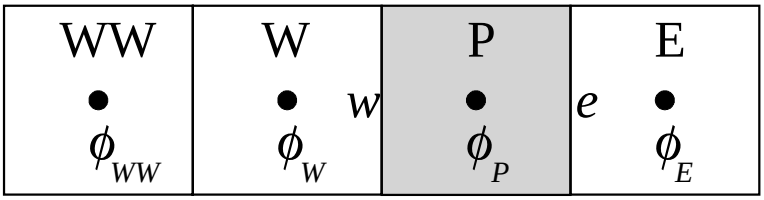

Figure 3.2: Control volume notation.

described in the CFX user manual [13].

Sections of the geometry, such as the piston and valves, move as the engine operates. The grid must then be capable of motion to model this behaviour. To allow for moving grids, equations 2.1, 2.2 and 2.4 are modified to account for this movement. This modification is also described in the CFX user manual [13].

3.2 Discretisation

As the code is a finite-volume code, both spatial and temporal discretisation is required. Equations 2.2, 2.4 and 2.8 are modified to the general form

$$\frac{\partial \overline{\rho}\phi}{\partial t} + \nabla \cdot \left(\overline{\rho}\widetilde{\mathbf{U}}\phi - \Gamma \nabla \phi \right) = S; \tag{3.1}$$

in which ϕ is the variable to be solved for, and can be either a velocity component, pressure, enthalpy, a turbulence parameter or a scalar quantity. In the SIMPLEC algorithm the pressure equation requires special treatment; refer to the many works on this area for details [13, 96, 270, 284, 98, 99].

Equation 3.1 can be integrated over the control volume to give

$$\int \frac{\partial \overline{\rho}\phi}{\partial t}\, dV + \int \overline{\rho}\phi\widetilde{\mathbf{U}} \cdot \mathbf{n}\, dA - \int \Gamma \nabla \phi \cdot \mathbf{n}\, dA = \int S\, dV, \tag{3.2}$$

in which $\mathbf{n}$ is the face unit vector, V is the cell volume and A is the cell face area.

Discretisation is performed in computational space. Consider the control volume shown in figure 3.2. Only a one-dimensional arrangement of cells will be considered here, the extension into two- and three-dimensions is similar.

The variable being considered is ϕ. The value of ϕ which exists in the mesh cell, P, is denoted by ϕ_P. The cell to its right (or "East") will be cell E, and the value of ϕ in this cell is ϕ_E. Similarly, the cell to the left ("West") is cell W, and it has a

value of ϕ_W. There is also a second cell, two nodes to the left side, called cell WW, with a value of ϕ_{WW} existing there.

The cell P has two faces, w ("west") and e ("east"). These faces are shared with neighbouring nodes.

Equation 3.2 gives the four terms we need to discretise, that is:

- $\int \frac{\partial \overline{\rho}\phi}{\partial t}\, dV$, or the temporal term;
- $\int \overline{\rho}\phi\widetilde{\mathbf{U}} \cdot \mathbf{n}\, dA$, or the advection term;
- $\int \Gamma \nabla\phi \cdot \mathbf{n}\, dA$, or the diffusion term; and
- $\int S\, dV$, or the source term.

Each of these terms have different properties and are handled differently. The various methods used in this work will now be discussed, using the w face of the P cell in figure 3.2 as an example.

3.2.1 Temporal Terms

Two temporal discretisation schemes were used in this work, first-order backward difference and second-order backward difference.

First-Order Backward Difference

The temporal term of equation 3.2 can be written as

$$\frac{\partial \phi}{\partial t} = F(\phi), \tag{3.3}$$

which is discretised as

$$\frac{\phi^n - \phi^{n-1}}{\Delta t} = F(\phi^n), \tag{3.4}$$

where ϕ^n is the value of the variable at the nth time step, ϕ^{n-1} is the value of the variable one time step earlier, and Δt is the time step. This technique is first order accurate in time.

Second-Order Backward Difference

In this case, the temporal term of equation 3.2 is discretised as

$$\frac{2\Delta t + \Delta t_0}{\Delta t\,(\Delta t + \Delta t_0)}\phi^n - \frac{\Delta t + \Delta t_0}{\Delta t \Delta t_0}\phi^{n-1} + \frac{\Delta t}{\Delta t_0\,(\Delta t + \Delta t_0)}\phi^{n-2} = F(\phi^n), \tag{3.5}$$

in which Δt_0 is the time difference on the previous time step. More memory is required when using this technique compared to first-order temporal differencing, as the variable needs to be stored at an extra time step.

3.2.2 Diffusion Terms

The diffusion term in equation 3.2 at the west face of the control volume is treated as

$$\begin{aligned} \int \Gamma \nabla \phi \cdot \mathbf{n}\, dA &= \frac{\Gamma A_w}{h_w} \left(\phi_P - \phi_W\right) \\ &= D_W \left(\phi_P - \phi_W\right), \end{aligned} \tag{3.6}$$

where A_w is the area of the west face, h_w is the distance between the west and central nodes (nodes W and P) and D_W is the west diffusion coefficient, defined as $D_W = \frac{\Gamma A_w}{h_w}$. The east face is treated similarly. Thus all diffusion terms are discretised as second-order accurate centred differences.

3.2.3 Advection Terms

The treatment of the advection terms is more complicated, and a number of different schemes were used. The advection term from equation 3.2 at the west face of the control volume is re-cast as

$$\begin{aligned} \int \overline{\rho} \phi \widetilde{\mathbf{U}} \cdot \mathbf{n}\, dA &= \overline{\rho} \mathbf{U}_w A_w \phi_W \\ &= C_W \phi_W \end{aligned} \tag{3.7}$$

where C_W is the convection coefficient at the west face, defined as $C_W = \overline{\rho} \mathbf{U}_w A_w$. A similar treatment is applied to the east face.

Central Differencing (CDS)

This is analogous to the central differencing used for the diffusion terms in section 3.2.2. The value of ϕ assumed to exist at the w face is the average of the cells P and W, that is

$$\phi_w = \frac{1}{2} \left(\phi_W + \phi_P\right). \tag{3.8}$$

It is second order accurate.

Upwind Differencing (UDS)

The Upwind differencing scheme assumes the value of the advected variable at the w face is that of the W cell, that is, ϕ_W. Using the standard terminology for the matrix coefficients [13, 96, 270, 284, 98, 99], it is defined as

$$A_W = \max\left(C_W, 0\right) + D_W, \tag{3.9}$$

and is first order accurate.

Hybrid Differencing (HDS)

This is a modification to the upwind differencing scheme which uses central differences if the mesh Peclet number (see equation 3.21) is less than 2, and upwinding (but ignoring diffusion) if greater than 2. It is defined as

$$A_W = \max\left(\frac{1}{2}C_W, D_W\right) + \frac{1}{2}C_W, \tag{3.10}$$

and is generally first order accurate, but can become second order accurate in areas of low flow or across the flow where the central differencing scheme is used.

Higher-Order Upwind Differencing (HUW)

This is an upwinding scheme made second order accurate by extrapolating to the face from two upwind points, as

$$\phi_w = \frac{3}{2}\phi_W - \frac{1}{2}\phi_{WW}, \tag{3.11}$$

where ϕ_{WW} is the variable at the cell centre two nodes upwind. If this scheme was implemented as equation 3.11, it would increase the bandwidth of the resulting matrix, so equation 3.11 is re-cast as

$$\phi_w = \phi_W + \frac{1}{2}\left(\phi_W - \phi_{WW}\right) \tag{3.12}$$

where the second term is included in the source term to maintain the matrix structure. At the east face

$$\phi_e = \frac{3}{2}\phi_P - \frac{1}{2}\phi_W, \tag{3.13}$$

which will not expand the matrix, so requires no modification. This results in the advection term being

$$A_W = \max\left(C_W, 0\right) + \frac{1}{2}\max\left(C_E, 0\right) + D_W. \tag{3.14}$$

Van Leer (TVD)

The Van Leer differencing scheme is one of a family of schemes developed for high Mach number flows. It is useful in flows with shocks and steep gradients as it is a second-order accurate method, but it has a flux limiter to ensure the solution retains boundedness. This family of schemes is sometimes referred to as Total Variation Diminishing (TVD) schemes. The TVD schemes are based on the higher order upwind (HUW) scheme with a modification of the ϕ_w term. The advection term

(equation 3.14) remains the same. In the Van Leer scheme, the value of the variable at the cell face is defined as

$$\phi_w = \left(1 + \frac{1}{2}\psi\right)\phi_W - \frac{1}{2}\psi\phi_{WW}, \tag{3.15}$$

where

$$\psi = \frac{r + |r|}{1 + |r|} \tag{3.16}$$

is the flux limiter, and r is the ratio

$$r = \frac{\phi_P - \phi_W}{\phi_W - \phi_{WW}}. \tag{3.17}$$

3.2.4 Source Terms

Source terms are written as

$$\int S\, dV = SU + SP\,\phi_P \tag{3.18}$$

where SP is negative. The SP term them enhances the diagonal dominance of the matrix which improves convergence.

3.2.5 Numerical Considerations

The equations describing fluid flow are complex non-linear partial differential equations, so the numerical solution of these equations not trivial. There are many issues that need consideration in obtaining an accurate numerical solution, these have already been discussed in a number of other works [98, 99, 237, 270]. However two issues of particular relevance to the current work will be discussed, being artificial dissipation and spurious "wiggles".

Artificial Dissipation

Discretisation schemes with an upwind bias (for example the UDS, HUW and TVD schemes, and HDS when it reverts to upwinding) exhibit some numerical diffusion, or artificial viscosity. Roache [237] shows that a one-dimensional, incompressible differencing model which uses the upwind first order scheme in time and space can be shown to be equivalent to

$$\frac{\partial\phi}{\partial t} = -\frac{\partial\,(u\phi)}{\partial x} + \alpha_e\frac{\partial^2\phi}{\partial x^2} + HOT, \tag{3.19}$$

in which HOT are the higher order terms to be neglected. The method has introduced a non-physical coefficient α_e of $\frac{\partial^2 \phi}{\partial x^2}$, which is shown to be given by

$$\alpha_e = \frac{1}{2} u \, \Delta x \, (1 - c) \,, \tag{3.20}$$

in which Δx is the grid spacing and c is the Courant number, $c = \frac{u \, \Delta t}{\Delta x}$. The scheme is only stable for $c \leq 1$. When $c < 1$, then α_e is non-zero and artificial dissipation occurs, that is, dissipation caused by the numerical solution technique rather than dissipation that exists in the actual system being modelled. As this dissipation has a similar effect to an increase in viscosity, it is also known as artificial viscosity.

The higher order schemes (HUW, TVD) also display artificial dissipation, but the effect is reduced as it occurs in terms of higher order than the first order upwinding scheme.

Artificial dissipation has a number of effects. As suggested by the name artificial viscosity, it can increase the viscosity of the fluid being modelled. If a solution of a system at a given Reynolds number is performed, the resulting numerical solution will be for a Reynolds number less than desired, as the artificial viscosity has, in effect, increased the fluid viscosity.

A second and related effect is that it tends to smooth the solution. This is apparent when attempting to resolve steep gradients such as shock waves, where the steep gradient is "smeared". This effect is discussed more in the shock tube validation case in section 5.2. The smoothing effect can also eliminate flow details such as small vortices or separations.

These effects make UDS unsuitable for modelling the flows presented in this work. The higher order schemes, HUW and TVD still have artificial dissipation, but its effect is reduced. Hence the HUW and TVD schemes are suitable, however a small amount of artificial dissipation is still occurring.

"Wiggles"

Discretisation schemes that are symmetrical about the cell (CDS and HDS when it is reverts to central differencing) are prone to creating spurious "wiggles" in the solution. It can be shown [237, 96, 270, 284, 98, 99] that the CDS is stable and accurate only if $Pe < 2$, where Pe is the cell Peclet number, defined as

$$Pe = \frac{C}{D} \tag{3.21}$$

in which C is the convection coefficient and D is the diffusion coefficient. If CDS is used and $Pe > 2$, the solution can still converge, but will converge to a spurious solution with "wiggles". This effect is demonstrated in section 5.2.

Due to the high velocities in engine simulations, satisfying the $Pe < 2$ criterion would require an excessively fine grid. This means CDS is not appropriate for engine modelling, and so has not been used in this work.

The HDS avoids the problem of wiggles by using central differencing when it will give a good solution, and reverting to upwind differencing when the scheme is prone to generating wiggles. However, as discussed in the previous section, first order upwind differencing is not suitable due to its artificial dissipation, so the HDS is also unsuitable for use in IC engine modelling.

3.2.6 Application to the SIMPLEC Algorithm

As the discretisation scheme has now been described, the SIMPLEC algorithm can be described in more detail. Figure 3.3 shows the structure of the solution procedure with regard to advancing the solution through time. SIMPLEC is one of the blocks in this procedure.

Figure 3.4 shows the structure of the SIMPLEC algorithm, to obtain coupled solutions of the fluid variables. It is well known [96, 98, 99, 237, 270, 284] that the SIMPLEC algorithm is numerically unstable if the new values of velocity, pressure and other variables found during one iteration are used directly for the next iteration. To control this instability, "under-relaxation" is used, where only a fraction of the difference between variable on the current iteration and the last iteration is used. Under-relaxation is a number between zero and one, with one being no under-relaxation and zero meaning that variable never updates.

The under-relaxation must be "tuned" to an appropriate value, as too high a value means that the solver can be unstable, give non-physical solutions or diverge; and too low a value will slow the solver and increases computational time. Optimum values for under-relaxation vary between solutions, and are difficult to determine precisely. It is up to the user to determine an appropriate level of under-relaxation for each equation. Fortunately the SIMPLEC algorithm is not very sensitive to the exact value of under-relaxation used [99, 270, 284], so approximate values are usually adequate.

Inside the SIMPLEC algorithm, there is a requirement to solve a velocity component in each dimension, and a pressure correction, enthalpy, turbulence and scalar equation. This is performed by the linear solvers, and a generalised block diagram of their structure is shown in figure 3.5. The user has three main parameters to set here, being the minimum ($i_{\min}$) and maximum ($i_{\max}$) number of iterations to perform, and the desired accuracy required or reduction factor (RFC). Again these

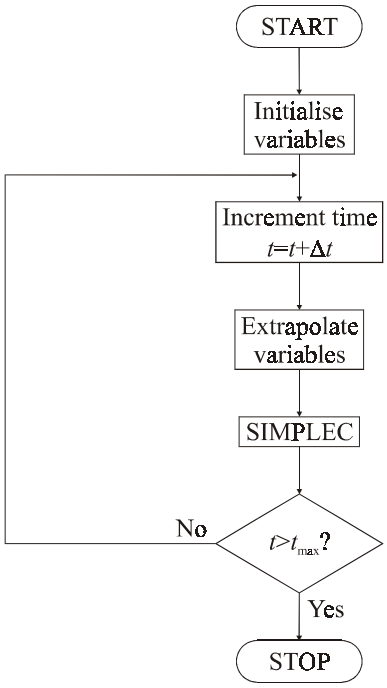

Figure 3.3: Block diagram of the time stepping loop of the CFX code. The process inside the "SIMPLEC" block is shown in figure 3.4.

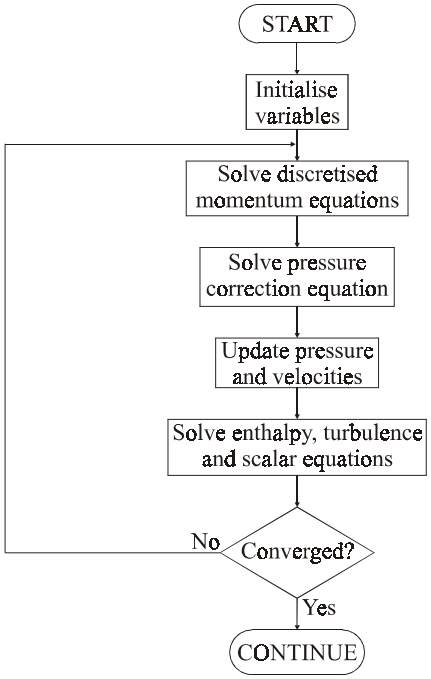

Figure 3.4: Block diagram of the SIMPLEC algorithm. The process inside each "solve" block is detailed in figure 3.5.

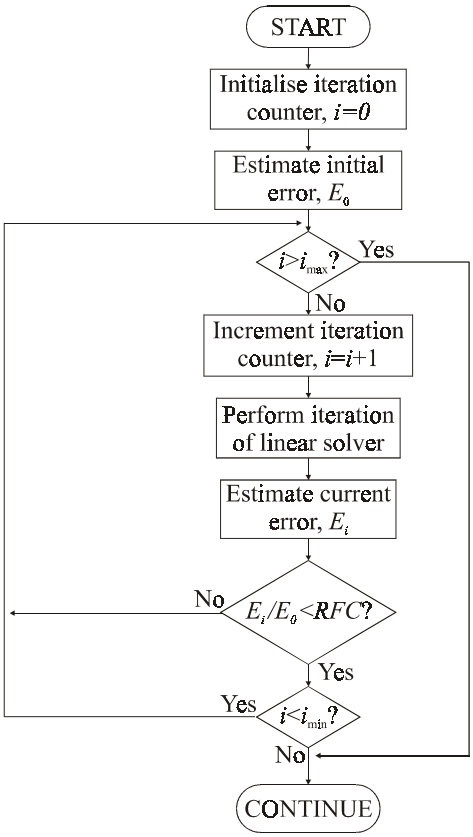

Figure 3.5: Block diagram of a linear solver. The parameters $i_{\max}$, $i_{\min}$ and the reduction factor (RFC) are set by the user.

parameters are to be determined by the user, and appropriate values depend on many factors.

The CFX code includes many different linear solvers for the user to select between, including two varieties of Stone solver [262] and two varieties of algebraic multi-grid solvers [183]. These solvers are described in the CFX manual [13] and will not be repeated here.

3.3 Boundary Conditions

Two forms of boundary condition are used in this work, being wall boundary conditions and pressure boundary conditions. Wall boundary conditions occur at any surface. Pressure boundary conditions allow gas to enter or leave the domain, and are used to simulate a region open to the atmosphere.

3.3.1 Wall Boundary Conditions

The generalised boundary conditions used for the walls of a domain can be written as

$$A\widetilde{\mathbf{U}} + B\widetilde{\boldsymbol{\tau}} = C, \tag{3.22}$$

in which $\widetilde{\mathbf{U}}$ is the fluid velocity at the wall, $\widetilde{\boldsymbol{\tau}}$ is the wall shear stress and A, B and C are constants. For a no-slip, stationary wall, $A = 1$, $B = 0$ and $C = 0$ are used. For moving walls the effect of wall motion can be included by setting $A = 1$, $B = 0$ and $C = \mathbf{U}_w$ where $\mathbf{U}_w$ is the tangential wall velocity. The constant B is used to specify wall shear stress and was not used explicitly in this work, however it is used to implement the wall functions caused by the turbulence model.

To assist in analysis of turbulent boundary layer flow, some non-dimensional numbers will be defined. If we define a parameter τ_k, known as the turbulent wall shear stress, as

$$\tau_k = \sqrt{C_\mu}\overline{\rho}k, \tag{3.23}$$

this may be used to define dimensionless variables

$$u^+ = \frac{\sqrt{\overline{\rho}\tau_k}}{\tau}\widetilde{\mathbf{U}_t} \tag{3.24}$$

which represents the non-dimensional velocity tangential to the wall, where $\widetilde{\mathbf{U}_t}$ is the dimensional tangential component of the velocity; and

$$y^+ = \frac{\overline{\rho}\tau_k^{1/2}}{\mu}y \tag{3.25}$$

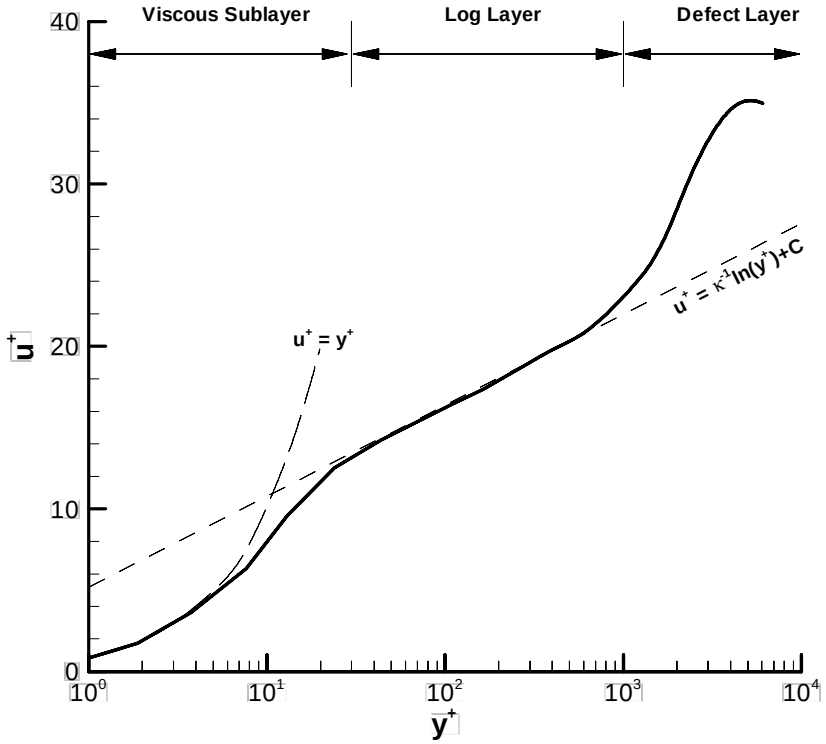

Figure 3.6: Typical velocity profile for a turbulent boundary layer, adapted from Wilcox [298].

which represents the non-dimensional distance normal from the wall, where y is the dimensional distance from the wall.

Figure 3.6 shows a typical profile for a turbulent boundary layer. This profile is found in simple boundary layer flows, such as flow over a flat plate. The viscous sublayer is the layer closest to the wall and in this region $u^+ \approx y^+$. Beyond this is the log layer, so called because u^+ and y^+ can be approximately related by the logarithmic function, $u^+ = \frac{1}{\kappa} \ln y^+ + C$, in which κ is the Kármán constant and C is an integration constant. The extreme section of the boundary layer is the defect layer where the boundary layer flow interacts with the rest of the flow and no simple relationships exist.

This profile will not exist if recirculations, transient effects, adverse pressure gradients or other complicating issues are present.

The regions near the walls of a turbulent numerical simulation require special attention, since near the wall steep gradients of fluid variables occur and this would

require a prohibitively fine mesh to resolve. A second and more fundamental problem is that the equations derived in section 2.3.3 and 2.3.4 do not hold in the viscous sublayer immediately adjacent the wall, as in this region viscous effects dominate over turbulent effects.

To overcome these problems "wall functions" are used so that the effect of the wall boundary layer is implemented on the node adjacent to the boundary rather than allowing the turbulent equations to be integrated right to the boundary. This allows the first node of the simulation to be placed in the log layer section of the boundary layer, which simultaneously addresses both problems mentioned in the previous paragraph—it dramatically reduces the mesh density required, and it places the first node in a region where the turbulence equations are valid. Further details on turbulent boundary layers and its modelling can be found in Wilcox [298] or Rodi [239].

The wall functions will now be described, which will require a modification to the wall boundary condition, equation 3.22. The non-dimensional velocity parallel to the wall is assumed to be a function of its non-dimensional distance from the wall in the near wall region, that is

$$u^+ = \left\{ \begin{array}{cc} y^+ & \text{for } y^+ < y_0^+ \\ \frac{1}{\kappa}\log\left(Ey^+\right) & \text{for } y^+ > y_0^+ \end{array} \right\} \tag{3.26}$$

where the cross over point, y_0^+, denotes the transition from the viscous sub layer to the log layer region. It is defined as the upper solution of

$$y_0^+ = \frac{1}{\kappa}\log\left(Ey_0^+\right), \tag{3.27}$$

where E is the log layer constant and κ is the Kármán constant. In this work $E = 9.793$, and $\kappa = 0.419$ was used, values which have been found typical for smooth walls [298]. This makes the transition point $y_0^+ = 11.22$.

Boundary values for velocity components can now be calculated from the wall shear stress,

$$\widetilde{\boldsymbol{\tau}} = T_M\left(\mathbf{U}_w - \widetilde{\mathbf{U}}_t\right), \tag{3.28}$$

where T_M is the turbulent wall multiplier, defined as

$$T_M = \frac{\mu}{y} \tag{3.29}$$

for laminar flows or if $y^+ < 11.22$, or

$$T_M = \frac{C_\mu^{1/4}\kappa\rho k^{1/2}}{\ln\left(Ey^+\right)} \tag{3.30}$$

for turbulent boundary layers where $y^+ > 11.22$. The k equation is solved in the cell adjacent to the boundary, and the boundary value for ϵ is given by

$$\epsilon = \frac{C_\mu^{3/4} k^{3/2}}{\kappa y}. \tag{3.31}$$

A similar approach is used for the boundary conditions for the Reynolds stresses in the RSM turbulence model.

The boundary conditions for enthalpy follows a similar procedure as those developed for velocity. A non-dimensional number scaling enthalpy in the boundary layer is developed as

$$H^+ = \frac{\sqrt{\overline{\rho}\tau_k}}{\dot{H}} \left(H_w - H_t\right) \tag{3.32}$$

where H^+ is the non-dimensional enthalpy at a small distance from the wall, where the total enthalpy is H_t. The enthalpy of the fluid in contact with the wall is H_w, which is determined by the temperature of the wall. The heat flux at the wall is $\dot{H} = \left(\frac{\partial H}{\partial \mathbf{n}}\right)_w$, where $\mathbf{n}$ is the unit vector normal to the wall. The Prandtl number of the fluid is defined as $\Pr = \frac{\mu}{\lambda}$. Again the boundary layer is split into two sections representing the viscous sub layer and the log layer, that is,

$$H^+ = \left\{ \begin{array}{cc} \Pr\ y^+ & \text{for } y^+ < y_H^+ \\ \frac{\sigma_H}{\kappa} \log\left(E_H y^+\right) & \text{for } y^+ > y_H^+ \end{array} \right\} \tag{3.33}$$

where σ_H is the turbulent Prandtl number for enthalpy, taken as $\sigma_H = 0.9$. The transition point, y_H^+, is the upper root of the equation

$$\frac{\sigma_H}{\kappa} \log\left(E_H y_H^+\right) = \Pr\ y_H^+ \tag{3.34}$$

and E_H is calculated from the formula of Jayatilleke [152]. This leads to $E_H = 4.406$ and $y_H^+ = 12.09$. The boundary condition can now be implemented as

$$AT_w + BQ_w = C \tag{3.35}$$

where T_w is the temperature of the wall and Q_w is the heat flux at the wall, that is, $Q_w = \left(\lambda \frac{\partial T}{\partial \mathbf{n}}\right)_w$; and A, B and C are constants set by the user to impose Neumann or Dirichlet boundary conditions at the wall. By adjusting these constants it is possible to model the boundary as a constant known temperature, a known heat flux or a function of temperature and heat flux.

3.3.2 Wall Functions Limitations

Although the wall function approach addresses the main difficulties in imposing wall boundary conditions on k-ϵ and RSM turbulence models, it does create some new limitations. The following argument is developed using the velocity boundary condition, however a similar argument can be used for the limitations in the enthalpy boundary condition.

Despite the fact that equation 3.26 can predict the shear stress in the viscous sub layer with reasonable accuracy, the turbulence equations (for example equations 2.44 and 2.41) do not hold in this region. Hence it is common practice to make the first node point in the domain lie outside the laminar sublayer to prevent the turbulence equations from being applied in a region where they are inappropriate. This is done by ensuring the y^+ of the boundary cells does not fall below 11.

If grid refinement is performed keeping y^+ above 11, the simulation can converge to a mesh independent solution. If grid refinement is continued, and y^+ falls below 11, the consistency of the simulations will be lost as the turbulence equations will be applied in the laminar sublayer, where they are not valid. This is the basis of a major issue with wall functions, being that grid refinement does not converge to the exact solution if $y^+ < 11$ at the boundaries. This means that grid refinement needs to be performed cautiously when using wall functions, and that care must be taken to ensure that the boundary cells do not drop below $y^+ = 11$. This imposes a minimum size for the boundary cells of the simulation.

It is common practice to attempt to make $y^+ > 30$, as this allows for some areas of the flow to be slightly less than the targeted figure, but still be above 11. Additionally, if $y^+ > 30$, the wall function model is a marginally more accurate description of a fluid's true boundary layer profile, as shown in figure 3.6.

Additionally, the log layer extends to around $y^+ = 1000$, so there is an upper limit on the acceptable range of y^+. This upper limit is less critical than the lower limit as the flow is fully turbulent in this region so the turbulence equations do provide an accurate model. This means using high values of y^+ is only reducing the resolution of the simulation, rather than applying the boundary inappropriately.

A further problem with the wall function approach is that it is not applicable to separations or re-attachments. The wall function approach is based on analysis of steady-state, flat plate boundary layers so its application to highly transient, three-dimensional flows would appear invalid [284, 298]. However, it has been found that the wall function approach does produce a reasonable approximation for many engineering flows, and has become the "normal" method of applying boundary

conditions in simulations of turbulence typical of engineering flows.

Analysis of wall functions used in the CFX code has been performed by Clarke et al [67], Ciofalo and Collins [65], Date and Turnock [82] and by the current author in Horrocks et al [142]. These studies confirm that wall functions are generally successful, however they do have limitations. They are used in this work as with current computing resources and numerical techniques they are the best model available.

3.3.3 Pressure Boundaries

Pressure is specified at pressure boundaries and Neumann conditions are applied to the velocities, that is

$$\frac{\partial \widetilde{\mathbf{U}}}{\partial \mathbf{n}} = 0, \tag{3.36}$$

where $\mathbf{n}$ is the unit vector normal to the boundary.

The treatment of other variables depends on the flow direction.

- At inflow, the entrance velocity is restricted to be subsonic. Temperature and additional scalars are specified by the user. Turbulence parameters, k, Reynolds stresses and ϵ are extrapolated from downstream, and pressure is set to the user specified value.

- At outflow, temperature, additional scalars, k and ϵ are extrapolated from upstream, and pressure is set to the user specified value. If the flow is supersonic the pressure is also extrapolated from upstream and the user-specified pressure is ignored.

An additional option is to replace the user specified pressure, p, with a user specified total pressure, p_t. In this case, for a compressible gas, the pressure at the boundary is set to

$$p = \frac{p_t}{\left(1 + \frac{\gamma-1}{2} M^2\right)^{\frac{\gamma}{\gamma-1}}}. \tag{3.37}$$

The mathematical model of fluid flow in an internal combustion engine and the numerical method of solving the equations used in this thesis have now been described. In chapter 4, existing numerical and experimental studies of engine flows will be discussed, with reference to their application in modelling the flows in the BRV engine.

Chapter 4

Literature Review

The major engine processes involving gas flows dealt with in this thesis are combustion, in-cylinder flow and manifold flows. Existing knowledge in these fields is discussed in sections 4.1, 4.2 and 4.3 respectively. Techniques used by other researchers to numerically model flows in engines are discussed in section 4.4, where one-dimensional (section 4.4.1), two-dimensional (section 4.4.2) and three-dimensional (section 4.4.3) methods are discussed.

Finally, existing knowledge regarding turbulence in engines is discussed. This is the major complicating factor in engine flow modelling, and is discussed in section 4.5.

4.1 Combustion

The fundamental source of power in an internal combustion engine is the combustion of the charge. The combustion generates the heat and pressure which is extracted during the expansion stroke and converted into crankshaft torque. Obviously, improving the effectiveness of the combustion in an IC engine will directly improve engine performance.

Factors affecting the combustion in an internal combustion engine include:

- Fuel properties, including air to fuel ratio, fuel vapourisation and fuel chemistry;
- Air properties, including air temperature and pressure, and quantity of residual exhaust gases from previous strokes;
- Gas motion factors, including charge velocity and turbulence during combustion;

- Ignition factors, including spark plug design, spark energy and spark duration;
- Geometric factors, including combustion chamber geometry, spark plug location and crevice volume[1]; and
- Combustion chamber wall temperatures.

For many of these factors, the BRV engine and the traditional poppet valve engine share common characteristics. For example, the fuel and spark plugs used in the BRV engine are the same as those in a normal high performance poppet valve engine, so in these aspects of combustion their behaviour is similar. Both fuel behaviour [232, 20, 167, 22, 287, 86, 62, 291, 275, 247, 125, 244, 135, 305, 201, 137, 214, 301, 163] and spark plug design [71, 203, 137, 236, 255] has been widely researched, so existing knowledge of these issues is transferrable to rotary valve engines.

The effect of combustion chamber wall temperatures and related heat transfer will also be similar in the BRV engine and traditional poppet valve engines, and has been extensively studied [201, 19, 146, 88, 182, 88]. The effect of wall temperatures in the BRV engine will be studied later in this work, in section 8.5.

The primary difference between combustion in BRV and poppet valve engines is that the BRV engine will allow the engine designer to create new combustion chamber geometries not previously possible with the poppet valve engines, thereby allowing the opportunity for new flow structures. Thus, this study will focus on predicting engine air flow, with the aim of simulating turbulence levels present at ignition of the charge.

High levels of turbulence during combustion are required in engines for a number of reasons. Hill and Zhang [137] summarises the effects of high turbulence as beneficial for engines as it:

- Reduces burning time. This is due to the fact that the propagation speed of the flame during the main burning period of combustion (10–90% mass burned) is roughly proportional to turbulence intensity;
- Has been shown to reduce cycle to cycle variations; and

[1] Crevice volumes are small, thin volumes in the combustion chamber with a high surface area to volume ratio. They exist in the clearance between the piston and cylinder bore to the piston rings, and in a rotary valve engine between the cylinder head and rotary valve to the sealing element. Crevice volumes do not burn properly as the gas cannot reach ignition temperature, and causes a reduction in engine performance and fuel efficiency. See Ramos [232] for further details.

- Has been shown to allow combustion of leaner mixtures than would otherwise be possible.

Of these points, it is the first two points which are the most critical for high performance engines. Rapid and repeatable combustion allows for the reduction of the ignition advance which in turn leads to better engine performance due to a reduction in negative work required before TDC, but after ignition. It can also reduce heat transfer losses by reducing the length of time the hot burnt gases are exposed to the cold cylinder walls. A reliable and rapid combustion is also critical so the engine can supply a consistent level of torque.

There is evidence to suggest that limits exist to the amount of turbulence that is beneficial to the combustion in an engine. Hill and Zhang [137] suggest excessive turbulence can lead to higher heat transfer losses due to a thinning of the cylinder wall boundary layer, and mechanisms of generating turbulence can reduce volumetric efficiency. There are also indications that excessive turbulence can extinguish the flame during the initial period of combustion (0–10% mass burned). However, this appears to only happen in engines with extremely high levels of flow velocity at spark ignition, and is generally only found in research engines specifically designed to study these extreme conditions.

A detailed analysis of the interaction between turbulence, combustion and engine performance is beyond the scope of this work. Readers interested in the details of turbulent combustion are referred to the large amount of existing literature on the subject [52, 150, 86, 291, 201, 286, 160, 301, 163, 88, 19]. However, the fundamental mechanism of turbulent combustion in an engine is usually accepted to be [263]:

1. An initial laminar burn period, where the flame kernel is too small to be significantly influenced by turbulence. This occurs during the first few percent of mass burnt;

2. A turbulent mixing burn, characterised by a large flame front and extensive interaction with the turbulence field; and

3. A final burn, where the final few per cent of fuel in the cold wall regions of the cylinder is burnt. It is also possible that some regions do not burn at all. This final burn is slow due to the low fluid velocities and high heat transfer rates near the walls.

The review performed by Hill and Zhang [137] is an excellent summary of current thinking on combustion in internal combustion engines. They state:

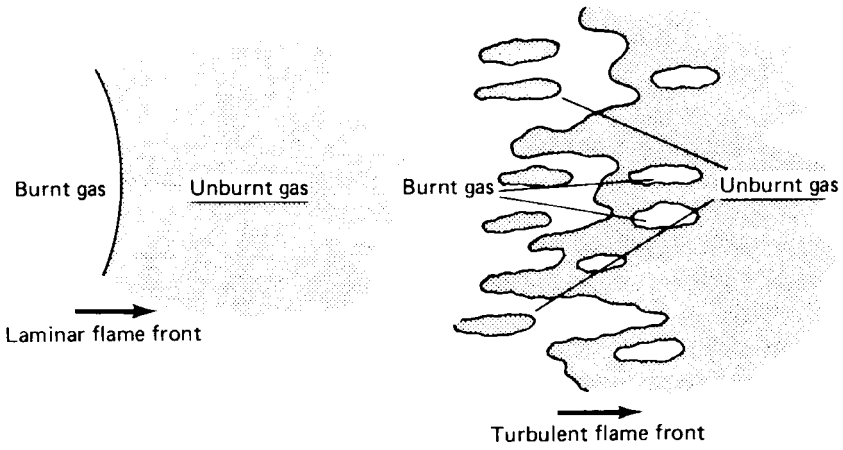

Figure 4.1: Comparison between laminar and turbulent flame fronts during combustion, adapted from Stone [263].

> "Much experimental work has shown the strong effect of the rms turbulence velocity u' on flame propagation speed. Most of the experimental data seem consistent with the idea that the turbulent flame speed divided by the laminar one varies with the ratio of the turbulence intensity u' to the laminar flame speed." [137]

The mechanism by which turbulence is understood to increase flame speed is due to the wrinkling of the flame front by the turbulent eddies, which increases the area of the flame front. The increased flame front area allows increased heat transfer to nearby unburnt gas. Since the temperature of the unburnt gas increases more quickly due to the increased heat transfer, it can reach ignition temperature and commence combustion more quickly than without a wrinkled flame front. A schematic diagram indicating the comparison between a laminar and turbulent flame front is shown in figure 4.1. It shows the laminar flame front to be smooth, and the turbulent flame front to be wrinkled, with pockets of burnt and unburnt gas in front of and behind the main flame front.

Hill and Zhang go on to state:

> "In recent years considerable work has been done on fractal analysis of turbulent flame propagation. As an example of the result of fractal analysis, and in good agreement with experimental data, Guelder [119] has shown that the ratio of turbulent flame propagation speed u_t to the

laminar flame speed u_l can be related to the turbulence intensity u' by

$$\frac{u_t}{u_l} = 1 + 0.62 \left(\frac{u'}{u_l} \right)^{\frac{1}{2}} \mathrm{Re}_L^{\frac{1}{4}} \tag{4.1}$$

in which $\mathrm{Re}_L = u'L/v$ and L is the integral length scale. Under engine conditions this can mean that turbulent flame speed may be 5–10 times as large as u_l; it shows the great importance of increasing u' in promoting burning rate in engines. Guelder also showed how, in the range of u' of interest to engine combustion, the dependence of u_t on u' given by equation 4.1 can appear to be linear. The apparent slope depends on the Reynolds number based on u' and the turbulence length scale, and is usually in the range 1–2." [137]

The supposition that the turbulent flame speed in an engine is approximately proportional to the turbulence intensity has also been demonstrated by Naitoh et al [201]. In developing their numerical simulation, they use the turbulent flame speed model of Tabacznsky [267], and justify the use of this model against a number of published experimental and direct numerical simulation models, which are summarised in figure 4.2.

A reasonable amount of scatter is apparent; this could be due in part to the difficulty in performing accurate measurements of flame speed in operating engines. However, the trend of turbulent flame speed being approximately proportional to turbulence intensity in the region of interest to engine combustion is clear.

The laminar flame speed is a function of the state of the combustion mixture, with fuel chemistry being the fundamental factor. Other factors, such as air to fuel ratio, gas temperatures and gas pressures have a smaller effect on laminar flame speed in the range of conditions encountered in an IC engine.

Arcoumanis and Whitelaw [23] performed an experiment in which they produced images of the flame front at various engine speeds directly. Pictures of the wrinkling of the flame front in an engine are shown in figure 4.3. The images show the flame front as having a small number of large imperfections at low speeds, increasing to many small "wrinkles" as the engine speed increases.

For the current work, it will be assumed that the optimum situation is to have maximum levels of turbulence at the end of the compression stroke, from the time of ignition of the spark to TDC. Hence no combustion model was used in this work, it is assumed that increased turbulence around the time of spark ignition will lead to improved combustion and engine performance. Thus, in the remainder of this

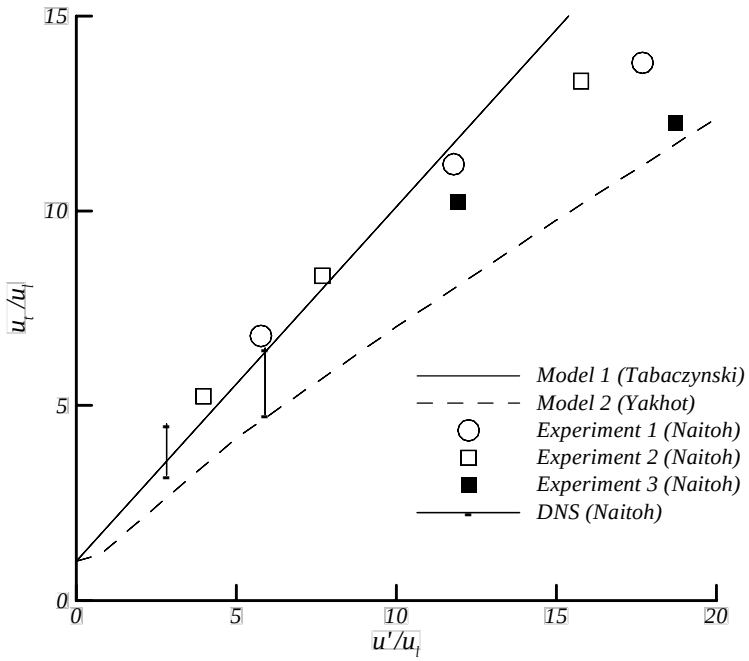

Figure 4.2: The relationship between turbulence intensity and burning velocity, adapted from Naitoh et al [201].

work, the question of increasing engine performance becomes an issue of maximising turbulence around the time of ignition of the charge.

Mechanisms which can be used to enhance turbulence levels for ignition are described in the following section.

4.2 In-Cylinder Flow

The in-cylinder flows of poppet valve engines are generally characterised by "squish", "swirl" and "tumble". Each of these flows are generated by different mechanisms, and each has different effects on the performance of an engine. An outline of these flows and their effects will now be presented.

4.2.1 Definitions

Squish

Squish is defined as a jet of gas acting along the piston face, occurring shortly before TDC. An example of a squish flow is shown in figure 4.4, and an example

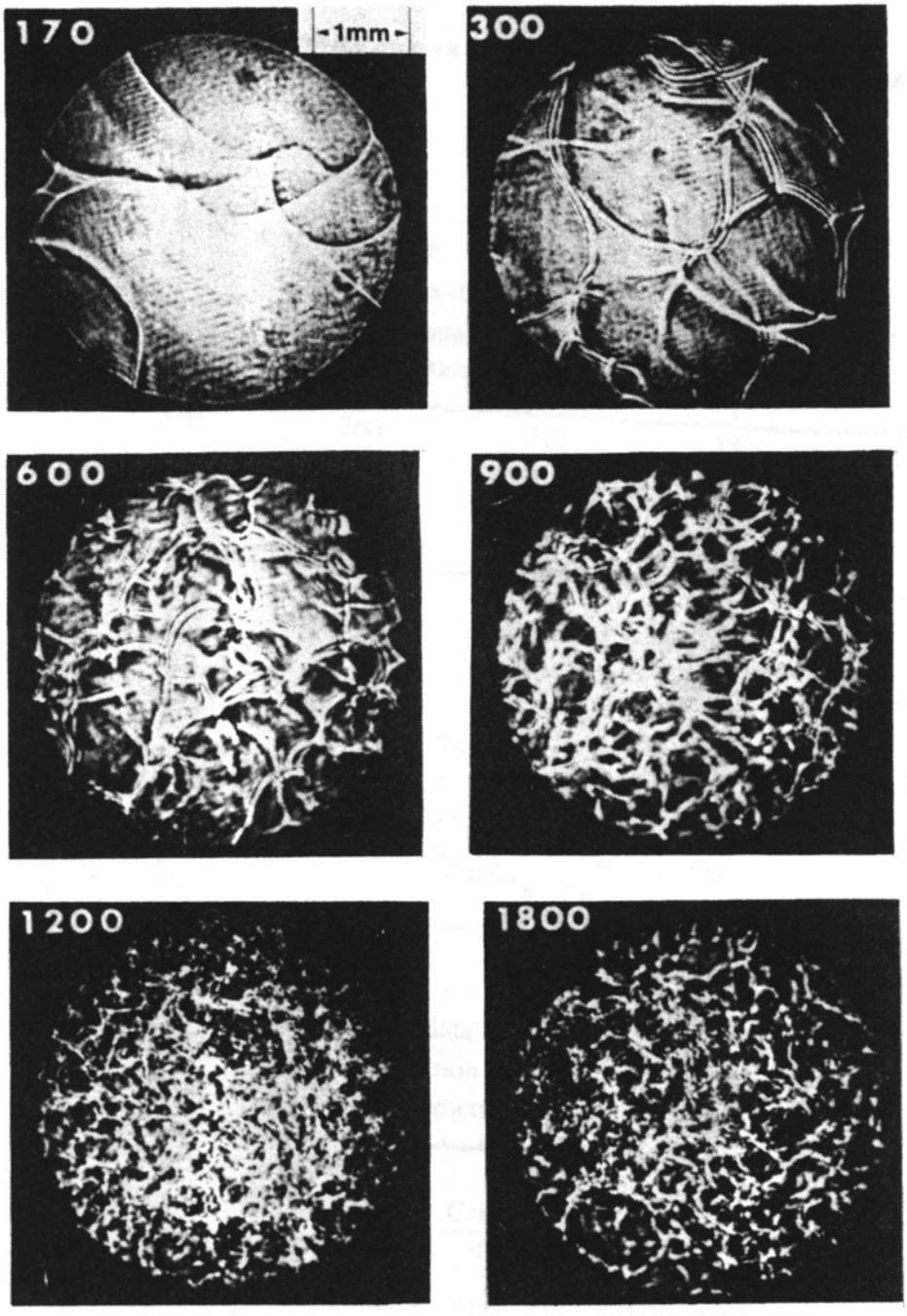

Figure 4.3: Microshadowgraphs of the flame propagation in an internal combustion engine from Arcoumanis and Whitelaw [23]. The flame is travelling towards the viewer, and the engine speed (in rpm) is indicated in the upper left hand corner of each photograph.

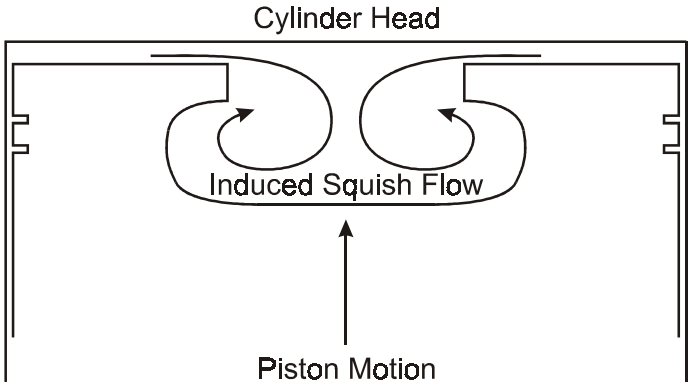

Figure 4.4: Example of an induced squish flow caused by sections of the piston coming into close proximity to the cylinder head.

Figure 4.5: A typical piston used for high squish applications, common in modern direct injection Diesel engines. Adapted from Northam and Rivers [210].

of a piston designed for squish is shown in 4.5. As the piston travels towards TDC the gas which is trapped in the areas where the piston and head surfaces come into close proximity is forced to flow at high velocity across the piston face. This high velocity jet is known as "squish", and in both the examples shown in figures 4.4 and 4.5 the resulting squish jet is radially inwards towards the centre of the combustion chamber.

Squish flows have been recognised as able to enhance turbulence levels since the earliest internal combustion engine designs. Squish was extensively used by researchers such as Ricardo in early side valve engines [236], an example of which is shown in figure 4.6. Here the squish jet is not radial, but into a combustion chamber offset to the side of the piston.

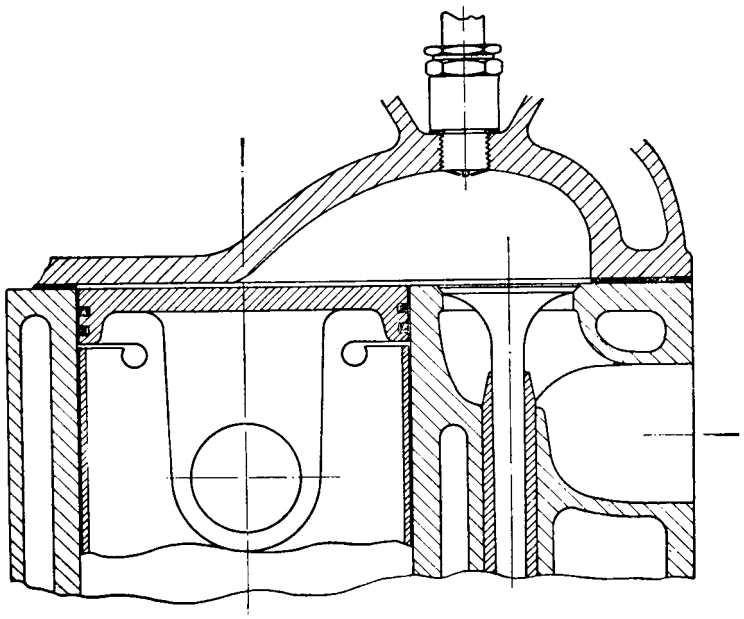

Figure 4.6: An engine configuration to generate a large squish flow. Just before TDC a high velocity jet of gas will be forced from the left side of the piston across the piston face and into the spark plug and valve region. Shown is the 1919 "Ricardo Turbulent Head" side valve engine [236].

Swirl

Swirl is defined as a large scale vortex in the gas in the combustion chamber, with a rotation axis parallel to the line of piston motion. An example of a swirl flow on a modern Diesel engine is shown in figure 4.7.

Tumble

Tumble is defined as a large scale vortex with a rotation axis perpendicular to both the axis of piston motion and the plane of the intake manifold. An example of a tumble flow in a three valve pentroof combustion chamber is shown in figure 4.8. It is sometimes known as "barrel swirl". Another type of flow, known as "cross tumble" is very similar to normal tumble, being a large scale vortex with a rotation axis perpendicular to the axis of motion of the piston, and parallel to the plane of the intake manifold. The behaviour of a cross tumble flow is similar to that of a tumble flow field.

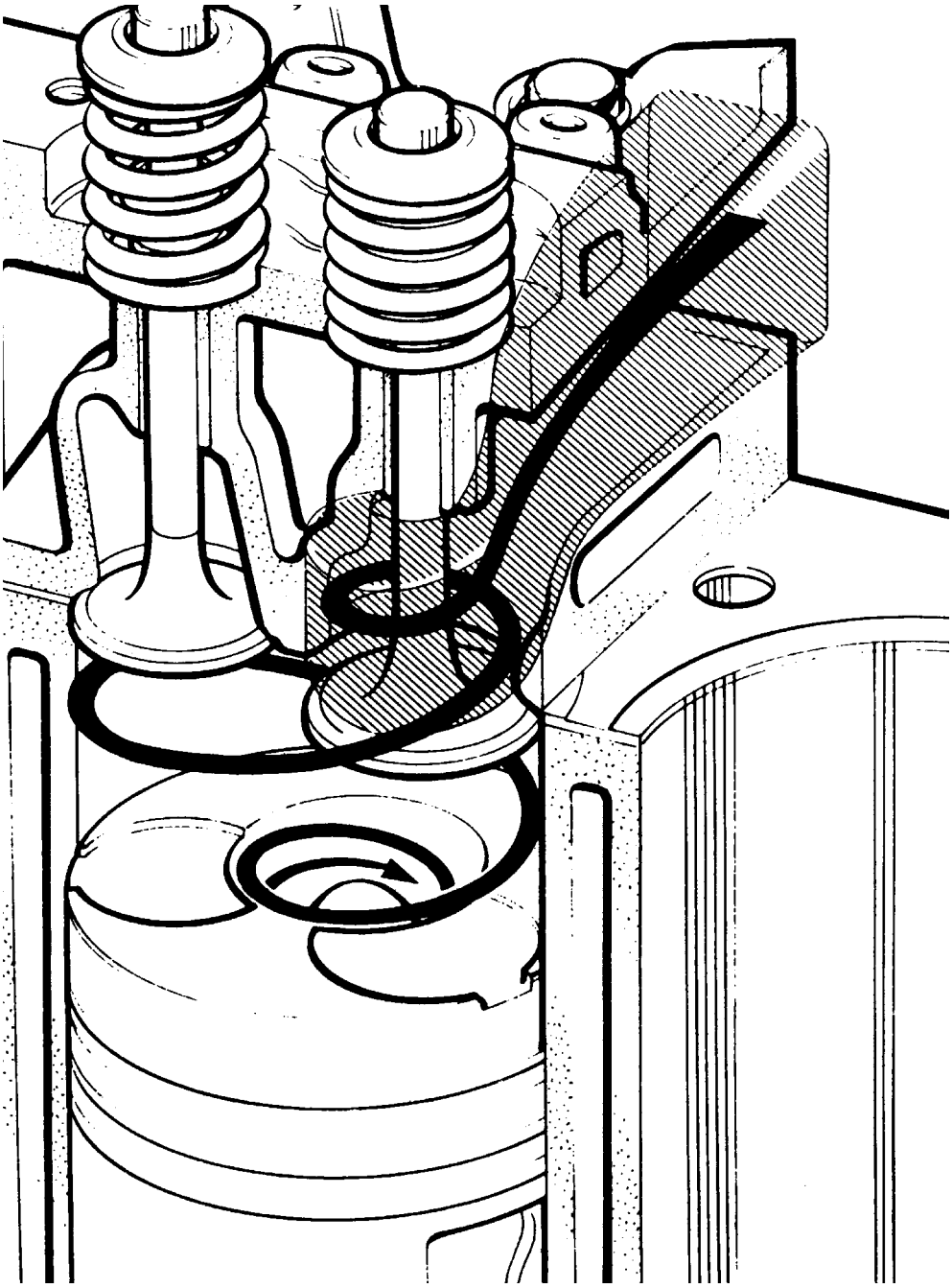

Figure 4.7: A swirl vortex, depicted on the direct-injection 2.5 L Ford Diesel engine from Stone [263].

Figure 4.8: A tumble vortex, adapted from [5].

4.2.2 Parameterisation

Squish

A common method of measuring the quantity of squish in the cylinder of an engine is by the squish ratio, SQ, defined as

$$SQ = \frac{A_{squish}}{A_{total}}, \tag{4.2}$$

in which A_{squish} is the projected squish area, and A_{total} is the projected piston area, as shown in figure 4.9. The squish area, A_{squish} is the shaded area shown, and $A_{total} = A_{squish} + A_{bowl}$.

A second factor which determines the level of squish is the piston to head clearance at TDC. For squish to have a significant effect the clearance must be very small—Taylor [272] suggests that it should be smaller than 0.005 times the bore for the effect to be useful.

Swirl, Tumble and Cross Tumble

Swirl (SR), tumble (TR) and cross tumble (CR) ratios are generally defined as the ratio of the angular momentum of the in-cylinder flow about each of the three orthogonal axes. It is normalised against the same gas rotating as a solid body about the same axes at crankshaft speed. The usual method for determining these ratios is the following process. First, the centre of mass of the combustion chamber gas is determined. Then axes X, Y and Z are defined with the origin at the centre of mass. The Z axis is defined as being parallel to the line of piston motion. The Y axis is defined as perpendicular to Z and parallel to the central axis of the inlet

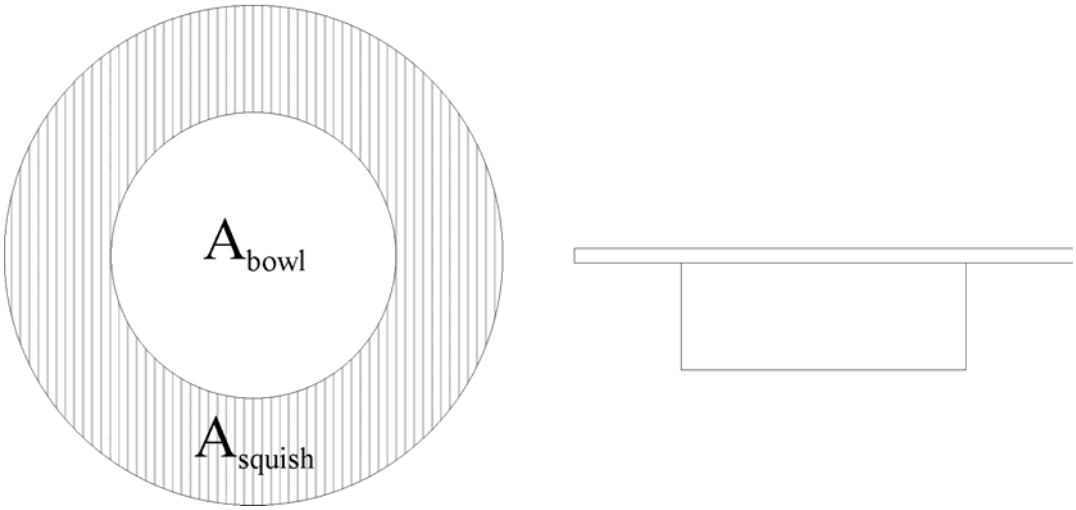

Figure 4.9: Definition of squish areas.

manifold. Finally, the X axis is defined as perpendicular to Z and Y. The swirl, tumble and cross tumble can now be defined as

$$TR = \frac{\int_\Omega \rho\,(\mathbf{r} \times \mathbf{U}) \cdot \mathbf{i}\, d\Omega}{\omega \int_\Omega \rho\,(\mathbf{r} \times (\mathbf{i} \times \mathbf{r})) \cdot \mathbf{i}\, d\Omega}, \tag{4.3}$$

$$CR = \frac{\int_\Omega \rho\,(\mathbf{r} \times \mathbf{U}) \cdot \mathbf{j}\, d\Omega}{\omega \int_\Omega \rho\,(\mathbf{r} \times (\mathbf{j} \times \mathbf{r})) \cdot \mathbf{j}\, d\Omega}, \text{ and} \tag{4.4}$$

$$SR = \frac{\int_\Omega \rho\,(\mathbf{r} \times \mathbf{U}) \cdot \mathbf{k}\, d\Omega}{\omega \int_\Omega \rho\,(\mathbf{r} \times (\mathbf{k} \times \mathbf{r})) \cdot \mathbf{k}\, d\Omega}; \tag{4.5}$$

in which $\mathbf{r}$ is the position vector from the origin and $\mathbf{U}$ is the gas velocity vector, $\mathbf{i}$, $\mathbf{j}$ and $\mathbf{k}$ are the unit vectors in the X, Y and Z directions respectively, ρ is the fluid density, ω is the crankshaft rotational speed and Ω is the combustion chamber volume. These parameters have been shown to be nearly independent of speed in a given engine geometry at a given crank angle for the typical range found in engines [63, 240].

4.2.3 Turbulence Enhancement Mechanisms

Squish

The existing levels of turbulence in the cylinder of an engine at the end of the compression stroke is increased by squish flows due to the following effects:

- Shear between the high velocity jets and the lower velocity fluid in the open section;
- Establishment of a flow field in the open section of the combustion chamber from the energy contained in the high velocity jets. The flow field then decays which generates turbulence through a process similar to swirl or tumble breakdown; and
- Acceleration of existing swirl or tumble vortices and subsequent breakdown.

Squish flows can also cause other aspects of engine performance to decline, so determining the optimum level of squish is often a compromise. Squish is known to lead to flame quenching in the thin sections in the extremities of the squish region [149, 236, 263]. The quenching is due to the metal walls of the combustion chamber being cold relative to the temperature of the combusting gases, and as the advancing flame front travels into the more confined regions in the squish areas the walls conduct more heat away from the flame. Eventually this removes enough heat from the gas so that it does not possess enough energy to continue the combustion process at a sufficient rate. This leads to a reduction in engine performance.

Some of the unburnt gas in the squish regions may burn later in the expansion stroke after the piston has moved away from the TDC position, but often a significant proportion remains unburnt. These unburnt gases then exit the engine during the exhaust stroke, and the fuel and air it contains are wasted. Hence, excessive squish can lead to large amounts of unburnt charge in the exhaust. This unburnt gas results in wasted fuel and engine capacity, so a compromise must be reached between the advantages of squish enhancing combustion through increased turbulence levels, and the extremities of the squish regions creating areas of unburnt charge.

Excessive squish can also lead to problems with engine knock, as discussed by Towers and Hoekstra [275].

Squish flows have also been used as a mechanism to speed the flame front reaching the extremities of the cylinder after TDC, when the flow direction reverses. This mechanism is described by Adachi et al [12], and is used in the Toyota 1ZZ-FE

engine. This engine was used in many Toyota vehicles, such as the 1998 Toyota Corolla.

Squish is often ineffective as a turbulence enhancement mechanism by itself for high performance spark ignition engines as the turbulence enhancement is localised around the edge of the squish jet [23, 282]. Also, as is discussed by Auriemma et al [29], the squish effect by itself only has significant effect between 5 °CA and 10 °CA before TDC. Thus the turbulence enhancement occurs after a significant fraction of the charge has already been burnt, and too late to be of real benefit for high speed spark ignition engines. However, Towers and Hoekstra [275] suggest that squish occurring after the charge has been ignited can be beneficial in promoting the main, middle stage of combustion.

It is commonly accepted that the optimum design for a spark ignition engine combustion chambers is to use squish in combination with other mechanisms such as tumble or swirl [49, 137, 166, 269, 23, 288, 297, 160, 86]. Not only can squish enhance turbulence at spark ignition, but it can also reduce cycle-to-cycle variations (see section 4.5) which are inherent in internal combustion engines [126].

Strong squish is often used in direct injection Diesel engines, often combined with swirl. In these engines a "bowl" type piston is used, such as the example shown in figure 4.5. The fuel injector is placed centrally in the bowl, and injects fuel along the central axis of the combustion chamber. The high levels of swirl combined with squish generate the turbulence, and a toroidal vortex is generated in the bowl. Both the turbulence and vortex contribute to mixing the fuel and enhancing combustion. This configuration is part of the mechanism commonly used in modern direct injection Diesel engines, and many example of its use can be found [297, 166, 126, 112, 243, 166, 29, 61, 181, 21, 261, 66, 307, 190, 136].

Deliberately separating the combustion chamber into areas of very lean charge and charge rich enough to support combustion can also be used in spark ignition engines, and is known as "stratified charge". This mechanism is being coupled with direct injection in the latest generation of production car spark ignition engines. Generally a tumble type flow field is used in combination with a degree of squish as the primary in-cylinder flow mechanism for these engines. Most major engine manufacturers are developing stratified charge, direct injection engines, for instance the Mitsubishi GDI engine [5], the NSDI-3 engine by the Institut Français du Pétrole [134], the Ricardo G-DI engine [95] and the HPi engine by PSA Peugeot Citroën [230]. This technology has the potential to significantly reduce fuel consumption and emissions, and it has the most dramatic effect at part load. In high performance engines, fuel consumption is of secondary significance, and they rarely operate at

part load. This makes gasoline direct injection and stratified charge technology not suitable for high performance engines.

As has previously been mentioned, the second parameter which determines the level of squish is the piston to head clearance at TDC. For a typical modern high performance engine with a bore of around 93 mm, using Taylor's [272] suggestion of a clearance of 0.005 times the engine bore indicates a clearance of 0.47 mm. In practise, the conrod tends to stretch under the large forces required to move a piston at high engine speeds, making such small clearances difficult to achieve.

The BRV engine piston to head clearance was designed so that at speed the piston would have very nearly touched the head at TDC during scavenging. Clearances during the compression stroke would have been slightly larger due to the high pressure gas pushing the piston down more than during the scavenge phase.

Swirl

Creating a swirling vortex in the cylinder has also been recognised as a way of enhancing turbulence levels during the compression stroke since the earliest days of internal combustion engines, for instance Ricardo used it in some of his early engines [236]. If a swirling velocity field is established at the time the inlet valve closes in an axisymmetric cylinder, it has been shown (as reviewed by Hill and Zhang [137]) that the in-cylinder velocity field becomes essentially two-dimensional solid body rotation, with the only major exception being the wall boundary layers. As this pattern has zero shear stress throughout most of the flow one might expect the enhancement of turbulence to be small, however this proves to be not the case. Hill and Zhang [137] state that swirl enhances turbulence during the compression stroke through the following processes:

- Turbulence generated by shear at the walls is transported throughout the bulk of the flow by diffusion and swirl generated secondary flows;
- Any protruding object not on the rotation axis of the swirl vortex, for instance off-centre spark plugs or valve heads will create turbulence through shear and vortex shedding; and
- A swirl vortex in conjunction with a squish flow will cause an acceleration of the rotational speed of the vortex as the piston approaches TDC to conserve angular momentum. This will increase turbulence production late in the compression stroke from the first two factors.

Swirl flows are commonly used in modern Diesel engines [11, 139, 249, 289], or in combination with squish [297, 166, 126, 112, 243, 166, 29, 61, 181, 21, 261, 66, 307, 190, 136].

As mentioned in the previous section many researchers report that a combination of swirl and tumble are better than purely one or the other [87, 90, 137, 192, 242]; however this is contradicted by Trigui et al [277] who report that pure swirl, tumble or cross-tumble appear to be superior. The exact reason for the unusual result of Trigui et al is not clear, it is possible they found an unusual engine geometry where their conclusion is true, or that they made an error in obtaining results. The strong weight of opinion is that a combination of swirl and tumble is optimum.

Some researchers report that the axis of the swirl vortex precesses during the compression stroke [242, 90]. This precession will cause a complicated breakdown of the flow field into turbulence in a manner similar to tumble flows.

It is likely that swirl decays into turbulence later than tumble [158, 207]. Turbulence levels rapidly decay during the final stages of the compression stroke, so it is likely that a late decay into turbulence will cause more turbulence to be present during combustion. However, as previously mentioned, swirl is likely to be most effective when used in combination with tumble.

A well known feature inherent in swirl flows is that they require energy to generate the vortex during the intake stroke. This energy comes primarily from the kinetic energy of the gases entering the cylinder through the inlet valve. So to increase the swirl intensity, the gas velocities in the inlet valve must be high, requiring a small cross section area at the inlet valve [14, 106, 122, 132]. This is the basis of one of the major compromises of swirl flows—between the requirement for the inlet valve cross sectional area to be large for adequate intake air flow at high engine speeds on one hand, and the requirement for small valve cross sectional areas to generate a high gas velocity for a strong swirl vortex on the other. A compromise must be reached between these two competing factors. A similar compromise also exists for tumble type flows, to be discussed in the next section.

In modern high performance spark ignition engines swirl flows are not used very often. For instance, the pentroof combustion chamber described in section 1.2 does not generate a significant swirl flow, as this configuration is almost symmetrical through the centre of the inlet valves. The reason for this is because tumble flows have shown a superior ability to produce turbulence for spark ignition engines. Examples of modern high performance engines with little swirl are found in [63, 168, 169].

Tumble

The exact process by which tumble enhances turbulence is not fully understood, however the fundamental mechanism has been identified. During the intake stroke a tumble vortex is established, as shown in figure 4.8. As the piston moves from BDC, the tumble vortex is compressed and increases its rate of rotation to conserve angular momentum. Only a small amount of energy is dissipated from the tumble vortex at this stage.

As the compression stroke continues, the aspect ratio of the combustion chamber starts to rapidly increase causing the vortex to become increasingly non-circular. The exact timing varies, but at around 30 °CA before TDC, the vortex exceeds a critical aspect ratio causing it to breakdown and form a number of smaller vortices. By a process which is not fully understood these vortices decay to a similar size as the turbulent structures, thereby enhancing the turbulence levels.

An early high performance engine to use a strong tumble flow was the famous 1967 Cosworth DFV V8 Formula One engine. The strong tumble flow is generated from its "cross flow" head, dual intake valves and small included valve angle. It is not clear whether the designer of this engine deliberately designed this engine for a high tumble flow, or whether it was a fortunate accidental discovery. Certainly there was no rigorous scientific analysis of this type of flow until the work of researchers such as Witze et al in 1983 [300], Gosman et al in 1985 [117] and Vafidis et al in 1987 [282]. Regardless of whether the Cosworth DFV engine designer knew the flow mechanism by which the engine operated, it has been the standard design for high performance engine design ever since[2].

Despite its widespread use, the exact trigger for the tumble vortex breakdown and the flow behaviour during the subsequent breakdown of the smaller vortices in the final stages of the compression stroke are not fully understood. A detailed mechanism of the triggering for the initial breakdown has been proposed recently by Marc et al [46], and is discussed in more detail in Marc [187]. The proposed mechanism is based on an elliptical instability of vortices in compression, and the adverse pressure gradient on the piston and head faces causing the separation of the tumble vortex. This has been studied by the current author in Horrocks et al [142], and will be discussed further in chapter 6.

Tumble is the flow regime preferred by most modern spark ignition engine designers to enhance compression stroke turbulence. It is now being extensively used

[2] The Cosworth DFV engine also pioneered other aspects of high performance combustion chamber design, such as the use of four valves, a central spark plug, and a small included angle between inlet and exhaust valves.

Tumble Ratio (TR)	0.52	1.27	1.89
Output (kW)	4.33	4.68	4.57
Combustion Duration (°CA)	73	62	58
Volumetric Efficiency (%)	76.9	77.0	76

Table 4.1: Tumble ratio versus engine output parameters from Miyachi [194].

on high performance and normal production car engines [160, 277, 87, 269, 174, 207, 63, 30, 291, 94, 233, 234, 240, 106, 80, 41, 60, 184, 241, 258, 156, 155].

Tumble is also critical for the functioning of the new direct inject spark ignition engines, as the combustion in these engines is very lean and requires large amounts of turbulence to stabilise it. In addition, the increased turbulence enhances the brief mixing period of the fuel spray before ignition. Examples of its use in direct injection spark ignition engines can be found in [230, 134, 125, 260, 246, 95].

Turbulence enhancing mechanisms, usually tumble, have been found to be essential when fuels with lower laminar flame speed are used, or when high levels of exhaust gas recirculation is present. Examples of this use can be found in [137, 22].

Tumble shares the characteristic of swirl in that it requires high inlet velocities to establish a strong vortex. Again, this creates a compromise which must be reached between the competing requirements for large inlet cross section areas for high flow rates against small inlet cross section areas for high gas velocity. This compromise is described by Miyachi et al [194], who describes a small engine with tumble ratio measurements from a steady state flow rig. Measurements of tumble taken from a steady state experiment must be treated with caution as tumble is an inherently transient process with the piston motion, but the results can be taken as a guide. The engine was run at 4000 rpm using a number of different configurations, and a summary of their results is shown in table 4.1. As expected, the combustion duration decreases with increasing tumble, but the high tumble ($TR = 1.89$) engine produces less power output than the mid tumble ($TR = 1.27$) engine. This reduction was due to the volumetric efficiency dropping because of the smaller cross section inlet manifold reducing inlet mass flow. Miyachi et al suggest for their engine, shortening of the combustion duration is the most significant effect below a tumble ratio of 1.6, and volumetric efficiency reduction is the most significant effect above a tumble ratio of 1.6. It is unlikely that $TR = 1.6$ is optimum in general. However, the concept of an optimum tumble ratio existing for an engine, above which the performance decreases is likely to be general.

Some researchers report that tumble seems to increase cycle-to-cycle variations. Belmont et al [34] state that this is caused by the inherent instability of the collapse

of the vortex. He says some of the issues causing the instability are:

1. the highly variable conditions prevailing in the 'spin-up tumble flow' period, around 60 °CA before TDC;

2. the large number of mode bifurcations of the flow that are passed through in the collapse to turbulence; and

3. the extreme sensitivity of the flow on initial and boundary conditions.

This disadvantage is somewhat offset by the fact that the enhanced levels of turbulence from tumble flows tend to reduce cycle to cycle variations in the combustion.

Some researchers have assumed that the symmetry of the geometry in the plane of the inlet and exhaust valves will lead to a flow field which is also symmetrical, and therefore simulations need only model half the cylinder volume. This assumption has been used by many researchers [174, 41, 115, 291]. Such an assumption is questionable, as cycle to cycle variations are likely to mean the flow will break symmetry, and it is unlikely to do so with repeatability. However, it may be possible that the "average" cylinder flow may in fact be close to symmetrical. This "averaging" can take place as ensemble averaging of experimental results, or use of a Reynolds averaged Navier Stokes turbulence model which has enough dissipation to stop the small instabilities occurring. This issue is more fully discussed in section 4.5.

Research performed by Kuwahara et al [168] has uncovered that the flow field generated by a four-valve pentroof combustion chamber produces a mixture of swirl and tumble where the swirl vortex is actually two geared vortices next to each other, as shown in figure 4.10. This work is significant in that engine flows have been discovered which can no longer be classified as "squish", "swirl" or "tumble". They report that their "triple vortex" structure appears as the energy from the tumble vortex gets distributed to the two swirl plane vortices through the common streamline in the centre of the chamber. They report the structure appears to be stable until quite late in the compression stroke, resulting in turbulence scale eddies of quite large size.

Cross tumble behaves in a similar manner to normal tumble during the compression stroke. However, since most pentroof combustion chamber engines generate very little cross-tumble in the intake stroke, its effects are often not significant compared to the effects of tumble. The effects of cross tumble in non-symmetric engines has not been analysed in detail.

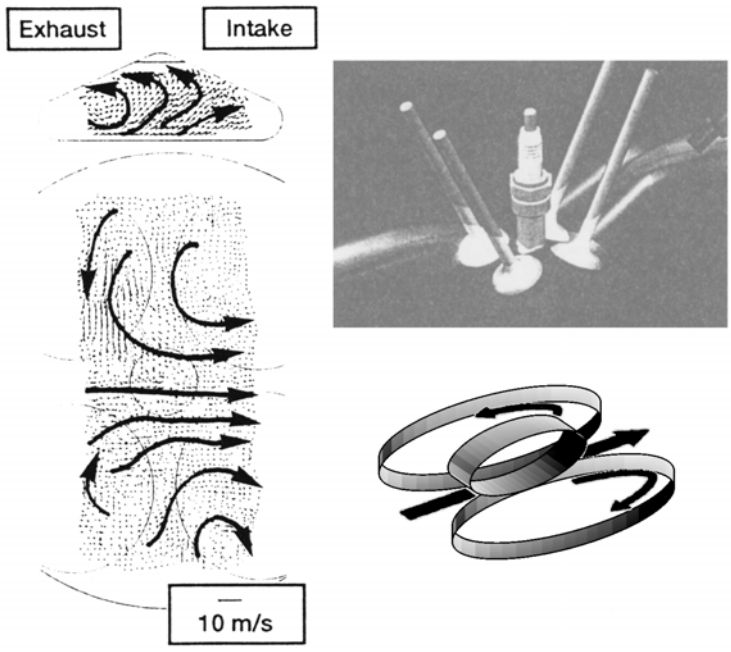

Figure 4.10: Laser Doppler Velocimetry (LDV) results of Kuwuhara et al [168], left, observed in a pentroof head engine 15 °CA before TDC. His schematic interpretation of the "triple-vortex" is also indicated.

4.3 Manifold Flows

The intermittent action of the valves in internal combustion engines cause pressure waves to be generated in the intake and exhaust manifolds. These waves travel up and down the manifold as they reflect between the inlet trumpet or exhaust pipe and valve ends of the manifold. The waves interact with internal features of the manifolds, such as manifold junctions or cross-sectional area changes; as well as interacting with the gas in the cylinder when the valve is open.

Manifold pressure waves can be harnessed to increase the performance of internal combustion engines by:

- Increasing the scavenging efficiency, by blowing gas directly from the inlet valve, across the combustion chamber, and out through the exhaust valve. This reduces the quantity of exhaust gas left in the cylinder for the following intake stroke;
- Supercharging the cylinder at the end of the intake stroke, by utilising the fact that manifold pressure behind the valve is, at times, above atmospheric.

Pressure waves have been utilised in the design of internal combustion engines

since the earliest internal combustion engines. For instance, the "Crossley Scavenging Engine" of the late 19th century [253] utilised pressure waves with a valve overlap to improve scavenging efficiency. The engine ran at 200 rpm, and was claimed to have a pressure of 13 kPa below atmospheric near the exhaust port during the scavenging period. To generate this favourable pressure system at this low speed, the exhaust pipe was 20 m long!

When the motor car became popular in the early 20th century, utilising the energy present as pressure waves in the manifolds (or "induction ramming") was only occasionally used in high performance engines. Engines specifically designed to make use of the induction ramming effect in Grand Prix class racing cars only appeared after rule changes enacted for the 1952-3 season, where unsupercharged engine capacities were restricted to 2.5 L, down from 4.5 L in the previous season [69]. This dramatic reduction in allowable engine capacity forced engine designers to look for more elegant forms of maximising engine performance, for instance, the use of the induction ramming effect.

Over the following decades chassis and body aerodynamics design advances created demands for smaller, lighter engines with better fuel efficiency. This made induction ramming effects essential for high performance engines [253]. In the 1960s, Bristol, Jaguar and Chrysler manufactured engines with "tuned" inlet and exhaust systems. The "tuning" was generally estimated using empirical relationships, and fine tuned experimentally by monitoring engine power and inlet manifold pressures whilst running the engine on a dynamometer.

As the velocities in the manifolds of an engine vary approximately in proportion with the engine speed, the additional pressure possible in the manifolds will vary approximately as the engine speed squared, due to the total pressure increasing as approximately the square of velocity. This is developed from the stagnation pressure of a compressible gas, being [283]

$$p_t = p_s \left(1 + \frac{\gamma - 1}{2} M^2\right)^{\frac{\gamma}{\gamma - 1}}, \tag{4.6}$$

where p_s is the fluid static pressure and p_t is the fluid total or stagnation pressure and M is local Mach number. The gas constant, γ, is the ratio of specific heat for the gas, $\gamma = C_p/C_v$.

Equation 4.6 can be expanded by the binomial theorem [283] to

$$p_t = p_s + \frac{1}{2}\rho V^2 \left[1 + \frac{1}{4} M^2 + \ldots\right], \tag{4.7}$$

in which V is the fluid velocity and ρ is the fluid density. Therefore for the low Mach numbers typical of engines, the bracketed term approaches one, so $(p_t - p_s) \propto V^2$.

This means that as high performance engines run faster, the total pressure available increases rapidly. Modern racing engines run at far higher speeds than those of the 1960's—estimates of the maximum speeds used in the top engines during the 1999 Formula One season are between 17000 rpm and 17500 rpm [4, 227]. This means tuned manifolds are essential for modern high performance engines.

4.4 Engine Flows Modelling

A number of different methods have been used for modelling engine manifold flows. Only those capable of predicting volumetric efficiency or in-cylinder flows will be discussed here. Other techniques, such as engine acoustics modelling are discussed in Davies [83] or Winterbone [299].

4.4.1 One-Dimensional Models

One-dimensional models were developed to allow modelling of the transient flow in engine manifolds. This allows the designer to analyse parameters affecting the inlet and exhaust manifold waves, such as tract length, valve timing and gas temperatures. It also allows crude modelling of manifold area profiles or pipe junctions through the use of empirical models. Of course, a one-dimensional model cannot simulate in-cylinder flows, such as squish, swirl or tumble. One-dimensional models are often used, however, as a method for designing manifold sizes, lengths and valve timing. The two common methods of performing one-dimensional simulations will now be discussed, being the method of characteristics and Lax-Wendroff scheme.

One-Dimensional Modelling Techniques

Method of Characteristics A widely used type of one-dimensional model is known as the method of characteristics (MOC). It is based on the one-dimensional transient Navier Stokes equations (see section 2.2), and in its simplest form assumes the gas to be homentropic[3]. A detailed derivation can be found in Benson [39], with the final result for homentropic flow being that the Navier Stokes equations are

[3]Homentropic flow occurs when the entropy in the gas is constant over all space and time. A consequence of this is that the gas temperature is assumed constant.

reduced to two families of equations, a λ family,

$$\begin{aligned} \frac{dx}{dt} &= u + a \\ \frac{da}{du} &= -\frac{\gamma - 1}{2} \end{aligned} \tag{4.8}$$

and a β family,

$$\begin{aligned} \frac{dx}{dt} &= u - a \\ \frac{da}{du} &= +\frac{\gamma - 1}{2} \end{aligned} \tag{4.9}$$

in which x is the length, t is the time, u is the fluid velocity, a is the fluid acoustic velocity and γ is the ratio of specific heats for the gas.

These families of equations propagate on the position diagram (which determines the velocity of the gas), and the state diagram (which determines the acoustic velocity of the gas). Boundary conditions and initial conditions are quite simple to implement, and define the way the families of characteristics "reflect" from the ends of the domain.

The method was later extended to include non-homentropic effects including heat transfer and friction, this is also described by Benson [39].

Lax-Wendroff An alternative technique is to use the hyperbolic nature of the equations describing the flow, and explicitly advance the equations in time using a two step technique. The technique is known as the Lax-Wendroff method, and an example of its derivation is given by Ramos [232]. The continuity, momentum and energy conservation equations are written in the form

$$\frac{\partial \mathbf{U}}{\partial t} + \frac{\partial \mathbf{F}}{\partial x} = \mathbf{G}, \tag{4.10}$$

where

$$\mathbf{U} = \begin{bmatrix} \rho \\ \rho u \\ \frac{1}{2}\rho u^2 + \frac{p}{\gamma - 1} \end{bmatrix}, \tag{4.11}$$

$$\mathbf{F} = \begin{bmatrix} \rho u \\ \rho u^2 + p \\ u\left(\frac{1}{2}\rho u^2 + \frac{\gamma}{\gamma - 1} p\right) \end{bmatrix}, \text{ and} \tag{4.12}$$

$$\mathbf{G} = \begin{bmatrix} -\frac{\rho u}{A}\frac{dA}{dx} \\ -\frac{\rho u^2}{A}\frac{dA}{dx} - \rho\frac{4f}{d}\frac{u|u|}{2} \\ \frac{q\pi d}{A} - \frac{1}{A}\frac{dA}{dx} u\left(\frac{1}{2}\rho u^2 + \frac{\gamma}{\gamma - 1} p\right) \end{bmatrix}. \tag{4.13}$$

Here A is the manifold cross section area, d is the manifold diameter, f is the friction factor for the manifold walls and q is the rate of heat transfer. Equations 4.11 to 4.13 assume that the manifold is circular in cross section, but they can be easily extended to other cross section profiles. Equation 4.10 can be marched through time in a two step process. The "half step" is first calculated with

$$\mathbf{U}_{i+\frac{1}{2}}^{n+\frac{1}{2}} = \frac{1}{2}\left[\mathbf{U}_i^n + \mathbf{U}_{i+1}^n\right] - \frac{\Delta t}{\Delta x}\left[\mathbf{F}\left(\mathbf{U}_{i+1}^n\right) - \mathbf{F}\left(\mathbf{U}_i^n\right)\right] + \frac{\Delta t}{2}\left[\mathbf{G}\left(\mathbf{U}_i^n\right) + \mathbf{G}\left(\mathbf{U}_{i+1}^n\right)\right], \tag{4.14}$$

and the next full time step is calculated from

$$\mathbf{U}_i^{n+1} = \mathbf{U}_i^n - \frac{\Delta t}{\Delta x}\left[\mathbf{F}\left(\mathbf{U}_{i+\frac{1}{2}}^{n+\frac{1}{2}}\right) - \mathbf{F}\left(\mathbf{U}_{i-\frac{1}{2}}^{n+\frac{1}{2}}\right)\right] + \frac{\Delta t}{2}\left[\mathbf{G}\left(\mathbf{U}_{i+\frac{1}{2}}^{n+\frac{1}{2}}\right) + \mathbf{G}\left(\mathbf{U}_{i-\frac{1}{2}}^{n+\frac{1}{2}}\right)\right], \tag{4.15}$$

where the subscript i represents the node number along the manifold, and the superscript n represents the time step number. This method is second order accurate in both space and time.

One-Dimensional Model Development

The first applications of one-dimensional, transient, compressible gas modelling were performed with MOC, using graphical methods. It was used during the 1940s and 1950s to model flows such as a valve on a high pressure reservoir suddenly opening and discharging through a pipe to the atmosphere [84, 111, 250]. These graphical methods were also applied to internal combustion engine manifold design by researchers such as Benson [37] and Wallace [290]. Both these researchers used the homentropic MOC to model the pressure waves in the exhaust manifold of a two stroke engine. The graphical MOC was subsequently used by many researchers, however detailed graphical constructions are required, with the result that the solutions were slow, tedious, and prone to error. Additionally, the homentropic equations had limited accuracy as they could not reproduce the effects of temperature variations or friction. More complicated solutions, such as non-homentropic flows, or multi-cylinder engine models were rarely attempted.

When computers became available to engine researchers, more ambitious simulations of engine flows could be attempted. Benson [40] was one of the first researchers to computationally model the homentropic MOC equations. The previously impractical non-homentropic MOC was successfully modelled by Benson [38] after computing power had developed a little further. This allowed MOC to develop into a more general design tool for engine manifolds.

Subsequently the MOC has been extensively used as an engine manifold design tool. An example is given by Shimamoto et al [252], who used MOC to model a six

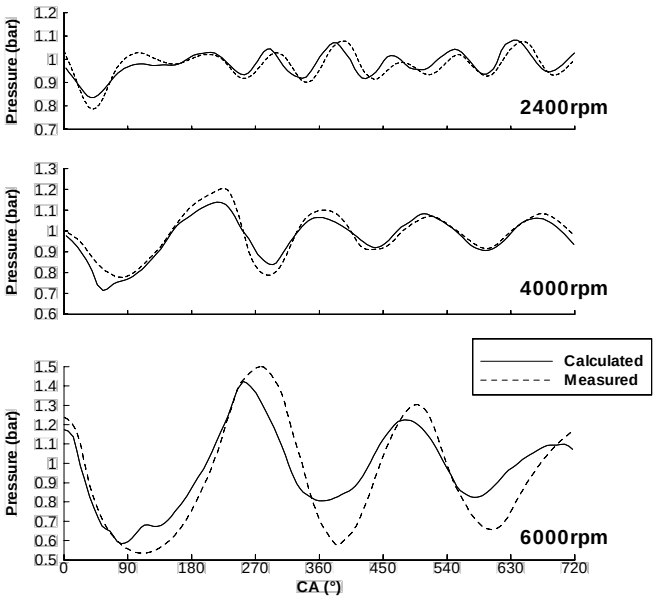

Figure 4.11: Comparison of measured and calculated pressure in the inlet manifold of the engine studied by Takeyama et al [268]. The results for 2400 rpm, 4000 rpm and 6000 rpm are shown.

cylinder engine inlet manifold, including pipe branches and intake plenums. Results compared well to experimental results, the volumetric efficiencies predicted being within 4% of measured results.

During the 1980s the Lax-Wendroff method was applied to engine manifold modelling, and proved faster and more accurate than the MOC. A comparison was performed by Poloni et al [228], who compared the homentropic and non-homentropic MOC to the two step Lax-Wendroff scheme. It was found that large overshoots occurred in the Lax-Wendroff model at regions of high gradients due to the second order nature of the scheme, so a flux corrected scheme was implemented which successfully controlled the overshoots. For homentropic flow, they found that the MOC with a fixed mesh was most accurate. For non-homentropic flow, the non-homentropic MOC and two step Lax-Wendroff scheme gave similar results, however the two step Lax-Wendroff scheme was twice as fast.

The MOC is still used by some researchers, such as Douglas et al [91] who studied the effect of temperature discontinuities in engine manifolds in 1991, and Blair and Blair [43] who studied the effects of pressure ratio and engine speed on the accuracy of a MOC simulation in 1987. However, the majority of researchers use the Lax-Wendroff technique now due to its improved computational speed and accuracy.

A good example of the use of the Lax-Wendroff technique is given by Takeyama et al [268]. They used the two step Lax-Wendroff scheme to predict wide open throttle performance in a four valve engine. They developed one-dimensional empirical models for friction, junctions, plenums, cylinder and combustion, heat transfer in cylinders and appropriate boundary conditions. The model was applied to a four and six cylinder engine. Intake pipe pressure were accurately predicted for the slower speed runs at 2400 rpm and 4000 rpm, but significant differences appear between predicted and measured values at the highest speed tested, 6000 rpm, shown in figure 4.11. However, the volumetric efficiency predicted at all speeds, including 6000 rpm, was remarkably good with an error of only 2%. They suggested that a connecting pipe between collecting chambers, with a butterfly valve controlled by the engine management system could increase low speed performance while not reducing high speed performance. This connecting pipe was modelled numerically and experimentally, and was shown to achieve the desired effect.

One-dimensional modelling has become quite mature with many researchers also reporting excellent accuracy. More complicated models have been developed, for instance, the model of the transport of chemical species developed by Onorati and Ferrari [214].

One-dimensional manifold modelling has become a standard tool for engine manifold and valve timing design. There are a number of commercial codes available which specifically model one-dimensional engine manifold flows, for instance WAVE by Ricardo USA [8], BOOST by AVL [2] and PC Dyno2000 by Motion Software [6]. No information on how these programs solve the equations could be found in the literature associated with the codes; it is assumed that they use the Lax-Wendroff technique. These codes have simple user interfaces and make this type of modelling easy to perform by any engineer, rather than requiring a numerical modelling specialist. Most high performance and production car engine manufacturers would use this type of modelling as part of the design process for engines, but as their designs and the results are confidential it is rarely published.

Despite the success of one-dimensional models, they have a number of disadvantages. These disadvantages will be discussed in the following section.

One-Dimensional Modelling Limitations

One of the inherent disadvantages of one-dimensional modelling is that it cannot deal with multi-dimensional effects. Where the flow is significantly multi-dimensional, an empirical relationship must be used to account for it. This is the case, for instance, as the flow passes through the valves. In one-dimensional mod-

els the effect of the valves is usually assumed to be predicted by "valve discharge coefficients". Valve discharge coefficient, C_D, is defined as

$$C_D = \frac{A_e}{A_c}, \tag{4.16}$$

where A_c is the smallest cross section area in the inlet manifold, usually the valve curtain in a poppet valve engine; and A_e is the valve effective area, defined as

$$A_e = \frac{\dot{V}}{v_0}, \tag{4.17}$$

where $\dot{V}$ is the measured volumetric flow rate and v_0 is the ideal flow velocity through an orifice of the same area and pressure drop based on an incompressible fluid, that is,

$$v_0 = \sqrt{\frac{2\,\Delta p}{\rho}}, \tag{4.18}$$

where Δp is the pressure drop across the valve and ρ is the fluid density. This measurement is typically done on a device called a "flowbench", which simultaneously measures pressure drop across the valve and volumetric flow rate. The valve is fixed to the lift to be tested, the pressure gradient is applied and the resulting flow rate is measured.

Flowbenches can usually only create a pressure drop of the order of 10 kPa, whereas in high speed engines the pressure across the valve can be over 100 kPa. At pressures of under 10 kPa, the flow is generally at a low Mach number, so few significant compressibility effects occur. In a high speed engine with driving pressures of over 100 kPa, the flow can reach sonic velocity and the flow can choke, and flow at this condition is obviously highly compressible. It is clearly inaccurate to extrapolate an incompressible result into the compressible flow regime. In addition, the flow in an engine operating at high speed has rapid transients and flow reversals, but the standard experimental methods of measuring valve discharge coefficients (that is, a flowbench) can only operate at steady state. Clearly the accuracy of using valve discharge coefficients determined through steady state flows at a low pressure gradient and applying them to high speed engines needs to be tested.

The difference between valve discharge coefficients determined by traditional steady state testing and the true dynamic situation was assessed by Blair and Blair [43]. They used non-homentropic MOC to model a 2.0 L, 4 stroke spark ignition engine. They experimentally determined the valve discharge coefficients at a number of pressure ratios in steady flow, and found the discharge coefficient of the inlet valve in the normal flow direction (manifold to cylinder) to be largely independent

of pressure ratio up to a pressure ratio of three, but the inlet valve in the reverse direction or the exhaust valve showed variations of up to 20%.

Blair and Blair also developed a simplified engine geometry to assess the effect of using a moving valve, and compared the pressure wave generated to a one-dimensional simulation. They found the simulation gave good agreement at low speeds between the predicted and measured pressure wave, but that the agreement deteriorated with increasing speed. They conclude by suggesting that the correlation is acceptable for the range of a "typical automotive engine". This conclusion is difficult to justify as they only tested speeds between 1000 rpm and 2500 rpm, and most automotive engines regularly operate above this speed range. This conclusion is doubtful for high performance engines as they operate far in excess of this speed.

The work of Fukutani and Watanabe [103] concentrates on the effect of engine speed on valve discharge coefficient, at speeds of up to 9000 rpm. They found that the flow coefficient measured on an actual engine could be reduced by up to 30% from the steady state coefficient, with the greatest variation found at high engine speeds.

A more recent publication by Blair [44] analyses the use of one-dimensional models in high performance engines, and assesses the accuracy of C_D as a means of measuring valve performance. He arrives at a very different conclusion to his earlier study, finding that the steady state case varies substantially from the dynamic case, and effects such as the proximity of the valve to the cylinder bore has a large effect on valve discharge coefficient. The driving pressure used in the steady state test was also found to significantly vary the results. He performed a one-dimensional simulation using the range of valve discharge coefficients they found with the steady state tests and found the pressures predicted varied by a considerable margin. Blair found the errors to vary from about 5% at 6000 rpm to about 10% at 9500 rpm. The paper concludes with:

> "It is recommended that the use of the traditional discharge coefficient is discontinued within an engine simulation if accuracy is required from that simulation. It is even questionable if it should be retained as a simple means of experimental comparison of the discharge coefficient of one valve system geometry to another.
>
> ...
>
> It is clearly quite inadequate to use within an engine simulation an 'effective valve area' which has been determined by a traditional analytic process, i.e. as [valve discharge coefficient], at a single pressure ratio alone, and for only one flow direction." [44]

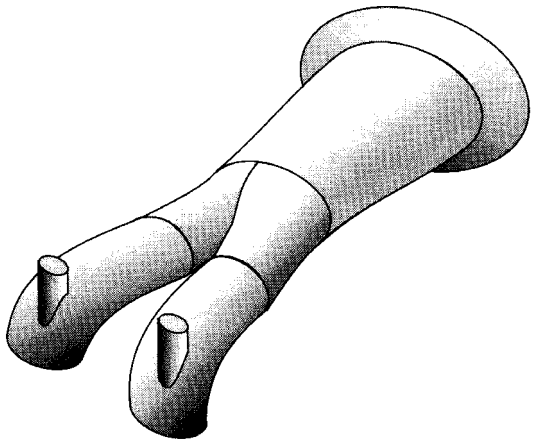

Figure 4.12: The Formula One engine inlet geometry modelled by Ferlet [299].

Valve discharge coefficients in high performance engines were also studied by Fleck and Cartwright [97]. They used a variation on the normal flowbench device which allowed them to produce driving pressures of up to 90 kPa, far greater than a standard flowbench can achieve, and comparable to the pressures found in high performance engines. Using this device they found that the valve discharge coefficient at high driving pressures varied by a factor of up to 20% from those found at low driving pressures.

A further problem with this type of modelling is the assumption that a single friction factor predicts the wall friction accurately. As noted by Ramos [232], the friction coefficient may not be valid in manifolds due to flow reversals, resonance and unsteady effects. Again, the accuracy of using a friction factor is likely to be good at lower engine speeds, but deteriorate with increasing engine speed as the complicating issues such as flow reversals and separations become more significant. The simple heat transfer models also used in one-dimensional models are also likely the have significant errors for similar reasons.

High Performance Engine Applications of One-Dimensional Modelling

Despite the problems with applying one-dimensional models to high speed internal combustion engines described previously, many examples of their use have been published. An example is the work of Ferlet [299], who reports on the modelling of the manifold of an early 1990s Formula One engine. The geometry modelled is shown in figure 4.12.

A major problem with using one-dimensional models on very high speed engines,

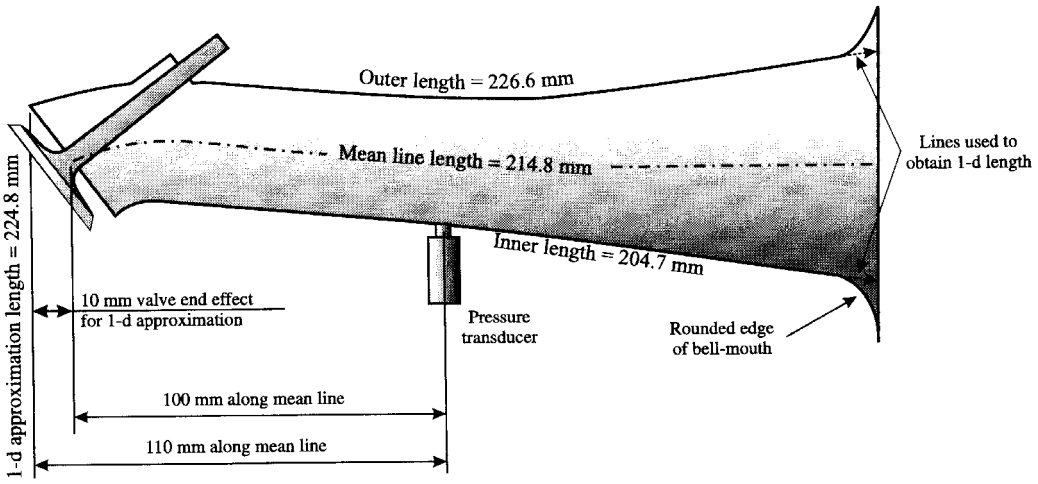

Figure 4.13: The inlet geometry dimensions used by Ferlet [299] to model a Formula One inlet manifold, showing the modifications made for the one-dimensional model.

is due to their short and wide inlet manifolds. The Formula One engine manifold modelled by Ferlet [299], shown in figure 4.12, is a typical example. Here the curve in the manifold and the valve angle relative to the manifold result in a significantly shorter path along the lower wall compared to that along the upper wall—in this example the length along the top wall of the manifold is 226.6 mm, and 204.7 mm along the lower wall. In engines with longer manifolds the 22 mm difference in lengths might not be a significant fraction of the manifold length, but in this case the variation is of the order of 10% of the entire manifold length. Thus there is a significant source of uncertainty as to which length to use in a one-dimensional model to represent this geometry.

A second source of uncertainty in determining the appropriate length to use is the fact that with manifolds that have a significant width to length ratio, the reflection point does not occur precisely at the end of the manifold, but a small distance outside it. This extra length adds an additional uncertainty into the true length to be modelled. In this example the manifold is around 200 mm long, and the diameter at the trumpet is around 50 mm, an aspect ratio of around 4. Thus the manifold is quite short and wide, so that significant end effects will occur.

To account for this length uncertainty, Ferlet determined an "end correction". A number of manifold lengths were modelled, and compared with the experimentally measured pressure waves. He found that a length of 224.8 mm gave the best reproduction of the inlet wave as shown in figure 4.13.

When the manifold length of 224.8 mm was used he reported good agreement

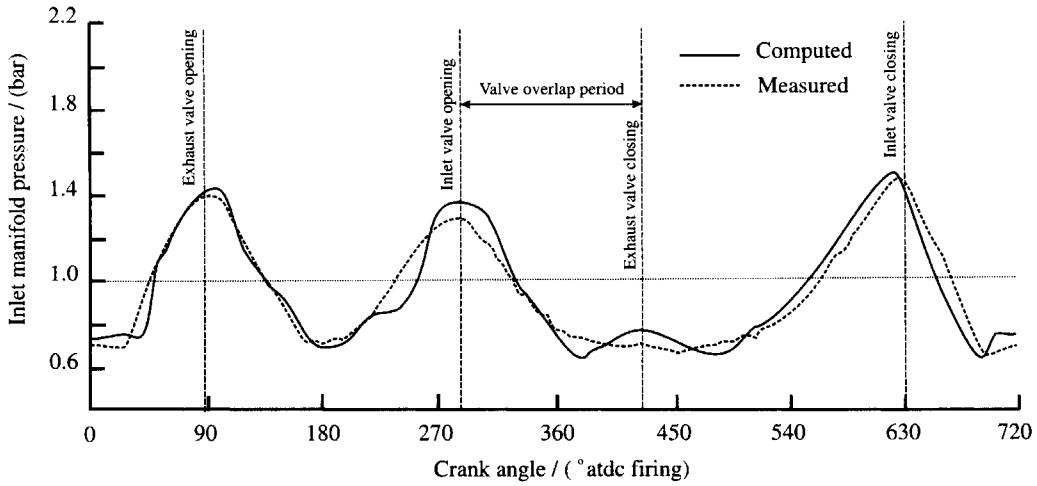

Figure 4.14: Comparison of measured and calculated pressure in the inlet manifold of a Formula One engine at 13000 rpm by Ferlet [299].

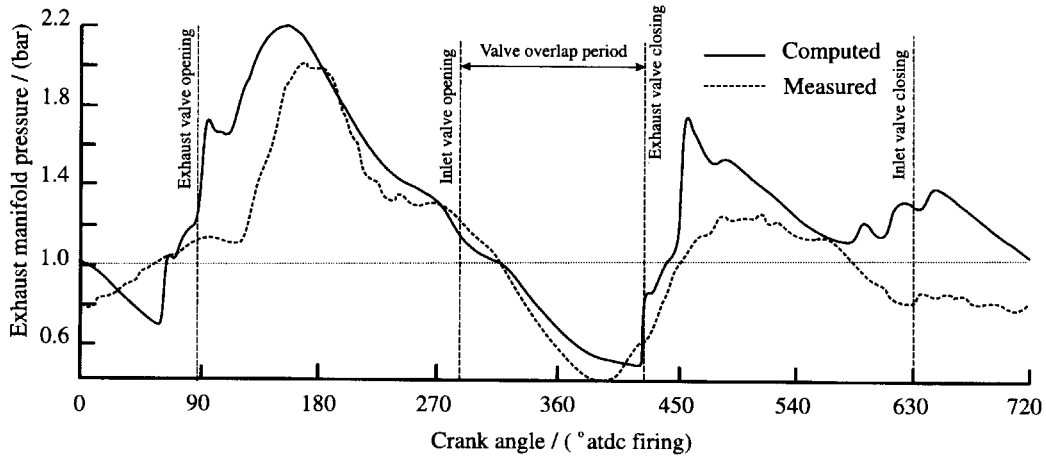

Figure 4.15: Comparison of measured and calculated pressure in the exhaust manifold of a Formula One engine at 13000 rpm by Ferlet [299].

between the model and the experimental results for the inlet manifold wave at speeds of 10000 rpm and 13000 rpm (the 13000 rpm result is shown in figure 4.14). However the agreement was poorer for the exhaust manifold wave, especially at 13000 rpm, as shown in figure 4.15.

Arbitrary adjustment of parameters until they fit experimental results to some extent defies the purpose of simulations, and certainly cannot be used where the design to be simulated is significantly different from that upon which the original end correction is based. It may be possible to determine a model for the end correction based on engine geometry and speed, but this is introducing yet another empirical relationship to the model. The model presented by Ferlet [299] incorporating its end correction in the inlet manifold would be a good tool for modelling the effects of minor changes to valve timing, engine speed or manifold geometry. The results are likely to be accurate provided that the reflection of the wave at the open end of the manifold remains similar, as would be the case if this section of the geometry is unchanged. His model would perform poorly if applied to a manifold of significantly different design, as a new end correction would need to be found.

Other examples of using one-dimensional models for high performance engines include:

- Novak and Kach [211] modelled a Ford NASCAR V8 engine, however no comparison with experimental results was included so no assessment of accuracy of the model can be made. The study is a use of the one-dimensional model to analyse the effects of valve timing and opening profile and the authors claim to have increased engine power by 40 hp;

- Boretti et al [48], who modelled a generic Formula One engine from 6000 rpm to 19000 rpm. Again, no comparison with experimental results is given so no assessment of accuracy can be made. The study analysed the effects of variable intake and exhaust manifold lengths, variable valve timing and resonance chambers and claims to have improved the engine's performance (maximum *BMEP* was increased from 14.0 bar at 12000 rpm to 15.8 bar at 10500 rpm) and smoothness of the torque versus speed curve;

- Boretti et al [50], who modelled a two cylinder 955 cc motorcycle engine between 7500 rpm and 12000 rpm. The results were in good agreement with experimental results in predictions of gross engine parameters. For instance engine power was predicted within 3% accuracy between 8500 rpm and 12000 rpm,

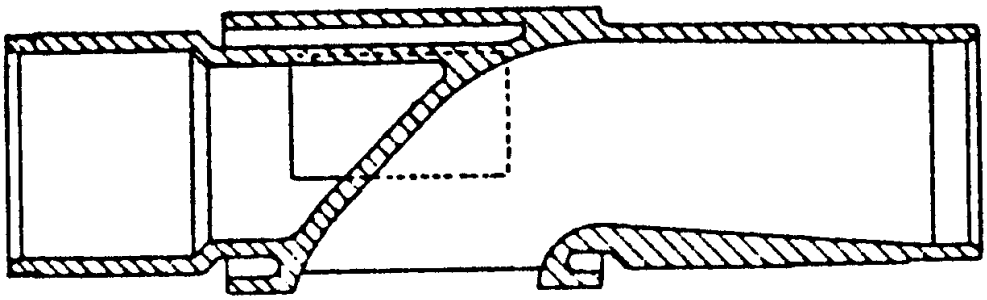

Figure 4.16: Cross section of the 1997 BRV geometry from Horrocks [141]. Cross section shown is through centre of the inlet port.

BMEP was predicted within 2% over the same range, and fuel consumption was predicted within 10%.

- Boretti et al [47], who studied a four cylinder, 16 valve motorcycle engine from 2500 rpm to 17000 rpm. Again, no comparison with experimental results was made so no absolute assessment of accuracy can be made, but a three-dimensional model was also performed and the one-dimensional results were in good agreement.

Clearly, despite the well known problems of applying one-dimensional models to high speed engines, many researchers have used them anyway. Generally the accuracy of these simulations remains acceptable, occasionally due to the addition of end corrections and other empiricisms. This type of model is most often used as a method of quickly estimating the trends in valve timing changes in a modification of manifold geometry, rather than as a way of predict the exact performance.

One-Dimensional Modelling of the BRV Engine

One-dimensional modelling was applied to the BRV engine by the current author [141] with limited success. The Method of Characteristics was used to model the flows in both a homentropic and non-homentropic configuration. The range of speeds tested was from 1800 rpm to 7200 rpm.

Using a one-dimensional model on the BRV engine not only suffers from the problems mentioned in the previous section, but introduces a new difficulty unique to rotary valve engines. In the BRV engine the valve window length is a significant proportion of the entire inlet manifold length, which causes a further uncertainty

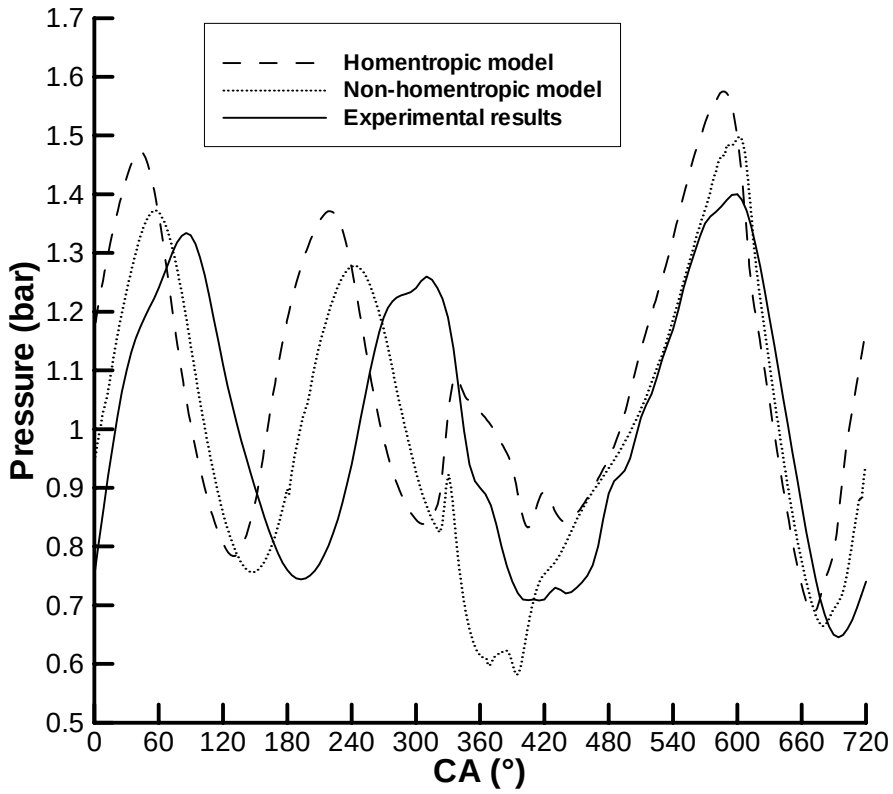

Figure 4.17: Comparison of modelled and experimental pressures in the 1997 BRV engine inlet manifold from Horrocks [141]. Engine speed is 5300 rpm, 610 mm inlet tract length, and pressure is taken at a point 122 mm from valve window centre.

as to the appropriate length to use in modelling the manifold. This is similar to the problem reported by Ferlet [299], who had a 10% difference in lengths along the top and bottom walls of the intake manifold. In the BRV engine studied by the current author [141], the inlet valve window length was 52 mm and the manifold mean line length was around 610 mm, as shown in figure 4.16. Thus the BRV engine also suffers from a variation in lengths of around 10%. No attempt was made to account for end effects.

Figure 4.17 shows an example of the simulation of pressure in the intake manifold. The model was able to predict gross engine parameters such as the effect of varying manifold lengths, valve timing or gas temperatures on volumetric efficiency. However, its accuracy was limited and this meant that it was not used as a design tool.

The BRV engine modelled in this study was an early design used for proof-of-concept testing. Since the early modelling performed in 1997 [141], the BRV engine design has progressed substantially such that it is now uses a much larger window of 80 mm length, and typical inlet manifold lengths have reduced to between 128 mm and 155 mm. This means that in the current configuration the valve window length is over half the entire manifold length. Obviously in this configuration the assumption that the valve boundary condition acts at a point at the end of the manifold is even less plausible than it was in the early geometry.

As has been discussed in section 1.3, one of the main features of a rotary valve engine is that it allows new combustion chamber shapes which were not previously possible with poppet valve engines. This feature manifests itself as a multi-dimensional flow in the cylinder. Obviously a one-dimensional model is unsuited for modelling this type of flow. Additionally, it has been shown that one-dimensional models are likely to be quite inaccurate in the short and wide inlet manifolds used in high speed engines and in particular the BRV engine. Hence a multi-dimensional model is required for this study.

4.4.2 Two-Dimensional Models

Multi-dimensional engine flows present a formidable challenge to simulate due to the complicated and moving geometry, high levels of turbulence, and wide range of flow regimes varying from almost stationary to the speed of sound. To successfully perform a full three-dimensional simulation to predict all of these aspects requires a high level of computing power. This power was not available to early engine simulation researchers so a common method of simplification was to model the

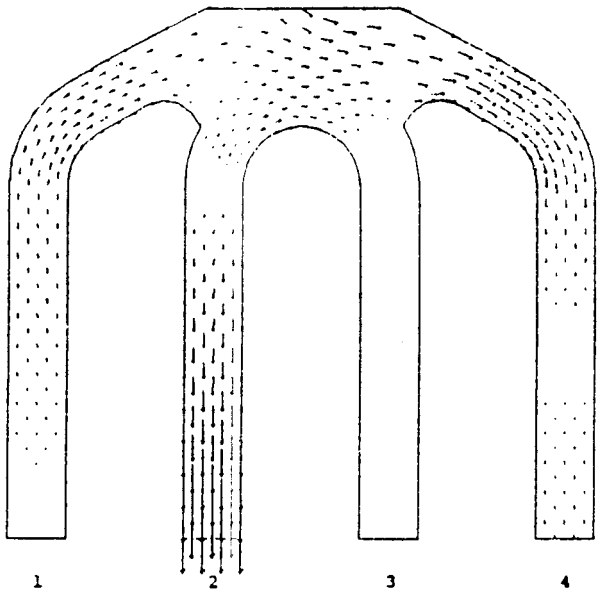

Figure 4.18: The flow field predicted in a four cylinder engine intake mainfold at 224 °CA by Chapman [59].

engine or component in two-dimensions.

An early use of two-dimensional numerical simulation of an engine manifold flow was the work of Chapman [59] who modelled the transient wave behavior in the intake manifolds of a four cylinder engine, as shown in figure 4.18. The cylinder was not modelled and the boundary conditions of the valves were approximated by valve discharge coefficients in a manner similar to that used in the one-dimensional simulations described in section 4.4.1. The geometry was assumed to be represented by a two-dimensional plane taken through the central plane of the inlet manifold.

Chapman's numerical model used the two-dimensional compressible Euler equations, which allowed modelling of the manifold pressure waves. However, the model failed to capture important real flow features such as separations, boundary layers, turbulence, friction and heat transfer. No experimental results are presented, and it is likely that the results are significantly in error as it could not resolve these important flow features. The work is significant, however, in that it appears to be the first application of multi-dimensional modelling to internal combustion engines.

Another example of an early work in multi-dimensional modelling was the work of Gosman et al [116], who employed a simplified engine model with no valve and an axisymmetric cylinder and piston arrangement. The simulation was performed only at low speeds of 10 rpm and 200 rpm, as it included no turbulence model.

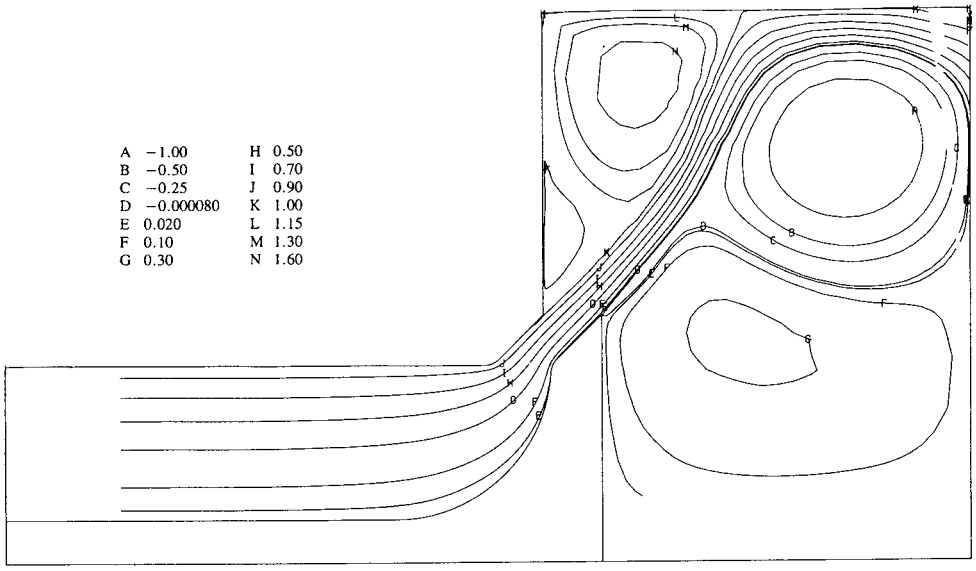

Figure 4.19: Streamlines predicted in an axisymmetric inlet valve by Naser and Gosman [204]. The configuration shown is at a moderate valve lift, and modelled using a composite turbulence model using a modified k-ϵ model in the main flow, and a one equation turbulence model near the wall.

Quite reasonable agreement was achieved between the simulation and experimental results for the velocity fields. This is the earliest study known to the current author of modelling in-cylinder flow.

Naser and Gosman [204, 205] performed two studies using a two-dimensional, axisymmetric finite volume numerical model on an exhaust and inlet valve respectively. These were performed to predict the valve discharge coefficient, C_D, at various valve lifts in comparison with experimental results. The k-ϵ turbulence model was used in both papers, with modifications to the empirical constants in the turbulence model to suit the particular flow of inlet and exhaust valves.

The inlet valve was modelled by Naser and Gosman [204] with an incompressible fluid as the pressure and temperature differences across the valve were small. An example of the streamlines predicted by their model is shown in figure 4.19. The numerical model results were compared with steady state experimental data with reasonable agreement, and they claimed that their modified treatment of turbulence allowed improved accuracy in prediction of valve discharge coefficients.

Other two-dimensional engine modelling studies have been performed by

- Huh et al [146], who analysed boundary layer and heat transfer models;

- Gorokhovskii and Khlynin [113] who modelled an axisymmetric two-dimensional compression stroke in an engine with a piston bowl;
- El Tahry [92] who assessed the accuracy of the Reynolds Stress turbulence model in an axisymmetric two-dimensional flow;
- Benjamin et al [35] who used an axisymmetric two-dimensional model to simulate flow in a pre-chamber stratified charge engine; and
- Hawkins and Wilkes [127] who used two-dimensional engine simulations as validation cases for the HARWELL-FLOW3D computational fluid dynamics code.

These works are further steps in the process of developing the modern three-dimensional models.

Two-dimensional simulations are used in contemporary engine research as a method of isolating and simplifying the part of engine behaviour which the researcher wishes to study. A good example is the recent work of Senecal et al [248], where a Diesel engine was optimised computationally. Variables adjusted included boost pressure, amount of exhaust gas recirculation, start of injection point, duration of injection and injection pressure. The cylinder was modelled as a two-dimensional axisymmetric geometry, and only the compression and expansion strokes were simulated. It was that assumed the gas exchange parameters would remain essentially the same for all combinations of optimisation variables. The two-dimensional model allowed simulation of the fundamental combustion effects, but ignored complicating issues such as inlet port geometry. The simplified nature of the geometry allowed the simulation to take only a short amount of time. Short run times are required as this type of optimisation method requires many simulations to be performed.

A two-dimensional simplified engine flow study is presented by the current author. It is used to simplify flow during the intake and compression stroke to allow modelling of a tumble vortex formation and breakdown. This is discussed in chapter 6.

4.4.3 Three-Dimensional Models

Three-dimensional models of internal combustion engine manifolds and in-cylinder flow evolved with increasing computer power. Early researchers modelled only one section of an engine's geometry to reduce the size of the simulation. Later

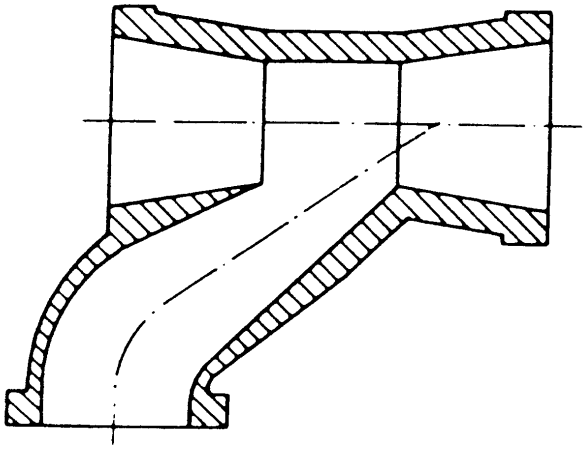

Figure 4.20: The exhaust manifold junction modelled by Leschziner and Dimitriadis [177].

three-dimensional steady state simulations became possible, and recently three-dimensional transient simulations have became practical. These areas have received much research attention recently, and a summary is presented below.

Engine Component Models

Early three-dimensional models of engine flows were only used to investigate one component of the system, for instance, the valve or a pipe junction. This was done to reduce the problem size to be suitable for the computing power available at the time. More recently, some researchers continue to model only one section of an engine so that the flow in that section can be analysed in more detail than is possible when it is part of a larger model.

This type of model introduces the problem of what conditions to specify at the boundaries. This is an obvious limitation of this type of simulation.

A pioneering series of papers in the multi-dimensional simulation of internal combustion engine flows was presented by Dimitriadis and Leschziner [89, 177], who modelled an exhaust manifold pipe junction. They used a three-dimensional finite-volume method, and an incompressible, steady state fluid with the k-ϵ turbulence model. The equations were solved using the SIMPLER algorithm proposed by Patankar [223]. The geometry modelled is shown in figure 4.20. Results were in reasonable agreement with experiment, and all major effects such as recirculations were successfully modelled.

The purpose of Dimitriadis and Leschziner's works was to develop a three-

dimensional sub-model of a pipe junction to incorporate into a MOC or Lax-Wendroff one-dimensional model of the entire engine. To the current author's knowledge this has never been performed using the numerical model developed by Dimitriadis and Leschziner. However, the significance of these works is that they are pioneering multi-dimensional models which have helped to pave the way for the more complex simulations of today.

Kuo and Chang [167] used a three-dimensional model of a section of the intake manifold of a port fuel injection spark ignition engine to analyse injection spray behaviour. Spray behaviour in intake manifolds is quite a major research area as fuel behaviour in the intake manifold can have a significant effect on engine emissions. With emissions regulations becoming increasingly strict it is necessary to analyse in detail what is happening to the fuel as it is injected. Understanding of the behaviour of fuel in the inlet manifold of a production car engine is vital to minimise emissions.

Roberts et al [238] used a CFD analysis of an intake manifold to estimate losses on a concept high performance production car engine design. The aim was to develop a 4.3 L V10 engine suitable for sporting luxury vehicle within a period of one year. To allow engine development to be completed in this short time schedule, a simple CFD model was used in the concept design phase of the inlet manifold system to identify the best inlet manifold size. This allowed the design to be optimised on the computer before any prototype manifolds were made, significantly reducing the number of design iterations.

Flowbench Models

A three-dimensional model which has been performed by many researchers is that of steady state flow through the engine manifolds, or a flowbench model.

Aïta et al [16] did some early modelling of three-dimensional steady state flow in engine inlet manifolds. The mesh used had 40000 nodes, which is coarse by today's standards. The work showed significant differences between experimental and simulated results, however the results were good enough to be useful as a guide to design.

Luo and Bray [184] modelled two- and three-dimensional steady state flow using k-ϵ and Reynolds Stress turbulence models. The two-dimensional models were cross sections of the geometry through the centre of the inlet valves. When compared to experimental hot wire anemometry data, the three-dimensional model was found to predict the flow field with far better agreement than the two-dimensional models, but the turbulence was predicted better by the two-dimensional Reynolds

Case	Initial	1	2	3	4	5
Quantity to maximise		C_D	SR	C_D	C_D	C_D
Restrictions		none	none	$SR > 0.4$	$SR > 0.35$	$SR > 0.3$
$\mathbf{C_D}$	0.61	0.64	0.50	0.607	0.613	0.626
SR	0.24	0.25	0.42	0.4	0.35	0.3

Table 4.2: Optimised valve discharge coefficient (C_D) and swirl ratio (SR) for an intake port design. Adapted from Trigui et al [276].

Stress model then the two- or three-dimensional k-ϵ model. They suggested a three-dimensional Reynolds Stress model would give the most accurate simulation, but did not perform the simulation. This presumably is due to the high computational cost of performing three-dimensional Reynolds Stress simulations.

In a series of papers from a collaboration between Clemson University and Diesel engine manufacturer Caterpillar [79, 219, 273, 274], the flow in the intake manifolds of a series of Diesel engines was modelled in detail to identify areas of losses. The meshes used were extremely detailed and included up to $850,000$ cells. There was very good agreement with experimental results, ranging between 5% and 8% discrepancy depending on the valve lift simulated.

The fine grid allowed them to identify areas of losses in the intake manifold and valves, as shown in figure 4.21. Figure 4.21b shows simulation results of the original design near the valve area which had a constriction at the valve trailing edge and a head design that caused the flow from the valve to leave at a large angle. The cylinder head design was modified to eliminate these problems, and the simulation of the new design is shown in figure 4.21c, where it shows no valve training edge constriction and a shallower angle of departure from the valve region. The modifications made to the design reduced pressure loss by up to 33% over the original design.

The Ford Motor Company has produced a series of papers [14, 276] using automatic CFD optimisation of steady state intake flow. No experimental work is reported. The intake manifold was parametised using factors describing its width, height and curvature. An in-house code was used to develop the port geometries and project the grid onto them, and a commercial code (Star-CD) was used to perform the numerical simulation. They applied their model to the optimisation of the compromise between swirl ratio and valve discharge coefficient, and a summary of their results is shown in table 4.2. The trade-off between swirl ratio and volumetric efficiency (expressed here as valve discharge coefficient) as described in section 4.2.3

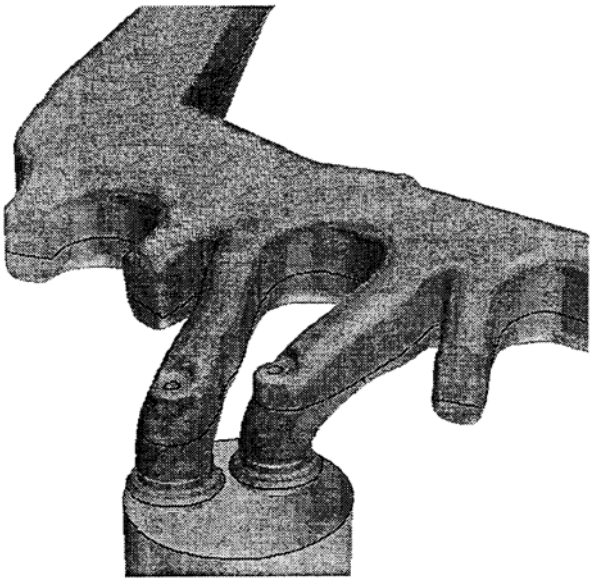

(a)

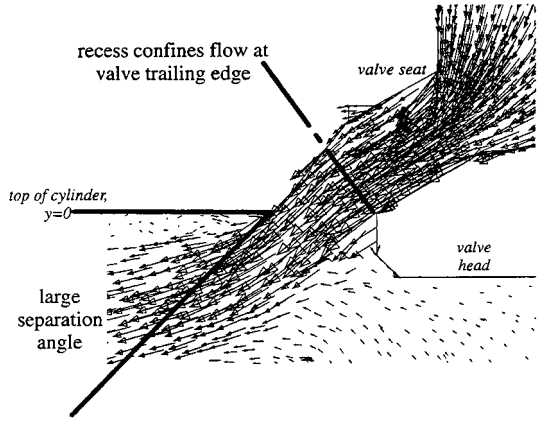

(b)

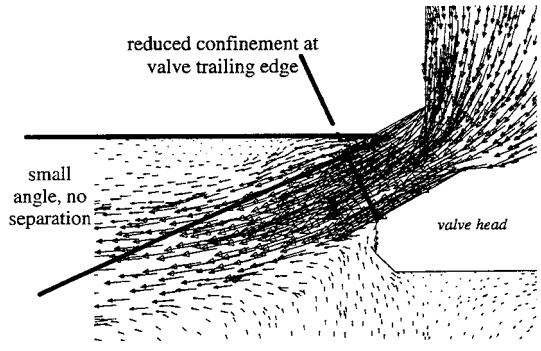

(c)

Figure 4.21: The inlet geometry and results from Taylor et al [273]. (a) – Section of geometry modelled; (b) – Detail of results from valve region, original design; and (c) – Detail of results from valve region, modified design.

is also shown here in table 4.2.

As mentioned in section 1.4.2, a feasibility study was performed by Storer and Nelson [265] on a rotary valve system for a small G-Kart racing engine. The study included a CFD analysis of steady state flow in the proposed engine. The model used was crude and simple in comparison with other flowbench simulations, for instance, the finest grid used only had 4800 cells. This is more than an order of magnitude less dense than some other studies, and would certainly not be grid independent. No experimental work was performed, and it is unlikely that their analysis was very accurate or picked up all flow features. However, it is a demonstration of CFD being used at the concept design stage to establish the major features of the flow, where a quick analysis is performed to establish if the concept is worth pursuing to the detailed design stage. CFD can be useful as a quick method of analysing initial design concepts where absolute accuracy is not required, just general trends. Of course, this assumes that the simulations have sufficient accuracy to give at least a quantitative idea of the flow.

Recently, using a one-dimensional model to predict the behaviour in the long sections of the manifolds and a three-dimensional solver to predict flow in complicated regions such as valves and junctions has become practical. Examples of commercial codes which can do this are Ricardo's WAVE [8] which can link to the three-dimensional solver STAR-CD, and AVL's BOOST [2] which can link to the three-dimensional solver FIRE.

An example of combining one- and three-dimensional simulations is the work of Boretti et al [47], who modelled air flows in a high performance motorcycle engine. They initially performed a traditional three-dimensional simulation to predict valve discharge coefficients, which were then used in a one-dimensional simulation of the flow in the inlet and exhaust manifolds. They carried out a second simulation for the maximum torque point (13000 rpm), in which a section of the exhaust manifold was modelled using a three-dimensional code, and the inlet manifold was modelled using a one-dimensional simulation. The results from the combined one- and three-dimensional model was quite similar to the full one-dimensional model results, no doubt due to the fact that the only section of the exhaust manifold that was modelled in three-dimensions was a pipe junction and the muffler. The flow around the inlet and exhaust valve was still modelled using valve discharge coefficients.

The accuracy of combined one- and three-dimensional simulations is assessed by Sinclair et al [254]. They report promising accuracy in the results of the simulations; however a number of factors, such as turbulence and boundary layer issues require

further investigation.

A further variation on the standard use of a flow bench is presented by McLandress et al [190], in which a Diesel engine intake manifold and dual intake valve arrangement was studied experimentally and by CFD simulation. A traditional flowbench was modified so that the valves could be actuated to represent an engine speed of 600 rpm, eliminating the steady state nature of the flow. Results predicted by a k-ϵ and RNG k-ϵ turbulence model were compared to experimental results, and showed moderate agreement. Large scale flow features were captured, but some smaller vortices predicted by the CFD did not appear on the experimental results.

A method used by some researchers to reduce the fluid velocities to make experimental analysis easier is to use a different working fluid. Generally water is the fluid used in these models, resulting in a $1:23$ velocity ratio after scaling with Reynolds number. This technique is only useful for performing a flowbench type analysis where the Mach number is low and there are no significant compressibility effects. Examples of this technique include Bensler et al [36] and O'Connor and McKinley [213].

O'Connor and McKinley [213] performed a CFD and experimental study of a dual intake valve engine in a steady state flow situation, using both water and air as working fluids. They used an automatic meshing procedure which simplified the generation of the complicated meshes required, an example of which is shown in figure 4.22. Their results show reasonable agreement with experiment, with swirl ratio being predicted to within 5%, and major flow structures being successfully captured. However, the predictions of turbulence levels had considerable error and it was found that increasing the mesh density did not significantly improve accuracy. No comparison of air and water results was performed so the accuracy of the change in working fluid cannot be assessed.

Other working fluids have also been used. For instance, Mahmood et al [185] used an oil based fluid. They performed an analysis of three-dimensional flow through a dual intake port Ford Zetec spark ignition engine, achieving good agreement with experimental results. Again, no comparison to results using air as the working fluid was performed, so the accuracy of using the oil based fluid cannot be assessed.

It is well known that steady state testing and the related CFD simulations are extensively used by engine manufacturers. Examples of this include the report of Pierson and Richardson [226] of CFD modelling at Jaguar of their AJ-V8 engine

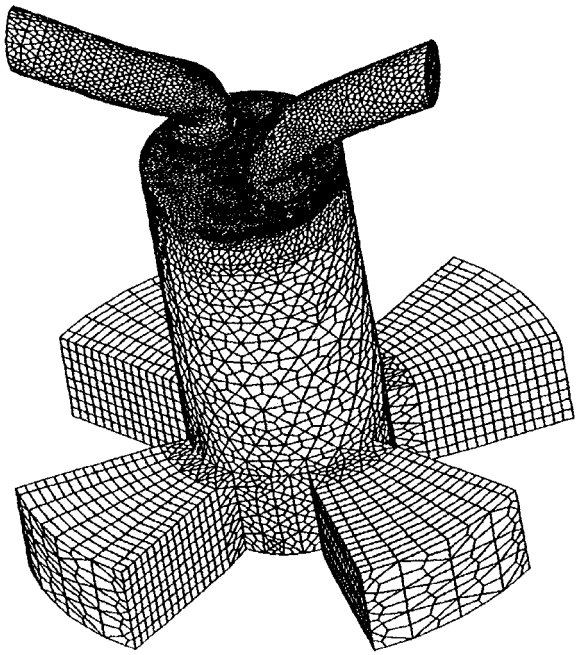

Figure 4.22: The mesh used in the water analog steady flow geometry modelled by O'Connor and McKinley [213].

intake manifold, the work of Miyauchi et al [194] which outlines development done on the GM132 and GM182 engines by engineers at Mitsubishi, Blaxill et al [45] report on work done by Cosworth Technology on spark ignition engine intake ports, and Caulfield et al [58] report on a comparison of CFD codes for steady state flow-bench simulations performed by Mercury Marine, Briggs and Stratton, Kohler and Harley-Davidson Motors. This demonstrates that despite the limitations involved in extrapolating flowbench data to real engine applications as described in section 4.4.1, flowbench models, either as experimental models or CFD simulations, are an essential part of modern engine development.

Full Three-Dimensional Engine Models

Although flowbench models are widely used in the engine design industry today, only the full three-dimensional, transient models of an engine offer the possibility of capturing all of the features of engine flows. Of course, this comes at the expense of complicated simulations requiring large computers and long run times.

Early engine modellers wrote their own codes as no existing computer programs were available. Examples of this early work include Wakisaka et al [289], who developed a three-dimensional model of an engine cylinder to analyse swirl and

tumble flows. Their model was greatly simplified with the domain being cylindrical and the valve being modelled as a disk just below the inlet manifold port. The model showed trends of swirl and tumble ratios during the intake stroke, but as the geometry had to be drastically simplified from that of a real engine, their results cannot be extrapolated to realistic engine geometries with certainty.

The work of Gosman et al [117] is another early study. The geometry was a simple axisymmetric valve and cylinder, where the valve had a mask on one side to create a tumble flow field. They note that the accuracy of their simulation was "at best moderate", but sufficient accuracy existed to describe the fundamental processes occurring during tumble vortex break down.

Very few researchers develop their own codes today. Commercial codes have been developed that are reasonably easy to use, contain all of the required sub-models and can be quite accurate. The knowledge required to write these codes is now very specialised skill due to the complicated nature of the numerical and physical modelling required. The development of a viable code takes many years. The use of a commercial code allows the researcher to access this high level of development to perform simulations far quicker than is possible when developing their own code.

An early code used to model transient engine flows was the CONCHAS SPRAY code developed by Los Alamos National Laboratory. This family of codes was developed by Amsden et al [18], and incorporated models for all major engine functions, including compressible three-dimensional flow, spray modelling, species transport, mixing and combustion. The CONCHAS SPRAY code was used by a number of researchers [57, 281], and it has now been superseded by the KIVA family of codes. KIVA is now by far the most commonly used code in engine modelling publications, and is well known for engine modelling. Many new or improved physics models in the code have been published [216]. Examples of its use are extensive [249, 94, 134, 169, 164, 231, 174, 166, 41, 203, 220, 246, 307, 243, 242, 11, 261, 136, 80, 86, 125, 19, 248, 304, 131, 165, 162], from low speed Diesel engines [94] to high speed Formula One engines [41]. Recently the Los Alamos National Laboratories group announced the development of a new code, CHAD, to supersede KIVA [218, 128, 217].

An example of the use of the KIVA code on high performance engines is presented by Bianchi et al [41], who performed simulations on a Formula One engine cylinder. The primary purpose of the research was to determine the effect of bore to stroke ratio on engine performance. The simulations were only run for the compression stroke, and used initial conditions at inlet valve close from predictions of the intake stroke performed by other researchers, as shown in figure 4.23b. Only half the

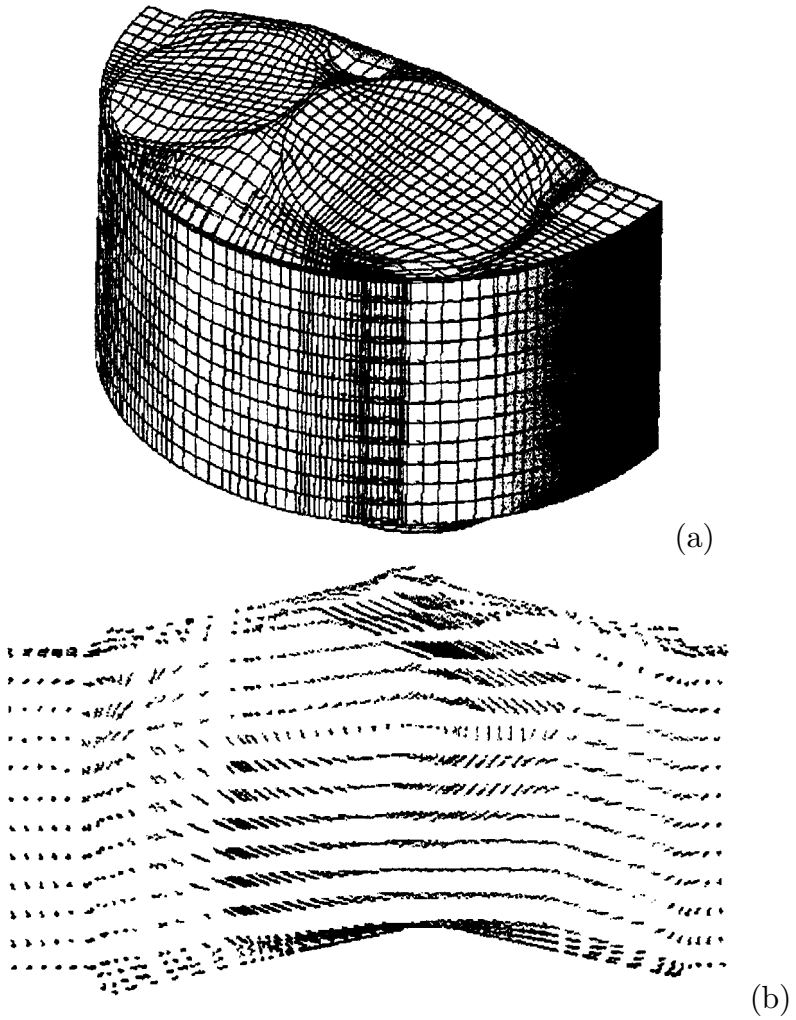

Figure 4.23: Simulation of Ferrari Formula One engine by Bianchi et al [41]. (a) – Computational grid; and (b) – Initial flow field at IVC, at $Y = 15\,\text{mm}$.

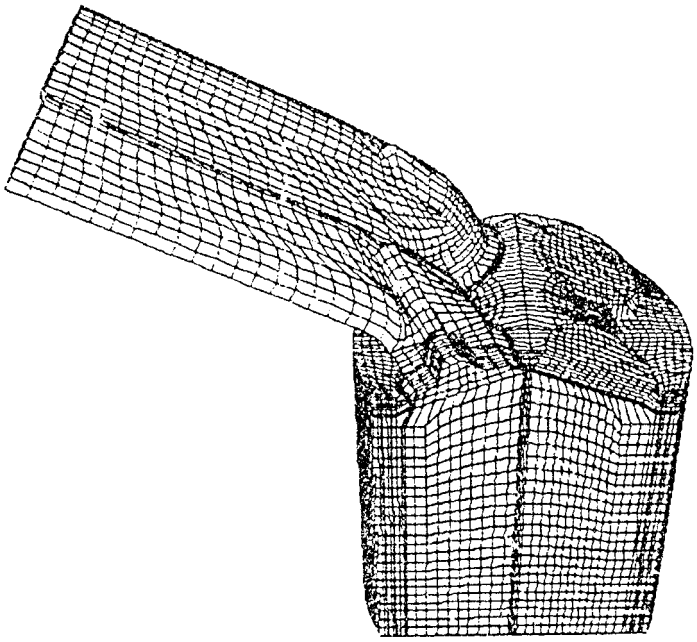

Figure 4.24: The direct injection spark ignition engine simulated by Han et al [125]. Grid is shown at BDC, and a slice is taken through an inlet valve.

combustion chamber was modelled as the geometry was symmetrical, as shown in figure 4.23a. The accuracy of this assumption was not tested. Results showed reasonable agreement with experimental results.

A study analysing the effects of bore to stroke ratio on the BRV engine has been performed as part of the current work, and will be discussed in section 8.6.

KIVA has also been used to model the intake stroke of engines. Han et al [125] simulated a direct injection spark ignition Ricardo research engine. Part of the mesh used is shown in figure 4.24. Agreement with experimental results was reasonable, with an example of the flows predicted in this work shown in figure 4.25, where the flow field at BDC is shown.

A second very widely used code in modern engine simulations developed from the early work at Imperial College by Gosman and his colleagues [21, 117, 114]. The early unnamed code was used by a number of other researchers [279, 297, 288, 66, 202]. This code then developed into the Star-CD code, which is used often in modern engine simulations [115, 181, 151, 33, 61, 49, 41, 145]. An example of a simulation performed using this code is presented by Gosman [115], who describes the simulation of a Mercedes-Benz M111 spark ignition, four valve engine, including sub-models of fuel behaviour and combustion. The model achieved very

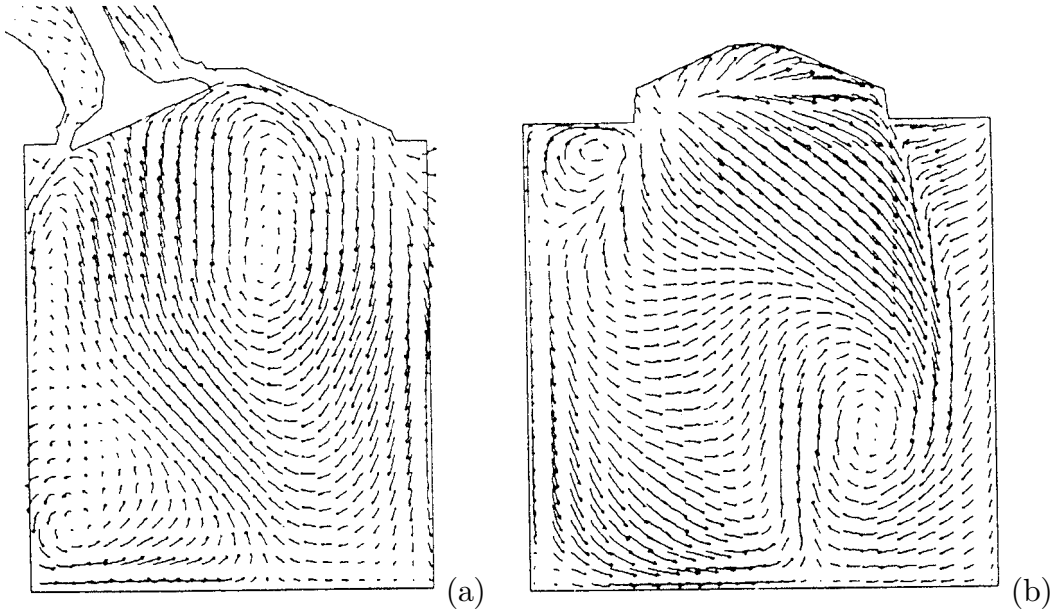

Figure 4.25: Flow fields predicted by Han et al [125] in a direct injection spark ignition engine. (a) – Plane through inlet valve at BDC; and (b) – Plane through cylinder symmetry plane between inlet valves at BDC.

good agreement with experimental results, an example is shown in figures 4.26 and 4.27. A further feature obvious from figure 4.26a is that visualisation techniques have advanced significantly. The three-dimensional data produced by the simulations can now be viewed as a three-dimensional data set, rather than merely as two-dimensional slices. Effective visualisation is a vital, and often undervalued component of an effective CFD simulation. Unless the flow is adequately visualised it is not possible to understand what is happening. The study presented by Gosman [115] is an example of the development of better simulation models, as well as better visualisation techniques.

Other commercial codes which have been used for engine modelling include the CFX family of codes. CFX has been used by a small number of researchers in engine modelling [100, 264, 184]. The FIRE code developed by AVL-List has also been used [85, 170, 258, 140, 291], Fluent has also been used to a small extent [197] and the VECTIS code developed by Ricardo is used occasionally [95]. Some engine manufacturers have developed their own in-house codes, such as the N3S-Natur code developed by Renault [30], CRUNCH by Ford [256] and ESP by General Motors [159, 160].

A common method used to simplify simulations is to only model the combustion chamber of the engine. This approach simplifies the geometry substantially as the manifold and valve geometry are no longer required. This type of model is

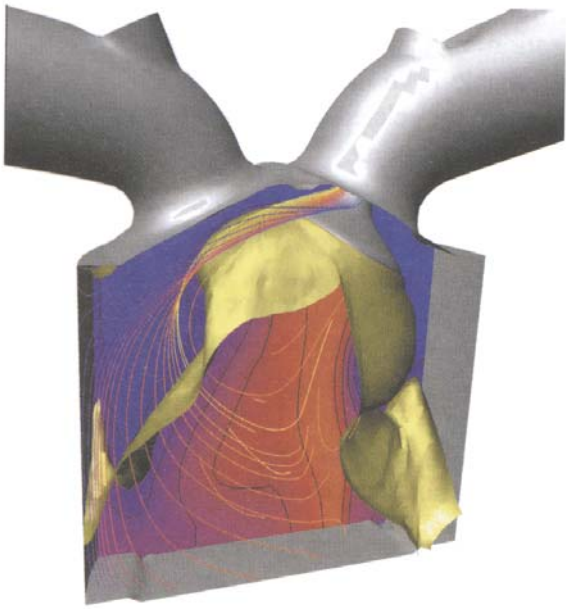

(a)

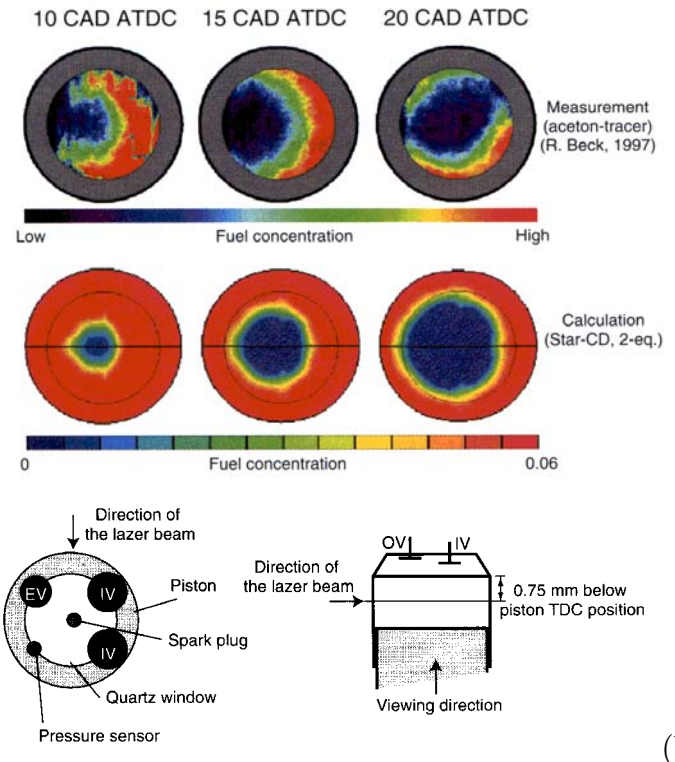

(b)

Figure 4.26: Simulation of Mercedes-Benz M111 four valve spark ignition engine, reproduced from Gosman [115]. (a) – Flow visualisation during intake stroke; and (b) – Flame propagation.

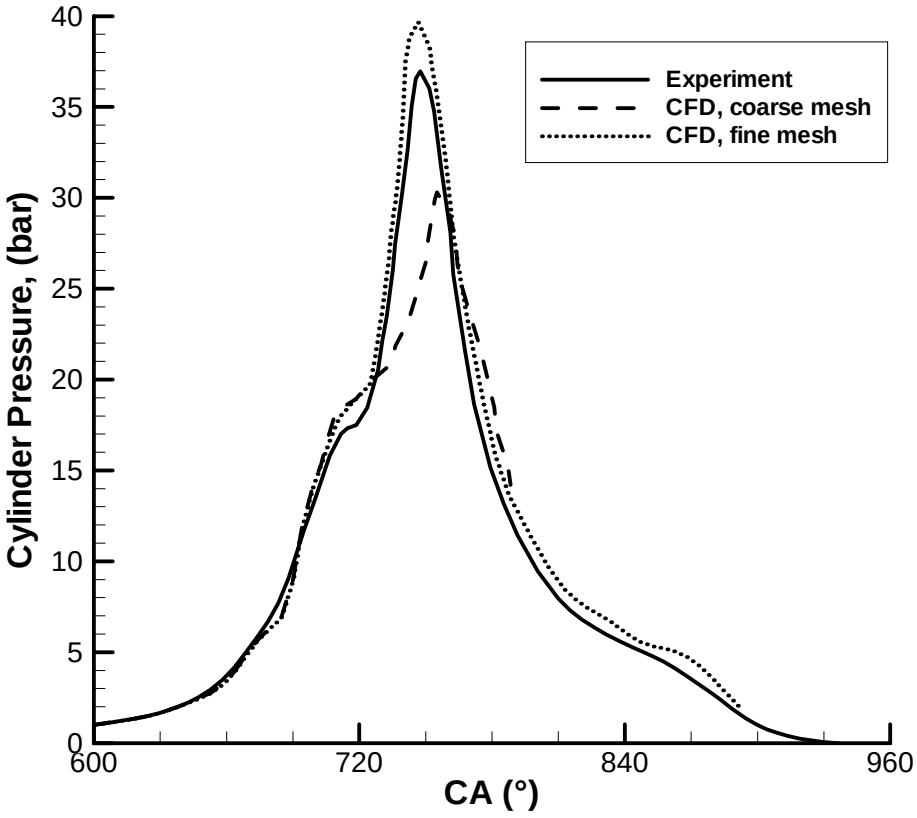

Figure 4.27: Cylinder pressure predicted for the Mercedes-Benz M111 four valve spark ignition engine, reproduced from Gosman [115].

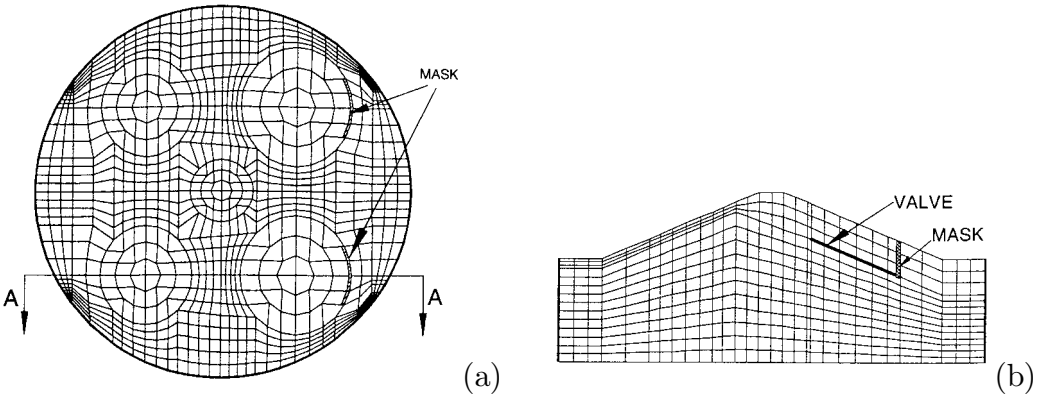

Figure 4.28: The cylinder mesh used by Das and Dent [80]. (a) – Mesh cross section, (b) – Mesh through plane A-A. Note valve modelled by a thin surface and a mask.

often used when only the compression and expansion strokes are simulated, such as when simulating of combustion [18, 264, 85, 166, 203, 220, 246], two stroke engine scavenging [281, 57], spark ignition direct injection fuel spray behaviour [246], or to study in-cylinder flow, such as swirl or tumble [289, 139, 117, 21, 297, 66, 288, 279, 242, 80].

This method has the disadvantage that the effect of the inlet manifold must be artificially imposed. If the intake stroke is modelled then the valves can be replaced by a flow of a known direction [279, 281, 85, 289, 288], or by assuming the valve to be a disk around which the inlet flow passes [246, 80, 57, 66, 21, 117, 288, 289]. If the compression stroke only is modelled, an initial flow must be assumed, usually near inlet valve close [297, 203, 220, 166]. Both of these techniques result in an initial condition or inlet valve boundary condition which is only an approximation of the true inlet flow, and accurate predictions cannot be expected. This type of approach is useful in studying the basic nature of in-cylinder flow [80, 279, 281, 297] or the fundamental processes of combustion [166, 203, 85], but the results cannot be transferred to a real engine with any certainty.

An example of a simulation using the combustion chamber only is the work of Das and Dent [80], who analysed the behaviour of tumble flow fields during the intake and compression strokes. The mesh used in this study is shown in figure 4.28. To reproduce the effects of the intake manifolds the valves were modelled as disks with masks to create the tumble flow field. Das and Dent claim that the results are "generally in agreement" with experimental results, but this conclusion is difficult to justify as the only correctly predicted result appears to be the direction of rotation of the tumble vortex. None of the other structures seen on the simulations appear in the experimental results. This lack of accuracy highlights the problem in

performing simulations using simplified inlet manifolds.

In simulating three-dimensional in-cylinder flows most researchers use the cylinder and intake manifold geometry. This method is suitable for modelling the intake, compression and expansion strokes. Most researchers only model the final section of the intake manifold before the cylinder, assuming the entry boundary condition to be either a constant pressure [33, 60, 125, 287] or a varying pressure described by a one-dimensional simulation or experimental results [19, 86, 95, 174, 231, 258]. None of these works appear to have had interaction between the one-dimensional simulation and the three-dimensional simulation of the valve and cylinder region, so that the interaction between the valve region of the intake manifold and the rest of the manifold is not captured. Most of this research describes studies of Diesel engines [61, 249, 307] or spark ignition engines designed for production cars [95, 174, 231, 86, 19, 287, 60, 125, 197, 169, 258, 33] where the highest speed modelled is 3000 rpm. At these low engine speeds the wave effects in the intake manifold are small, or adequately predicted by a predetermined pressure against time function.

A second approach, which is a better method for capturing the dynamic wave effects but is obviously more computationally costly, is to model the entire intake manifold from the throttle (in a part-throttle simulation) or the inlet trumpet or plenum (in a full throttle simulation). This allows the model to capture the flow in the entire inlet manifold, together with all interactions. This has the added benefit of being able to capture any three-dimensional flows occurring in the intake manifold, including separations and boundary layer growth. This type of model does not suffer from any of the problems encountered with one-dimensional modelling discussed in section 4.4.1.

A few researchers model the entire intake manifold using incompressible flow, so that the intake wave is not resolved, but separations, fuel behaviour and boundary layer effects are resolved [100, 94]. Most researchers, however use a compressible formulation of the Navier Stokes equations so that all inlet manifold behaviour can be resolved [136, 261, 243, 160, 159, 49, 169, 115, 125, 133]. A number of these studies are on Diesel engines [243, 261, 136], where the engine speed is low so the inlet manifold wave effects will be small. The heating and increase in pressure of the charge during the compression stoke can only be modelled by a compressible version of the Navier Stokes equations, so presumably these researchers use the compressible Navier Stokes equations so the same code can be used for both intake and compression strokes. Most studies of spark ignition engines use the compressible Navier Stoke equations [169, 49, 159, 160, 115, 125, 133].

Very few publications involving a three-dimensional model of an entire engine

cycle were found. One example is the work of Lisbona [181], who presents a full cycle simulation of a JTD 10V engine developed by Fiat, for the Alfa Romeo 156 automobile. They comment that the exhaust part of the simulation is "extremely delicate", because of the large pressure and temperature gradients that occur in the early part of the exhaust stroke. An example of the flows predicted in the exhaust stroke is shown in figure 4.29. Figure 4.29a shows the early exhaust stroke, where the exhaust gas is being driven by the high cylinder pressure. The pressure gradient here is large, causing high velocity flow with large separations. Figure 4.29b shows the exhaust flow later in the stroke, where the flow is being driven by the piston pushing the exhaust gas out of the cylinder. This period of flow is typified by lower pressure gradients, smaller separations and lower velocities. The flow is also seen to bend more before separating than is seen in figure 4.29a. Experimental results for the cylinder pressure are presented and agree reasonably well with the simulations, however no experimental results are presented for validation of the exhaust stroke flow.

A simulation of both intake and exhaust strokes is also presented by Sinha et al [256]. The paper is presented as a demonstration of the capabilities of the code rather than as a serious study of an engine and thus the results are not examined in detail and no comparison with experimental results is included.

Soltani and Veshagh [258] wrote a brief description of performing a "repeated cycle calculation" where the simulation is run for a complete cycle and the intake stroke is repeated to assess whether the change in initial conditions for the second stroke effects results. They found that after an initial "adjustment" phase of around 60 °CA from the start of the intake stroke that the results between the first and second strokes were very similar and the maximum differences between averaged in-cylinder quantities such as pressure, temperature, swirl or tumble were at most 5%. They do not state how they performed the exhaust stroke or the scavenge parts of the simulation.

Other researchers show solid models of exhaust manifolds, but do not describe the simulations including exhaust strokes [30, 115, 151].

The geometry of two stroke engines is quite different to that of four stroke engines, especially for engines with crankcase scavenging [170, 140]. This field presents similar difficulties to those found in modelling the full cycle of a four stroke engine, with similar techniques used to overcome them.

Only two studies could be found which describe three-dimensional modelling performed on high speed engines. The first is the study of bore to stroke ratio in Formula One engines by Bianchi et al [41], which has already been discussed. The

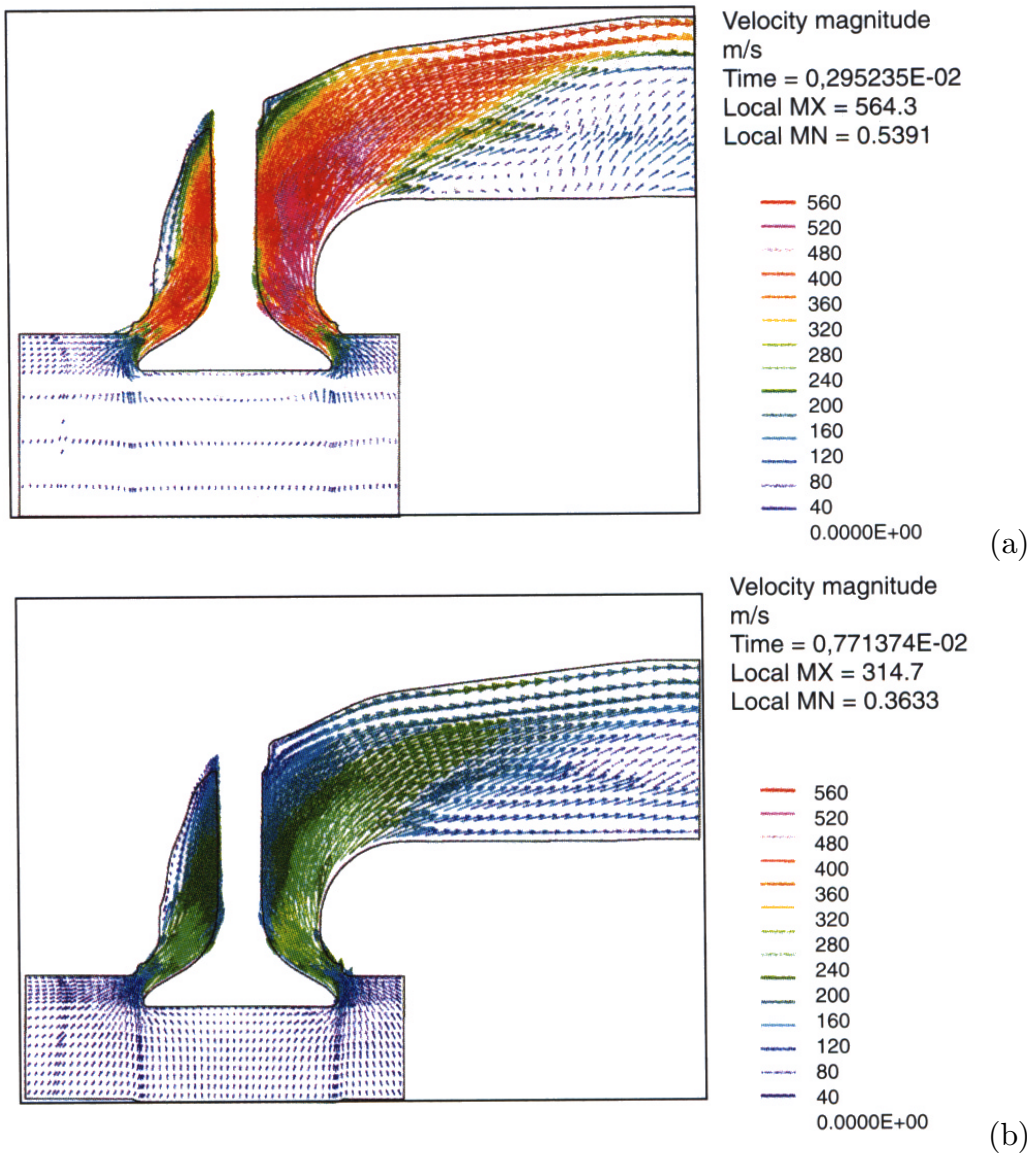

Figure 4.29: Simulation of the exhaust stroke of a spark ignition engine from Lisbona [181]. (a) – Velocity field at 150 °CA before TDC and (b) – Velocity field at 50 °CA before TDC.

second is by Boretti et al [49], who presents work on a high speed motorcycle engine using the Star-CD and SPEED codes. A simple combustion model was included in the model. No comparison to experimental results was performed. Their simulations predicted a relationship between high volumetric efficiency and high turbulence levels in the compression stroke, which lead to reduced combustion duration. They also found back flow during the valve overlap period to not only reduce volumetric efficiency, but to also lessen turbulence during the compression stroke. These effects have also been found by the current author on the BRV engine, and are discussed in section 8.1.

New Developments in Engine Modelling

New techniques of modelling the Navier Stokes equations are being developed by a small number of researchers. Some researchers have tried a radical departure from existing methods, including Sugiura et al [266] who developed a "method of lines" for use in engine modelling, Nkonga and Guillard [208] who developed a Godunov method for unstructured grids and used an engine geometry as an example of its use, or Tu and Fuchs [280] who developed an overlapping grid method for application to engine modelling to simplify the modelling of poppet valves. All of these models are in the developmental stage only, and have not been used as a serious engineering design tool at this stage.

A small number of researchers are testing very different methods for engine modelling. Haworth and El Tahry [129] performed some simulations using probability density function (PDF) methods coupled with a Monte Carlo Lagrangian solver. The PDF approach is potentially superior to traditional Reynolds-averaged turbulence models in complex flow fields with chemical reactions, such as combustion. Also, a Lagrangian "boundary vortex" method has been applied to a number of simplified engine geometries by Gharakhani and Ghoniem [109, 108, 110]. Again, neither of these methods have been applied to realistic engine geometries to the current author's knowledge, and have not progressed beyond the developmental stage.

Halliday et al [124] simulated a single intake valve engine using a statistical kinetic theory model rather than the traditional Navier-Stokes based models. Recent increases in computing power and developments in gas kinetics theory have made this type of modelling possible. It is based on the assumption that the gas can be represented with a large number of "particles", each of which represent a large number of individual gas molecules. The particles interact with each other and their surroundings in a comparatively simple manner. There is no requirement to solve

complicated non-linear partial differential equations as exists with Navier-Stokes based methods. The models presented used up to 3.9×10^6 cells, far more than is possible in all but the largest Navier-Stokes simulations. The accuracy of the predictions was quite good at 3.2%, 2.3% and 6.0% respectively for the low, medium and high lift cases. Swirl ratio was predicted within a similar accuracy. This type of method is in its infancy now, but shows great promise for the future.

4.5 Turbulence in In-Cylinder Flows

4.5.1 Reynolds Averaging

Superficially, ensemble averaging appears to be the most appropriate method of averaging fluid variables in an internal combustion engine as the flow in an engine repeats every engine cycle. An instantaneous "snapshot" of the flow is measured at a specific point in the engine cycle, and repeated over a large number of cycles until a statistically significant average value is determined. This is the method used in the majority of experimental analyses of engine in-cylinder flows [242, 241, 168, 64, 95].

In multi-dimensional in-cylinder flow simulation, however, a time averaged approach is usually used. The standard technique used to model in-cylinder flow is the Reynolds averaged Navier Stokes equations, with turbulence modelling provided by a k-ϵ based turbulence model. This technique is described in chapter 2, and has been used by almost all of the multi-dimensional engine simulations mentioned in the previous section.

All three forms of Reynolds averaging are equivalent in the case of stationary, homogeneous turbulence. This is known as the ergodic hypothesis [298]. However, in an internal combustion engine the turbulence is neither stationary nor homogeneous. A problem can now be seen, being that experimental models and numerical simulations often use different definitions of turbulence, and that they are not necessarily equivalent.

Attempts to fix this lack of a direct comparison have been published recently, for instance Marc [187] performs spatial Reynolds averaging on experimental PIV and LDA data; and Haworth [128] and Haworth and Jansen [130] have simulated engine flows over a number of cycles, which allows an ensemble average to be performed. These publications can only be regarded as preliminary, and at the time of writing no thorough validation of numerical and experimental results using equivalent definitions of turbulence for engine flows has been performed.

4.5.2 Limitations of Reynolds Averaging

Reynolds averaging suffers from some fundamental problems.

Time averaging assumes that there is a clear distinction between the turbulent time scales and the mean flow time scales so that the averaging time can be an intermediate time interval. This has also been found not to be the case for in-cylinder flow, as the low frequency turbulent time scales and the high frequency average flow time scales are of similar durations [23].

Volume averaging assumes that there is a clear distinction between the turbulent length scales and the mean flow length scales so the averaging volume can be an intermediate length interval. This has also been found to be not the case in in-cylinder flow, as the larger turbulent length scales and the smaller average flow length scales have similar sizes [23].

Ensemble averaging has also been found to be a poor representation of engine turbulence as variations between engine cycles have been found which cannot be called turbulence fluctuations. That is, variations occur between cycles which do not affect the shear stresses, combustion or mixing in the way that normal turbulence would [23, 128].

These problems of there being no distinction between turbulence and average flow length and time scales and non-turbulent fluctuations between engine cycles are related to each other. Collectively, their effect is to cause variations between cycles which are not turbulent (from a Reynolds averaging viewpoint), and so are called cycle to cycle variations.

4.5.3 Cycle to Cycle Variations

As a demonstration of the effect of cycle to cycle variations in an internal combustion engine, Maurel et al [189] gave the example shown in figure 4.30. Their experiment was performed on a model square cylinder and piston engine configured to give a high tumble ratio. This geometry will be discussed in more detail in chapter 6. However, an important result of this research was the visualisations produced of cycle to cycle variations.

The ensemble averaged velocity field and three instantaneous fields in the central region of the cylinder at TDC is shown in figure 4.30. The ensemble averaged field is the result of averaging 120 instantaneous fields.

Figure 4.30a shows the ensemble averaged field to have a simple and well defined structure with a large central vortex, and top and bottom extremities of the frame showing little flow. It is quite amazing that such a simple and ordered field could

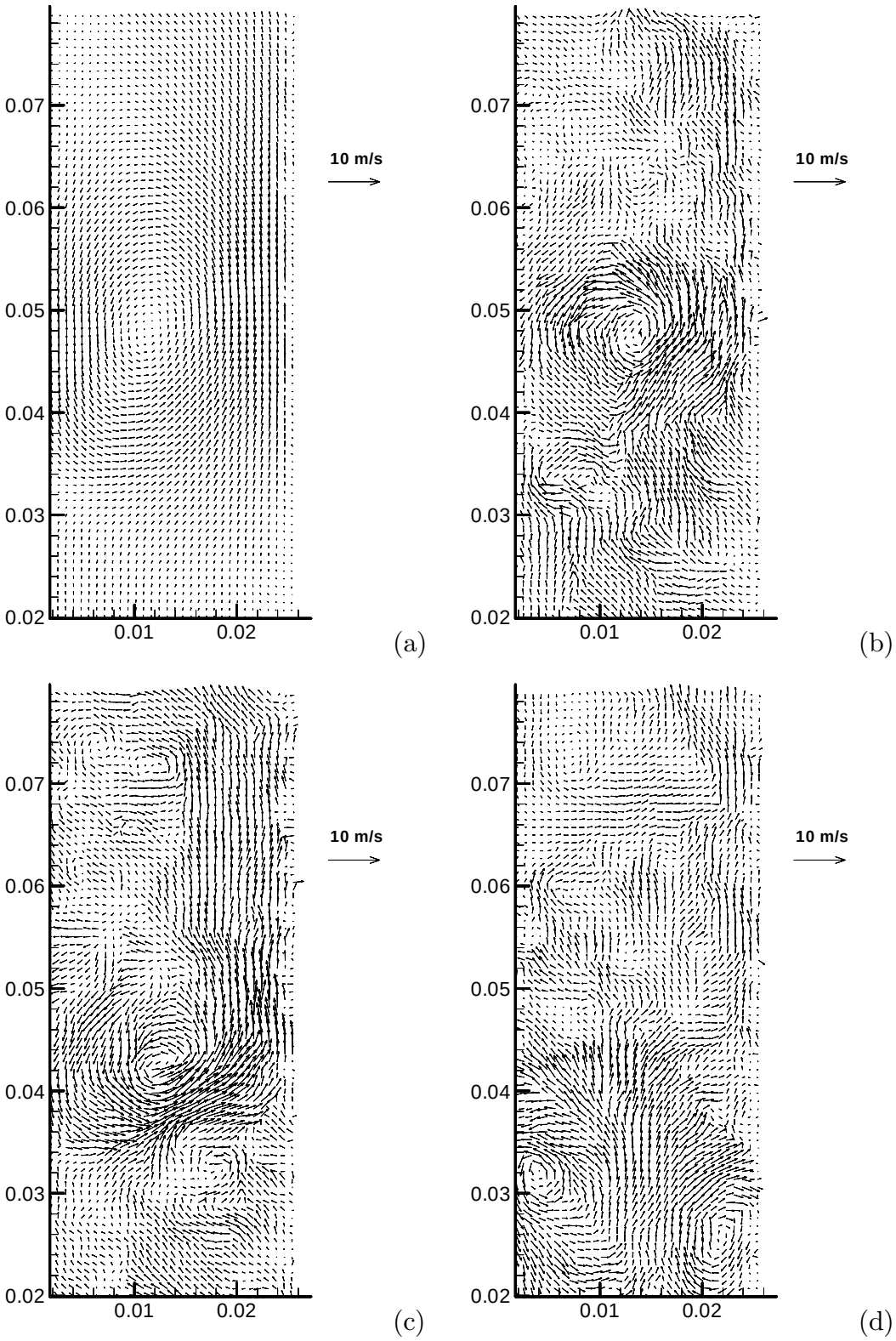

Figure 4.30: Comparison of averaged and instantaneous velocity fields at TDC of a square piston engine, from Maurel et al [189]. (a) – Ensemble averaged results; and (b)–(d) – Examples of instantaneous velocity fields.

result from the average of fields such as figures 4.30b to 4.30d, which at first glance appear to have little in common with the averaged result. There are clearly many features in the instantaneous results which have been removed with the averaging process, and even the main central vortex moves significantly. Additionally, the central vortex does not appear at all in figure 4.30d! It is clear in this case that the averaging process has been brutal, and removed all but a passing resemblance to the individual fields which created it.

It is a matter for debate amongst turbulence researchers whether cycle to cycle variations are caused by large scale turbulent fluctuations or whether it is bifurcations of the bulk flow [128]. Both of these possible causes are likely to be related to the so called "coherent structures", an area of much current turbulence research [178, 53].

This behaviour has been known for some time, and some approaches to handle it have been discussed by Wilcox [298], Arcoumanis and Whitelaw [23], and El Tahry and Haworth [93]. Methods are generally based around changing the decomposition of an instantaneous velocity into an averaged component, a fluctuating mean flow component and a fluctuating turbulent component. This is a modification of Reynolds averaging where the fluctuating quantity is averaged twice by different methods. El Tahry and Haworth [93] suggest a decomposition as

$$f(\mathbf{x},t) = \overline{f_E(\mathbf{x},t)} + f_{cv}(\mathbf{x},t) + f'(\mathbf{x},t) \tag{4.19}$$

in which $f(\mathbf{x},t)$ is the instantaneously fluctuating variable, $\overline{f_E(\mathbf{x},t)}$ is the normal ensemble averaged flow field, $f'(\mathbf{x},t)$ is the instantaneous turbulent fluctuation, and the additional term $f_{cv}(\mathbf{x},t)$ represents the cycle to cycle variability. A definition of $f_{cv}(\mathbf{x},t)$ which has been used by a number of researchers is to take a time average over a short fraction of the engine cycle, El Tahry and Haworth [93] suggest around 40 °CA.

Secondly, the additional term means the traditional Reynolds Averaged Navier Stokes equations no longer apply, and they must be replaced with a more complicated set of equations including the effect of the non-turbulent fluctuation, $f_{cv}(\mathbf{x},t)$. To the current author's knowledge, a simulation of this type has never been attempted. The standard way of accounting for the additional variation is to use the combined term $\left[\overline{f_E(\mathbf{x},t)} + f_{cv}(\mathbf{x},t)\right]$ as the averaged variable in the normal Reynolds Averaged Navier Stokes equations, and to accept that the mean flow predicted is no longer a fixed average, but will vary between cycles. Whether the Reynolds Averaged Navier Stokes equations is capable of performing this type of simulation is a matter of debate [128].

El Tahry and Haworth [93] suggest an alternative decomposition based on temporal frequency. Here the instantaneous velocity is decomposed as

$$f(\mathbf{x},t) = f_{lf}(\mathbf{x},t) + f_{hf}(\mathbf{x},t) \tag{4.20}$$

where *lf* and *hf* denote low and high frequency components. The low frequency component is assumed to be the "mean flow" component, and the high frequency component is assumed to be the turbulent fluctuation component. These components are determined by a Fourier analysis of the raw signal $f(\mathbf{x},t)$, and the cut-off frequency used to split low and high frequency components is based on the characteristic time scale of the event of interest. This method is not a Reynolds averaging approach as an "average" is not calculated.

This frequency based decomposition approach has been used on experimental results, for instance Rouland et al [241]. More complicated frequency based decompositions have also been suggested [196].

It is not possible to use this approach with a traditional Reynolds averaged Navier Stokes numerical simulation as the decomposition now is based on filtering rather than averaging. This method is suitable, however for the large eddy simulation (LES) technique.

4.5.4 Large Eddy Simulation

This type of modelling is now starting to become possible for IC engine simulations, but the method is far from mature. The first application of LES modelling to IC engines found in the current study was performed by Naitoh et al in 1992 [199], who extended the work to include a few other simple geometries later that year [200], and republished in 1993 with a few minor changes [201]. The simulation modelled a four valve spark ignition engine, and only modelled the cylinder of the engine with the valves being modelled as boundary conditions. It included a simple combustion model. They simulated engine speeds ranging from 700 rpm to 2100 rpm. Only one or two engine cycles were run at each speed, so only a very limited analysis of cycle to cycle variations was performed, however significant variation between cycles was found. Predictions of cylinder pressure and combustion were in moderate agreement with experiment, however the turbulence predicted was quite dramatically different to measured values. The accuracy of the simulations presented are no better than normal Reynolds averaged simulations being performed at the time.

A number of other researchers report more recent LES simulations of IC engines. These include Haworth and Jansen [130], who modelled a simplified axisymmetric

valve and cylinder arrangement over 18 individual engine cycles. This made it possible to compare to experimental results on an ensemble averaged basis. The accuracy of their results was reasonable, but only of a similar order of accuracy as modern Reynolds averaged simulations. This same geometry has also been modelled by Verzicco et al [285], who used an orthogonal mesh using body forces to implement the effects of piston motion and walls; and Yavuz and Celik [303], who used this geometry to assess a new sub-grid model suitable for application to IC engine simulation. Other geometries simulated include Sinha et al [257], who modeled a two valve spark ignition engine using an unstructured grid LES simulation; and Pomraning and Rutland [229], who modelled a Diesel engine intake stroke. All of these studies are only preliminary applications of LES to engine modelling, and none of these studies has shown significantly increased accuracy over modern Reynolds averaged simulations.

The state of LES modelling in IC engines is reviewed by Haworth [128]. His review is biased towards his own works [130, 242, 285], however it is a useful summary of current thinking in the area. It also includes an extension to the experimental work of Ruess et al [242], who performs a LES simulation of a two valve engine geometry.

All of these works show that encouraging progress is being made in this area, but the technique still suffers from some fundamental flaws which have not been addressed in these pioneering studies, namely:

- As LES can directly simulate the cycle to cycle variations, an individual realisation of the flow field is of limited value. Turbulence is a statistical phenomenon, and requires a number of realisations to be performed so as to build up a statistical sample. Only introductory studies in this area (such as [130]) have been performed to date.

- A true LES study requires a grid fine enough to resolve inertial sub-range of the turbulence spectrum. This requires the mesh to resolve flow features with a size of the integral length scale. Haworth and Jansen [130] estimate the integral length scale of their simplified geometry at TDC to be 2.5 mm, and their grid resolution is of the order of 1 mm, so it is likely their simulation could resolve the integral length scale. Similarly, Verzicco et al [285] and Yavuz and Celik [303] also have a grid resolution of around 1 mm, so it is likely that the integral length scale has been resolved in both these simulations. However, the studies performed on real engine geometries, such as Sinha et al [257] do not have sufficient resolution; partly due to the smaller length scale in a real

engine caused by higher speeds and smaller clearances, and partly due to the coarser grids necessary in the complicated real engine geometry. Thus LES simulations on real engine geometries are at the limits of currently available computing power;

- LES models require a sub-grid turbulence model, and sub-grid models suitable for engine modelling are still being developed. For example, Sinha et al [257] use the Smagorinsky sub-grid model; Pomraning and Rutland [229] use a one-equation sub-grid model; Verzicco et al [285] use the Smagorinsky sub-grid model and a modified dynamic Smagorinsky model; and Yavuz and Celik [303] develop a sub-grid model based on Smagorinsky, but using length scale parameters derived from the engine geometry. This is a sign of the immaturity of this form of simulation.

- Depending on which sub-grid model is chosen, LES poses problems near the wall boundary conditions. Physically, turbulence structures decrease in size as you approach walls, and the anisotropy increases. This would require a prohibitively fine mesh if it had to be resolved by the simulation. Two main approaches are used to overcome this problem; either a wall damping term is used to relax this restriction [298], or alternatively wall functions similar to that used by Reynolds averaged Navier Stokes equations (see section 3.3.1) can be used. Both of these approaches mean that the turbulence is not being resolved over the entire flow, and an increased level of empiricism is required.

With developments in LES modelling techniques and the current rapid increases in computing power, LES simulations will certainly become the standard modelling technique for internal combustion engines in the future. Currently, however, they are on the frontiers of knowledge and require further development work before they can be reliably applied to engine modelling.

As the current work was focussed on studying the aerodynamics of the BRV engine with the most suitable method available at the time, it was decided that a Reynolds-averaged Navier Stokes method would be used. The development of this method has been described in chapters 2 and 3; and its validation is described in chapters 5 and 6. However, a preliminary study of a LES simulation is performed as part of the validation described in chapter 6.

Chapter 5

Validation of Numerical Simulation Code

As CFX-4.3 is a widely used commercial code it has been extensively validated for a wide range of flows. As an example of the wide application of the code, the CFX user magazine, "CFX Update", in its Autumn 1999 edition describes studies in which CFX is used to model reacting flow in a mixer, impeller driven mixing in a tank, separation of oil droplets in water, air flow in a pneumatic silencer, crystal growth, water flow in a Pelton wheel turbine and pool fire combustion.

A number of validations of the CFX code with particular relevance to the present work will be described in this chapter. Examples of validations published by the authors of the code that are summarised in this chapter are laminar flow over a backstep (section 5.1.1) in which various differencing schemes are compared to experimental data, turbulent flow over a backstep (section 5.1.2) in which various turbulence models are compared to experimental data, transient grid motion (section 5.1.4) in which the transient grid motion section of the code is assessed, the effect of various differencing schemes on results (section 5.1.3), and a benchmarking exercise (section 5.1.5) which used a number of standard laminar and turbulent flow benchmarks to test the accuracy of the code.

CFX has also been validated by users of the code as part of their own research. Some relevant examples have been summarised, including flow over an aerofoil with a separation (section 5.1.6), turbulent boundary layer skin friction (section 5.1.7) and external automobile aerodynamics (section 5.1.8).

AEA Technologies claims that CFX-4.3 is capable of internal combustion engine modelling. The web page of CFX states that it can be used for modelling in-cylinder flows [3], and the CFX magazine contains a number of reports of people using CFX

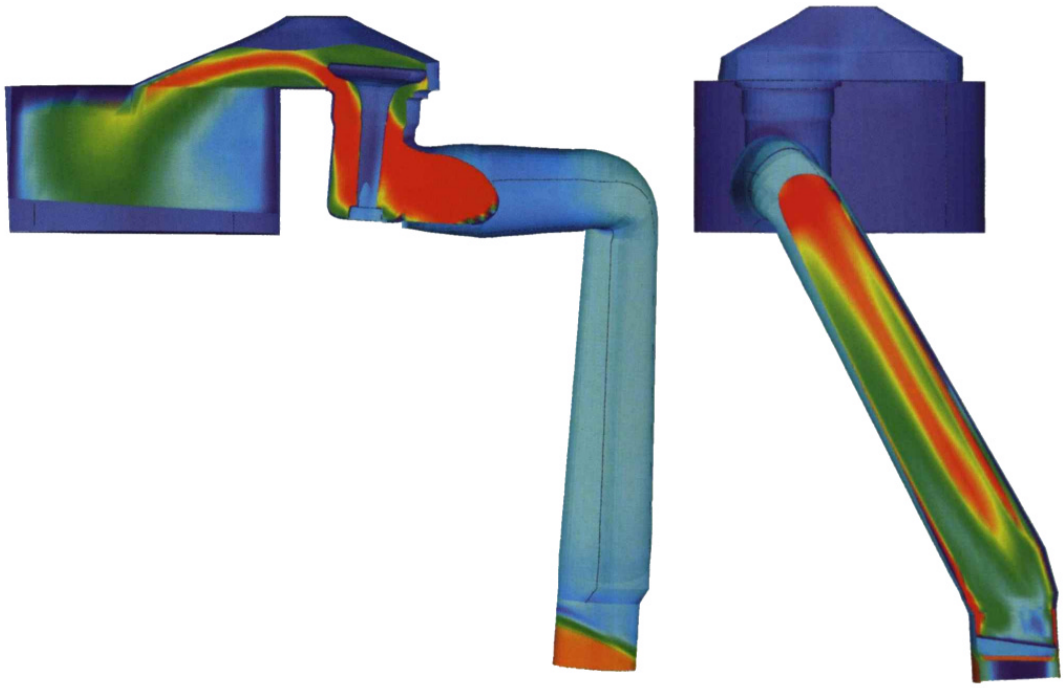

Figure 5.1: Model of a Tecumseh small utility engine from Foster [100]. Walls of the model are coloured by pressure, and a velocity slice is taken through the inlet valve (left) and the throttle (right).

to model in-cylinder flows.

Examples of the use of CFX-4 in modelling in-cylinder flows include:

- Foster [100] used CFX-4 to model transient flow including piston motion and valve motion in a small Tecumseh spark ignition "utility" engine—possibly a lawn mower engine or small pump engine, shown in figure 5.1. The engine was modelled using isothermal conditions, so it is assumed that the gas was modelled as an incompressible fluid and that the inlet manifold wave is negligible.

- Stopford [264] used CFX-4 to model the combustion in a Diesel engine. The particle tracking capabilities of CFX were used to track fuel particles in the spray, and linked to a separate chemical kinetics package for the modelling of combustion and soot formation.

Both of these reports were written primarily for marketing purposes rather than as scholarly reports. They have many "pretty pictures", but no data suitable for making an objective assessment of accuracy. It is not clear what reliance can be

placed on these works when they report reasonable accuracy and useful results. However, it does show that CFX-4 has been used for engine in-cylinder modelling, and has been accepted as a useful tool in engine design by a number of engine researchers.

Due to the scarcity of objective validations of the CFX-4 code for modelling internal combustion engine manifold and in-cylinder flows, validation work to establish its suitability was performed as part of the current work.

Firstly a validation of the effectiveness of CFX-4.3 in modelling compressible gas waves was performed. As has been mentioned in section 4.4.1, waves occur in the inlet and exhaust manifold of high speed internal combustion engines, so it is important to be able to capture their behaviour. As a validation of compressible fluid waves, a simulation of the one-dimensional shock tube problem is performed in section 5.2. To the author's knowledge, this is the first time the one-dimensional shock tube validation study has been performed using CFX.

Finally, the ability of CFX to predict the behaviour of flow fields during the compression stroke of an engine was assessed. This validation uncovered some important fundamental behaviour of flows in the compression stroke of internal combustion engines, so an entire chapter has been devoted to describing this study. This work modelling vortex breakdown due to compression will be discussed in more detail in chapter 6.

5.1 Summary of Existing Validations

5.1.1 Laminar Flow Over a Backstep

Moore and Wilkes [195] performed simulations of two-dimensional laminar flow over a backstep, and compared their simulations with the experimental results of Armaly [24]. The geometry modelled had a step height of 4.9 mm, an inlet height of 5.2 mm, and continued for 310 mm downstream of the step. The inlet boundary condition was prescribed as a fully developed, parabolic velocity profile with $u_{max} = 1.9075\,\mathrm{ms}^{-1}$, which yields a Reynolds number of 882. The Reynolds number is based on mean inlet velocity, twice the inlet height, and using water as the fluid. Armaly found flow at these conditions generated a second recirculation on the top wall of the domain.

Moore and Wilkes simulated this flow with a number of different grids and differencing schemes. The grids used are shown in table 5.1. All grids were uniformly graded across the flow. The size of the primary recirculation predicted by the various

Grid	Nodes	Inlet Location	Node Size	
			At Step	100 mm Downstream
1	40 × 40	one node upstream of step	7.5 mm	7.5 mm
2	43 × 40	25 mm upstream of step	7.5 mm	7.5 mm
3	47 × 40	25 mm upstream of step	1.7 mm	8.0 mm
4	69 × 60	25 mm upstream of step	1.0 mm	6.1 mm

Table 5.1: Grids tested by Moore and Wilkes [195].

Differencing	Grid 1	Grid 2	Grid 3	Grid 4
HDS	14.8	14.6	6.9	6.6
UDS	13.0	13.0	9.5	7.6
HUW	12.7	12.6	11.1	10.6
CCCT	6.5	7.6	11.0	11.7
Quick	5.3	6.3	10.6	12.1
CONDIF	5.2	5.4	diverged	diverged
Experiment [24]	15.1			

Table 5.2: Length of primary recirculation bubble from Moore and Wilkes [195].

differencing schemes and grids is shown in table 5.2 and the size of the secondary recirculation is shown in table 5.3.

The differencing schemes tested were UDS, HDS and HUW, described in section 3.2.3. A further three schemes tested by Moore and Wilkes that have not been described in the current work are CCCT, Quick and CONDIF. The Quick scheme is a commonly used third order accurate scheme. CCCT is a modification of Quick that is bounded. CONDIF is a modification of the CDS scheme to reduce its tendency to cause spurious oscillations in the solution. These differencing schemes are further discussed in the CFX manual [13].

The secondary recirculation was only predicted with high order differencing (HUW, CCCT, Quick, CONDIF) or with a fine grid. The accuracy of predicting the recirculation sizes was poor by the HDS and UDS schemes, as shown in tables 5.2 and 5.3. The apparent accuracy of the HDS and UDS schemes on grid 1 is misleading as these simulations failed to predict the existence of the secondary recirculation.

The higher order schemes, especially the Quick differencing scheme on the fine grid, are shown to be reasonably accurate in predicting both the primary and secondary recirculation sizes.

This study shows that high order differencing schemes and fine grids are required to produce accurate results if separation and reattachment occur. The study also

	Separation	Reattachment
Experiment [24]	12.4	20.8
HDS Grid 2	8.9	11.4
HDS Grid 4	4.7	11.6
Quick Grid 2	4.0	14.3
Quick Grid 4	9.7	21.5

Table 5.3: Length of secondary recirculation bubble from Moore and Wilkes [195].

confirms that graded grids are useful for providing local grid refinement without increasing the size of a simulation, and that this can improve the accuracy of a simulation.

5.1.2 Turbulent Flow Over a Backstep

Clarke and Wilkes [68] included a validation of the FLOW3D code primarily to validate the Reynolds stress turbulence model, but they also assessed the k-ϵ model. The paper describes validations of a number of simulations; a summary of their turbulent flow over a backstep validation will be presented here.

The backstep problem was simulated at a Reynolds number of 51615, which indicates that the flow is turbulent. Simulations were performed with the standard k-ϵ, RSM and the algebraic stress (ASM) turbulence models, and compared with experimental results of Bates et al [32]. The ASM turbulence model is a modification of the RSM where algebraic equations for the Reynolds stresses are solved rather than partial differential equations, reducing the number of equations modelled.

The results in figure 5.2 show that all three turbulence models resolve the overall trends of the experimental results; however, no model predicts the experimental results precisely. All models predict the u velocity with reasonable accuracy, with the RSM model being marginally better than the other models in figure 5.2a. The predictions of the $\overline{uu}$ Reynolds stress in figure 5.2b are good from $Y = 0$ to $Y = 0.016$ for all models; however, no model predicted the turbulence dropping as rapidly as the experimental results show beyond $Y = 0.016$. Overall, however, all models predict the turbulence trend reasonably well, with the RSM and ASM models being slightly more accurate than the k-ϵ model.

Overall, the RSM model is marginally more accurate than the k-ϵ or ASM models in predicting the axial velocity, and the ASM and RSM models predicted the $\overline{uu}$ Reynolds stress better than the k-ϵ model which significantly underpredicted the turbulence level. All models predicted the correct overall trend for the flow. This validation demonstrates that the k-ϵ model, RSM model and ASM model are all ca-

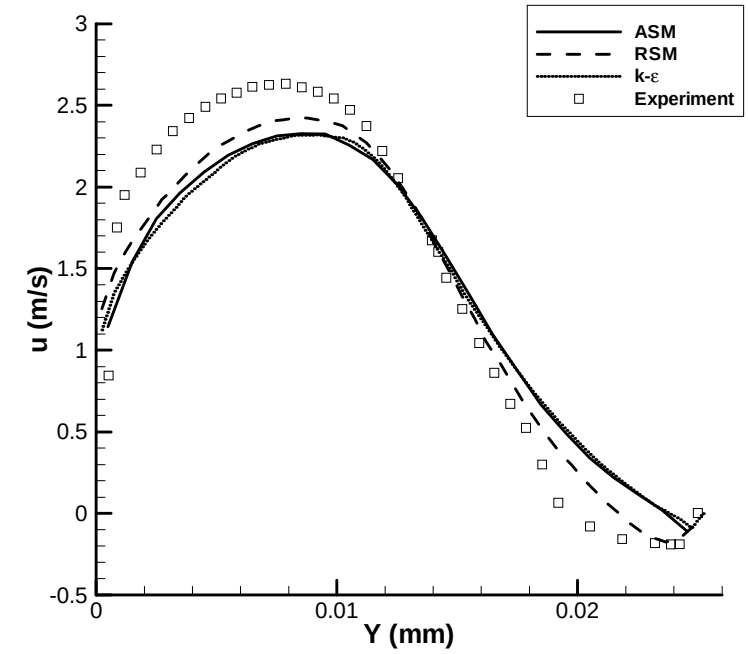

(a)

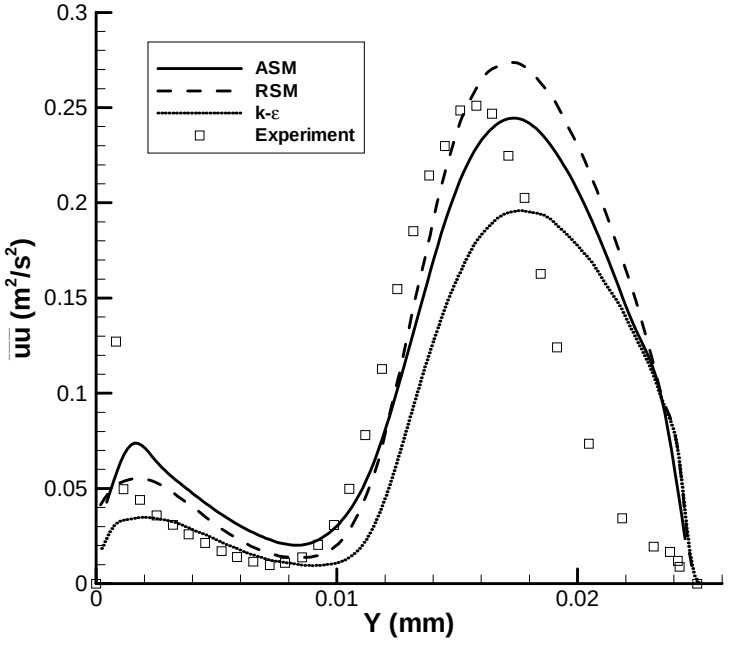

(b)

Figure 5.2: Comparison of predictions using various turbulence models for flow over a backstep at Re = 51615. Adapted from Clarke and Wilkes [68], and experimental results from Bates [32]. (a) – Axial velocity profile, located in the recirculation at a distance half the step height downstream of the step; and (b) – Mean square axial velocity fluctuation profile, located in the recirculation at a distance half the step height downstream of the step.

pable of predicting simple turbulent separated flows. It also shows that the velocity components are likely to be better predicted than the turbulence components.

5.1.3 Differencing Schemes

Alderton and Wilkes [17] included a validation of the FLOW3D code (the forerunner of the CFX code), to assess the effects of various differencing schemes on solutions. They tested laminar flow over a backwards facing step and compared the results to a published and accepted accurate finite-element solution. They also tested a number of other models, but they did not present benchmark data to validate the results and so these models will not be discussed.

The laminar flow over a backwards facing step was simulated at $\mathrm{Re} = 300$, with a step size to inlet ratio of one. Simulations performed using various differencing schemes were compared with solutions obtained from a previously published finite-element simulation. The exact details of the geometry that was modelled were not specified.

Figure 5.3a shows a comparison of wall shear stress after the step modelled by the various differencing schemes, and are compared to the finite-element solution. All finite differencing schemes show excellent accuracy, with all of them predicting essentially the same result, which agrees with the finite-element results. The only differencing scheme with a significant departure from the finite element results is the hybrid differencing scheme in the region of the recirculation ($3 < X < 5.5$), and in the early section of the reattachment region ($5.5 < X < 9$).

The results from the model simulating turbulent flow through a pipe with a splitter plate is shown in figure 5.3b. Here two streams, initially separated by a thin annular wall parallel to the flow, are allowed to mix. Again, the four differencing schemes tested all produced very similar results. It was noted, however, that the QUICK differencing scheme failed to converge as it had a tendency to make the turbulent kinetic energy negative at the end of the splitter plate, which is not physically possible. This is a well known problem with the QUICK differencing scheme, and is the reason why it was not used in the engine simulations in this work.

Alderton and Wilkes conclude that the higher-order differencing schemes assessed (HUW, QUICK, CCCT, CONDIF) are successfully implemented in CFX as shown by a range of validation studies, and that for general use a higher-order differencing scheme will achieve more accurate results on a given grid than will a simpler low-order differencing scheme such as UPWIND or HYBRID. However, an

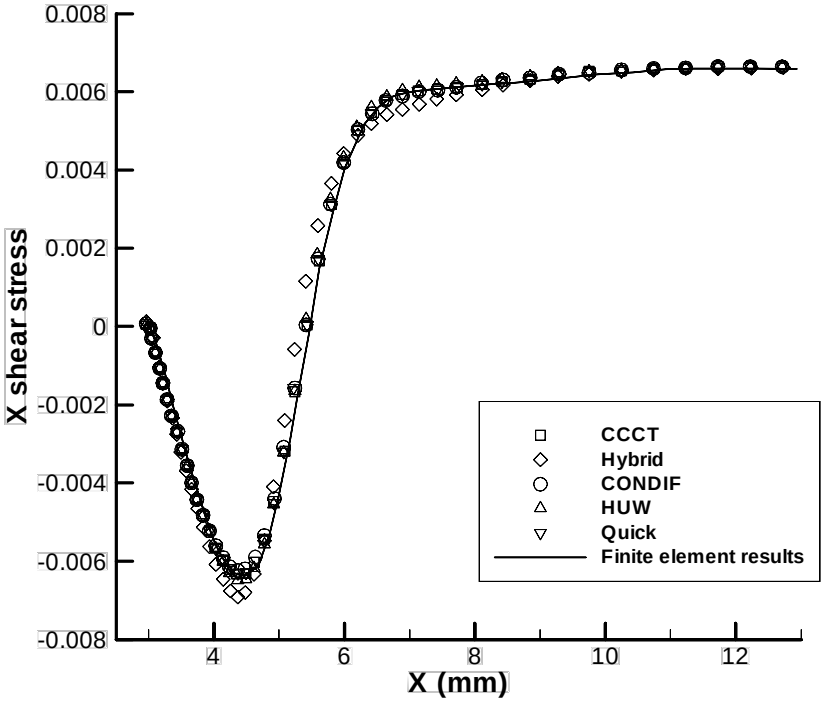

(a)

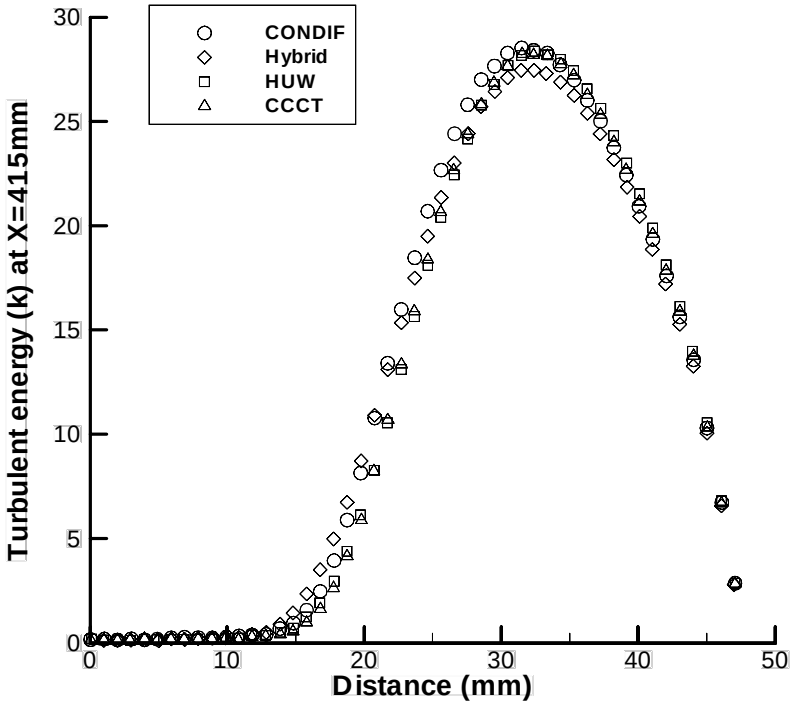

(b)

Figure 5.3: Validation simulations from Alderton and Wilkes [17]. (a) – Wall shear stress on the stepped wall for backwards facing step flow, Re = 300; and (b) – Turbulent kinetic energy (k) profile at $X = 0.415\,\mathrm{m}$ for turbulent flow in a pipe with a splitter plate.

important limitation is that the higher-order schemes, QUICK in particular, can be difficult to converge, or may give non-physical solutions.

5.1.4 Moving Grids

Hawkins and Wilkes [127] describes the development and validation of the moving grid capability of the FLOW3D code. Four simple validation studies, and two more complicated validation studies using engine-like geometries are described.

The simple validation studies tested whether the moving grid caused spurious movement in the fluid, and whether it could reproduce simple analytical results, such as adiabatic compression. The two engine-like geometries that were tested were more of a demonstration of what can be done with the code rather than a validation as they did not compare the results of their modelling with experimental data.

The first simple validation test was performed to assess whether the grid motion caused spurious fluid motion. A square region with an orthogonal mesh and zero initial velocity and pressure variation had its mesh distorted, whilst keeping its outside boundaries unchanged. Since the outside boundary does not move, this test should result in zero flow after the grid motion. When this test was performed with an incompressible fluid, the simulation gave exactly zero velocity over the entire domain. When repeated with a compressible fluid, velocities of the order of $10^{-14}\,\mathrm{ms}^{-1}$ were created. This error is of the same order as the machine rounding error, and at least ten orders of magnitude less than the grid motion velocities, so it was concluded grid motion did not cause significant spurious fluid motion.

The second test was a translating, rigid box containing an incompressible fluid. Here the fluid should move at the velocity of the translation. The flow converged uniformly to the velocity of the box within 20 iterations.

The third test was similar to the second, however this time the incompressible fluid was driven by a moving piston described by a moving mesh, and fluid was allowed to enter the domain through a constant pressure boundary. The flow correctly converged to the velocity of the piston within 20 iterations.

The fourth test case was of a one-dimensional adiabatic compression and expansion of a compressible gas. The compression ratio was 10. When the simulation was performed with 18 time steps of around 1 s each (20 °CA per time step), the temperature and pressure fields were overestimated by 5%. This error was reduced to around 1% by using 36 time steps of 0.5 s (or 10 °CA).

The first of the more complicated and realistic validations of the transient grid

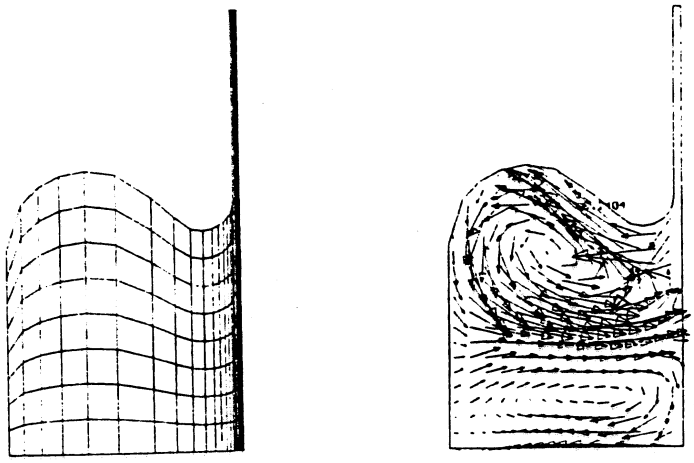

Figure 5.4: The grid used and velocity vectors predicted in the model of an axisymmetric Diesel engine cylinder at TDC, from Hawkins and Wilkes [127].

capabilities of the code was in modelling an axisymmetric Diesel engine cylinder with a central bowl during the compression and expansion strokes. Neither combustion nor gas exchange processes were modelled. The bore modelled was 100 mm, the stroke 110 mm, the crankshaft speed 1500 rpm, and the simulation started at BDC with a solid body swirl motion of magnitude $SR = 2.3$ in the cylinder.

The grid used and the predicted velocity vectors are shown in figure 5.4. The turbulent kinetic energy (k) predicted in this model is shown in figure 5.5. Peaks of turbulence are seen to be associated with the end of the squish zone near the open section of the piston and at the top of the piston bowl, showing that the turbulence generated by squish is localised around the edge of the piston bowl. Shortly after TDC the flow reverses, and smaller turbulence peaks are generated in the squish zones.

Figure 5.6 shows the second more realistic simulation, which was of a valve closing in a duct with a pressure gradient driving the flow. The flow is seen to form a jet as it passes through the valve seat, and the left jet is seen to curve and create a recirculation under the valve. However, as no benchmark data for this simulation is presented is it not possible to make a judgement of the accuracy on this simulation.

Both of these more realistic examples demonstrate that CFX can model transient geometries using its moving grid capability; however, no assessment of accuracy of these predictions can be made since no grid refinement study or comparison to experiment was included. The simple validation studies show that the transient grid does not cause spurious fluid motion and that simple analytical results such as

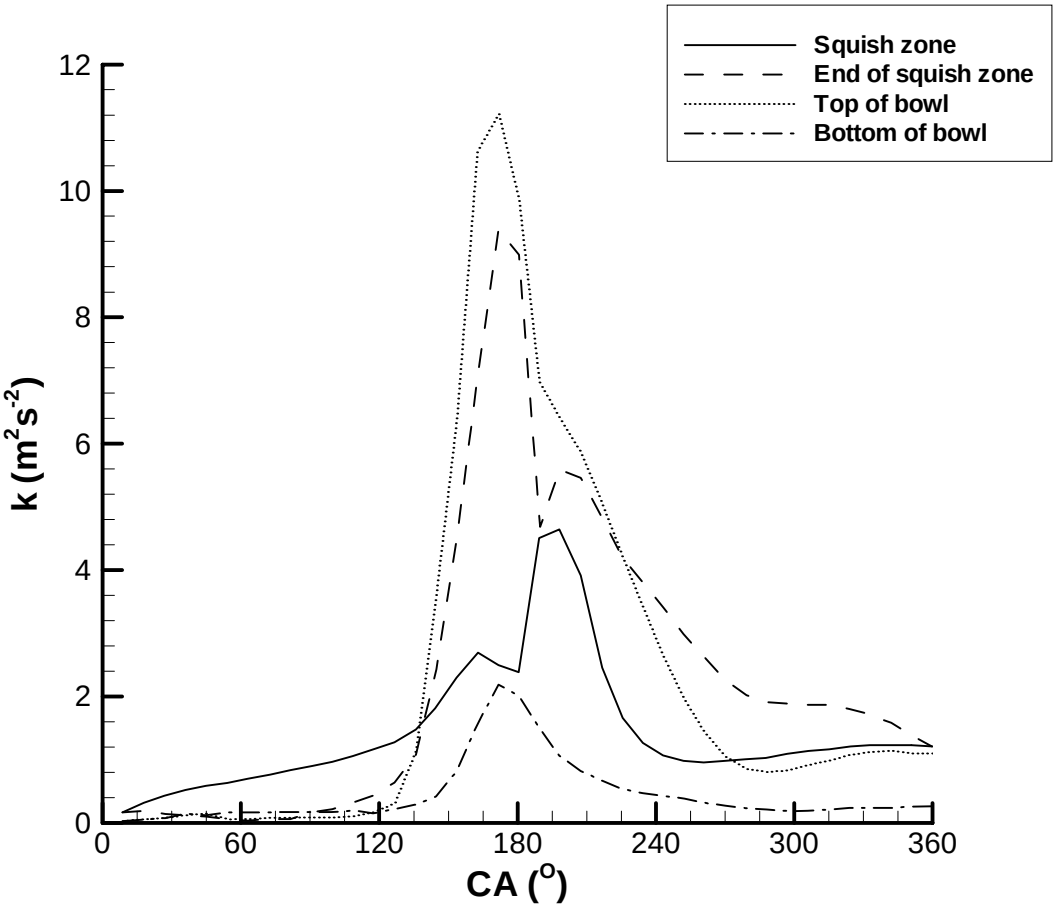

Figure 5.5: Turbulent kinetic energy (k) predicted for piston bowl compression stroke simulation at various points. Adapted from Hawkins and Wilkes [127].

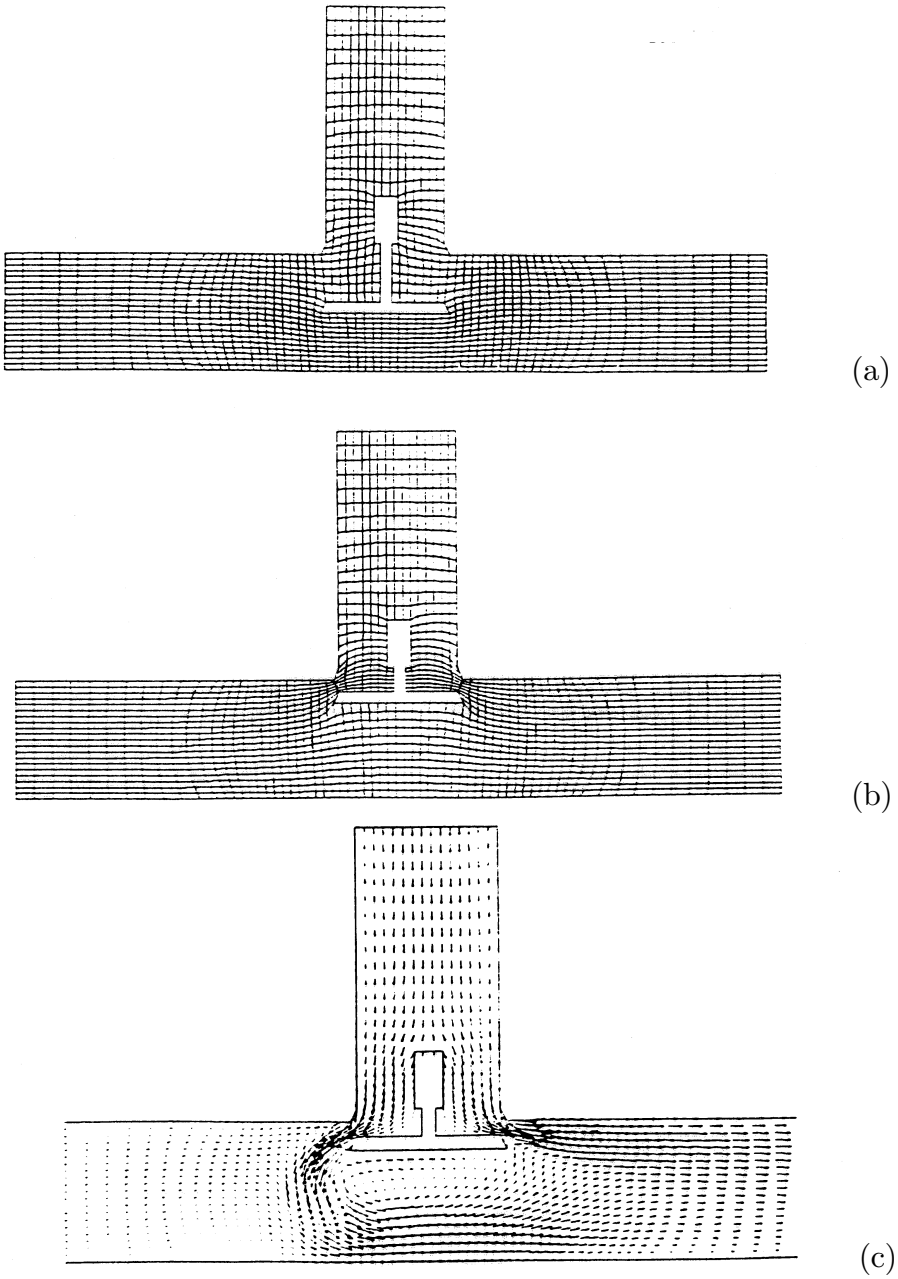

Figure 5.6: Simulation of moving valve poppet valve by Hawkins and Wilkes [127]. (a) – Grid at time 0.0 s; (b) – Grid at time 1.0 s; (c) – Velocity vectors predicted at time 1.0 s.

a translating box or an adiabatic compression can be accurately simulated.

5.1.5 General Benchmarks

CFX also participated in a CFD code benchmarking exercise published by Freitas [102]. The purpose of this benchmark was to compare commercial CFD codes on a series of five test cases, selected as being representative of a wide range of engineering flows. High quality experimental or numerical results were used as the benchmark solutions.

The selected test cases included three laminar flow problems and two turbulent flow problems:

- The backward-facing step problem at Re = 200, 450 and 1000;
- Uniform flow past a circular cylinder at Re = 60;
- Three-dimensional shear driven cavity flow at Re = 3200;
- Turbulent flow around a square cross-section cylinder at Re = 14000; and
- Developing turbulent flow in a 180 ° bend at Re = 56700.

Disappointingly, the CFX vendor chose only to submit results for the first three problems.

For the first problem, CFX predicted the reattachment point within 10% accuracy at Re = 200, but failed to predict the secondary recirculation region which forms at Re = 450 and 1000, and so failed to predict the correct flow structure. This is disappointing as the validation discussed in section 5.1.1 by Moore and Wilkes [195] tested this flow at a similar Reynolds number, and they successfully predicted the second recirculation and noted that reasonable mesh resolution and accurate discretisation schemes are required to obtain accurate results. Obviously the validation of the CFX code presented by Freitas was not done as carefully as the earlier work of Moore and Wilkes.

The second problem was very poorly done as the vendor assumed the flow to be symmetrical and steady, whereas it is well known that the flow at this Reynolds number is asymmetric and unsteady. As unsuitable models were chosen it was not possible to correctly predict the flow. Consequently, the drag coefficient was predicted with poor accuracy.

The third problem was also poorly modelled. The vendor assumed the flow to be symmetrical and steady-state, whereas in reality this flow is also asymmetric and

transient. The velocity profiles on the centre lines were predicted with reasonable accuracy, but the fundamental flow structure was not resolved due to the incorrect model being chosen.

This benchmarking exercise proved to be more of a demonstration of the lack of understanding by the code's vendor than a test of the accuracy of the code. As CFX does possess the transient three-dimensional models capable of simulating these flows correctly, one can only suggest that the vendor was ignorant of the true nature of the flows and therefore chose inappropriate models.

This benchmarking exercise should not be used to criticise the accuracy of CFX as it has been extensively validated elsewhere. It should, instead, be taken as a warning that one needs to understand the flow that one is trying to simulate. An accurate simulation will only occur if the correct model options are chosen.

5.1.6 Aerofoil Modelling

Date and Turnock used CFX-4.3 to model steady and transient flow over a NACA 0012 aerofoil section fitted with a Gurney flap at the trailing edge [81]. The flow was modelled over a range of Reynolds numbers between 0.77–0.89 $\times 10^6$, with an incompressible turbulent simulation. The flow was assumed to be two-dimensional, and the standard k-ϵ turbulence model was used.

A grid refinement study was performed. It was found that the grid resolution significantly affected the structure of the flow predicted behind the Gurney flap, but the lift coefficient changed only marginally (around 0.5%). The drag coefficient was more sensitive to grid resolution, varying by around 10%.

A further study tested the effect of modelling the flow using steady-state equations against using a full transient simulation. The steady-state simulation did not converge to a steady value of lift or drag coefficient, but converged by several orders of magnitude then oscillated slightly around a mean value about every 60 iterations. When the full transient model was performed, it was found that the flow oscillated slightly in a manner typical of bluff bodies. An example of an oscillating flow simulated by Date and Turnock is shown in figure 5.7.

If the iteration-averaged value of the steady-state simulation was compared to the time-averaged value of the full transient simulation, they found that the two models predicted very similar results, as shown in figure 5.8. Figure 5.8 shows that the only significant difference between the averaged steady-state simulation and the full transient simulation is a small difference in the lift coefficient at high angles of attack. The results are also in reasonable agreement with the laser Doppler

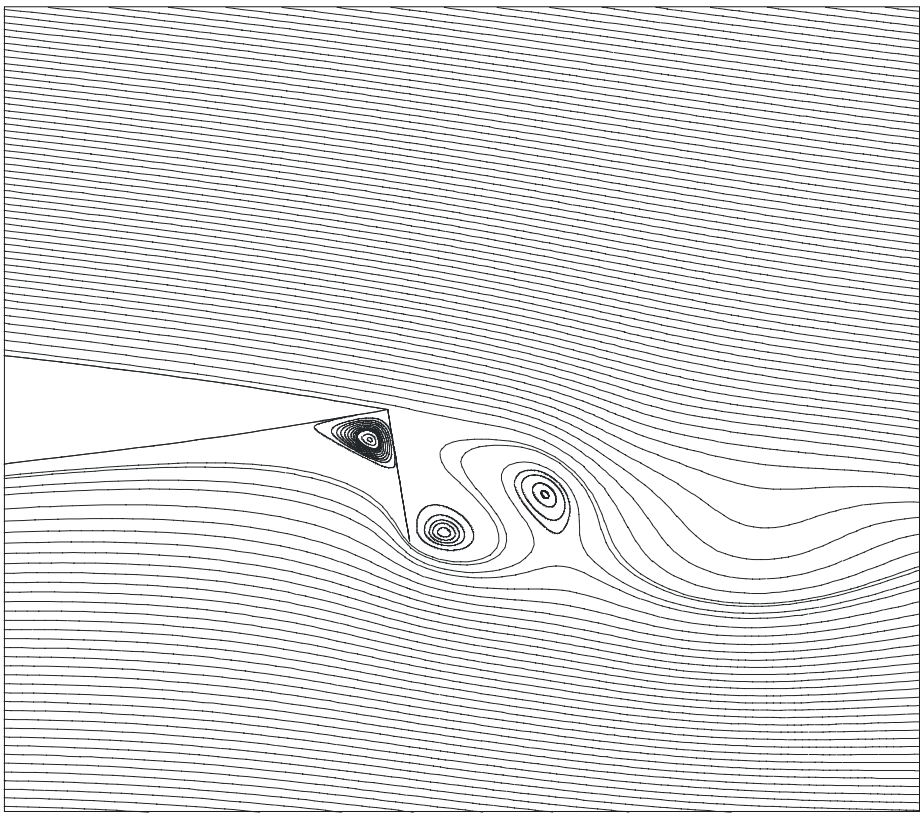

Figure 5.7: Instantaneous streamlines of a 4% Gurney flap aerofoil at zero angle of attack, from Date and Turnock [81].

anemometry results of Jeffrey [153].

A time step size study on the transient results found that the vortex shedding behaviour was accurately captured as long as the CFL number remained below four.

This result shows that CFX is capable of predicting complex multi-dimensional external flows. The k-ϵ turbulence model used was certainly a major limitation on the accuracy of the simulation due to its well known shortcomings, however the reasonable accuracy of the results predicted is encouraging.

5.1.7 Turbulent Boundary Layer

Date and Turnock used CFX-4.3 to model skin friction on a flat plate [82]. A wide range of Reynolds numbers was tested from 7×10^4 to 1.5×10^9. A two-dimensional domain was modelled with the incompressible Navier Stokes equations. Results using laminar equations, the k-ϵ turbulence model and RNG turbulence model were compared.

An extensive validation of the model by testing many different mesh density

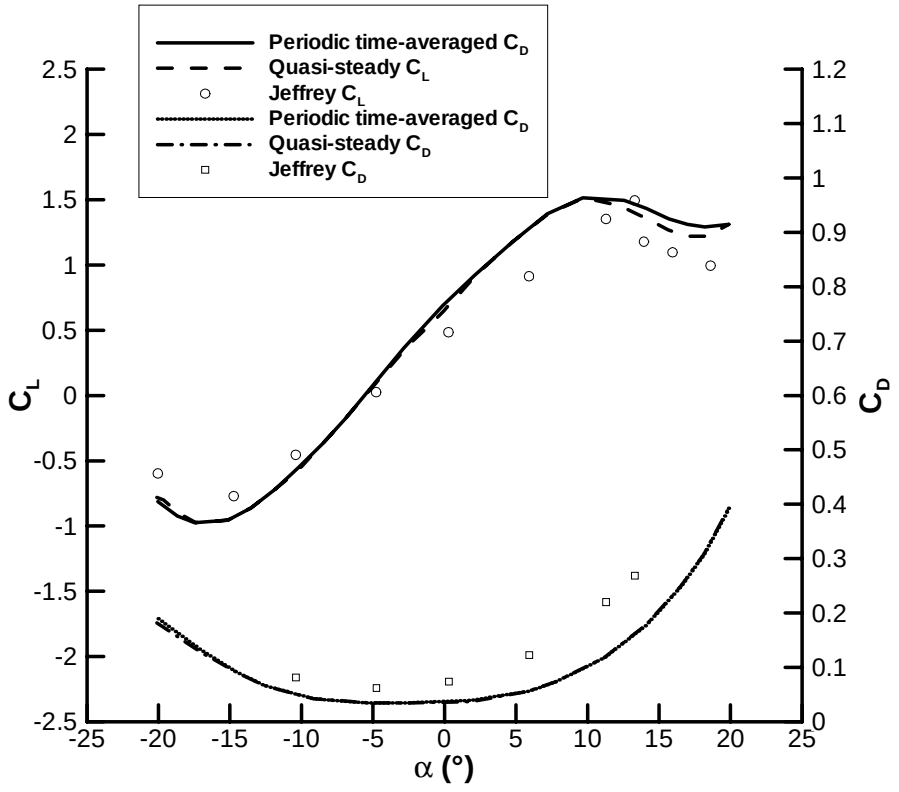

Figure 5.8: Time averaged C_L and C_D versus angle of attack (α) for a NACA 0012 aerofoil with a 4% Gurney flap. Comparison of numerical simulations using transient and steady state models against experimental results. From Date and Turnock [81].

parameters was performed, and boundary condition independent solutions reached. Parameters analysed included the position of the inlet, outlet and top boundary condition, grid density across and along the flow and the advection differencing scheme. It was found that the y^+ of the first node into the domain on the plate did not have a significant effect on the results, as long as it was within the range $30 < y^+ < 500$. This is in agreement with the comments made about the limitations of wall functions in section 3.3.2.

As shown in figure 5.9, the skin friction predicted by the turbulent simulations for the high Reynolds region of $\mathrm{Re} > 2 \times 10^6$ was very close to that predicted by the empirical correlations of Schoenherr and ITTC (1957) and the experimental results of Froude. In this high Reynolds number region the flow is highly turbulent, so the turbulence models can successfully model the physics of this type of flow.

Figure 5.9 also shows that the agreement of the numerical simulations with Froude's experimental results deteriorated for the range of $5 \times 10^5 < \mathrm{Re} < 2 \times 10^6$. In this region the laminar to turbulent transition plays a critical role in determining the total skin friction, and the standard k-ϵ or RNG turbulence models cannot capture the physics of transitional flow. It is interesting to note that the Schoenherr and ITTC (1957) data also compares poorly with the experimental results of Froude. This is surprising as these empirical correlations are regularly used in skin friction calculations in ship design.

It is likely that the laminar simulations were accurate for $\mathrm{Re} < 5 \times 10^5$, but as Froude presented no experimental results for this region no conclusions can be drawn. This low Reynolds number region is not applicable to ship design, and so was not studied intensively.

This study shows another limitation of the k-ϵ turbulence model, in that it cannot accurately model transitional flows. However, the k-ϵ model can yield accurate results when the flow is well into the turbulent region. Additionally, the importance of using suitable values of y^+ was demonstrated.

5.1.8 Simulation of Complex External Flows

A demanding test of fluid simulations and turbulence models is the prediction of turbulent external flows, such as automobile external aerodynamics. The flow over a simplified sedan vehicle geometry moving at $28\,\mathrm{ms}^{-1}$ was modelled by Shaw and Simcox [251] as part of the development of a CFD modelling capability for external flows for the Jaguar automobile company. The geometry modelled is shown in figure 5.10a. This was modelled using two grid densities, $49 \times 28 \times 16$ and $96 \times 54 \times 30$, and

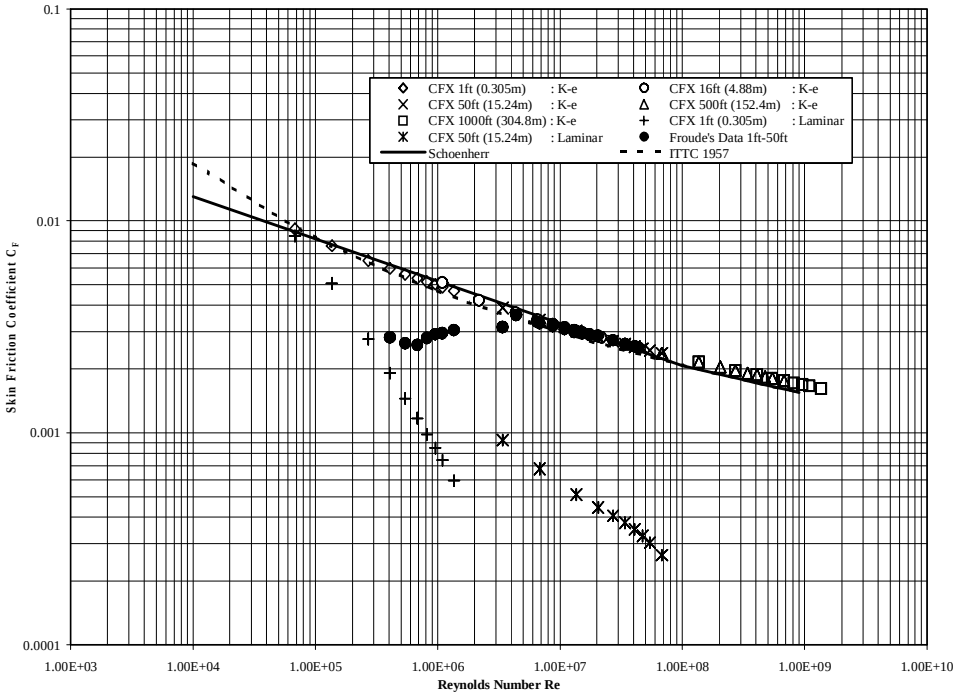

Figure 5.9: Skin friction coefficient versus Reynolds Number for various numerical models and experimental results. Adapted from Date and Turnock [82].

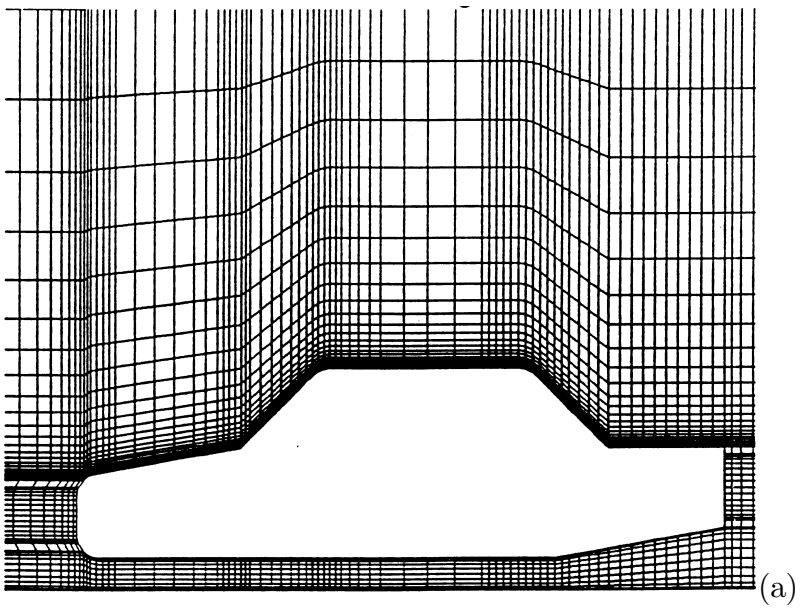

(a)

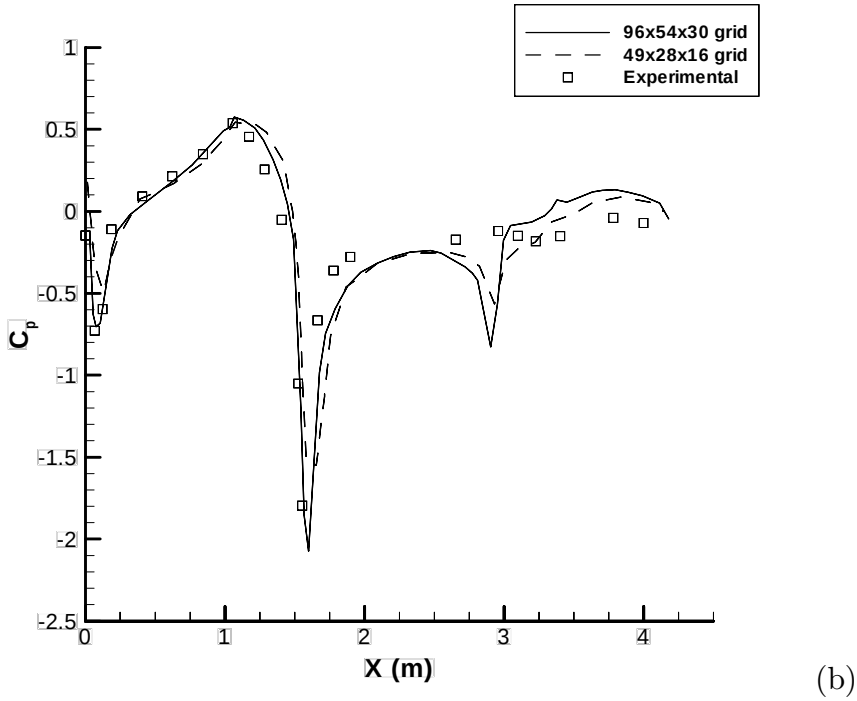

(b)

Figure 5.10: Simulations of a simplified vehicle geometry modelled by Shaw and Simcox [251]. (a) – Grid of vehicle geometry modelled. Cross section shown is the central symmetry plane; and (b) – Pressure coefficient predicted and experimental results. Results shown for the upper surface of the vehicle centreline.

Case	Total C_D	Front C_D	Rear C_D
Coarse Grid	0.517	0.313	0.204
Fine Grid	0.391	0.238	0.153
Experimental	0.156	0.000	0.156

Table 5.4: Experimental and predicted drag coefficients from Shaw and Simcox [251].

compared to experimental results. They report that most flow features, such as the separations at the base of the vehicle and at the top of the rear screen were predicted by both grids. A third smaller separation at the base of the front windscreen was not predicted by either grid. Figure 5.10b shows the pressure predicted along the centre line, showing good agreement for both grids against the experimental results, with the finer grid having additional accuracy in regions of pressure spikes at the front of the vehicle and the top of the windscreen.

The accuracy of predictions when drag coefficients are calculated over the front, rear and entire vehicle show a lower level of accuracy. Table 5.4 shows the comparison. The experimental results are based on an approximate technique that derives total drag coefficient from surface pressure measurements rather than total force measurements. Thus the experimental results in table 5.4 are likely to have significant error—the value of 0.000 for the drag coefficient for the front section of the car in particular looks doubtful. This error in experimental results means no conclusions about the accuracy of the simulated drag coefficients can be made.

It is clear in table 5.4 that grid convergence has not yet been achieved as significant variations in the drag coefficients occur between the two meshes. This is despite the centre line pressure (figure 5.10b) being similar for both meshes.

Shaw and Simcox show that CFX is able to predict complex turbulent external separated flows. The surface pressure was predicted quite accurately, but the prediction of total drag force was poor. A finer grid produced more accurate results, but it is likely a far finer mesh again is required before grid convergence can be achieved. This demonstrates the need for appropriate mesh size for accurate simulations.

5.2 One-Dimensional Shock Tube

In this section a validation study is performed which focusses on the ability of the CFX code to model the one-dimensional propagation of non-linear pressure waves. This has been performed to assess whether CFX can accurately capture the pressure

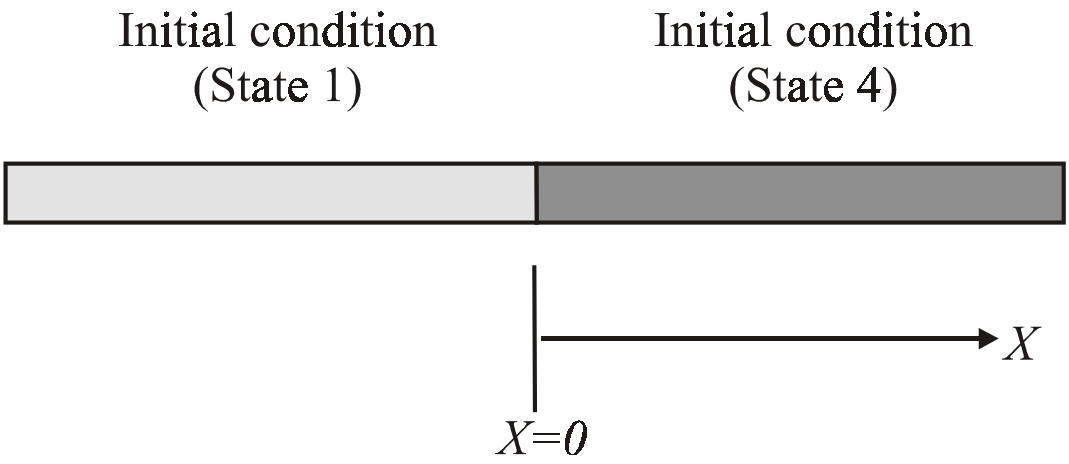

Figure 5.11: Geometry used for one-dimensional shock tube.

waves which occur in the manifolds of an internal combustion engine.

This is the first time this validation has been performed on CFX to the current author's knowledge.

5.2.1 Description

The one-dimensional shock tube problem is often used as a test for compressible fluid flow modelling. It has been extensively used as a test for one- and multi-dimensional engine manifold simulation codes [228, 214], and many other transient compressible flow simulations [157, 171, 172, 208, 209, 144, 143].

The configuration is shown in figure 5.11. It is a long, thin volume filled with a compressible gas. The section is initially divided into two subsections by a diaphragm, with the gas in the two subsections at different states. The diaphragm is at $X = 0$, and in the left hand side of the tube, $X < 0$, the initial state of the gas is defined as pressure, p_1 and temperature, T_1. For the right hand side, $X > 0$, the initial state of the gas is defined as pressure, p_4 and temperature, T_4.

At time $t = 0$ the diaphragm is instantaneously removed and the gases start to interact. It is assumed that the resulting flow is one-dimensional and that the fluid is inviscid and non-conductive. A compression wave is generated at the interface and propagates as a shock wave into the low pressure gas. A rarefaction wave is also generated, and propagates through the high pressure gas. After the compression wave has passed through the low pressure gas and the rarefaction wave has passed through the high pressure gas, the gases near the original location of the diaphragm are at the same pressure (that is, $p_2 = p_3$); however, the two regions of gas are

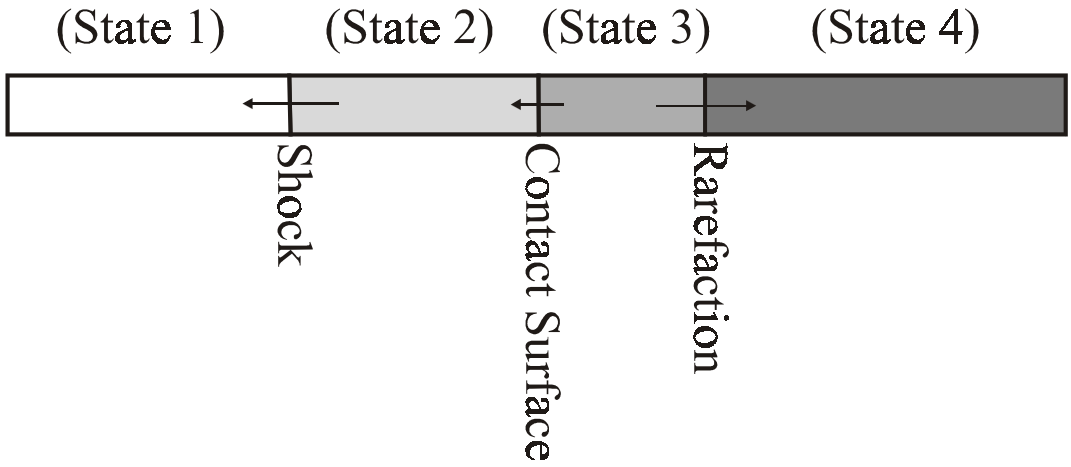

Figure 5.12: Diagram indicating the various gas states in the shock tube after a period of time has passed. The four main gas states are shown.

generally not at the same temperature (that is, $T_2 \neq T_3$). This temperature interface is called the contact surface. Figure 5.12 shows the state of the various gas regions, and figure 5.13 shows the typical gas state changes which occur.

The ends of the domain (X_{max}, X_{min}) are assumed to be far away, so no end effects or reflections occur.

The discontinuities occurring at the shock and contact surface present a severe test of the discretisation scheme. Additionally, the inviscid, non-conductive case has an analytical solution. These features make the shock tube simulation an excellent test of transient compressible flow simulations, and it has become a standard validation case.

5.2.2 Exact Solution

The exact solution, adapted from Liepmann and Roshko [179], for the pressure after the shock is given by

$$p_4 - p_2 \left(1 - \frac{(\gamma - 1)\left(\frac{a_1}{a_4}\right)\left(\frac{p_2}{p_1} - 1\right)}{\sqrt{2\gamma\left(2\gamma + (\gamma+1)\left(\frac{p_2}{p_1} - 1\right)\right)}} \right)^{\frac{-2\gamma}{\gamma-1}} = 0, \tag{5.1}$$

which must be solved for p_2. In equation 5.1, γ is the ratio of specific heats (taken as $\gamma = 1.4$ here), and a_1 and a_4 are acoustic velocities determined from $a = \sqrt{\gamma RT}$. Note that $p_2 = p_3$, as the post-shock and post-rarefaction pressures are equal.

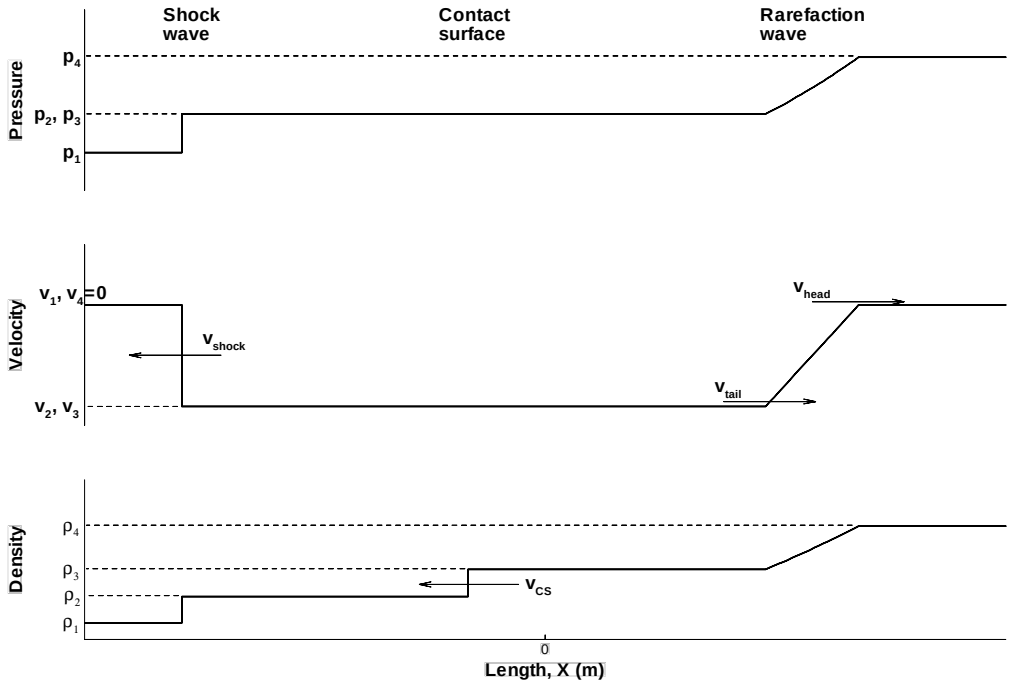

Figure 5.13: Representation of shock tube after some time has elapsed. In this example, a shock wave (left side) propagates to the left at velocity v_{shock}; the contact surface (centre) propagates left at velocity $v_{CS} = v_2 = v_3$; and the rarefaction wave (right side) propagates with the velocity at the head of the wave at v_{head}, and its trailing point propagates at v_{tail}.

Equation 5.1 can be solved for p_2 by a number of methods, a simple "halving the interval" or bisection method [107] was used here.

After the post shock pressure has been determined, the other parts of the exact solution are easily found. The post-shock fluid velocity, which is also the velocity of the contact surface, $v_2 = v_3 = v_{CS}$ is

$$v_2 = v_3 = \frac{2a_1}{\gamma - 1}\left(1 - \left(\frac{p_2}{p_4}\right)^{\frac{\gamma-1}{2\gamma}}\right). \tag{5.2}$$

It follows that the post-rarefaction density, ρ_3 is

$$\rho_3 = \rho_4\left(\frac{p_3}{p_4}\right)^{\frac{1}{\gamma}}, \tag{5.3}$$

and the post-shock density, ρ_2, is determined from

$$\rho_2 = \rho_1\left(\frac{p_2 + \frac{\gamma-1}{\gamma+1}p_1}{p_1 + \frac{\gamma-1}{\gamma+1}p_2}\right). \tag{5.4}$$

The velocity of the shock, v_{shock}, is

$$v_{shock} = \frac{v_2}{1 - \frac{\rho_1}{\rho_2}} \tag{5.5}$$

and the velocity of the tail of the rarefaction, v_{tail}, is

$$v_{tail} = a_2 - \frac{v_3}{1 - \frac{\gamma-1}{\gamma+1}}. \tag{5.6}$$

In the final solution, the position of the shock, X_{shock}, is determined by $X_{shock} = v_{shock}t$. The fluid to the left of the shock is at state ρ_1, T_1 and p_1, and has velocity $v_1 = 0$.

The fluid between the shock and the contact surface is at state ρ_2, T_2 and p_2, and has velocity v_2. The position of the contact surface, X_{CS}, is determined by $X_{CS} = v_2 t$.

The fluid between the contact surface and the tail of the rarefaction is at state ρ_3, T_3 and p_3, and has velocity v_3. The position of the tail of the rarefaction, X_{tail}, is determined by $X_{tail} = v_{tail}t$.

The fluid beyond the head of the rarefaction is at state ρ_4, T_4 and p_4, and has velocity $v_4 = 0$. The position of the head of the rarefaction, X_{head}, is determined by $X_{head} = a_4 t$.

The only part of the solution which remains to be determined is that which exists inside the rarefaction wave. For any X inside the rarefaction wave ($X_{tail} > X > X_{head}$), the density at can be evaluated by

$$\rho\left(X\right) = \rho_4 \left(\left(\frac{\gamma - 1}{\gamma + 1} \right) \left(\frac{X}{a_4 t} \right) + \left(1 - \frac{\gamma - 1}{\gamma + 1} \right) \right)^{\frac{2}{\gamma - 1}}, \tag{5.7}$$

the pressure by

$$p\left(X\right) = p_4 \left(\left(\frac{\gamma - 1}{\gamma + 1} \right) \left(\frac{X}{a_4 t} \right) + \left(1 - \frac{\gamma - 1}{\gamma + 1} \right) \right)^{\frac{2\gamma}{\gamma - 1}}, \tag{5.8}$$

and the velocity by

$$v\left(X\right) = - \left(1 - \frac{\gamma - 1}{\gamma + 1} \right) \left(\frac{X}{t} + a_4 \right). \tag{5.9}$$

The exact solution for any X or t can now be determined.

5.2.3 Numerical Modelling

In the configuration modelled here the initial conditions are $p_1 = 100\,\mathrm{kPa}$, $T_1 = 288\,\mathrm{K}$ and $p_4 = 200\,\mathrm{kPa}$, $T_4 = 288\,\mathrm{K}$. The gas is air, and is assumed to be an ideal gas with properties taken at 288 K, with negligibly small viscosity and thermal conduction coefficients. The simulation was run for $10^{-3}\,\mathrm{s}$ after the removal of the diaphragm. The length of the region modelled is 1 m, chosen so that no wave can reach the end of the domain in the simulation time, so no end reflections take place.

The Van Leer TVD differencing scheme was used on the momentum and enthalpy equations, and temporal differencing was performed using second order quadratic differencing. The default SIMPLEC algorithm was used as the solution technique. The under relaxation factors used were 1.0 for the velocity, density, temperature and enthalpy equations; and 0.9 was used for the pressure equation.

CFX cannot model zero viscosity or zero coefficient of conductivity fluids as these lead to divide by zero errors and cause the solver to crash. A molecular viscosity of $\mu = 1.0 \times 10^{-8}\,\mathrm{Pa\,s}$ and thermal conductivity of $\lambda = 1.0 \times 10^{-8}\,\mathrm{W\,m^{-1}\,K^{-1}}$ were used instead. It will be shown in section 5.2.5 that these values produce results which are effectively inviscid and non-conductive.

The result of the simulation is shown in figure 5.14. The exact solution is also shown for comparison. The simulation used 400 equally spaced nodes, and 400 time steps of $2.5 \times 10^{-6}\,\mathrm{s}$ (equivalent to a maximum CFL number of 0.46). The effect of the number of nodes and the time step size are discussed in section 5.2.6.

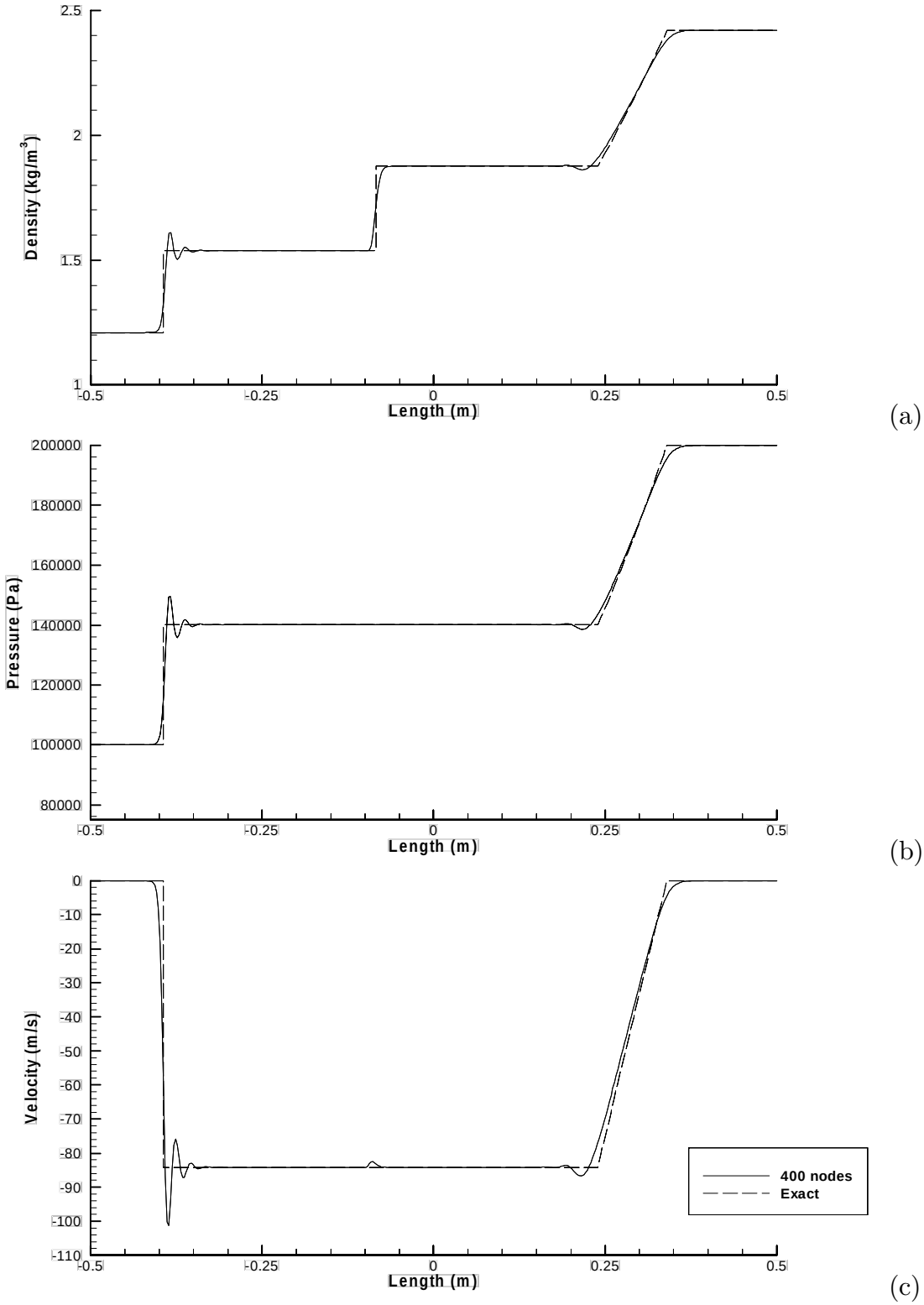

Figure 5.14: Density, pressure and velocity predictions from one-dimensional shock tube simulation, with comparison to exact solution at 10^{-3} s. (a) – Density; (b) – Pressure; and (c) – Velocity.

The simulated results predict the exact solution with very good accuracy. The post-shock and post-rarefaction gas states are predicted extremely accurately. The post-shock density, velocity and pressure are predicted with an error of 0.009%, 0.009% and 0.001% respectively.

The most obvious departure from the exact solution occurs near the shock, and to a lesser extent the rarefaction, where the simulated result cannot reproduce the very steep gradients, leading to an overshoot. There is also a smaller departure from the exact solution at the contact surface. Even though overshoots of around 10% occur near the shock, the density, velocity and pressure after the shock are predicted with as little as 0.009%, 0.009% and 0.001% error respectively. These overshoots or "wiggles" can be seen after the shock and, to a lesser extent, after the rarefaction wave. The overshoots are due to the second order time discretisation scheme causing overshoots and undershoots as it attempts to model the discontinuities.

The cause for the "wiggles" is described in section 3.2.5 for the advection terms, and the same concept applies here when using second order differencing for the temporal term. The effect of mesh density, time step size and numerical scheme will be further analysed in the following sections.

5.2.4 Overshoots and Shock Resolution

The effect of the mesh on the "wiggles" was tested by running the simulation detailed above, but with a range of mesh densities. Meshes consisting of 100, 200, 400 and 800 nodes were used. The results over the majority of the domain were essentially the same as has been detailed in section 5.2.3, for instance the post-shock pressure was predicted with a worst case error of 0.02%.

The only significant differences between meshes occurred near the shock. A magnified view of predictions near the shock is shown in figure 5.15. It shows that the peak of the overshoot has a similar magnitude for all mesh densities at around 148 kPa or around 20% of the pressure difference across the shock. It also shows that all the meshes required around four nodes to resolve the shock, so the gradient of the the discontinuity predicted is directly proportional to mesh density. Thus the size of the overshoot in the "wiggles" is largely independent of mesh density. How sharply the shock is resolved and the distance required before the simulation settles down to the correct post-shock value improves in proportion to mesh density.

The shock position is defined as the location where the simulation predicts half way between the analytical pre- and post-shock states, here called the 50% point. In general, this point occurs between node points so linear interpolation is used to

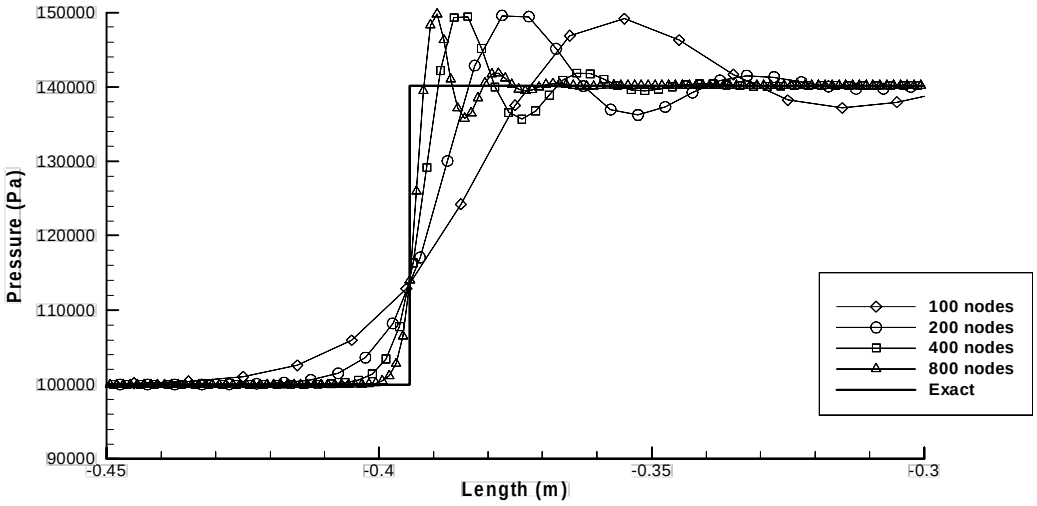

Figure 5.15: Detail of pressure near the shock from the one-dimensional shock tube simulation.

	Shock		**Contact Surface**		**Rarefaction Wave**	
	X	Error	X	Error	X	Error
Exact	-0.394		-0.0841		0.292	
100 nodes	-0.389	1.3%	-0.0848	0.7%	0.286	2.0%
200 nodes	-0.391	0.7%	-0.0847	0.6%	0.289	1.0%
400 nodes	-0.393	0.3%	-0.0846	0.5%	0.291	0.4%
800 nodes	-0.394	0.2%	-0.0845	0.4%	0.292	0.2%

Table 5.5: Position of the shock wave, contact surface and rarefaction wave for various mesh densities, in comparison to analytical solution. The errors are normalised against analytical solution.

determine the location between nodes. Similarly, the position of the contact surface and rarefaction wave can be calculated, and are shown for the various meshes in table 5.5.

Table 5.5 shows the position of the shock, contact surface and rarefaction wave is predicted with excellent accuracy, with the 100 node solution achieving accuracy of better than 2%, and the 800 node solution achieving accuracy of better than 0.4%. This shows that the accuracy of the predicted position of the shock wave, contact surface and rarefaction wave was very good, and improved with mesh refinement.

Run	μ (Pa s)	λ (W m^{-1} K^{-1})	Max. Difference	% Difference
1	1.0×10^{-8}	1.0×10^{-8}	–	–
2	1.0×10^{-8}	2.531×10^{-2}	3.9×10^{-5}	0.002
3	1.788×10^{-5}	1.0×10^{-8}	1.1×10^{-5}	0.0007
4	1.788×10^{-5}	2.531×10^{-2}	3.9×10^{-5}	0.002

Table 5.6: Combinations of viscosity and thermal conductivity tested in the one-dimensional shock tube.

5.2.5 Inviscid and Non-Conductive Assumptions

As stated in section 5.2.3, values of $\mu = 10^{-8}$ Pa s and $\lambda = 10^{-8}$ W m^{-1} K^{-1} were used for the molecular viscosity and thermal conductivity coefficient respectively. To assess the sensitivity of the results to μ and λ, a series of otherwise identical simulations were performed, using the combinations of μ and λ values listed in table 5.6. The values of $\mu = 1.788 \times 10^{-5}$ Pa s and $\lambda = 2.531 \times 10^{-2}$ W m^{-1} K^{-1} were chosen as they are typical values of air at 288 K, and approximately 10^3 and 10^6 times larger respectively than the other value used.

The results are shown in table 5.6. "Maximum Difference" is the greatest difference in density at any node between that run and run 1. "% Difference" is the maximum difference expressed as a percentage of that from run 1. The largest difference seen is 0.002%, an insignificant variation, even though the values of viscosity and thermal conductivity changed many orders of magnitude. This means using $\mu = \lambda = 10^{-8}$ is appropriate for the results to represent a fluid which is inviscid and non-conductive.

5.2.6 Time Step Size

The Courant-Friedrichs-Lewy (CFL) stability criterion for a compressible gas is

$$CFL = \frac{(a + |u|)\ \Delta t}{\Delta X}, \tag{5.10}$$

where a is the local acoustic velocity, u is the fluid velocity in the X direction, Δt is the simulation time step and ΔX is the node spacing in the X direction. This is the fundamental stability criterion for time step size in simulations of high Mach number flows [99, 237, 96].

The effect of various time step sizes was tested on a simulation with 400 nodes, and the pressure predicted from these simulations is shown in figure 5.16. The predictions are virtually identical over the entire domain except near the overshoot at the top of the shock. A magnified view of the shock overshoot is shown in figure

5.16b. The smaller time step simulations capture the shock fractionally more sharply than the larger time step simulations, but the size of the overshoot remains about the same. The simulation was found to diverge if time steps larger than $CFL = 0.62$ were used. It follows that maintaining $CFL \leqslant 0.5$ was the best compromise between simulation accuracy and simulation speed.

5.2.7 Other Numerical Schemes

It is possible to use other numerical schemes to reduce the "wiggles" near the shock. Some examples of the effects of these schemes are shown in figure 5.17. Here the results obtained from the numerical method outlined above are compared to the results using linear time differencing, and a further variation in which linear time differencing and a number of high-speed compressible flow options have been used. This "optimised" simulation makes use of a number of high-speed compressible flow options available in CFX-4.3, namely a modified Rhie-Chow algorithm using harmonic averaging, a modified pressure correction suitable for high Mach number flows which includes a density correction, linear time stepping and smaller time steps at $CFL = 0.23$. Further details about this scheme can be found in the CFX user manual [13]. All three simulations use 400 nodes.

Simply replacing the second order quadratic time differencing with first order linear time differencing is seen to eliminate the overshoots, but the shock is not captured as sharply. The optimised simulation resolves the shock almost as sharply as the quadratic time stepping, but has only very small overshoots. The optimised simulation is the best compromise between reducing overshoot size and sharp resolution of the shock.

If resolving shocks was the primary aim for this work this optimised scheme would be the best one to use. However, it was found that the optimised scheme did not perform well in three-dimensional internal combustion engine flows. In engine flows the fluid is often at low Mach numbers, and is strongly influenced by three-dimensional effects and turbulence. High Mach number effects such as shocks exist only for a small fraction of the engine cycle. It was found that the optimised scheme limited time step size to around $CFL = 0.5$ in engine simulations, whereas the scheme described in chapter 3 was not constrained by a maximum CFL criterion value. The scheme described in chapter 3 was found to be stable and accurate at very large time steps, up to $CFL = 50$.

Thus the quadratic time differencing scheme was used for IC engine modelling as it is the best compromise as it can resolve shocks reasonably well, whilst using

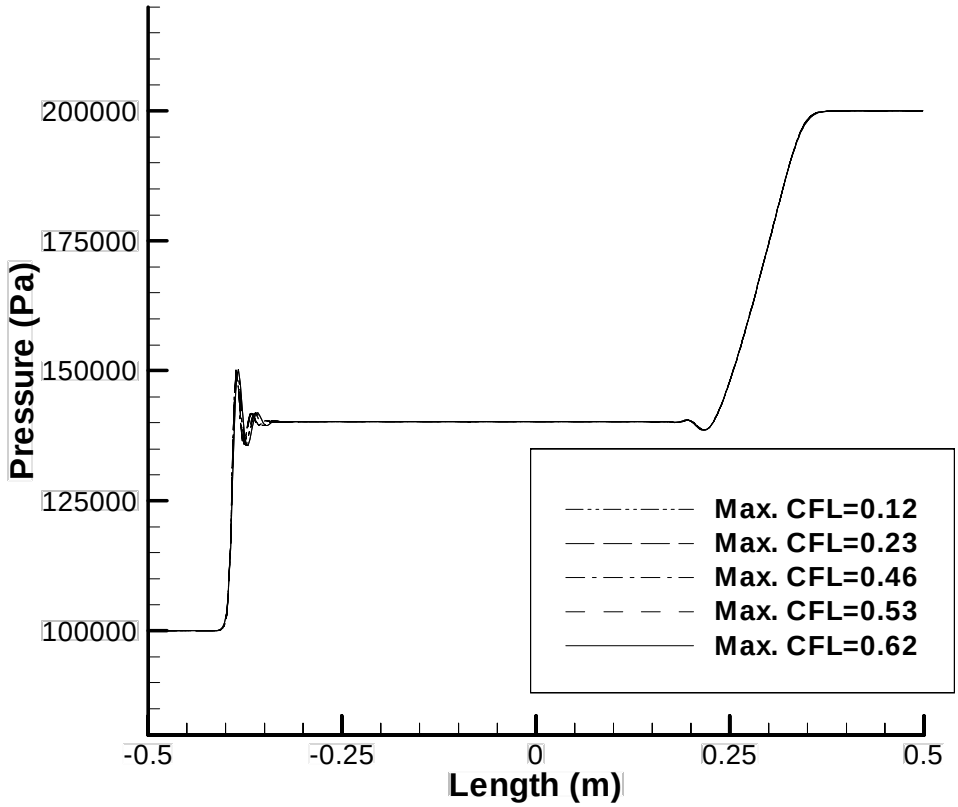

(a)

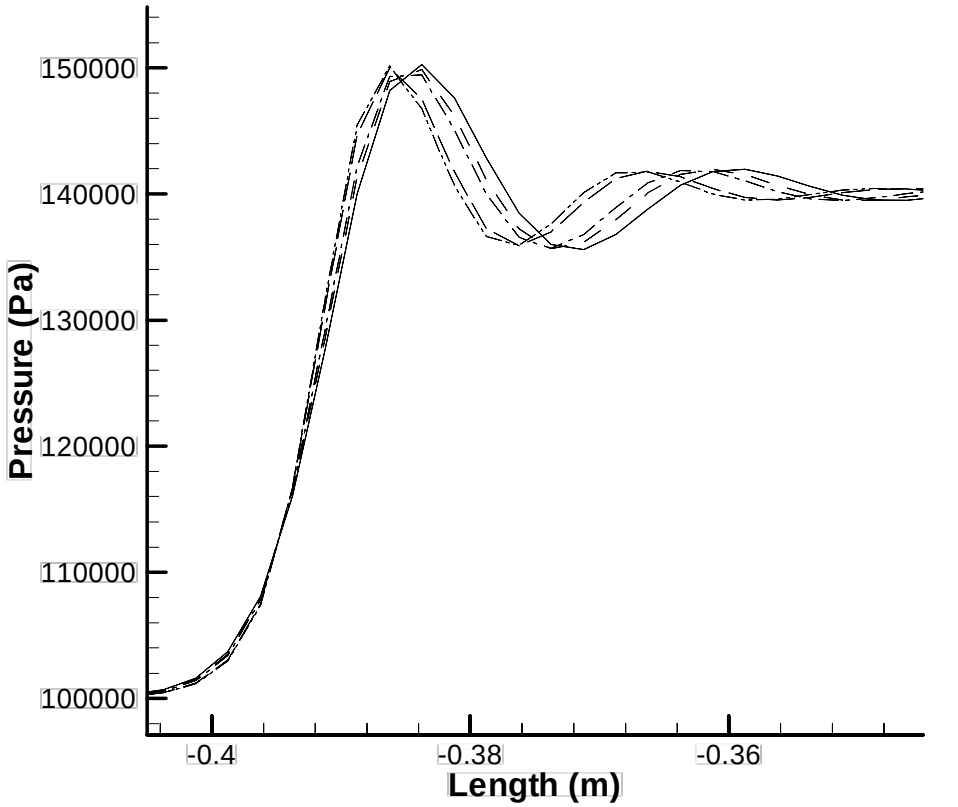

(b)

Figure 5.16: Results of the one-dimensional shock tube simulation using various time step sizes. (a) – Full field; and (b) – Magnification of the region around the shock wave.

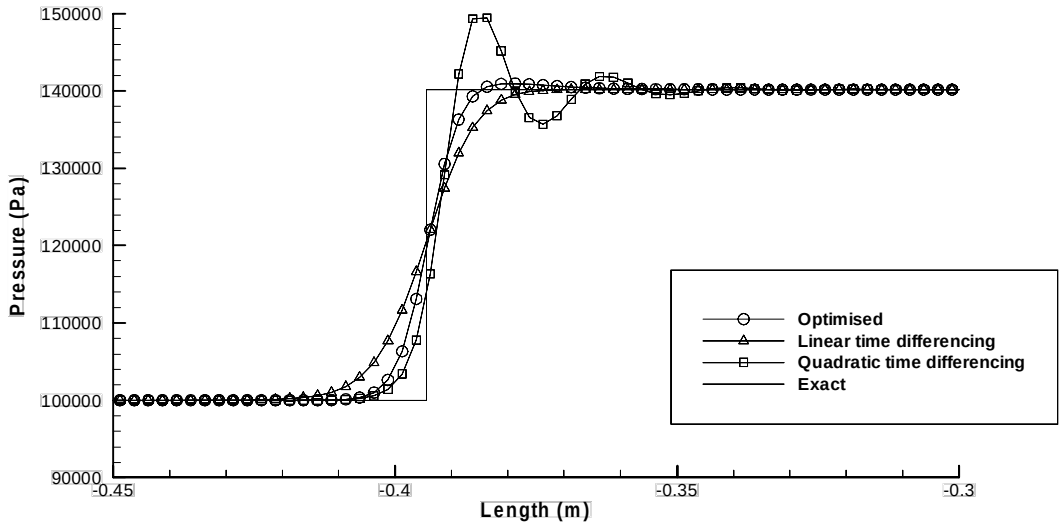

Figure 5.17: Detail of pressure near the shock for linear time differencing, quadratic time differencing and an optimised scheme for the one-dimensional shock tube simulation.

a time step up to 100 times larger than that allowed with the optimised algorithm in engine simulations.

5.3 Discussion

The validations discussed in this chapter show the accuracy of the CFX code in a number of types of flow. Flow over a backwards facing step is a standard benchmark validation for flows involving separations and reattachments. It is discussed in sections 5.1.1 and 5.1.2, where CFX is found to predict this flow in both laminar and turbulent regimes. The transient grid section of the code is assessed in section 5.1.4, and found to accurately predict simple validation exercises. Unfortunately the authors did not attempt to validate their IC engine simulations, so no conclusions can be drawn about its accuracy in more complicated transient grid flows. The effect of various differencing schemes on results (section 5.1.3) shows low order differencing schemes can cause inaccurate results. Higher order schemes are more accurate, but can cause boundedness problems.

The ability of CFX to simulate simple turbulent flows is assessed in section 5.1.7 by studying predictions of a turbulent boundary layer. More complicated turbulent flows are assessed in sections 5.1.6 and 5.1.8, and found to show good accuracy. The importance of adequate grid resolution to predict the flow structure is shown to be

vital in these flows.

Finally, a validation is performed by the current author using the one-dimensional shock tube problem. This is a standard benchmark validation exercise for compressible transient flows, yet to the author's knowledge this is the first time this validation has been performed on the CFX code. The code is found to very accurately model the post-shock and post-rarefaction gas state very accurately, with errors less than 0.02%. The position of the shock wave, contact surface and rarefaction wave were also very accurately predicted, to an accuracy of 0.4% or better by the 800 node simulation.

The code does, however, predict significant "wiggles" at the shock, contact surface and rarefaction wave discontinuities. It is possible to reduce the wiggles by using a numerical scheme more suited to shock wave flows, however this scheme is unsuitable for modelling general engine flows.

The flows found in engines are turbulent, compressible, transient, and have many separations. These validations show the CFX code to accurately model these flow phenomena. However, the code has not yet been directly assessed for the ideal validation for the current work—that of engine in-cylinder flow. This direct validation is discussed in chapter 6, where a validation of the CFX code in modelling in-cylinder flow by comparing the simulation results to high quality experimental data is presented.

Chapter 6

Compression Stroke Tumble Vortex Breakdown

Simulation of the breakdown of a tumble vortex into turbulence during the compression stroke of an internal combustion engine is a very complicated process, and is not fully understood. It is also a demanding test of a numerical model. In this chapter the CFD simulations of the current author, part of which has been published [142], are compared with experimental data. The experimental data is derived from Particle Image Velocimetry (PIV), Laser Doppler Anemometry (LDA) and Laser Doppler Velocimetry (LDV) measurements from a group of researchers including Marc, Charnay, Bazile, Borée, Ben, Moreau, Lecordier and Maurel from the Institut De Mechanique des Fluides de Toulouse (IMFT), France [46, 187, 188, 189].

This work was performed because a validation of the ability of the CFX code to model in-cylinder flows was required. Further, the simplified nature of the configuration allows the physical mechanism and nature of tumble breakdown to be understood more readily.

6.1 Previous Works

6.1.1 Experimental Studies

Many experimental studies of tumble flows have been performed [207, 168, 156, 155, 90, 234, 241, 137]. A good example of an experimental study of tumble flow is performed by Rouland et al [241], who presented a study of a motored pentroof combustion chamber engine. Baffles were placed in the intake manifold to increase the strength of the tumble flow. An example of the results achieved is shown in figure 6.1, which shows the velocity vector field measured in the combustion chamber

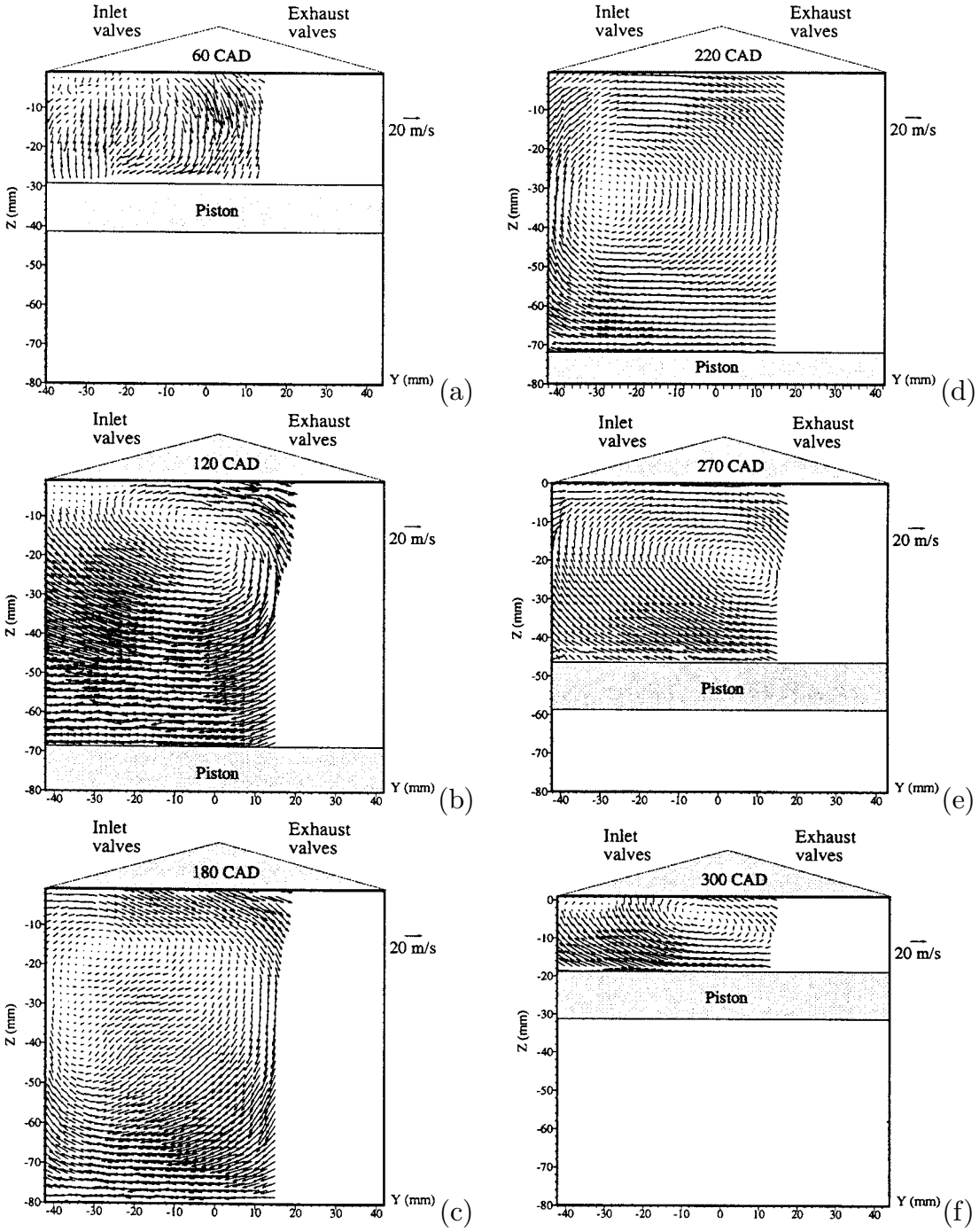

Figure 6.1: PIV ensemble averaged velocity fields in a pentroof combustion chamber at 2000 rpm, from Rouland [241]. (a) – 60 °CA; (b) – 120 °CA; (c) – 180 °CA; (d) – 220 °CA; (e) – 270 °CA; and (f) – 300 °CA.

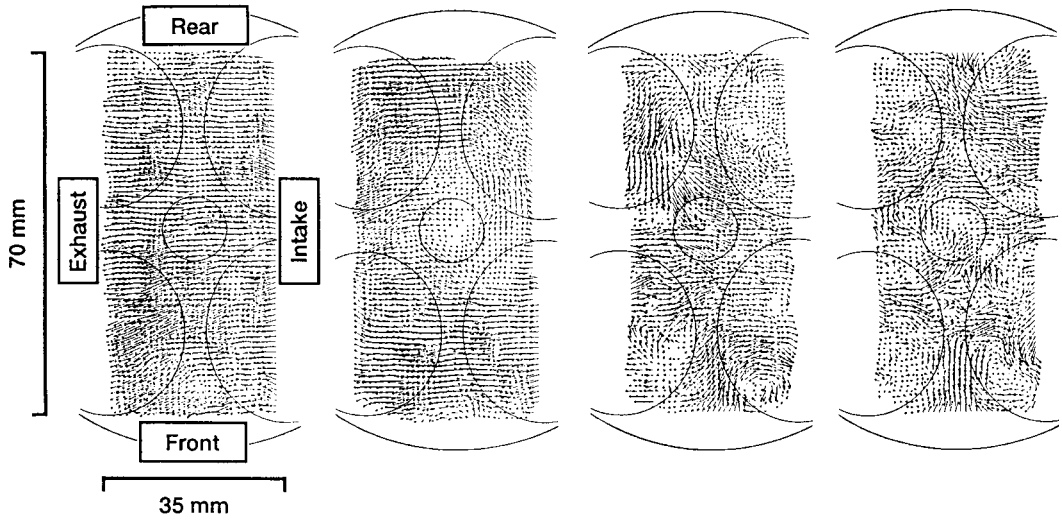

Figure 6.2: Flow field structures 8 mm below spark plug during the compression stroke of a pentroof combustion chamber engine. Shown, from left to right, is 270 °CA, 315 °CA, 345 °CA and TDC. Reproduced from Kuwahara and Ando [168].

symmetry plane at 2000 rpm. The tumble vortex forms during the intake stroke, and persists through the entire compression stroke. In the final frame at 300 °CA significant flattening of the tumble vortex is seen, but the tumble flow field still remains.

This study did not proceed far enough into the compression stroke to measure a peak of turbulence associated with tumble breakdown. It also did not pick up a breakdown of the tumble vortex.

Kuwahara and Ando [168] report measuring the decay of swirl and tumble flow fields into turbulence at the end of the compression stroke. However they only display a flow field perpendicular to the tumble plane, as shown in figure 6.2. It does show, although not very clearly, a fairly uniform flow field at 270 °CA progressing to a highly disorganised and turbulent field at TDC. The TDC visualisation does show many small eddies, understood to be the result of the breakdown of the tumble vortex. However, this plane cannot show the process of tumble vortex breakdown.

Kang and Baek [155, 156] and Dimopoulos and Boulouchos [90] confirm tumble as a turbulence enhancement mechanism, based on velocity fluctuation measurements. No measurements of the actual breakdown of the tumble flow were reported.

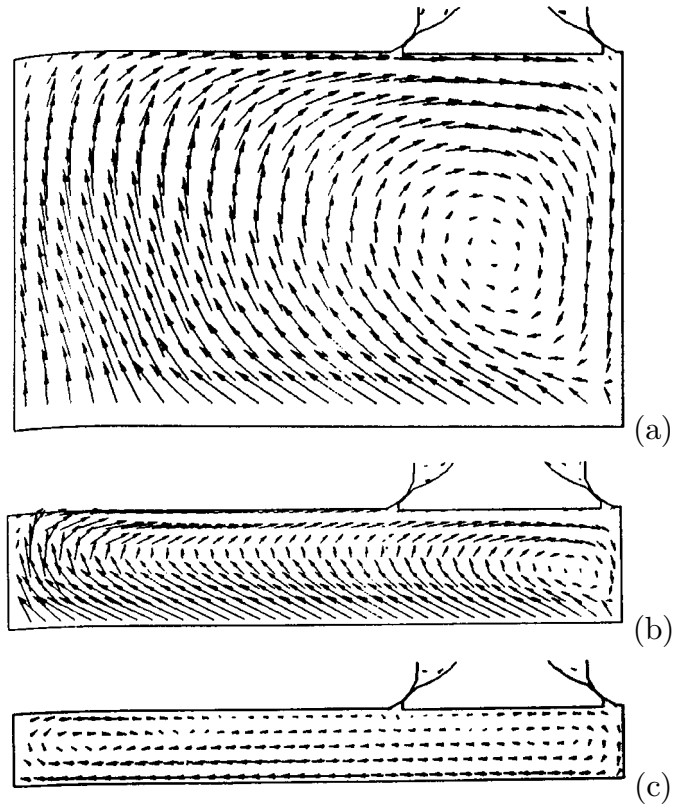

Figure 6.3: Development of in-cylinder flow during the compression stroke, reproduced from Khalighi [159]. (a) – 270 °CA; (b) – 330 °CA; and (c) – TDC.

6.1.2 Numerical Studies

The current study is not the first time tumble vortex decay during the compression stroke of an internal combustion engine has been simulated. Many numerical studies have been performed focussing on the flow evolution during the compression stroke [159, 126, 202, 198, 199, 200, 201, 176, 175], and dozens more works are described by Hill and Zhang in their review of the topic [137].

A typical example of the types of flows predicted is given by Khalighi [159]. The simulations were performed using a finite volume solver and the k-ϵ turbulence model. The model only possessed a single valve as only the inlet and compression strokes where studied. Figure 6.3 shows the flow simulated during the compression stroke in his engine. Mid-way through the compression stroke (figure 6.3a), a strong tumble vortex is visible. As the compression proceeds (figure 6.3b), the vortex is seen to move to one side of the domain and weaken considerably. By the end of the compression stroke, the vortex has all but disappeared. Figure 6.4 shows that as the tumble vortex weakens, it corresponds to a reduced tumble ratio, and a peak of turbulence just before TDC.

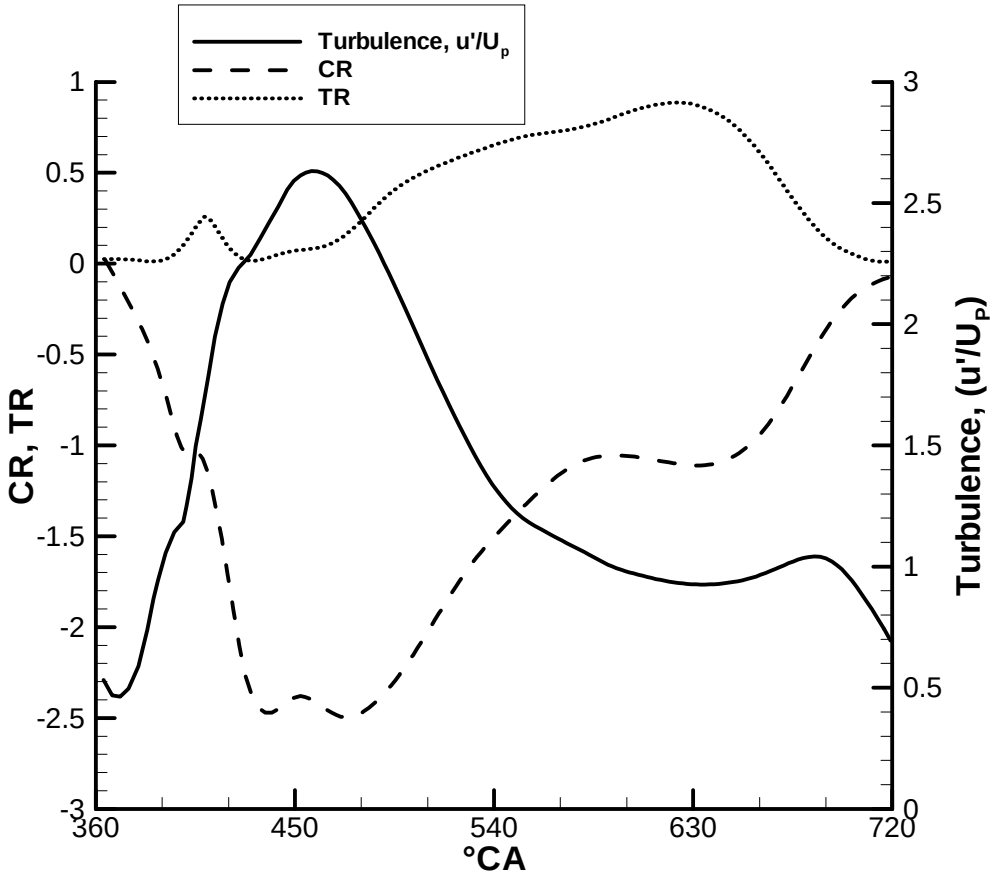

Figure 6.4: Normalised mass averaged turbulence, TR and CR against crank angle during the compression stroke. Turbulence is normalised against U_P, the mean piston velocity. Adapted from Khalighi [159].

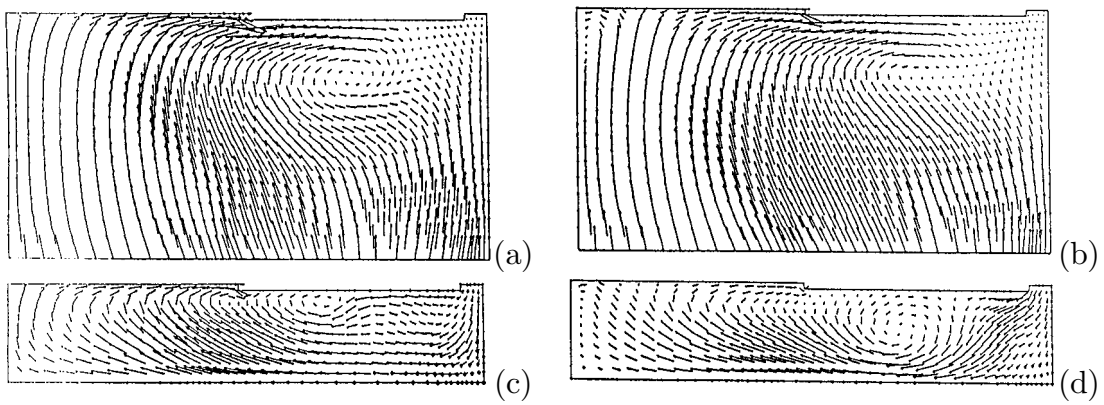

Figure 6.5: Velocity field predicted by various turbulence models during the compression stroke in the cylinder symmetry plane, from Lebrère and Dillies [176]. (a) – 300 °CA, k-ϵ model; (b) – 300 °CA, Reynolds stress model; (c) – TDC, k-ϵ model; and (d) – TDC, Reynolds stress model.

A comparison of compression stroke simulations using k-ϵ and RSM turbulence models has been performed by Lebrère and Dillies [176] and Lebrère et al [175]. The geometry tested generated a weak tumbling flow, rather than the very strong tumble flow considered in the current study. The Reynolds stress turbulence model was found to be marginally more accurate, however the differences between the two models were only small. An example of their results is shown in figure 6.5, which shows simulated flows during the compression stroke of the motored engine. Figure 6.5a and 6.5b shows the flow at 300 °CA to be very similar between the two turbulence models. More variation is seen at TDC in figure 6.5c and 6.5d, however the fundamental structure of the two flows is still similar.

The mechanism described by Khalighi [159], Lebrère et al [175, 176] and the many other studies in this area, is in general agreement with the way tumble breakdown is thought to occur (section 4.2). These papers are typical of the many studies published on compression stroke flow; they all predict the tumble vortex weakening but staying coherent throughout the entire compression stroke.

Despite this general agreement on tumble behaviour, there remains a fundamental problem. Rodi indicates that:

> "The large eddies interact with the mean flow (because the scales of both are similar), thereby extracting kinetic energy from the mean motion and feeding it into the large-scale turbulent motion. The eddies can be considered as vortex elements which stretch each other. Due to this vortex stretching, which is an essential feature of the turbulent motion, the energy is passed on to smaller and smaller eddies until

> viscous forces become active and dissipate the energy. This process is called energy cascade." [239]

This means that the energy cascades from the mean flow to the large turbulent structures to the medium turbulent structures to the smallest turbulent structures. Herein lies the problem; if a large tumble vortex is to break down into many small vortices, the energy cascade principle tells us it does it by "cascading" the energy down through successively smaller structures. None of the studies mentioned previously has actually identified a tumble vortex breaking down, it is only shown as weakening and the turbulence increasing. One would expect the tumble breakdown would begin with the tumble vortex breaking up into a small number of vortices as the start of the "energy cascade". All of the previously mentioned studies had sufficient grid resolution to follow this initial breakup, yet none of them had predicted it in their simulations.

Hill and Zhang [137] also suggest that there are two possible vortex break down processes. The first is the mechanism described previously, being that the tumble vortex instantly (or at least quickly) is destroyed and generates small scale turbulent structures simultaneously. The second mechanism is that of a gradual breakdown, where the tumble vortex breaks down into a small number of vortices, which break down into a large number of smaller vortices, and so on until the vortices are very large in number and the size of the turbulent structures. This second mechanism is in better agreement with the turbulent energy cascade concept.

The only studies found by the current author which describes a large scale mean flow vortex breaking up into smaller vortices during the compression stroke are those of Naitoh et al [202, 198, 200]. These works use an early LES model to simulate intake and compression stroke flows on various engine geometries.

An example of his early results is shown in figure 6.6. A comparison with experimental results was performed, but it was only qualitative since, inexplicably, the numerical and experimental configurations were completely different. For example, the engine speed was different between the simulation and the experimental model, and the fluid was air in the CFD simulation and freon-12 in the experimental model. The comparison is not an objective assessment of the accuracy of the numerical simulation.

Later Naitoh and Kuwahara [200] performed a direct comparison with experimental results. The engine geometry is remarkably similar to the geometry considered in the current work, being a model engine with a rectangular piston 100 mm × 200 mm, with a stroke of 100 mm. In the numerical model it was only modelled as 100 mm × 20 mm with periodic boundaries on either side. This reduction of the

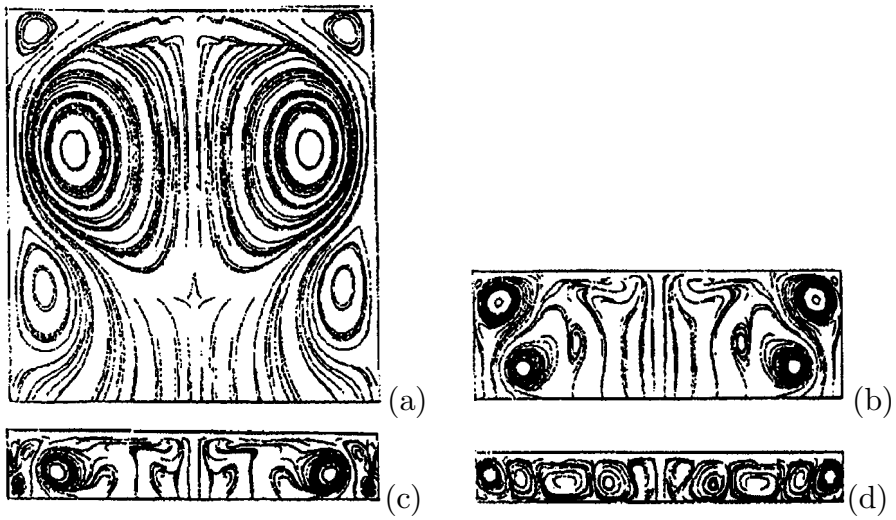

Figure 6.6: Streamlines modelled during the compression stroke of an axisymmetric flat piston engine from Naitoh et al [202]. Engine speed is 1400 rpm, and compression ratio is 10.0. (a) – BDC (180 °CA); (b) – 240 °CA; (c) – 330 °CA; and (d) – TDC (360 °CA).

piston width was not justified by the authors. It would lead to an artificial restriction on the flow, as structures larger than 20 mm could not form. Whether this assumption had a significant effect on results is not clear.

The experimental and numerical model was run at 998 rpm and a compression ratio of 3.9, and the intake channel was offset and angled to create a tumble flow field. Two engine cycles were calculated. No information is given as to how many experimental cycles were performed, it is assumed only one cycle result was used. The fluid used was freon-12 as it has a low acoustic velocity, allowing the use of Mach-Zehnder interferometry to experimentally visualise density contours.

A sequence of images showing the entire intake and compression stroke of the first engine cycle is shown in figures 6.7 and 6.8. Unfortunately the quality of reproduction of the images was very poor, however the detail is sufficient to make judgements as to the effectiveness of the numerical simulations.

During the intake stroke, shown in figure 6.7, the intake jet is seen creating regions of high density gradients. This is displayed by both the experimental and numerical models. The motion of the main vortex is captured accurately by the numerical simulation at 80 °CA and 100 °CA, however the other images show the numerical model varying somewhat from the experimental results.

The quality of the reproduction of the compression stroke is even poorer, and makes comparisons difficult. Generally there appears to be some agreement, but the critical final three images are not sufficiently clear to make an informed comparison.

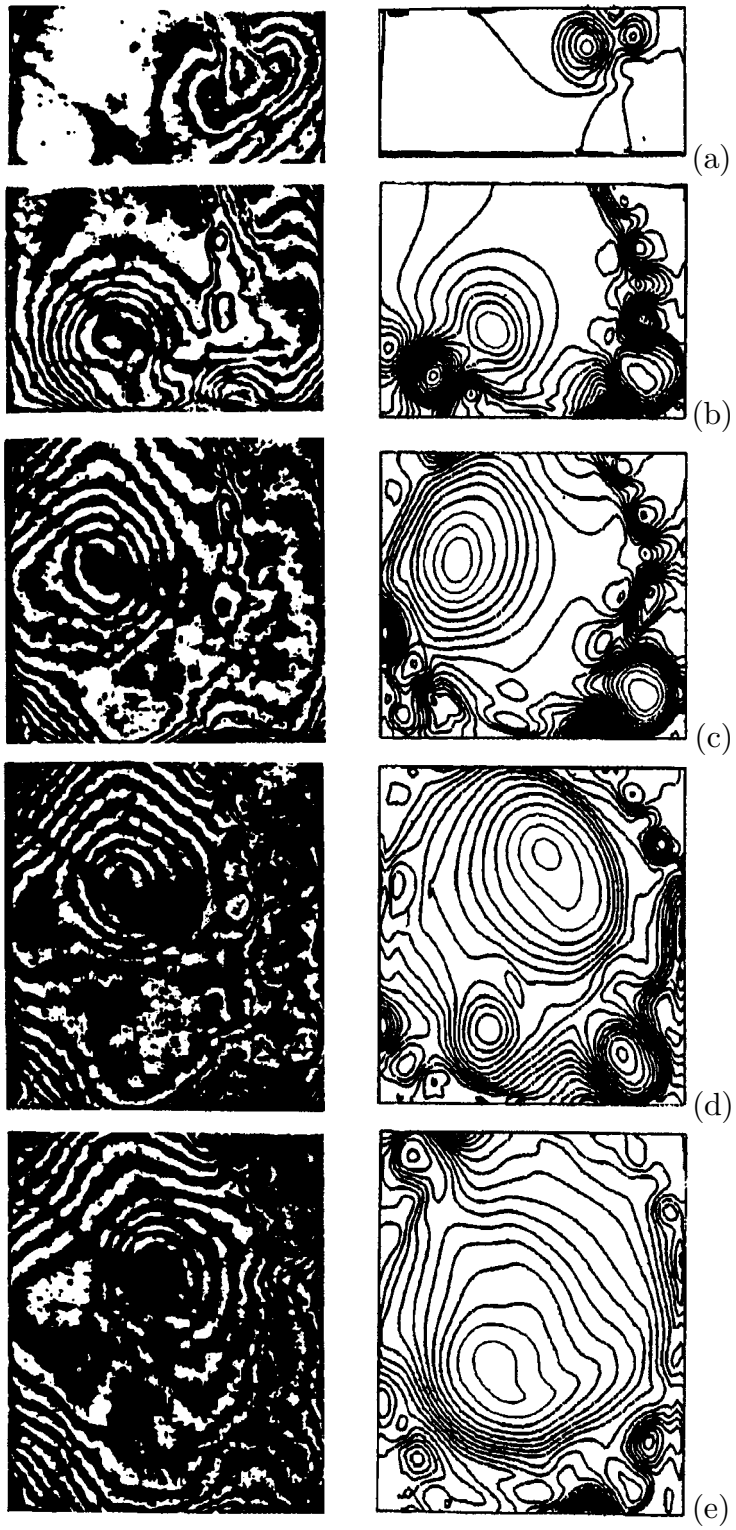

Figure 6.7: Experimental (left) and simulated (right) density contours in the intake stroke of rectangular piston engine, from Naitoh and Kuwahara [200]. (a) – 40 °CA; (b) – 80 °CA; (c) – 100 °CA; (d) – 120 °CA; and (e) – 140 °CA.

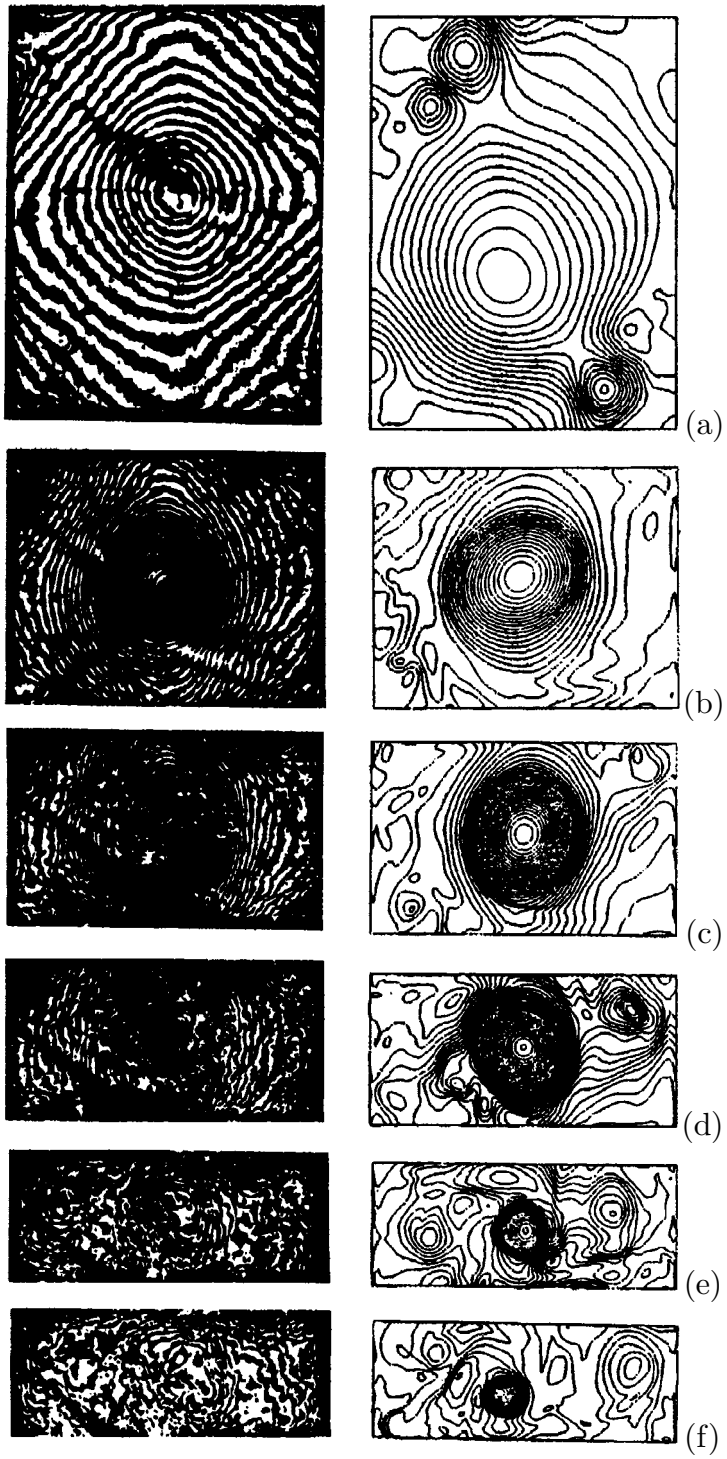

Figure 6.8: Experimental (left) and simulated (right) density contours in the compression stroke of rectangular piston engine, from Naitoh and Kuwahara [200]. (a) – 200 °CA; (b) – 280 °CA; (c) – 300 °CA; (d) – 320 °CA; (e) – 340 °CA; and (f) – 360 °CA.

There appear to be small structures predicted at the edges of the domain by the numerical model at 200 °CA and 280 °CA which do not appear experimentally. The numerical results at 320 °CA, 340 °CA and TDC predict a number of smaller vortices indicating that the main tumble vortex is breaking up, however the structure of the flow cannot be clearly seen in the experimental results.

Overall, Naitoh and Kuwahara's work [200] appears to simulate tumble vortex breakdown, and perform an elementary comparison with experimental data. Unfortunately, the results and the comparison can only be described as basic. The assumption that the experimental geometry piston width of 200 mm can be represented by a width of 20 mm is a further limitation with this work.

This leads to the rather surprising conclusion that tumble vortex breakdown is accepted as the mechanism by which tumble flows enhance engine performance and is used extensively in modern engine design, yet only one team of researchers have managed to numerically simulate this breakdown. In the few publications to report simulating the breakdown, the comparison with experimental data is poor and uncertain.

This chapter presents a detailed and rigorous comparison of a numerical simulation to quality experimental data of tumble vortex breakdown in the compression stroke of an engine. To the current author's knowledge, this is the first comparison to be performed in such detail.

6.2 Description

6.2.1 Geometry

The geometry being studied is a square piston model engine, shown in figure 6.9. The square piston arrangement was developed by the IMFT researchers as it allows easy optical access for experimental observations of fluid velocities.

Fortunately, the rectilinear geometry also considerably simplifies the numerical model required. This is due to the orthogonal nature of the domain, which means a body fitted grid transformation is not required. The orthogonal grid version of the numerical code is considerably simpler and faster.

The dimensions of the Z mid plane of the geometry used by Marc et al [188, 187, 46, 189] is shown in figure 6.10. The dimensions in the Z direction are not shown for clarity, however the cylinder region extends 100 mm in the Z direction, and the intake channel extends 96 mm in the Z direction.

The simulations presented here were performed using two compression ratios

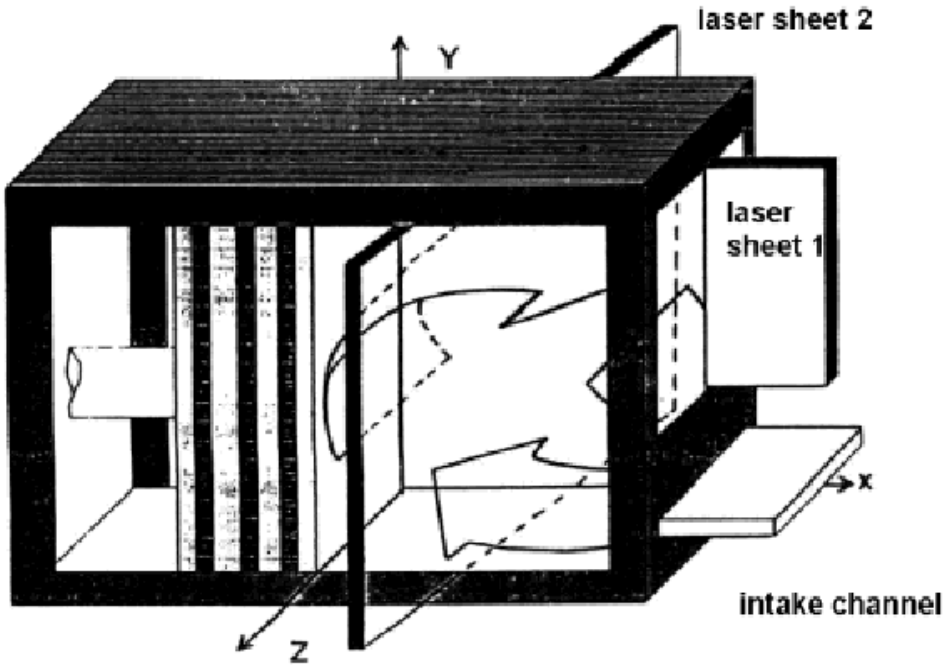

Figure 6.9: Geometry used by IMFT researchers, from Borée et al [46].

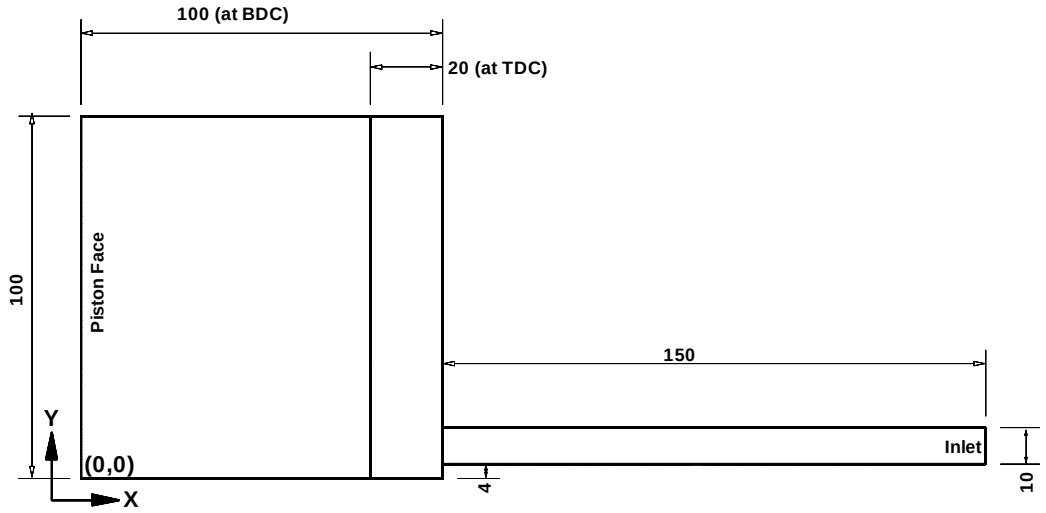

Figure 6.10: Dimensions of the geometry in the Z mid plane from Marc et al [188, 187, 46, 189]. Geometry shown for $CR = 5$.

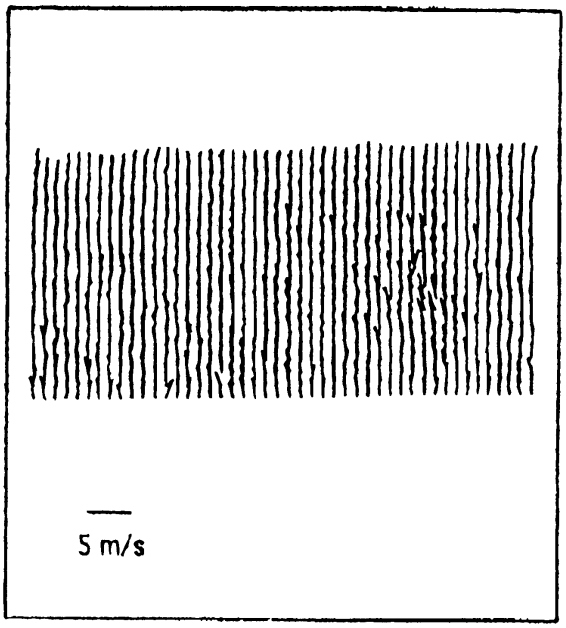

Figure 6.11: Velocity vectors in YZ plane ($X = 90\,\text{mm}$), at BDC from Marc et al [188].

(CR), being $CR = 4$ to match the results presented in Maurel et al [189], and $CR = 10$ to match the results presented in Marc [187].

6.2.2 Dimensionality

In the early work of Marc et al [188], the level of two-dimensional flow was investigated. They presented the visualisation shown in figure 6.11, which shows velocity vectors in the YZ (cross tumble, see figure 6.9) plane at BDC. As the visualisation showed no significant flows in the Z direction, it was assumed the flow was two-dimensional in the XY plane. Additionally, as the width to height ratio used for the intake channel is 96 mm to 10 mm, or a ratio of 9.6, Marc et al suggested that the intake flow was two-dimensional over the central 80% of the channel width. They then supposed that the central section of the flow could be assumed as two-dimensional flow, and analysed the flow on this basis.

This assumption that the flow is two-dimensional is a dramatic simplification for both the experimental and numerical models. The remainder of the work of Marc et al [188], and the publication by the current author based on it [142], then analysed the flow on this basis.

The later works by Marc [187], Borée et al [46] and Maurel et al [189] found that

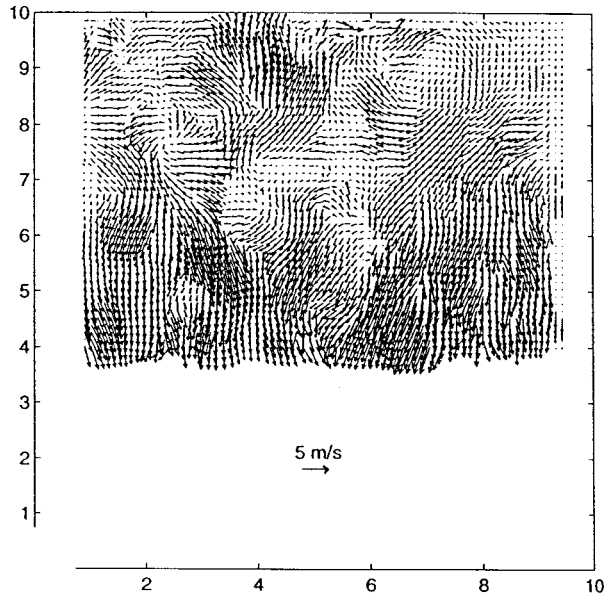

Figure 6.12: Velocity vectors in YZ plane at 61 °CA, from Marc [187].

the two-dimensional flow discovered in their earlier work by Marc et al [188] was only true for a small section of the flow near BDC, and not representative of the flow in general. Both the intake and compression strokes generated considerable three-dimensional flows which were not observed in their earlier work, as can be seen in figure 6.12, a frame from early in the intake stroke. Many three-dimensional flow structures can be seen. The current author has also found numerically that the flow departs significantly from two-dimensional behaviour.

It is clear that the flow contains large three-dimensional structures, and cannot be adequately described by a two-dimensional flow. For completeness, both two- and three-dimensional simulations will be presented in the following analysis.

6.2.3 Other Numerical Factors

The fully compressible Navier Stokes equations, as specified in section 2.2 were used to describe the flow. The Van Leer differencing scheme was used on the momentum, enthalpy and turbulence equations, as specified in section 3.2.3. Central differencing was used on the pressure correction equation. The temporal differencing scheme was second order backward differencing, as described in section 3.2.1.

The linearised momentum equations were solved using a Stone solver, the linearised turbulence equations by line relaxation and the pressure correction equation by the Algebraic Multi-Grid (AMG) solver. At each time step, convergence was de-

clared when the residual from every equation had improved by a factor of 5.0×10^{-4} from the first iteration at that time step.

The time step of the simulation was an increment of 0.25 °CA. The effects of halving the time step interval was investigated and found to have no significant effects.

The working fluid was air, and fluid properties were assumed constant. Fluid properties were taken as that of air at 298 K.

The fluid entering the domain through the inlet boundary condition was set to a pressure of 100 kPa and a temperature of 298 K. All walls were assumed to have a temperature of 293 K.

In Marc [187], the valve is specified as closing over a range of 150 °CA to 200 °CA. The details of the valve motion inside this range was not specified. For the current work the valve motion was assumed to be instantaneous, and to occur at BDC. The valve action was modelled numerically by removing the inter-block boundary between the intake manifold block and the cylinder block at BDC.

Marc [187] studied the motion of the piston in his experiment, and found that it was very close to sinusoidal, but slight discrepancies from sinusoidal were found in the velocity. For the current work the piston motion was assumed to be a pure sine wave, and was modelled by stretching the cylinder grid in the X direction. No node elimination or creation was performed, so the number of node points is the same at TDC and BDC.

The speed of the engine was set to 206 rpm, to match the results from Maurel et al [189] and Marc [187].

6.2.4 Initial Conditions

The simulation starts at TDC with zero velocity and atmospheric pressure (100 kPa) and temperature (298 K) over the entire domain. Initial values of turbulence parameters were set using the method described by Soltani and Veshagh [258], where the initial value of the turbulence kinetic energy intensity, k_{init}, is given by

$$k_{init} = 0.3V_P^2, \tag{6.1}$$

in which V_P is the mean piston velocity. This simulation was also run using a RSM model, where the initial turbulence level was defined by assuming the initial turbulence to be isotropic, so that the three normal Reynolds stresses can be determined by

$$\overline{uu}_{init} = \overline{vv}_{init} = \overline{ww}_{init} = \frac{2}{3}k_{init}. \tag{6.2}$$

The initial value of the turbulent dissipation, ϵ, is derived from assuming the length scale, l_{init}, of the initial turbulence field is a function of bore size [258], that is

$$l_{init} = 0.125B, \tag{6.3}$$

in which B is the cylinder bore. Initial dissipation rate, ϵ_{init}, can now be evaluated from the relationship between turbulence intensity, dissipation rate and the turbulence length scale [298], being

$$\epsilon_{init} = \frac{C_\mu k_{init}^{3/2}}{l_{init}}. \tag{6.4}$$

This leads to initial values of $k_{init} = 0.115\,\mathrm{m^2\,s^{-2}}$, or $\overline{uu}_{init} = \overline{vv}_{init} = \overline{ww}_{init} = 0.076\,\mathrm{m^2\,s^{-2}}$ and $\epsilon_{init} = 0.28\,\mathrm{m^2\,s^{-3}}$ at 206 rpm for the $CR = 10$ simulation. The off diagonal terms in the Reynolds Stress tensor are assumed to be initially $\overline{uv}_{init} = \overline{vw}_{init} = \overline{uw}_{init} = 0$.

6.3 Mesh Independence

The simulation was run using six different mesh densities to determine whether mesh independence could be achieved. This was assessed using both the k-ϵ and RSM turbulence models, in the two-dimensional simulations. Due to the long run times involved in performing three-dimensional simulations with fine meshes, no mesh independence tests was performed on three-dimensional simulations. As the magnitudes of the flows predicted by two- and three-dimensional meshes are similar it is assumed that mesh sensitivity will be also comparable.

The two-dimensional meshes tested had 21×15, 31×24, 42×30, 63×45, 84×60 and 126×90 nodes defining the combustion chamber. For the 63×45 mesh, the inlet manifold was meshed with 45×12 nodes, and was scaled accordingly for the other mesh densities. The mesh used in the inlet manifold/cylinder junction region is shown for all the meshes in figure 6.13.

A critical parameter in simulating turbulent flows is the y^+ value at the walls of the domain, as defined in equation 3.25. As stated in section 3.3.2, logarithmic wall functions are only valid for $y^+ > 11$, and it is common practice to keep $y^+ \gtrsim 30$ to ensure a "margin of safety".

This places a restriction on the degree of grid refinement possible at the walls. Due to this restriction, it was not possible to simply scale the same mesh between grid refinements. The three coarsest meshes required mesh points to be graded towards the wall to allow adequate resolution of near-wall behaviour, however the

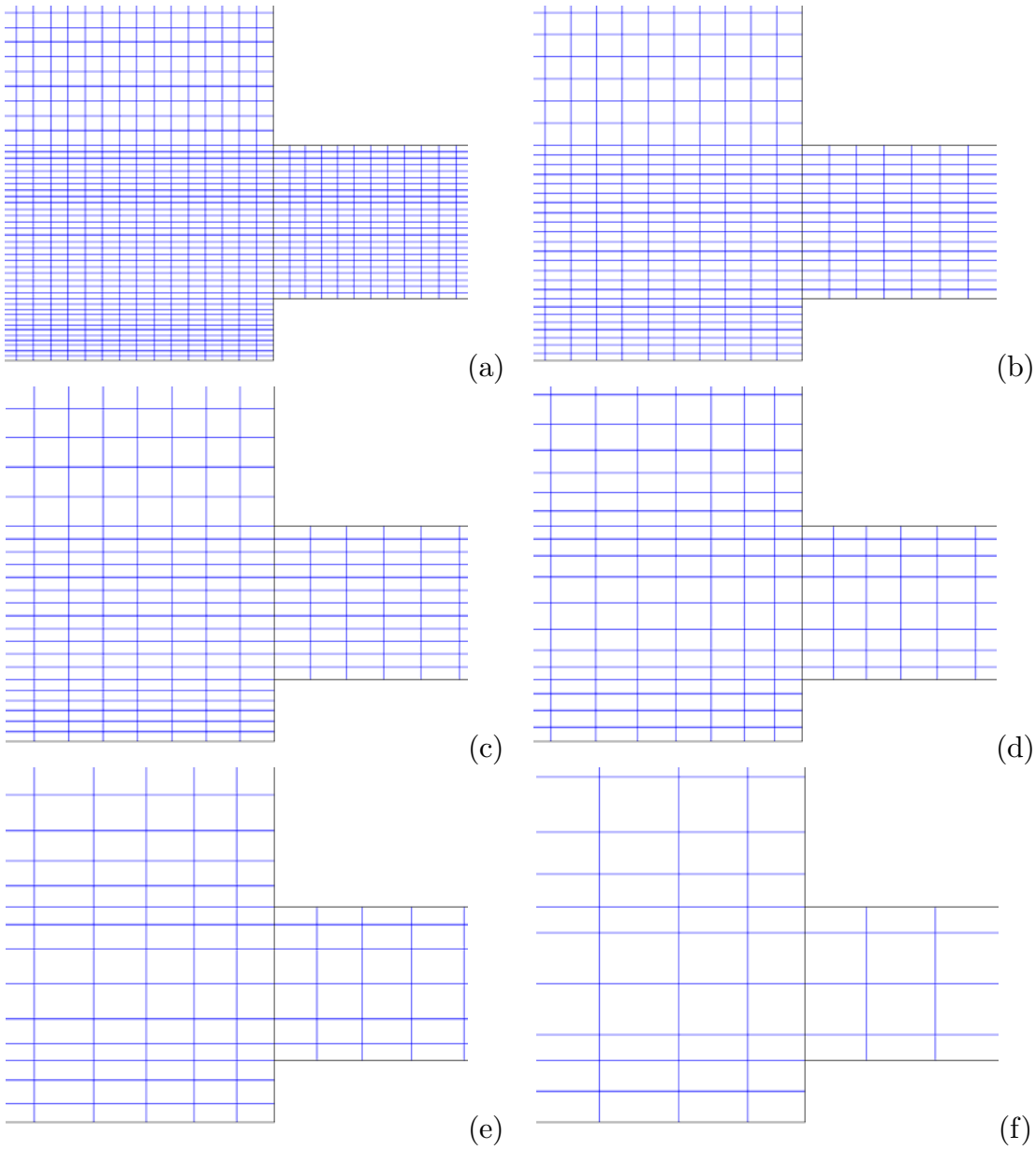

Figure 6.13: Detail of mesh used around inlet manifold/cylinder junction. Variables are stored at the centre of the cells shown. (a) – 126×90 mesh; (b) – 84×60 mesh; (c) – 64×45 mesh; (d) – 42×32 mes; (e) – 31×24 mesh; and (f) – 21×15 mesh.

Mesh	BDC		TDC	
	k-ϵ	RSM	k-ϵ	RSM
21×15	52.2	49.1	13.5	14.0
31×24	36.6	35.4	13.5	10.8
42×30	27.6	26.7	7.1	8.5
63×45	33.9	31.8	8.4	19.5
84×60	25.3	24.2	6.6	17.0
126×90	16.6	16.0	4.7	12.0

Table 6.1: y^+ for various meshes at BDC and TDC. Values at BDC taken at $X = 0$, $Y = 50\,\text{mm}$; values at TDC taken at $X = 100\,\text{mm}$, $Y = 50\,\text{mm}$.

two finest meshes used a uniform mesh so as to not infringe the minimum y^+ criterion. This can see seen in table 6.1, which shows the y^+ values at the centre of the piston at BDC and the centre of the head at TDC. At BDC all simulations have $y^+ > 11$, so it appears the wall functions are being appropriately applied for all meshes. Both the k-ϵ and RSM models predict similar y^+ values on the same grid, which is an indication that the two simulations are predicting similar flows. The y^+ values away from the centre of the piston are likely to be significantly lower, and in the corners of the domain y^+ will approach zero. As previously mentioned, this problem of y^+ approaching zero is unavoidable in geometries such as this.

The y^+ values at TDC show the k-ϵ simulation to have y^+ below 11 for all but the coarsest meshes. The RSM model has $y^+ > 11$ for the coarsest and three finest meshes. The difference between the k-ϵ and RSM simulations is due to the different compression stroke flow fields predicted by the two models, this will be discussed further in following sections.

Figure 6.14 shows the grid convergence achieved for the global parameters averaged across the domain. Figure 6.15 shows the grid convergence achieved for selected parameters at the central point of the domain at BDC.

Figure 6.14a, 6.14c, 6.15a and 6.15c show the k-ϵ simulation has reached grid independence. All grids, except the coarse 31×22 grid, are predicting essentially the same result. The velocity based comparisons (figure 6.14a and 6.15a) show a maximum variation of around 10% at BDC, with the differences reducing during the compression stroke to around 2% at 270 °CA. The turbulence based comparisons (figure 6.14c and 6.15c) show a similar trend where the maximum variation (when the coarse 31×22 grid is discounted) of around 20% at BDC and around 10% at 270 °CA. Again the grids all converge to a very similar value during the compression stroke. All graphs show the same trends for all grids.

The RSM grid convergence study shows a greater variation as the grid density

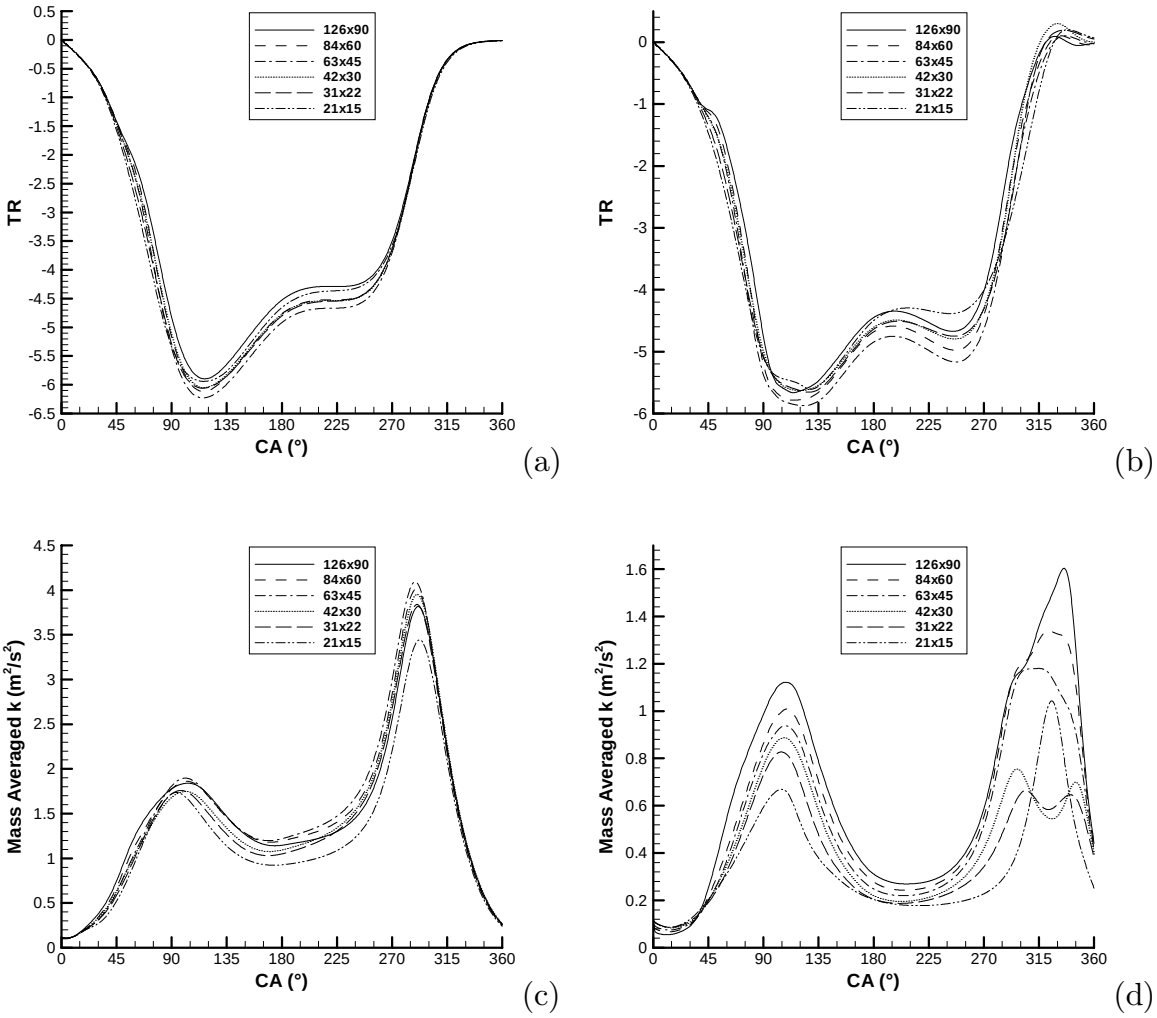

Figure 6.14: Grid convergence of cylinder averaged parameters in the square piston engine. (a) – Tumble ratio, k-ϵ simulation; (b) – Tumble ratio, RSM simulation; (c) – Mass averaged turbulent energy, k-ϵ simulation; and (d) – Mass averaged turbulent energy, RSM simulation.

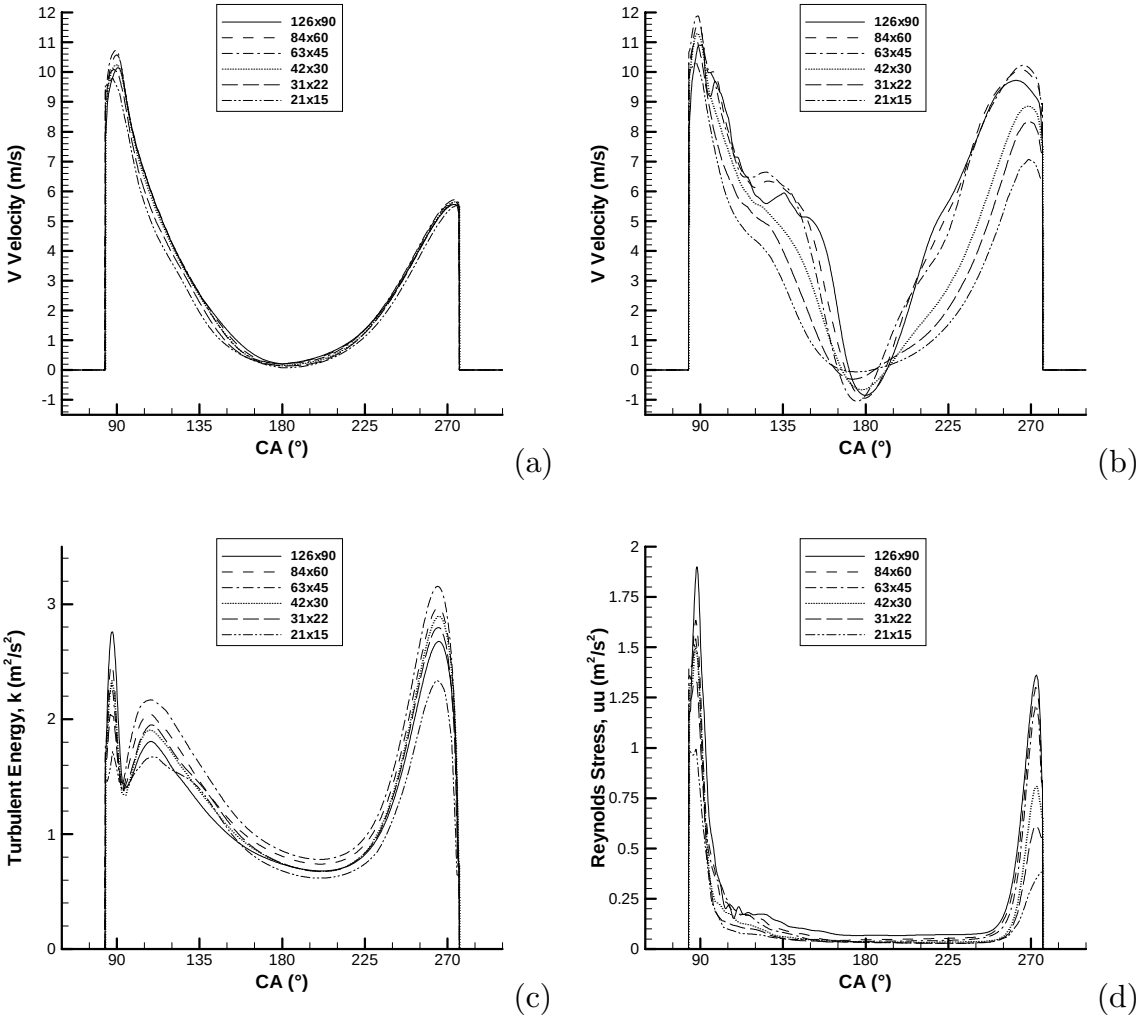

Figure 6.15: Grid convergence at point 55 in the square piston engine. (a) – V velocity, k-ϵ simulation; (b) – V velocity, RSM simulation; (c) – Turbulent energy, k, k-ϵ simulation; and (d) – Reynolds stress, $\overline{uu}$, RSM simulation.

is changed. Figures 6.14b and 6.15b show that the RSM simulations have achieved mesh independence in the velocities predicted for the 63×45 and finer grids. Figure 6.14b shows that the three finest meshes are similar within around 10%, and all predict similar trends. Figure 6.15b shows that the three finest meshes predict results within a few percent. The coarser meshes, however, fail to predict the "kink" present around 135 °CA, or the sharpness of the dip near BDC.

The turbulence results shown in figures 6.14d show that full grid independence has not been achieved even for the finest grids. Here there are large differences between the results from the three coarsest meshes (21×15, 31×24 and 42×32), and grid independence has clearly not been achieved. The three finest meshes (63×45, 84×60 and 126×90), show an adequate level of grid convergence between 120 °CA and 320 °CA, but still show considerable differences during the initial turbulence peak before 120 °CA with a variation of around 20% between the results from the three finest meshes. At 315 °CA, the three finest meshes differ by approximately 5%, which can be considered reasonable agreement, however there are large differences between the results from the grids during the final period of turbulence decay after 315 °CA. This discrepancy after 315 °CA is a significant problem as the turbulence during the final stages of the compression stroke is of critical importance to engine performance. Closer to TDC, however, the results all converge to similar values again.

The turbulence at the centre of the domain, shown in figure 6.15d, appears to be almost grid independent. When the three coarsest meshes are excluded the variations between meshes are minor, around 10% at 270 °CA. However the variations displayed in 6.14d do not occur here as the point being sampled is no longer in the domain after 280 °CA, and the variations appear after 315 °CA.

Part of the reason for the grid refinement characteristics is shown in figure 6.16. Here the results of the RSM simulations are shown, at TDC of the compression stroke. Displayed are velocity vectors, and a single contour line at $u = 0$. This contour allows the vortices to be seen more clearly as there is a vortex at each sign change of u. The finer meshes shown in figures 6.16a through to 6.16c are largely similar, showing nine vortices, with possibly a further very small vortex in the top left and bottom right corners. The vortices are all in approximately the same position. The three coarser meshes, figures 6.16d to 6.16f show that the simulation did not have sufficient resolution to simulate the structure—figures 6.16d and 6.16e depict seven vortices and fail to predict the flow being close to symmetrical about $Y = 50\,\text{mm}$, and figure 6.16f depicts only three major vortices.

This means that the three coarse meshes had insufficient resolution to predict

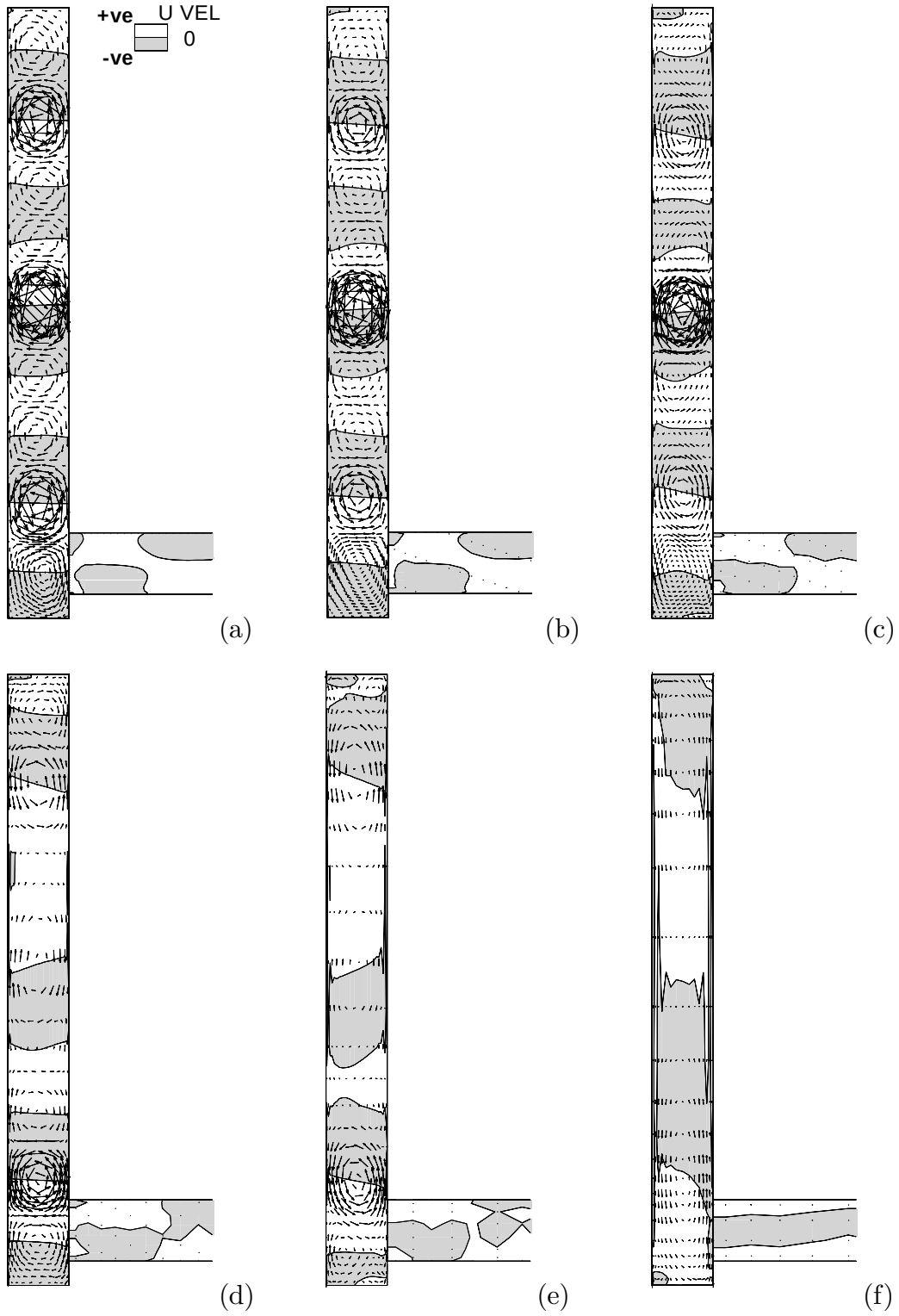

Figure 6.16: Effect of grid density on flow field predicted at TDC by the RSM model. Velocity vectors and $u = 0$ contour shown. (a) – 126×90 grid; (b) – 84×60 grid; (c) – 63×45 grid; (d) – 42×30 grid; (e) – 31×22 grid; and (f) – 21×15 grid.

Mesh	k-ϵ	RSM
21×15	0.39	0.59
31×22	0.80	1.29
42×30	1.65	3.02
63×45	4.20	9.49
84×60	8.95	20.2
126×90	25.49	58.9

Table 6.2: Computation time, in hours, required for various mesh densities.

the flow structure, and the three finest meshes all predicted the same flow structure. This confirms the previous conclusion from figures 6.14 and 6.15, that the 63×45 and finer grids yield results that are largely grid independent, but the 42×32 and coarser grids are not sufficiently fine.

The flow fields predicted for the k-ϵ simulations were essentially the same flow structure for all grid densities. That is, all grids predicted essentially zero flow at TDC.

The critical flow whose structure was simulated is the decay of the bulk fluid motion to turbulence during the compression stroke. This establishes the turbulence level present during spark ignition and the early phases of combustion. The later phases of combustion are dramatically affected by the heat released by the earlier combustion. Since ignition occurs between about 60 °CA and 30 °CA before TDC for most engines, it was concluded that the reasonably grid independent solutions obtained by the RSM model at 315 °CA would be adequate for these purposes.

The computation times for these simulations are shown in figure 6.2. Based on this result, all subsequent work using both the k-ϵ and RSM turbulence models was performed using a 63×45 node mesh, as this mesh demonstrates the best compromise between accuracy and computational time.

The difficulty in achieving grid independent solutions in internal combustion engine modelling is well known [93, 118]. It comes from the wide range of flows encountered in IC engine modelling—for instance the flows in a high performance engine running at speed has a Reynolds number in the range $0 \leq \mathrm{Re} < 10^6$ based on the inlet manifold diameter, and Mach numbers of between 0 and 1.0. As the wall functions are only valid for a limited range of roughly $11 < y^+ < 500$ [298, 284, 239, 296], a compromise must be achieved between a high grid density to resolve flow features, and a grid which is adequately coarse to keep y^+ above 11 during the important phases of low flow velocity. This is very difficult to achieve.

A second deficiency of the wall function approach is that the structure of the

turbulent boundary layer must be assumed. It is assumed that there exists a viscous sublayer extending to around $y^+ = 11$, and a log-layer extending to around $y^+ = 1000$. This has been shown to be a good model for simple, steady state, fully developed, turbulent boundary layers in geometries such as pipe flow [298]. However, this profile takes time and distance to develop, and factors such as separations, flow reversals and streamline curvature can dramatically effect the boundary layer, and can render the wall function approach inappropriate [118, 298]. As shown in table 6.1, the meshes used for these simulations have been designed so the y^+ remains above 11 as much as possible.

These problems are in addition to the deficiencies of Reynolds averaging discussed in section 4.5, namely that there is no clear distinction between turbulent and "mean" length or time scales in engines.

These problems make it impossible to achieve total grid independence when modelling an engine with a Reynolds Averaged turbulence model simulation using wall functions. Therefore the level of grid independence achieved in this section is viewed as the best possible with current techniques.

6.4 Initial Conditions Independence

The effect of various turbulence initial conditions was tested to establish the effects of turbulence remaining from previous cycles. All simulations were performed starting from TDC of the induction stroke with zero velocity and atmospheric pressure (100 kPa) over the entire domain. Hill and Zhang [137] suggest that the turbulence level during the compression stroke is largely independent of the turbulence conditions at the start of the intake stroke, and Soltani and Veshagh [258] suggest that the turbulence initial condition has little effect on the flow field after around 30 °CA of calculation. To confirm this for the current situation, three models were run at 200 rpm, with $CR = 5$. The RSM turbulence model was used. Initially the turbulence was assumed to be uniform and isotropic over the entire domain. The only difference between the configuration of the three runs was the magnitude of the turbulence initial conditions. The three initial conditions tested are shown in table 6.3. The initial k levels differed by a factor of around 20, and the ϵ levels varied by a factor of around 6 over the three tests.

Figure 6.17 shows the results of this test. After 120 °CA, the three simulations have converged to the same value, and remain essentially identical for the remainder of the intake stroke and the entire compression stroke. The maximum variation occurs at around 320 °CA, where the difference between the tests is 2%.

Test	k_{init} $(\mathrm{m^2\,s^{-2}})$	ϵ_{init} $(\mathrm{m^2\,s^{-3}})$
1	0.0855	0.18
2	0.15	10
3	1.5	10

Table 6.3: Turbulence initial conditions tested for engine run at $CR = 5$ and 200 rpm.

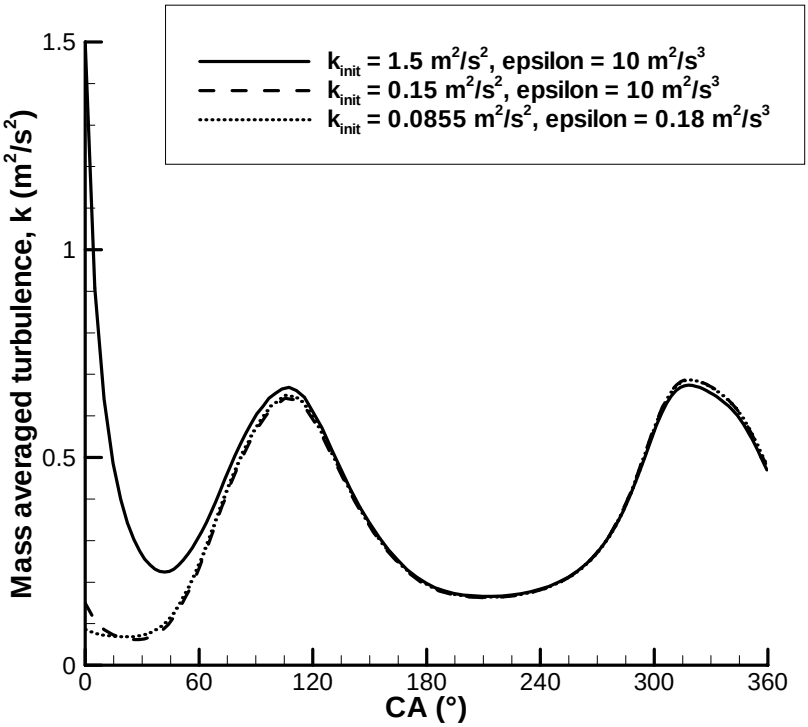

Figure 6.17: Effect of initial turbulence conditions on $CR = 5$ simulation.

Simulation	k-ϵ Time, (hours)	RSM Time, (hours)
Two-dimensional, $CR = 4$, 63×45	4.1	10.4
Two-dimensional, $CR = 10$, 63×45	4.2	9.5
Three-dimensional, $CR = 4$, $63 \times 45 \times 44$	216.6	342.0
Three-dimensional, $CR = 10$, $63 \times 45 \times 44$	278.0	361.5

Table 6.4: CPU time for two- and three-dimensional simulations.

This demonstrates that the turbulence predicted in the compression stroke of the simulation is effectively independent of the initial turbulence field. A 1000% change in initial turbulence levels resulted in only a 2% change in results later in the simulation.

The initial condition for the inlet manifold pressure wave also will not have a significant effect on results. At 200 rpm, with a manifold only 150 mm long, a pressure wave travelling at the acoustic velocity of air at 298 K can travel up and back along the inlet manifold around 170 times in just one intake stroke. This means that there are so many high and low pressure waves during one intake stroke that the effects of the pressure peaks and troughs are lost. Also, the mean piston velocity for this model is $0.62\,\mathrm{m\,s^{-1}}$, which indicates a mean inlet manifold velocity of around $6.2\,\mathrm{m\,s^{-1}}$. The dynamic pressure resulting from this velocity is $p_t = \frac{1}{2}\rho V^2 = 22\,\mathrm{Pa}$, which is an insignificantly small pressure variation in atmospheric pressure of 100 kPa.

6.5 Two- and Three-Dimensions

The effect of three-dimensional flow on the model was assessed by performing a three-dimensional simulation. Due to the long computational times required by three-dimensional modelling, a single grid of $63 \times 45 \times 44$ and initial conditions specified in equations 6.1 to 6.4 was used. Two simulations were run, one using $CR = 4$ to match the experimental results of Maurel et al [189], and one using $CR = 10$ to match the experimental results of Marc [187]. Both the RSM and k-ϵ models were used to simulate the flow. Other simulation parameters were the same as the two-dimensional simulations.

The large increase in computational times in three-dimensional modelling is shown in table 6.4. The simulation time increased by a factor of around 50 for the k-ϵ simulations, and a factor of around 40 for the RSM simulations.

6.6 $CR = 4$ Model

The simulation was run using $CR = 4$ and a speed of 206 rpm. These conditions match the experimental conditions of Maurel et al [189]. A two-dimensional 63×45 grid and a three-dimensional $63 \times 45 \times 44$ grid were used, and the simulation was performed using k-ϵ and RSM turbulence models. The turbulence field predicted mid-way through the intake stroke is shown in figure 6.18, and the velocity field in figure 6.19. No results from the compression stroke were presented by Maurel et al.

The turbulent energy shown in figure 6.18 shows some variation from the experimental results. The RSM and k-ϵ models predict very similar turbulence levels for the shear layer below the intake jet, and are in reasonable agreement with the experimental results. The k-ϵ model predicts a larger, more intense turbulent region in the shear layer above the intake jet than is predicted in the RSM model, and the k-ϵ model is in reasonable agreement with experimental results. The RSM model underpredicts the turbulence associated with this top shear layer.

The "tongue" of turbulence, seen in the experimental results to curl around the top region of the domain is predicted by the k-ϵ model, however the magnitude of the turbulence in the tongue is slightly underestimated. The turbulence magnitude of the tongue is substantially underpredicted by the RSM model.

Maurel et al analysed the turbulence associated with the shear layers above and below the intake jet, and found that the turbulence in the upper shear layer is reduced due to the upwards curvature of the intake jet streamlines. This effect is seen in their experimental results (figure 6.18a) as a reduction in turbulence intensity in the shear layer above the jet compared to below. They note that this turbulence damping process includes a reverse cascade process, a process which the k-ϵ turbulence model is unable to capture. This result is confirmed in the current results, as the two k-ϵ simulations (figures 6.18b and d) show the jet upper and lower shear layer turbulence to be of approximately equal magnitude, whereas the two RSM simulations (figures 6.18c and e) show the upper shear layer to have significantly less turbulence than the lower region. This confirms that the k-ϵ simulations are unable to simulate a significant difference in turbulence levels due to streamline curvature, but that it is successfully simulated using the RSM simulation.

The small area of turbulence located at the vortex centre in the experimental results was analysed in Maurel et al, and found to be caused by the ensemble averaging technique used to determine the turbulent fluctuations. They report that small variations in the location of the main vortex centre cause a peak of turbulence intensity at the vortex centre, however this is the result of cycle to cycle variations

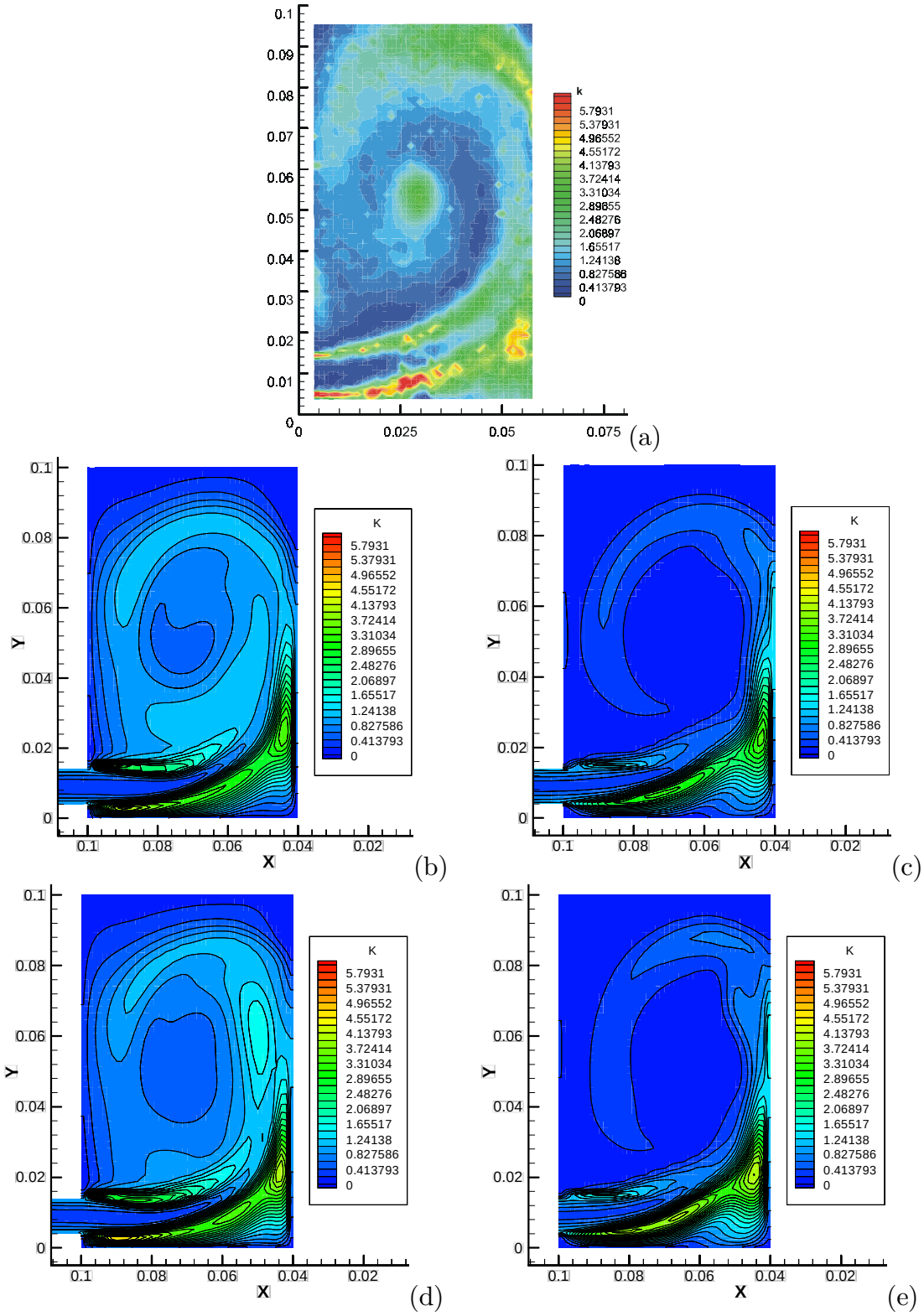

Figure 6.18: Comparison of turbulent kinetic energy (k) from experimental results and numerical simulation for model with $CR = 4$, speed= 206 rpm at 86 °CA. a) – Ensemble averaged turbulent kinetic energy from PIV experiments of Maurel et al [189]; b) – 2D k-ϵ simulation; c) – 2D RSM simulation; d) – 3D k-ϵ simulation; and e) – 3D RSM simulation.

Model	X (mm)	Y (mm)	**Error** (mm)
PIV	30	55	
Two-dimensional k-ϵ	30	54	1
Two-dimensional RSM	30	54	1
Three-dimensional k-ϵ	31	64	9
Three-dimensional RSM	32	60	5

Table 6.5: Vortex centre location for $CR = 4$ model at 86 °CA. PIV data from Maurel et al [189]

of the location of the vortex rather than true turbulent fluctuations. Thus, the fact that the peak of turbulence is not predicted by the k-ϵ or RSM models is to be expected.

Figure 6.19 shows the RSM and k-ϵ turbulence models both predict essentially the same velocity field, and in close agreement with experimental results. The location of the vortex centre was calculated, and compared to that found in the experimental results. The position of the centre of the main vortex from the PIV results of Maurel et al, and the various CFD models is given in table 6.5. All models predict the position with reasonable agreement with the experimental results. Interestingly, the two-dimensional models appear to be the most accurate, varying from the experimental results by only 1 mm. Why the two-dimensional model is in better agreement than the three-dimensional models is unclear.

Position of the vortex centre was calculated on the numerical results by linear interpolation to zero u and v velocity. The velocity component in the w direction was ignored in the three-dimensional results.

The turbulence field predicted at BDC is shown in figure 6.20, and the velocity field in figure 6.21. The turbulence results in figure 6.20 show the k-ϵ model appears to have predicted the turbulence intensities at the outside of the domain well, but significantly overpredicted the intensity in the centre of the domain. The RSM model appears to have underpredicted turbulence intensities over the entire domain. Again, the turbulence peak visible in the centre of the experimental results is spurious, and so is not predicted by the simulations.

Figure 6.21 shows the RSM and k-ϵ turbulence models both predict essentially the same velocity field, but this time a significant variation from experimental results is seen. The vortex centre measured by PIV was at $X = 52$ mm, $Y = 36$ mm which is significantly below the centre point of the domain, as shown in table 6.6. None of the CFD models predicted the vortex centre to lie this far below the centre of the domain. Again, the two-dimensional models give the most accurate results in

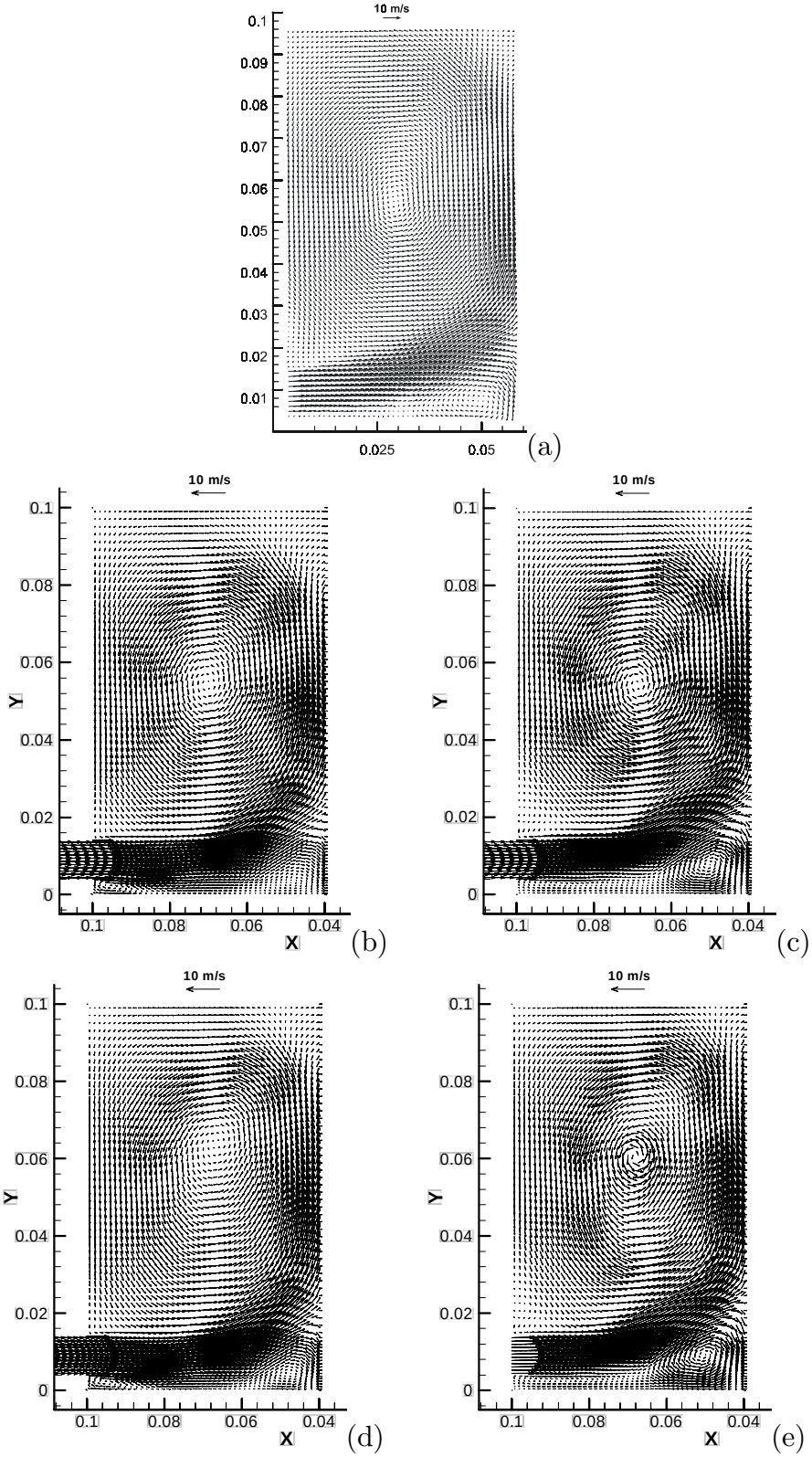

Figure 6.19: Comparison of velocity vectors from experimental results and numerical simulation for model with $CR = 4$, speed= 206 rpm at 86 °CA. a) – Ensemble averaged velocity vectors from PIV experiments of Maurel et al [189]; (b) – 2D k-ϵ simulation; (c) – 2D RSM simulation; (d) – 3D k-ϵ simulation; and (e) – 3D RSM simulation.

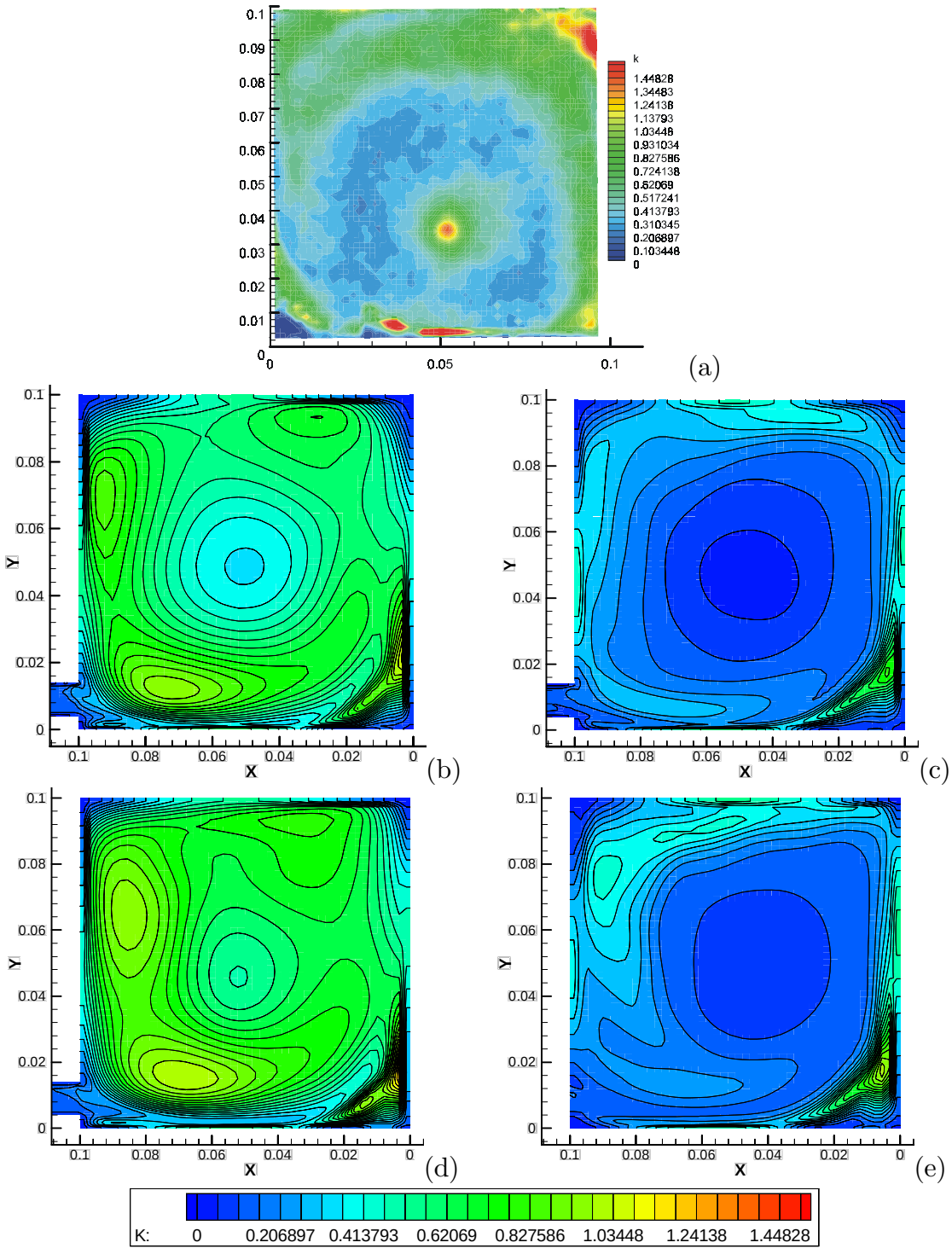

Figure 6.20: Comparison of turbulent kinetic energy (k) from experimental results and numerical simulation for model with $CR = 4$, speed= 206 rpm at BDC. a) – Ensemble averaged turbulent kinetic energy from PIV experiments of Maurel et al [189]; b) – 2D k-ϵ simulation; c) – 2D RSM simulation; d) – 3D k-ϵ simulation; and e) – 3D RSM simulation.

Model	X (mm)	Y (mm)	**Error** (mm)
PIV	52	36	
Two-dimensional k-ϵ	50	45	9
Two-dimensional RSM	47	44	6
Three-dimensional k-ϵ	51	46	10
Three-dimensional RSM	53	48	12

Table 6.6: Vortex centre location for $CR = 4$ model at BDC. PIV data from Maurel et al [189]

predicting the vortex centre location.

These results show that during the intake stroke, the turbulence models and two- and three-dimensional models predict similar results. The velocity field predicted by all simulations had only small variations, however the two-dimensional simulations were slightly more accurate. The levels of turbulence predicted by the k-ϵ turbulence model were in reasonable agreement with the experimental results. The levels of turbulence predicted by the RSM simulations were significantly less than that found experimentally.

6.7 $CR = 10$ Model

The simulation was run using $CR = 10$ and a speed of 206 rpm. These conditions match the experimental conditions of Marc [187]. A two-dimensional 63×45 grid and a three-dimensional $63 \times 45 \times 44$ grid was used, and the simulation was performed using k-ϵ and RSM turbulence models.

6.7.1 Intake Stroke

Table 6.7 shows the positions of the vortex centre for the various models through the intake stroke. Both the three-dimensional RSM and k-ϵ models compare favourably against the experimental results, with an error at BDC of around 4 mm.

Figure 6.22 shows the velocity field at 87 °CA. All models predict reasonably similar results. However, the region of the flow which varies the most between simulations appears to be the intake jet region, and this region was out of the visible region in the PIV data so it is not possible to draw conclusions regarding accuracy.

Note that the visualisations of Marc show the flow reversed about the Y axis compared to the results of Maurel [189] in the previous section. Only the top part

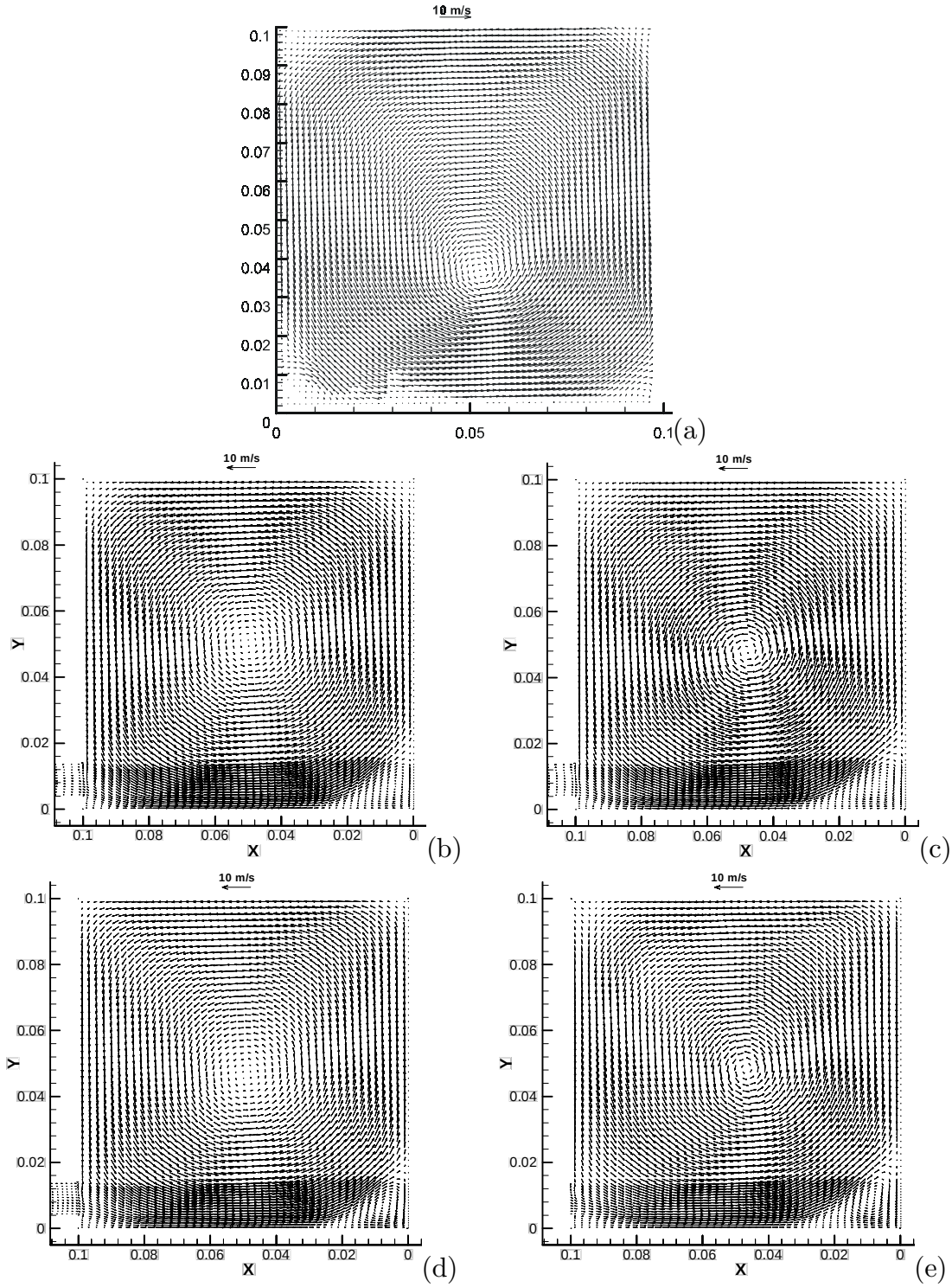

Figure 6.21: Comparison of velocity vectors from experimental results and numerical simulation for model with $CR = 4$, speed= 206 rpm at BDC. a) – Ensemble averaged velocity vectors from PIV experiments of Maurel et al [189]; (b) – 2D k-ϵ simulation; (c) – 2D RSM simulation; (d) – 3D k-ϵ simulation; and (e) – 3D RSM simulation.

	X			Y			Error	
°CA	RSM	k-ϵ	PIV	RSM	k-ϵ	PIV	RSM	k-ϵ
87	76	69	78	56	58	57	2.2	9.1
127	64	62	66	55	50	67	12.2	5.0
BDC	44	46	47	52	45	49	4.2	4.1

Table 6.7: Comparison of intake stroke vortex centre location for three-dimensional simulations, $CR = 10$. PIV results from [187], and all results are in mm. Note that Marc [187] presents a number of visualisations of the flow at BDC, and they show a range of vortex centre locations. The X location varies in these visualisations from 45 mm to 48 mm, so 47 mm was used as an "average". Similarly the Y location varies in these visualisations from 45 mm to 52 mm, so 49 mm was used here.

of the flow field is visible due to the inlet manifold and valve obstructing the laser sheet.

Figure 6.23 shows the turbulence energy (k) at 87 °CA. No experimental data of the turbulence field is available at this location. The most obvious difference is that the k-ϵ model predicts substantially more turbulence in the central section of the domain than that predicted by the RSM model. This is especially true for the three-dimensional k-ϵ model, where a large region of strong turbulence is located at $X = 60$ mm, $Y = 60$ mm, which is not predicted by any of the other models.

Figure 6.24 shows a slice in the YZ or cross tumble plane, at $X = 93$ mm. The PIV results show a chaotic flow which is possibly resolving some turbulent structures or cycle to cycle variations. Additionally, the flow is clearly asymmetric. Both the k-ϵ and the RSM model do not predict this complexity, but predict a far more ordered flow with only small three-dimensional effects.

The turbulence in the YZ plane is shown in figure 6.25. As shown in figure 6.23, the k-ϵ model predicts significantly more turbulence than the RSM model. No experimental data on turbulence was presented in this plane so a comparison to experimental results cannot be performed.

6.7.2 Bottom Dead Centre

Marc [187] performed a detailed analysis of the flow at BDC, and a comparison of the CFD results from the current author are presented here. The flow in the central tumble ($Z = 50$ mm) plane is shown in figure 6.26. The two- and three-dimensional k-ϵ and RSM models all predict very similar results, being a large main vortex with a smaller secondary vortex in the lower left corner. They are in good agreement with the PIV results for the section of flow measured.

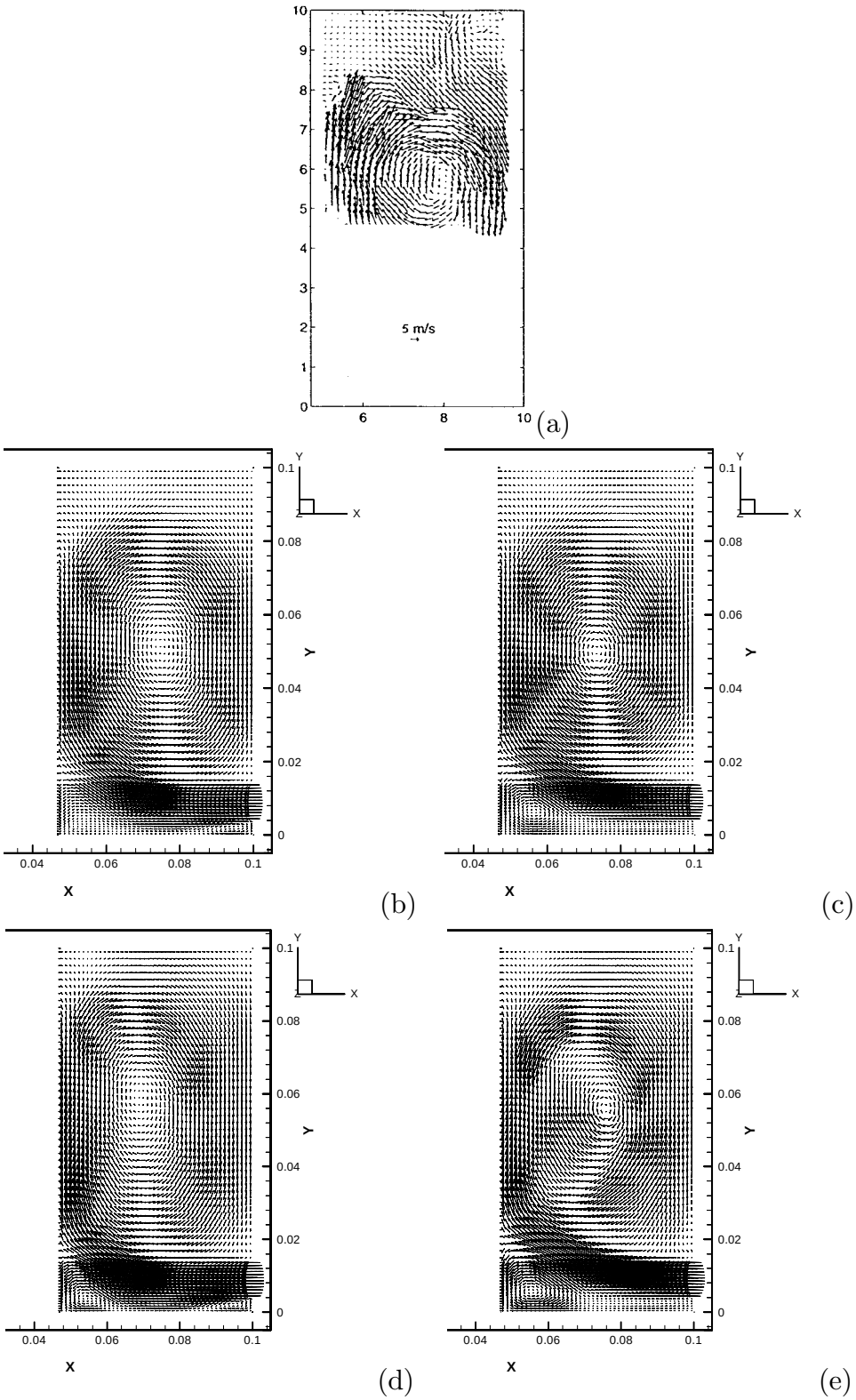

Figure 6.22: Comparison of velocity predictions in the $Z = 50\,\text{mm}$ plane for $CR = 10$, at 87 °CA. (a) – PIV result from Marc [187]; (b) – 2D k-ϵ simulation; (c) – 2D RSM simulation; (d) – 3D k-ϵ simulation; and (e) – 3D RSM simulation.

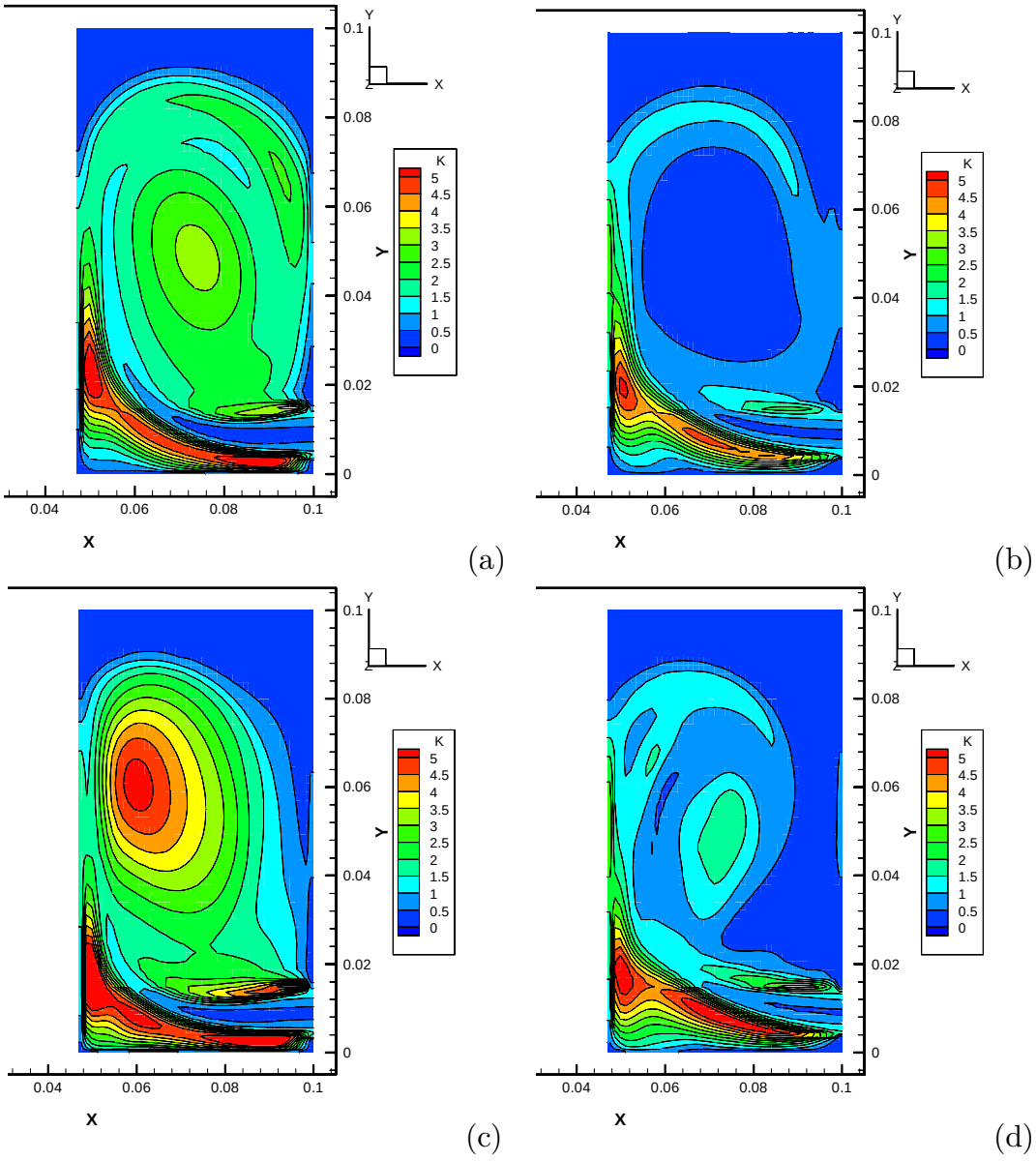

Figure 6.23: Comparison of turbulent energy (k) predictions in the $Z = 50\,\text{mm}$ plane for $CR = 10$, at 87°CA. (a) – 2D k-ϵ simulation; (b) – 2D RSM simulation; (c) – 3D k-ϵ simulation; and (d) – 3D RSM simulation.

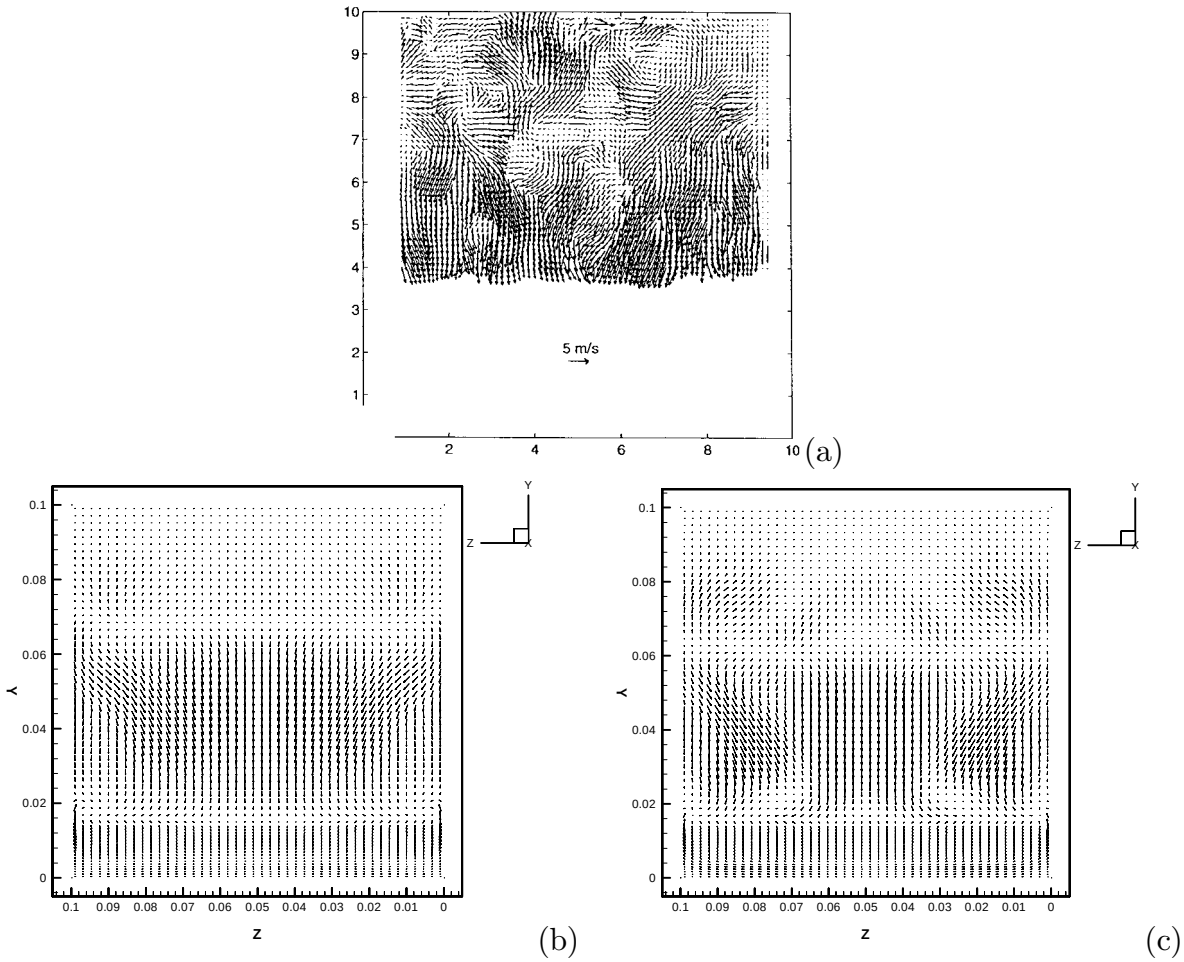

Figure 6.24: Comparison of velocity predictions in the $X = 93\,\text{mm}$ plane for $CR = 10$, at 64 °CA. (a) – PIV results from Marc [187]; (b) – 3D k-ϵ simulation; and (c) – 3D RSM simulation.

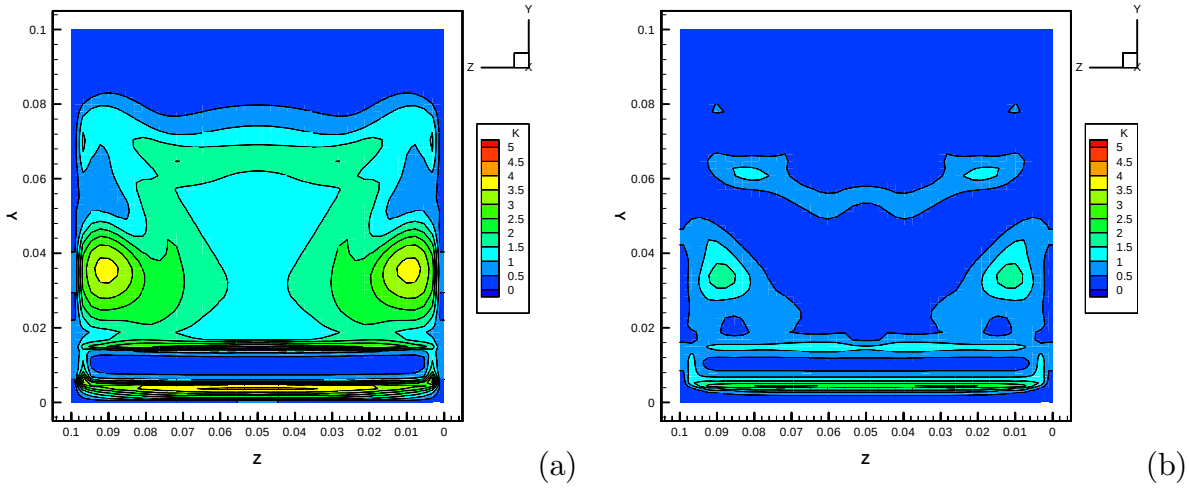

(a) (b)

Figure 6.25: Comparison of turbulent energy (k) predictions in the $X = 93\,\text{mm}$ plane for $CR = 10$, at 64 °CA. (a) – 3D k-ϵ simulation; and (b) – 3D RSM simulation.

Figure 6.27 shows the flow in the cross tumble (YZ) plane. No structures are seen, so the flow near this plane must be a vortex in the tumble plane only, with very little flows in the third (Z) dimension. This is in close agreement with the original PIV study of Marc et al [188], shown in figure 6.11 on which they based their earlier assumption of two-dimensional flow.

The location of the tumble vortex centre has been extracted from the data in figures 6.26 and 6.27, to allow a more objective assessment of accuracy. Figure 6.28 shows the position of the vortex centre for all the CFD models, together with individual cycles recorded by PIV and the centre recorded by the ensemble averaged PIV result. Neither the k-ϵ nor the RSM simulation predicted the same position as the ensemble averaged PIV result, however they are all within the typical spread of vortex centre locations measured for individual cycles.

Figure 6.29 shows a velocity profile through the centre of the tumble vortex. Marc [187] obtained the experimental results by two independent methods, so their close agreement indicate they are likely to be accurate. An interesting feature of this profile is that it shows the tumble vortex is not in solid body rotation. If the vortex was simply rotating as a solid body, the vortex tangential velocity would be proportional to the distance from the centre of rotation. The sections of the profile between $60\,\text{mm} < X < 90\,\text{mm}$ and $10\,\text{mm} < X < 30\,\text{mm}$ clearly depart from solid body rotation.

The three-dimensional RSM model most accurately agrees with the experimental results, reproducing this departure from solid body rotation. The two-dimensional

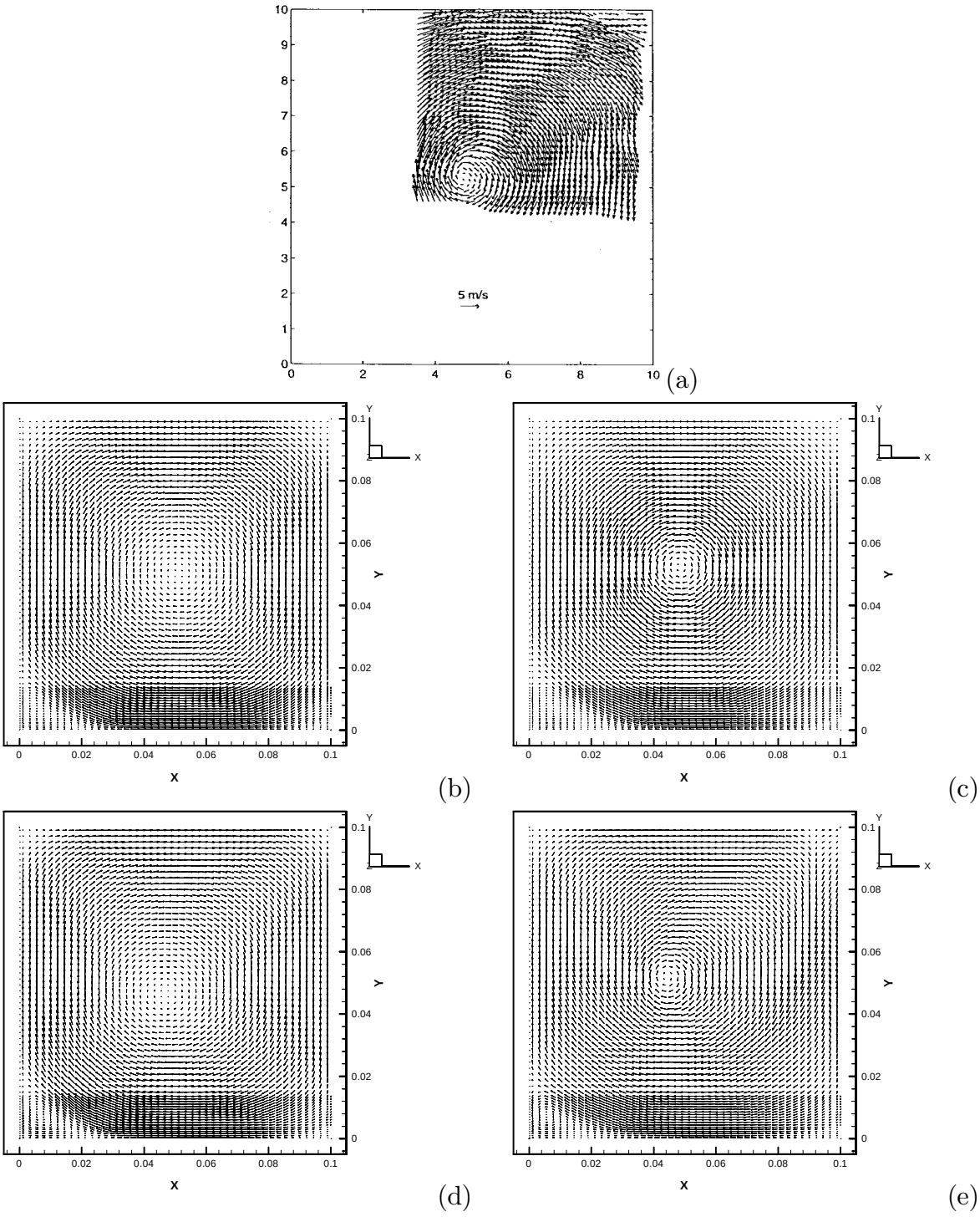

Figure 6.26: Comparison of velocity predictions in the $Z = 50\,\text{mm}$ plane for $CR = 10$, at BDC. (a) – PIV result from Marc [187], (b) – 2D k-ϵ simulation; (c) – 2D RSM simulation; (d) – 3D k-ϵ simulation; and (e) – 3D RSM simulation.

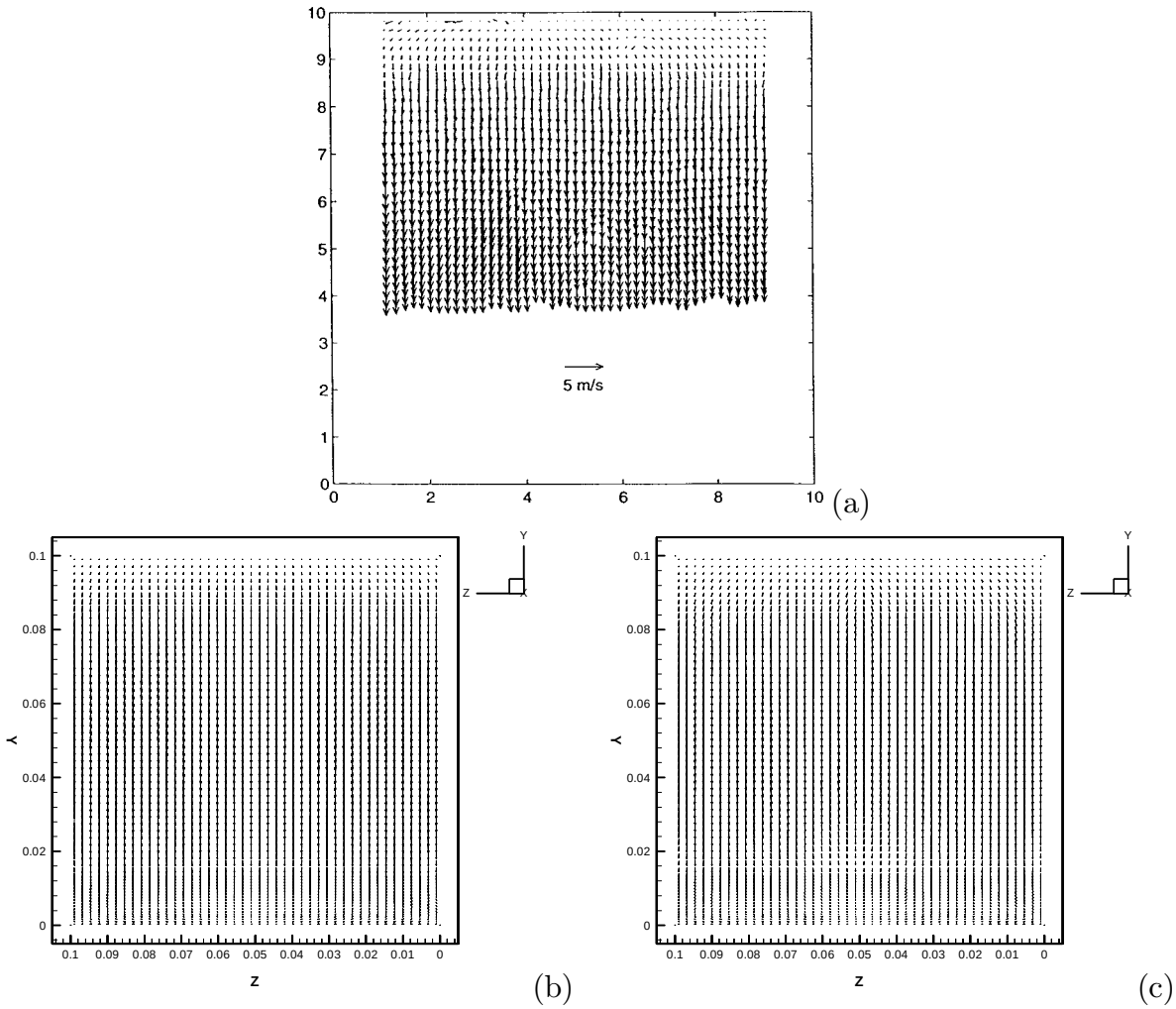

Figure 6.27: Comparison of velocity predictions in the $X = 93\,\text{mm}$ plane for $CR = 10$, at BDC. (a) – PIV results from Marc [187]; (b) – 3D k-ϵ simulation; and (c) – 3D RSM simulation.

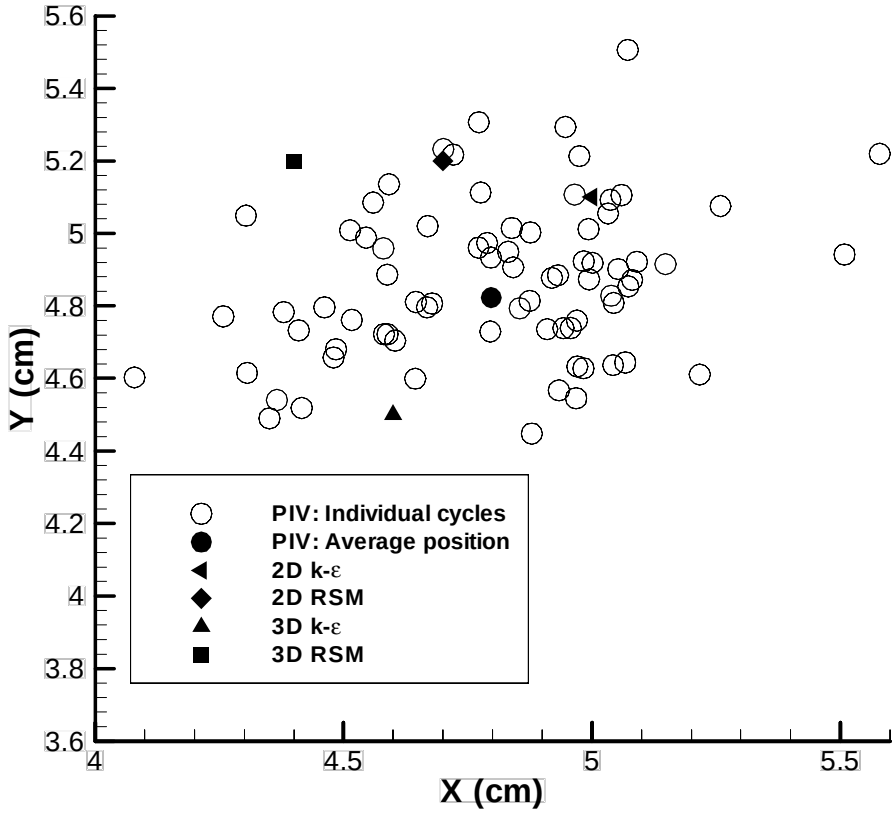

Figure 6.28: Vortex centre positions for $CR = 10$ model at BDC. PIV data from Marc [187].

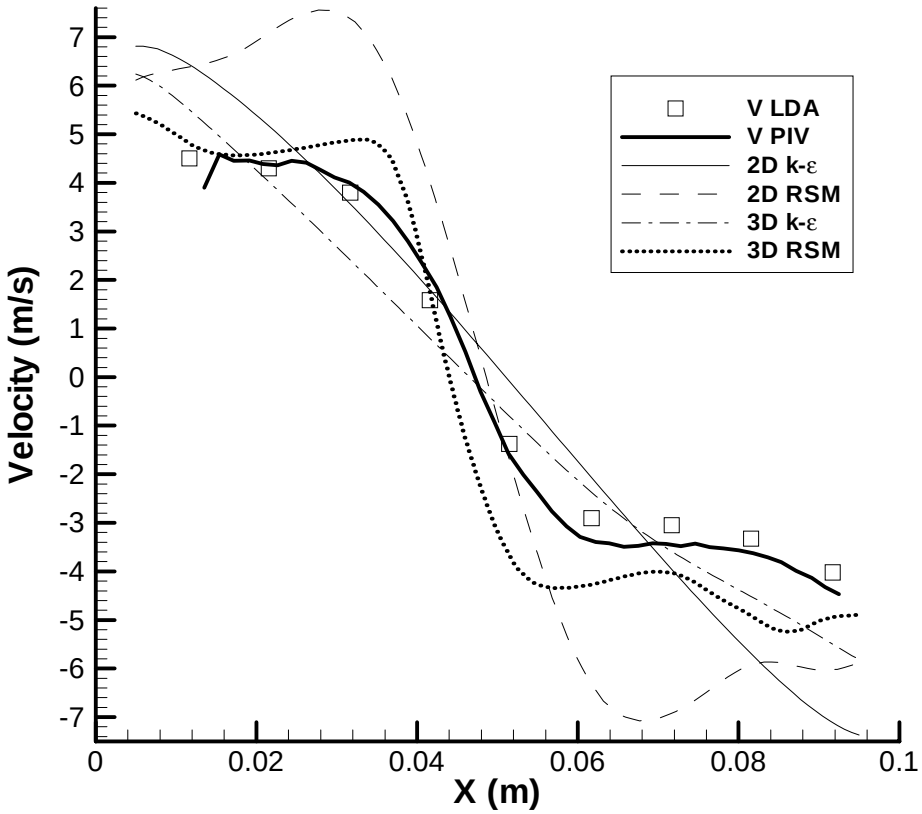

Figure 6.29: Comparison of velocity profiles from $CR = 10$ model at BDC for $Y = 50\,\text{mm}$, $Z = 50\,\text{mm}$. LDA and PIV results from Marc [187].

RSM model also predicts a departure from solid body rotation, however the magnitude of the velocities are significantly over-estimated.

Both the two- and three-dimensional k-ϵ models do not predict the experimental results very well, instead predicting a flow which closely resembles solid body rotation (that is tangential velocity is proportional to distance from rotation axis). This appears to be a fundamental failing of the k-ϵ turbulence model.

The turbulence profiles across the domain at BDC, as shown in figure 6.30, are in poor agreement with the experimental results for all simulations. It is not clear why this agreement is so poor when the other results are in good agreement, especially for the three-dimensional RSM model.

Figure 6.31 shows the turbulent energy (k) at BDC for the $CR = 10$ simulation. As expected, the two- and three-dimensional k-ϵ simulations predict significantly more turbulence than the RSM models. Marc [187] presents no experimental data for this result to be compared against, so no comparison to experimental data can be performed.

The Reynolds stresses displayed in figures 6.32, 6.33 and 6.34 all show very similar results between the two- and three-dimensional simulations. The only major differences appear to be the two-dimensional simulation predicting a region of high $\overline{uu}$ at $X = 80\,\text{mm}$, $Y = 60\,\text{mm}$ which is much weaker in the three-dimensional results, and a region of high $\overline{ww}$ in the two-dimensional simulation at $X = 60\,\text{mm}$, $Y = 60\,\text{mm}$ which does not occur in the three-dimensional simulation.

Marc [187] calculated the $\overline{uv}$ Reynolds stress from his PIV results, and the comparison to the current RSM results is shown in figure 6.35. The RSM simulation appear to capture the region of high $\overline{uv}$ at the left region of the top wall, and correctly predicted the near zero $\overline{uv}$ throughout most of the domain, but the large region of low $\overline{uv}$ seen at $X = 80\,\text{mm}$, $Y = 80\,\text{mm}$ in the PIV results is not resolved by either of the CFD simulations.

Figure 6.32, 6.33 and 6.34 also show an interesting feature about the nature of turbulence at BDC. The centre section of the domain for all visualisations has quite similar levels of the three normal Reynolds stresses, indicating isotropic turbulence. There are small regions where the turbulence displays anisotropic behaviour, such as the $\overline{ww}$ peak seen in figure 6.34 at $X = 60\,\text{mm}$, $Y = 60\,\text{mm}$; but overall the flow is largely isotropic.

The anisotropic sections of the flow appear to be concentrated in narrow regions next to the walls. For instance, there is a region of high $\overline{uu}$ very close to the top wall at $X = 50\,\text{mm}$; and a region of high $\overline{vv}$ on the left wall at $Y = 60\,\text{mm}$. Both of these regions do not have a corresponding peak of $\overline{uu}$ or $\overline{vv}$, and so represent a

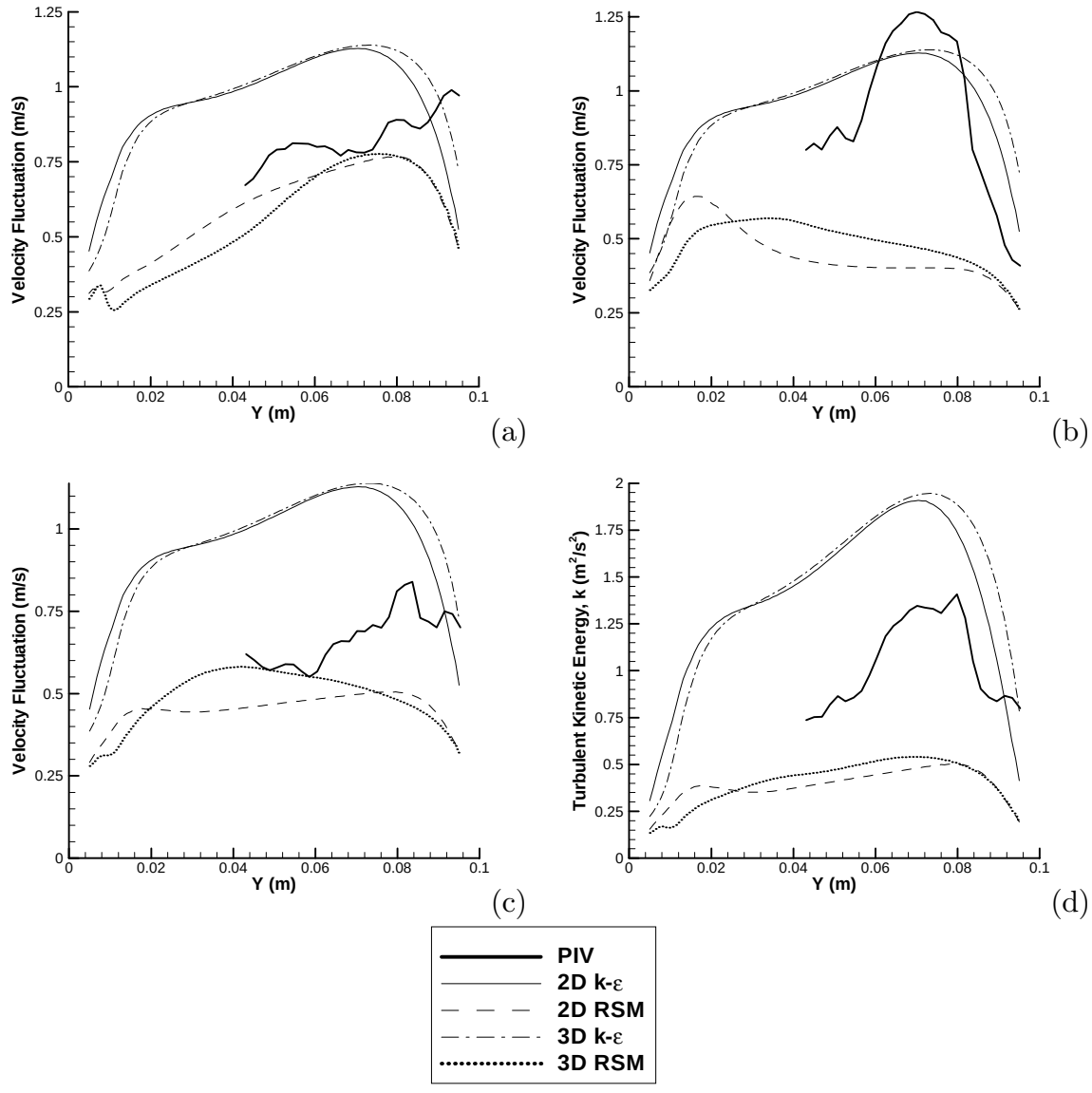

Figure 6.30: Turbulence profile at BDC along line $X = 93\,\text{mm}$, $Z = 50\,\text{mm}$. PIV results from Marc [187]. (a) – u'; (b) – v'; (c) – w'; and (d) – k.

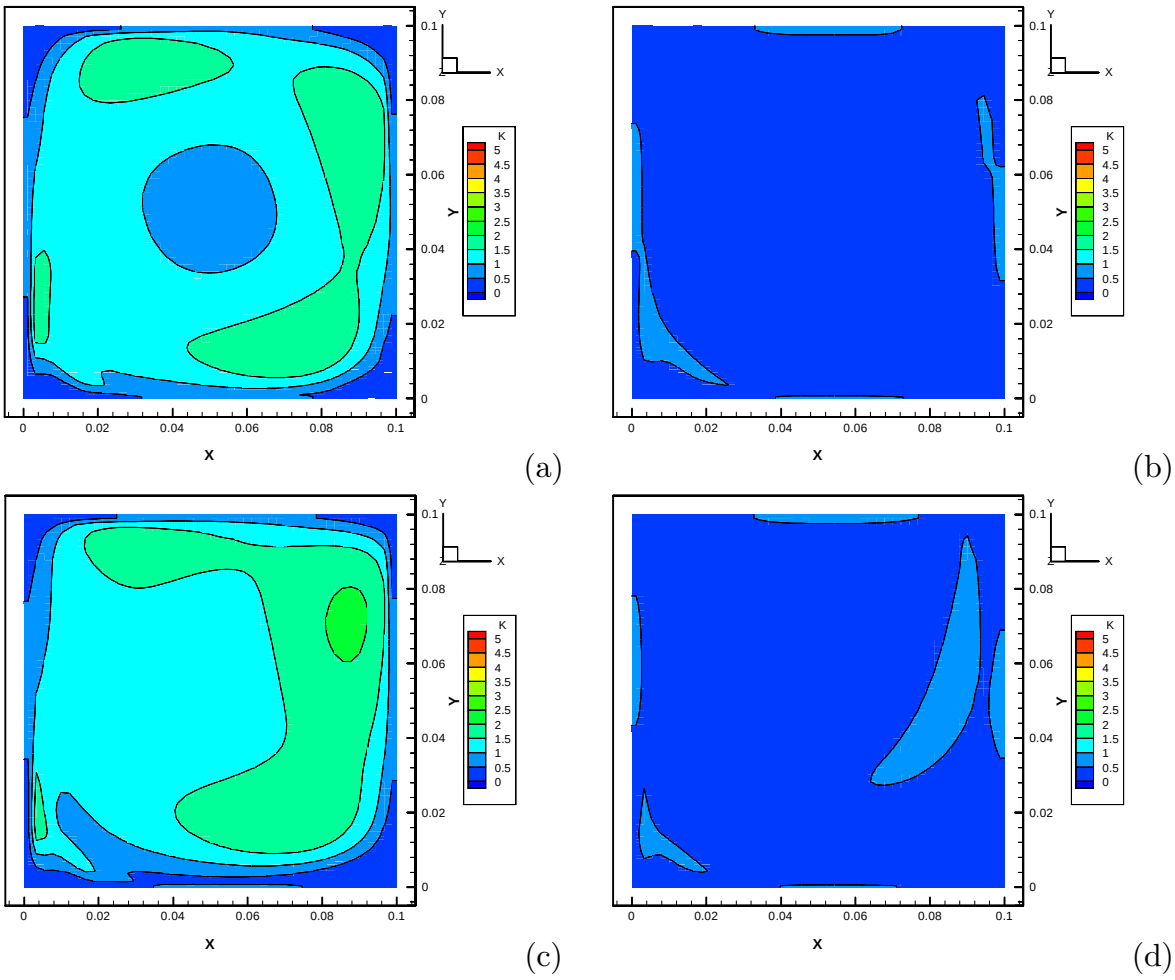

Figure 6.31: Comparison of turbulent energy (k) predictions in the $Z = 50\,\text{mm}$ plane for $CR = 10$, at BDC. (a) – 2D k-ϵ simulation; (b) – 2D RSM simulation; (c) – 3D k-ϵ simulation; and (d) – 3D RSM simulation.

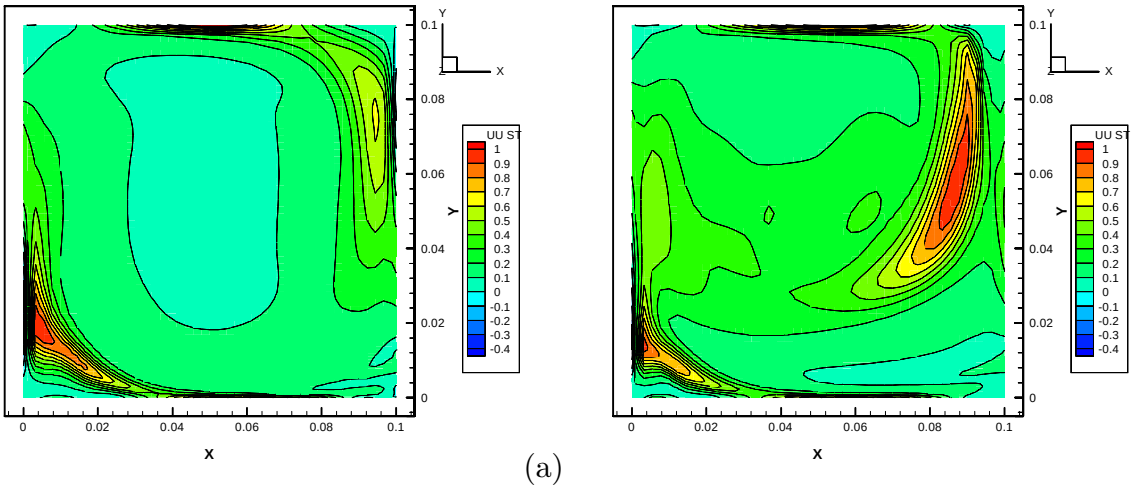

Figure 6.32: Comparison of $\overline{uu}$ predictions in the $Z = 50\,\text{mm}$ plane for $CR = 10$, at BDC. (a) – 2D RSM simulation; and (b) – 3D RSM simulation.

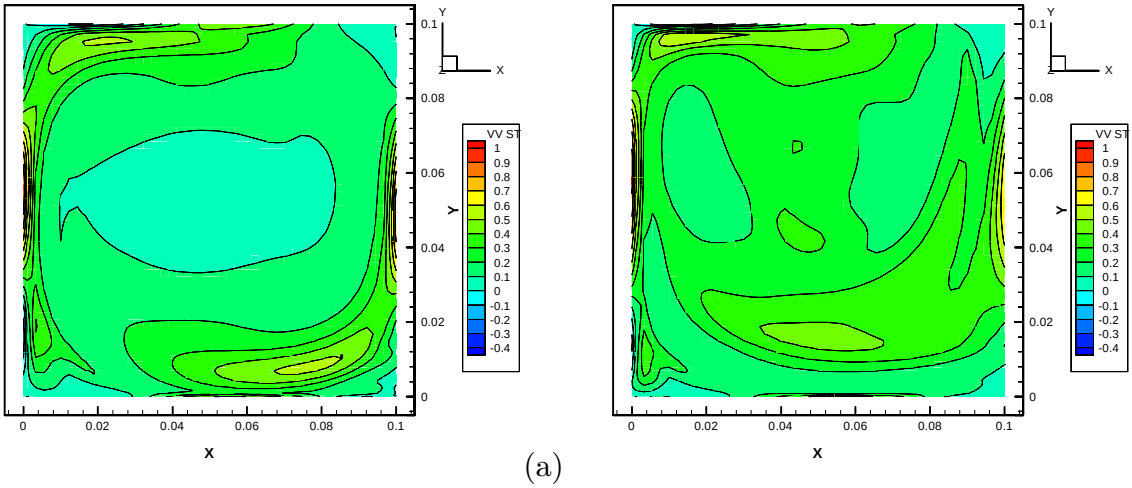

Figure 6.33: Comparison of $\overline{vv}$ predictions in the $Z = 50\,\text{mm}$ plane for $CR = 10$, at BDC. (a) – 2D RSM simulation; and (b) – 3D RSM simulation.

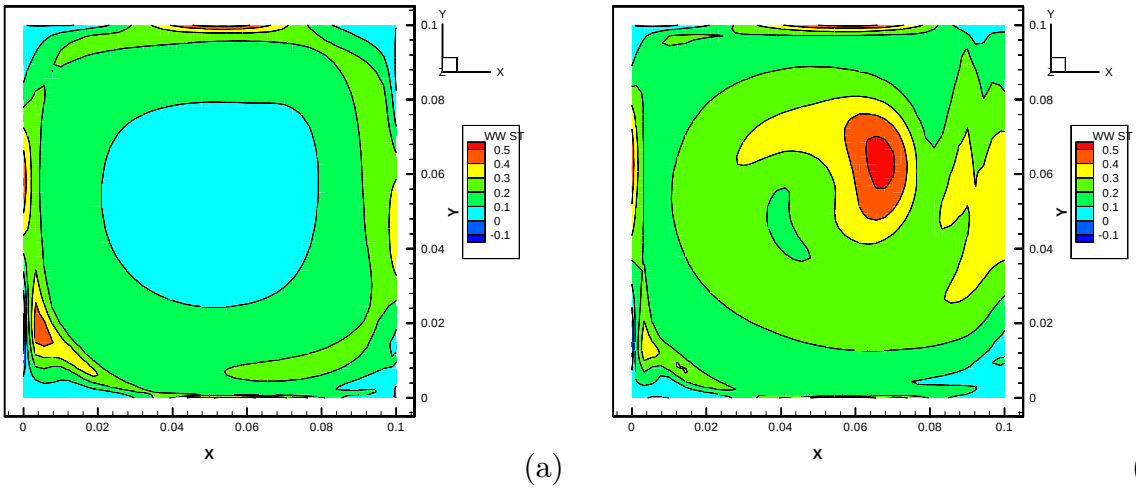

Figure 6.34: Comparison of $\overline{ww}$ predictions in the $Z = 50\,\text{mm}$ plane for $CR = 10$, at BDC. (a) – 2D RSM simulation; and (b) – 3D RSM simulation.

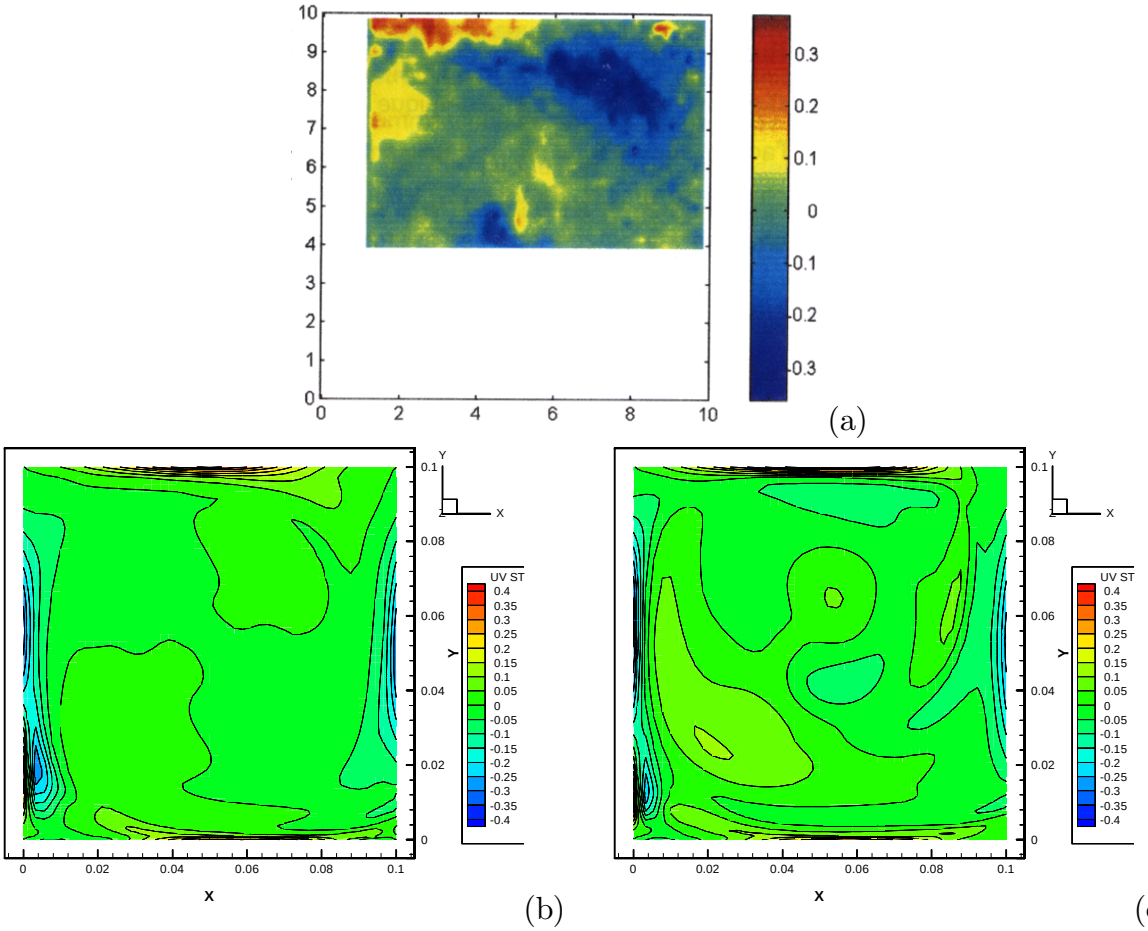

Figure 6.35: Comparison of $\overline{uv}$ predictions in the $Z = 50\,\text{mm}$ plane for $CR = 10$, at BDC. (a) – PIV results from Marc [187]; (b) – 2D RSM simulation; and (c) – 3D RSM simulation.

region of anisotropic turbulence.

These regions of anisotropy obviously cannot be modelled by the k-ϵ model, and is possibly a reason for the failure of the model to predict the tumble vortex breakdown process.

6.7.3 Compression Stroke

The compression stroke is a critical section of the engine cycle. It is also a challenging flow to simulate with a computer simulation, as the flow undergoes many changes during this stroke as the tumble vortex breaks down into many smaller vortices. Additionally, the aspect ratio of the geometry changes significantly, making accurate numerical simulation challenging.

Marc [187] presents visualisations of the flow in the compression stroke at 276 °CA, 299 °CA, 312 °CA, 321 °CA, 328 °CA and 335 °CA. The results from the current simulations will now be compared to these experimental results.

Results at 276 °CA

Figure 6.36 shows the velocity field predicted at 276 °CA. Even at this early stage of the compression stroke a fundamental difference is apparent between the RSM and k-ϵ models. The RSM models appear to maintain a strong vortex in the centre of the domain, which is roughly elliptical in shape. The top and bottom regions of the domain only have a weak flow. The k-ϵ models on the other hand predict that the vortex takes up the entire domain, taking on the rectangular shape of the domain. The PIV shows a strong central vortex similar to that predicted by the RSM simulations, but with a little more flow in the top and bottom of the domain than is shown in the RSM model.

These regions of low velocities in the top and bottom of the domain are explained by Marc [187] as separations, caused by the central vortex detaching from the head and piston faces due to the adverse pressure gradient on those faces. This causes the tumble vortex to decrease in size (as is seen in the PIV and RSM results in figure 6.36). This decrease in size consequently causes the tumble "spin-up" process where the tumble vortex rotation rate increases, to conserve angular momentum.

The position of the centre of the vortex at 276 °CA is shown in figure 6.37. The two-dimensional RSM model very accurately predicts the averaged position of the centre of the vortex. The three-dimensional RSM model is a little higher in the domain than the normal spread of PIV results, about 10 mm from the experimentally measured average position. The two- and three-dimensional k-ϵ models are

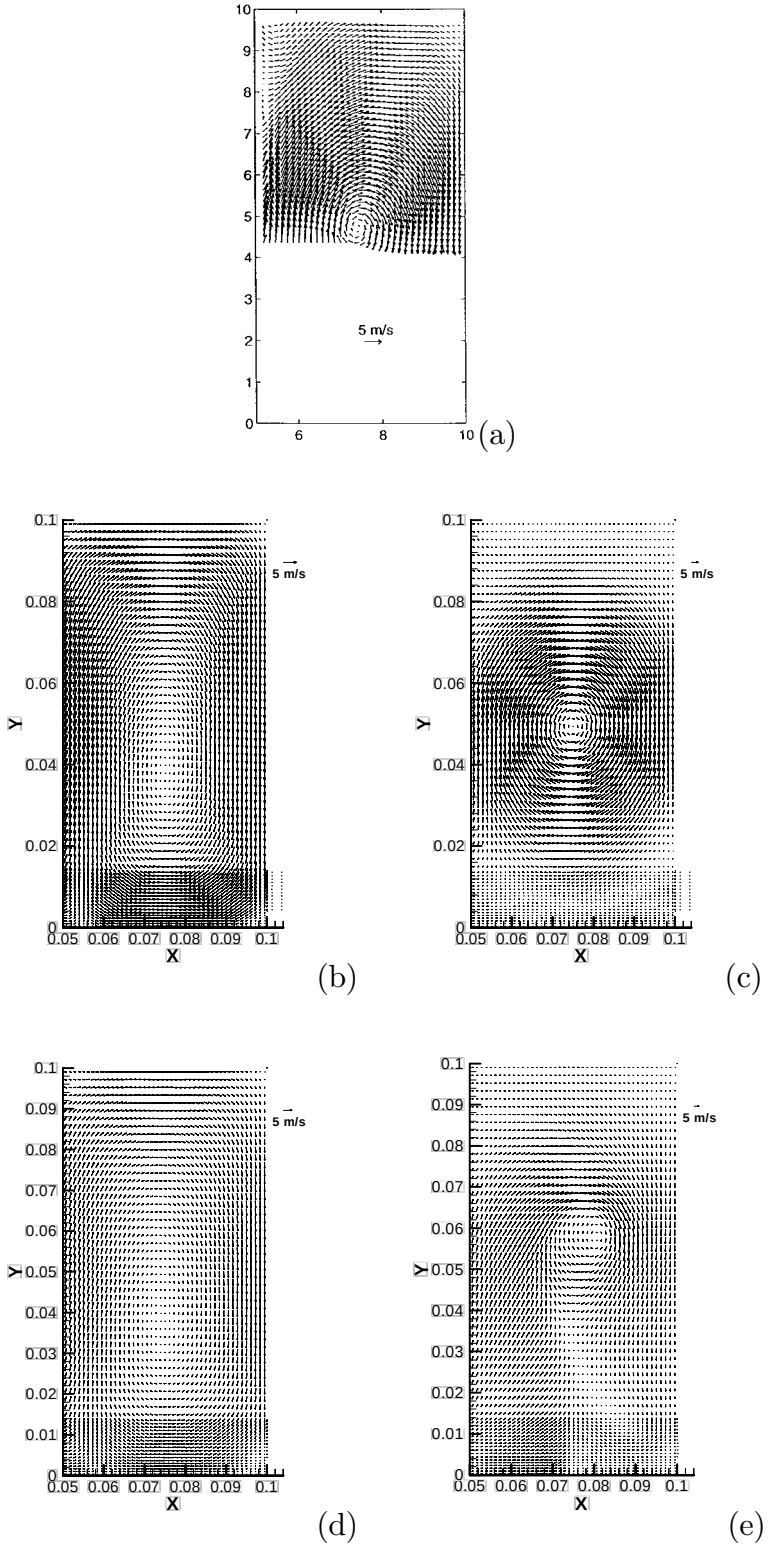

Figure 6.36: Velocity vectors in $Z = 50\,\text{mm}$ plane at 276 °CA. (a) – PIV results of Marc [187]; (b) – 2D k-ϵ simulation; (c) – 2D RSM simulation; (d) – 3D k-ϵ simulation; and (e) – 3D RSM simulation.

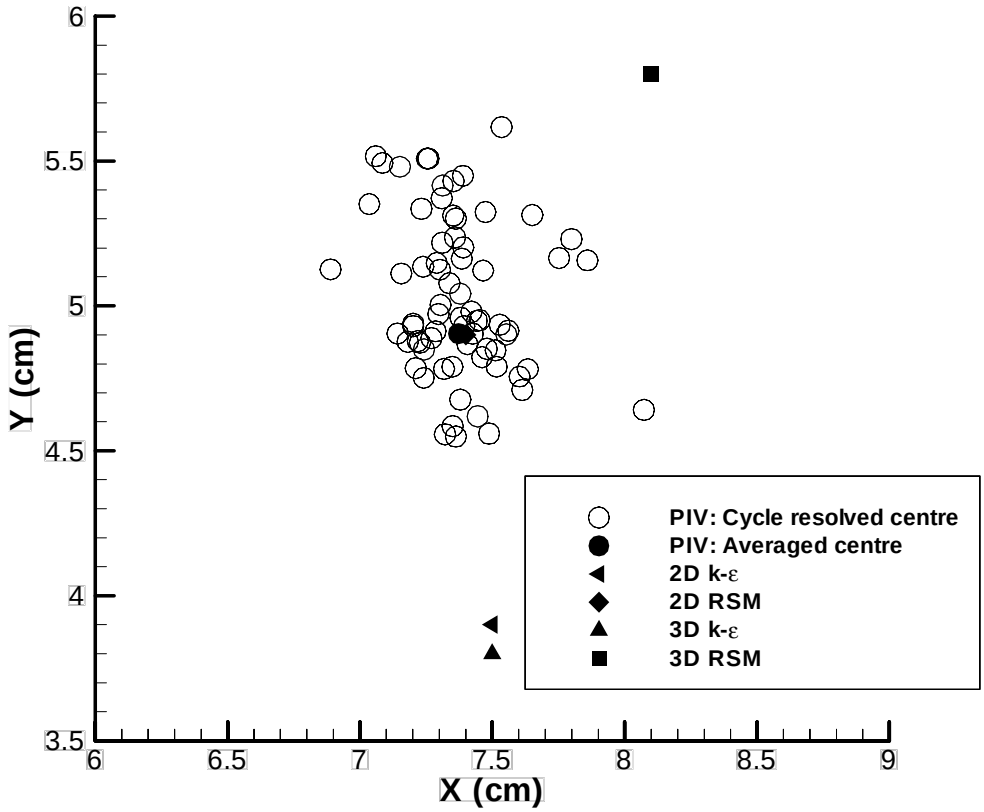

Figure 6.37: Position of the centre of the vortex at 276 °CA.

similar to each other, about 10 mm below the PIV results. These results show that all simulations are predicting the position of the central vortex with agreement to the experimental results of better than 10 mm.

The turbulence in the XY plane (figure 6.38) shows that the RSM models generate comparatively little turbulence, and the k-ϵ models generate a comparatively large amount of turbulence. There are also some differences between the two- and three-dimensional RSM models, fundamentally caused by the slightly different size and shape of the central vortex shown in figure 6.36.

The $X = 93$ mm plane (figure 6.39) shows very little structures occurring in this plane, and the flow is still dominated by a vortex in the tumble plane.

The turbulence in the $X = 93$ mm plane (figure 6.40) has a similar characteristic to that shown in the XY plane in figure 6.38, with a large region of high turbulence predicted by the k-ϵ model in the centre of the domain. The RSM model predicts

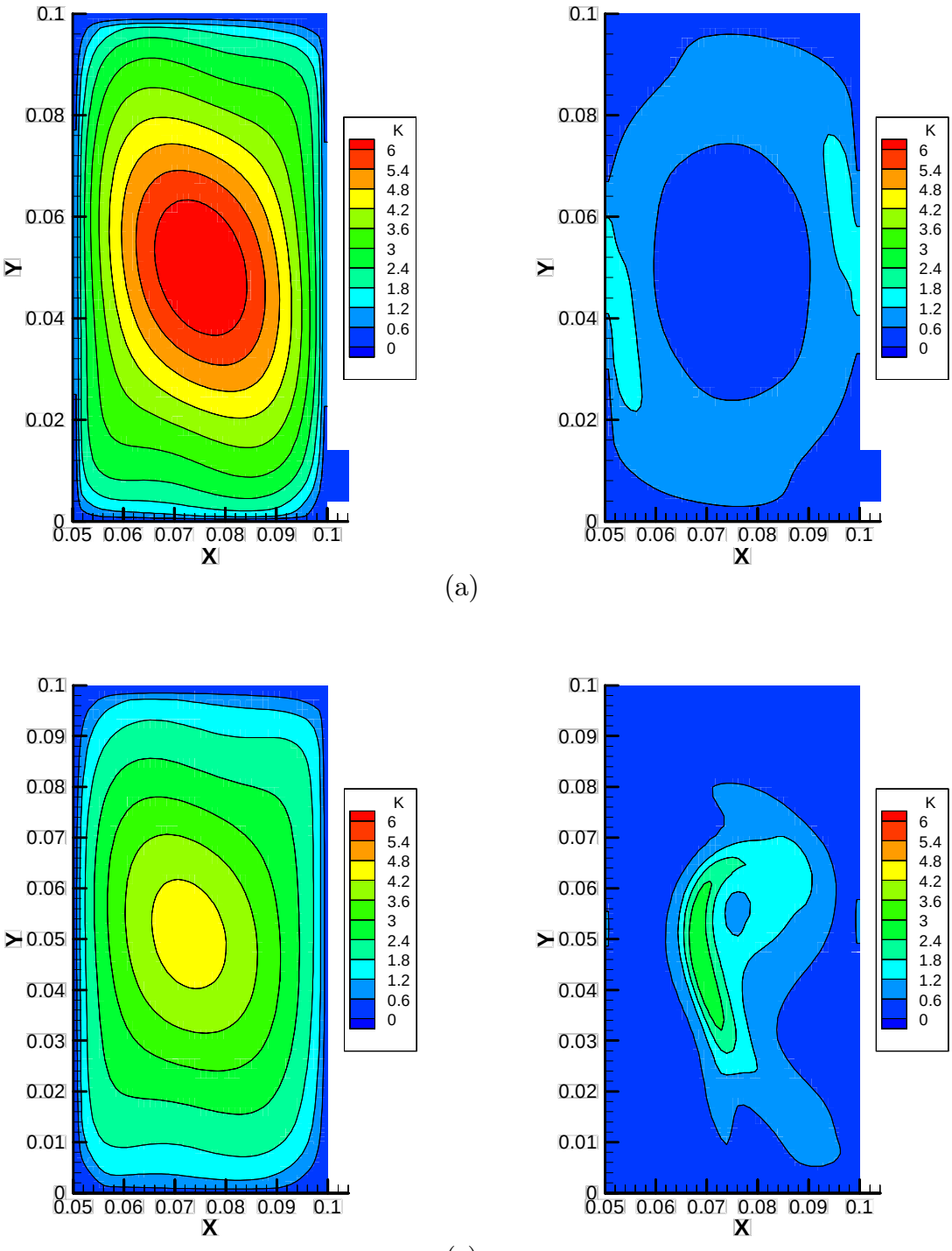

Figure 6.38: Turbulent kinetic energy, (k) in $Z = 50\,\text{mm}$ plane at 276 °CA. (a) – 2D k-ϵ simulation; (b) – 2D RSM simulation; (c) – 3D k-ϵ simulation; and (d) – 3D RSM simulation.

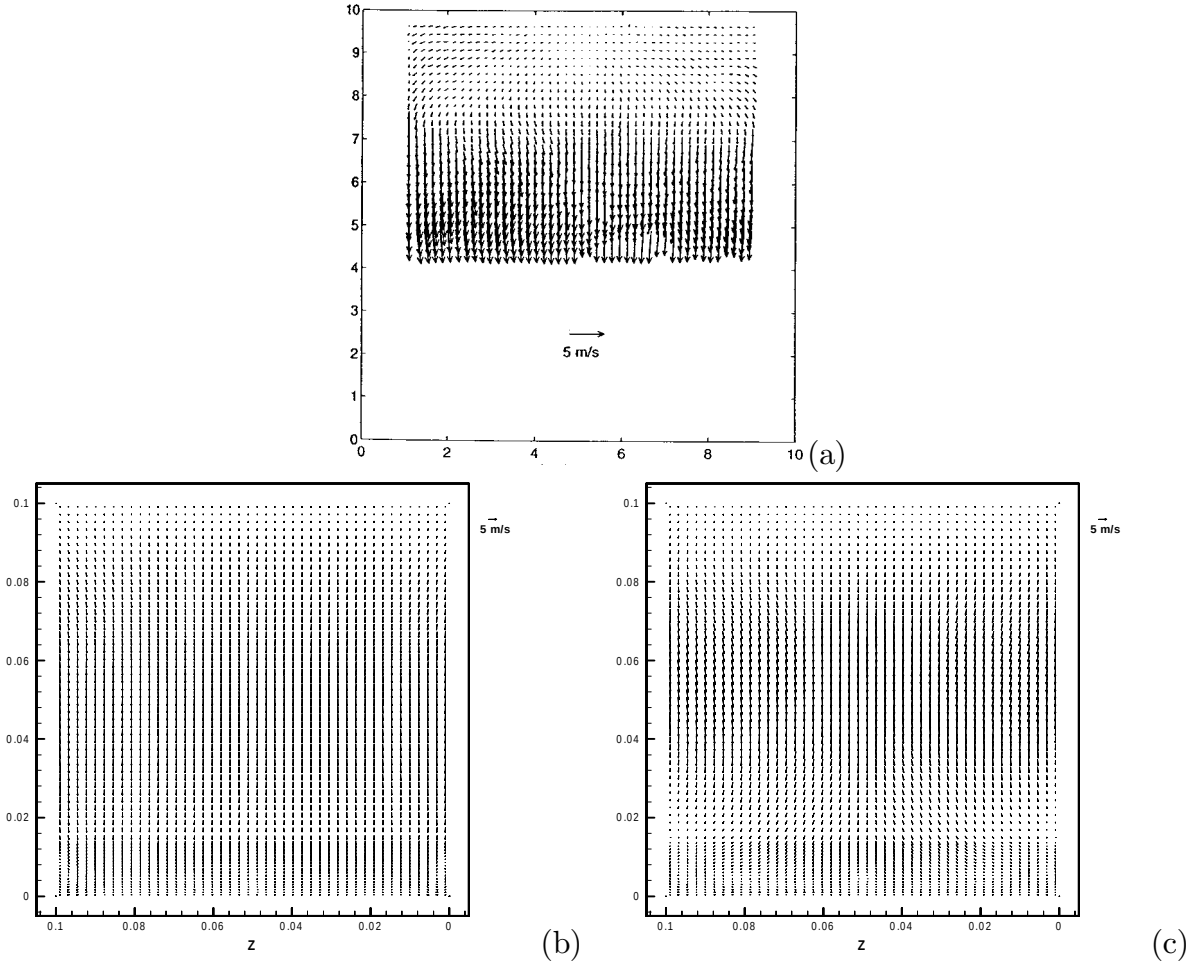

Figure 6.39: Velocity vectors in $X = 93\,\text{mm}$ plane at 276 °CA. (a) – PIV results of Marc [187]; (b) – 3D k-ϵ simulation; and (c) – 3D RSM simulation.

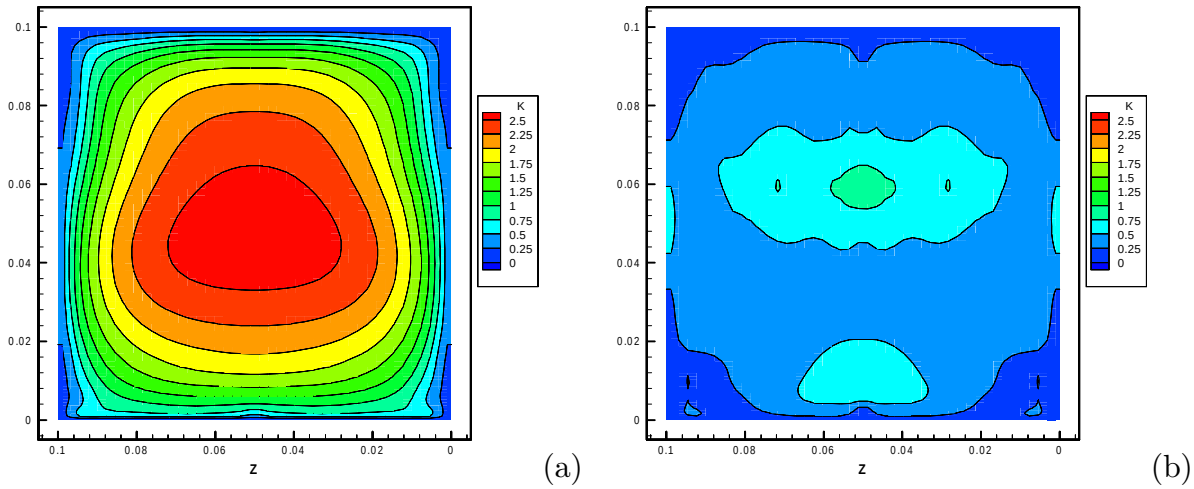

Figure 6.40: Turbulent kinetic energy, (k) in $X = 93\,\text{mm}$ plane at 276 °CA. (a) – 3D k-ϵ simulation; and (b) – 3D RSM simulation.

a far lower level of turbulence.

These results show that the compression stroke is around half complete, and the tumble breakdown process is commencing. The experimental results show the tumble vortex to be moving to the centre of the cylinder, and this process has been captured by the two- and three-dimensional RSM models. The k-ϵ models are already showing a significant departure from the experimental results, in that they do not predict any separation and decrease in size of the tumble vortex.

Results at 299 °CA

The compression stroke continues in figure 6.41 to 299 °CA, and the trends shown at 276 °CA continue. The PIV data indicates that the central vortex strengthens and becomes smaller, and the separated regions at the top of the domain grow to accommodate this. Again this is predicted by the two- and three-dimensional RSM models. The two-dimensional RSM model predicts a very strong central vortex, with weaker vortices in the top and bottom regions beginning to form. The three-dimensional RSM model also predicts the central vortex, but it is not as strong as that predicted by the two-dimensional RSM model, and the upper and lower secondary vortices have not formed. Both the two- and three-dimensional k-ϵ models predict the flow to be a rectangular vortex taking up the entire region.

Figure 6.42 shows the position of the vortex centres at 299 °CA. The two-dimensional and three-dimensional RSM models predict the location of the centre with good agreement with the experimental results.

The failure of the two- and three-dimensional k-ϵ models to correctly predict the

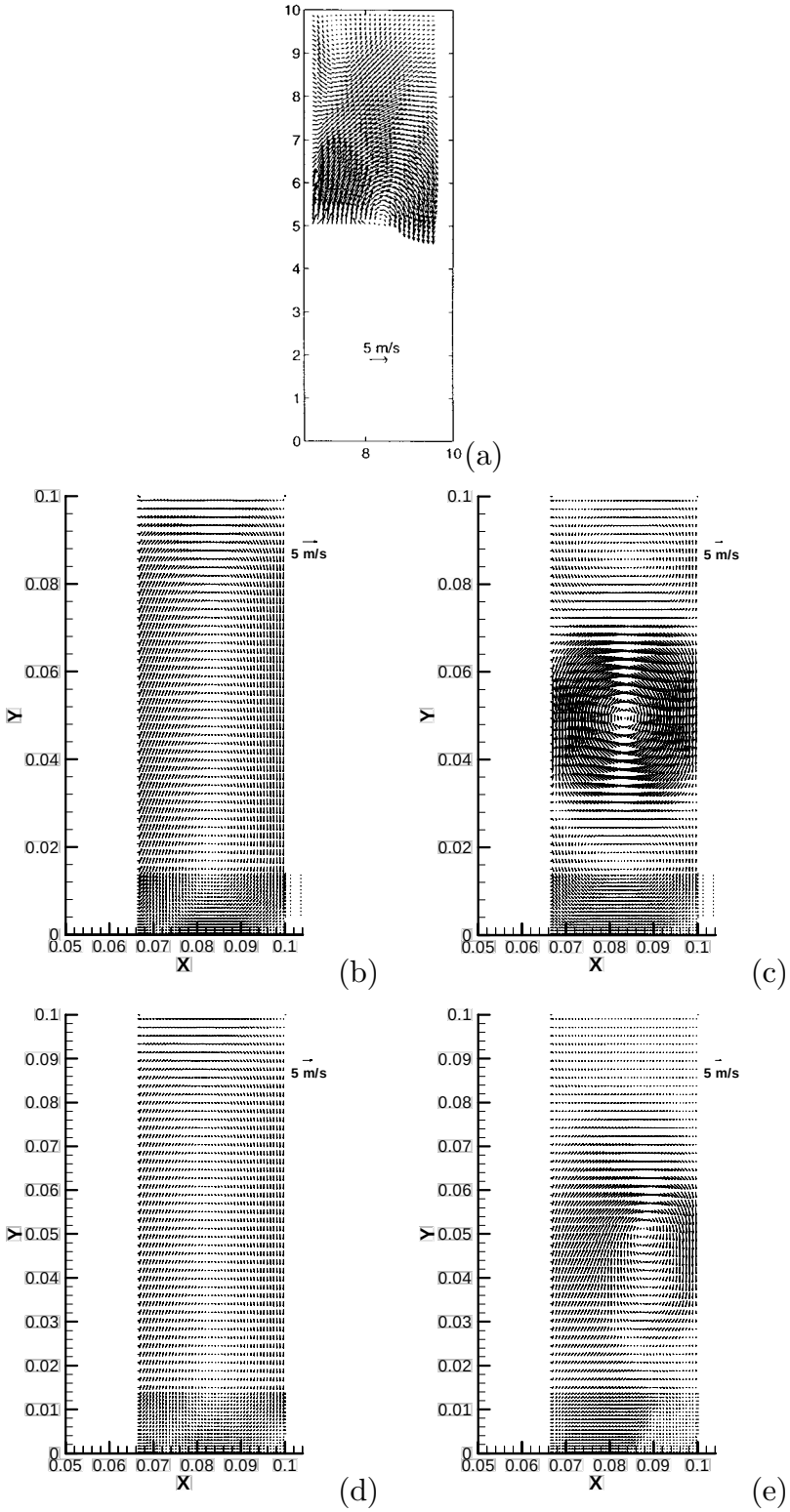

Figure 6.41: Velocity vectors in $Z = 50\,\text{mm}$ plane at 299 °CA. (a) – PIV results of Marc [187]; (b) – 2D k-ϵ simulation; (c) – 2D RSM simulation; (d) – 3D k-ϵ simulation; and (e) – 3D RSM simulation.

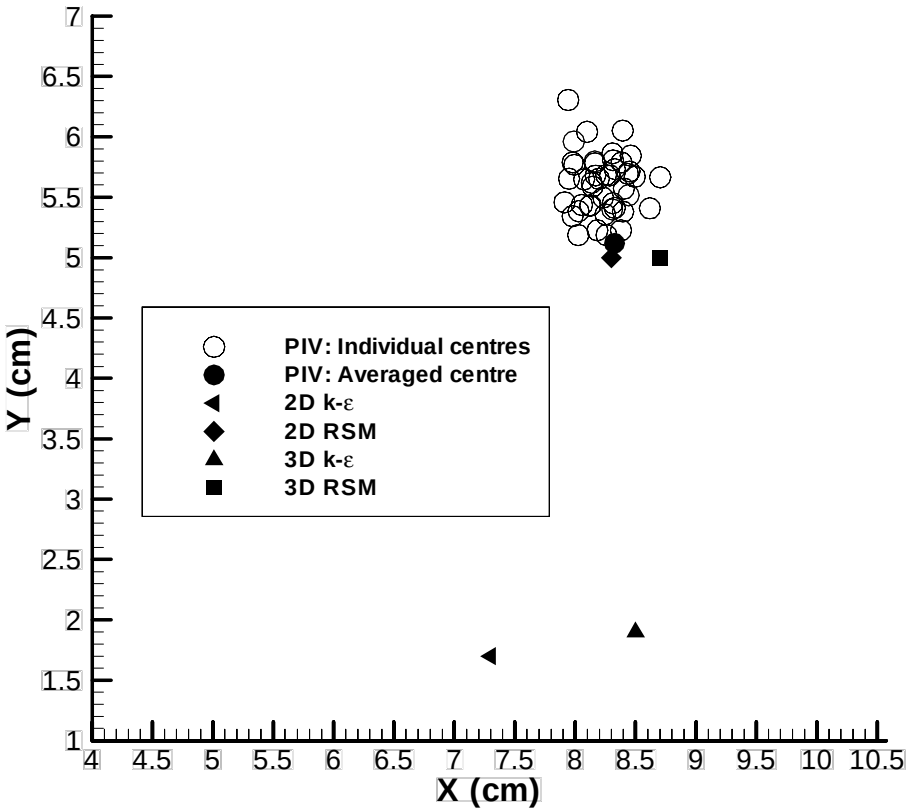

Figure 6.42: Position of the centre of the vortex at 299 °CA.

flow during the compression stroke now makes the vortex centre location predicted a long way from that measured experimentally—about 32 mm error, or one third of the total length of the domain.

An interesting point of interest about figure 6.42 is that the ensemble averaged PIV vortex centre does not lie in the middle of the region of the individual vortex centres. This is a result of the ensemble averaging process.

The turbulence levels in the XY plane, shown in figure 6.43 continue the trend seen in figure 6.38, where the k-ϵ models predict significantly higher turbulence levels than the RSM models, and the RSM models only predict a low turbulence level associated with the central vortex. Again, there is a small difference between the two- and three-dimensional RSM models associated with the different shape of the central vortex, seen in figure 6.41.

The YZ plane ($X = 93$ mm), shown in figure 6.44, shows the first signs of three-

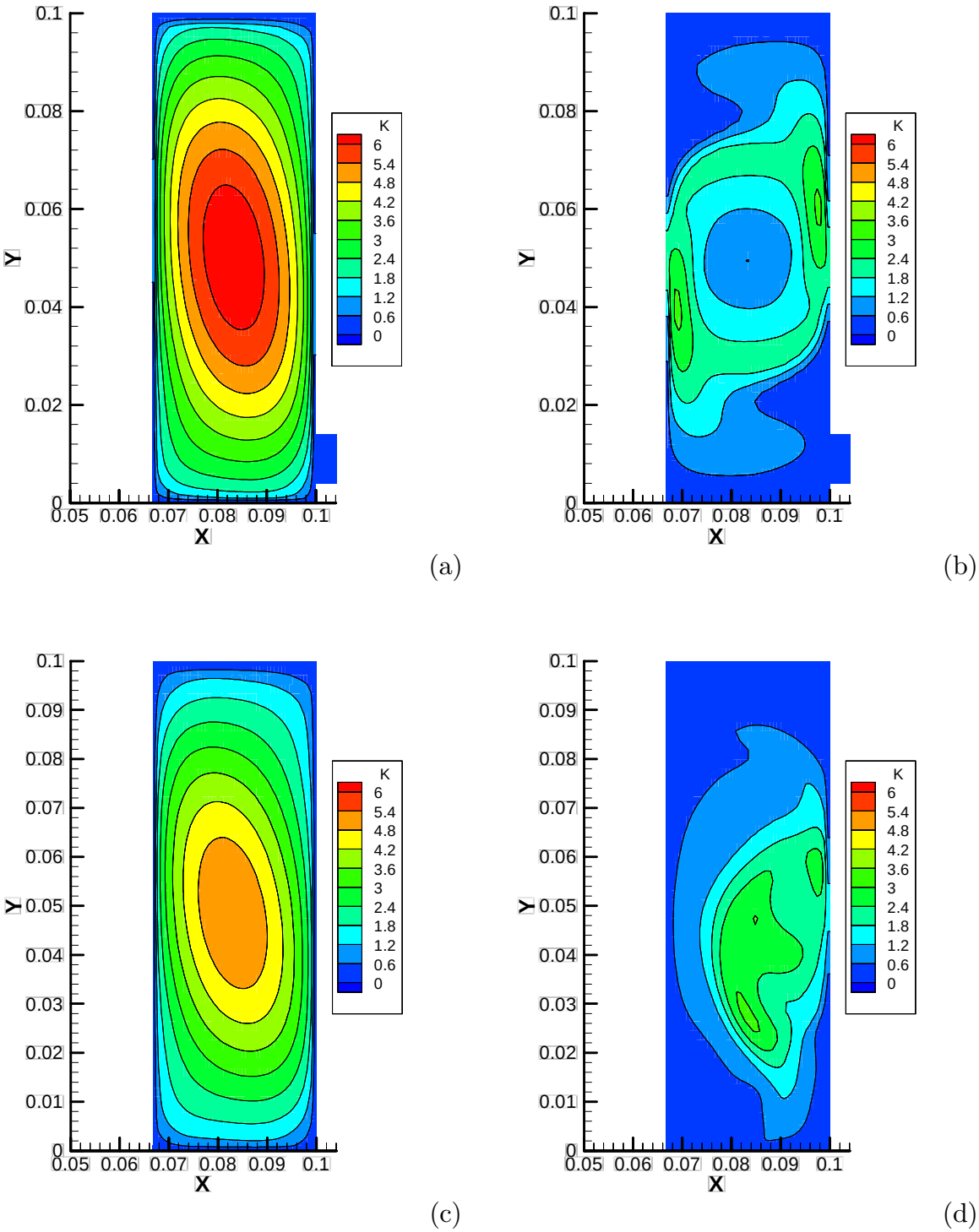

Figure 6.43: Turbulent kinetic energy, (k) in $Z = 50\,\text{mm}$ plane at 299 °CA. (a) – 2D k-ϵ simulation; (b) – 2D RSM simulation; (c) – 3D k-ϵ simulation; and (d) – 3D RSM simulation.

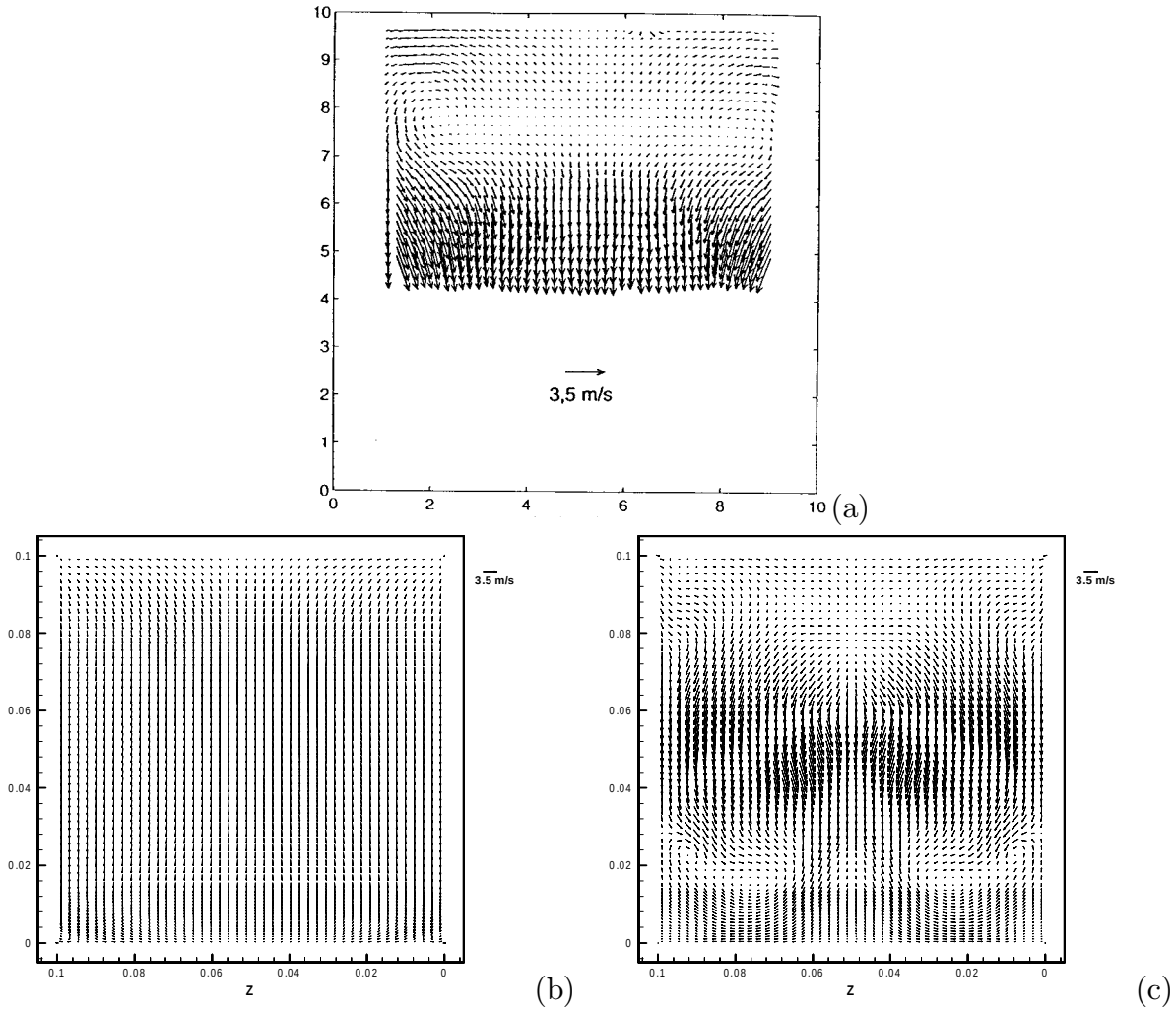

Figure 6.44: Velocity vectors in $X = 93\,\text{mm}$ plane at 299 °CA. (a) – PIV results of Marc [187]; (b) – 3D k-ϵ simulation; and (c) – 3D RSM simulation.

dimensional flows commencing in the compression stroke. The PIV results show a region of flow at the outside of the domain which is heading towards the centre of the domain, in a reasonably symmetrical fashion. The RSM model predicts symmetrical three-dimensional flow, but it appears to be the wrong shape. For instance, in the bottom left corner of the PIV results the flow is seen moving down and right (towards the centre of the cylinder), whereas the three-dimensional RSM results at the same location show the flow to be heading down and left (towards the outside wall of the cylinder).

The k-ϵ model fails to pick up any three-dimensional flows at all.

The turbulence intensity (k) in this YZ plane, shown in figure 6.45, continues the trend from 276 °CA (figure 6.40). However, the differences between the k-ϵ and RSM simulations have been reduced.

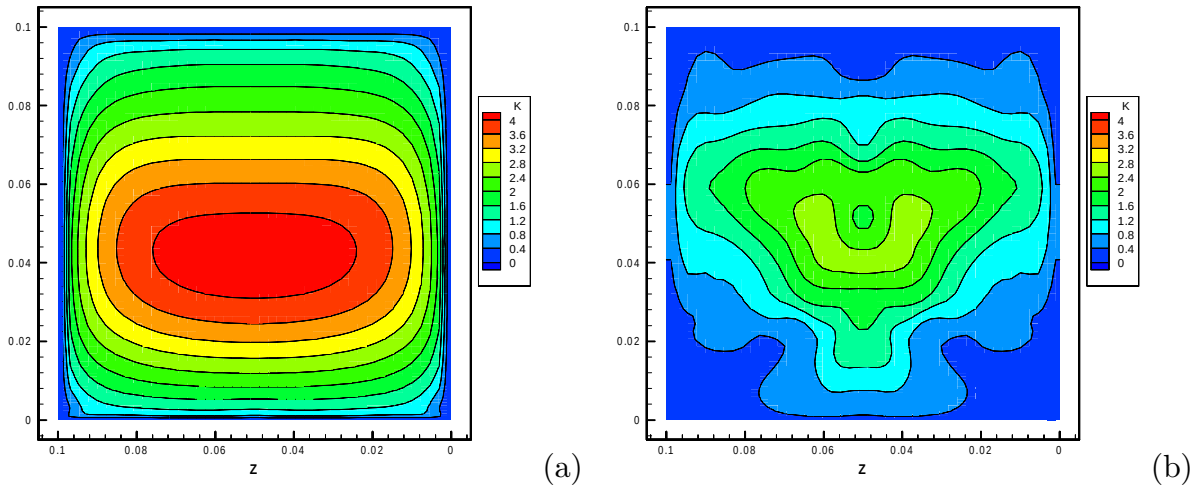

(a) (b)

Figure 6.45: Turbulent kinetic energy, (k) in $X = 93$ mm plane at 299 °CA. (a) – 3D k-ϵ simulation; and (b) – 3D RSM simulation.

Results at 312 °CA

The compression stroke is now in its final stages, at 312 °CA. Figure 6.14 shows the two- and three-dimensional k-ϵ models have passed their peak turbulence values, and the levels of turbulence intensity are rapidly declining. The two- and three-dimensional RSM models show the turbulence peaks around this position.

Figure 6.46 shows the PIV data to have a strong central vortex, and a weaker vortex rotating in the opposite direction above it (and presumably below, it is out of the field of view). This velocity field has successfully been captured by the two-dimensional RSM model, which clearly resolves the three vortices. The three-dimensional RSM model does not show three vortices, however it does show the central vortex to have reduced in size. The two- and three-dimensional k-ϵ models completely fail to capture the field at all, continuing to predict one large rectangular vortex as shown in figures 6.41 and 6.36. The vortex predicted by the k-ϵ models has now significantly weakened.

The turbulence intensity in the XY plane is shown in figure 6.47. Again, it shows the k-ϵ model predicts a fairly even and high level of turbulence, with a maximum valve in the centre of the cylinder. In comparison, the RSM models predict the turbulence being concentrated around the central vortex. The three-dimensional RSM model is now predicting a higher level of turbulence in its central vortex than the k-ϵ model.

The three-dimensional RSM simulation predicts a complicated flow field. Several views of the three-dimensional nature of this flow can be seen in figure 6.48, showing instantaneous streamlines at 312 °CA viewed from various angles. The small central

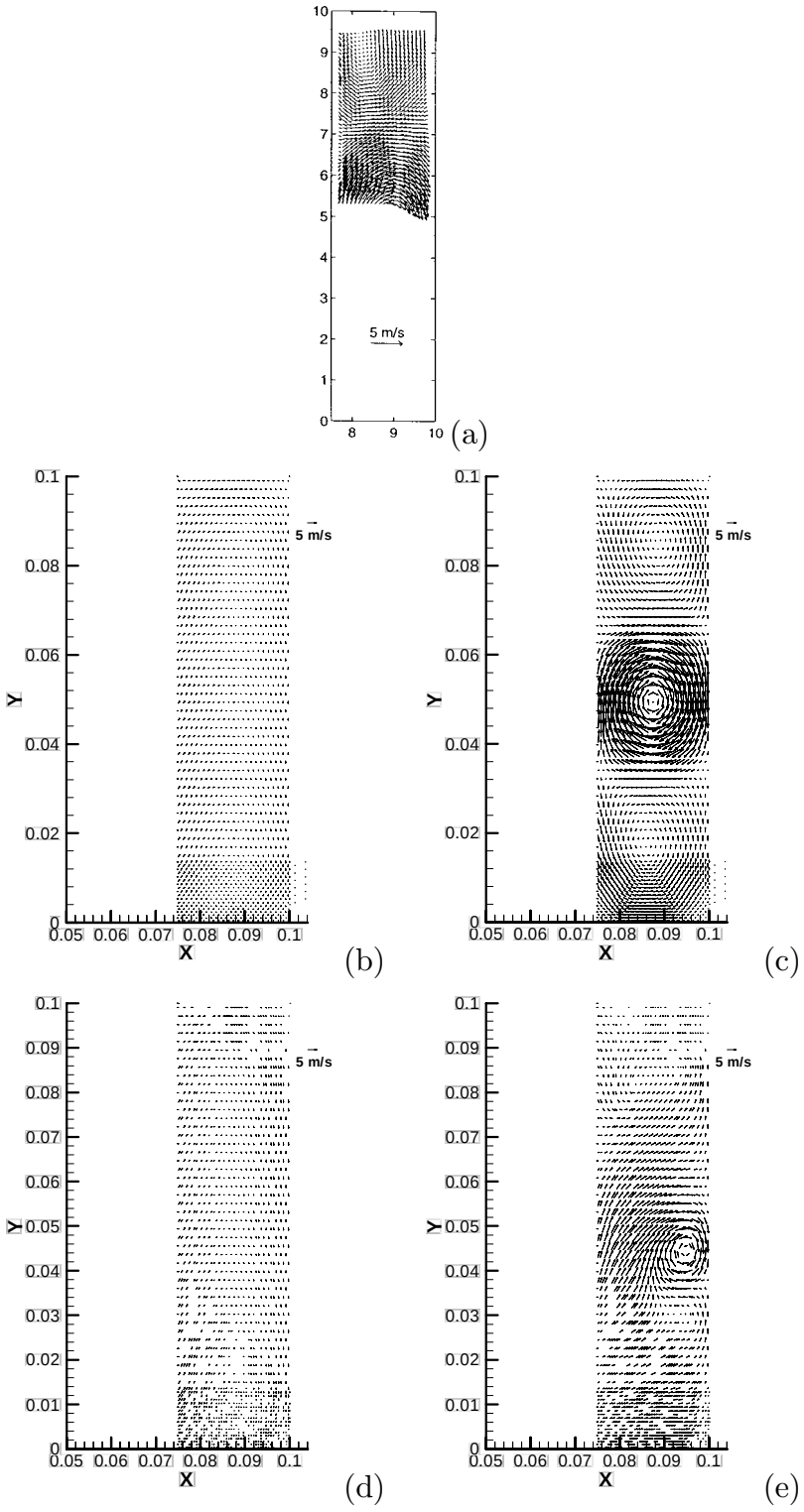

Figure 6.46: Velocity vectors in $Z = 50\,\text{mm}$ plane at 312 °CA. (a) – PIV results of Marc [187]; (b) – 2D k-ϵ simulation; (c) – 2D RSM simulation; (d) – 3D k-ϵ simulation; and (e) – 3D RSM simulation.

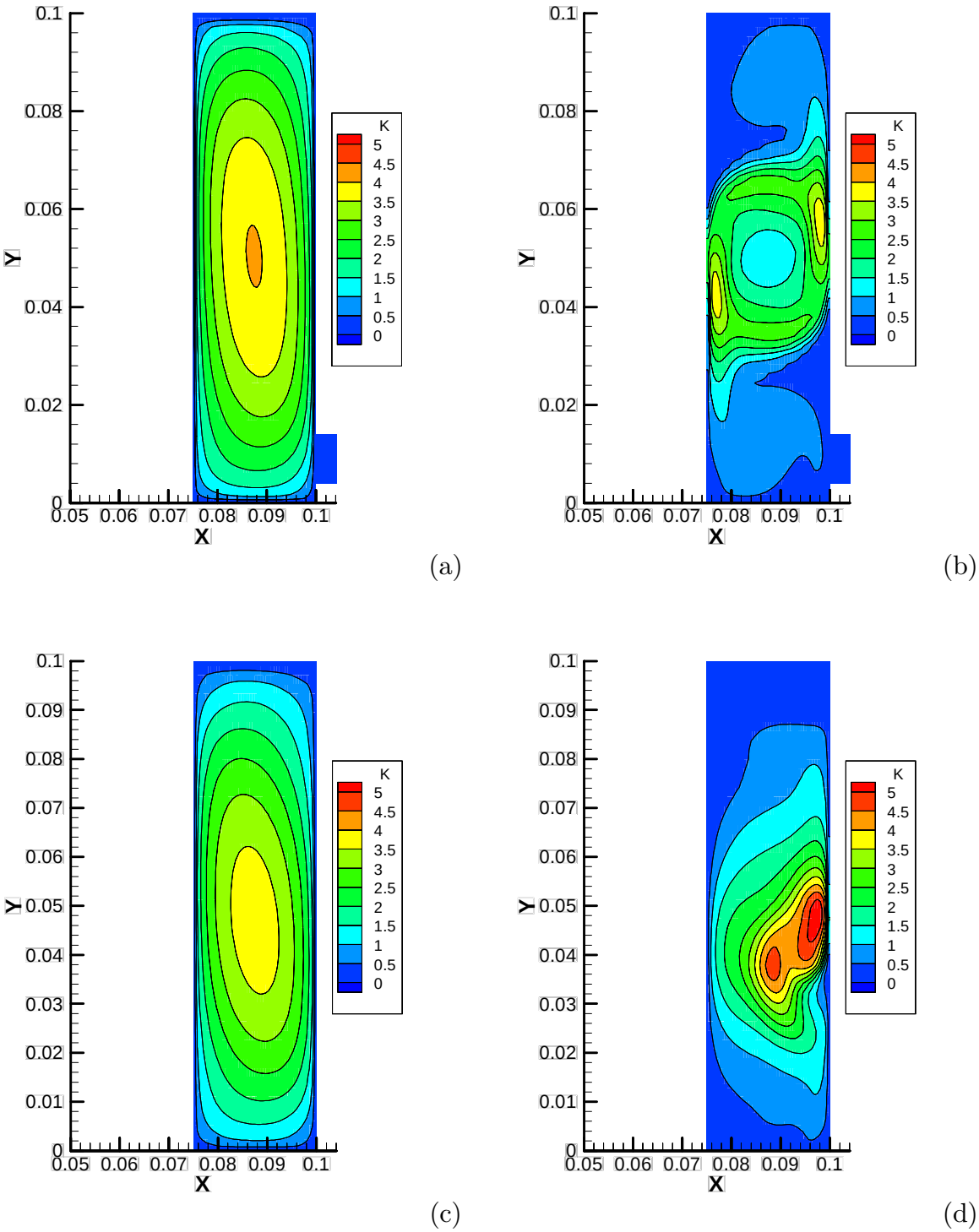

Figure 6.47: Turbulent kinetic energy, (k) in $Z = 50\,\text{mm}$ plane at 312 °CA. (a) – 2D k-ϵ simulation; (b) – 2D RSM simulation; (c) – 3D k-ϵ simulation; and (d) – 3D RSM simulation.

tumble vortex is seen to extend across the entire field in figure 6.48c, and the curve in the centre line of this vortex is visible. Structures above and below the central tumble vortex are also apparent.

The YZ plane, shown in figure 6.49, indicates that the three-dimensional flows seen commencing at 299 °CA in figure 6.44 are growing stronger. The PIV results show weak vortices in the top left and right corners, and significant three-dimensional flows over most of the rest of the domain, in a reasonably symmetrical fashion. The RSM model continues to predict symmetrical three-dimensional flow, but it is still the wrong shape. The k-ϵ model fails to pick up any significant three-dimensional flows at all.

The turbulence intensity in this plane is shown in figure 6.50. The three-dimensional k-ϵ and RSM models predict reasonably similar levels of turbulence in the centre of the domain, but the k-ϵ model predicts it to be evenly spread across the domain and the RSM model predicts it to be focussed at the centre and significantly distorted in shape.

Results at 321 °CA

All simulations are now predicting the turbulence to rapidly decrease until the end of the compression stroke.

Figure 6.51 shows the PIV results to clearly resolve a strong central vortex, a slightly weaker top vortex and presumably a similar third vortex on the bottom. This is correctly predicted by the two-dimensional RSM model, however the central vortex is too strong. The three-dimensional RSM model predicts the strength of the central vortex better and does show a weak top vortex, but does not clearly resolve it. The central vortex of the three-dimensional RSM model is also seen to be offset from the centre of the domain significantly, which is not shown on the PIV results. The two- and three-dimensional k-ϵ models completely fail to pick and significant flows at all, predicting that the flow has essentially stopped. Presumably the extra turbulence generated earlier in the compression stroke has dissipated the energy from the mean flow field.

Figure 6.52 continues the trend shown in this plane in previous visualisations. The two- and three-dimensional k-ϵ models both predict uniform levels of turbulence across the entire domain. As the velocities generating turbulence have now effectively stopped in the k-ϵ simulations, there is very little turbulence generation for the remainder of the compression stroke. The turbulence currently present will rapidly dissipate.

The two- and three-dimensional RSM simulations, shown in figure 6.52b and

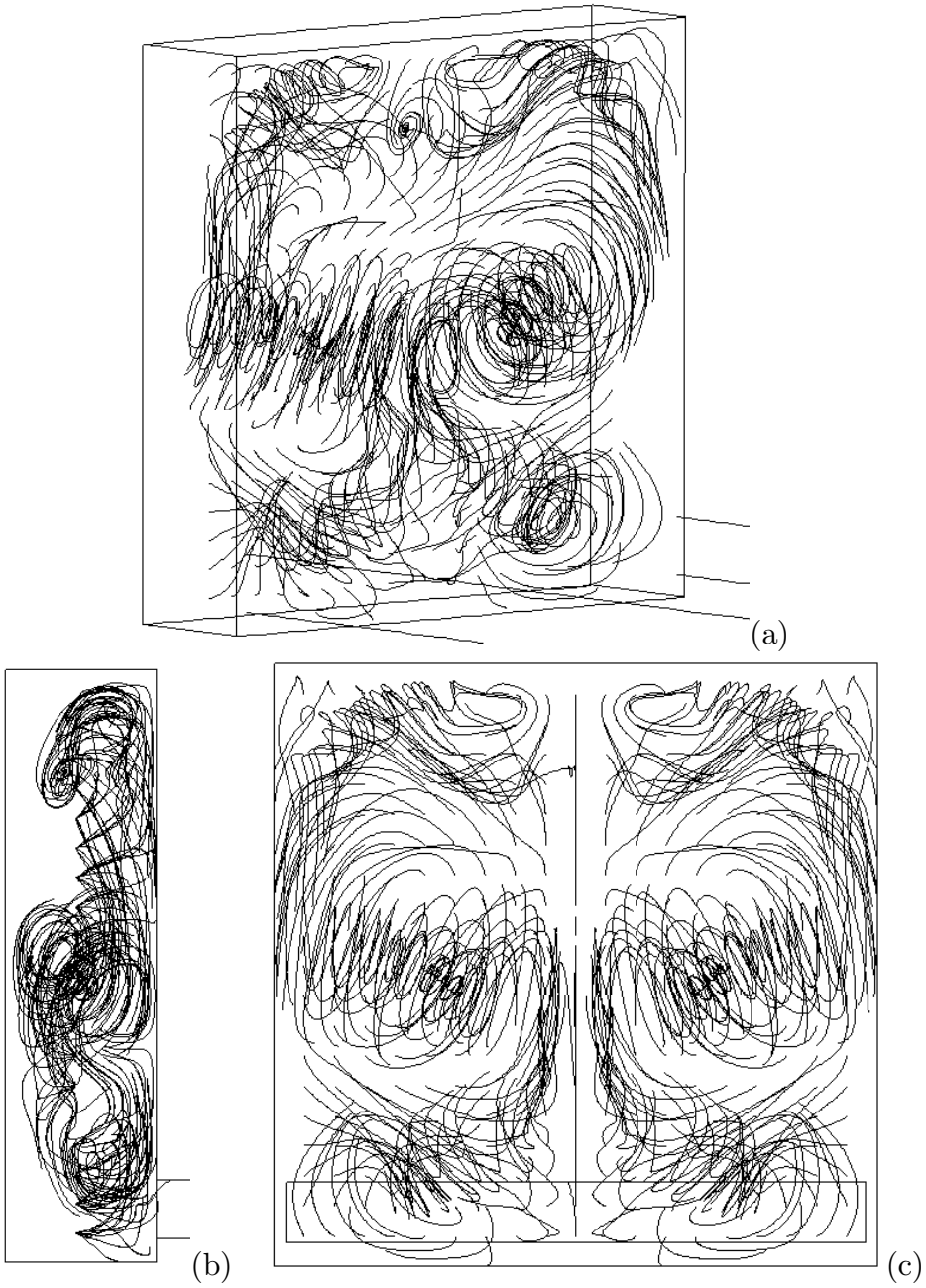

Figure 6.48: Instantaneous streamlines from the three-dimensional RSM simulation at 312 °CA. (a) – Isometric view; (b) – Tumble plane view; and (c) – Cross tumble plane view.

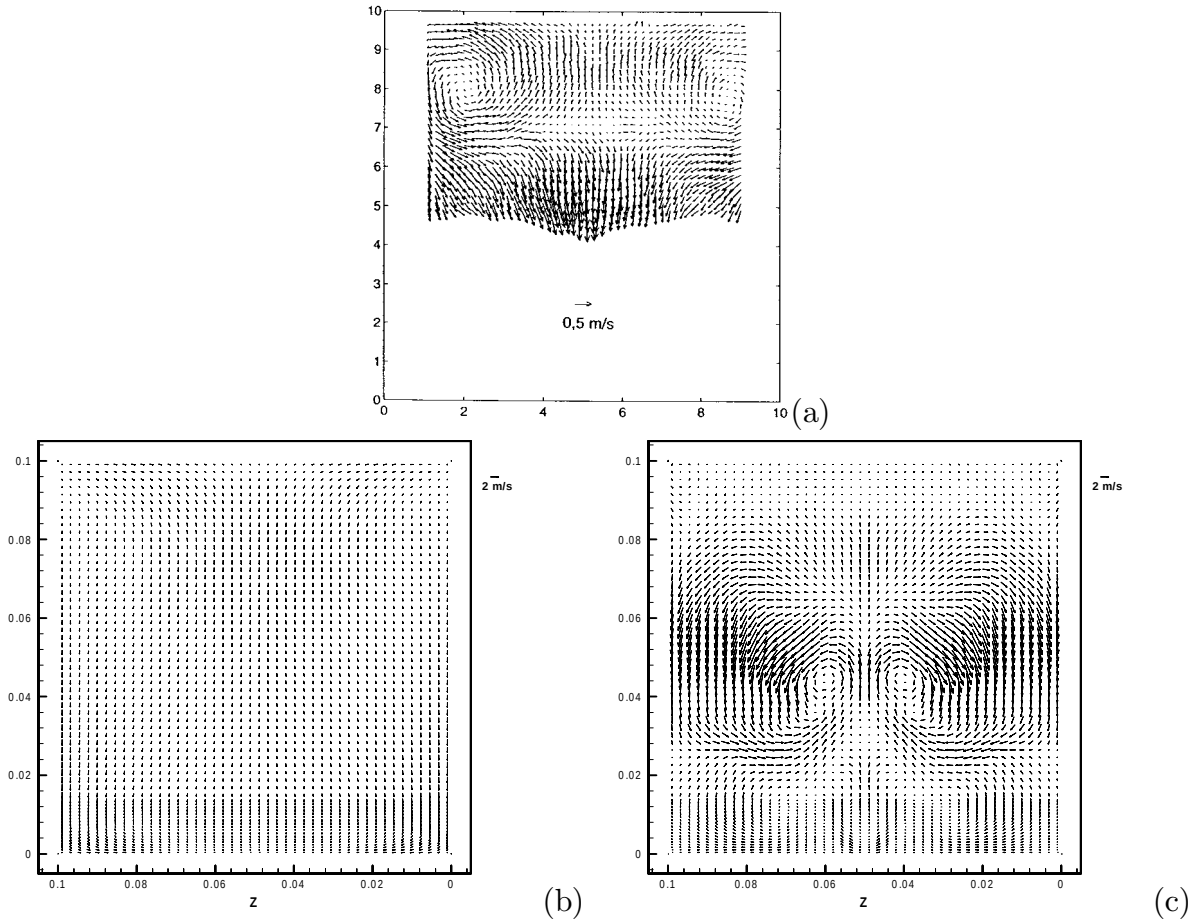

Figure 6.49: Velocity vectors in $X = 93\,\text{mm}$ plane at 312 °CA. (a) – PIV results of Marc [187]; (b) – 3D k-ϵ simulation; and (c) – 3D RSM simulation.

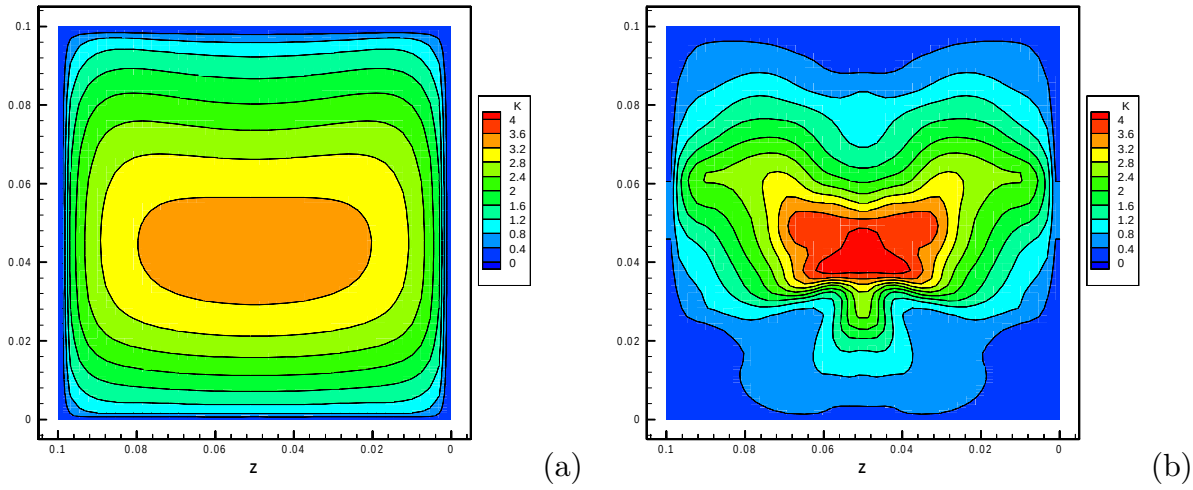

Figure 6.50: Turbulent kinetic energy, (k) in $X = 93\,\text{mm}$ plane at 312 °CA. (a) – 3D k-ϵ simulation; and (b) – 3D RSM simulation.

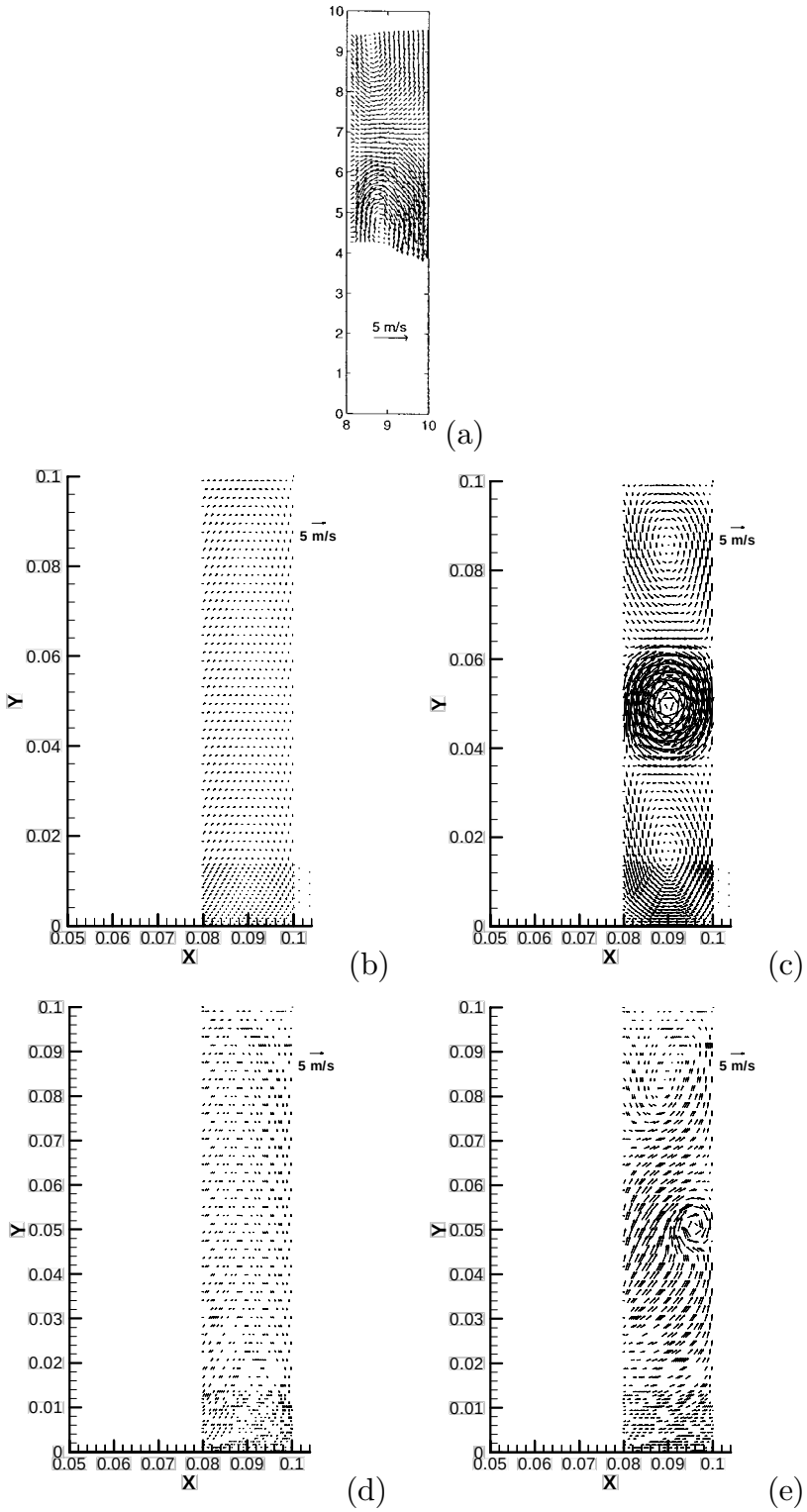

Figure 6.51: Velocity vectors in $Z = 50\,\text{mm}$ plane at 321 °CA. (a) – PIV results of Marc [187]; (b) – 2D k-ϵ simulation; (c) – 2D RSM simulation; (d) – 3D k-ϵ simulation; and (e) – 3D RSM simulation.

6.52d, predict similar turbulence fields centred around the strong central vortex. However the two-dimensional RSM simulation displays an odd symmetry about the central plane[1], whereas the three-dimensional RSM model is asymmetric.

The YZ plane vector field shown in figure 6.53 at 321 °CA was the furthest through the compression stroke that Marc was able to record PIV data for this plane. He explains that an excessive amount of reflections occurred as the piston approached the measurement plane, making the data unusable. The PIV results shown in figure 6.53 show that the top left and right vortices first seen at 312 °CA in figure 6.49 remain, and the flow is still largely symmetric. However, there is a large amount of "noise" in the diagram, possibly indicating large variations due to turbulence, cycle to cycle variations or difficulties in performing accurate measurements. The structure of the flow is clear, however.

Again all simulations failed to predict this flow. The k-ϵ model again predicted essentially no flow. The RSM model predicted structures of around the correct size, but they are in the wrong position.

The turbulence levels in this plane (figure 6.54) now shows that the k-ϵ model now drops below the levels predicted by the RSM model. The turbulence in the RSM model is still concentrated around the central vortex.

Results at 328 °CA

Figure 6.55 shows the PIV results, still showing the structure of two visible vortices and presumably a third vortex out of the field of view. It is not as clearly seen as at 321 °CA in figure 6.51, however. Again this is clearly captured by the two-dimensional RSM model, but the central vortex is now far too strong. The three-dimensional RSM model also captures the central and top vortex, but no clear bottom vortex is seen and the central vortex is still off-centre. As the experimental results did not resolve the flow in the lower half of the cylinder, whether a vortex exists in the lower half of the cylinder is a matter of speculation.

All motion has essentially stopped in the two- and three-dimensional k-ϵ models predictions.

The turbulence intensity predictions follows the same trend as before, and are shown in figure 6.56. The two-dimensional RSM model predicts a region of strong turbulence associated with the strong central vortex. The three-dimensional RSM model predicts a lower level of turbulence, also concentrated at the central vortex. The k-ϵ models predicts a uniform spread of turbulence intensity, which is now

[1] Odd in the mathematical sense, that is, $f(-x) = -f(x)$ for all x.

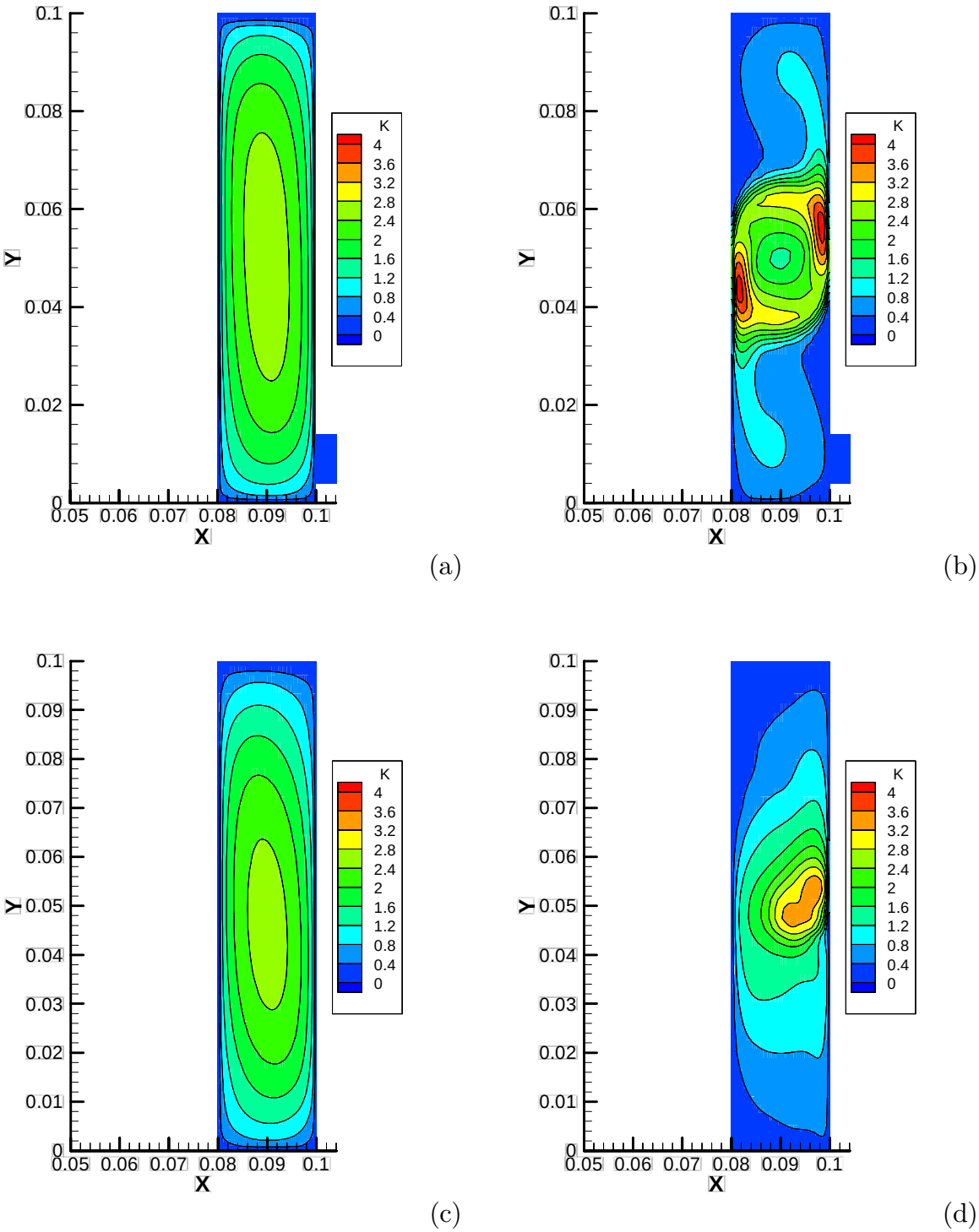

Figure 6.52: Turbulent kinetic energy, (k) in $Z = 50\,\text{mm}$ plane at 321 °CA. (a) – 2D k-ϵ simulation; (b) – 2D RSM simulation; (c) – 3D k-ϵ simulation; and (d) – 3D RSM simulation.

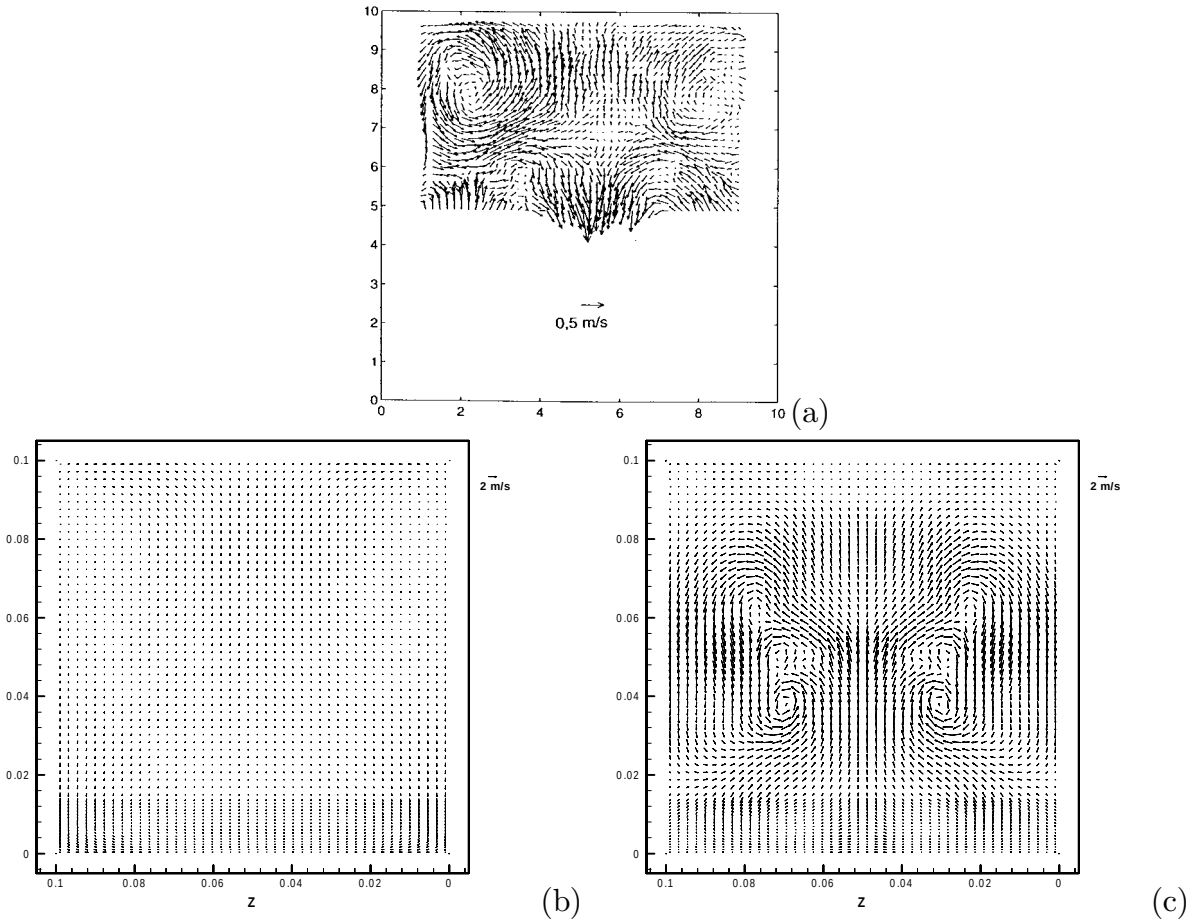

Figure 6.53: Velocity vectors in $X = 93\,\text{mm}$ plane at 321 °CA. (a) – PIV results of Marc [187]; (b) – 3D k-ϵ simulation; and (c) – 3D RSM simulation.

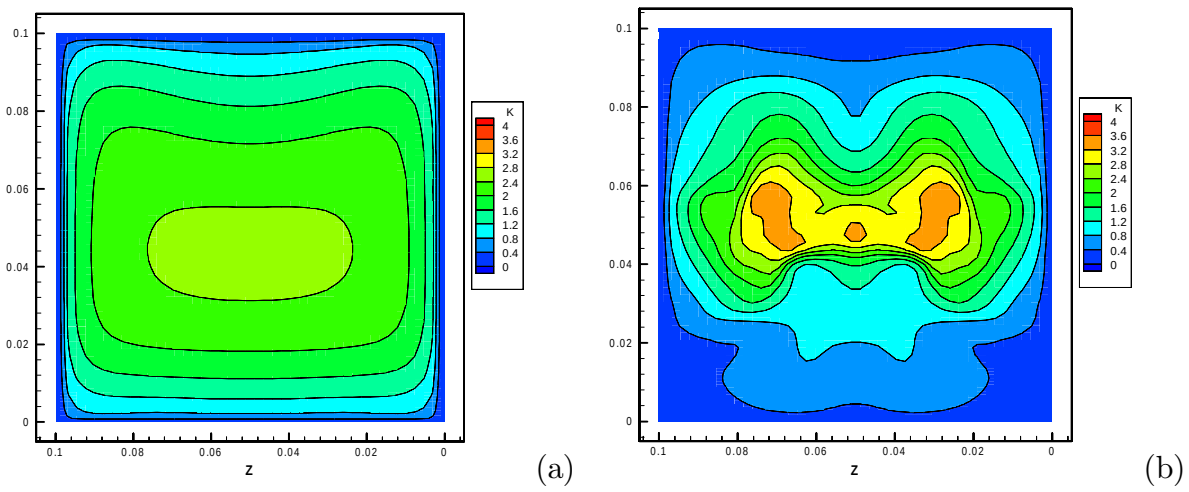

Figure 6.54: Turbulent kinetic energy, (k) in $X = 93\,\text{mm}$ plane at 321 °CA. (a) – 3D k-ϵ simulation; and (b) – 3D RSM simulation.

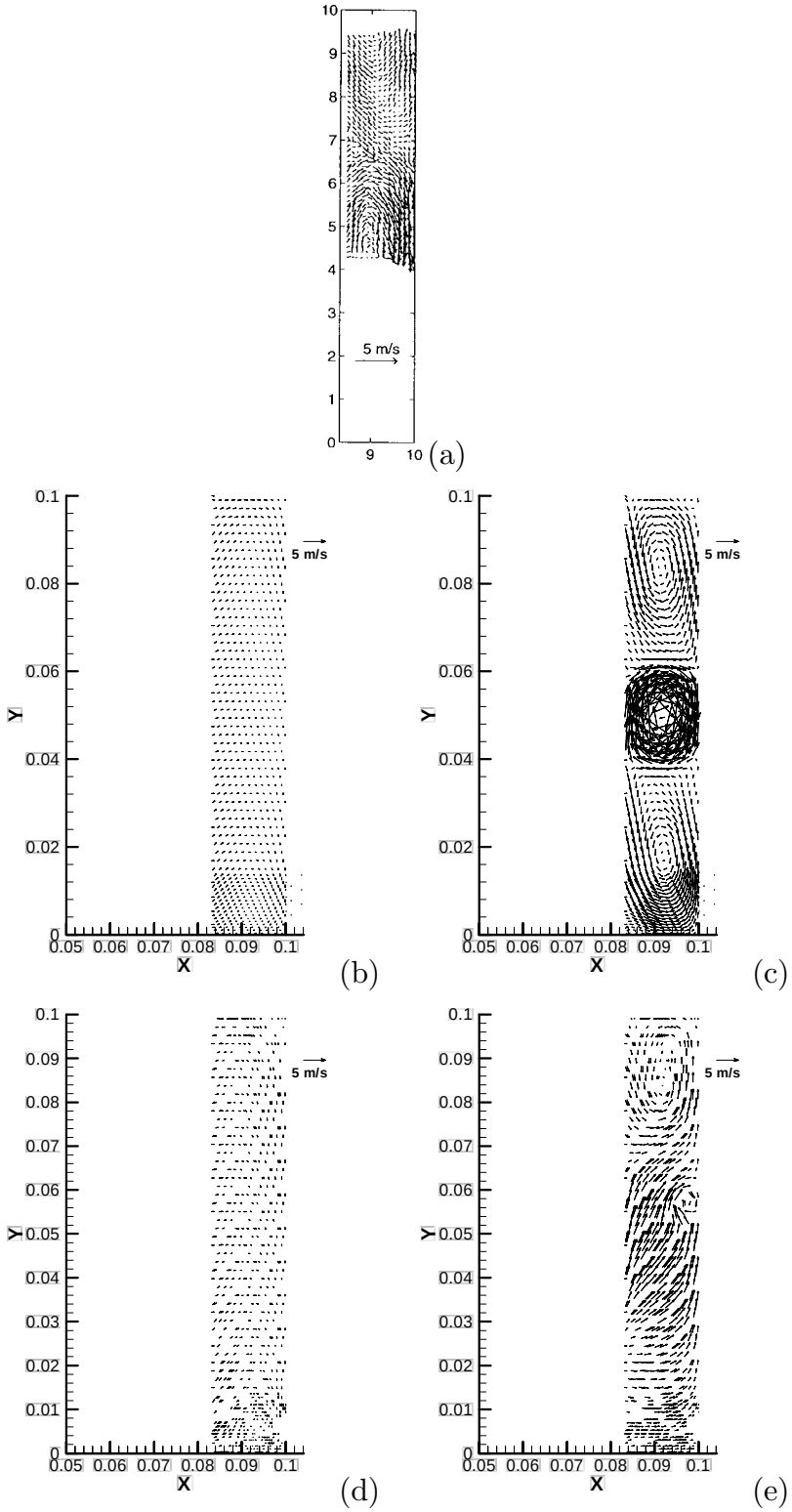

Figure 6.55: Velocity vectors in $Z = 50\,\text{mm}$ plane at 328 °CA. (a) – PIV results of Marc [187]; (b) – 2D k-ϵ simulation; (c) – 2D RSM simulation; (d) – 3D k-ϵ simulation; and (e) – 3D RSM simulation.

dissipating rapidly as there is little remaining energy for turbulence generation.

Results at 335 °CA

This visualisation at 335 °CA was as close to TDC as Marc could measure PIV data in the tumble ($Z = 50\,\text{mm}$) plane. Figure 6.57 shows that the PIV results do not clearly resolve the three vortex structures seen before; the only feature clearly visible is the top of the central vortex. The two-dimensional RSM simulation still clearly resolves the three vortices, but the central vortex appears to have almost disappeared in the three-dimensional RSM model. The k-ϵ models continue to predict essentially zero flow.

The turbulence shown in figure 6.58 shows that the two-dimensional RSM model has the turbulence concentrated around the central vortex, as does the three-dimensional RSM model but with a lower level of turbulence. The k-ϵ models continue to predict low and reasonably uniform levels of turbulence across the domain.

Results at 360 °CA, TDC

Marc [187] presents no PIV data for this position, it is included here for completeness. Figure 6.59 shows the velocity vectors, and the trends shown in the previous visualisations continue. The two-dimensional RSM model has now broken down further, and is displaying around 9 vortices, again with the central one being the strongest. Many small vortices are seen, they are possibly being "born" and have not yet interacted with their neighbouring vortices and equally distribute the available volume between themselves. The three-dimensional RSM model predicts a single vortex in the top half of the chamber, but the strong upwards flow indicates significant flows in the third dimension which is not shown on this cross section. The k-ϵ model continues to show essentially zero flow over the entire domain.

The turbulence intensity, as shown in figure 6.60, indicates that all the simulations have arrived at reasonably similar results at TDC. Again the two-dimensional RSM model has a peak of turbulence intensity at the central vortex and is now displaying two more peaks where the top and bottom secondary vortices were once located. The three-dimensional RSM model is showing the turbulence concentrated at the top vortex and where the central vortex was once located. The k-ϵ models yield reasonably uniform turbulence across the entire domain, as they have done for the entire compression stroke.

Instantaneous streamlines predicted for the three-dimensional RSM simulation

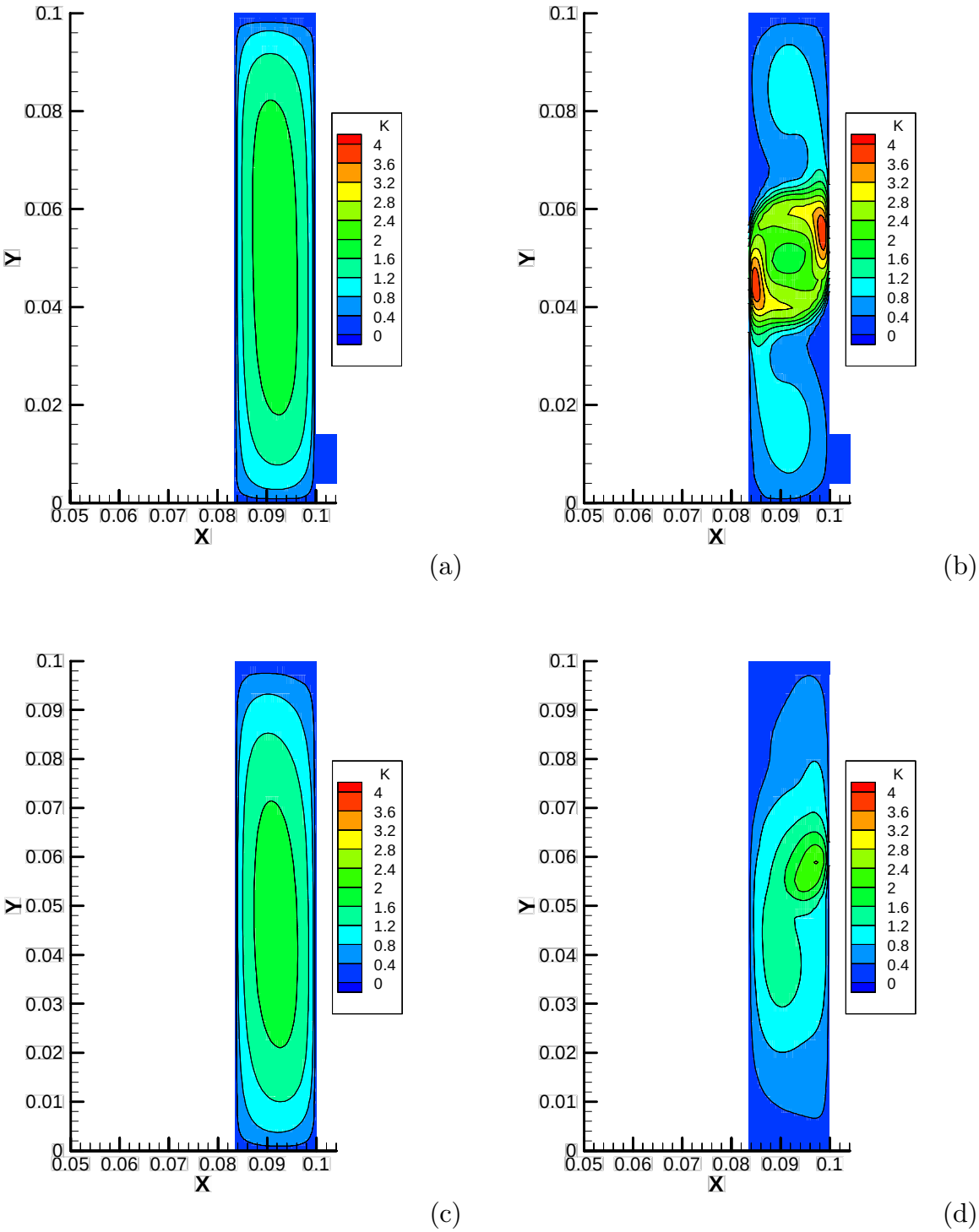

Figure 6.56: Turbulent kinetic energy, (k) in $Z = 50\,\text{mm}$ plane at 328 °CA. (a) – 2D k-ϵ simulation; (b) – 2D RSM simulation; (c) – 3D k-ϵ simulation; and (d) – 3D RSM simulation.

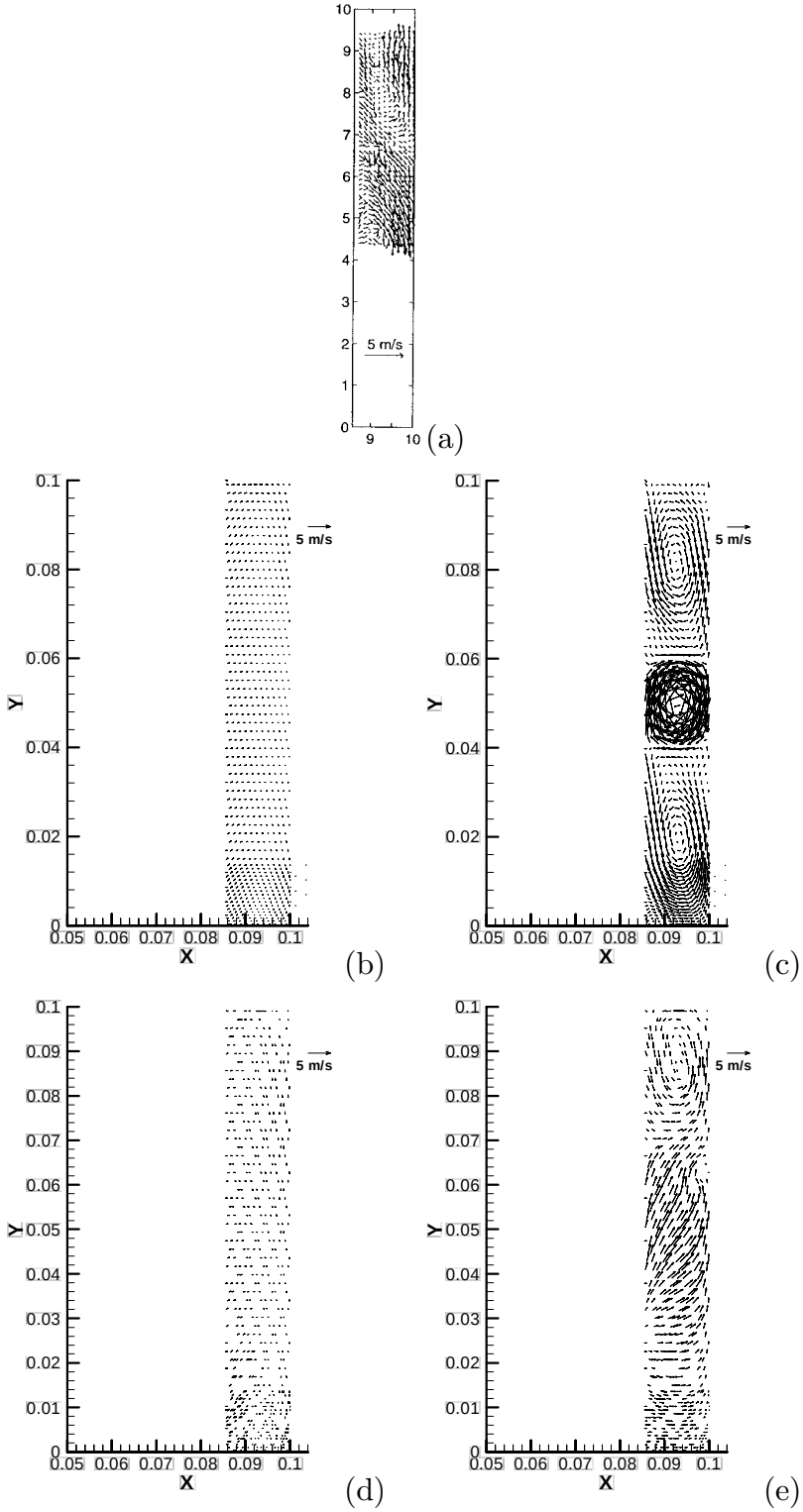

Figure 6.57: Velocity vectors in $Z = 50\,\text{mm}$ plane at 335 °CA. (a) – PIV results of Marc [187]; (b) – 2D k-ϵ simulation; (c) – 2D RSM simulation; (d) – 3D k-ϵ simulation; and (e) – 3D RSM simulation.

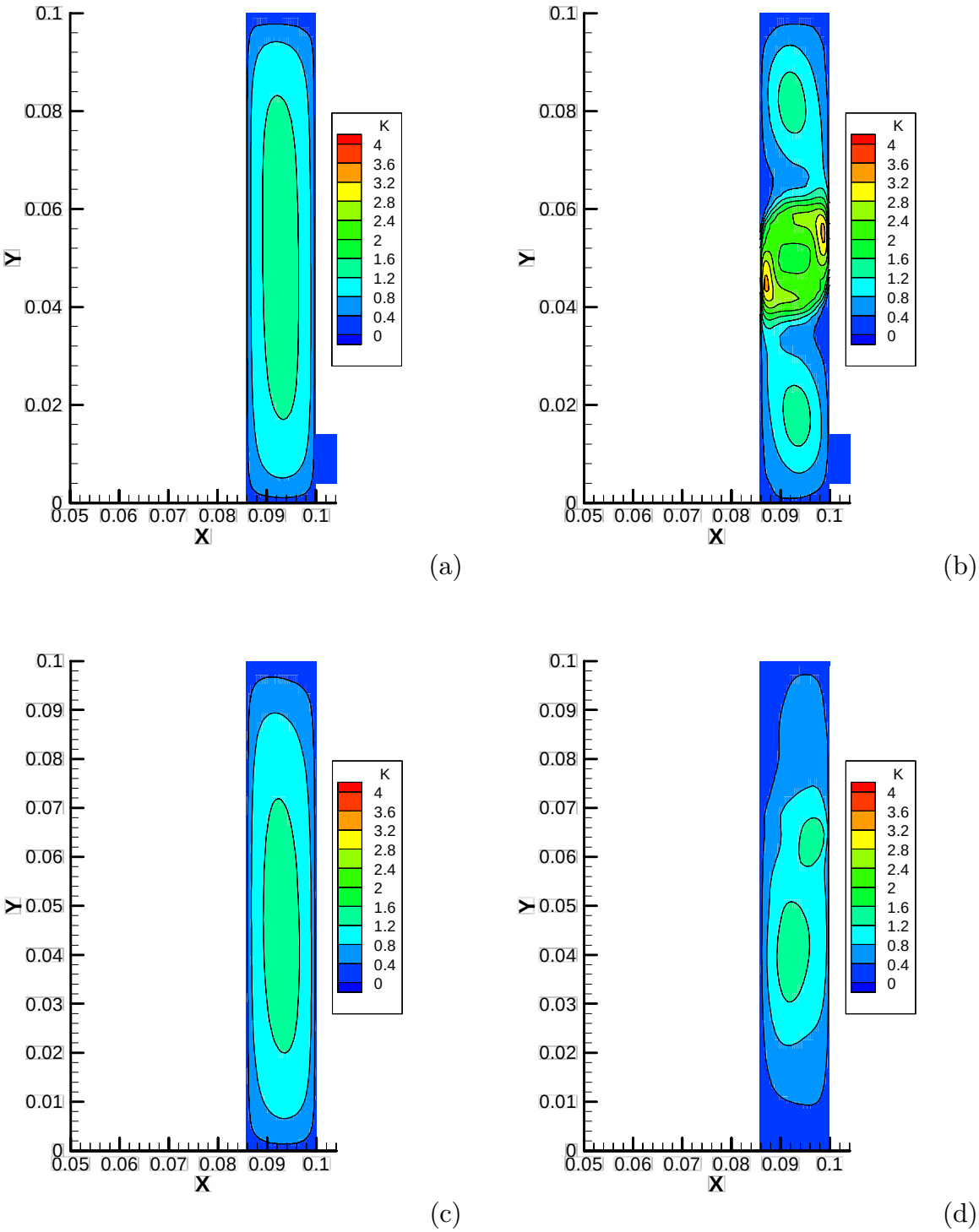

Figure 6.58: Turbulent kinetic energy, (k) in $Z = 50\,\text{mm}$ plane at 335 °CA. (a) – 2D k-ϵ simulation; (b) – 2D RSM simulation; (c) – 3D k-ϵ simulation; and (d) – 3D RSM simulation.

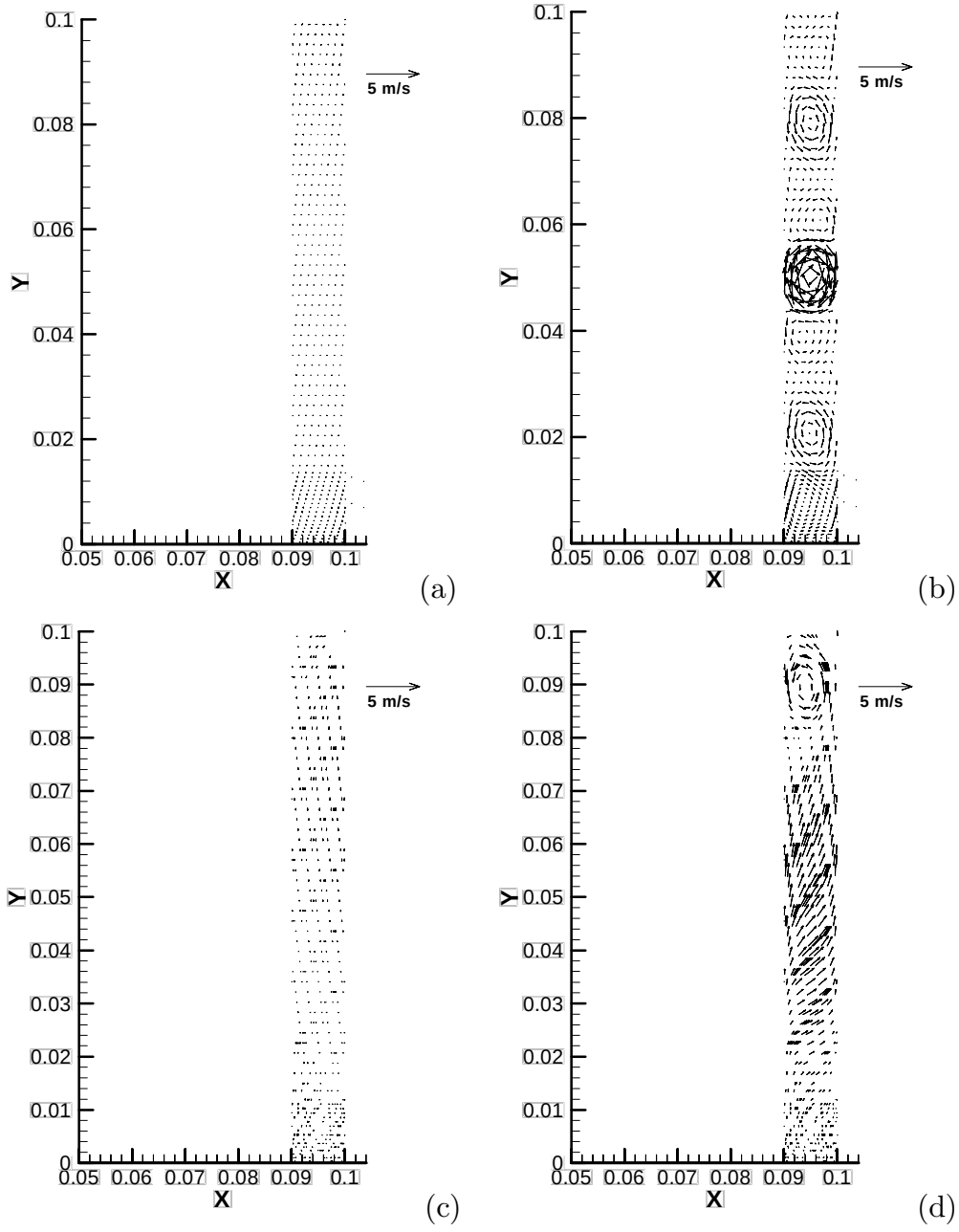

Figure 6.59: Velocity vectors in $Z = 50\,\text{mm}$ plane at TDC. (a) – 2D k-ϵ simulation; (b) – 2D RSM simulation; (c) – 3D k-ϵ simulation; and (d) – 3D RSM simulation.

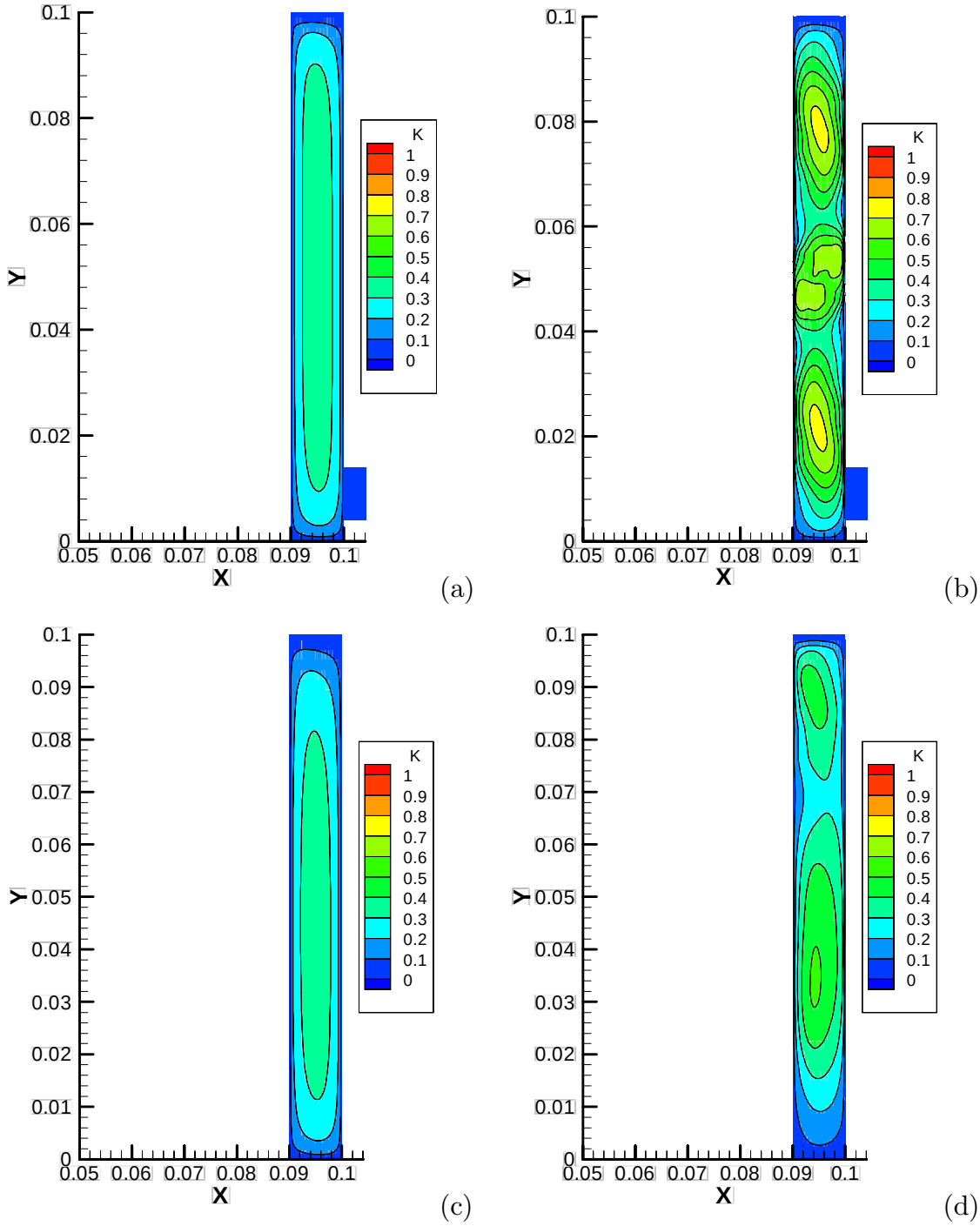

Figure 6.60: Turbulent kinetic energy, (k) in $Z = 50\,\text{mm}$ plane at TDC. (a) – 2D k-ϵ simulation; (b) – 2D RSM simulation; (c) – 3D k-ϵ simulation; and (d) – 3D RSM simulation.

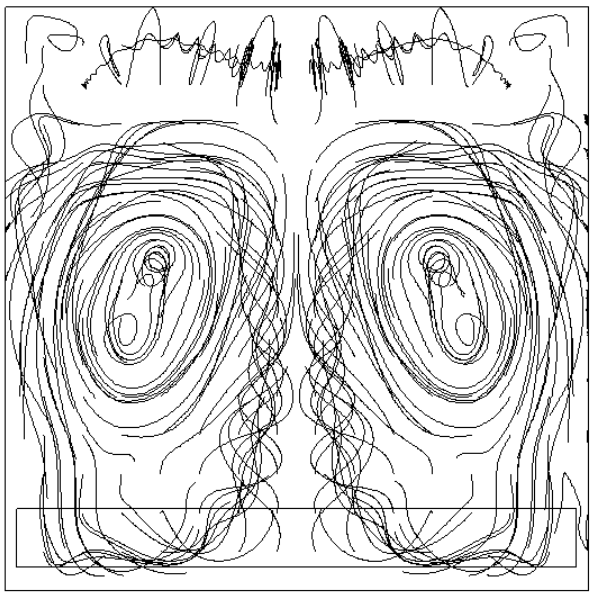

Figure 6.61: Instantaneous streamlines from the three-dimensional RSM simulation at TDC, viewed on the cross tumble plane.

at TDC are shown in figure 6.61. It confirms the three-dimensional structure of the flow, however the flow remains symmetrical about $Z = 50\,\text{mm}$. Two large vortices are visible on either side of the central symmetry plane, and numerous smaller vortices.

6.7.4 Averaged Parameters

The averaged turbulence, kinetic energy and tumble ratio results of the simulations are presented in figures 6.62, 6.63 and 6.64. Two sets of results are shown for each three-dimensional simulation; "full domain", in which the parameter is averaged over the entire domain of the cylinder; and "central plane only", in which the results are averaged only over the central plane ($Z = 50\,\text{mm}$). The $Z = 50\,\text{mm}$ plane is the plane for which Marc et al present their results in all their publications from the tumble plane [188, 187, 46, 189], and is the most direct comparison to the two-dimensional simulations.

Figure 6.62 shows that the turbulence in the k-ϵ model varies by a factor of about two between the two- and three-dimensional simulations at 300 °CA, and converges to similar values around 330 °CA. The RSM simulations are seen to show similar levels of turbulence between two- and three-dimensional models. The k-ϵ model predicts much higher levels of turbulence than the RSM model, varying from

a factor of about two during the intake stroke, up to a factor of about four during the compression stroke. The peak of turbulence occurs earlier in the k-ϵ simulation (300 °CA) than the RSM simulation (315 °CA), and this is the case for both two- and three-dimensional models.

Figure 6.63 shows the mass averaged velocity squared. All curves show a similar trend of a peak during the intake stroke, and decaying to a small value over the compression stroke. Physically, this means that the flow velocity (that is, the in-cylinder mean flow kinetic energy) is built up during the intake stroke, and dissipates to almost zero by the end of the compression stroke as the mean flow energy is converted to turbulent energy. The k-ϵ simulations decay to zero mean flow energy at about 315 °CA, significantly earlier than the RSM simulations who decay to near zero at TDC.

The most significant departure from this behaviour is the two-dimensional RSM model which predicts a second peak during the compression stroke. This second peak is associated with the tumble "spin up" and breakdown into turbulence, and is visible on the other models only as a kink in the decay curve. The peak seen in the compression stroke of the two-dimensional simulation is a result of the insufficient dissipation of mean flow energy in the two-dimensional RSM model, and was also seen as an over-estimate of the velocities predicted in section 6.7.3.

An interesting phenomenon is displayed by the three-dimensional RSM simulation (figure 6.63b). The "central plane only" results for this model are depicted as fluctuating significantly above and below the "full domain" results. This behaviour is typical of turbulent flows, with instantaneous point values fluctuating about an average value. Thus it appears that the three-dimensional RSM simulation predicts turbulent-like behaviour in the mean flow velocity (U, V and W) variables. This suggests that averaging the results over the full domain is behaving as an additional volume Reynolds averaging function. The significance of this second level of Reynolds averaging is not clear.

Figure 6.64 shows both three-dimensional models predicting similar tumble ratios during the simulation, with the two-dimensional models predicting more pronounced peaks cause by "tumble spin up" than any of the three-dimensional models. Again, the three-dimensional RSM central plane results appear the fluctuate around the full domain values.

It is interesting to note that the three-dimensional RSM simulation predicts a reversal of the tumble vortex just before TDC. This can be seen in the tumble ratio shown in figure 6.64b, where just before 360 °CA the central plane tumble ratio changes sign. The reversal is also seen with a smaller magnitude on the full domain

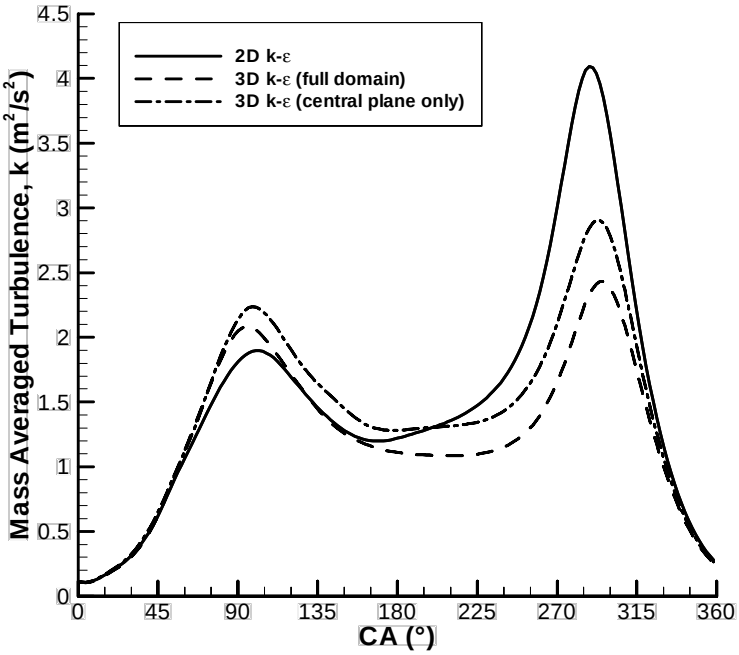

(a)

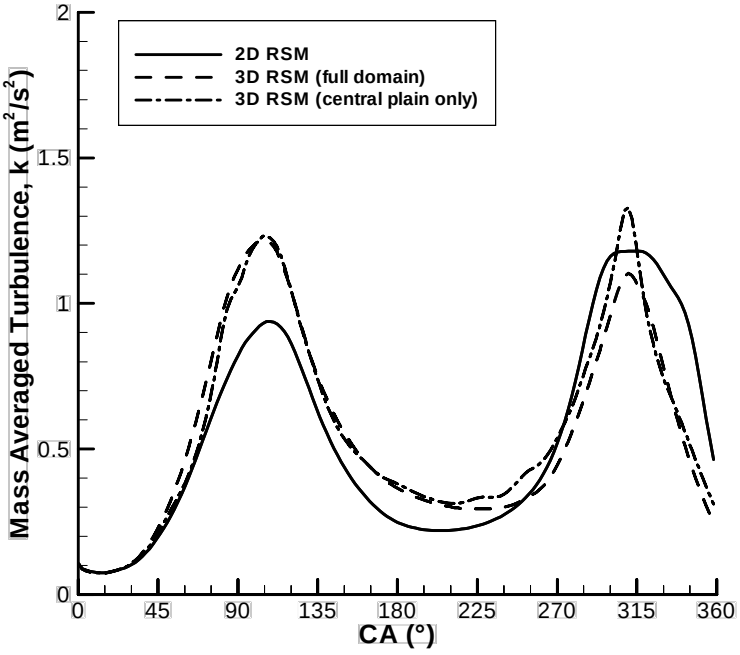

(b)

Figure 6.62: Mass averaged turbulence (k) for two- and three-dimensional $CR = 10$ CFD models. (a) – k-ϵ turbulence model; and (b) – RSM turbulence model.

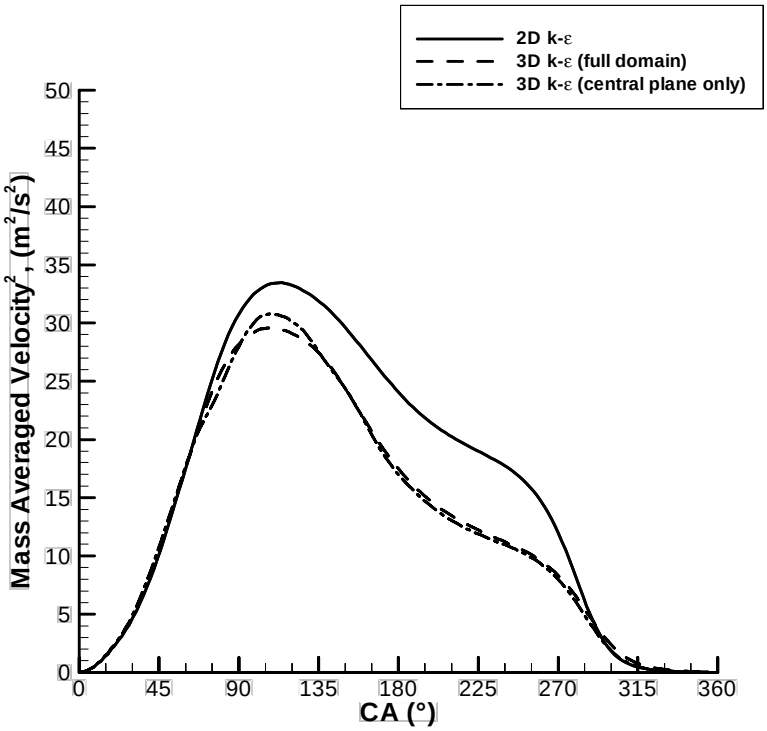

(a)

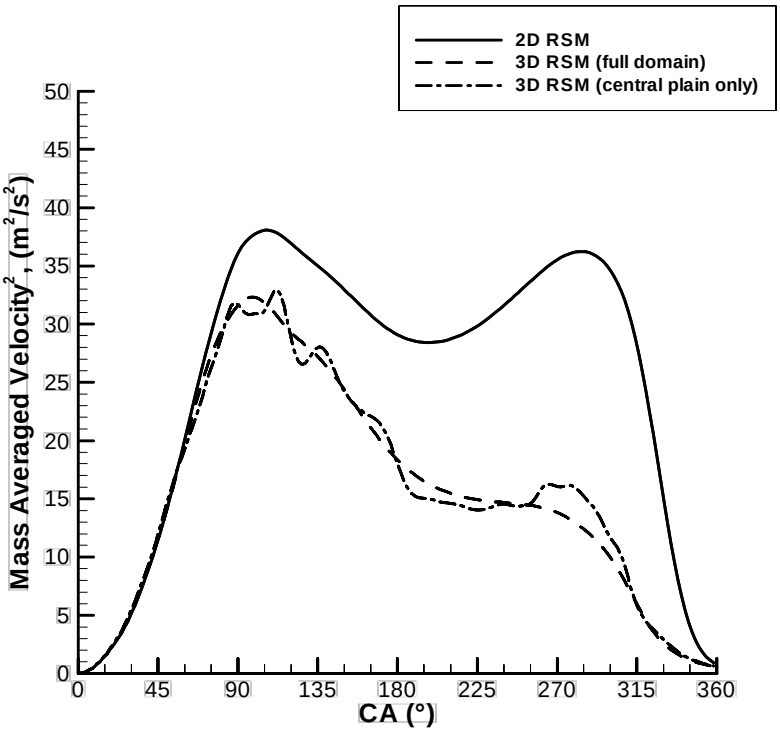

(b)

Figure 6.63: Mass averaged velocity squared for two- and three-dimensional $CR = 10$ CFD models. (a) – k-ϵ turbulence model; and (b) – RSM turbulence model.

and two-dimensional simulation results.

6.7.5 Conditions at Various Points

Marc [187] performed extensive Laser Doppler Anemometry (LDA) analysis of the $CR = 10$ model engine. The LDA results were based on averaging 500 samples, which he estimates to give an error of $\pm 0.1\,\mathrm{m\,s^{-1}}$ for the velocity components, and $\pm 10\%$ for the velocity fluctuations. Readings are reported for six points in the model, and were only recorded during the compression stroke. The CFD simulation was adapted to produce data at these points to allow a direct and objective assessment of the accuracy of the CFD simulation. The points at which Marc [187] took LDA measurements are defined in figure 6.65.

The results from point 15, shown in figure 6.66a and 6.66b, indicate that no model has accurately predicted the u or v velocity. Most notable is the three-dimensional RSM model predicting wildly fluctuating values of u velocity between 300 °CA and 330 °CA which is not seen experimentally at all, and the two-dimensional k-ϵ model overpredicted the v velocity by a factor of almost three.

The three-dimensional RSM predicted turbulent fluctuations in excellent agreement with experimental results, as seen in figures 6.66c and 6.66d. The two- and three-dimensional k-ϵ model appears to substantially over-predict turbulence between 180 °CA and 300 °CA, and predict the peak of turbulence to be earlier than was measured experimentally.

Point 55 is in the middle of the cylinder at BDC. The predictions in figure 6.67 at point 55 have poor agreement with the experimental data. No model predicted u, u' or v' well, however all models (with the possible exception of the two-dimensional RSM model) predicted the v velocity with reasonable accuracy. The main feature of the turbulence measured by the LDA, shown in figures 6.67c and 6.67d is the peak of turbulence at around 210 °CA. This peak was not captured by any simulation.

Figure 6.68, taken at point 12, shows the averaged velocity, v, is predicted well by the three-dimensional k-ϵ model, but the two-dimensional k-ϵ simulation and both RSM simulations show some discrepancy. The two-dimensional RSM model, and to a lesser extent the three-dimensional RSM model predicted u' reasonably well. No model predicted the v' at this point accurately, with the peak measured at 210 °CA not being predicted by any model.

The results at point 12 (figure 6.68), show that the experimental results have significant anisotropy in the turbulence. This is shown by the u' and v' turbulence intensities differing, for instance u' in figure 6.68b at 270 °CA is around $0.4\,\mathrm{m\,s^{-1}}$,

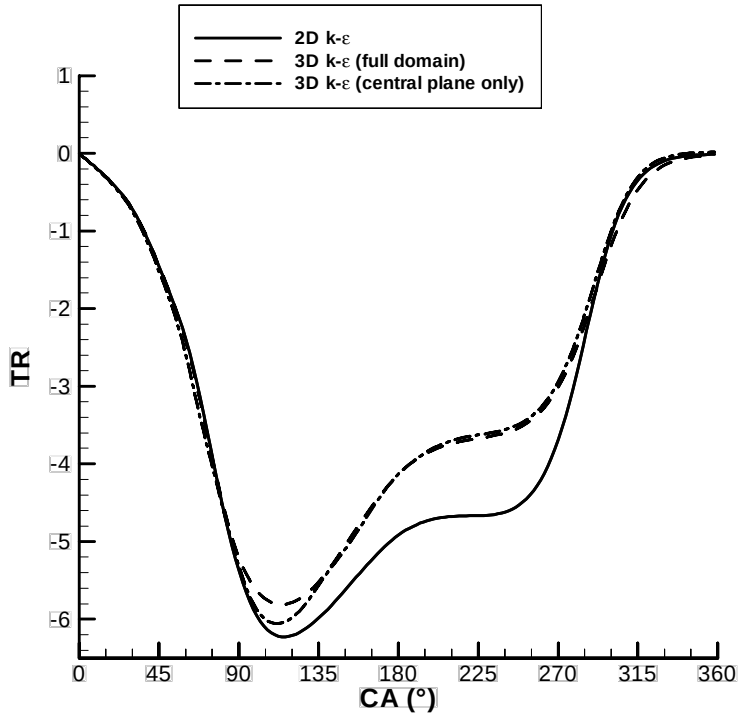

(a)

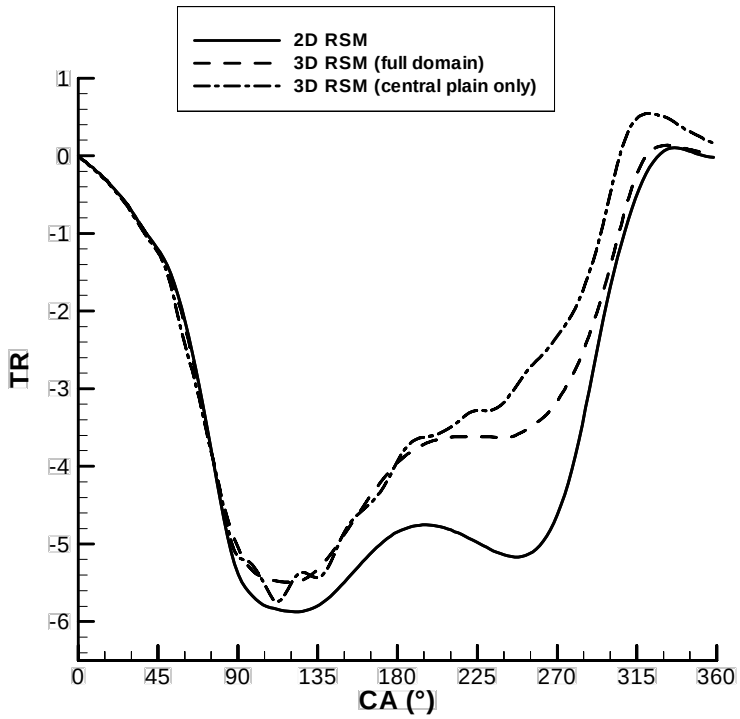

(b)

Figure 6.64: Tumble ratio for two- and three-dimensional $CR = 10$ CFD models in the square piston engine. (a) – k-ϵ turbulence model; and (b) – RSM turbulence model.

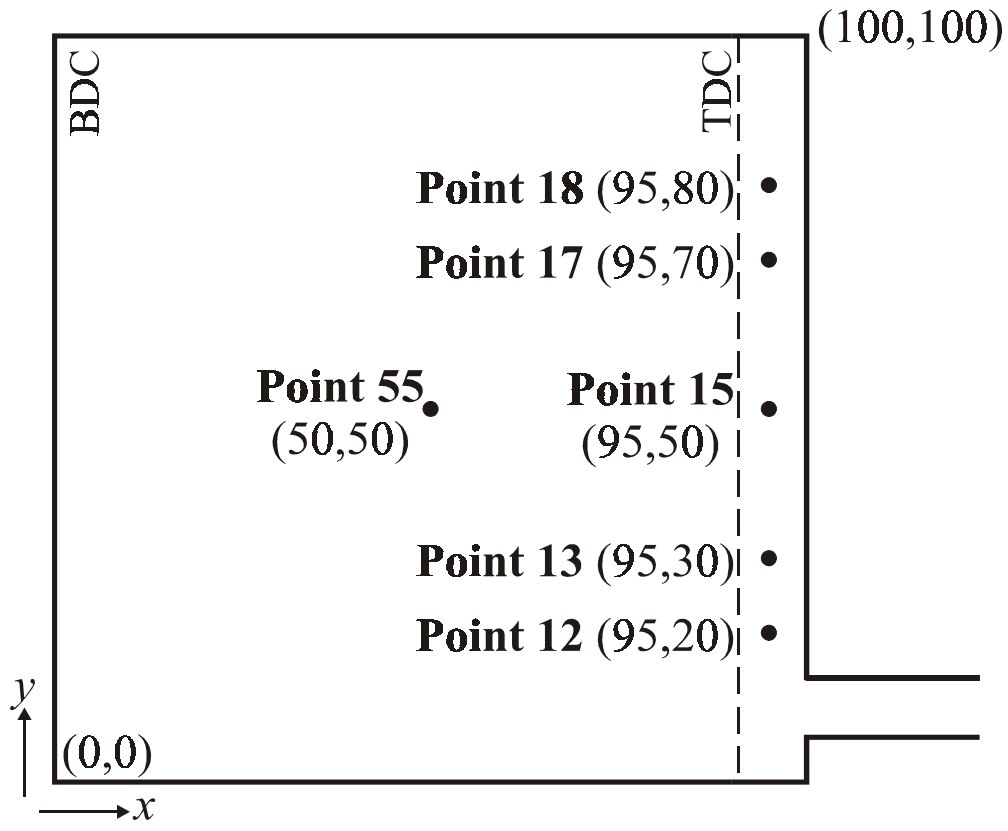

Figure 6.65: The definition of the LDA points analysed, from Marc [187].

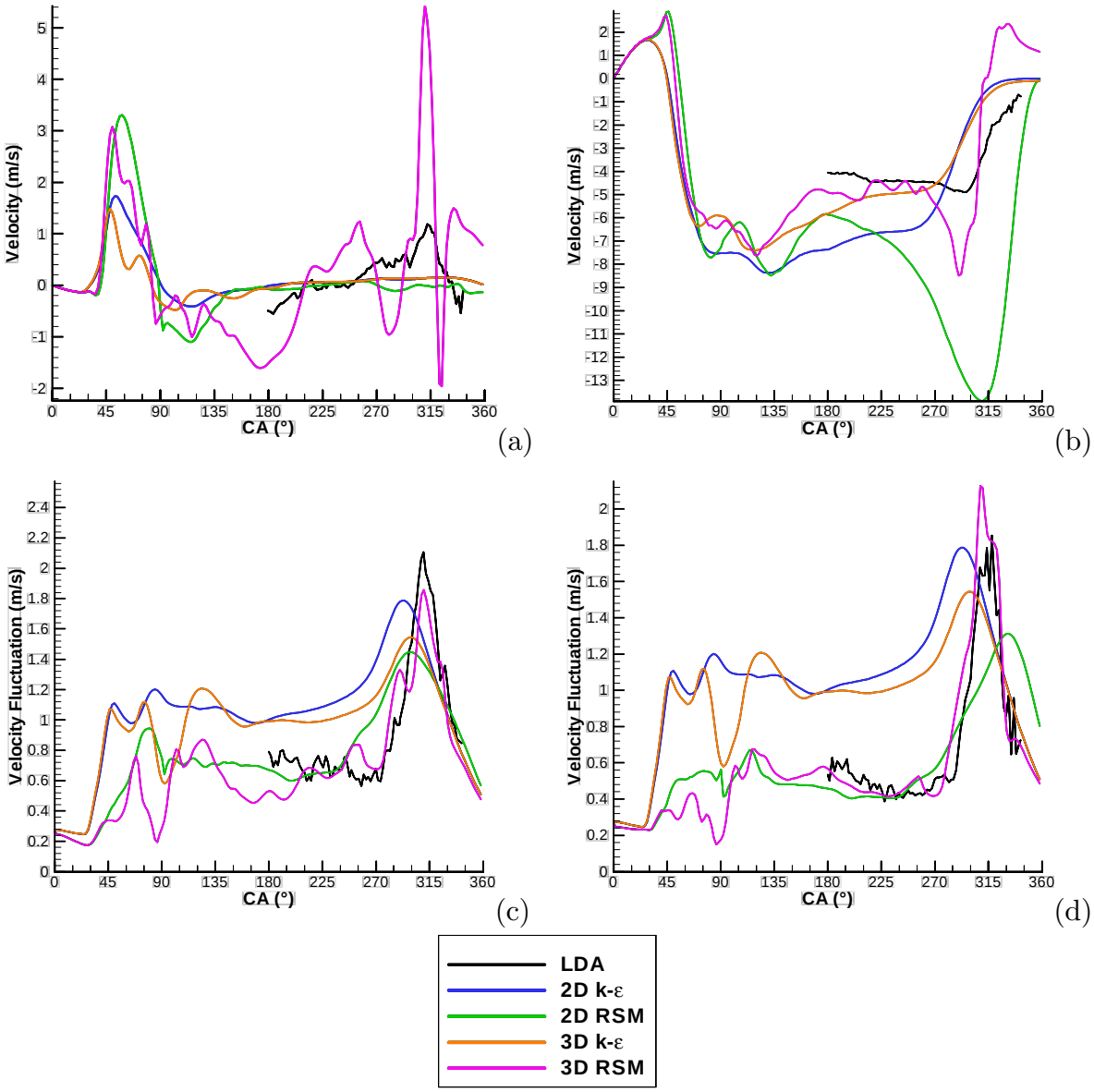

Figure 6.66: Comparison of LDA and CFD results at point 15 ($X = 95\,\text{mm}$, $Y = 50\,\text{mm}$). LDA data from Marc [187]. (a) – u velocity; (b) – v velocity; (c) – u' turbulent velocity fluctuation; and (d) – v' turbulent velocity fluctuation.

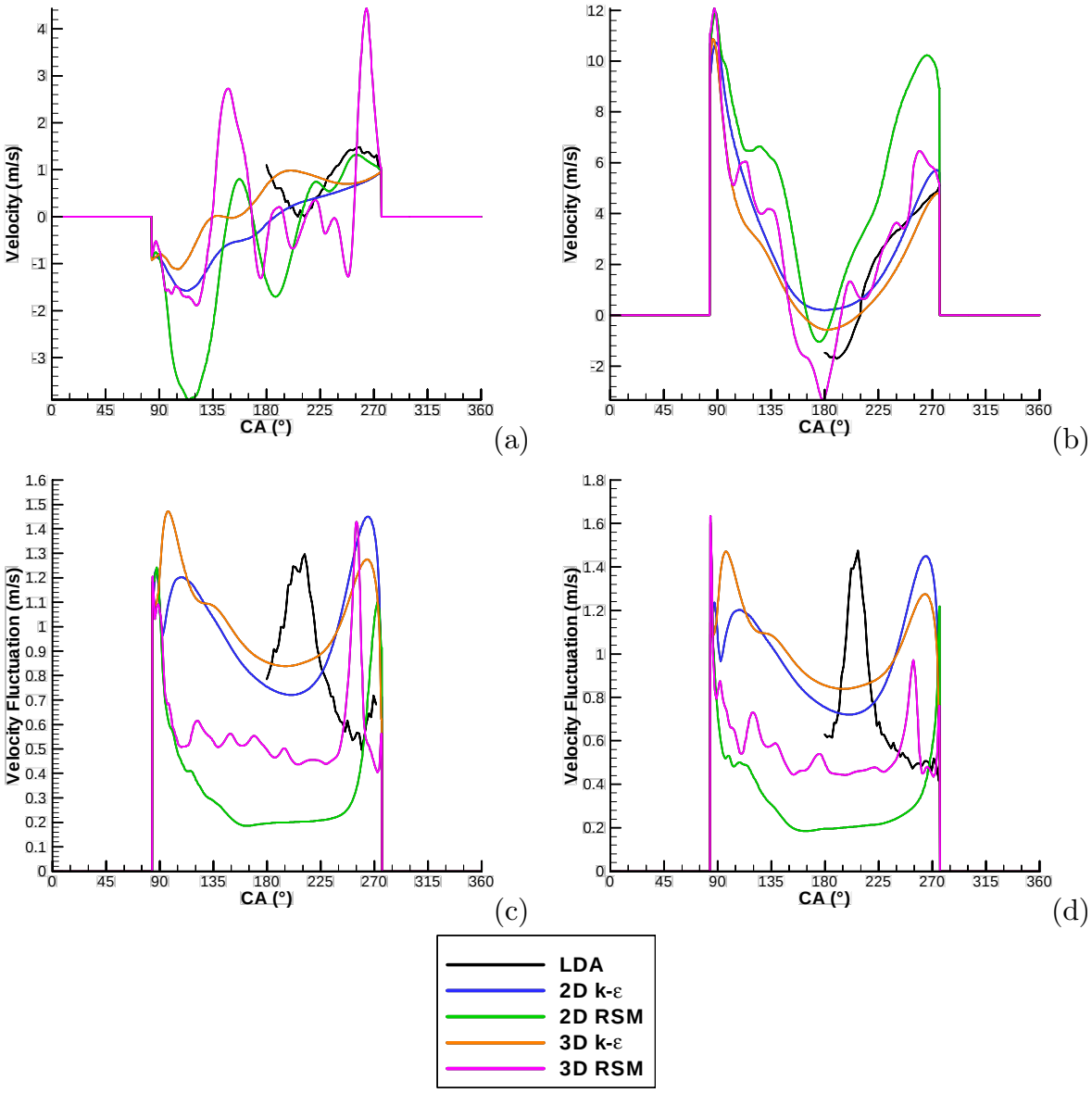

Figure 6.67: Comparison of LDA and CFD results at point 55 ($X = 50\,\text{mm}$, $Y = 50\,\text{mm}$). LDA data from Marc [187]. (a) – u velocity; (b) – v velocity; (c) – u' turbulent velocity fluctuation; and (d) – v' turbulent velocity fluctuation.

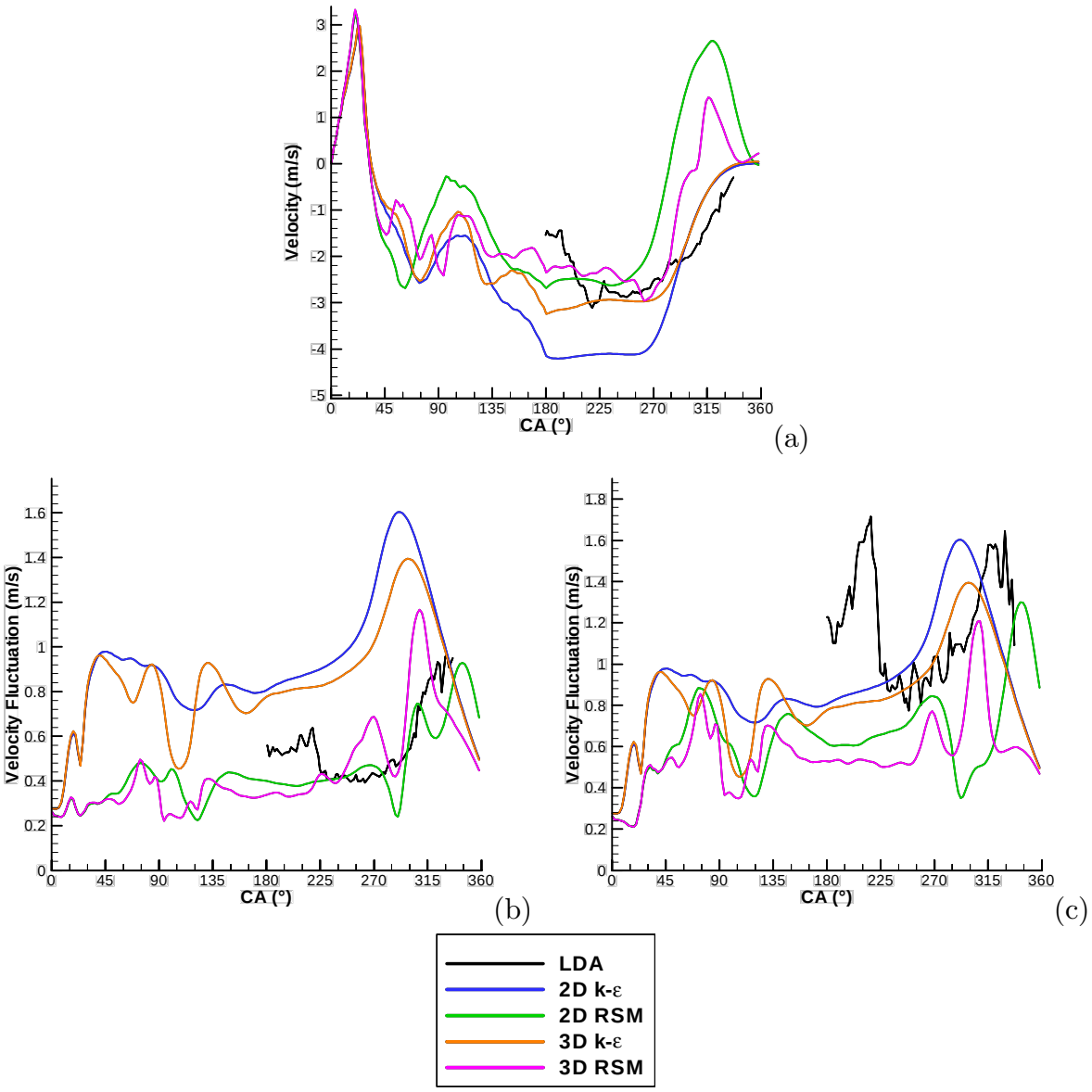

Figure 6.68: Comparison of LDA and CFD results at point 12 ($X = 95\,\text{mm}$, $Y = 20\,\text{mm}$). LDA data from Marc [187]. (a) – v velocity; (b) – u' turbulent velocity fluctuation; and (c) – v' turbulent velocity fluctuation.

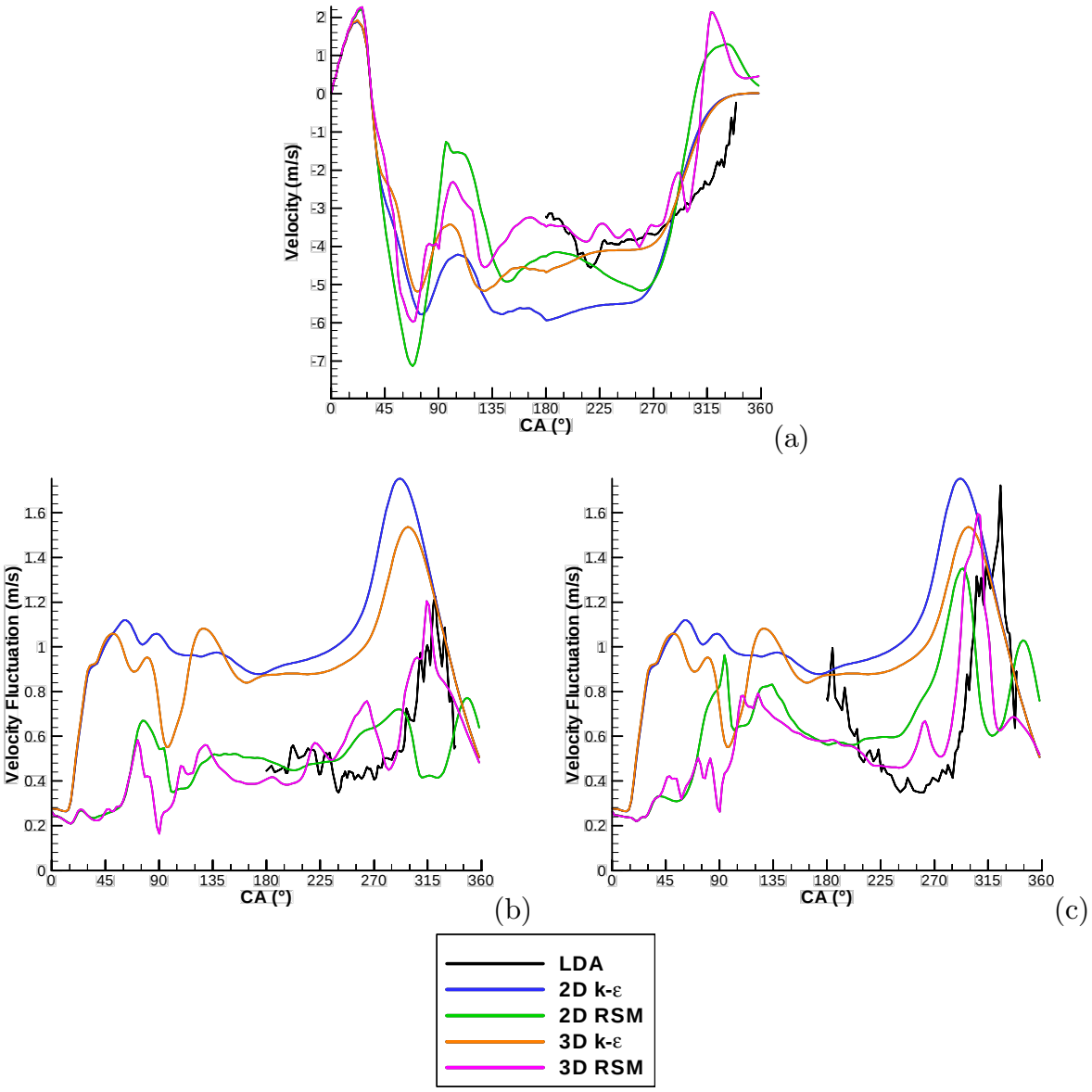

Figure 6.69: Comparison of LDA and CFD results at point 13 ($X = 95\,\text{mm}$, $Y = 30\,\text{mm}$). LDA data from Marc [187]. (a) – v velocity; (b) – u' turbulent velocity fluctuation; and (c) – v' turbulent velocity fluctuation.

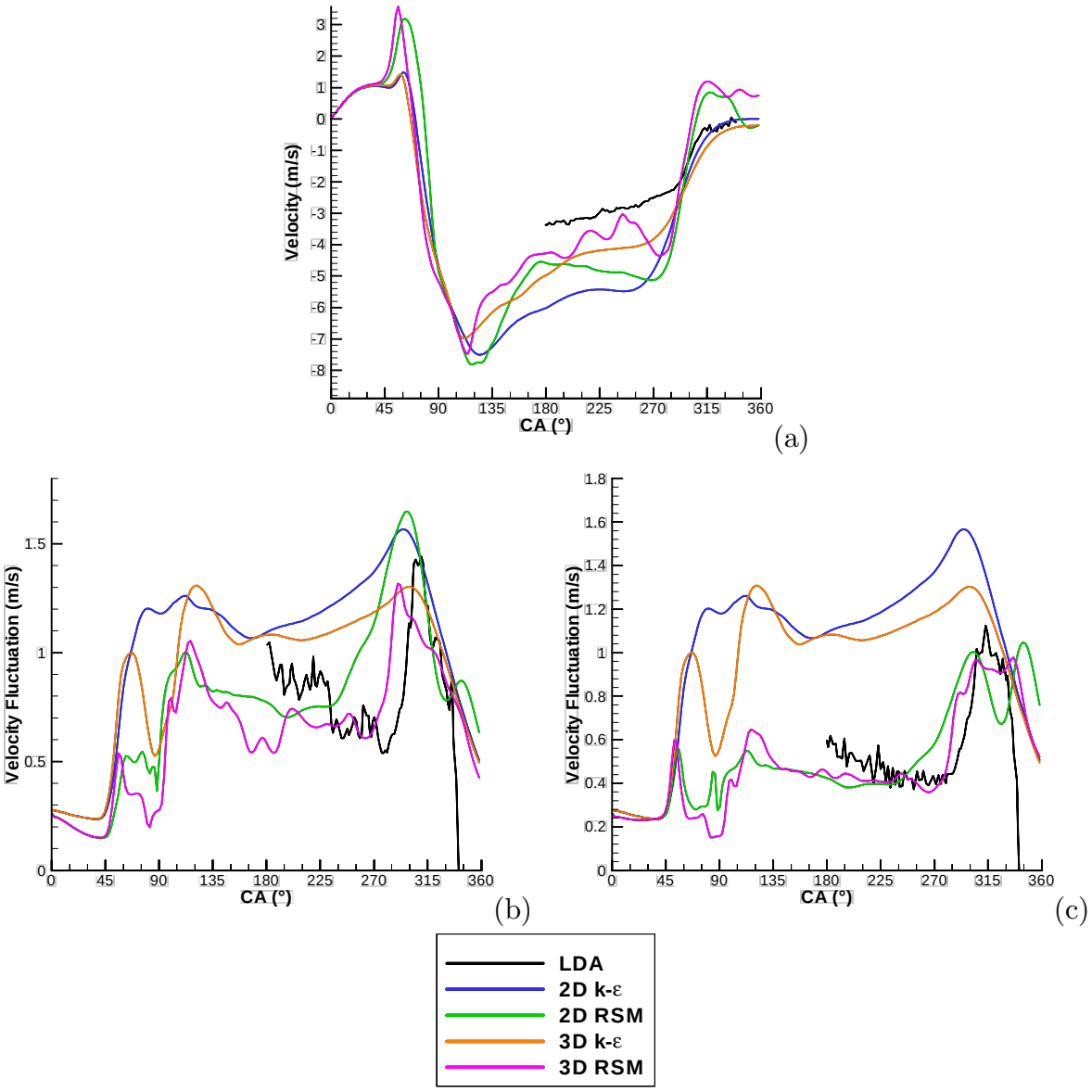

Figure 6.70: Comparison of LDA and CFD results at point 17 ($X = 95\,\text{mm}$, $Y = 70\,\text{mm}$). LDA data from Marc [187]. (a) – v velocity; (b) – u' turbulent velocity fluctuation; and (c) – v' turbulent velocity fluctuation.

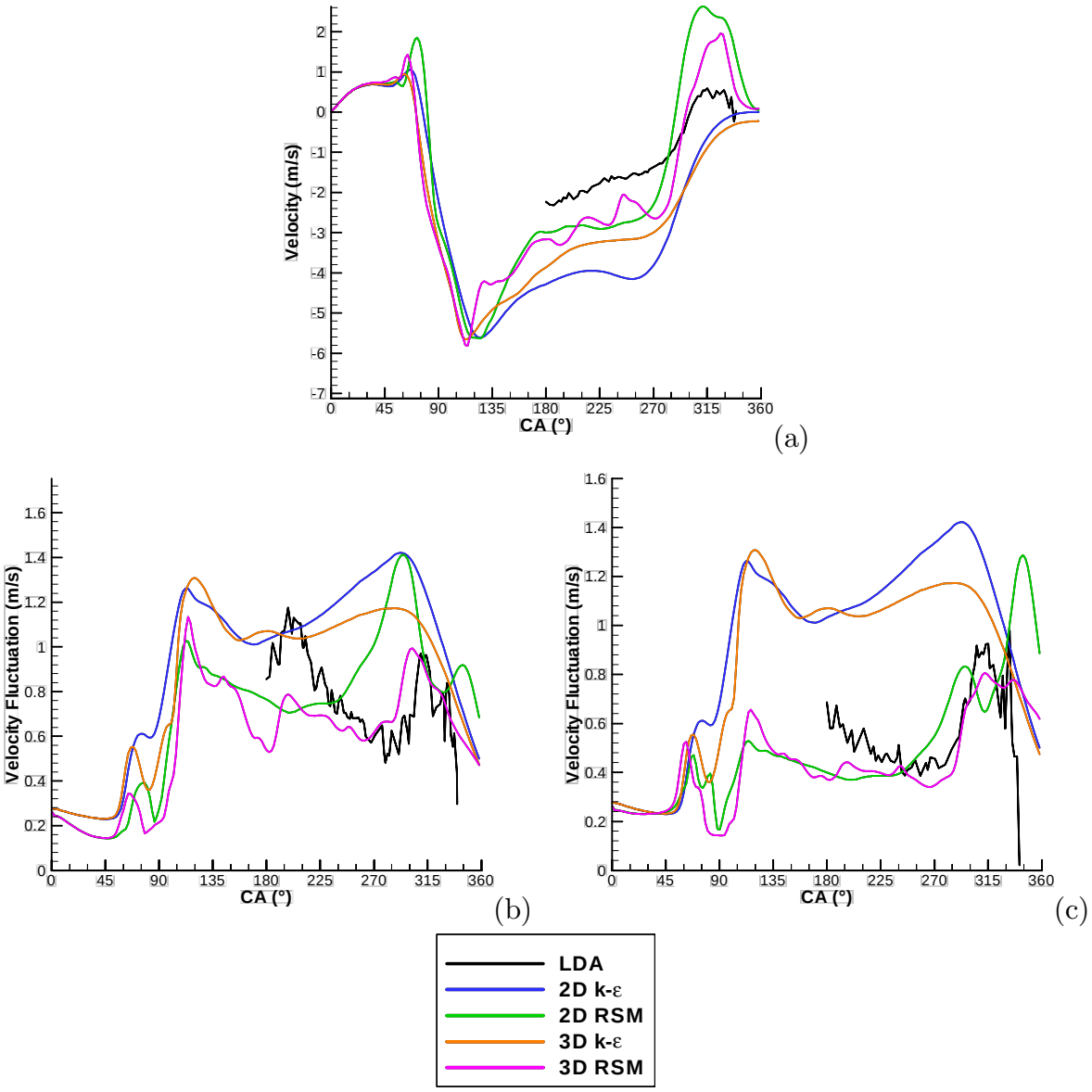

Figure 6.71: Comparison of LDA and CFD results at point 18 ($X = 95\,\text{mm}$, $Y = 80\,\text{mm}$). LDA data from Marc [187]. (a) – v velocity; (c) – u' turbulent velocity fluctuation; and (d) – v' turbulent velocity fluctuation.

yet the v' turbulence in figure 6.68c is around $1.0\,\mathrm{m\,s^{-1}}$. This obviously poses a problem for the k-ϵ turbulence model, as it assumes the turbulence is isotropic. Consequently, the v' turbulence level is simulated by the k-ϵ model to be in approximately agreement with the experimental results (with the compression stroke turbulence peak occurring around 40 °CA too early, however), but the u' turbulence level is over-estimated by a factor of around two.

Figure 6.69, taken at point 13, shows the averaged velocity, v, to be generally predicted by most simulations, however significant deviations are seen. No simulation predicted v accurately. Both the u' and v' turbulence was predicted with excellent accuracy by the three-dimensional RSM model, but the k-ϵ simulation achieves poor accuracy, over-predicting u' by a factor of about two up to 315 °CA.

At point 17, shown in figure 6.70, all models predicted the experimental results reasonably well, with the three-dimensional models being marginally more accurate. All models predicted the turbulence reasonably well, however the best agreement was the three-dimensional RSM model which yielded excellent agreement to experimental results. Again, the k-ϵ simulation significantly over-predicts the turbulence levels of both u' and v'.

Point 18, shown in figure 6.71, shows that all models predicted the mean velocity, v, poorly. The two RSM simulations correctly predicted the sign change of v at 300 °CA, however all simulations significantly over-predicted the magnitude of the velocities. The three-dimensional RSM model predicted the turbulence parameters (u' and v') with excellent agreement between numerical and experimental results, and again, the k-ϵ simulations greatly over-predicted the turbulence before 315 °CA.

Overall, the accuracy of the three-dimensional RSM model appears to be quite good as it produced excellent agreement to experimental results for the magnitude of the turbulent fluctuations for four of the six points. Both of the k-ϵ simulations substantially over-predicted the turbulence levels present until 315 °CA. All models predicted the mean velocities with only reasonable accuracy.

6.8 Discussion

The square cylinder model engine developed by Marc et al [46, 187, 188, 189] was modelled using RSM and k-ϵ turbulence models in both two- and three-dimensions. The simulated results were compared to the PIV, LDV and LDA results of Marc [187] and Maurel et al [189].

Overall, the three-dimensional RSM simulation is in best agreement with the experimental results. It managed to predict the turbulence intensities at a num-

ber of points in the domain with excellent accuracy, and successfully captured the fundamental process of tumble vortex breakdown occurring during the compression stroke. This is to be expected, as it is known that tumble vortex breakdown is a complex three-dimensional process; involving anisotropic turbulence, separations in adverse pressure gradients, strongly curved streamlines and adverse pressure gradients. The Reynolds stress turbulence model is known to be superior to k-ϵ models in simulating these flow features [298].

The two-dimensional RSM model was also reasonably accurate, and captured the tumble breakdown process in good agreement with the experimental results. It predicted the turbulence intensities less accurately. Even though it correctly modelled the tumble breakdown process, it significantly overestimated the vortex strengths. This is probably due to a two-dimensional model's reduced ability to dissipate energy as it cannot generate flows in the third dimension.

The two-dimensional and three-dimensional k-ϵ models predicted the intake flow reasonably successfully, and predicted turbulence intensities at various points in the flow with only moderate accuracy. The main feature apparent with this model is its complete failure to model the tumble compression breakdown process.

The failure of the k-ϵ model to predict the breakdown process may be caused by its well known deficiencies in modelling separations, strongly curved streamlines and adverse pressure gradients [298], and the assumption of isotropic turbulence used in its derivation. Many researchers report the in-cylinder flow to be essentially isotropic [137], and the results of RSM simulations presented confirm that the bulk of the flow is isotropic. However, it appears there are small, but very important, regions of anisotropic turbulence close to the walls. The failure to resolve the anisotropic turbulence in these regions may be the cause of the inability of the k-ϵ turbulence model to simulate the breakdown process.

It should also be noted that the results predicted here by the k-ϵ model are qualitatively very similar other k-ϵ simulations of engine flows, for example the results presented by Khalighi [159], shown in figure 6.3. In both the current k-ϵ simulation and Khalighi's, the tumble vortex is shown to weaken and move off-centre during the final stages of the compression stroke, but remain as a single vortex with no break-up. Khalighi's results shows the TDC flow to have two weak vortices at either end of the cylinder. However, the flow at TDC essentially stops; just as the k-ϵ turbulence model predicts in the current work. As the k-ϵ predictions presented in this work have been shown to fail to predict the tumble breakdown process, this raises doubts about the accuracy of the results presented by Khalighi. The work of Khalighi is typical of many numerical studies of compression stroke

	300 °CA	%	330 °CA	%	360 °CA	%
Two-dimensional k-ϵ	3.583	237	1.166	57	0.280	10
Two-dimensional RSM	1.159	9	1.099	48	0.467	50
Three-dimensional k-ϵ	2.788	162	1.076	44	0.265	15
Three-dimensional RSM	1.064	0	0.745	0	0.312	0

Table 6.8: Comparison of mass averaged turbulence, (k), for various simulations at the end of the compression stroke. The percent variation from the three-dimensional RSM simulation is also shown.

flow, so the validity of the flow fields predicted in many of these k-ϵ turbulence model simulations during the compression stroke are likely to be significantly in error.

Despite the failure of the k-ϵ turbulence model to predict the tumble break-down process, the levels of turbulence predicted as the simulation approached TDC was quite similar between all models. This was shown in figure 6.62, and is summarised in table 6.8. The three-dimensional RSM simulation has been used as the basis of the calculation of variations, as it appears to be the most accurate simulation.

The variations seen at 300 °CA are quite large, with the k-ϵ model predicting around three times the turbulence level of the RSM simulations. However, as the compression stroke proceeds, all simulations start to converge to similar values. At 330 °CA, the variations have reduced to below 60% of the three-dimensional RSM result. At TDC, 360 °CA, the three-dimensional k-ϵ and RSM give the same result within 15%, and the two-dimensional k-ϵ simulation agrees within 10%. This suggests that even though the k-ϵ turbulence model has been shown to be unable to predict the mechanism of the tumble breakdown process, it can still predict the turbulence levels near the end of the compression stroke with moderate accuracy.

Unfortunately, using the RSM turbulence model in simulations of the BRV engine was unsuccessful due to the extra seven equations to be solved, and the numerical stiffness of the turbulence model equations. The RSM model is difficult to use in complicated geometries, and the model never converged in the heavily distorted grids required for the BRV engine, described in chapter 7. Thus the k-ϵ model was the only turbulence model used for the modelling of the BRV engine, as it is the best model available. It has been shown here that the k-ϵ model fails to predict the tumble breakdown process during the compression stroke of an engine, however it does predict the turbulence existing at the end of the compression stroke with moderate accuracy. The turbulence existing at the end of the compression stroke is the critical parameter for determining engine performance, so the k-ϵ model is cautiously justified for IC engine simulations providing its shortcomings are acknowledged.

The simulations of the BRV engine are discussed in chapters 7 and 8.

6.9 LES Model

Because of the simple geometry and the low engine speed, the square cylinder engine is an ideal subject for a large eddy simulation (LES) study. A simple LES model was developed as an introductory investigation into this type of simulation. As has been mentioned in section 4.5.4, LES models with an explicit sub-grid model solve the filtered Navier Stokes equations rather than the Reynolds averaged equations. This means existing Reynolds averaged simulation models are not suitable for LES simulations, and a new solver is required. However, to make the development of this model practical within the scope of the current work, the LES model was implemented as an extension to the existing solution technique.

6.9.1 Model Description

The purpose of a sub-grid model in LES is to dissipate the energy cascading to the smaller turbulent scales from the larger scales. This dissipation is modelled as an increase in the local viscosity [298].

As discussed in section 3.2.5, a characteristic of upwinding discretisation schemes in finite volume simulations is that they tend to cause "numerical dissipation", or an additional non-physical viscosity caused by the numerical solution technique, and not part of the physical model [237].

The effect of numerical dissipation is similar to a sub-grid model in LES. This suggests the interesting idea that the numerical dissipation in an upwinding finite volume simulation could be used to represent the dissipation of the small turbulent scales, rather than using an explicit sub-grid model. Although this appears to be a very crude formulation, Haworth [128] makes the following points about what he calls "model-less" LES:

- numerical inaccuracy provides a subgrid scale model that is at least as reliable as any explicit model;
- the numerical dissipation of the low-order numerical methods generally used in engineering CFD dominates the modeled subgrid scale stresses; and
- numerical inaccuracy behaves in a manner that is qualitatively similar to an explicit subgrid stress model.

Although this type of model has not been as widely used as the normal sub-grid turbulence model LES, a number of researchers report successful simulations. "Model-less" LES has been legitimised and justified by Boris et al [51], Oran and Boris [215], Spalart [259], Mankbadi [186] and Fureby and Grinstein [104]. It has been used in a LES model of flow over a cylinder by Mittal and Moin [193] and Tsuboi et al [278]. Naitoh et al [202] applied it to a simple engine geometry, and successfully modelled the breakdown of a small number of large vortices into a large number of small vortices. Naitoh et al [198] used a similar LES model on a four valve pentroof and two valve hemispherical combustion chamber, and achieved reasonable agreement with experimental results in predicting the intake stroke flow.

The fundamental limitation of model-less LES is in dealing with the wall regions [259]. The only way this type of sub-grid model can accurately deal with wall regions is by approaching DNS in the boundary layer. This is not possible with current resources. This restriction has been avoided by some researchers by modelling flows without walls, such as the free shear layer modelled by Fureby and Grinstein [104].

In the present work a model-less LES simulation was performed on the square piston engine. The laminar, or non-averaged Navier Stokes equations were solved, using the second order Van Leer differencing scheme to provide the dissipation in the momentum and energy equations. Only three-dimensional simulations were performed with this technique since LES is inherently three-dimensional.

It is included in the current work only as a preliminary study of the application of LES models to an engine geometry to establish whether future work is warranted.

There is no special treatment of the wall regions, the unfiltered Navier Stokes equations were integrated directly to the walls. This is likely to be a fundamental inaccuracy in the model [259], however the preliminary nature of the work makes this simplification acceptable. The development of an accurate wall treatment is beyond the scope of the current work.

A breakdown of the entire LES modelled flow field into mean and turbulent components has not been performed since this requires the storage of many complete flow fields, which requires a prohibitively large amount computer memory. Hence, the only comparison to the turbulence measured in the experimental results will be from data taken at a few selected points in the cylinder, presented in section 6.9.6, and only based on results from a single stroke of the engine.

LES modelling requires a significant number of simulations to be performed to establish a statistical trend (see section 4.5.4), as individual simulations can be effected by cycle to cycle variations. This has not been performed here due to insufficient computing resources, so the LES results presented here are only from a

single simulation. This means the LES results presented here must be viewed with some caution, as no attempt the remove these effects has been performed. However, as this study is only a preliminary investigation, this is acceptable.

6.9.2 Turbulent Length Scales

A fundamental issue regarding the application of LES simulation to engine simulation is adequate grid resolution to resolve the turbulent vortices. A true LES study requires a filter width of the integral length scale or finer to resolve the turbulent fluctuations. This leaves the unresolved motions as nearly isotropic. It is possible to estimate the turbulence length scale present from the turbulence parameters predicted by a Reynolds averaged Navier Stokes simulation, using the k-ϵ or RSM turbulence models. This will be performed based on the simulations presented in sections 6.6 and 6.7.

The integral length scale, l, is defined as a length scale typical of the larger eddies. It is a guide as to the size of the largest eddies which can be considered turbulent. In the k-ϵ turbulence model it is assumed that the length scale can be given by

$$l = \frac{C_\mu k^{3/2}}{\epsilon}, \tag{6.5}$$

and this can be calculated for both the k-ϵ and RSM simulations. Length scale has been calculated at TDC of the $CR = 4$ simulations, and the results are shown in figure 6.72. This relationship is not strictly applicable to RSM simulations, however it can be used as a reasonable measure of the turbulent length scale.

The k-ϵ model predicts the length scale of the turbulence to be of the order of 3 mm at TDC in figure 6.72a, and the RSM model predicts the length scale to be around 1.2 mm at TDC in figure 6.72b.

The size of the elements for the $63 \times 45 \times 44$ grid in the $CR = 4$ simulation at TDC is 2.2 mm in the Z direction, 1.9 mm in the Y direction, and 0.4 mm in the X direction. If the length scale of the turbulence in the central section of the domain is around 3 mm to 1.2 mm (as predicted by the Reynolds averaged simulations), this indicates the simulations presented here are approaching the integral length scale of the turbulence. This means the LES model presented in this work is likely to resolve the larger turbulent scales.

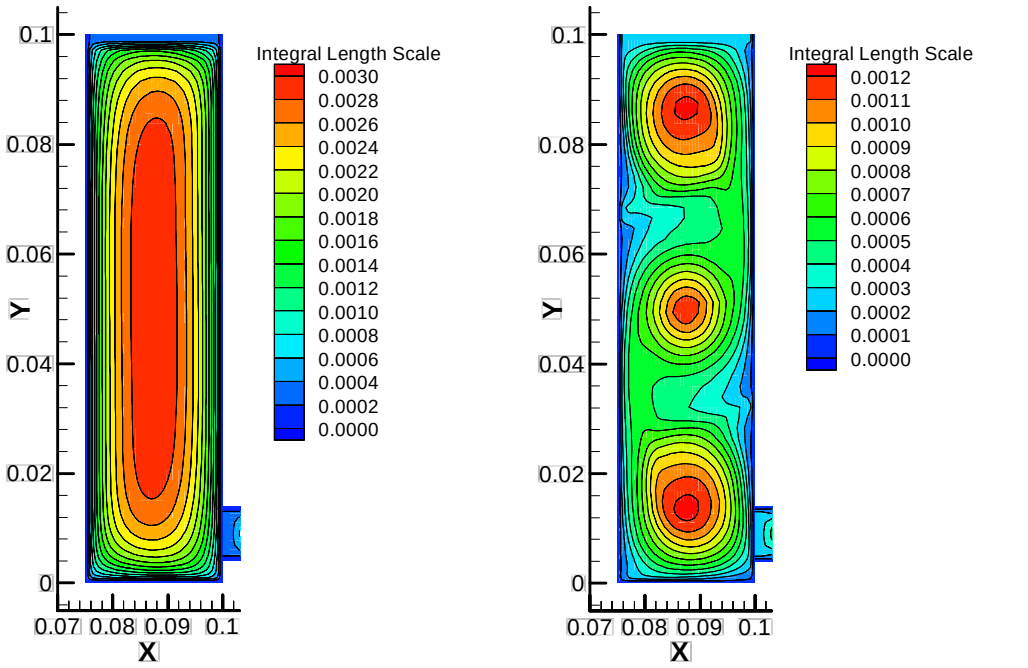

Figure 6.72: Integral length scale, in metres, at TDC for the $CR = 4$ simulation, 84×60 grid. (a) – k-ϵ simulation; and (b) – RSM simulation.

Simulation	**LES** Time, (hours)
$CR = 4$, $63 \times 45 \times 44$	196.2
$CR = 10$, $63 \times 45 \times 44$	207.2

Table 6.9: CPU time for LES simulations.

6.9.3 Computation Time

Due to the long computational time involved in LES simulations, only two LES models were performed. One simulation was performed using $CR = 4$ to match the conditions of Maurel et al [189], and the second simulation used $CR = 10$ to match the conditions of Marc [187]. The computation times required for both of these simulations is listed in table 6.9, and can be compared to the Reynolds averaged simulations in table 6.4. As the mathematical model in the LES model is simpler than the Reynolds averaged model presented in sections 6.6 and 6.7, the computation time for the LES simulations is reduced. For example, the $CR = 4$ LES simulation was 10% faster than the three-dimensional k-ϵ simulation, and 40% faster then the three-dimensional RSM simulation, shown in table 6.2.

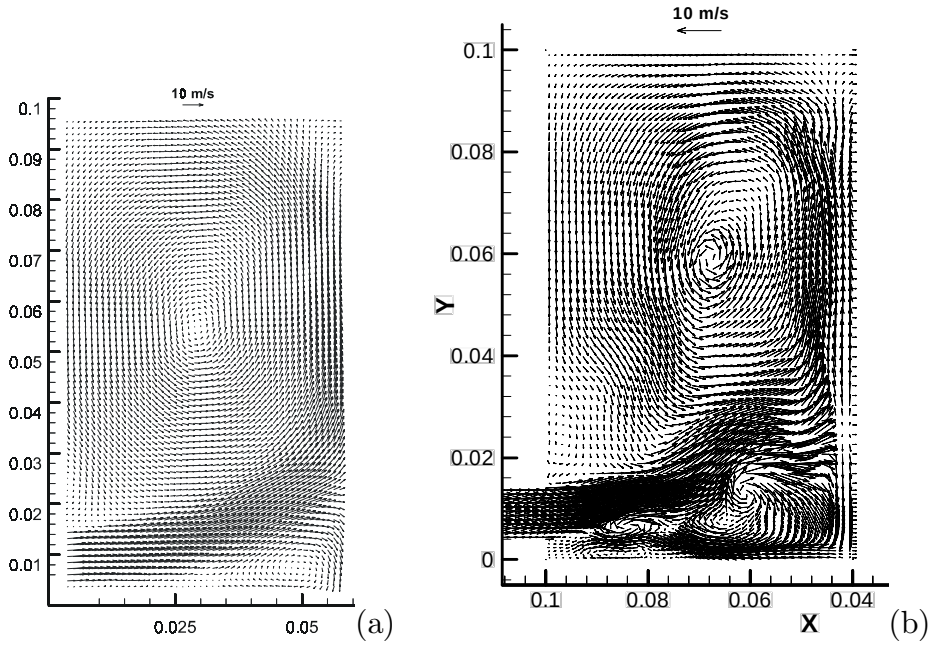

Figure 6.73: Comparison of velocity vectors from experimental results and numerical simulation for model with $CR = 4$, 206 rpm at 86 °CA. a) – Ensemble averaged turbulent kinetic energy and velocity vectors from PIV experiments of Maurel et al [189]; and (b) – 3D LES simulation.

6.9.4 $CR = 4$ Results

The $CR = 4$ results was compared to the PIV results of Maurel et al [189], and are shown in figure 6.73 for 86 °CA, and figure 6.74 for BDC. These figures can be compared to the Reynolds averaged simulations shown in figures 6.19 and 6.21.

At 86 °CA, the LES simulation has correctly predicted the formation of the large tumble vortex, however many small vortices and other structures not seen on the PIV data appear. This is also seen in the results at BDC, where the large tumble vortex is seen, but the PIV results show few small structures, whereas the LES simulation predicts many small vortices and other small perturbations.

These small vortices and perturbations are likely to have turbulent properties, and so would need to be averaged with a number of simulations to obtain a statistically significant average flow. This would make the LES results directly comparable to the PIV data. As this has not been performed at this stage no conclusions about accuracy can be reached.

Despite no averaging process being applied, the location of the centre of the tumble vortex is predicted with reasonable accuracy. This is shown for 86 °CA in table 6.10 and for BDC in table 6.11. This accuracy (4 mm at 86 °CA, 18 mm at BDC) is comparable to that of the Reynolds averaged simulations.

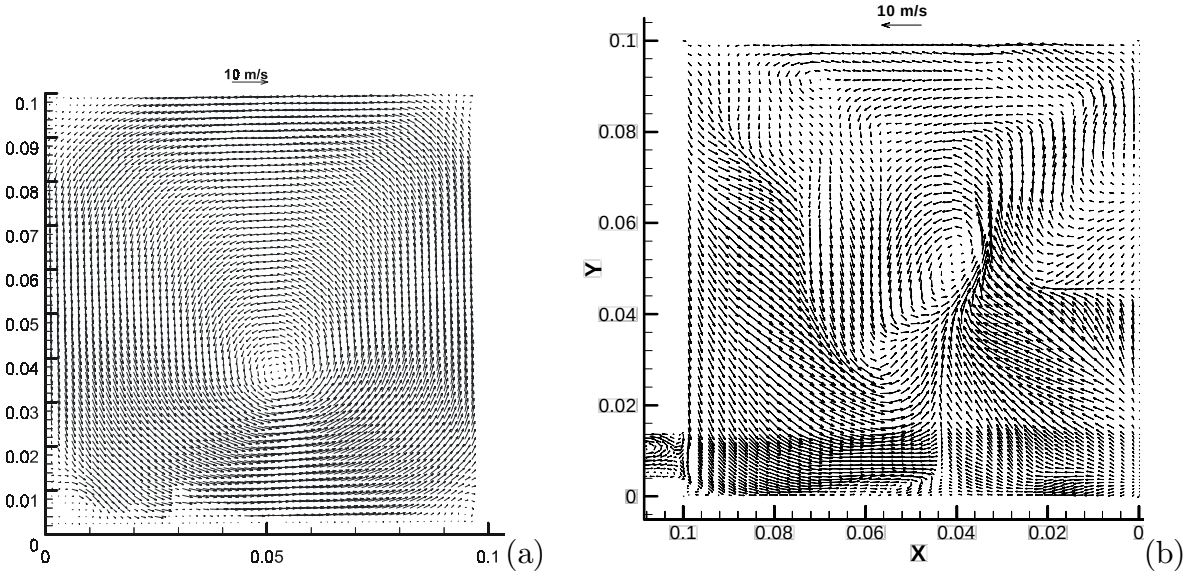

Figure 6.74: Comparison of velocity vectors. Experimental results and numerical simulation for model with $CR = 4{,}206$ rpm at BDC. a) – Ensemble averaged turbulent kinetic energy and velocity vectors from PIV experiments of Maurel et al [189]; and (b) – 3D LES simulation.

Model	X (mm)	Y (mm)	Error (mm)
PIV	30	55	
Three-dimensional LES	32	59	4

Table 6.10: Vortex centre location for $CR = 4$ LES model at 86 °CA. PIV data from Maurel et al [189]

Model	X (mm)	Y (mm)	Error (mm)
PIV	52	36	
Three-dimensional LES	59	53	18

Table 6.11: Vortex centre location for $CR = 4$ LES model at BDC. PIV data from Maurel et al [189]

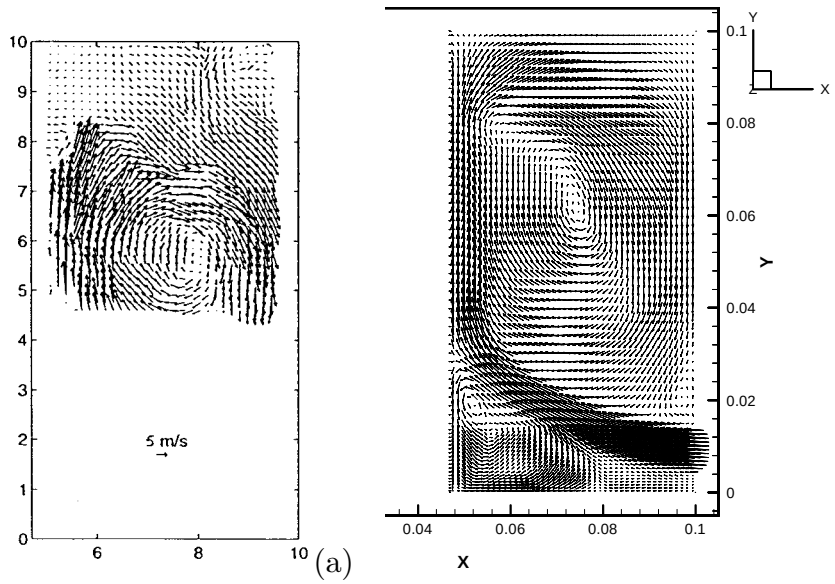

Figure 6.75: Comparison of LES velocity predictions in the $Z = 50\,\text{mm}$ plane for $CR = 10$, at 87 °CA. (a) – PIV result from Marc [187]; and (b) – 3D LES simulation.

6.9.5 $CR = 10$ Results

Intake Stroke

The flow during the intake stroke of the engine was measured by Marc [187] using PIV, and is shown in figure 6.75 in the tumble plane ($Z = 50\,\text{mm}$) at 87 °CA, and in figure 6.76 in the cross tumble plane ($X = 93\,\text{mm}$) at 64 °CA. The tumble plane, shown in figure 6.75, shows the LES model to reproduce the experimental results with good agreement. At this early stage of the simulation, however, all simulations predict very similar results (see figure 6.24).

The vortex centre location predicted by the LES model is shown in table 6.12. It shows the LES model predicts the location of the vortex centre with good agreement throughout the intake stroke. However, the error of the LES model at BDC (12.1 mm) is significantly greater than the Reynolds averaged simulations shown in table 6.7.

The velocity vectors in the cross tumble plane (figure 6.76) show that the LES model has predicted many small structures and vortices. The predicted flow is still symmetrical, however the experimental results show significant asymmetry and additional structures.

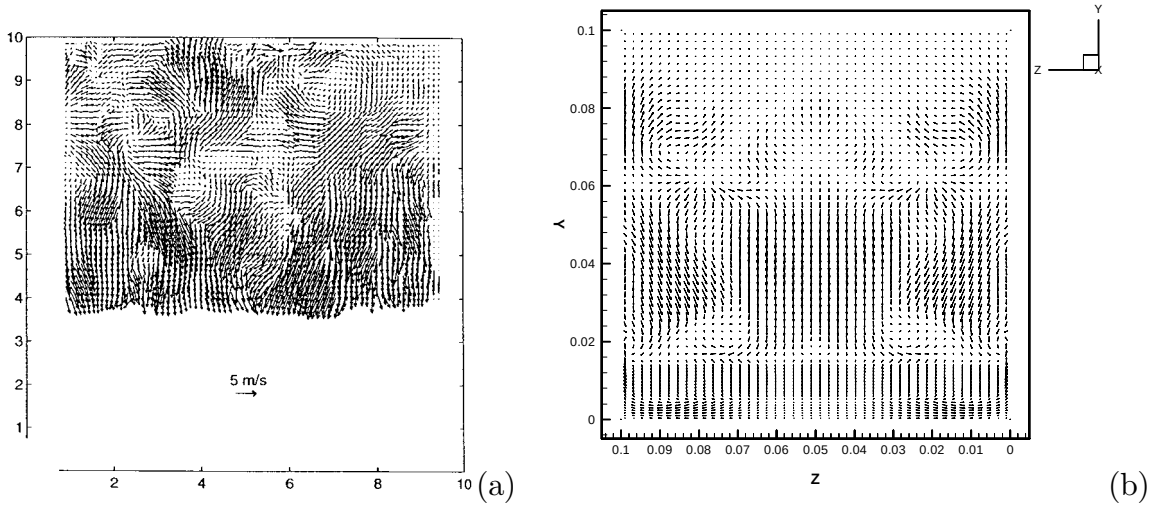

(a) (b)

Figure 6.76: Comparison of LES velocity predictions in the $X = 93\,\text{mm}$ plane for $CR = 10$, at 64 °CA. (a) – PIV results from Marc [187]; and (b) – 3D LES simulation.

	X		Y		Error
°CA	LES	PIV	LES	PIV	LES
64	80	n/a	32	n/a	n/a
87	77	78	62	57	5.1
127	74	66	61	67	10.0
BDC	52	47	38	49	12.1

Table 6.12: Intake stroke vortex centre location for the LES model, $CR = 10$. PIV results from [187], and all results are in mm.

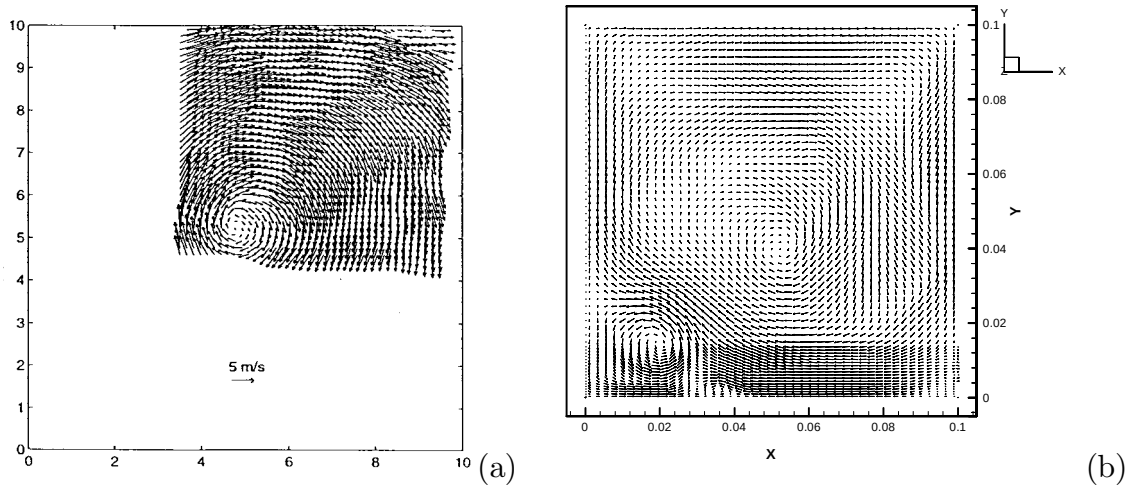

Figure 6.77: Comparison of LES velocity predictions in the $Z = 50\,\text{mm}$ plane for $CR = 10$, at BDC. (a) – PIV result from Marc [187]; and (b) – 3D LES simulation.

Bottom Dead Centre

The flow in the central tumble ($Z = 50\,\text{mm}$) plane is shown for the LES simulation in figure 6.77. The LES simulation shows many small structures superimposed on the main vortex, and the secondary vortex in the lower left corner is much stronger and larger than the Reynolds averaged simulations presented in figure 6.26. These structures are possibly turbulent fluctuations, and might be removed by ensemble averaging in a fashion similar to the PIV results.

Figure 6.78 shows the position of the vortex centre for the LES simulations, and the location of the experimentally measured vortex centre locations. Unlike the Reynolds averaged simulations shown in figure 6.28, the LES simulation is the only simulation to fail to predict a vortex centre within the typical spread of the PIV results.

Figure 6.79 shows the flow in the cross tumble (YZ) plane. No structures are seen in the PIV results, however a small amount of three-dimensional flow has developed in the LES simulation. The LES simulation has also broken symmetry.

Figure 6.80 shows a velocity profile through the centre of the tumble vortex, previously shown for the Reynolds averaged simulations in figure 6.29. As mentioned in section 6.7.2, the experimental results clearly show a significant departure from solid body rotation. This departure was captured by the RSM models, however the k-ϵ models failed to predict this fundamental behaviour. Figure 6.80 shows the LES model has predicted a departure from solid body rotation and the agreement with the experimental results is good between $50\,\text{mm} > X > 100\,\text{mm}$. However,

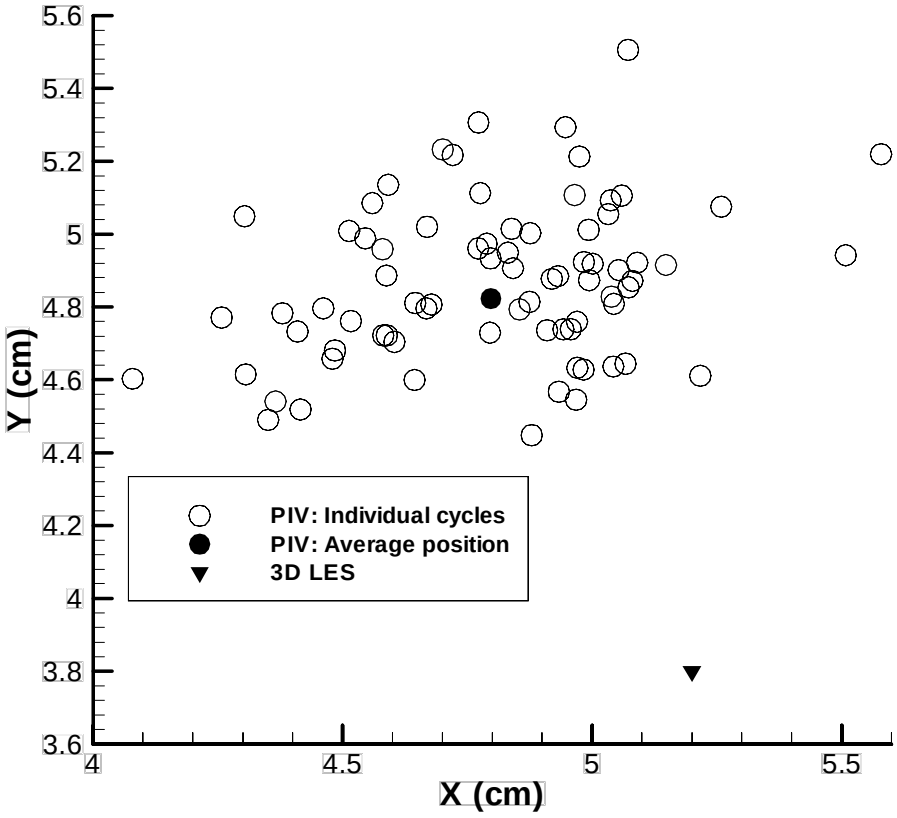

Figure 6.78: Vortex centre positions for $CR = 10$ LES model at BDC. PIV data from Marc [187].

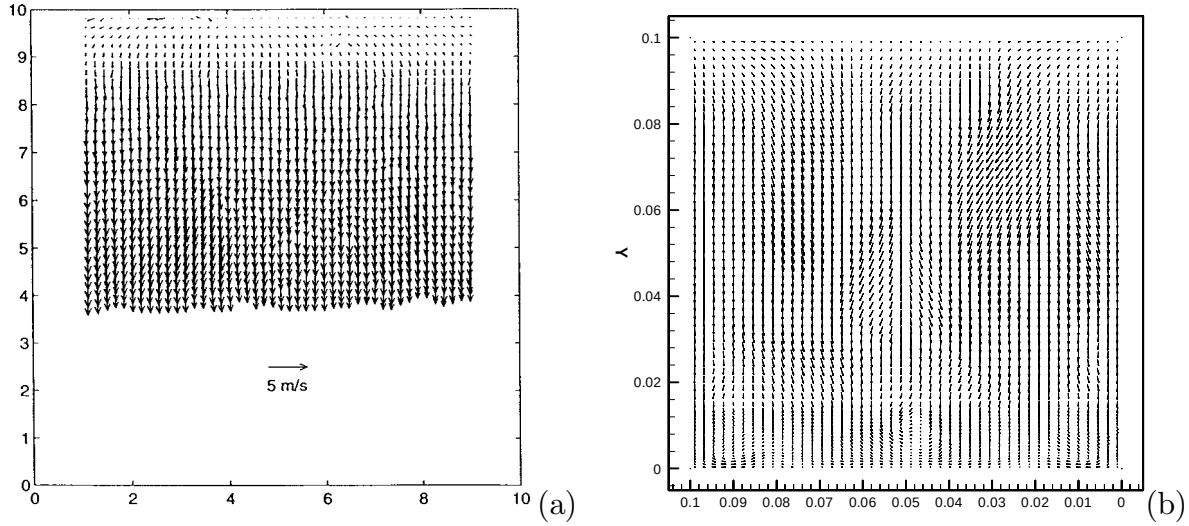

Figure 6.79: Comparison of LES velocity predictions in the $X = 93\,\text{mm}$ plane for $CR = 10$, at BDC. (a) – PIV results from Marc [187]; and (b) – 3D LES simulation.

significant errors occur in the region $0 > X > 50\,\text{mm}$.

Instantaneous streamlines for the LES model and BDC are shown in figure 6.81. It confirms the dominant flow structure is a large tumble vortex, however many small perturbations are seen, and the flow is asymmetrical.

Compression Stroke

Figures 6.82 to 6.87 depict the tumble plane flow fields predicted at various stages in the compression stroke, and compare them to experimental PIV data by Marc [187]. At 276 °CA (figure 6.82), the LES model shows a strong central vortex, with weaker flow above and below it. This is in reasonable agreement with the experimental data, so the LES model appears to be modelling the commencement of the tumble vortex break down process.

At 299 °CA (figure 6.83), the LES simulation predicts a result similar to the three-dimensional RSM model (figure 6.41e), but the vortex is shifted above the centre somewhat. Small structures are obvious in the field as "kinks" in the the velocity field of the LES simulation. As the simulation progresses to 312 °CA (figure 6.84), the LES simulation has predicted the central vortex moving significantly off-centre, and many smaller structures. Clearly it is modelling some turbulence-like structures. At 321 °CA (figure 6.85), the three-dimensional LES simulation predicts a complicated field with at least 11 vortices visible, and no one vortex being dominant. This simulation is now predicting many turbulence-like structures. The

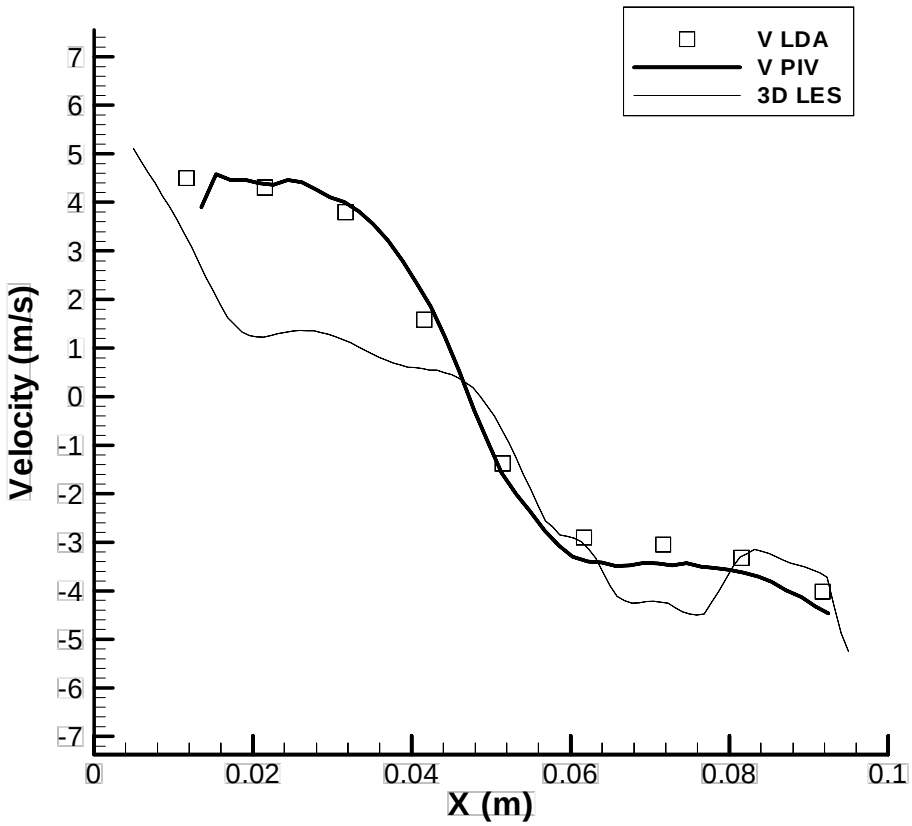

Figure 6.80: Comparison of LES simulation velocity profiles from $CR = 10$ model at BDC for $Y = 50\,\text{mm}$, $Z = 50\,\text{mm}$. LDA and PIV results from Marc [187].

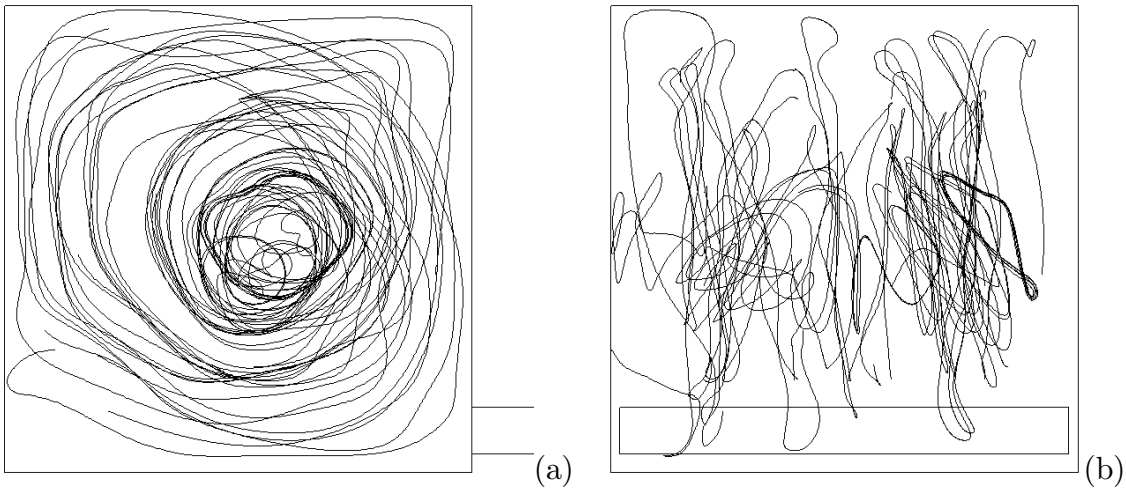

Figure 6.81: Instantaneous streamlines for the LES model at BDC. (a) – Tumble plane view; and (b) – Cross tumble plane view.

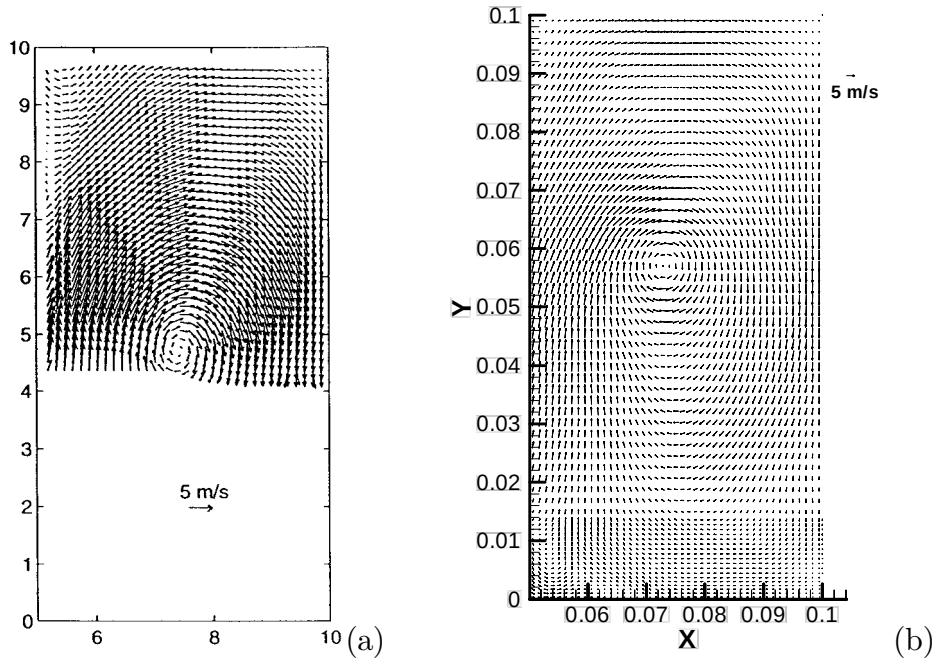

Figure 6.82: Velocity vectors in $Z = 50\,\text{mm}$ plane from the LES simulation at 276 °CA. (a) – PIV results of Marc [187]; and (b) – 3D LES simulation.

structures decrease in size and increase in number as the compression continues through 328 °CA (figure 6.86) and 335 °CA (figure 6.87). At 335 °CA, LES predicts a central vortex reforming, however it is rotating the opposite direction to the original tumble vortex!

Similarly as for figures 6.37 and 6.42, the vortex centre can be extracted from the LES simulation and compared to the experimental results. The position of the centre of the vortex for the LES simulation at 276 °CA is shown in figure 6.88, and is seen to be in a region typical of the experimentally measured individual cycles. Figure 6.89 shows the position of the vortex centres at 299 °CA, and the vortex centre predicted by the LES simulation differs from the ensemble averaged PIV result by about 15 mm, however it is close to the spread of PIV results taken from individual cycles.

The flow in the cross tumble ($X = 93\,\text{mm}$) plane is shown in figures 6.90 to 6.93. At 276 °CA (figure 6.90), the LES simulation shows a small departure from symmetrical flow, but few structures have formed. As the simulation advances to 299 °CA (figure 6.91), some strong vortex structures have formed, the largest of which is centred at $Y = 10\,\text{mm}$, $Z = 20\,\text{mm}$. The flow is now highly asymmetric, and does not resemble the PIV results. By 312 °CA (figure 6.92), three major vortices have formed, and several smaller ones exist. The final vector field in this

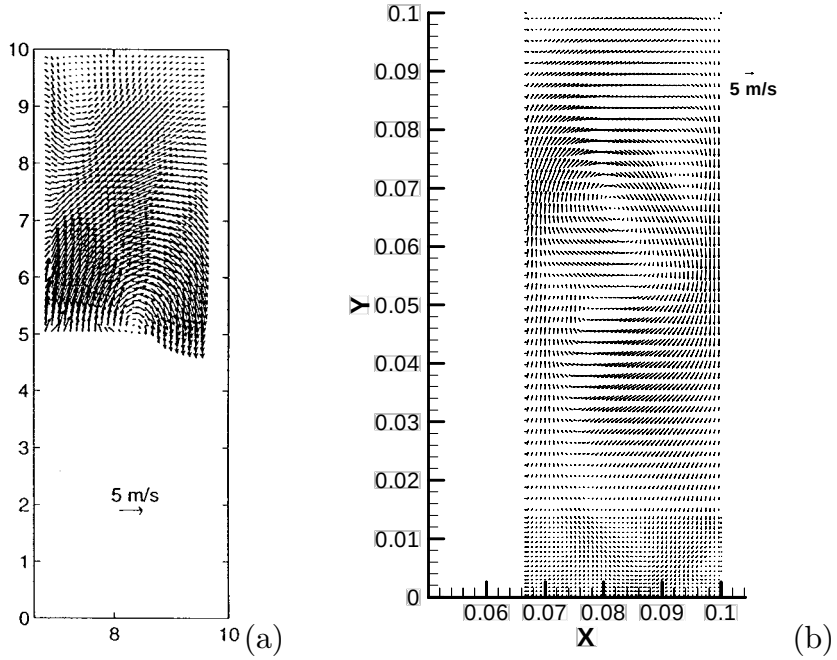

Figure 6.83: Velocity vectors in $Z = 50\,\text{mm}$ plane from the LES simulation at 299 °CA. (a) – PIV results of Marc [187]; and (b) – 3D LES simulation.

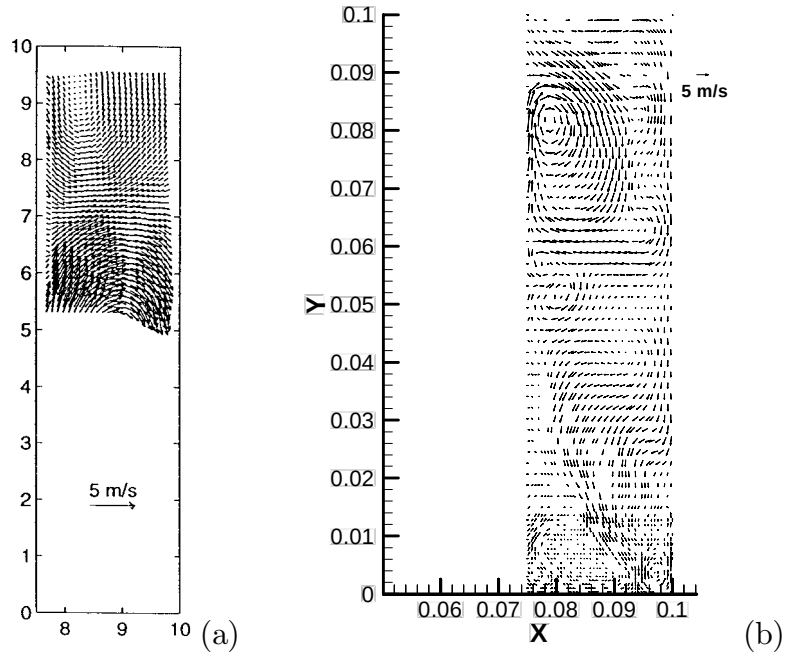

Figure 6.84: Velocity vectors in $Z = 50\,\text{mm}$ plane from the LES simulation at 312 °CA. (a) – PIV results of Marc [187]; and (b) – 3D LES simulation.

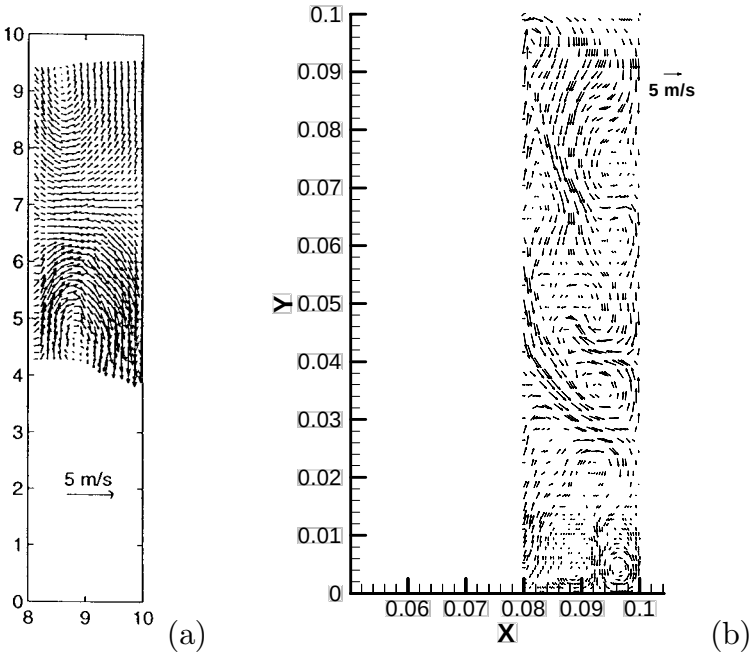

Figure 6.85: Velocity vectors in $Z = 50\,\text{mm}$ plane from the LES simulation at 321 °CA. (a) – PIV results of Marc [187]; and (b) – 3D LES simulation.

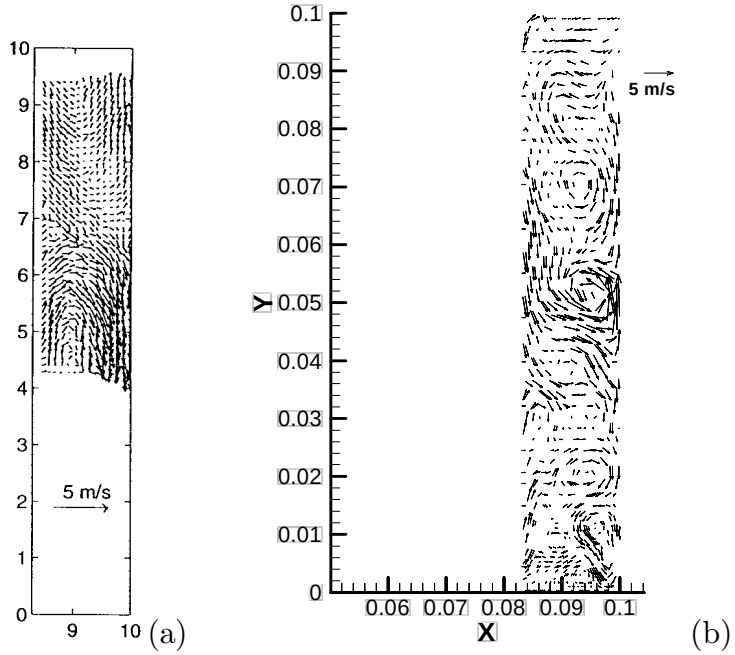

Figure 6.86: Velocity vectors in $Z = 50\,\text{mm}$ plane from the LES simulation at 328 °CA. (a) – PIV results of Marc [187]; and (b) – 3D LES simulation.

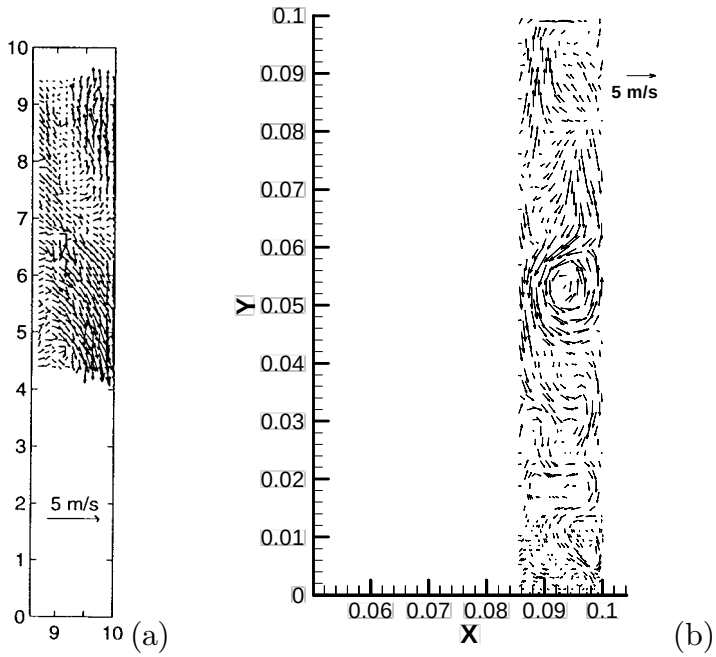

Figure 6.87: Velocity vectors in $Z = 50\,\text{mm}$ plane from the LES simulation at 335 °CA. (a) – PIV results of Marc [187]; and (b) – 3D LES simulation.

plane is shown at 321 °CA, and shows that the three main vortices still remain together with a number of smaller structures. Again the LES simulated flow does not resemble the PIV results for either of the final two visualisations.

The effects of the turbulence and cycle to cycle variations have large effects on the flow field during the compression stroke. This means that to obtain an objective comparison to experimental results, a large number of simulations would need to be performed and averaged to gain a mean flow, similar to that done to the PIV data. Until this can be performed it is not possible to make conclusions about the accuracy of the method.

Top Dead Centre

The three-dimensional LES model at TDC (figure 6.94) continues to show a complicated structure with many vortices. It shows many small structures near the bottom of the cylinder, and a few larger vortices in the remainder of the cylinder. This flow field obviously contains a number of turbulent-like structures.

Instantaneous streamlines for the LES model at TDC are shown in figure 6.95. It shows a few large structures and many small structures. Again, this flow obviously needs to be averaged to gain a statistically significant mean flow for comparison to experimental results.

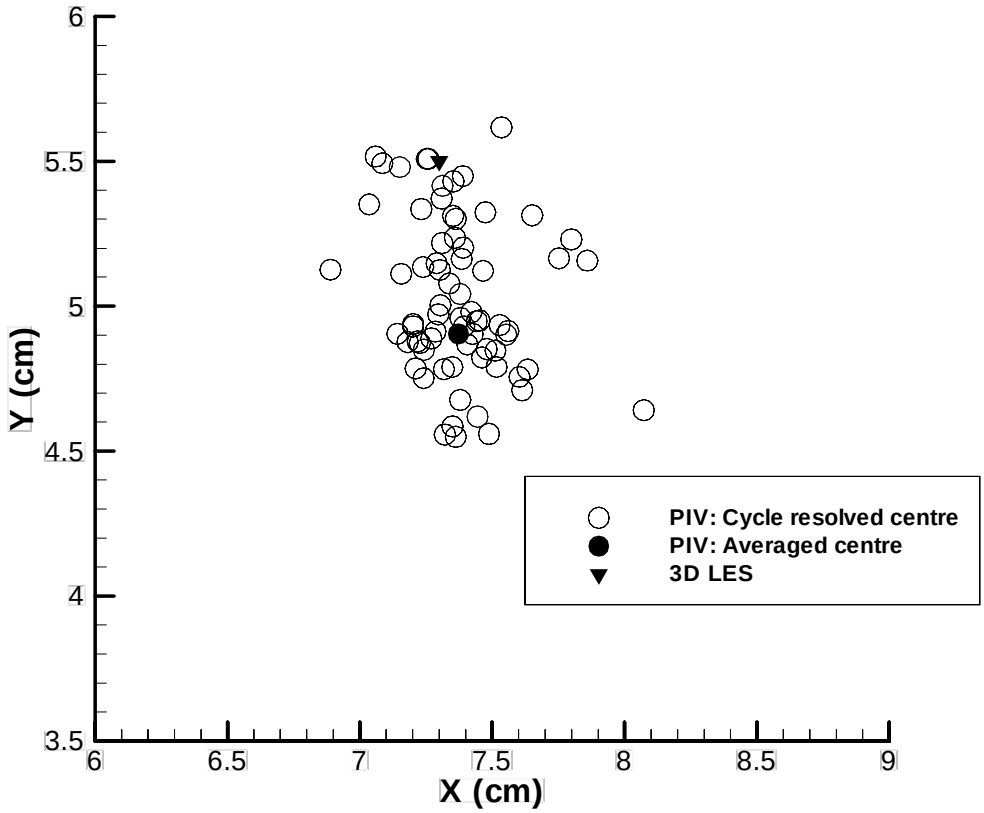

Figure 6.88: Position of the centre of the vortex predicted by the LES simulation at 276 °CA.

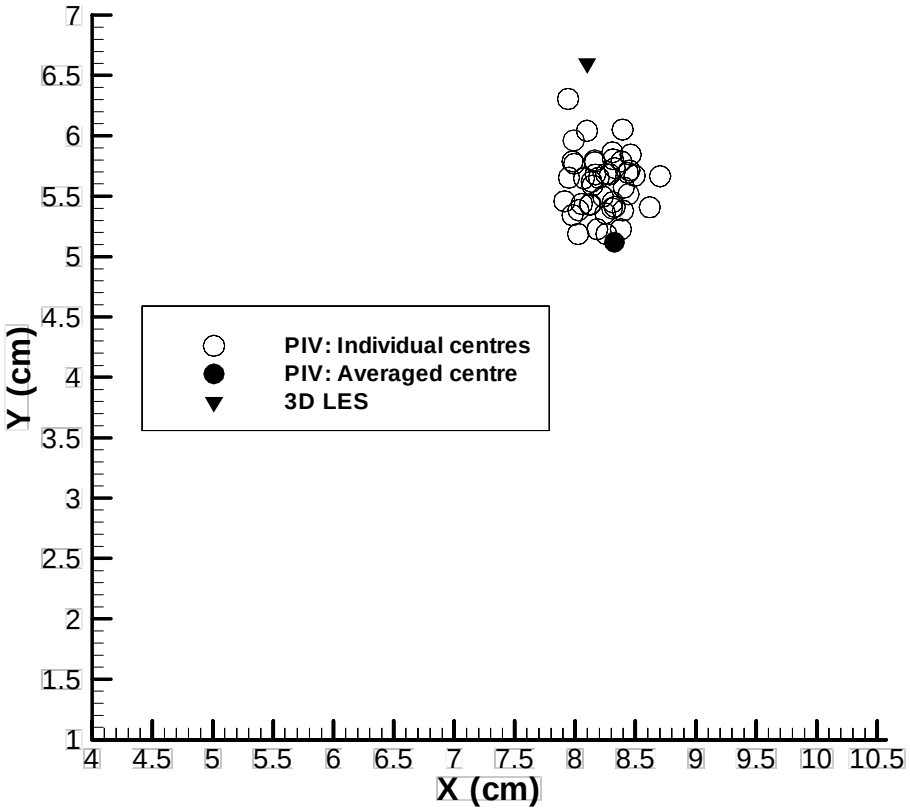

Figure 6.89: Position of the centre of the vortex predicted by the LES simulation at 299 °CA.

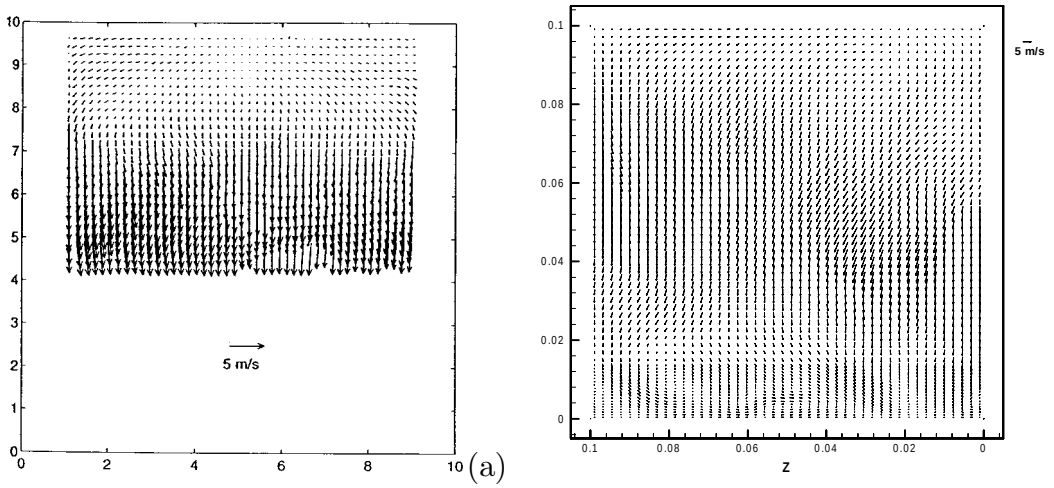

(a) (b)

Figure 6.90: Velocity vectors in $X = 93\,\text{mm}$ plane from the LES simulation at 276 °CA. (a) – PIV results of Marc [187]; and (b) – 3D LES simulation.

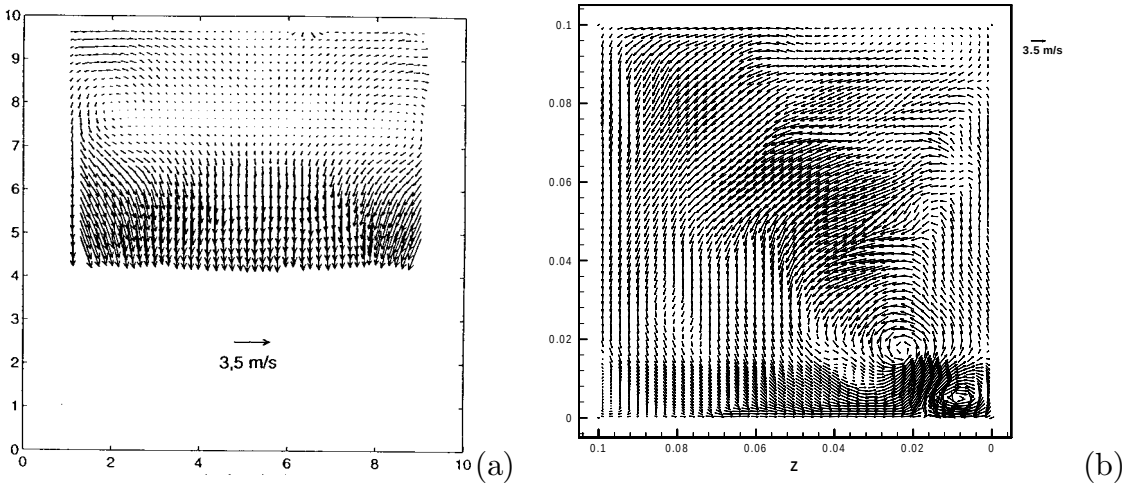

Figure 6.91: Velocity vectors in $X = 93\,\text{mm}$ plane from the LES simulation at 299 °CA. (a) – PIV results of Marc [187]; and (b) – 3D LES simulation.

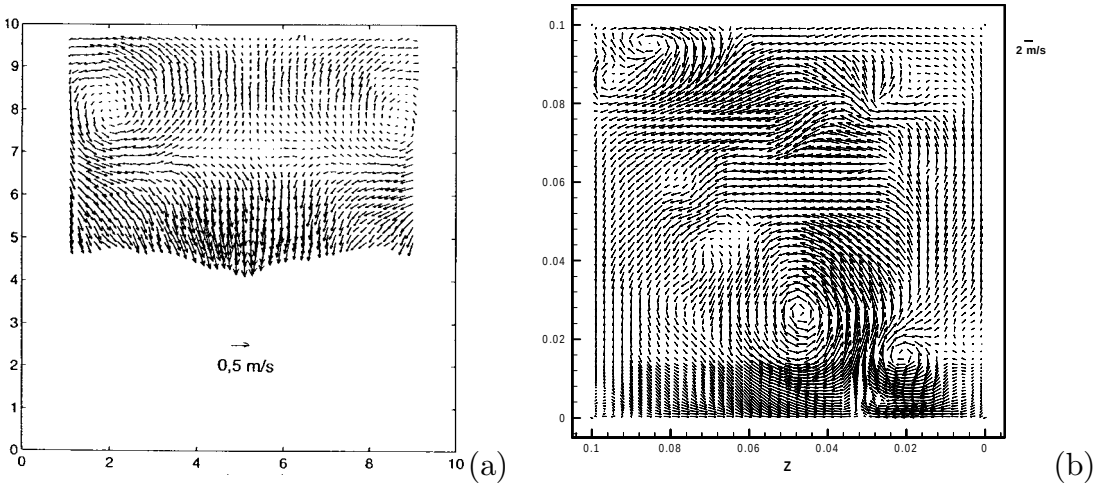

Figure 6.92: Velocity vectors in $X = 93\,\text{mm}$ plane from the LES simulation at 312 °CA. (a) – PIV results of Marc [187]; and (b) – 3D LES simulation.

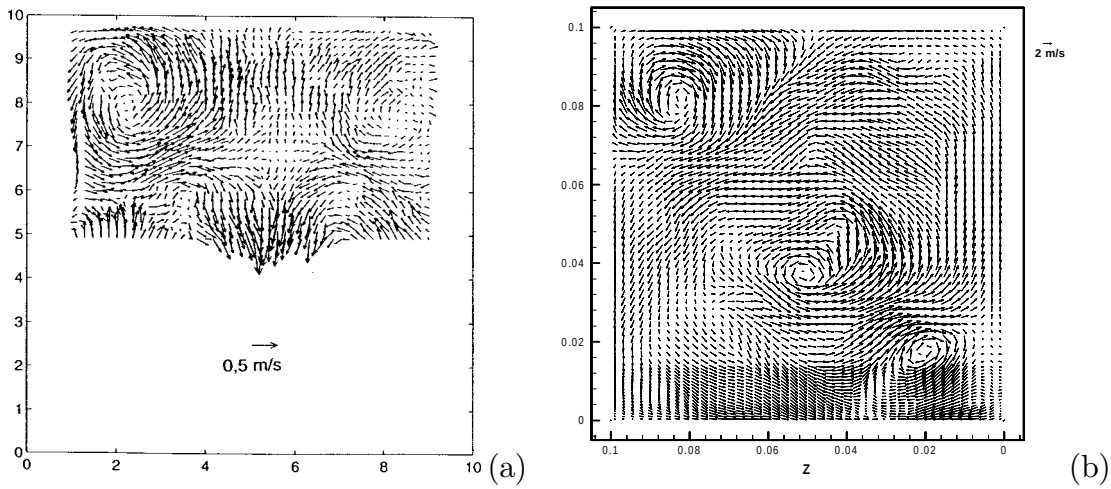

Figure 6.93: Velocity vectors in $X = 93\,\text{mm}$ plane from the LES simulation at 321 °CA. (a) – PIV results of Marc [187]; and (b) – 3D LES simulation.

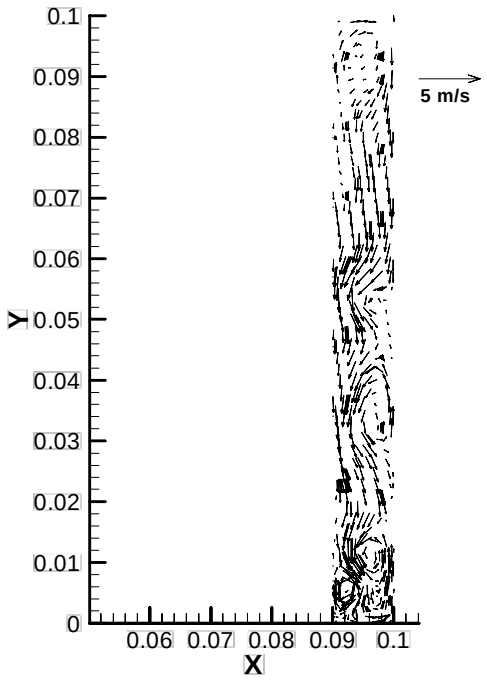

Figure 6.94: Velocity vectors from the LES simulation in the $Z = 50\,\text{mm}$ plane at TDC.

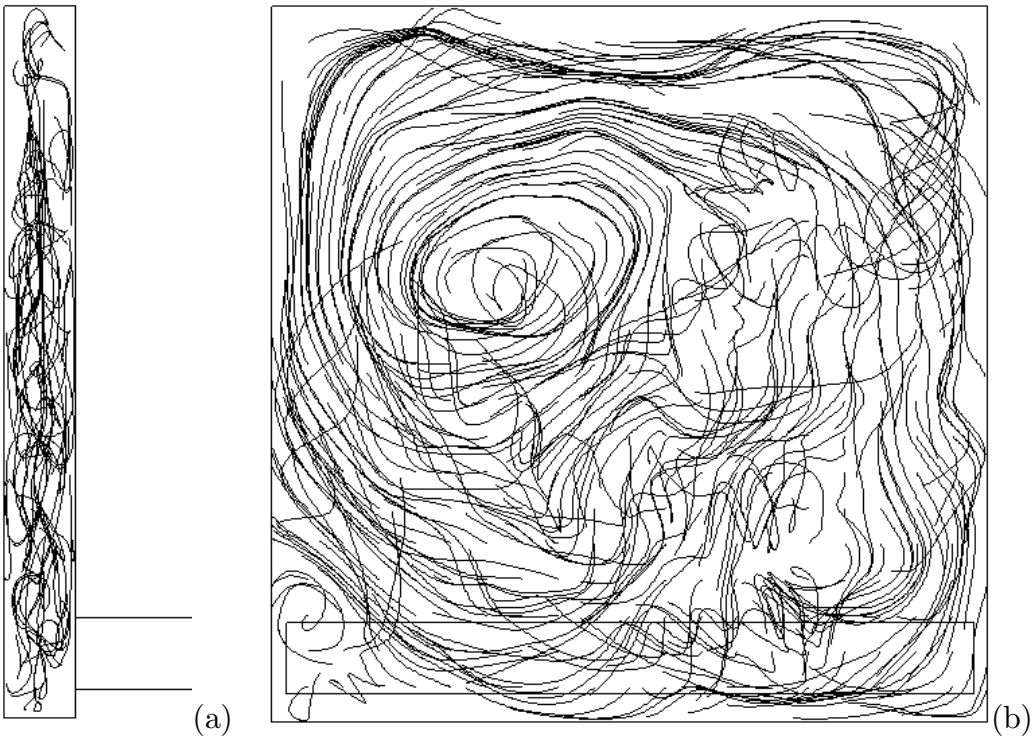

Figure 6.95: Instantaneous streamlines for the LES model at TDC. (a) – Tumble plane view; and (b) – Cross tumble plane view.

Averaged Results

Figure 6.96 shows the mass averaged velocity squared and tumble ratio predicted by the LES simulation, and can be compared to the Reynolds averaged simulations in figures 6.63 and 6.64. The equivalent result from the three-dimensional Reynolds averaged RSM model has been shown from figures 6.63b and 6.64b as a comparison.

A large amount of fluctuations can be seen in the central plane results on both the mass averaged velocity graph (figure 6.96a) and tumble ratio graph (figure 6.96b). This indicates that turbulent-like fluctuations are affecting the central plane results. The fluctuations do not appear to affect the full domain results, so it appears that averaging over the entire domain has removed the turbulent fluctuations and only left the mean flow component. As discussed in section 6.7.4, this is likely to be due to the full domain results behaving like volume Reynolds averaging to remove the turbulent fluctuations.

The tumble spin-up during the compression stroke is seen in both the mass averaged velocity squared and the tumble ratio.

The mass averaged velocity squared and tumble ratio predicted by the LES model are similar to those predicted by the three-dimensional RSM simulation.

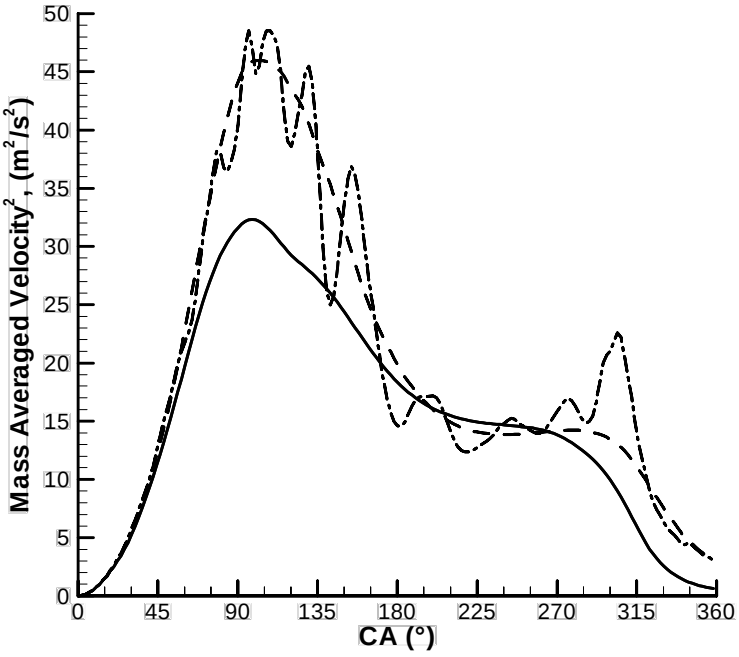

(a)

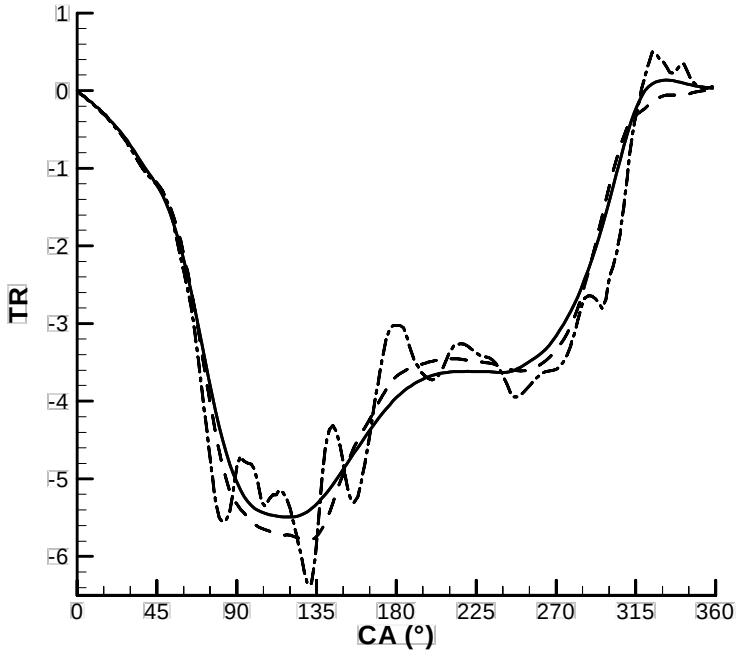

(b)

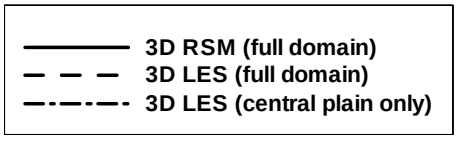

Figure 6.96: Mass averaged velocity squared and tumble ratio for the LES model. (a) – Mass averaged velocity squared; and (b) – Tumble ratio.

The previous section showed that this was the most accurate Reynolds averaged simulation tested, so this shows the LES model has encouraging accuracy in this comparison.

The LES model predicts a slight reversal of the tumble vortex just before TDC of the compression stroke, mainly seen on the central plane (figure 6.96b). This was also predicted by the three-dimensional RSM simulation.

6.9.6 Velocity Decomposition

Marc [187] presents experimentally determined velocity and turbulence histories at a small number of points in the flow, as presented in section 6.7.5. A decomposition of the three-dimensional LES results into mean and turbulent components allows comparison with experimental data. The method used is described in equation 2.12, where the mean value is defined as the average of the instantaneous valve over a small part of the engine cycle [93].

From the raw data from the model, the mean and turbulent components were calculated as

$$u_{mean}\left(CA\right) = \frac{1}{30}\int_{CA-15}^{CA+15} u_{raw}\left(CA\right)\, d\left(CA\right) \text{ and} \tag{6.6}$$

$$u'\left(CA\right) = \frac{1}{30}\sqrt{\int_{CA-15}^{CA+15} \left[u_{raw}\left(CA\right) - u_{mean}\left(CA\right)\right]^2\, d\left(CA\right)}, \tag{6.7}$$

in which $u_{raw}\left(CA\right)$ is the velocity predicted by the model at the point as a function of crank angle, $u_{mean}\left(CA\right)$ is the running average of that velocity over a 30 °CA range, and $u'\left(CA\right)$ is the turbulent fluctuations, calculated as an root mean square (rms) average over the same 30 °CA range. The averaging time was chosen as 30 °CA as it includes one to two wavelengths of the high frequency component of the velocity, and is thus the shortest time interval possible which can remove the high frequency fluctuations. This averaging time is similar to that suggested by El Tahry and Haworth [93] of 40 °CA. The results of performing this averaging on results is shown in figure 6.97. The mean velocity appears to successfully remove the high frequency fluctuations from the raw velocity, and agrees well with the experimentally measured mean velocity.

The LES model results were analysed using equations 6.6 and 6.7, and compared to the LDA results of Marc at various points throughout the domain. The points analysed were point 12 (figure 6.98), point 13 (figure 6.99), point 15 (figure 6.100), point 17 (figure 6.101), point 18 (figure 6.102), and point 55 (figure 6.103).

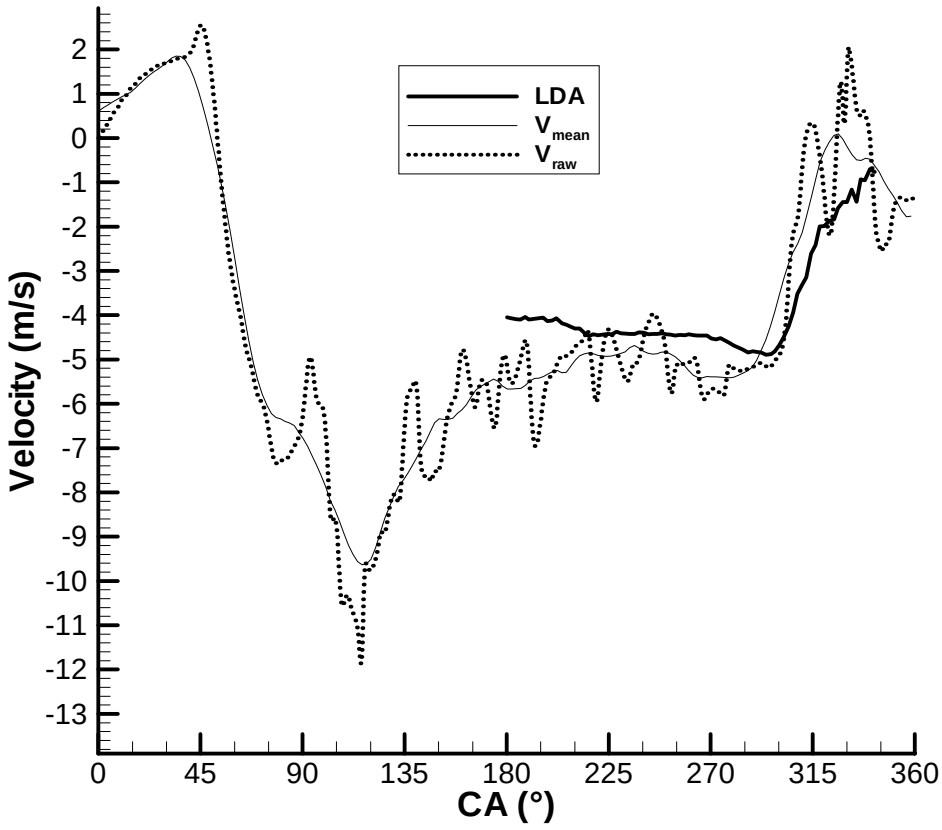

Figure 6.97: v velocity at point 15 ($X = 95\,\text{mm}$, $Y = 50\,\text{mm}$). v_{raw} is directly from $CR = 10$ LES model, v_{mean} is a $30\,^{\circ}\text{CA}$ running average of v_{raw}. LDA results from Marc [187].

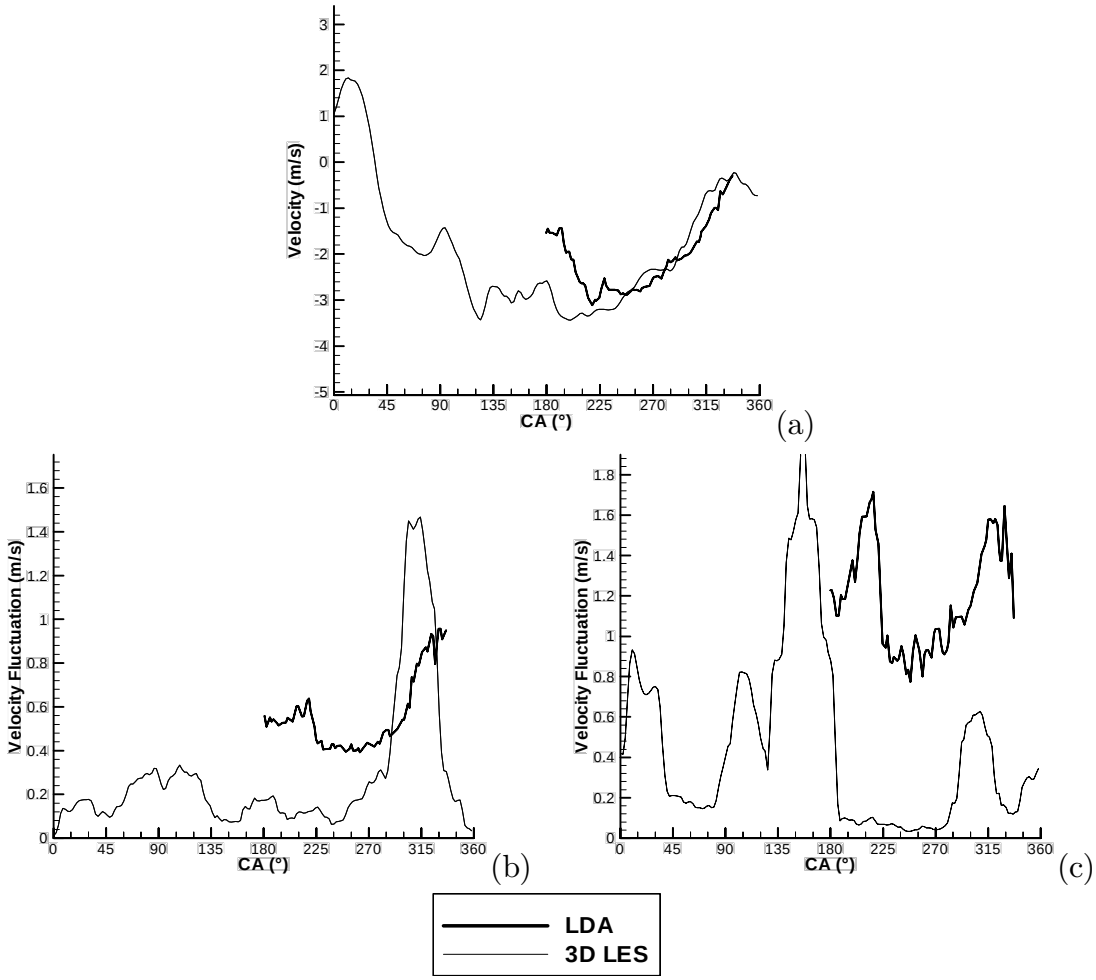

Figure 6.98: Comparison of LDA and LES results at point 12 ($X = 95\,\text{mm}$, $Y = 20\,\text{mm}$). LDA data from Marc [187]. (a) – v velocity; (b) – u' turbulent velocity fluctuation; and (c) – v' turbulent velocity fluctuation.

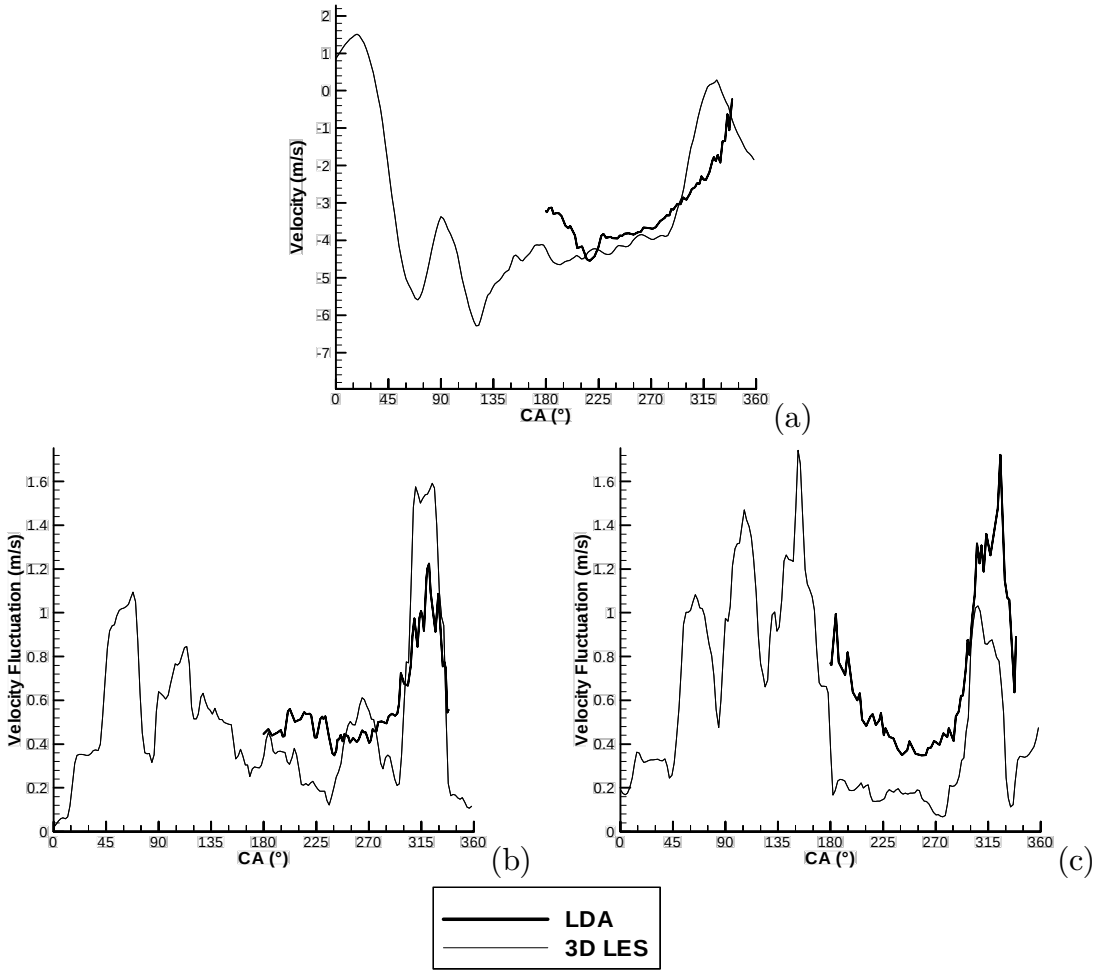

Figure 6.99: Comparison of LDA and LES results at point 13 ($X = 95\,\text{mm}$, $Y = 30\,\text{mm}$). LDA data from Marc [187]. (a) – v velocity; (b) – u' turbulent velocity fluctuation; and (c) – v' turbulent velocity fluctuation.

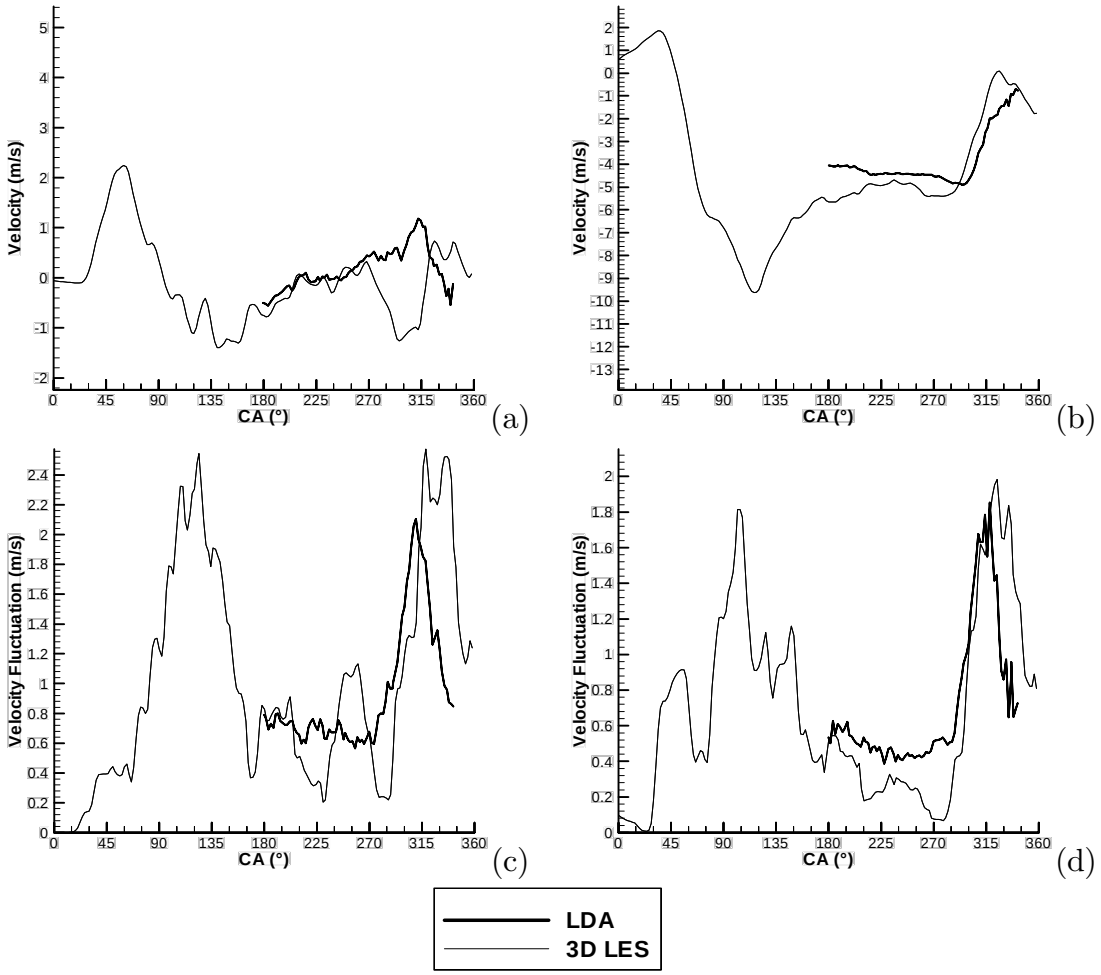

Figure 6.100: Comparison of LDA and LES results at point 15 ($X = 95\,\text{mm}$, $Y = 50\,\text{mm}$). LDA data from Marc [187]. (a) – u velocity; (b) – v velocity; (c) – u' turbulent velocity fluctuation; and (d) – v' turbulent velocity fluctuation.

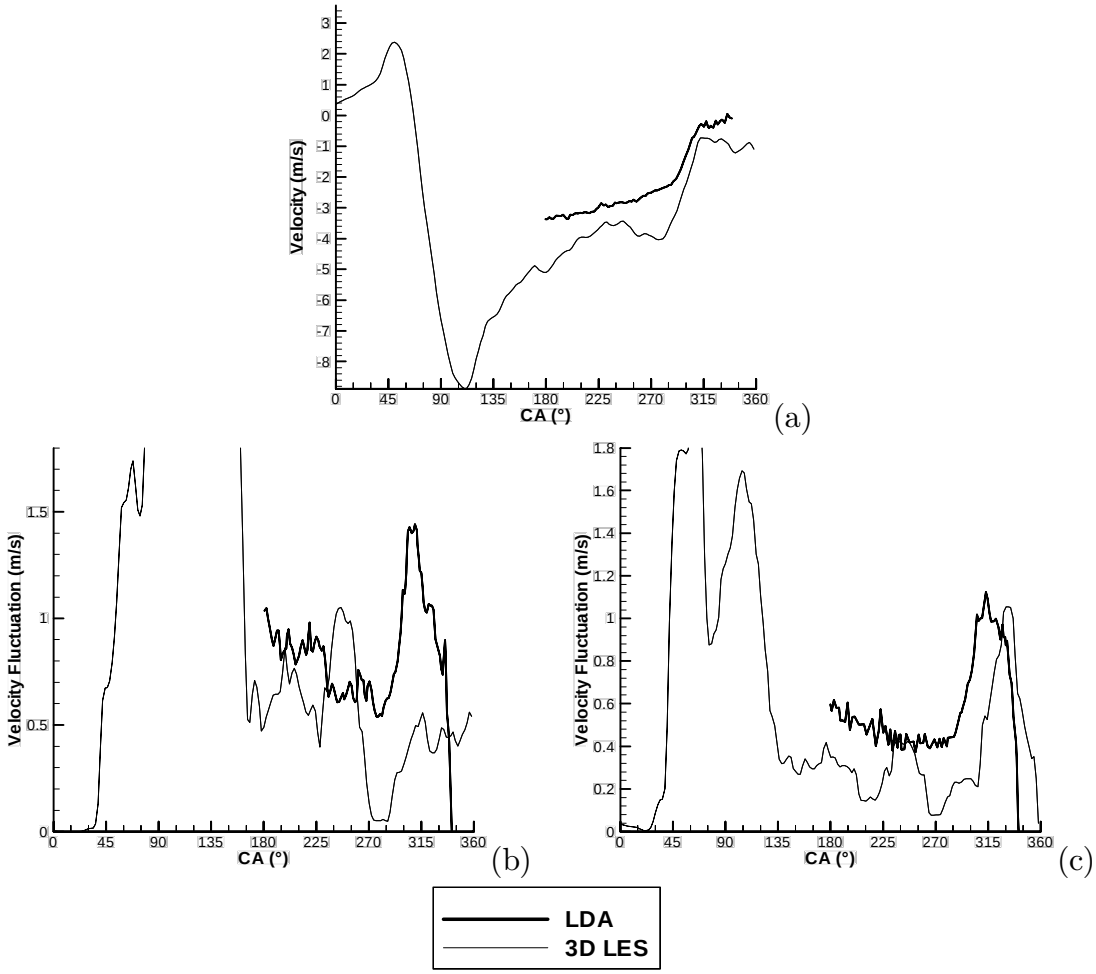

Figure 6.101: Comparison of LDA and LES results at point 17 ($X = 95\,\text{mm}$, $Y = 70\,\text{mm}$). LDA data from Marc [187]. (a) – v velocity; (b) – u' turbulent velocity fluctuation; and (c) – v' turbulent velocity fluctuation.

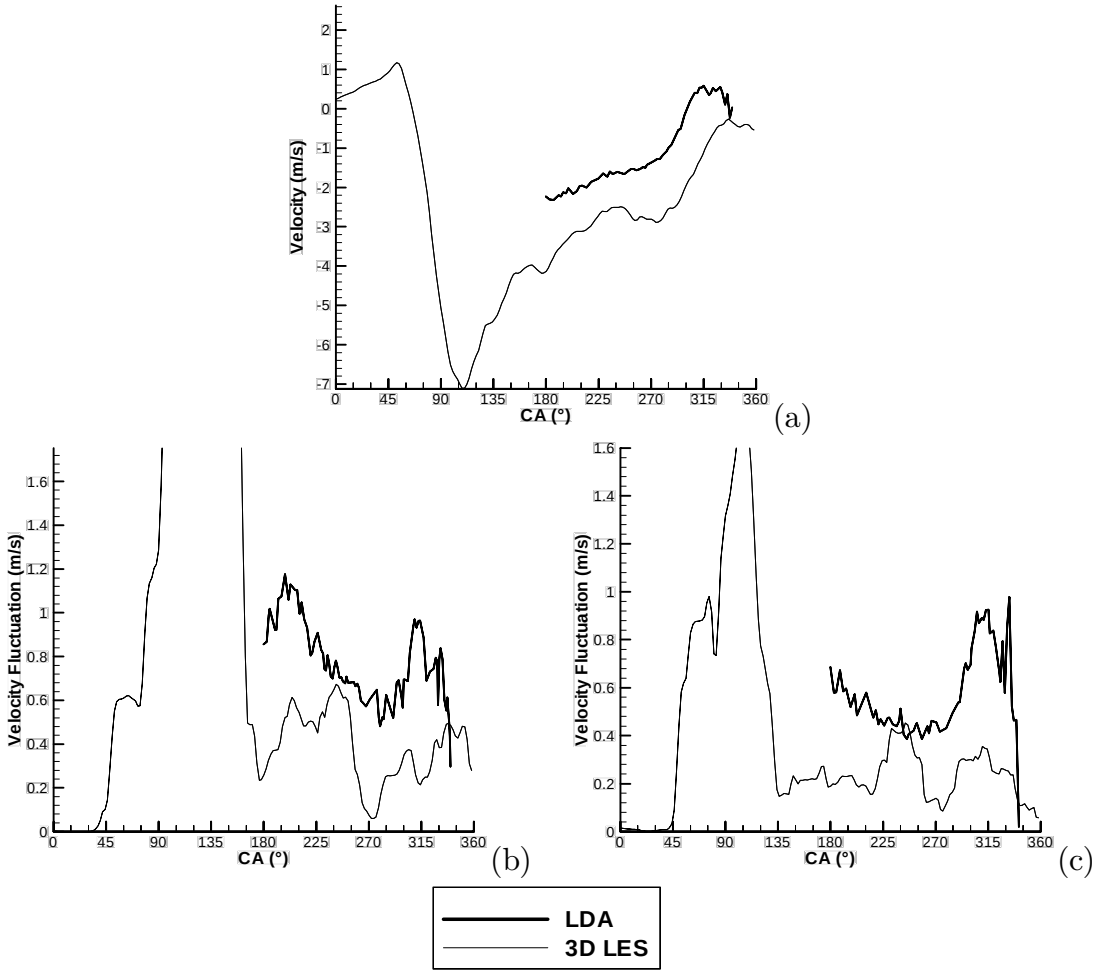

Figure 6.102: Comparison of LDA and LES results at point 18 ($X = 95\,\text{mm}$, $Y = 80\,\text{mm}$). LDA data from Marc [187]. (a) – v velocity; (b) – u' turbulent velocity fluctuation; and (c) – v' turbulent velocity fluctuation.

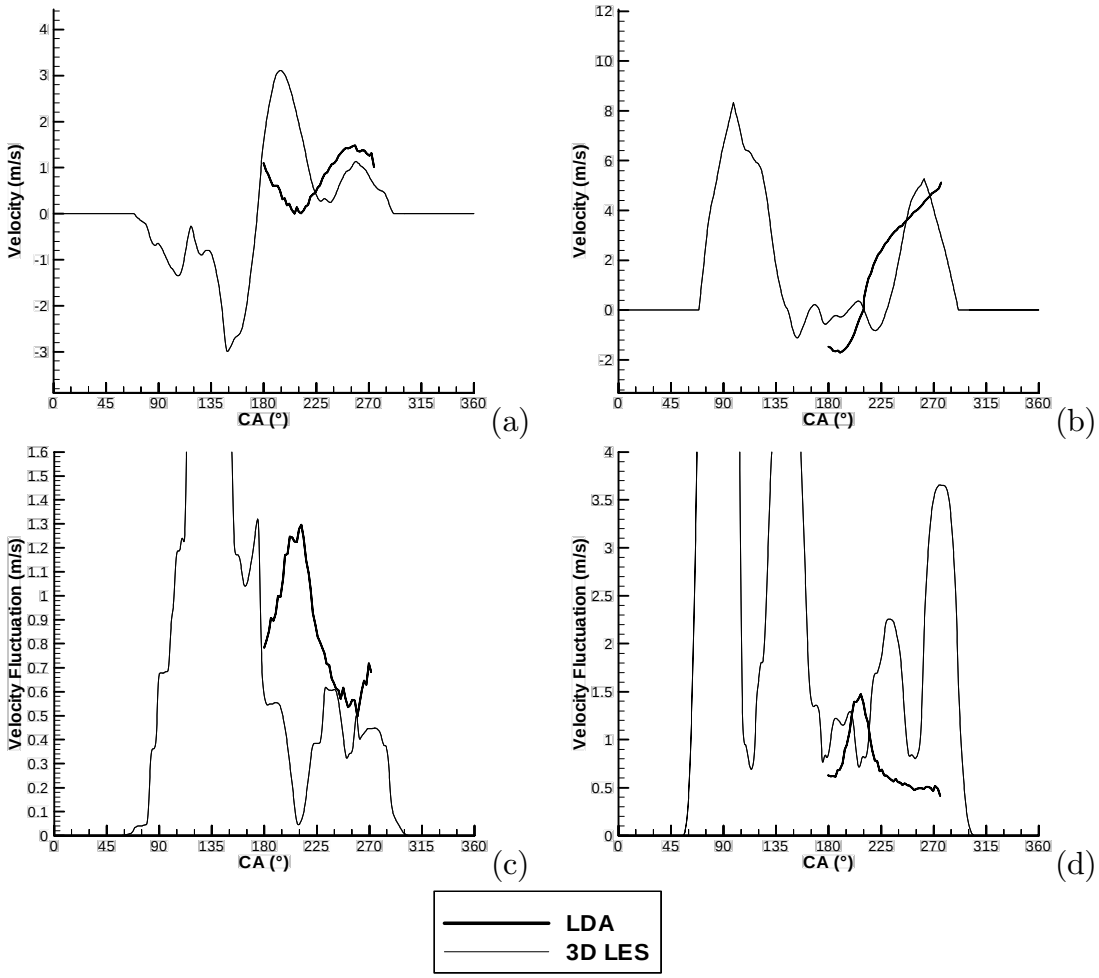

Figure 6.103: Comparison of LDA and LES results at point 55 ($X = 50\,\text{mm}$, $Y = 50\,\text{mm}$). LDA data from Marc [187]. (a) – u velocity; (b) – v velocity; (c) – u' turbulent velocity fluctuation; and (d) – v' turbulent velocity fluctuation.

The velocities predicted at these points are shown in figures 6.98a, 6.99a, 6.100a and b, 6.101a, 6.102a and 6.103a and b. The LES results agree with the experimental results as well as the best Reynolds averaged simulations (figures 6.66 to 6.71), and in many cases better. For instance the LES model has good agreement in calculating the v velocities at points 12, 13, 15 and 55. In many cases it proves more accurate than any of the Reynolds averaged simulations. The velocities predicted at points 15 (u velocity), 17, 18 and 55 (u velocity) have reduced agreement, however in only one of these cases does a Reynolds averaged simulation perform better (being the three-dimensional RSM simulation at point 18).

The turbulence (u' and v') predicted at these points are shown in figures 6.98b and c, 6.99b and c, 6.100c and d, 6.101b and c, 6.102b and c, and 6.103c and d. In general the agreement is reasonable, however the turbulence predicted by the RSM Reynolds averaged simulation reproduces the experimental results better. At points 12, 13, 15, 17 and 18 the RSM model, especially the three-dimensional RSM model predicts the turbulence levels more accurately than the LES model. At these same points, the LES model also proves to be at least as accurate than the k-ϵ models (with the only exception being point 12 v' where the two- and three-dimensional k-ϵ models are better). Point 55 is poorly predicted, however no Reynolds averaged model predicts this point well either.

6.9.7 Discussion

The three-dimensional LES model was found to do remarkably well despite its simplicity. It successfully captured features such as the fact that the BDC flow was not solid body rotation—a feature the k-ϵ model failed to predict. It also managed to predict velocities and turbulence at various points in the domain with reasonable accuracy. The LES model also predicted a form of tumble vortex breakdown, however it is quite different to that found in the ensemble averaged experimental results.

The LES model shows reasonable agreement with experimental results for the velocity components described in section 6.9.5, and proves to be as accurate in many respects (or possibly more accurate) than the three-dimensional RSM model. It predicts the velocity components with greater accuracy than the k-ϵ model. The turbulence components are predicted with moderate accuracy, with the three-dimensional RSM model proving to be significantly more accurate than the LES model. However, the LES model has proved to be significantly more accurate than the two- or three-dimensional k-ϵ model.

This reduced accuracy in the turbulence compared to the velocity is caused by a combination of the LES model and the turbulence decomposition technique (equations 6.6 and 6.7). A detailed study of the source of this error is beyond the scope of this work, and is left to future research.

Since any LES model resolves some turbulent structures, a number of simulations must be performed and ensemble averaged (or some other form of averaging) to get a proper comparison to the experimental data. This has not been performed as part of this work, however the success of the simple model presented here encourages further work in this area. Areas for future work include performing a number of simulations to establish a statistical pattern, analysis of the predicted turbulence energy spectrum, development of a specialised LES solver and development of a more rigorous sub-grid model.

Chapter 7

Modelling of the BRV Engine

The numerical model developed and validated in the previous chapters will now be used to simulate air flows inside the BRV engine.

7.1 BRV Engine Layout

The basic layout of the BRV engine is shown in figure 7.1. The valve rotates at half engine speed along an axis parallel to the crankshaft, and perpendicular to the piston motion axis, as shown in figure 7.2. The valve has an inlet port and exhaust port in the same valve. The bottom end of the engine, that is, the crankshaft, sump, cylinder barrel, valve drive mechanism and other ancillary items, are not significantly different to those used in traditional poppet valve engines.

7.2 Method of Creating the CFD Model

The geometries used in this work were designed and drawn at Bishop Innovation, and given to the author as either engineering drawings or "parasolid" files. Parasolid is a file format used to export geometries in three-dimensional solid modelling programs. The system at Bishop Innovation used the package "Unigraphics" to draw the geometries, and the pre-processor for CFX, "CFX-Build" was used by the current author to transform the solids into a mesh usable by the CFX solver.

There is as much art as science in developing a good mesh for use in a CFD model. This is especially so in complicated geometries with movement, such as an internal combustion engine. Demands to be satisfied for an internal combustion engine CFD model include:

- The mesh must adequately define the geometry;

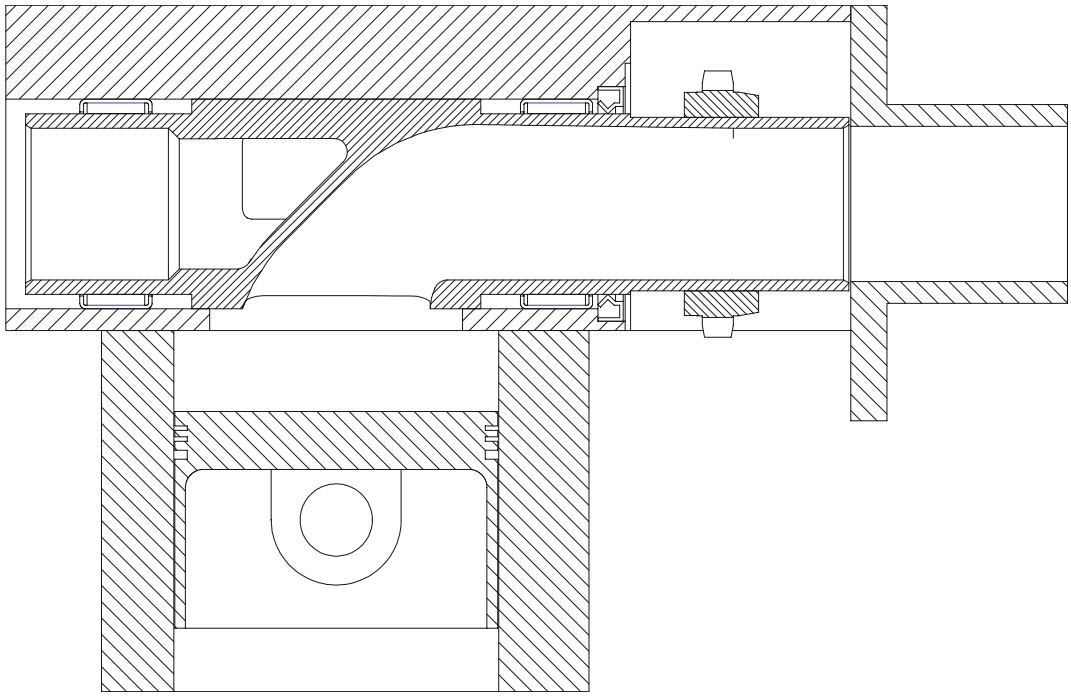

Figure 7.1: Diagram of the overall layout of the BRV engine, showing piston, valve and cylinder head.

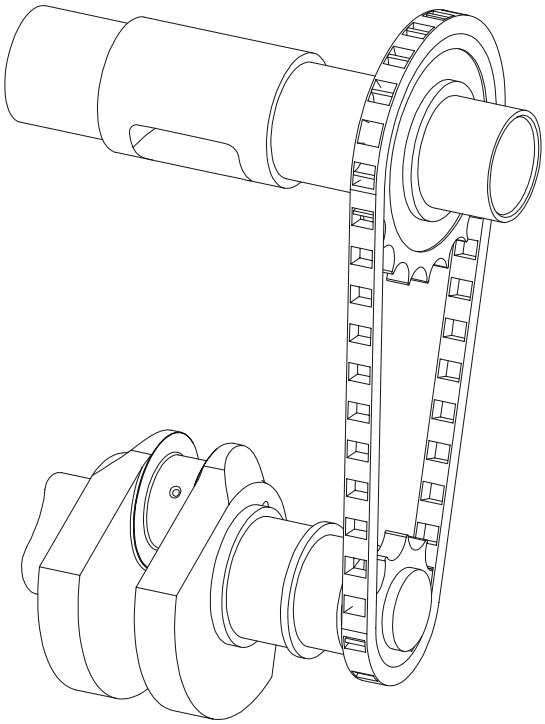

Figure 7.2: Diagram of the overall layout of the BRV engine, showing crank and valve drive system.

- The mesh must allow implementation of the motion of the piston and valves;
- The mesh must minimise grid distortion. The main factors of grid distortion are:
  - Cell aspect ratio;
  - Relative size of adjacent cells; and
  - Orthogonality of cells.
- The mesh must allow increased resolution at the walls; and
- The mesh must be of a size practical to run on the available computing resources.

All the meshes used in this work were made with the above demands in mind. The procedure used to create the engine mesh involves many individual steps, and will not be described in detail. The main steps used to create one of the meshes used for this study will be briefly described as an example.

The raw geometry imported from the parasolid file is shown in figure 7.3. The geometry shown is a solid model used during the manufacturing of the valve, and therefore it contains detail not relevant to the CFD model.

The first step was to extract the region of the model needed for the CFD model. Similarly, the geometry for the cylinder head and trumpet were also imported. The result of this is shown in figure 7.4, which shows the geometry in their correct locations in space. Note that in figure 7.4 there is a small section of the inlet manifold missing between the valve and trumpet. This section is the throttle assembly in the engine, and this is a simple circular cylindrical section. It was added later during the processing of the geometry.

The first part of the geometry to be processed was the cylinder head, shown in various views in figure 7.5a and 7.5b. This geometry includes the top surface of the cylinder head, the cylindrical surface swept by the valve periphery and the conical surface of the piston crown. The piston is located at the nominal TDC location.

The top surface of the cylinder head is meshed using two different techniques. The central section of the region (just below the valve window) is roughly rectangular, so it is meshed using a simple surface mesh as shown in figure 7.5c. The window has the dimensions of 85 mm $\times$ 34 mm, and was meshed using 30 $\times$ 20 nodes. The resolution was finer across the window to allow for better resolution of the valve motion as it sweeps across the head face.

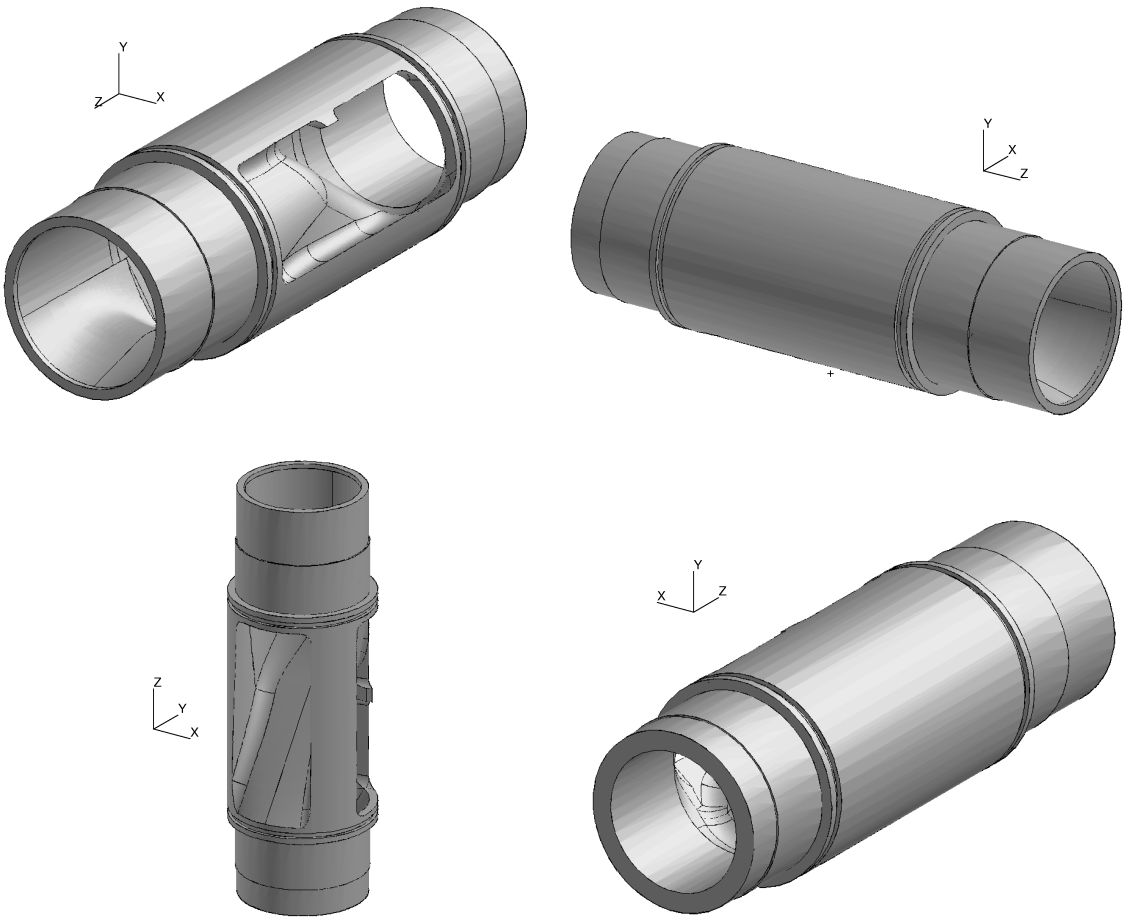

Figure 7.3: Various isometric views of the valve geometry, as originally imported.

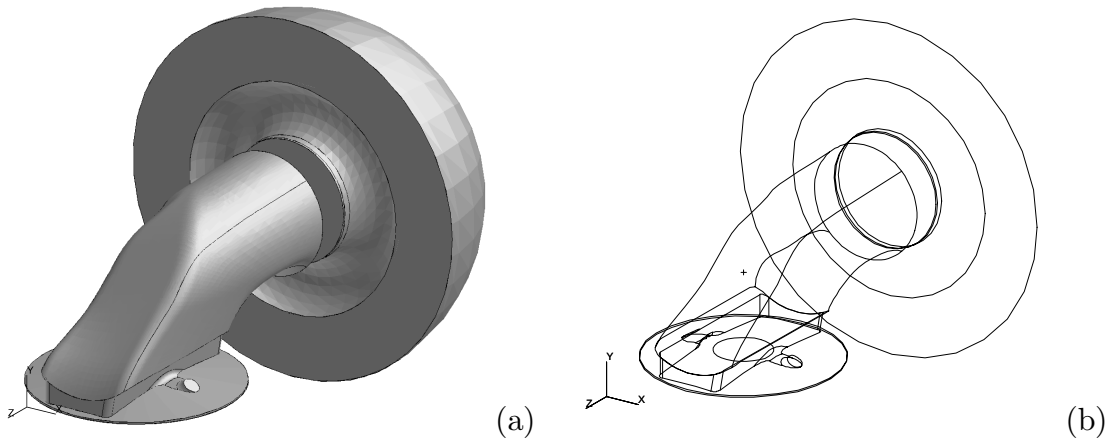

(a) (b)

Figure 7.4: Isometric view of the imported BRV engine geometry. (a) – Shaded view; and (b) – Wireframe view.

The outer section of the head was meshed using an unstructured grid, as shown in figure 7.5d. The target element length was set to 2 mm for this operation, so all nodes in this region will have edge lengths of approximately 2 mm. The nodes at the outer edge of the cylinder were then split radially, such that the nodes against the cylinder wall had an edge length of approximately 1 mm. This is shown as the outer nodes in figure 7.5d. The entire cylinder head top surface mesh is shown in figure 7.5e.

The mesh on the top surface of the cylinder head was then projected onto the piston crown, as shown in figure 7.6. The mesh was projected with 20 nodes between the top surface and piston crown surfaces. This technique allows the mesh to include cylinder head details such as spark plug cavities and piston crown shape. The piston was placed at BDC for this operation.

The cylinder and combustion chamber have now been meshed.

The mesh in the cylinder head at the valve window is shown in figure 7.7a. The shape of the window in the valve is not necessarily the same as the head window. This can be seen in figure 7.7b, which shows the equivalent mesh in the valve window. Note it is wider than the head window, and the edges of the window are not parallel. It is, however, still meshed with a 30×20 mesh.

The valve is modelled as a single block. The valve geometry is a complex three-dimensional shape, as shown in figure 7.8, so the surfaces defining this block are complicated. The throttle body and trumpet sections of the inlet manifold are circular in cross section, and so can be modelled easily. The domain is extended beyond the trumpet a short distance so as to allow modelling of the inlet manifold wave reflecting from the trumpet. The blocks used to model the valve, trumpet and domain outside the trumpet are shown in figure 7.9.

As previously mentioned, the window surface in the valve is roughly rectangular, as shown in figure 7.7b, and is meshed as a single rectangular surface. The other surfaces of the valve are more intricate, and smoothing was required to give a good quality mesh on these faces. An example of the mesh used on one side of the valve is shown in figure 7.10a, after the smoothing has been applied. The surface where the valve interfaces with the throttle block is shown in figure 7.10b, and is circular. It is meshed as a rectangular region due to the other end of the valve (that is the valve window, shown in figure 7.7b) also being meshed as a rectangle. This causes some distortion of the cells in the corners of this surface, but this can be minimised through mesh smoothing. Using multiple blocks to model the valve was found not to improve mesh quality as it resulted in mesh distortion nearer the valve window. The technique outlined here was found to be the best compromise.

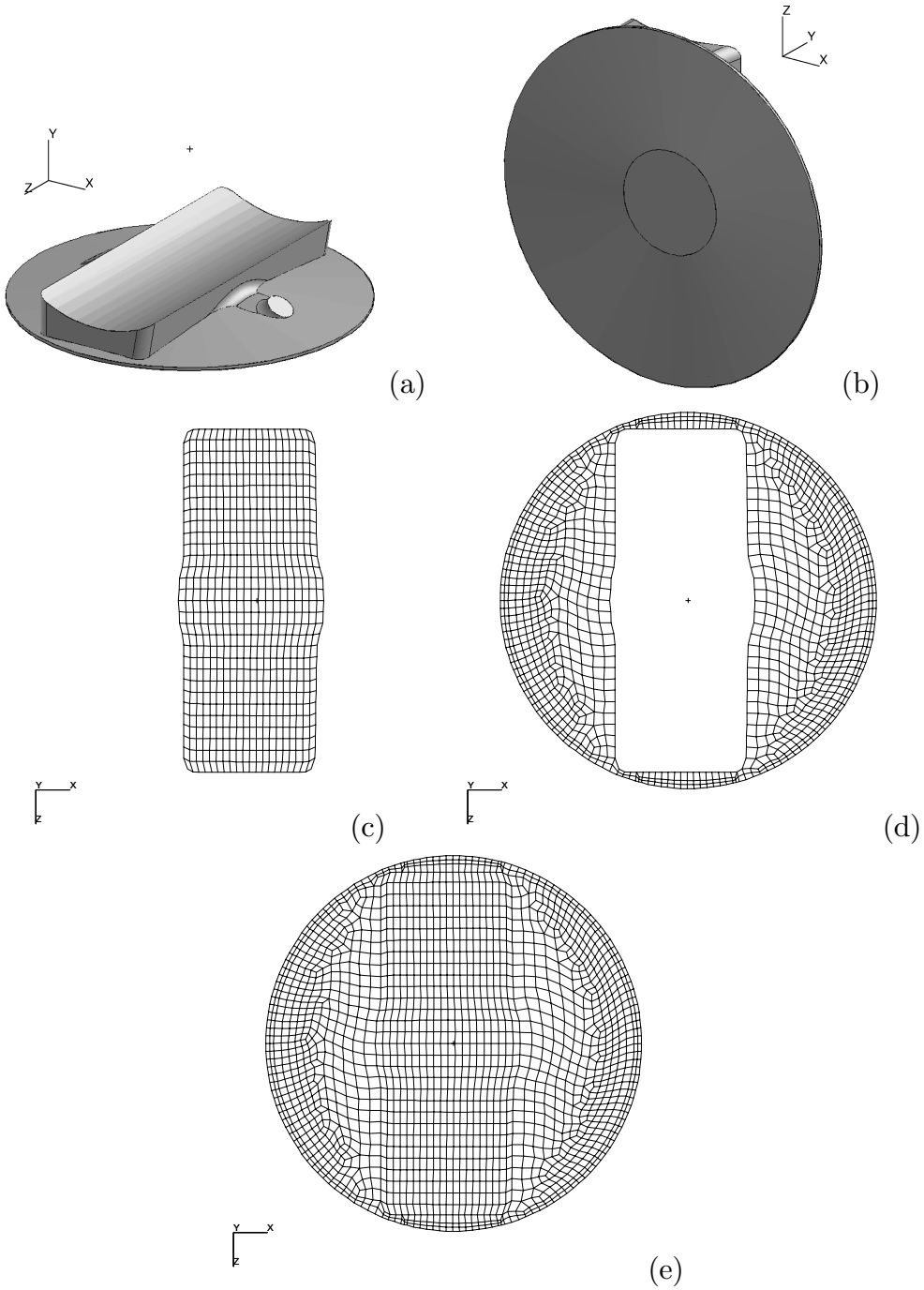

Figure 7.5: Cylinder head geometry meshing operations. (a) and (b) – Isometric views of the cylinder head surface as originally imported; (c) – Head mesh, rectangular section; (d) – Head mesh, unstructured section; and (e) – Complete head surface mesh.

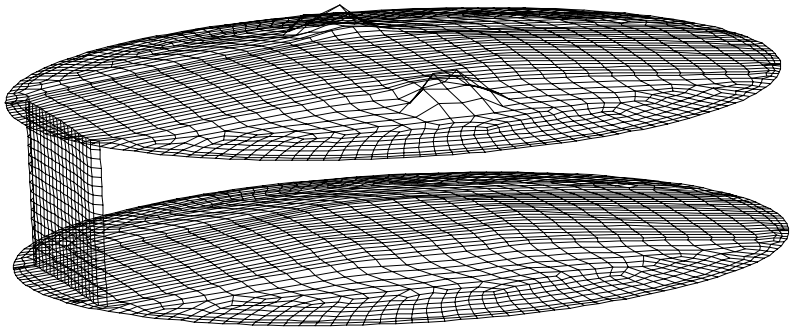

Figure 7.6: Cylinder head top surface mesh projected onto the piston crown.

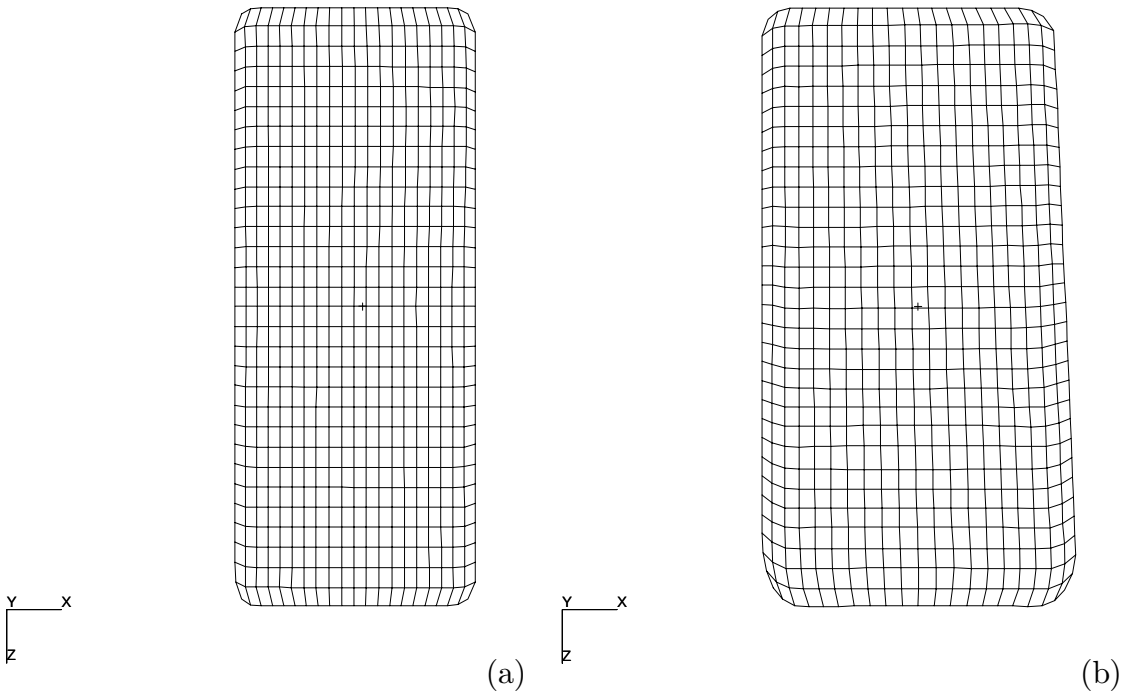

Figure 7.7: Mesh used in valve window. (a) – Mesh on cylinder head side; and (b) – Mesh on valve side.

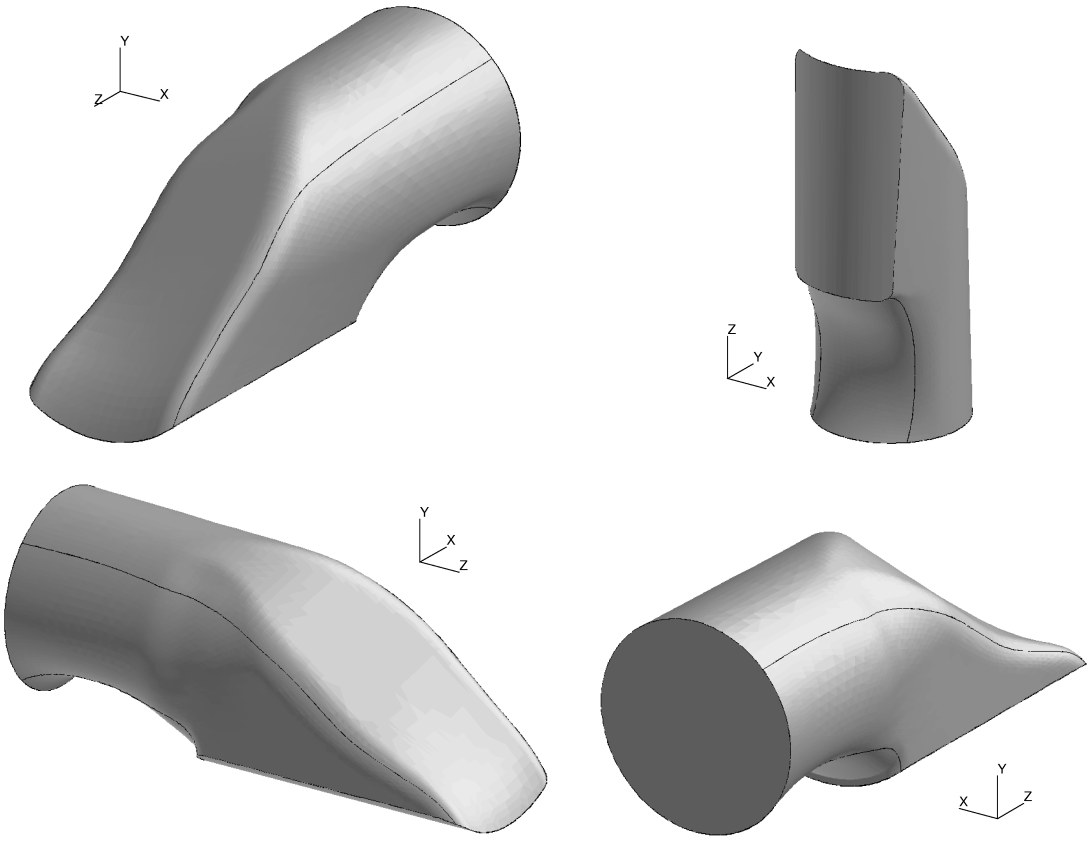

Figure 7.8: Isometric views of the valve surface geometry.

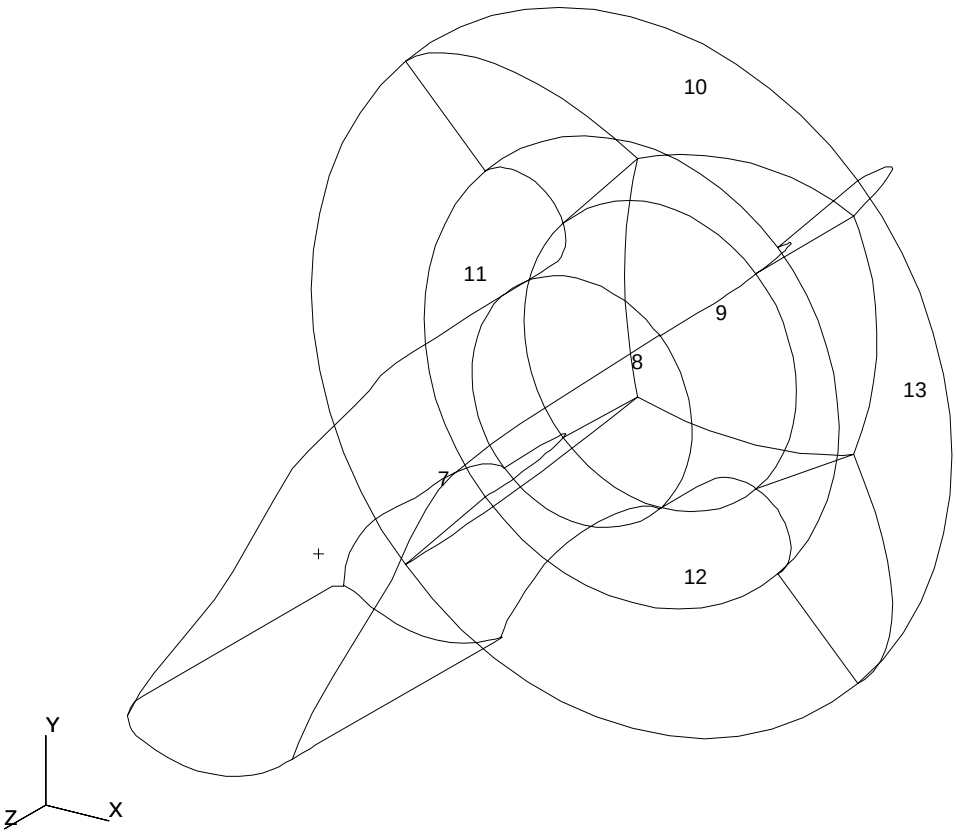

Figure 7.9: Isometric view of valve and inlet manifold blocks. The extension of the domain beyond the trumpet can be seen.

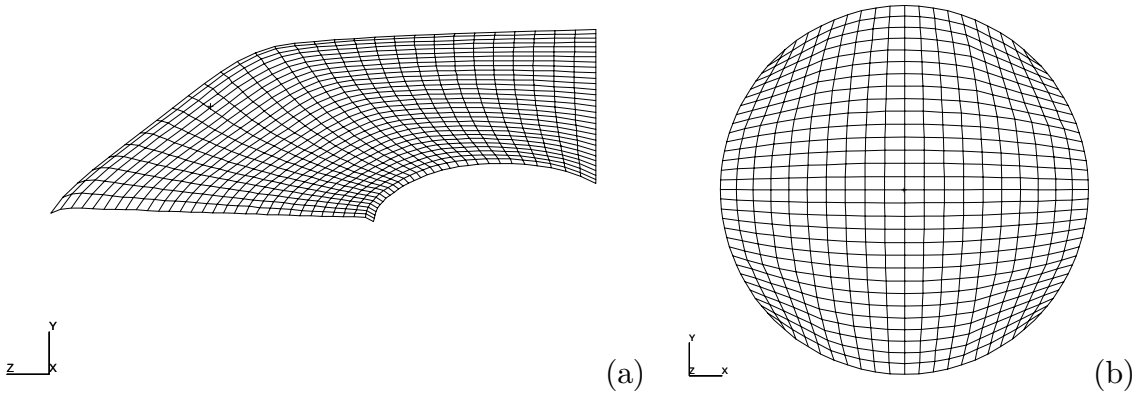

Figure 7.10: Example of mesh used in the valve. (a) – Mesh used on side faces; and (b) – Mesh used on throttle interface.

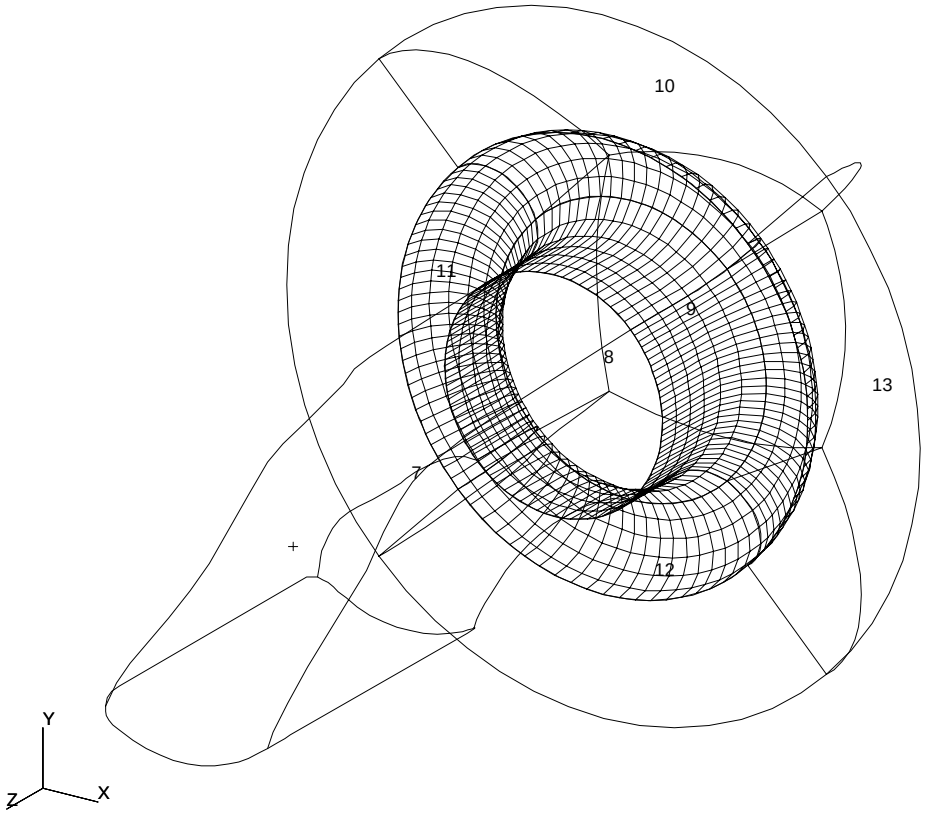

Figure 7.11: Meshing of the throttle and trumpet sections.

The remainder of the inlet manifold was meshed as a single block, with the end of the trumpet modelled as four blocks (as shown in figure 7.9). The meshing used for these blocks is shown in figure 7.12.

The meshing of the geometry is now complete. The final step of the processing of the geometry was to produce the "geometry file", which contains the grid information of the CFX solver. Since the grid consists of structured and unstructured regions, the grid needed to be "reblocked". This reblocking involves analysing the grid structure and attempting to define the geometry in as few blocks as possible, which helps convergence and reduces memory requirements over a non-reblocked grid.

Here, reblocking is used to make a structured grid of the unstructured section of the cylinder head, by defining it by many small blocks. Typically reblocking generated between 50 and 70 blocks. This means that some of these smaller blocks will only have $1 \times 1 \times 20$ nodes in them, but it was found that the good quality mesh resulting from this technique improved the convergence, and the large number of

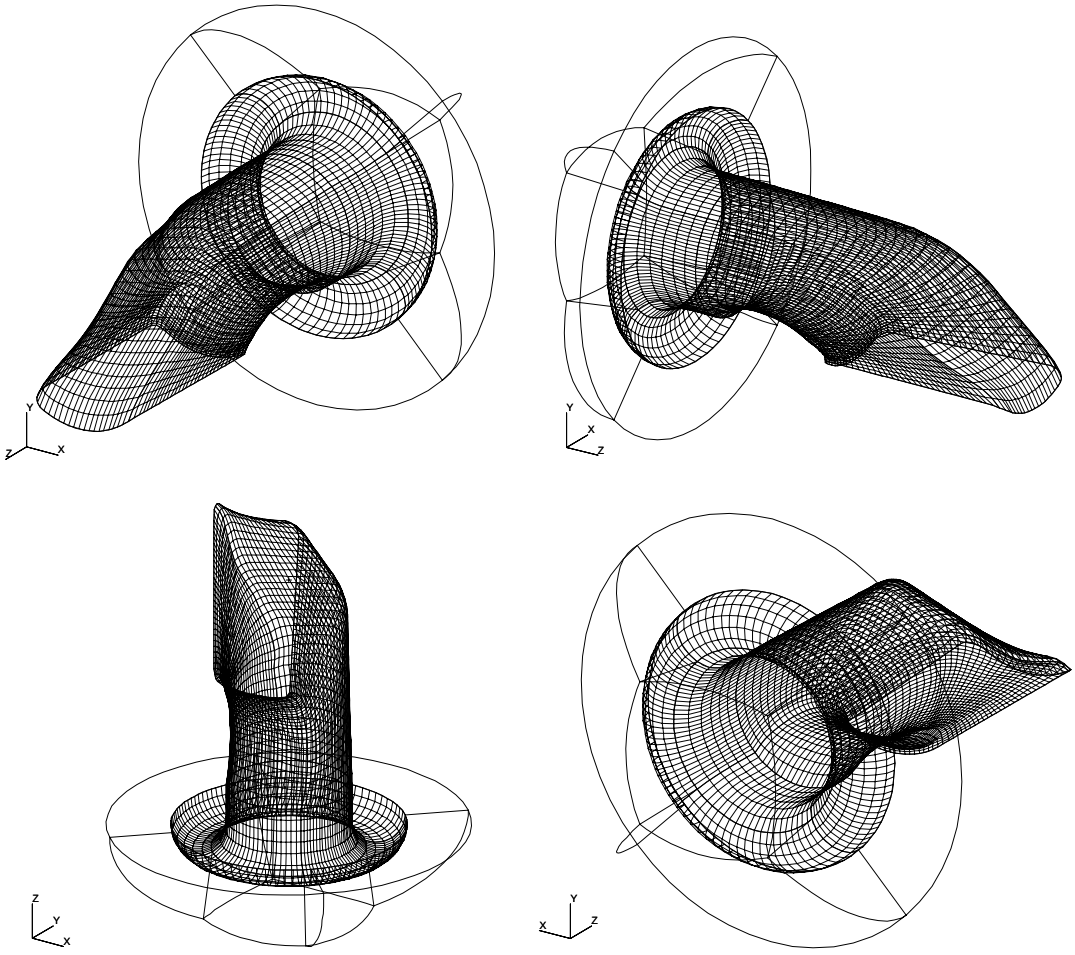

Figure 7.12: Various isometric views of the inlet manifold and valve mesh.

blocks did not reduce simulation speed excessively.

7.2.1 Mesh Motion

The motion of the grid was implemented using a fortran subroutine developed as part of this work, called from the CFX solver. Mesh motion is required to simulate the motion of the piston as it reciprocates and the valve as it rotates. The methodology used only a single geometry file (as developed in the previous section) for the entire run, and the mesh motion was defined as a transformation of the original geometry as a function of crank angle. The structure of this subroutine is:

1. Valve angle and piston displacement was defined as a function of crank angle;
2. The geometry file (from the previous section) is read from disk and loaded into memory;
3. A file, "blocks.txt" is read from disk which defines the type of transformation to apply to each block and how to apply it;
4. The nodes of each block are transformed according to the instructions from the "blocks.txt" file; and
5. The transformed node locations are written to memory for use by the CFX solver.

The two forms of mesh motion in the BRV engine simulation, being the piston motion and valve rotation, are imposed as different transformations of the geometry file. The transformations required to generate these motions will now be discussed.

Piston Motion

The configuration is shown in figure 7.13, where A is the stroke length, B is the conrod length and Θ_{CA} is the crank angle from TDC. If D is defined as the distance from the centre of the little end bearing of the conrod to the axis of rotation of the crankshaft, then it follows from figure 7.13 that

$$D = \frac{A\cos\Theta_{CA} + \sqrt{A^2\cos^2\Theta_{CA} - A^2 + 4B^2}}{2}. \tag{7.1}$$

The distance from the cylinder head surface to the piston crown surface, l, can now be specified as

$$l = B + \frac{A}{2} - D + D_{tdc}, \tag{7.2}$$

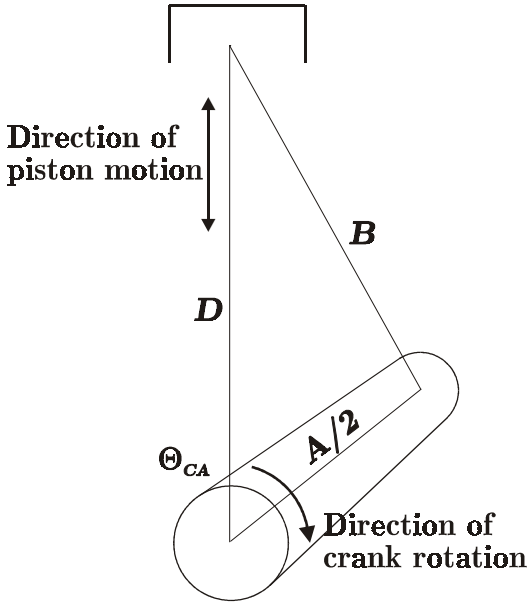

Figure 7.13: Definition of piston location against crank angle.

where D_{tdc} is the clearance of the piston crown to the cylinder head surface at TDC.

The cylinder node vertex transformation can now be expressed as

$$Y_t = \frac{(l + h + l_{geo})(Y_o + Y_{head})}{h} + Y_{head}, \tag{7.3}$$

in which Y_t is the transformed Y location of the node, Y_o the original Y location for the node as read from the geometry file (that is, at BDC), h is the distance from the piston crown to the head surface at that X and Z location in the geometry file, l_{geo} is the distance the piston crown has been projected from the head surface in the geometry file (as shown in figure 7.6), and Y_{head} is the Y location of the node on the head surface in the geometry file.

The X and Z location of the nodes in the cylinder do not change from the geometry file, that is

$$X_t = X_o, \text{ and} \tag{7.4}$$

$$Z_t = Z_o. \tag{7.5}$$

Valve Motion

The valve motion is a simple rotation transformation as a function of crank angle. The current angle of the valve, Θ_V, is defined as

$$\Theta_V = \frac{R\Theta_{CA}}{2} + \Theta_{offset}, \tag{7.6}$$

where Θ_{offset} is an offset angle used to define the phase of the rotor relative to the piston motion, and R determines the direction of rotation, and is either $+1$ or -1.

The transformation of the node locations is now

$$X_t = X_o \cos(\Theta_V) - Y_o \sin(\Theta_V), \quad (7.7)$$

$$Y_t = X_o \sin(\Theta_V) + Y_o \cos(\Theta_V), \text{ and} \quad (7.8)$$

$$Z_t = Z_o. \quad (7.9)$$

7.2.2 Valve Sliding Grid

This was the most complicated individual model added to CFX by the current author. It is an adaptation of the CFX existing "sliding mesh" routine to allow modelling of opening and closing ports. To the author's knowledge this is the only adaptation of the CFX-4.3 code to modelling this type of inter-block boundary condition.

Before the work done to allow CFX to model opening and closing ports is described, a brief description of the existing sliding grid model in the CFX code will be presented.

Existing Sliding Grid Modelling

The existing sliding mesh capability in CFX-4.3 is designed to be able to model flows with rotating components, such as a pump impeller [13]. The pump impeller is meshed with one mesh, and the volute is meshed with a second mesh, and the interface between these two meshes is modelled with a sliding mesh interface. This type of interface has a number of restrictions [13]:

1. At all times during the simulation, the nodes on both sides of the sliding interface must be in contact;
2. If any node looses contact with nodes on the opposite side of the interface the simulation the run stops and gives an error message;
3. The mesh motion must be finely resolved; and
4. Only first order advection discretisation is performed over the interface.

Restrictions 1 and 2 mean it is not possible to model a valve sliding shut with the sliding grid model as supplied with CFX, as this involves nodes leaving the sliding grid interface and becoming walls. Restriction 3 is not transgressed in this

case as the time steps used will already be sufficiently small due to the stricter requirement to resolve the mesh motion. Restriction 4 means that, regardless of which discretisation scheme is used globally, only first order differencing is used across the interface. This is not a major drawback as the lowered accuracy of a first order scheme is only applied in a small region of the flow field.

New Sliding Port Model Development

In the development of the model presented here, a sliding mesh boundary was developed in CFX-4.3 which allows modelling of a valve sliding shut. The methodology used is based on modelling the valve motion in many small steps, with each step being a separate run of CFX and using the previous run as an initial condition.

It is based around the following procedure:

1. At the start of the run, determine current crank angle and valve angle;
2. Loop over all cells on the valve block to determine which nodes line up with nodes in the head block;
3. Loop over all cell centres on the head block which have not already been determined as matching in step 2, and determine which additional nodes line up with nodes in the valve block. Add any nodes found to the list from step 2;
4. Reblock the valve window nodes and head window nodes;
5. Set the valve and head window nodes as normal CFX-4.3 sliding grid interfaces, set the remaining nodes as wall boundaries;
6. Perform simulation for a short period of time using this mesh topology; and
7. Stop the simulation before nodes across the sliding interface leave contact. Restart the simulation at step 1, incrementing the crank and valve angle.

When this procedure was first implemented it suffered from poor convergence and unexpected crashes. After contacting the CFX support staff, it was determined that the value of the variables in the dummy nodes in the new wall nodes after a restart was causing the instability, and was easily rectified by setting the value of all variables in the dummy nodes at walls to zero at each time step. This was found to fix the problem.

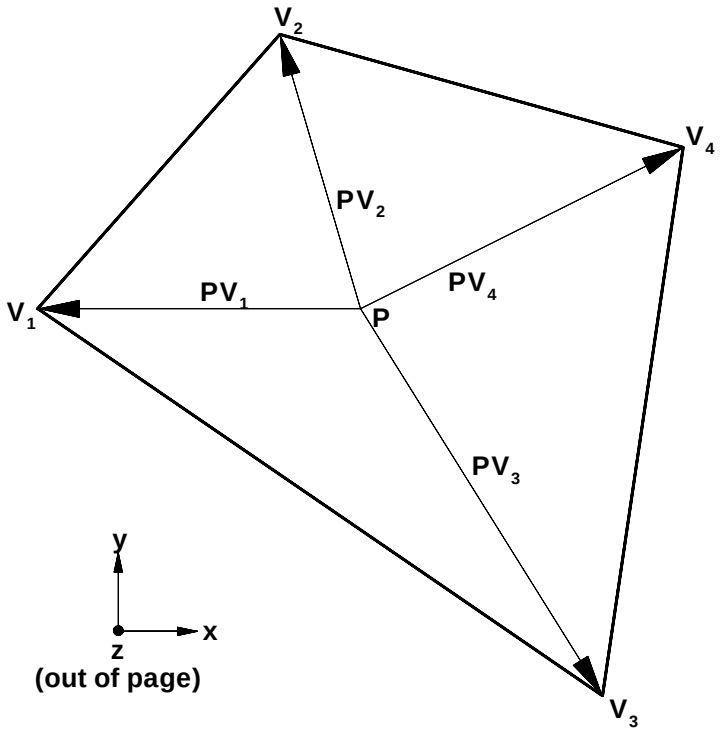

Figure 7.14: Definition of terms to determine if point P is in quadrilateral $V_1V_2V_3V_4$.

This procedure requires a number of new sub-procedures, firstly to determine matching nodes at the interface (step 2 and 3), and secondly the manual reblocking step (step 4).

Matching Node Determination A fundamental element of the procedure was the requirement for a computationally fast routine for determining whether a node lay inside or outside a cell element on the other side of the interface.

As the valve window sweeps out a two-dimensional surface, the problem can be simplified to whether a point lies inside a two-dimensional quadrilateral, defined by its four corner points. Consider the geometry shown in figure 7.14. A quadrilateral is defined by the four vertices V_1, V_2, V_3 and V_4. The vertices must be specified in the order shown in figure 7.14, and it must be a simple quadrilateral (that is lines V_1V_2, V_2V_4, V_4V_3 or V_3V_1 must not cross). Point P is a point anywhere on the plane. Vectors from P to all four vertices are generated, $\overrightarrow{PV_1}$, $\overrightarrow{PV_2}$, $\overrightarrow{PV_3}$ and $\overrightarrow{PV_4}$.

If the point P is inside the quadrilateral, it must lie between lines V_2V_4 and V_1V_3, and lines V_1V_2 and V_3V_4 simultaneously. Thus the problem can been broken down

into establishing whether point P is between two sets of lines.

If two non-parallel vectors are on the same plane, their cross product will be perpendicular to that plane. The magnitude of the cross product is a function of the vector magnitudes and their relative angle. However, the direction of the cross product must be either normal to the plane and in one of two directions (nominally called "up" and "down"), and the direction is purely dependant on whether the angle swept from the first vector to the second is clockwise or anti-clockwise.

The fact that the cross product allows the determination as to whether the angle swept between two vectors is clockwise or anti-clockwise allows a simple test for determining whether a point is between two lines.

If the angle swept from $\overrightarrow{PV_2}$ to $\overrightarrow{PV_1}$ is anti-clockwise (as it is in figure 7.14), the cross product $\overrightarrow{PV_2} \times \overrightarrow{PV_1}$ will have a k component which is positive. Conversely if the angle is clockwise, the cross product will have a negative k component. For the point P to be between lines V_1V_2 and V_3V_4, the direction of rotation from $\overrightarrow{PV_2}$ to $\overrightarrow{PV_1}$ and the rotation from $\overrightarrow{PV_4}$ to $\overrightarrow{PV_3}$ must be in opposite directions. In other words, the sign of the k component in $\overrightarrow{PV_2} \times \overrightarrow{PV_1}$ and $\overrightarrow{PV_4} \times \overrightarrow{PV_3}$ must be different.

This considerably simplifies the calculation since the only non-zero component is in the k direction, so i and j components in the cross product need not be calculated.

Similarly, for the point P to lie between lines V_2V_4 and V_1V_3, the sign of the k component of $\overrightarrow{PV_2} \times \overrightarrow{PV_4}$ and $\overrightarrow{PV_1} \times \overrightarrow{PV_3}$ must be different.

If point P lies between the lines V_1V_2 and V_3V_4; and lines V_2V_4 and V_1V_3 simultaneously, then the point P lies in the quadrilateral $V_1V_2V_3V_4$.

Thus the test for whether point P lies in quadrilateral $V_1V_2V_3V_4$ can be performed by:

1. Evaluate the vectors $\overrightarrow{PV_1}$, $\overrightarrow{PV_2}$, $\overrightarrow{PV_3}$ and $\overrightarrow{PV_4}$;
2. Evaluate the k component only of the cross products $\overrightarrow{PV_2} \times \overrightarrow{PV_1}$, $\overrightarrow{PV_4} \times \overrightarrow{PV_3}$, $\overrightarrow{PV_1} \times \overrightarrow{PV_3}$ and $\overrightarrow{PV_2} \times \overrightarrow{PV_4}$. This can be called $\left(\overrightarrow{PV_2} \times \overrightarrow{PV_1}\right)_k$, $\left(\overrightarrow{PV_4} \times \overrightarrow{PV_3}\right)_k$, $\left(\overrightarrow{PV_1} \times \overrightarrow{PV_3}\right)_k$ and $\left(\overrightarrow{PV_2} \times \overrightarrow{PV_4}\right)_k$;
3. If $\left(\overrightarrow{PV_2} \times \overrightarrow{PV_1}\right)_k * \left(\overrightarrow{PV_4} \times \overrightarrow{PV_3}\right)_k < 0$ and $\left(\overrightarrow{PV_1} \times \overrightarrow{PV_3}\right)_k * \left(\overrightarrow{PV_2} \times \overrightarrow{PV_4}\right)_k < 0$ then P is inside the quadrilateral[1]. If either equals zero and the other equals zero or is less than zero then P lies on the edge of the quadrilateral.

The code used to perform this operation in the simulations is listed in appendix A.1. This is a very effective method of determining whether the point is in the

[1]The symbol "$*$" is used here to represent the multiplication of two scalars. This is done to avoid confusion with the vector cross product.

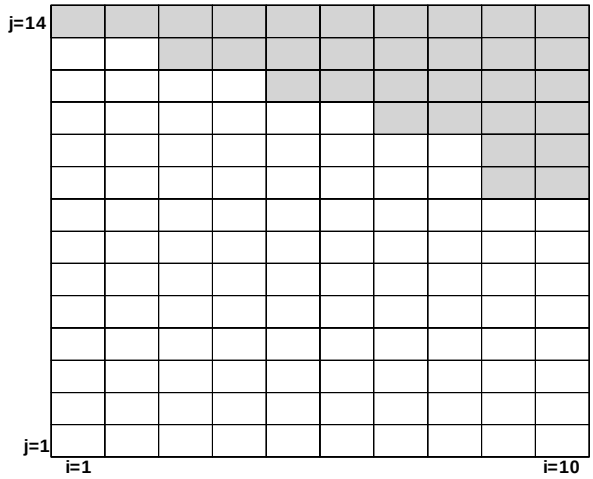

Figure 7.15: Example mesh after node state has been determined.

quadrilateral as the entire routine only needs 22 floating point operations, two "`if`" statements and a boolean operation. This small number of operations is desirable because the routine is called several hundred times each time a new simulation step is performed.

Manual Reblocking Figure 7.15 shows a generalised diagram of the node states after step 3 of the sliding mesh sequence from section 7.2.2. As an example of the methodology of the routine, a small rectangular block with 10×14 nodes will be reblocked, but the process described here is generalisable to any shape of domain. The example geometry presented here is rectangular only for simplicity.

In figure 7.15, the white nodes represent nodes which have been identified by the technique in the previous section to be sliding mesh inter-block boundary nodes, and the grey shaded nodes represent nodes which are to be wall boundary nodes. If the geometry was delivered to CFX in this form, this single surface would have 140 individual boundary conditions on it. This uses a large amount of additional memory and slows the solver due to the additional book-keeping required. To increase the efficiency of the solver it is necessary to manually reblock this region so that the large number of single node boundary conditions are specified as a smaller number of multiple node boundary conditions.

All boundary conditions in CFX must be specified as a rectangular range of nodes, for instance from $i = 5$ to $i = 8$; and $j = 3$ to $j = 6$ specifies a region with 4×4 nodes. This region could be specified as a single boundary condition.

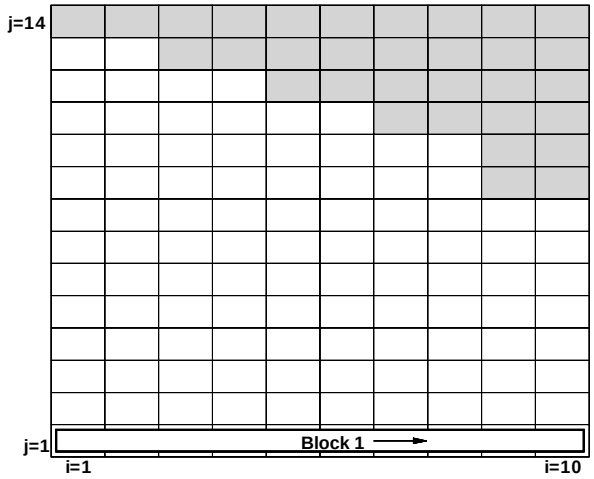

Figure 7.16: The first step in reblocking the window, extending the block in the i direction.

This was performed using a reblocking fortran subroutine, whose logic runs as follows. The first step is to find the first node to be reblocked. This is performed in a nested "`do`" loop checking each i and j location on the surface. In the example in figure 7.15, the first window node is node $(i = 1, j = 1)$. This location is set as the start of the first block.

The second step is to increment the block in i until either it spans the entire width of the block or it reaches a node which is not to be reblocked. This is shown in figure 7.16, where the new block has been extended to $i = 10$, the end of the block.

The third step is to increment the block in the j direction, again until it either spans the entire width of the block or it reaches a node which is not to be reblocked. Note that in this case the check must be performed at every i location along the block as the j is incremented. After this has extended as far as possible, the end of the first block can be determined. In this case, block one extends from $(i = 1, j = 1)$ to $(i = 10, j = 8)$.

This sequence must be repeated a number of times until all nodes are reblocked. Figure 7.18 shows the block after it has been completed. The reblocking has reduced the number of window boundary condition blocks from the original 108 to 5. This is a far more reasonable number of boundary conditions for the solver.

The wall section of the window is also reblocked. In this example this gives an additional 5 blocks, as shown in figure 7.19.

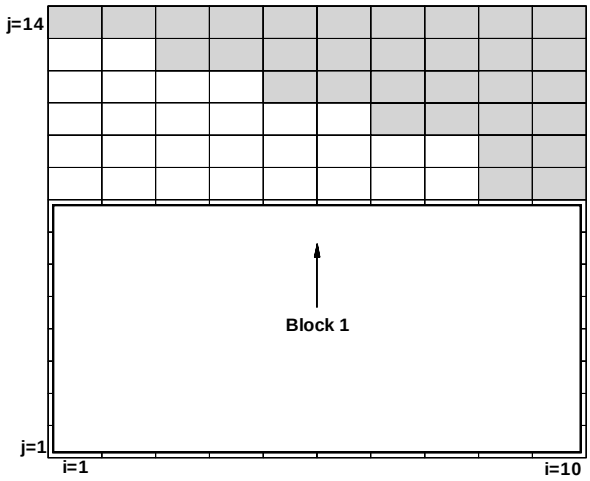

Figure 7.17: The second step in reblocking the window, extending the block in the j direction.

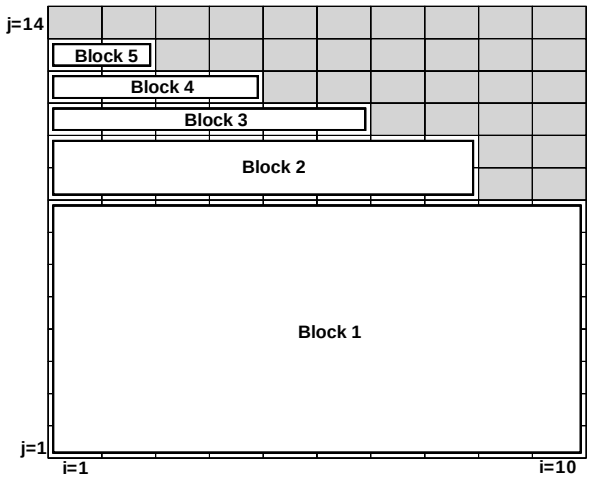

Figure 7.18: The window section completely reblocked.

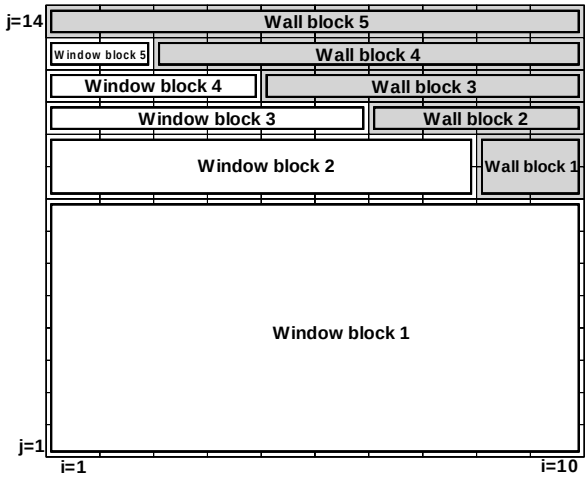

Figure 7.19: The region after both window and wall reblocking.

The fortran subroutine used to implement this method is listed in appendix A.2.

7.3 Parameters Used in BRV Simulation

7.3.1 "Two Cycle" Simulation

A number of researchers have investigated the effects of previous cycles on engine simulations, however the only published simulations modelling more than one engine cycle in three-dimensions are for moderate speed engines [181, 258]. No publications could be found analysing previous cycle effects in high performance engines, despite the fact that it will have a significant effect on results, as discussed in section 4.3.

Due to the well known dependence of results on previous engine cycles, the simulations presented here will be of two engine cycles. The structure of the simulation is shown diagrammatically in figure 7.20.

The simulation starts at TDC of the intake stroke with assumed initial conditions of atmospheric pressure, 278 K, a scalar concentration of 0.0, a turbulence intensity of $1\,m^2\,s^{-2}$, and a turbulent dissipation of $10\,m^2\,s^{-3}$ in the inlet manifold; and 81 kPa, 700 K, a scalar concentration of 1.0, a turbulence intensity of $50\,m^2\,s^{-2}$, and a turbulent dissipation of $500\,m^2\,s^{-3}$ in the cylinder. These initial conditions are approximations of the true conditions. It has already been shown that the turbulence initial condition is not important in section 6.4; and the temperature and pressure initial conditions will be shown in section 8.2 to have little effect on the

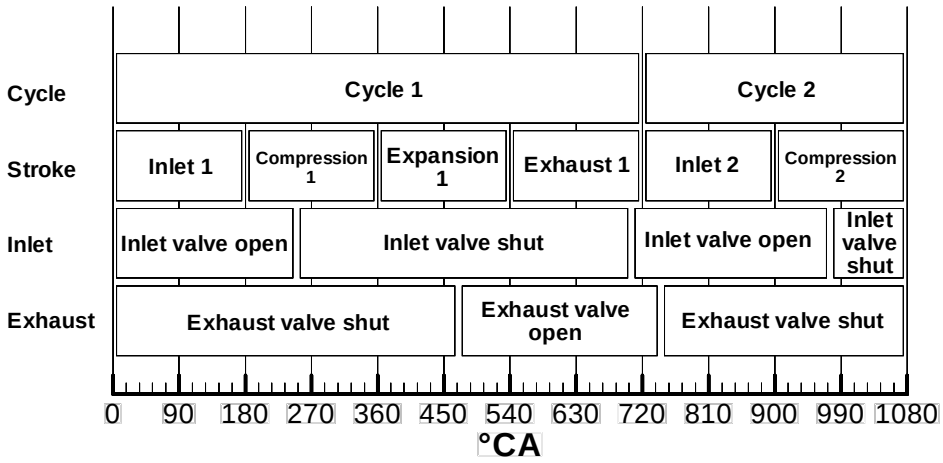

Figure 7.20: Diagram of engine strokes for the BRV engine simulation.

results of the second cycle of the engine. Thus, the approximate values given above were considered adequate for the initial conditions.

Even though in the engine the exhaust valve would normally be open for a short time after TDC of the intake stroke, the exhaust valve is assumed shut initially for the first intake stroke. The first intake stroke is only establishing the conditions for the remainder of the simulation, and the small amount of exhaust flow that would occur is not significant.

The simulation continues through the inlet and compression strokes. Combustion is not modelled. However, the effects of combustion on the gas exchange process are modelled by changing the state of the cylinder gas, just before the exhaust valve opens, to the experimentally measured cylinder pressure and an estimated cylinder gas temperature. This occurs at 460 °CA, where the cylinder pressure was set to 954 kPa the temperature set to 1714 K and the scalar concentration set to 1.0. This pressure was measured experimentally on the dynamometer, and the temperature was estimated from the work on similar engines by Bianchi et al [41].

The exhaust stroke starts shortly afterwards, and the exhaust valve opens. The exhaust valve was assumed be a constant pressure outlet on the head window, where the imposed pressure was the measured pressure in the exhaust manifold from the dynamometer. This allows gas to exit the cylinder in similar fashion to the real exhaust valve, however it does not allow pressure variation across the exhaust.

The inlet valve opens shortly before TDC of the exhaust stroke, and the exhaust valve shuts shortly afterwards, so the scavenging section of the inlet and exhaust strokes can be simulated. The second intake stroke is then modelled, followed by

the second compression stroke. It is the second inlet and compression strokes that are of most interest as they include the effects of the previous cycle on the inlet manifold pressure wave and in-cylinder conditions.

7.3.2 Fluid Parameters

The universal gas constant used was $8.314\,\mathrm{J\,mol^{-1}\,K^{-1}}$, the laminar viscosity of air was set to $1.835 \times 10^{-5}\,\mathrm{Pa\,s^{-1}}$, the thermal conductivity was set to $2.609 \times 10^{-2}\,\mathrm{W\,m^{-1}\,K^{-1}}$, the specific heat capacity $1005\,\mathrm{J\,kg^{-1}\,K^{-1}}$, and the molecular mass of air was set to $28.97\,\mathrm{kg\,kmol^{-1}}$.

As discussed in section 6.8, the k-ϵ model was used (section 2.3.4) to model the turbulence. Large eddy simulation (LES) techniques were unsuitable due to the requirement for high density grids, which was beyond the capacity of available computing resources for a real engine geometry. Reynolds stress turbulence models were not used, despite the promising results of chapter 6. This is because the RSM model is difficult to use in complicated geometries, such as an engine. No RSM turbulence model had successfully converged on a BRV engine simulation. This leaves the k-ϵ model as the best model available. Despite its shortcomings, it has been widely used and validated in engines [137].

7.3.3 Exhaust Gas Scalar

A scalar was used as a simple method of approximately tracking the motion of the exhaust gas in the cylinder during scavenging. The diffusion between exhaust gas and intake charge in a real engine has only a small effect due to the very short time available for mixing. Therefore it was decided to use a scalar with no diffusivity.

In CFX it is not possible to model a scalar with zero diffusivity. The figure of $10^{-6}\,\mathrm{kg\,m^{-1}\,s^{-1}}$ was chosen as a diffusivity coefficient so low as to cause negligible diffusion. A log layer constant and sublayer thickness also needs to be specified. The exact values of the log layer constant and sub-layer thickness are not important here as the diffusivity is set sufficiently low so that no significant boundary layer effects occur. The log layer constant was set at 10^{-3} and the sub-layer thickness was set to 10^{-3}.

7.3.4 Wall Boundary Conditions

The wall temperatures used are listed in table 7.1. The temperatures used are estimates of the temperatures from the real engine.

Wall Surface	Temperature
Cylinder	423 K
Head	423 K
Piston face	423 K
Interior surfaces of the valve	353 K
Valve surface exposed in head	353 K
Trumpet	283 K

Table 7.1: Surface temperatures used for various engine components.

Equation	Differencing Scheme	Under Relaxation	Linear Solver	RFC	$i_{\min}$	$i_{\max}$
Velocity	Van-Leer	0.65	Block Stone	0.25	1	5
Pressure	Hybrid	1.0	General AMG	0.1	3	30
k	Van-Leer	0.7	Line relaxation	0.25	1	5
ϵ	Van-Leer	0.7	Line relaxation	0.25	1	5
Enthalpy	Van-Leer	1.0	Block Stone	0.1	1	30
Exhaust Gas	Van-Leer	1.0	Block Stone	0.1	1	30
Temperature	n/a	1.0	n/a	n/a	n/a	n/a
Density	n/a	0.3	n/a	n/a	n/a	n/a

Table 7.2: Convergence parameters used for BRV engine simulations.

7.3.5 Convergence Parameters

The reference pressure used was 101.3 kPa and the reference temperature 288 K. The various differencing schemes selected for the various equations are listed in table 7.2. The range of under relaxation, linear solvers, reduction factors (RFC), minimum iterations ($i_{\min}$) and maximum iterations ($i_{\max}$) used are also shown in table 7.2. Refer to section 3.2.3 and 3.2.6 for definitions of these terms. Most of these values used are the default values of the CFX solver, and were found to be close to optimum for the simulations performed in this work.

Deferred Correction

The ϵ equation was found to be prone to divergence during the exhaust stroke due to the large velocity and pressure gradients present. To aid convergence during this phase, deferred correction was used to remove the effect of the cross derivative diffusion term in the epsilon equation. The effect of removing this term was tested and found to have a negligibly small effect on the final solution. This is to be expected since, in most flows, the epsilon equation is dominated by production, dissipation, advection and normal diffusion.

Deferred correction was only required at the start of the simulation and during the exhaust stroke when very high property gradients were encountered. It was turned off, that is the full equations were solved, for the second intake and compression strokes.

Cylinder Parameters

Cylinder Mass The mass of gas in the cylinder was calculated by numerically integrating over the cylinder blocks. This was done by summing the product of the density and volume at each node.

Other in-cylinder averaged quantities, such as mass averaged turbulence or velocity squared were calculated similarly. The technique used was to sum the product of density, volume and the variable in question at each node, then to divide the final quantity by the cylinder mass.

Valve Mass Flow Rate The valve mass flow rate is calculated from the change in the cylinder gas mass per unit time, that is, the cylinder mass numerically differentiated with respect to time. The differential was calculated using a first order backward differencing scheme. Second order central differencing was tested for calculating flow rates, and found to make negligible difference to results.

7.4 Validation of BRV CFD Model

An analysis of the air flows in the BRV engine using PIV, LDA or any other flow visualisation technique was beyond the scope of the current work. Thus, validation of the BRV CFD model was performed based on quantities which were measurable with the available equipment, that is pressure sensors, air flow and engine *IMEP*.

7.4.1 Description of Dynamometer Facility

The dynamometer system used for the experimental testing of the BRV engine was developed and operated by the staff of the BRV project at Bishop Innovation. The current author had no direct role in performing the dynamometer tests, however its results were used as the experimental data to which the numerical simulations performed as part of this work are compared.

The dynamometer facility is a Schenck test cell and dynamometer. It has a rated maximum engine speed of 18000 rpm. The retarder in the dynamometer is an AMK

AC retarder motor. The test cell is environmentally controlled, and includes an air-conditioning and steam injection unit to provide air to the engine at 101.4 ± 1 kPa, 25 ± 1 °C and $30 \pm 5\%$ relative humidity. The humidification unit can only increase humidity with steam injection, and has no capability of drying the air. This means with Sydney's warm and humid climate, the test cell humidity often climbed above the specified 30%.

The data acquisition uses AVL high speed and low speed data acquisition systems and is computer controlled. The overall system has an estimated repeatability of 0.25% for torque measurement, and ± 5 rpm for speed.

The air consumption of the engine is measured using a Sensyflow model P hot film air mass flow meter, made by Sensycon Hartmann and Braun. It is specified to have an accuracy of better than 2% of measured value. Temperature sensors are Platinum resistive temperature devices (RTD) with accuracy rated to better than ± 1 °C, and pressure sensors are piezoresistive strain gauge bridge type of varying specifications. Cylinder pressure was measured by a variety of piezoelectric Kistler pressure sensors.

7.4.2 Time Step Size

The effect on the simulation results of the size of the time step used was tested by performing an intake stroke of the simulation with time steps of 0.1 °CA, 0.25 °CA and 0.5 °CA. The results of this test are shown in figure 7.21.

All results shown in figure 7.21 show the 0.1 °CA and 0.25 °CA time step simulations give essentially the same results, and some small but noticeable differences occur for the 0.5 °CA simulation. The mass averaged turbulence (figure 7.21a) shows that the maximum difference between the simulations occurs near 50 °CA, where the 0.5 °CA time step simulation differs by 5% from the 0.1 °CA time step simulation, and the 0.25 °CA differs by only 0.3%. By the end of the simulation at 180 °CA the maximum difference between all three simulations is 0.5%.

The mass averaged velocity squared is shown in figure 7.21b. It shows that the 0.5 °CA simulation differs from the 0.1 °CA by 3% at 180 °CA, whereas the 0.25 °CA time step simulation differs by only 0.5%. The cylinder gas mass (figure 7.21c) shows even less variation between the simulations, the maximum deviation between the simulations being 0.3%. The tumble ratio (figure 7.21d) shows the 0.5 °CA time step simulation is predicting a small amplitude wave to be superimposed on the result. As the intake stroke progresses the agreement remains good—by 180 °CA, the 0.5 °CA time step simulation differs from the 0.1 °CA time step simulation by

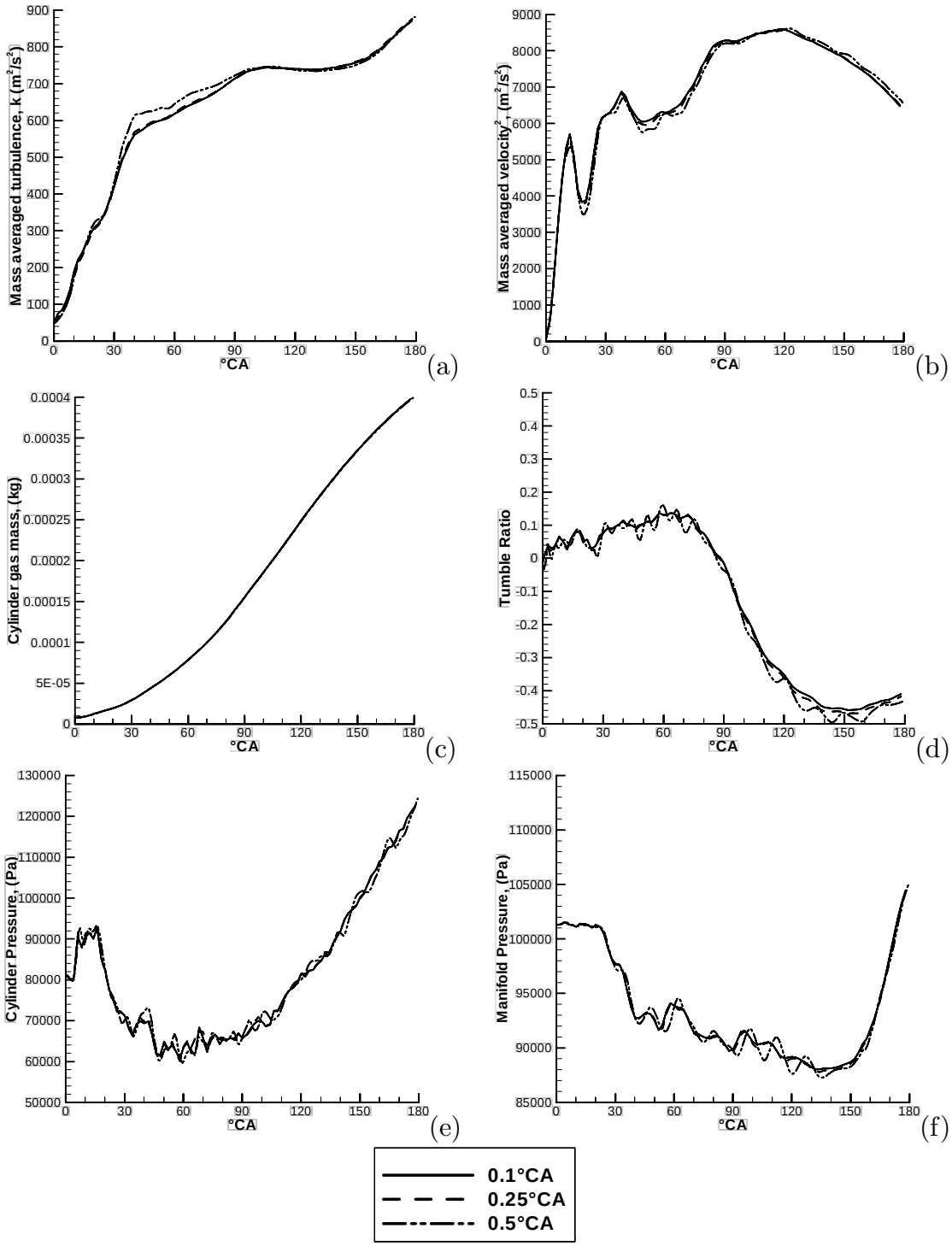

Figure 7.21: The effect of time step size on simulation results. (a) – Mass averaged turbulence (k); (b) – Mass averaged velocity squared; (c) – Cylinder gas mass; (d) – Tumble ratio; (e) – Cylinder pressure; and (f) – Pressure in the inlet maifold, 120 mm from the centre of the window.

6%, whereas the 0.25 °CA simulation differs by only 2%.

The pressure predicted in the cylinder is shown in figure 7.21e. Again, all simulations are predicting the same trends, however the 0.5 °CA simulation shows a wave superimposed with an amplitude of around 5 kPa. Figure 7.21f shows the pressure in the inlet manifold 120 mm from the centre of the window and 35 mm from the end of the trumpet. It also shows all simulations predicting the same trends, however the 0.5 °CA simulation also has a wave superimposed on it with an amplitude of about 3 kPa.

All time step sizes predicted the same result within a few percent for all parameters, however the 0.5 °CA simulation predicted a spurious small amplitude wave on the pressure results. As the coarser time step simulations use far less computer time, a 0.5 °CA time step was used for the first intake, compression, expansion and exhaust strokes. The second intake and compression strokes used a 0.25 °CA time step to increase accuracy. The majority of results are taken only from the second intake and compression strokes.

The sliding port boundary condition described in section 7.2.2 requires frequent restarts so that the window region can be remeshed. Remeshes during the intake stroke were performed at 3 °CA increments. Remeshes during the exhaust stroke were performed at 6 °CA increments. Remeshing is not required during the compression and expansion strokes.

The CFL stability criterion (equation 5.10) was found not to be a major restriction in this simulation. This is due to the implicit solution technique which means CFL number is not a fundamental stability criterion. This stability criterion is only applicable to explicit simulation techniques, high Mach number flows, and some other complex simulations such as free surface modelling and combustion.

7.4.3 Inlet Manifold Pressure

In early designs of the BRV engine the inlet manifold was quite long, and there was enough space to mount a pressure sensor in the inlet manifold just outside the rotating section of the valve. This allowed the inlet manifold pressure variations to be measured. A CFD model, recording the pressure at the same position was developed, and the results are shown in figure 7.23.

Two sets of CFD results are shown in figure 7.23. The fine mesh result is based on a mesh using 62967 cell vertices, and coarse mesh result is based on a 16302 cell vertex mesh. This equates to roughly halving the number of nodes in each of the three axes of each block. The cross-sections of the coarse (16302 cells) and fine

(62967 cells) meshes used are shown in figure 7.22 for the cross tumble, tumble and swirl planes.

As can be seen in figure 7.23, the agreement between experimental and both numerical simulations between 240 °CA and 700 °CA is excellent. Both models capture the shape, wavelength and decay of the fundamental wave with excellent accuracy. However, both CFD simulations show a small high frequency variation which is not seen in the experimental results, with the coarse mesh showing this spurious frequency most strongly. The fact that the CFD models fail to predict the behaviour before 240 °CA is due to the initial conditions of the CFD model, being zero velocity and atmospheric pressure at TDC at the start of the intake stroke. As the closing of the inlet valve is the "trigger" that starts the inlet manifold wave, from this point on the results are largely independent of the initial conditions. The inlet manifold is effectively a pipe with one end open to the atmosphere, and the other closed. It does not interact with the cylinder or exhaust systems during this time. During this part of the simulation the CFD model shows good agreement with the experimental data.

There is also a significant deviation from the experimental results after 700 °CA, however this variation is due to the re-opening of the inlet valve, and the inlet manifold pressure wave will then be affected by the cylinder conditions. It is difficult to accurately estimate the cylinder conditions at the start of the inlet stroke, so the variation seen in figure 7.23 is likely to be caused by an inaccurate estimate of in-cylinder initial conditions.

7.4.4 Mesh Refinement Study

As has been shown in section 7.4.3 and figure 7.23, the coarse and fine mesh simulations of the BRV engine give very good predictions of the flow in the inlet manifold. Figure 7.24 is a further comparison of fine and coarse mesh simulation results, this time for in-cylinder flow during the intake stroke.

The results shown in figures 7.24a to 7.24e are parameters that are based on the fluid velocity or state, and all show good agreement between coarse and fine meshes. For instance, the cylinder gas mass predicted by the fine mesh at 240 °CA is 4.54×10^{-4} kg, whereas the coarse mesh predicts 4.6×10^{-4} kg, a reduction of 1%; and the mass averaged velocity squared predicted by the fine mesh at 240 °CA is $3635\,\mathrm{m^2\,s^{-2}}$, whereas the coarse mesh predicts $3536\,\mathrm{m^2\,s^{-2}}$, a reduction of 3%.

We can conclude that the pressure and velocity fields predicted by the two meshes are similar, and appear to be mesh density independent. However, there is

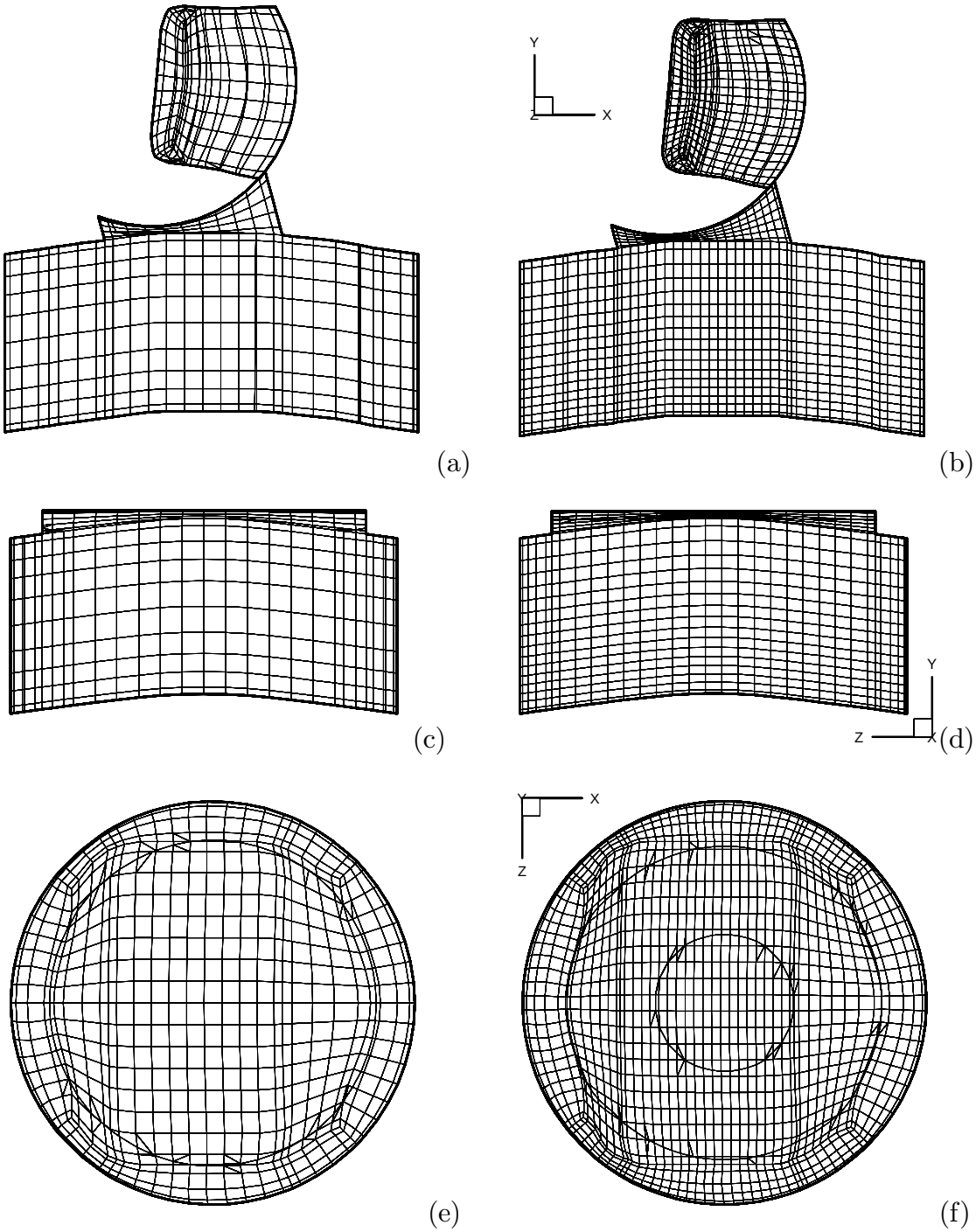

Figure 7.22: Cross sections through the coarse and fine mesh used to model the BRV engine. (a) – Coarse, cross tumble plane; (b) – Fine, cross tumble plane; (c) – Coarse, tumble plane; (d) – Fine, tumble plane; (e) – Coarse, swirl plane; (f) – Fine, swirl plane;

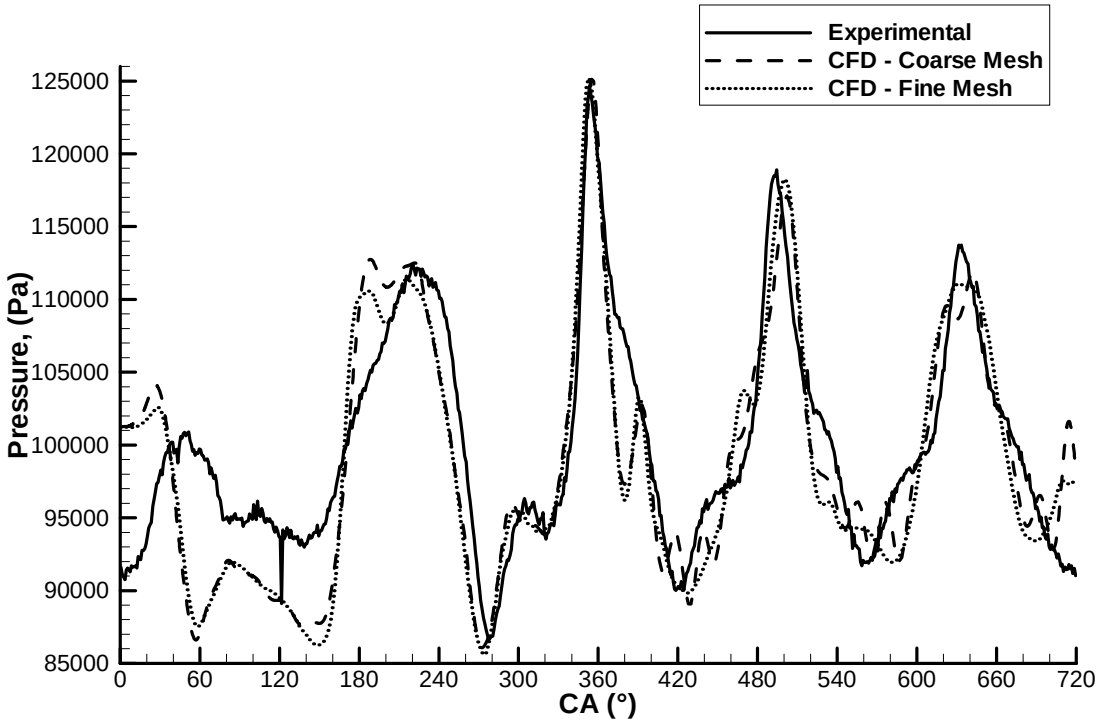

Figure 7.23: Comparison of inlet manifold pressure, experimental results versus coarse and fine mesh results.

a significant variation in the predicted turbulence levels, shown in figure 7.24f. At 240 °CA the fine mesh simulation predicts a mass averaged turbulence intensity of 641 $m^2 s^{-2}$, whereas the coarse mesh simulation predicts an intensity of 439 $m^2 s^{-2}$, a reduction of approximately 30%. This indicates mesh convergence has clearly not been achieved to the same extent for the turbulence parameters.

This conclusion is confirmed by observing the flow field for the two mesh densities. Figure 7.25 shows the velocity and turbulence field in the cross tumble plane, and figure 7.26 shows the velocity field in the tumble plane. The extra mesh resolution can be seen in the velocity field as more vectors, however the shape of the flow field and the position of the vortices are very similar between the two simulations. The small vortex in the tumble plane (figure 7.26) has some small differences, but overall the velocity fields are very similar, and show the same structure.

Figure 7.24f shows that the turbulence has a significantly higher intensity in the fine mesh simulation than in the coarse mesh simulation. This is confirmed in figures 7.25 and 7.26, where the magnitude of turbulence fields in the fine mesh result is significantly higher.

Unfortunately, however, it was not possible to redo the simulation using an even finer mesh as the memory and computational time requirements would have been excessive. Additionally, the comments made in chapter 6 about there not being a true grid convergent solution for the square cylinder engine would no doubt also hold here, so it is likely that there is no truly grid converged solution for this configuration using a Reynolds averaged solution technique with wall functions.

This means that we must accept the fine grid simulation, as modelled here, as the best simulation available. It has been shown that it is essentially grid independent for the predictions of the pressure and velocity fields, however it is not fully grid independent for the turbulence field.

Due to this lack of grid independence of the turbulence, the grids used for the following BRV engine models used a similar sized mesh as much as possible. This was done by using a nominal element size of 2 mm for internal nodes in the cylinder, and 1 mm for nodes at the wall for all meshes, as described in section 7.2. This means that the variations caused by mesh density changes are minimised.

7.4.5 Effect of Gas Initial and Boundary Temperature

The initial temperature of the gas in the domain at the start of the calculation and the temperature of the gas entering the domain at the trumpet pressure boundary was found to have a large effect on the wave set up in the inlet manifold and on

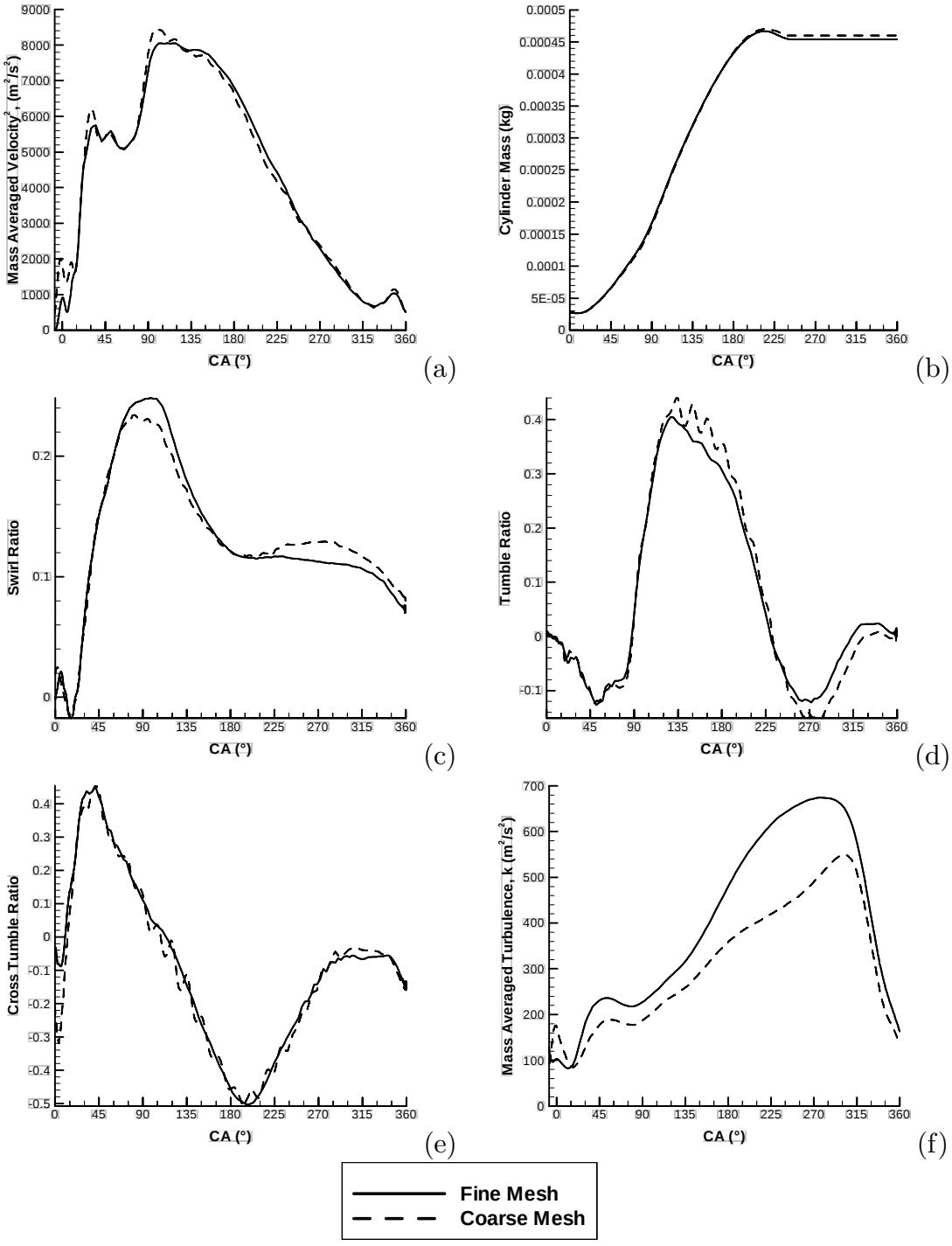

Figure 7.24: Comparison of various cylinder parameters for coarse and fine meshes. Results shown from the second cycle. (a) – Mass averaged velocity squared; (b) – Mass of gas in cylinder; (c) – Swirl ratio; (d) – Tumble ratio; (e) – Cross tumble ratio; and (f) – Mass averaged turbulence.

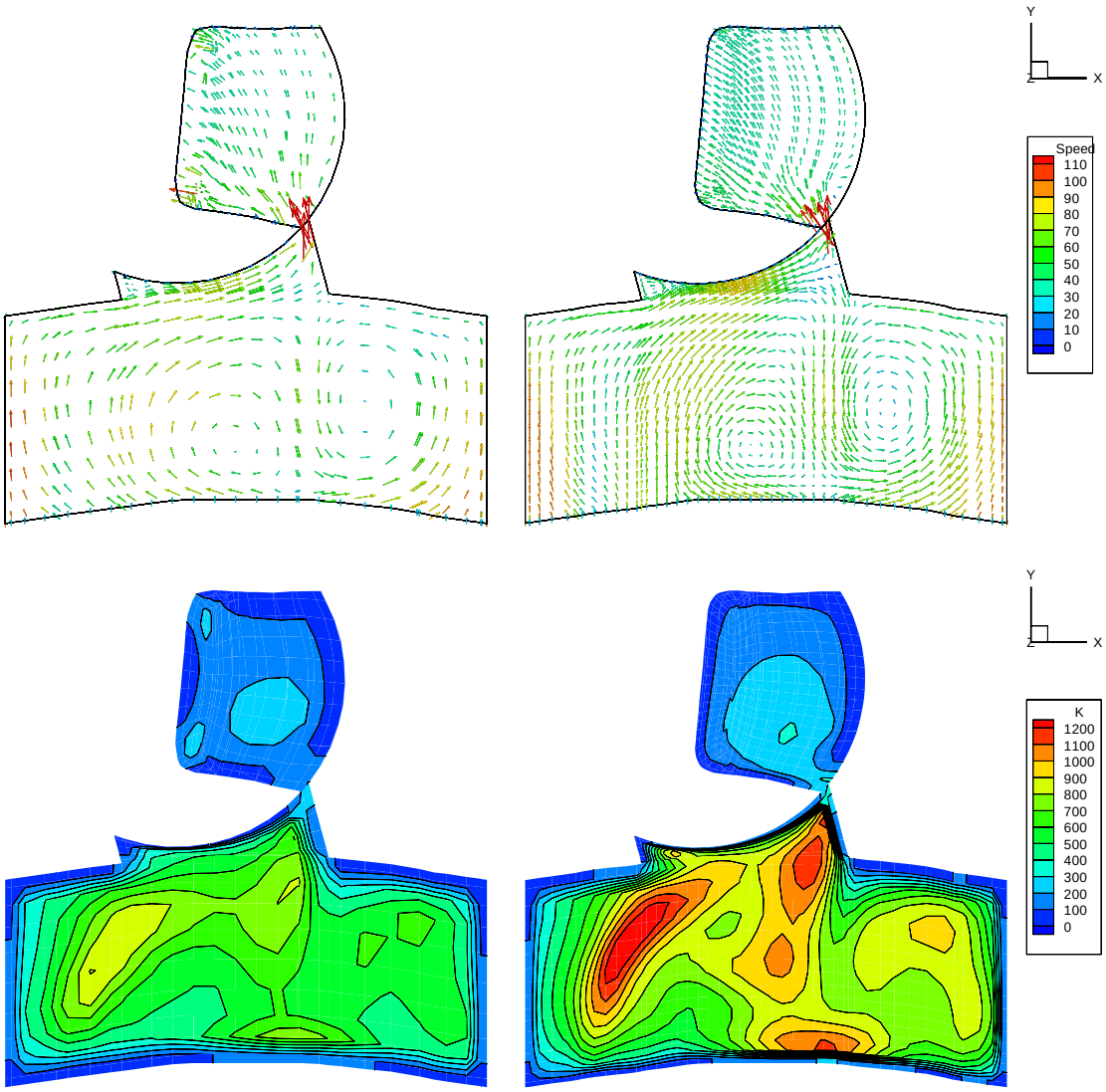

Figure 7.25: Comparison of coarse and fine mesh results in the cross tumble plane at 238 °CA. Top is velocity vectors and bottom is turbulence (k) contours, and left is coarse mesh and right is fine mesh.

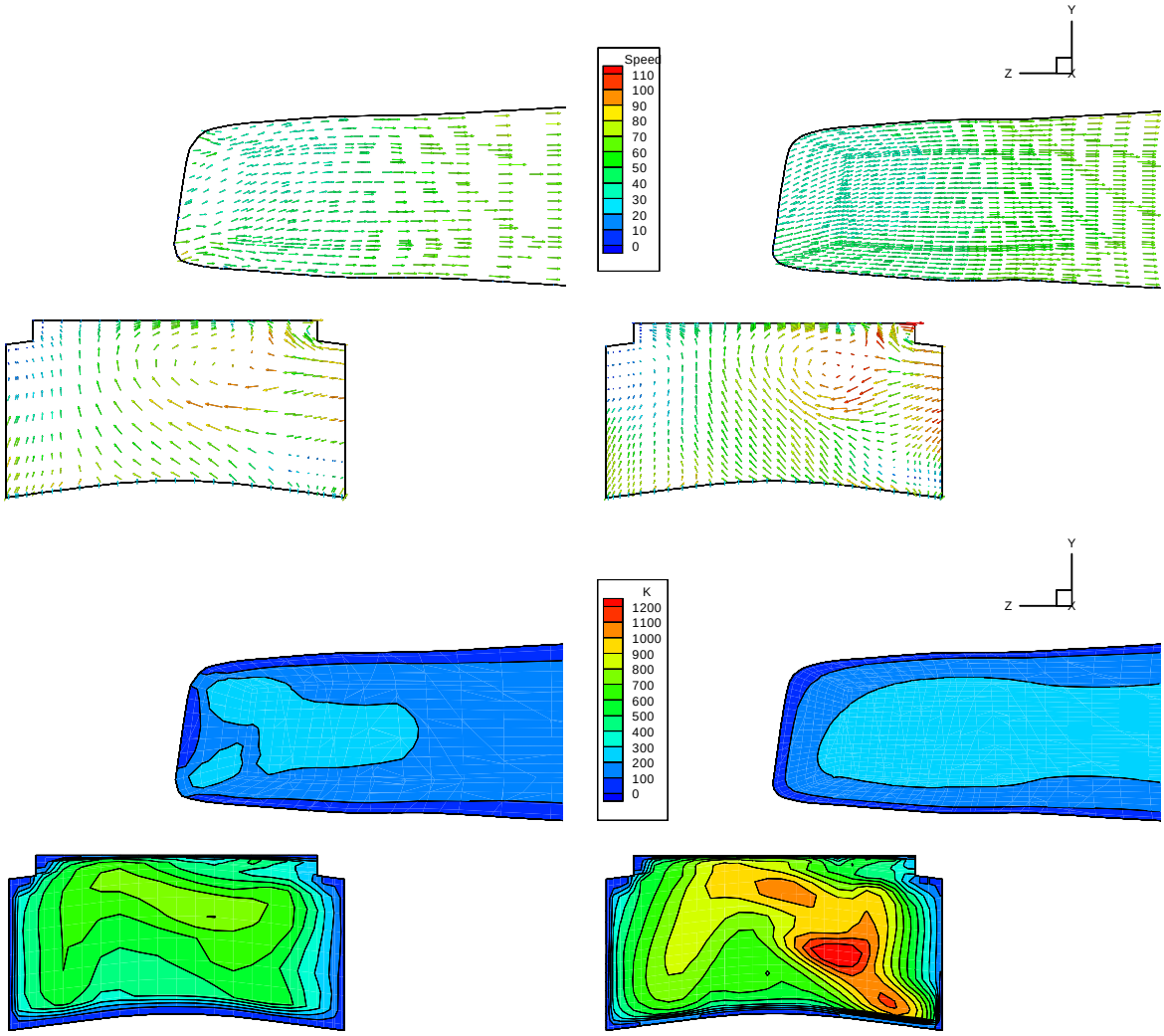

Figure 7.26: Comparison of coarse and fine mesh results in the tumble plane at 238 °CA. Top is velocity vectors and bottom is turbulence (k) contours, and left is coarse mesh and right is fine mesh.

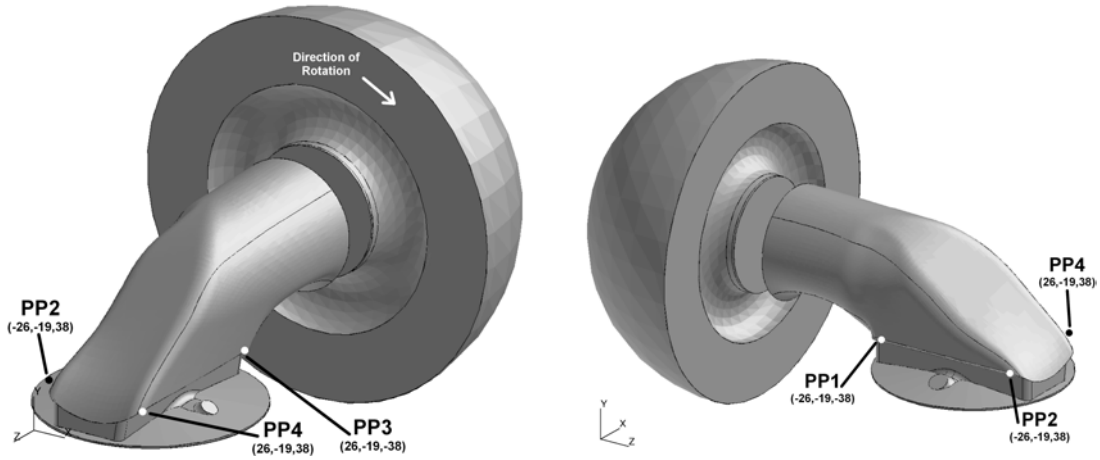

Figure 7.27: Isometric views of BRV engine showing location of port pressure sensors, labelled "PP1" to "PP4".

the state of the gas entering the cylinder. Thus it is important to use initial and boundary conditions which match the actual conditions for the simulation.

Temperature matching was done here by matching experimental and simulated inlet manifold waves. The acoustic velocity of air is

$$a = \sqrt{\gamma RT}, \tag{7.10}$$

and the natural frequency of the inlet manifold wave is proportional to the acoustic velocity. Thus the natural frequency of the inlet manifold wave can be adjusted within a small range by changing the temperature of the gas entering the inlet manifold. The small change in inlet manifold wave frequency will be seen as a phase difference between the measured and simulated waves later in the simulation.

The inlet manifold wave on the current BRV engine is measured by what are known as "port pressure" sensors. These sensors are located inside the head, facing the rotating valve surface. Figure 7.27 shows the position of these sensors on a isometric view of the engine. They measure the inlet manifold wave only during the time the inlet valve sweeps across their faces, and for the rest of the engine cycle they are shut off from the inlet manifold gas by the valve surface. Therefore, as the port pressure sensors are only exposed to the inlet manifold gas for a small section of the engine cycle, the inlet manifold wave must be inferred from a small section of data obtained when the inlet manifold is exposed to the pressure sensor.

A similar "sensor" was placed in the numerical simulation, where the pressure was recorded at the valve window surface at a location matching that of the experimental sensors. Thus both the experimental and numerical readings are equivalent, and only show a small section of the inlet manifold wave. This is shown in figure

7.28, where the small section of data read from the numerical model is compared to the relevant data from the real engine.

Even though only a small section of the wave is visible in figure 7.28, the edge of a wave can be seen in the experimental results between about 620 °CA and 690 °CA in figure 7.28a and b. This wave edge was the feature used to "tune" the simulation boundary condition temperatures.

Superficially, the correct boundary condition temperature appears to be the temperature of the air as it leaves the air conditioning unit in the dynamometer. The dynamometer is specified to provide air to the engine at 25 ± 1 °C, 101.4 ± 1 kPa and a relative humidity of $30 \pm 5\%$. When the simulation was run using an initial and boundary gas temperature of 25 °C, the simulation predicted the crank angle when the pressure measured at port pressure sensor 3 and 4 crossed 100 kPa to be around 14 °CA earlier than experimentally measured. This is shown in figure 7.28a and figure 7.28b. This indicates the model is predicting a frequency in the inlet manifold which is too high, even though the imposed gas inlet temperature agrees with that used in the dynamometer.

The reason for this discrepancy appears to be evaporation of the fuel lowering the temperature of the gas in the inlet manifold. This effect is increased by the fact that a gas/droplet mixture has a lower acoustic velocity than a gas with no suspended droplets. This means that the suspended fuel droplets in the manifold are likely to further lower the manifold acoustic velocity. However, at the relatively low droplet concentrations found in engine intake manifolds it is unlikely that the effect of the droplets on acoustic velocity is significant.

Modelling the fuel motion, droplet behaviour and evaporation is beyond the scope of the current work. To account for the effects of these processes, their effects on lowering the acoustic velocity in the manifold was accounted for by lowering the temperature of the initial gas and the gas which enters the domain through the trumpet boundary condition.

The temperature necessary to reproduce this effect was calculated from

$$\frac{CA_{elapsed} - CA_{error}}{CA_{elapsed}} = \frac{a_{sim}}{a_{true}} = \sqrt{\frac{T_{sim}}{T_{true}}} \tag{7.11}$$

where CA_{error} is the error in degrees crank angle of a section of the wave, in this case 14 °CA; $CA_{elapsed}$ is the crank angle which has passed since the "origin" of the inlet manifold wave which can be taken as inlet valve close, in this case 420 °CA. The simulated and true acoustic velocities are a_{sim} and a_{true} respectively, where the simulated acoustic velocity has a small error. Using $T_{sim} = 298$ K, this gives $T_{true} = 278$ K.

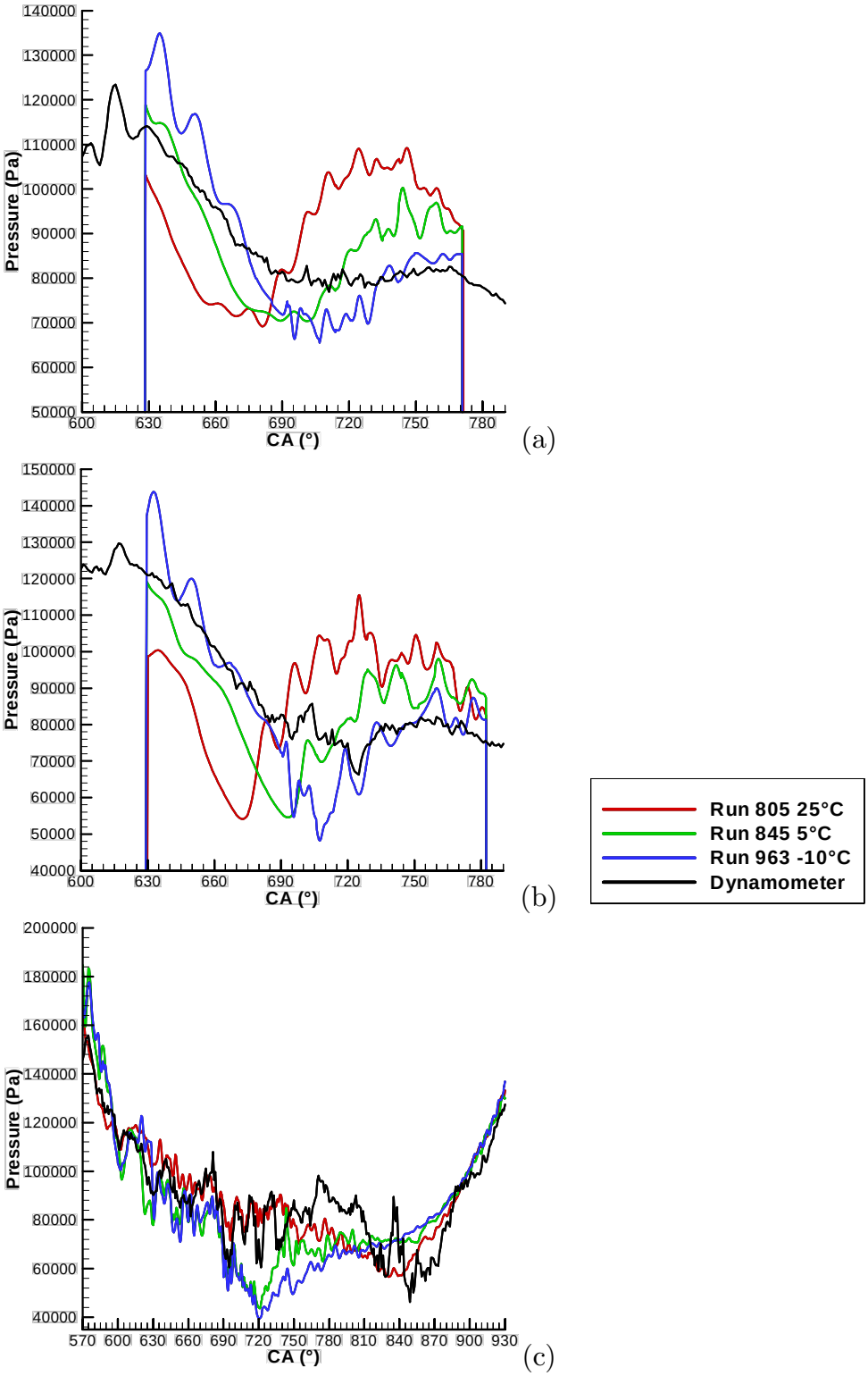

Figure 7.28: Comparison of inlet manifold cylinder pressure during overlap. Shown is dynamometer results, simulations for initial and boundary gas temperatures of 25 °C, 5 °C and −10 °C; at (a) – Port pressure sensor 3; (b) – Port pressure sensor 4; and (c) – Cylinder pressure sensor.

When the simulation is rerun using initial and boundary temperatures of 278 K (or 5 °C), the inlet pressure wave predicted is indicated by the green lines in figures 7.28a and 7.28b. A further simulation using initial and boundary temperatures of 263 K (−10 °C) was also performed, it is indicated by the cyan lines.

The 278 K simulation predicts the pressure at position 3 (figure 7.28a) with good agreement against the dynamometer results from 630 °CA to 660 °CA, and the 263 K simulation has good agreement at position 3 in the final section seen by the pressure sensor from 720 °CA to 770 °CA. Similarly pressure sensor 4 (figure 7.28b) shows the cooler simulations to have an improved accuracy, with the 263 K simulation predicting the experimental results very well. The only significant departure from the experimental results here is in a small section between 690 °CA and 720 °CA.

The results at the cylinder pressure sensor are shown in figure 7.28c. The pressure in the cylinder is a function of many more variables than just the inlet manifold wave, so moving the position of the inlet manifold wave does not have a simple effect on the cylinder pressure. The main differences appear to be that the 263 K and 278 K results predict a region of low pressure which is not found in the experimental results. Overall the 298 K simulation appears to predict the experimental results marginally better than the colder conditions, as it shows the best agreement at around 720 °CA and at 840 °CA.

As there was no clear choice as to which inlet temperature to use based on the results of figure 7.28, 278 K was used as the best compromise. It was used as the initial and boundary condition temperatures for all subsequent simulations.

7.5 Mark I Combustion Chamber

The cylinder head used at the commencement of the current author's work is shown in figure 7.29. This is the "Mark I" combustion chamber, and was the first combustion chamber design used by Bishop Innovation for the BRV engine.

The design philosophy at this time was:

1. An "open" combustion chamber so as not to impede flow of inlet or exhaust gas, giving maximum volumetric efficiency;

2. Maximum valve window area, again to maximise inlet and exhaust air flows for high volumetric efficiency;

3. Small squish areas at the periphery of the combustion chamber and a reasonably open central section for good combustion; and

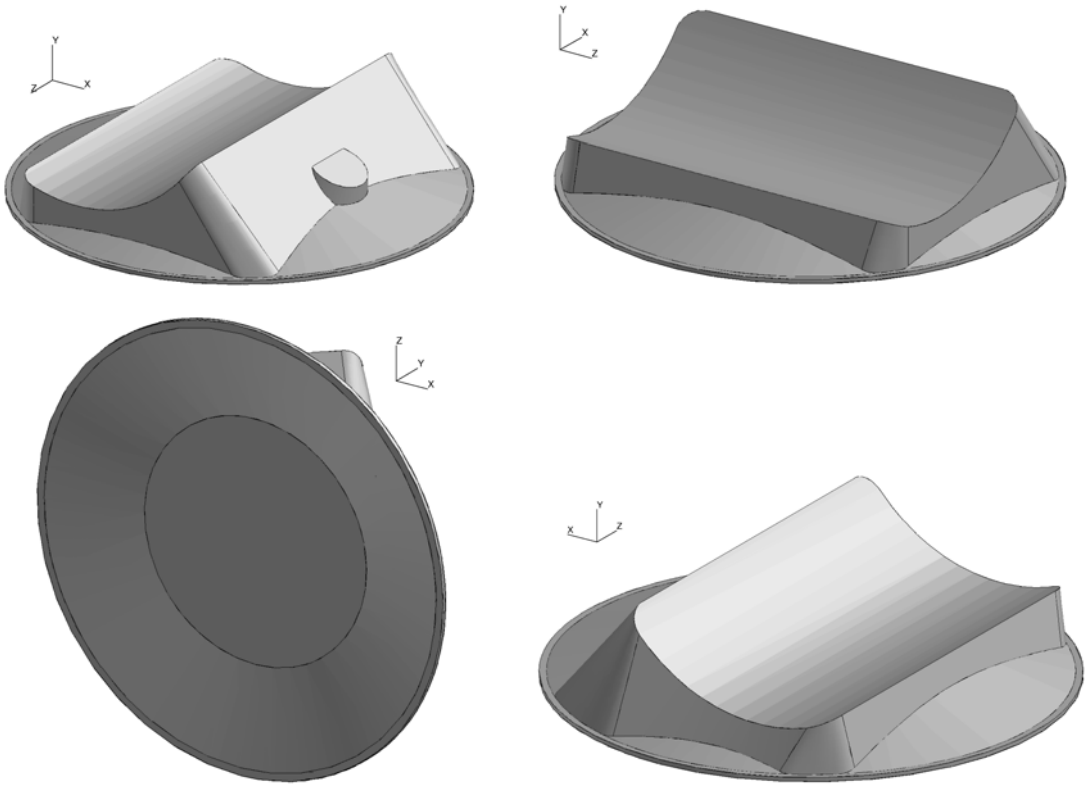

Figure 7.29: Various isometric views of the Mark I combustion chamber. Piston is located at TDC.

4. Steady state testing of the valve had indicated it should produce large amounts of tumble, and the head and valve was designed to utilise this.

The early versions of the BRV engine were designed with a 80 mm stroke to give 500 cc per cylinder. It was designed to run at speeds of up to 8000 rpm. As the design progressed, it was decided to shorten the stroke of the engine to allow it to run faster. The redesigned engine used the same cylinder head geometry, but had a stroke of 47 mm and 300 cc per cylinder. This engine could run at around 13000 rpm with the same piston velocity as the longer stroke engine.

Dynamometer tests showed the engine performed well when it was run with the long stroke configuration, but a number of performance parameters dropped sharply in the short stroke configuration. These changes in performance parameters included the *BMEP* decreasing and the spark advance required for peak torque increasing. The experimental results could not suggest a reason for the performance decrease, however analysis of the results of the CFD model successfully uncovered the reason.

It was known that the BRV engine produced high tumble ratios. Figure 7.30a is the tumble vector plane from the simulation at the end of the intake stroke of the long stroke engine. It shows a strong, roughly circular shaped tumble vortex, giving the tumble ratio of 1.1 at 180 °CA, as displayed in figure 7.31. This strong tumble at the end of the intake stroke results in high levels of turbulence during the compression stroke and good combustion.

When the same simulation was run using the short stroke engine, the tumble is found to reduce significantly. The short stroke engine (figure 7.30b) does not have the strong tumble vortex present found in the long stroke engine (figure 7.30a). The vortex is distorted into a non-circular shape and consequently the tumble ratio at this position is reduced to 0.65, as shown in figure 7.31. This is a reduction in tumble intensity of 40%.

It is apparent that the Mark I combustion chamber, which worked well on a long stroke configuration performs poorly on the short stroke configuration, and a significant part of the performance reduction is due to a large reduction in tumble flow strength.

7.6 Mark II and III Combustion Chamber

With the lack of success of the Mark I chamber on the short stroke engine, it was realised a fundamental change was required to the design philosophy for the short stroke engine combustion chamber. The combustion chamber shown in figure 7.32

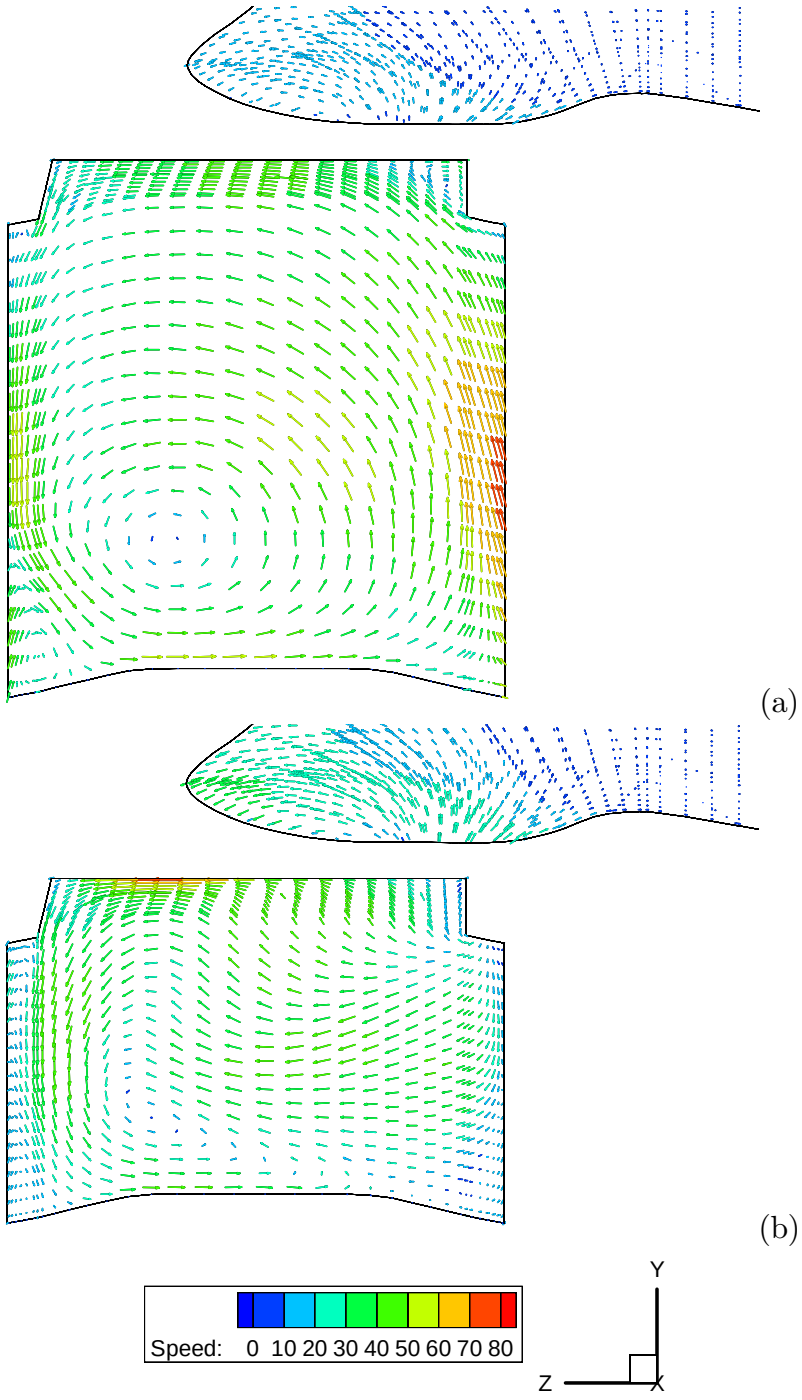

Figure 7.30: Comparison of the tumble generated by the short and long stroke Mark I combustion chamber BRV engines. Results shown from a incompressible intake stroke simulation, at BDC with plane shown taken through rotation axis of the valve. (a) – long (80 mm) stroke configuration at 6000 rpm, and (b) – short (47 mm) stroke confiuration at 10000 rpm. Engine speed has been increased in the 47 mm simulation to maintain equivalent piston velocities.

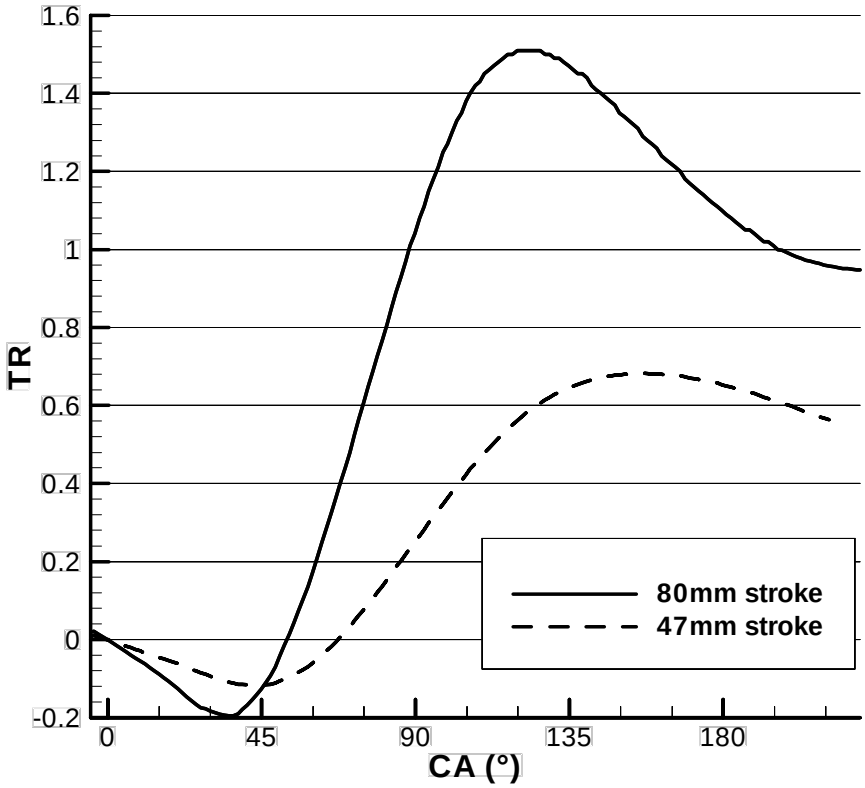

Figure 7.31: Tumble ratio versus crank angle for long and short stroke BRV Mark I engine configurations.

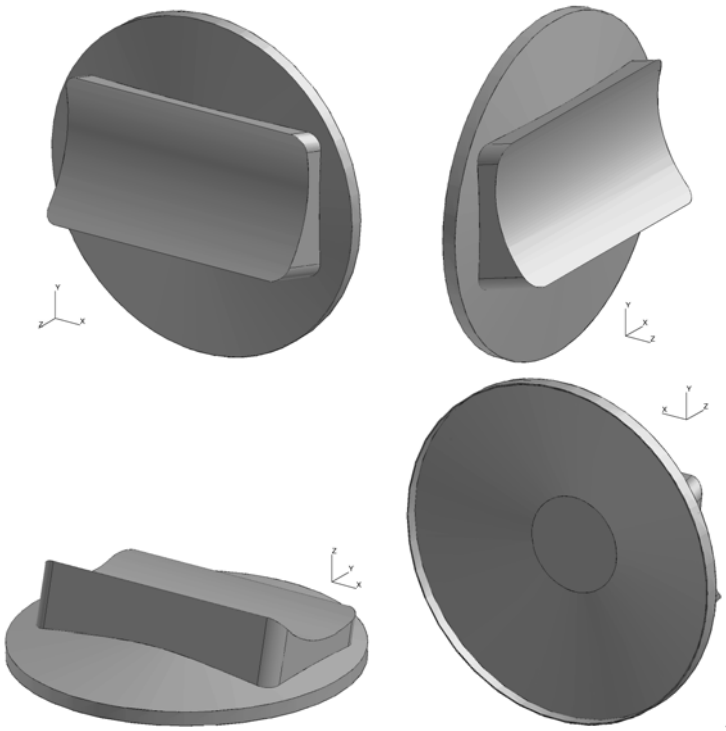

Figure 7.32: Various isometric views of the Mark II combustion chamber. Piston face is located at TDC.

was designed by the BRV design staff. This is the "Mark II" combustion chamber, and it was soon followed by the "Mark III" chamber shown in figure 7.33. Cross sections of the three head geometries are shown in figure 7.34.

Dynamometer testing showed that these combustion chambers dramatically lifted engine performance on the short stroke engines. Again, the experimental results could not indicate the reason for the increased performance with the measurements recorded.

The CFD simulation performed on these engine geometries indicated the reason for the improved performance of the Mark II and III cylinder heads. Comparison of the simulations of the Mark II (figure 7.36) and the Mark III (figure 7.37) chamber against the Mark I (figure 7.35) chamber showed that the in-cylinder flow clearly does not develop significant swirl, tumble or squish. On the other hand, the flow develops dual geared vortices in the cross tumble plain, and little of the traditional tumbling flow at all. The flow was named "dual cross-tumble", describing its structure of two vortices in the cross tumble plane.

The flow predicted in the Mark I head is shown in figure 7.35. As discussed in the previous section, this geometry has little tumble (as seen in figure 7.30b), and also little dual cross tumble. A small amount of dual cross tumble is present, but

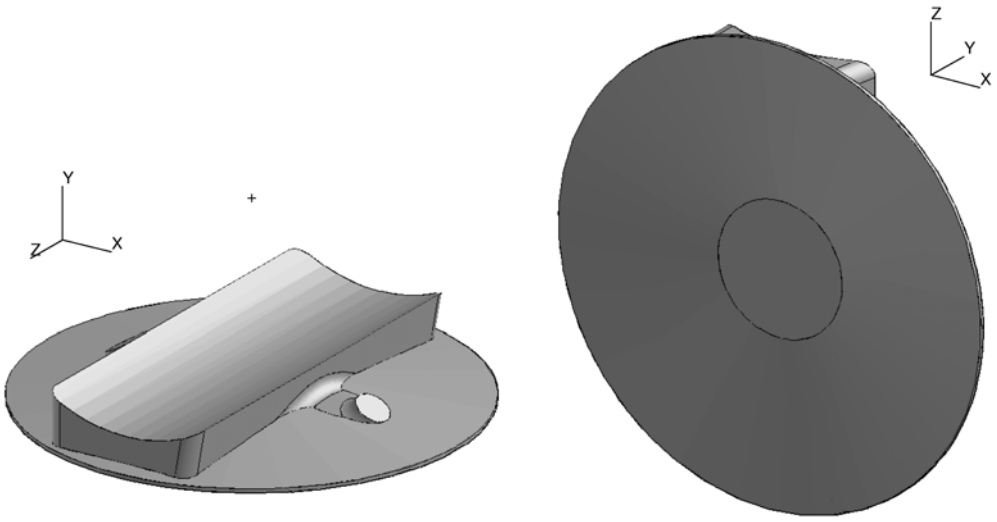

Figure 7.33: Various isometric views of the Mark III combustion chamber. Piston face is located at TDC.

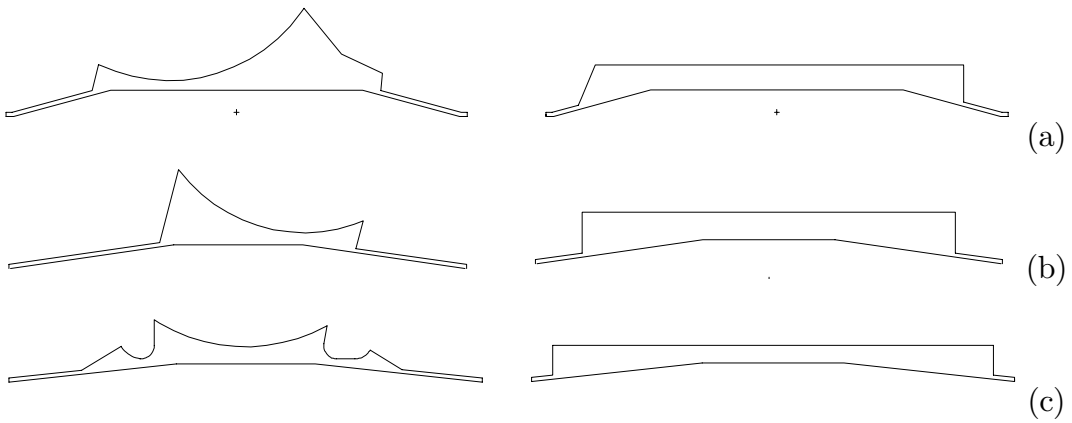

Figure 7.34: Cross sections of Mark I, II and III head geometries. (a) – Mark I; (b) – Mark II; and (c) – Mark III.

it is not as strong as that shown in the Mark II and III heads in figures 7.36 and 7.37. The Mark II geometry (figure 7.36) show a strong dual cross tumble flow in the cross tumble plane, and small weak structures in the tumble plane. The Mark III geometry (figure 7.37) also shows a strong dual cross tumble structure, this time with no vortices seen in the tumble plane at all.

It appears that the dual cross tumble flow field has replaced the tumble flow field of the Mark I long stroke engine as the fundamental turbulence generation mechanism.

7.6.1 Previous Work on Dual Tumble

This work appears to be the first research to recognise the importance of dual cross tumble flows, and to deliberately design engines to use it. However, there have been a small number of previous researchers who report finding flow fields similar to dual cross tumble, even if they did not recognise its significance.

One example is Muroki et al [197], who performed a CFD simulation on a concept rotary valve engine. The valve system they used is very different to the BRV concept: they used a "notch" style valve, similar to the MGN rotary valve engine discussed in section 1.4.2. The bore or stroke used for the simulations is not stated; however, measurements from their diagrams indicate the bore to stroke ratio to be 1.3. The design proposed by Muroki does not seem to have addressed any of the fundamental flaws of the MGN engine, so it is unlikely that their engine would have performed adequately.

However, the CFD simulations performed by Muroki et al show that their valve shares the central jet feature during the intake stroke which is fundamental to creating the dual tumble in the BRV engine. The flows they predicted are similar in overall structure to those presented in the current work, as can be seen in the vector diagrams shown in figure 7.38 and 7.39. They assumed that the flow was symmetrical about the centre of the cylinder and valve, so only half the dual cross tumble flow is resolved. It is more clearly seen in the schematic representation of the flow shown in figure 7.39, where the flow is shown to enter the central plane of the cylinder, and recirculate back following the outer edge of the cylinder. This recirculation is a combination of dual cross tumble and a swirl flow.

The simulations of Muroki et al are relatively crude—the grid they used had only 25000 nodes, so that it was far too coarse to resolve all flow features. They only present very basic results from their simulations; for instance, they do not present any results of the predicted magnitude of turbulence. Their simulation can be

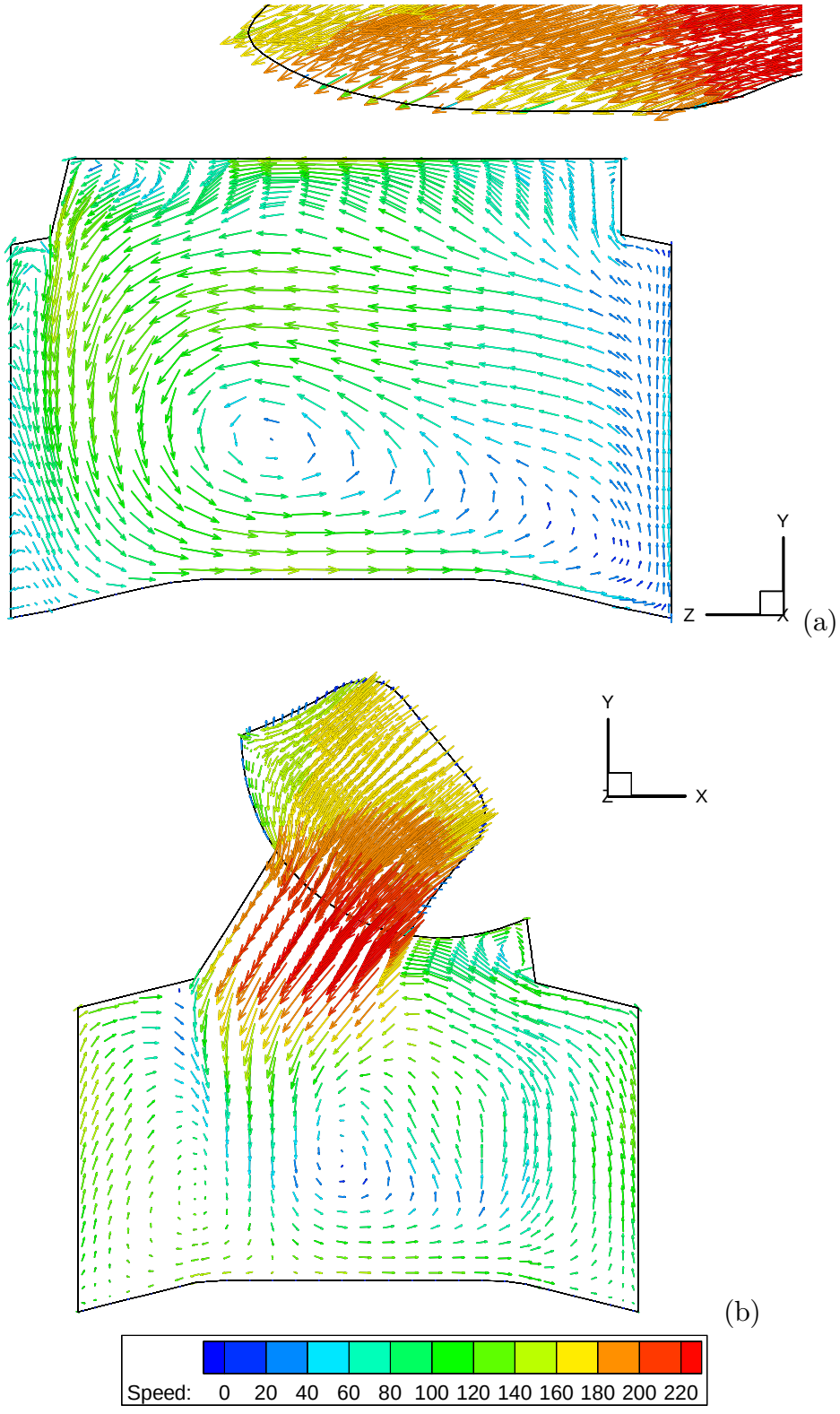

Figure 7.35: Visualisations of the flow in the Mark I cylinder head at BDC, 18000 rpm. (a) – Tumble plane and (b) – Cross tumble plane.

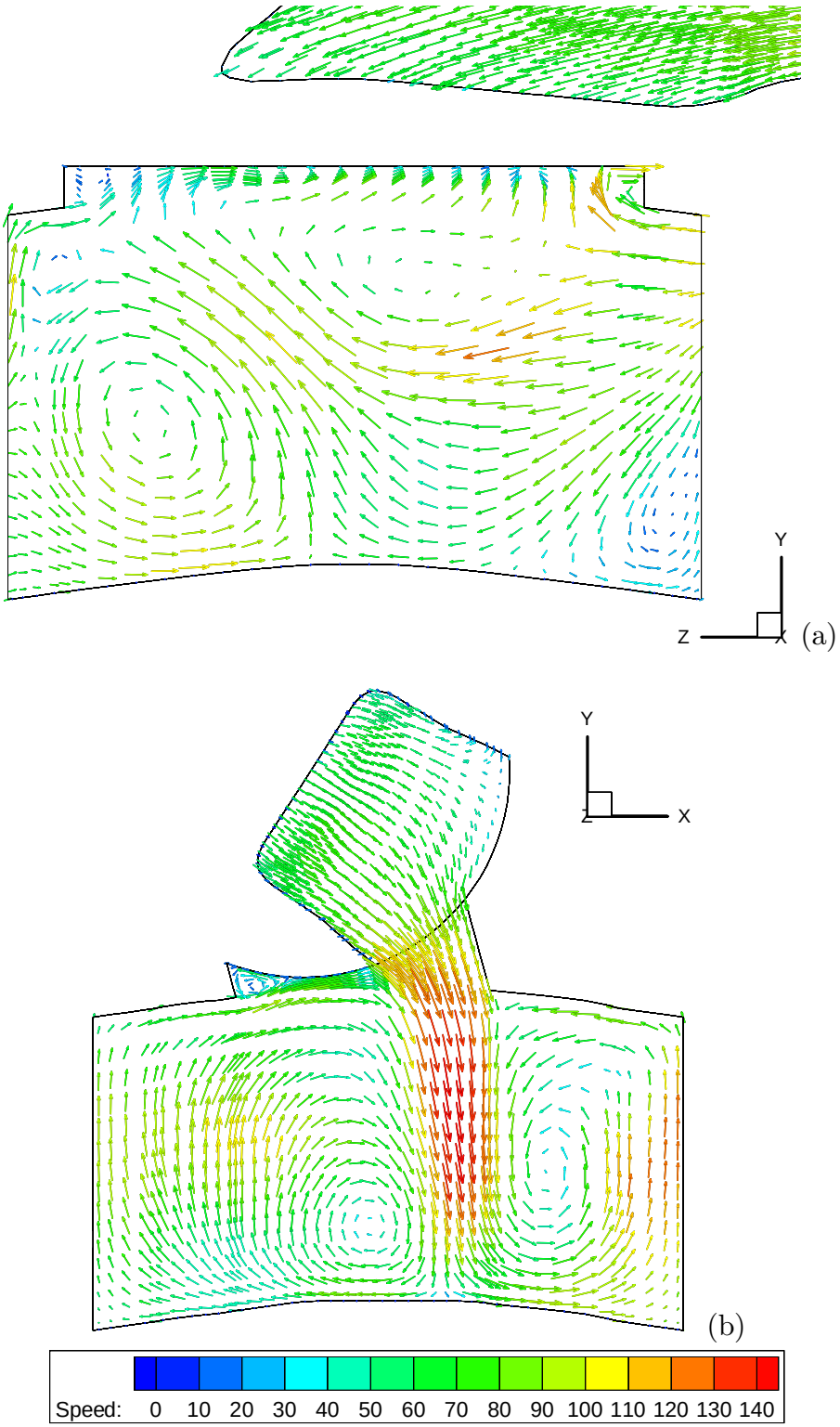

Figure 7.36: Visualisations of the flow in the Mark II cylinder head at BDC, 12000 rpm. (a) – Tumble plane and (b) – Cross tumble plane.

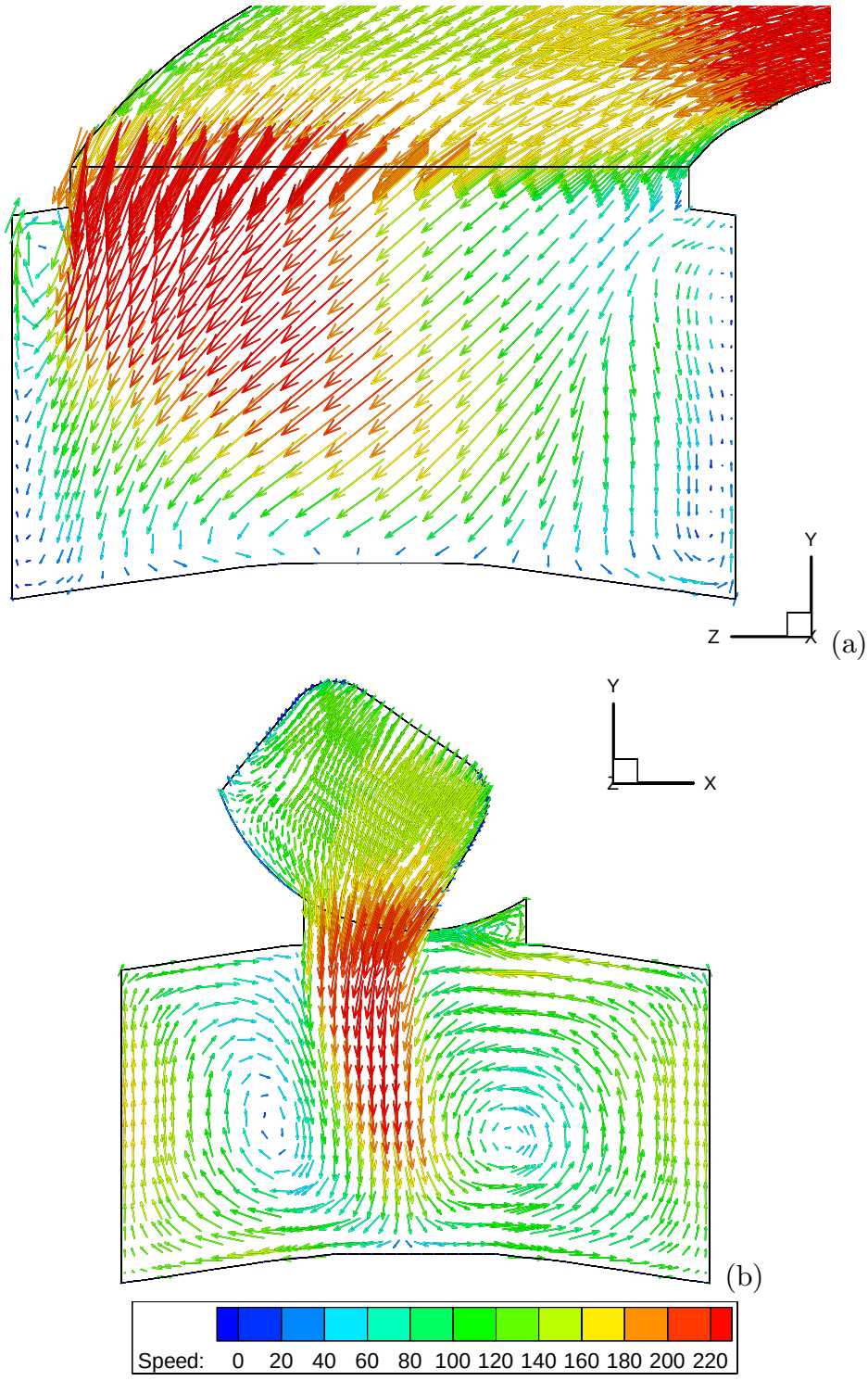

Figure 7.37: Visualisations of the flow in the Mark III cylinder head at BDC, 18000 rpm. (a) – Tumble plane and (b) – Cross tumble plane.

regarded as a preliminary analysis only. Despite this simplicity, they still managed to identify the fundamental flow structure inherent in their engine, which appears to be similar to the BRV dual tumble flow (figure 7.36b or figure 7.37b). The authors appear to not have discovered the significance of this new flow structure, and there is only a passing mention of the structure in the text of the paper.

In the review of Hill and Zhang [137], it is mentioned that turbulence enhancement can occur from the compression of flow fields with multiple vortices:

> "Turbulence production can be magnified by compression of tumbling vortices by piston motion; intense shear strain can be a feature of one vortex or multiple vortices compressed into a small space near TDC." [137]

Despite this realisation that turbulence enhancement can occur with multiple vortices, no analysis of a compressed multiple vortex flow field is presented.

The only other work known to the current author which discusses a dual cross tumble flow is presented in Han et al [125]. The tumble flow simulations performed in this publication have already been discussed in section 4.4.3. However, as shown in figure 7.40, a flow similar to dual cross tumble develops when the fuel spray of the direct injection engine is modelled.

The fuel spray is close to the centre axis of the cylinder head, and points roughly straight down. The spray is created by a "pressure-swirl" injector with a fuel pressure of 5 MPa, and creates a hollow cone shaped spray with a cone angle of approximately 55 °.

The spray released by the jet entrains air, and is predicted to significantly modify the flow field generating the dual cross tumble structure, seen in figure 7.40d. As shown in figure 7.40a, without fuel injection the flow did not exhibit a strong tumble flow field, and no large vortices in the cross tumble plane exist.

The dual tumble structure was found to have reduced turbulence in the centre of the domain, but increased turbulence slightly off centre, and is reproduced in figure 7.40e and 7.40f. Han et al attributes this increased turbulence to shear occurring between the central jet and slower moving fluid further away. Han et al reports that the net effect of the modified flow structure is a small increase in the turbulence levels.

No analysis is performed by Han et al on the dual cross tumble flow structure created by the fuel injection system, and they do not discuss any tumble generation mechanisms possible from dual cross tumble as opposed to normal tumble. The

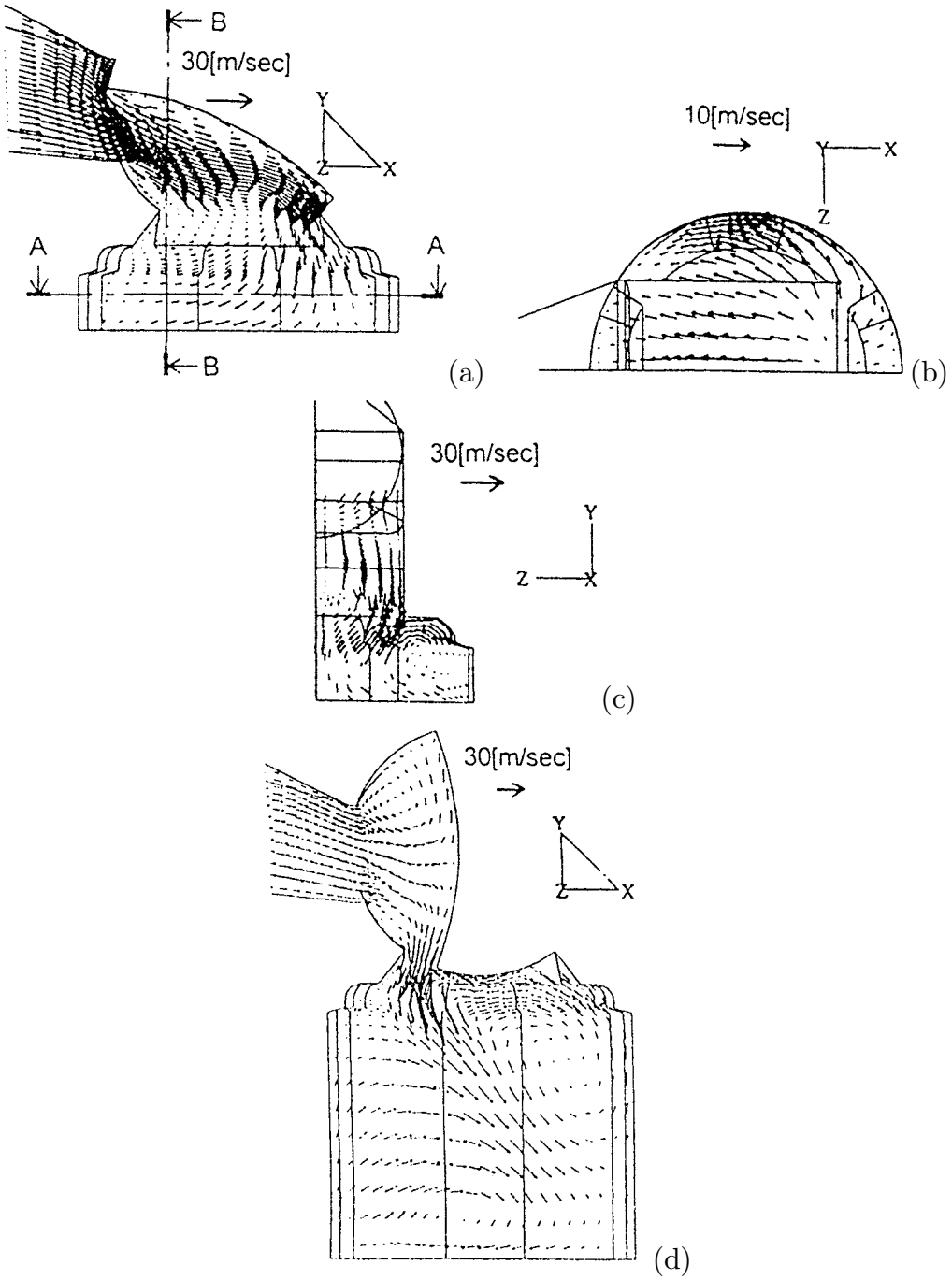

Figure 7.38: CFD model of mean velocity visualised at 1500 rpm for a rotary valve engine by Muroki et al [197]. (a) – Central (tumble) plane at 48 °CA; (b) – Swirl plane at 48 °CA; (c) – Cross tumble plane at 48 °CA; and (d) – Central (tumble) plane at BDC.

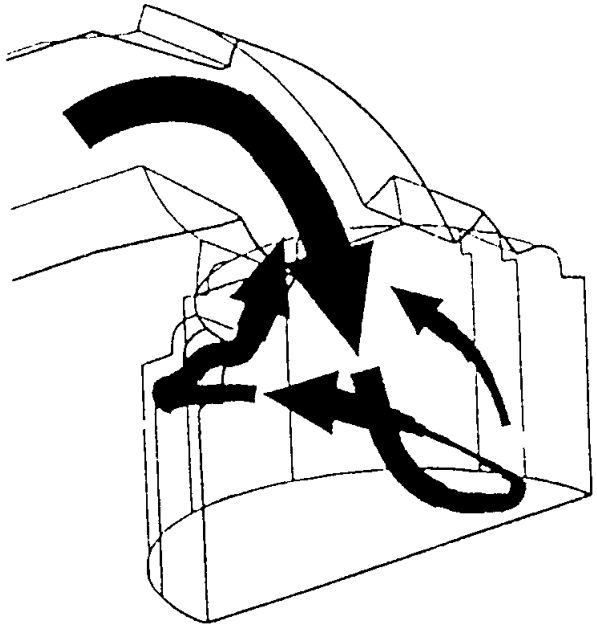

Figure 7.39: Schematic representation of rotary valve engine flow simulated by Muroki et al [197].

results presented in figures 7.40 are at BDC, they do not discuss the behaviour of the dual cross tumble flow during the compression stroke.

The engine studied by Han et al was a production car engine with a bore to stroke ratio of around one. As will be discussed in section 7.7.1, the benefits of the dual cross tumble structure are not likely to be apparent in this engine due to its low bore to stroke ratio.

This shows that the dual cross tumble flow field is not new as it has been visualised by a number of previous researchers—even by one study of a rotary valve engine. However, none of these previous works have recognised that the flow field has different properties to tumble, properties which may prove it superior to tumble for certain applications. This makes the analysis of the dual cross tumble flow field presented in section 7.7, the first analysis of this new class of engine flows.

7.7 Analysis of Dual Cross Tumble

When the properties of the dual cross tumble flow are analysed, some interesting properties become apparent.

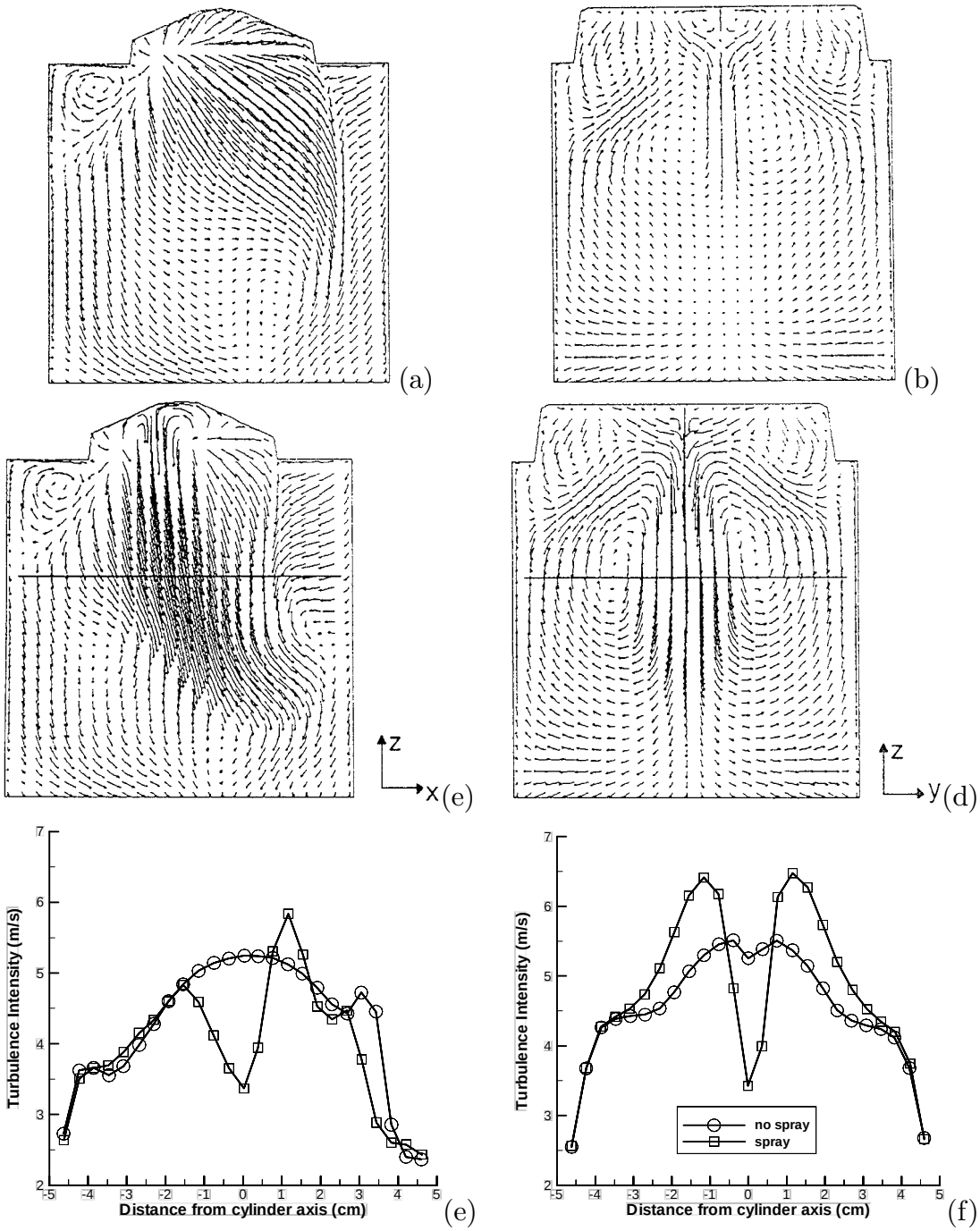

Figure 7.40: Effects of fuel injection on the velocity field predicted by Han et al [125], in a direct injection spark ignition engine at 150 °CA. (a) – Cylinder symmetry plane, tumble plane without fuel injection; (b) – Cylinder symmetry plane, cross tumble plane without fuel injection; (c) – Cylinder symmetry plane, tumble plane with fuel injection; (d) – Cylinder symmetry plane, cross tumble plane with fuel injection; and (e) – Gas turbulence intensity, 30 mm below head surface at BDC, XZ plane (symmetry plane between inlet valves); and (f) – Gas turbulence intensity, 30 mm below head surface at BDC, YZ plane (symmetry plane between inlet and exhaust valves).

7.7.1 Breakdown to Turbulence Mechanism

For traditional tumble flows, it is thought that the decay of the tumble vortex occurs at a critical aspect ratio of the tumble vortex during the compression stroke, generally occurring between 30 °CA to 60 °CA before TDC [137]. This has already been discussed in section 4.2.3.

As turbulence decays quickly, it is desirable to make this decay of the tumble vortex occur just before the turbulent combustion phase, to minimise the amount of turbulence lost through dissipation. Ignition timing in high performance engines is typically 30 °CA to 60 °CA before TDC, and the period between spark ignition and commencement of the rapid turbulent combustion is typically 15 °CA to 30 °CA at 2500 rpm [263], and can be significantly longer at high engine speeds. This means that the breakdown of the tumble vortex is usually significantly before the turbulent combustion phase, thus allowing significant turbulence decay before combustion.

Dual cross tumble has two vortices in the cylinder rather than one as in the case of tumble, so the aspect ratio of the vortices is reduced by a factor of about two. Thus it would seem that dual cross tumble would reach the critical aspect ratio triggering decay later than normal tumble, and would consequently decay later in the compression stroke than tumble. This means that less turbulence decay would occur before the turbulent combustion phase. This can potentially increase the amount of turbulence in the turbulent combustion phase, and increase engine performance.

7.7.2 Dual Cross Tumble Generation

The cylinder and manifold design required to generate high levels of normal tumble are well known, and are discussed in section 4.2. The pentroof combustion chamber (figures 1.2 or 1.3) is an example of a design to generate a strong tumble vortex flow.

The dual tumble flow field seems to require a very different method of generation than normal tumble. To generate strong dual cross tumble flows, the cylinder design requires the inlet gas jet central in the cross tumble plane, and straight down the axis of the cylinder. This vertical central jet is clearly seen in figures 7.36 and 7.37.

It would be difficult to design a poppet valve engine with the intake air jet aimed centrally, yet still maintain a good combustion chamber shape. The author suspects that this is the reason for this type of flow not being studied in poppet valve engines.

A rotary valve engine of the BRV design is able to produce this central intake

air jet, since the valve can easily be located reasonably centrally in the head, and the air directed to enter the cylinder directly without having to pass over a valve head.

7.7.3 Dual Cross Tumble Parameterisation

The traditional methods of calculating the magnitudes of swirl, tumble and cross tumble were described by equations 4.5, 4.3 and 4.4 respectively in section 4.2.2. These relations, however, fail to pick up dual cross tumble flows. This is due to the dual cross tumble flow being close to symmetrical, so that the momentum of the two counter-rotating vortices cancel each other out, and the result is near zero. This makes the traditional swirl, tumble and cross tumble calculations meaningless when designing an engine for dual cross tumble.

Hill and Zhang [137] also noted the failure of the traditional swirl and tumble number to indicate the turbulence generating potential of an in-cylinder flow with multiple vortices, however they did not propose an alternative method.

A definition to parameterise the flow strength of a dual cross tumble flow was therefore required. Methods proposed were based on dividing the cylinder into two regions, then a traditional tumble ratio calculation can then be performed in the two sub-regions. Methods devised to split the region include using the dividing streamline, using the point of maximum downward velocity as the dividing line, or to simply split the cylinder about its central axis. None of these methods proved useful as they were either difficult to implement, or gave another meaningless number.

The most promising method of analysing the flow was to use the mass averaged square of the velocity across the entire cylinder. This number is representative of the total mean fluid kinetic energy in the cylinder. Since the concept of vortex break down during the compression stroke is to convert a bulk motion into turbulent motion, the total amount of mean flow kinetic energy available at the beginning of the compression stroke is obviously vital. It is the "energy source" from which the turbulence enhancement is created, before the conversion of the mean flow kinetic energy to turbulent kinetic energy. This was thought to be the most meaningful measure of dual cross tumble, or indeed of any arbitrary engine flow.

Of course, using mass averaged velocity squared means that all in-cylinder motions are included, not just dual cross tumble. This can be misleading, for instance it is well known that the turbulence enhancement from a tumble vortex is usually more intense than the turbulence enhancement from an equivalent swirl vortex [137, 263]. However it is used in this work, as mass averaged velocity squared has

a sound physical basis, and it is able to pick up both traditional tumble and swirl flows, together with the new dual cross tumble flows.

7.8 Behaviour of Dual Cross Tumble

In this section the behaviour of a dual cross tumble flow will be described over an entire intake and compression stroke. Figures 7.41, 7.42 and 7.43 show the development of the velocity field and figures 7.44, 7.45 and 7.46 show the development of the turbulence field over the intake stroke and compression stroke. The engine configuration shown is a Mark III head running at 15000 rpm. The result shown here is from the second cycle of the simulation, so the effects of the inlet manifold wave and scavenging processes have been included.

The velocity and turbulence fields at TDC at the start of the intake stroke are shown in figure 7.41a and figure 7.44a. During these very early stages of the intake stroke the scavenging process results in gas flowing from the intake valve through the cylinder head and out the exhaust valve. Very high velocities are associated with this process, up to $300\,\mathrm{m\,s^{-1}}$. Very little flow is occurring in the very long, thin squish regions. A high level of turbulence is associated with the high velocity scavenge flow.

As the intake stroke progresses to 60 °CA (figure 7.41b and figure 7.44b), the dual cross tumble flow begins to develop. At this stage the vortices are weak. The flow is still accelerating since the piston has not reached its maximum velocity. In fact the peak of gas velocity occurs some time after the piston velocity peak due to a time lag caused by gas compressibility. An interesting feature is that on the right side of the cross tumble velocity field two vortices are visible. This third vortex in the cross tumble plane soon dissipates as the gas velocity increases. Very high levels of turbulence are seen on either side of the intake jet, caused by shear between the high velocity ($140\,\mathrm{m\,s^{-1}}$) jet and the slower flows in the vortices.

At 120 °CA (figure 7.41c and figure 7.44c), the piston has gone past maximum velocity and is now decelerating. The valve is also very close to fully open. The jet of gas entering the cylinder takes up the middle third of the cylinder, and strong cross tumble vortices are forming on either side. The jet has velocities of up to $140\,\mathrm{m\,s^{-1}}$, and shear at the edge of this jet intensifies the cross tumble vortices. The third vortex in the cross tumble plane is no longer present. The tumble plane shows that the central jet enters the cylinder at an angle, and has no large scale vortices in it. The cylinder region has a high level of turbulence across its entire domain, with localised areas of very high turbulence.

The simulation continues, and at BDC (figure 7.42a and figure 7.45a), the central intake jet is seen to shrink as the valve starts to close and the valve edge sweeps across the cylinder head. The velocity associated with this central jet is still high, around $140\,\mathrm{m\,s^{-1}}$. The pair of cross tumble vortices are still present. The turbulence at this instant is again generally quite high, with small localised areas of very high turbulence.

At 240 °CA (figure 7.42b and figure 7.45b), the valve has almost shut and the gas trapped in the cylinder has been significantly compressed. This causes a small amount of back flow, visible as a small high velocity jet in the valve window. The stabilising influence of the central jet during the intake stroke has now stopped, and the dual tumble vortices are beginning to break down in a process similar to the break down of a tumble vortex. In this case, the right side vortex remains in much the same position, but the left side vortex has travelled towards the piston face and towards the centre of the combustion chamber. Some small features are visible in the tumble plane, but no large scale structures are present. Again the turbulence levels across the cylinder are generally high, with the central regions having very high levels of turbulence (up to $2000\,\mathrm{m^2\,s^{-2}}$).

The compression stroke continues to 300 °CA (figure 7.42c and figure 7.45c), and the flow field has slowed considerably with peak velocities dropping to around $80\,\mathrm{m\,s^{-1}}$. The dual tumble flow field is no longer present. The remnants of the right hand vortex can still be seen, but the left vortex has completely dissipated. The energy from the velocity field has been transformed into turbulent energy, and very high levels of turbulence are seen across the entire cylinder, peaking at about $1800\,\mathrm{m^2\,s^{-2}}$.

At TDC of the compression stroke (figure 7.43 and figure 7.46) the remnants of the original flow field have completely disappeared. Now there are only two small vortices in the central section of the head caused by the squish jets. The turbulence in the squish regions has reduced to very low levels due to the close proximity of the walls, but there are small regions of high turbulence in the central section of the head caused by the squish jets.

An alternative way of visualising the flow field is by using instantaneous streamlines. Various views of instantaneous streamlines plotted on the BRV Mark III engine is shown early in the intake stroke (79 °CA) in figure 7.47, at BDC in figure 7.48, and at IVC (247 °CA) in figure 7.49. Early in the intake stroke (figure 7.47), the central intake jet is seen to be the predominant feature, with small dual cross tumble vortices on either side. A further small vortex is seen behind the intake jet.

As the flow progresses to BDC (figure 7.48), the dual cross tumble flow becomes

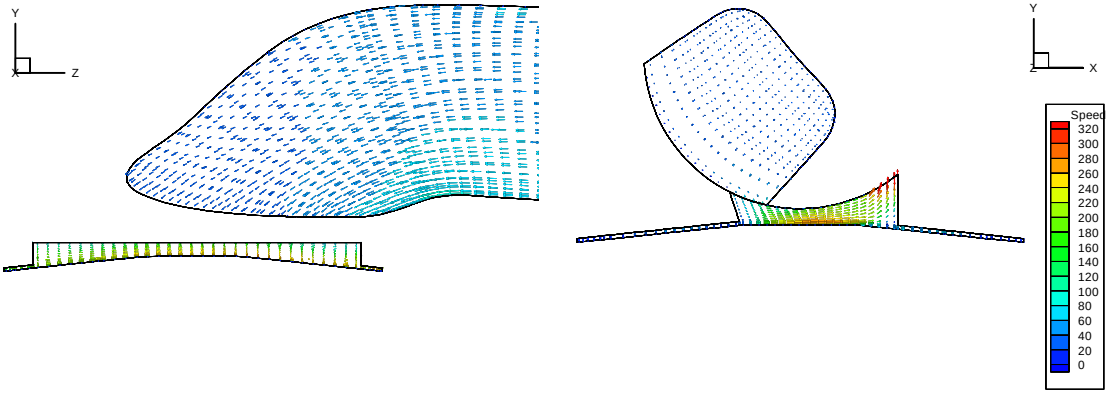

(a)

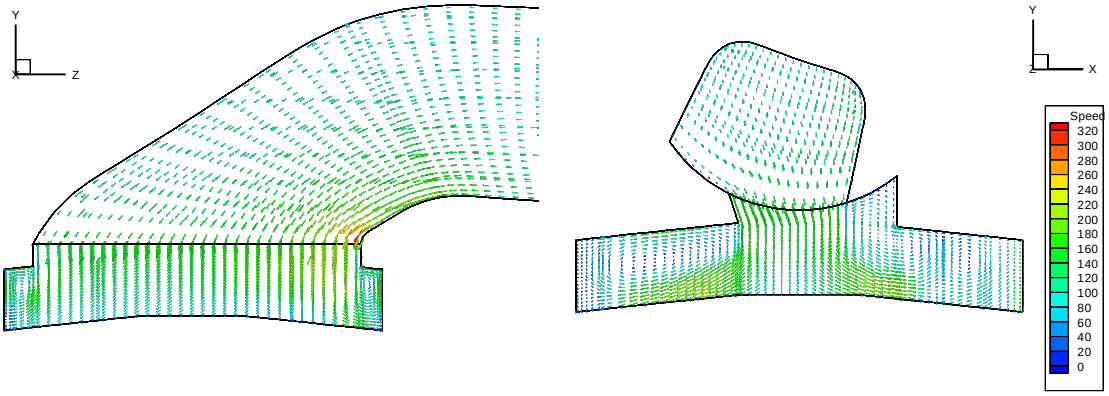

(b)

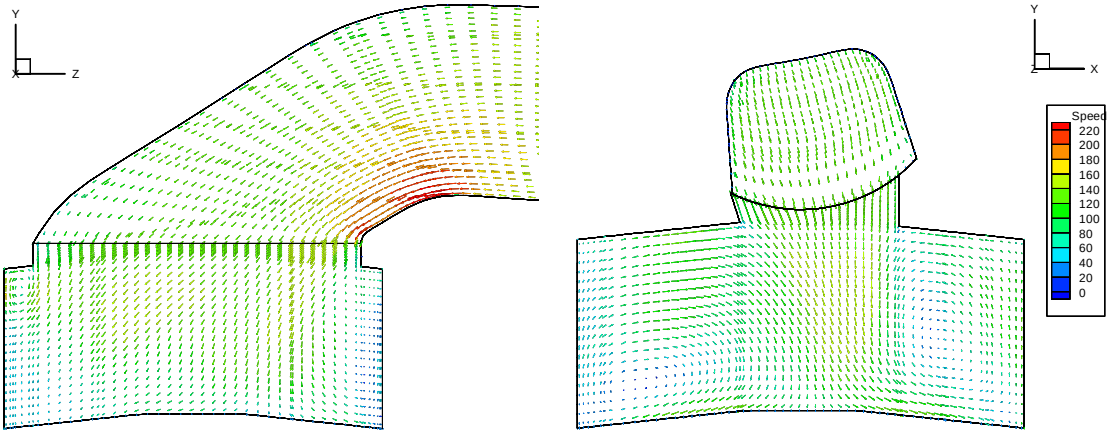

(c)

Figure 7.41: Flow field in tumble and cross tumble planes during the early intake stroke. Simulation is the Mark III head run at 15000 rpm. Results continued in figure 7.42. (a) – 0 °CA; (b) – 60 °CA; and (c) – 120 °CA.

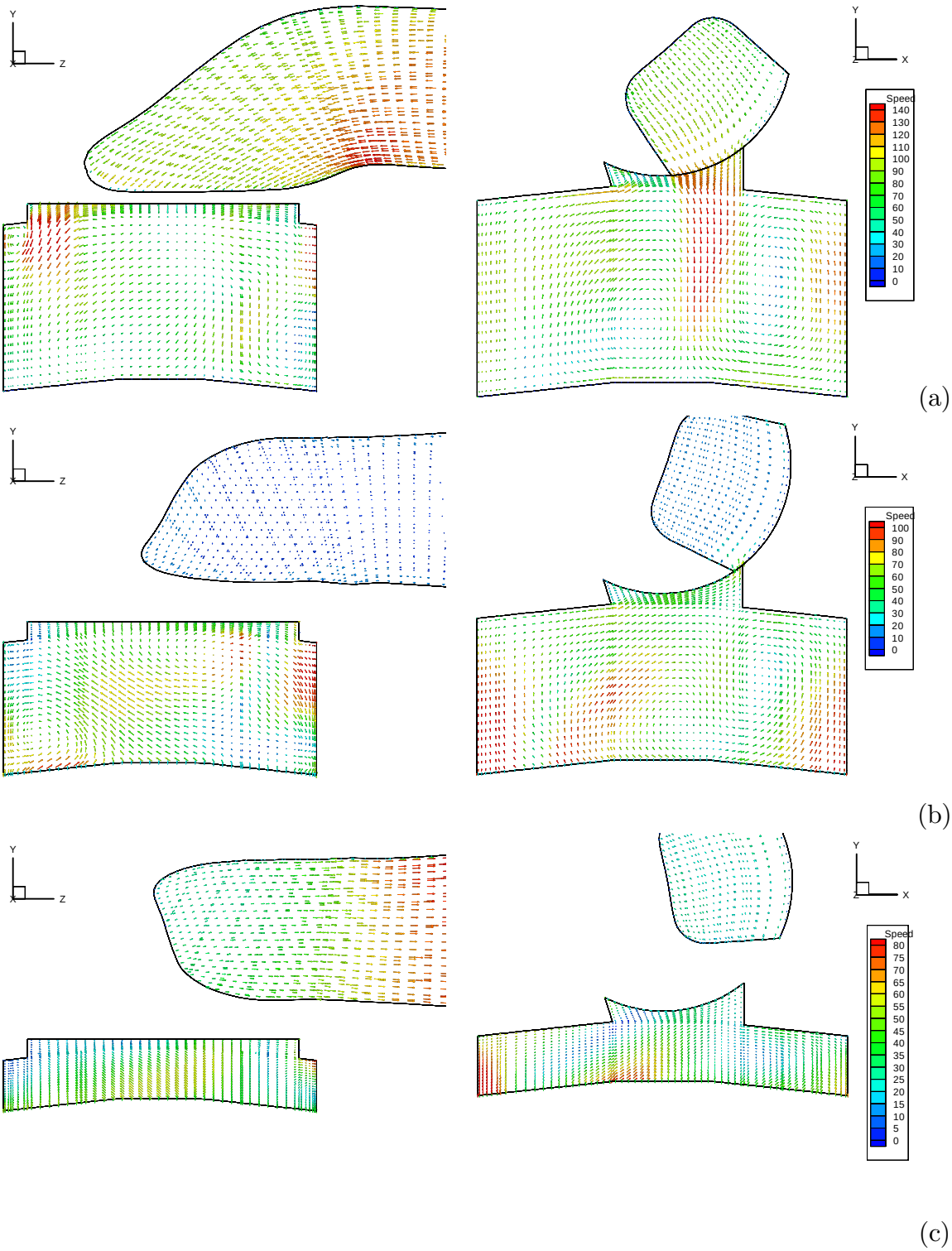

Figure 7.42: Flow field in tumble and cross tumble planes during the late intake and compression strokes. Simulation is the Mark III head run at 15000 rpm. Continues from figure 7.41, and results continued in figure 7.43. (a) – 180 °CA; (b) – 240 °CA; and (c) – 300 °CA.

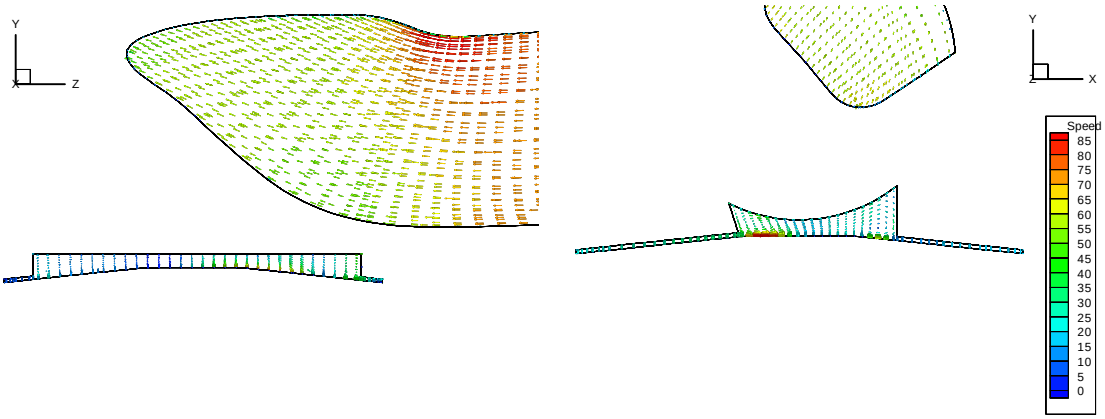

Figure 7.43: Flow field in tumble and cross tumble planes at TDC of the compression stroke. Simulation is the Mark III head run at 15000 rpm. Continues from figure 7.42.

more established. The two dual cross tumble vortices are the predominant feature in the flow. It should be noted that the cross tumble vortices are inclined due to the intake jet entering at an angle.

At IVC (figure 7.49) the dual cross tumble field remains, but is not as coherent as at BDC. The two vortices are now significantly different sizes, with the division between the two vortices sweeping across the cylinder head with the valve motion.

As the fundamental structure of the dual cross tumble flow structure has been identified, a new series of BRV engines was designed using this knowledge. The cylinder head shape used is based on the Mark III head, and the effect of variations in design can be tested as modifications to the existing basic design. This analysis of design variations of the Mark III head will be described in chapter 8.

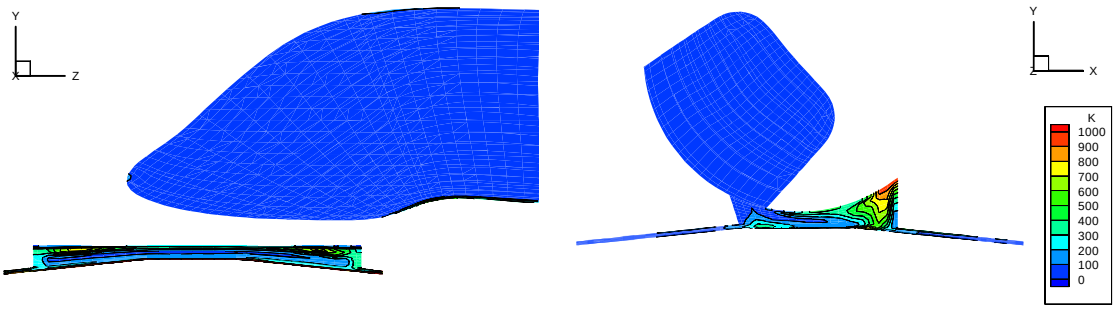

(a)

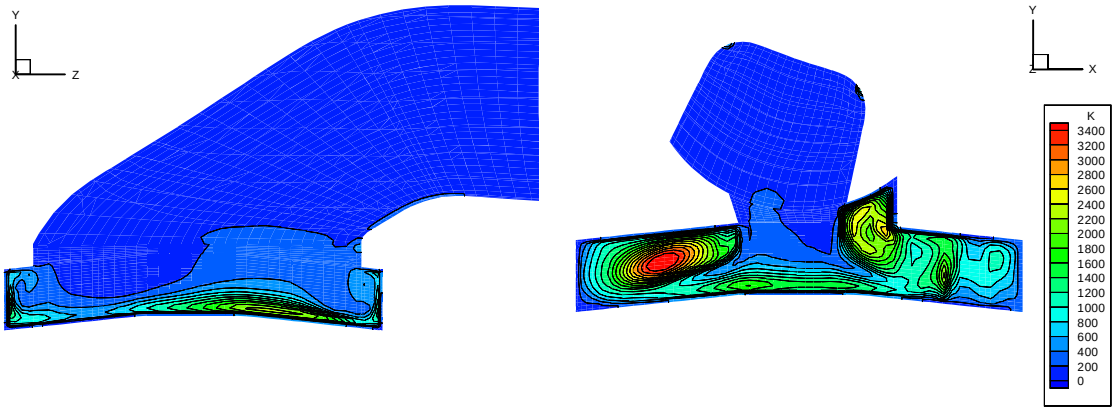

(b)

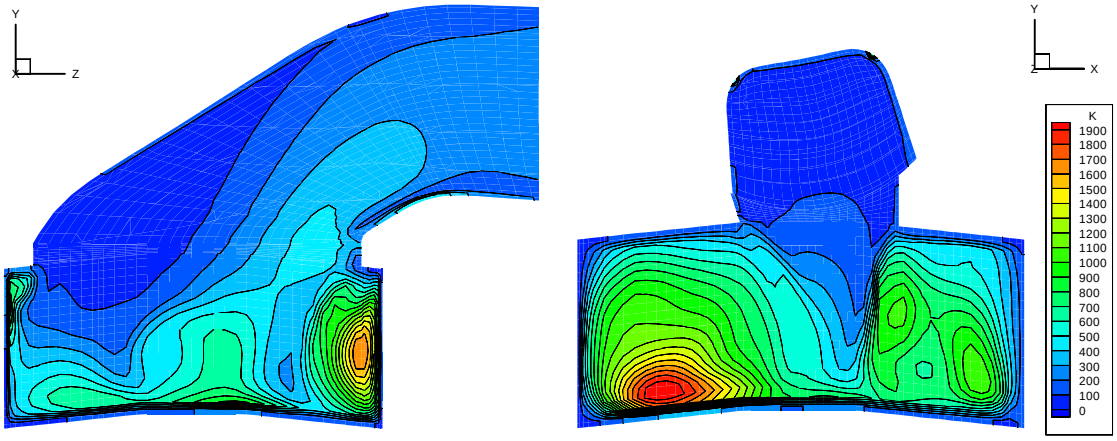

(c)

Figure 7.44: Turbulence field in tumble and cross tumble planes during the early intake stroke. Simulation is the Mark III head run at 15000 rpm. Results continued in figure 7.45. (a) – 0 °CA; (b) – 60 °CA; and (c) – 120 °CA.

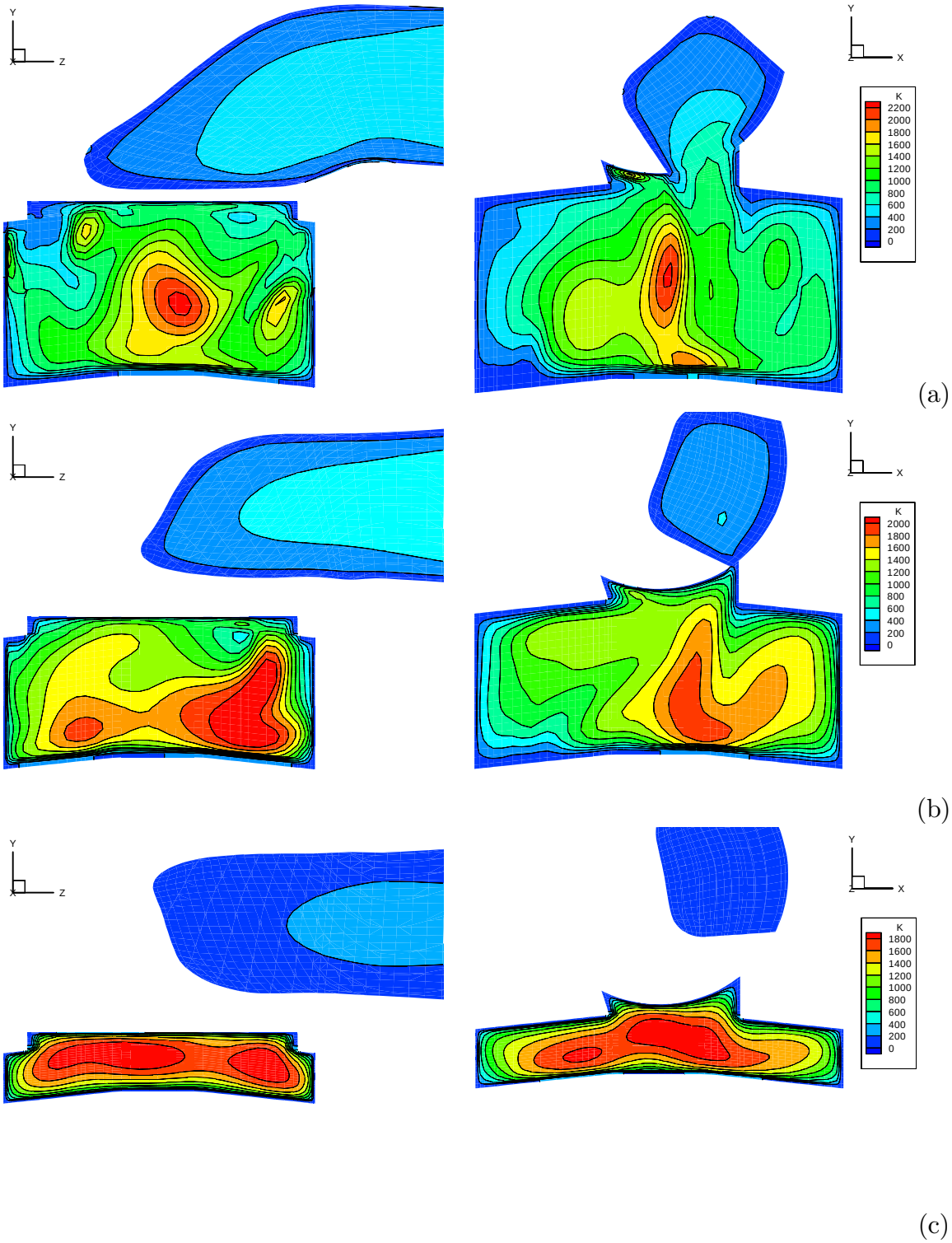

Figure 7.45: Turbulence field in tumble and cross tumble planes during the late intake and compression strokes. Simulation is the Mark III head run at 15000 rpm. Continues from figure 7.44, and results continued in figure 7.46. (a) – 180 °CA; (b) – 240 °CA; and (c) – 300 °CA.

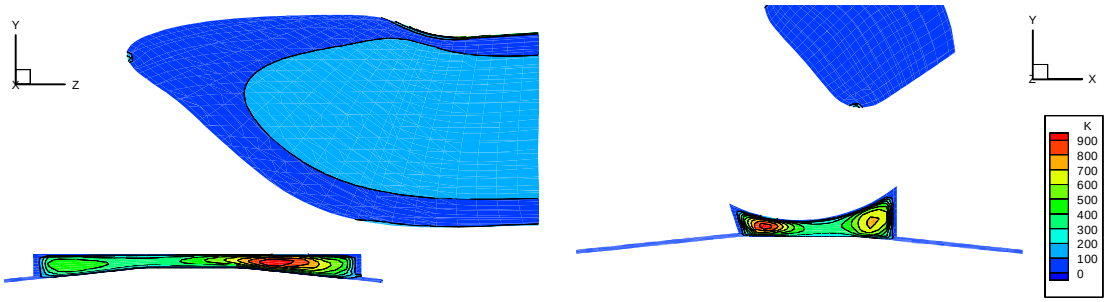

Figure 7.46: Turbulence field in tumble and cross tumble planes at TDC of the compression stroke. Simulation is the Mark III head run at 15000 rpm. Continues from figure 7.45.

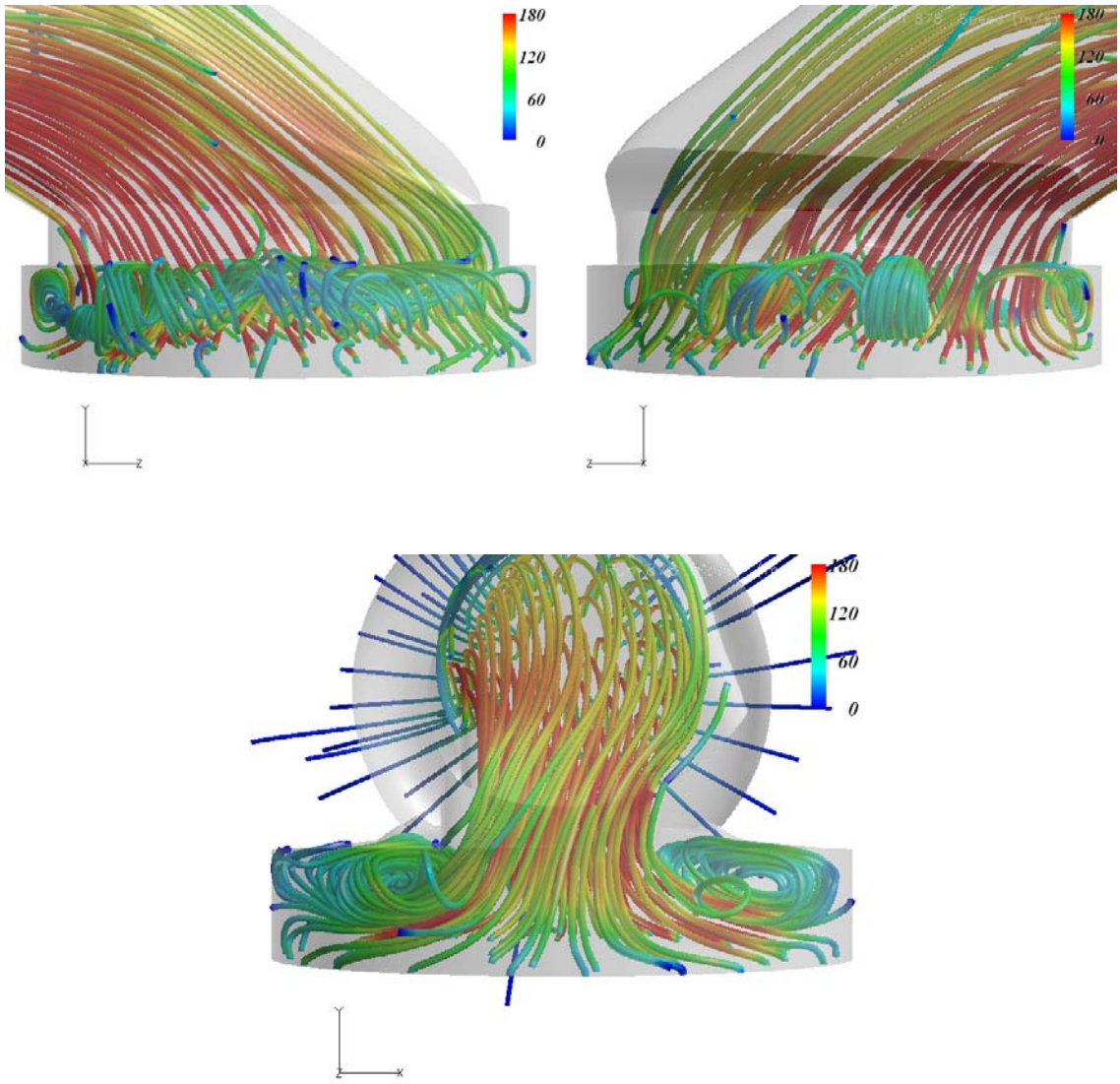

Figure 7.47: Various views of instantaneous streamlines at 79 °CA for BRV Mark III engine, 99 mm bore at 18000 rpm.

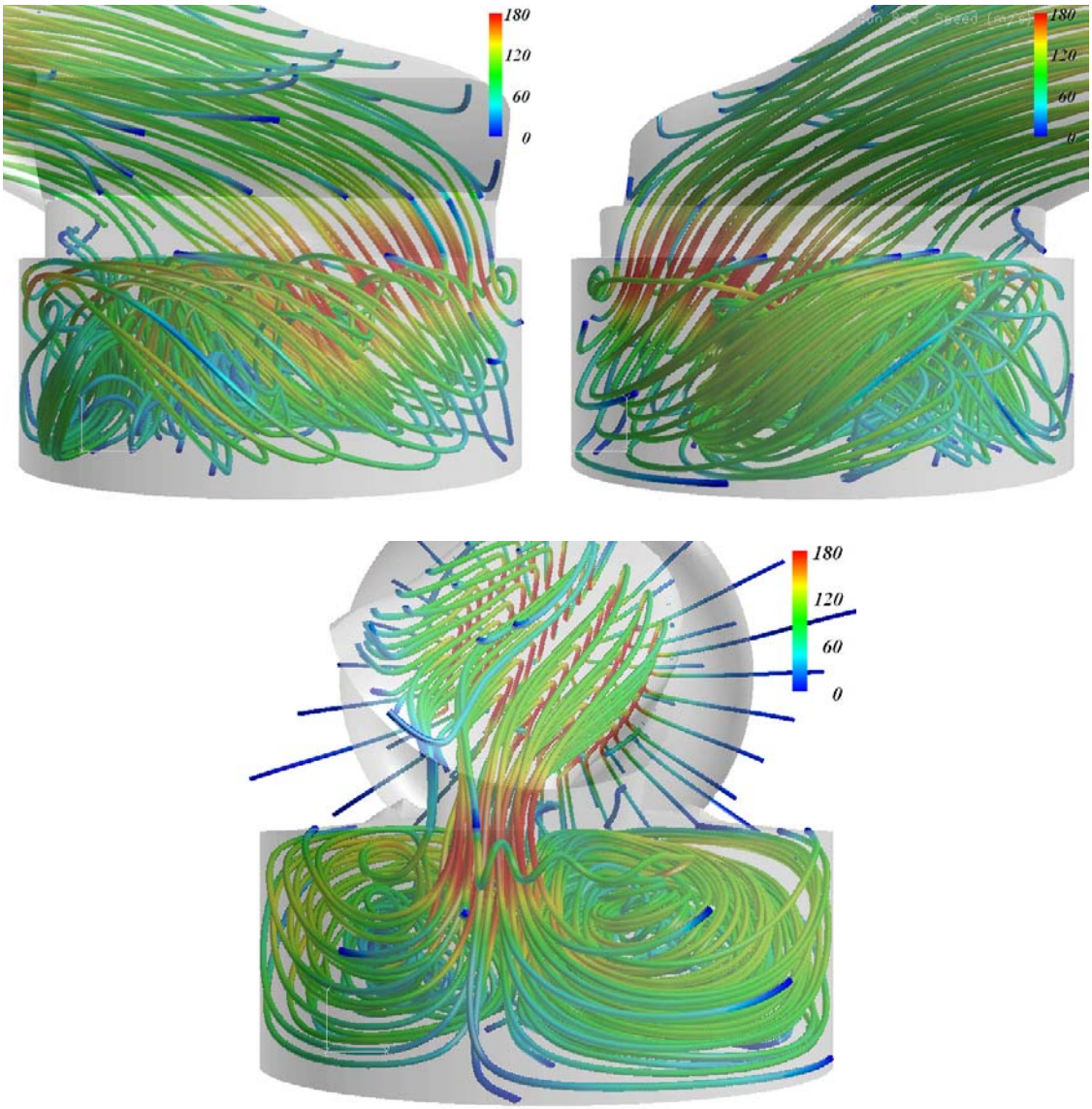

Figure 7.48: Various views of instantaneous streamlines at 178 °CA for BRV Mark III engine, 99 mm bore at 18000 rpm.

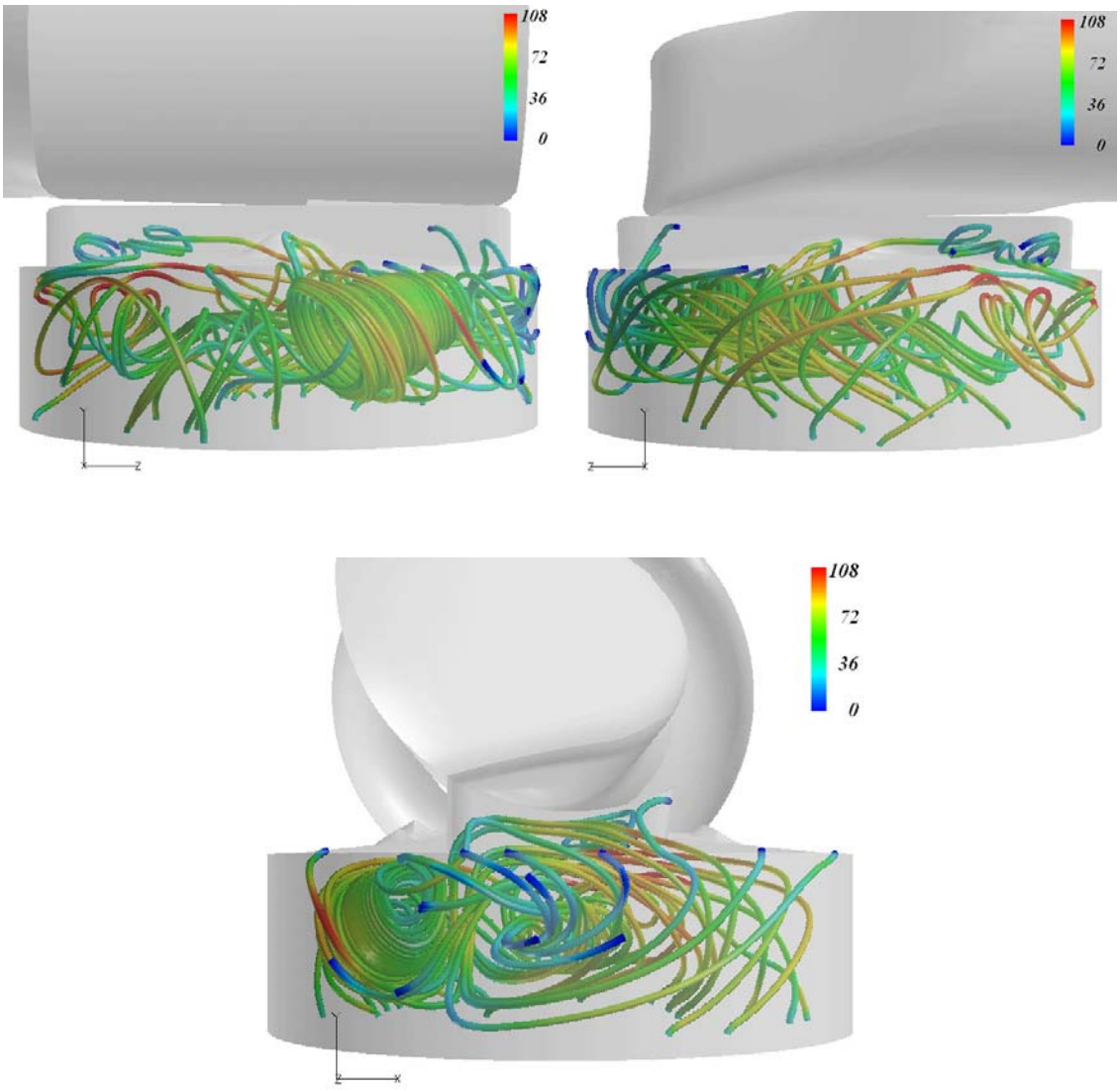

Figure 7.49: Various views of instantaneous streamlines at 247 °CA for BRV Mark III engine, 99 mm bore at 18000 rpm.

Chapter 8

Analysis of the BRV Engine

The CFD model, which has been validated in previous chapters, was applied to modelling the design of the BRV engine as it stood during 1999 and 2000. This time saw some significant developments in the project, including the development of the Mark II and Mark III combustion chambers using the dual cross tumble mechanism.

A series of 12 simulation runs were performed. Some of these runs reproduce dynamometer results, and so can be used as a further validation of the model. Some of the runs were used to test modifications impossible or impractical to test on a real engine, to further understand the BRV engine. The geometry and conditions simulated are tabulated in table 8.1 and continued in table 8.2.

These simulations have been used to assess the accuracy of the model in predicting volumetric efficiency (section 8.1), the effect of the inlet manifold wave on engine performance (section 8.2), the effect of reducing the valve cross-section area (section 8.3) and the related effect of increasing the valve size (section 8.4). The model is then used to establish the effect of heat transfer in the inlet manifold on engine performance (section 8.5) and the effect of bore to stroke ratio on the BRV engine (section 8.6). Finally, an analysis of the scaling of the in-cylinder turbulence with engine speed (section 8.7) is performed.

8.1 Prediction of Volumetric Efficiency

Of the simulations listed in tables 8.1 and 8.2, two runs were directly comparable to dynamometer runs and so direct comparisons can be made of the volumetric efficiency. The two simulations which are directly comparable are run 844 and run 851. Run 844 is of a 63 mm valve engine at 15000 rpm, and run 851 is of a 68 mm

Run Number	Valve Diameter	Window Dimensions	Engine Bore	Inlet Length
844	63 mm	78 mm × 34 mm	90 mm	156 mm
845	63 mm	78 mm × 34 mm	90 mm	156 mm
851	68 mm	85 mm × 34 mm	93 mm	155 mm
852	68 mm	85 mm × 34 mm	93 mm	155 mm
861	68 mm	85 mm × 34 mm	93 mm	128 mm
862	68 mm	85 mm × 34 mm	95 mm	128 mm
864	68 mm	85 mm × 34 mm	93 mm	128 mm
877	68 mm	85 mm × 34 mm	95 mm	128 mm
878	68 mm	85 mm × 34 mm	99 mm	128 mm
879	68 mm	85 mm × 34 mm	97 mm	128 mm
963	63 mm	78 mm × 34 mm	90 mm	156 mm
964	68 mm	85 mm × 34 mm	97 mm	128 mm

Table 8.1: Simulations performed on the BRV engine geometry and variations, part one.

Run Number	IVO °BTDC	IVC °ABDC	EVC °ATDC	Engine Speed	Comments
844	27	75	26	15000 rpm	
845	27	75	26	15000 rpm	"Throat" valve
851	15	73	15	15000 rpm	
852	15	73	15	18000 rpm	
861	30	73	15	18000 rpm	
862	30	73	15	18000 rpm	
864	30	73	15	15000 rpm	
877	30	73	15	18000 rpm	
878	30	73	15	18000 rpm	
879	30	73	15	18000 rpm	
963	27	75	26	15000 rpm	Air temp −10 °C
964	30	73	15	18000 rpm	Adiabatic walls

Table 8.2: Simulations performed on the BRV engine geometry and variations, part two.

valve engine also run at 15000 rpm.

The volumetric efficiency of an engine is defined as the mass of air in the cylinder at IVC divided by a reference mass of air. The reference air mass is defined as the mass of air which would exist in the cylinder volume at BDC, with the air being at a reference temperature and pressure. The CFD model was programmed to output the mass of air in the cylinder at every time step, which allows calculation of volumetric efficiency together with other mass flow parameters, such as valve mass flow rates.

Volumetric efficiency is difficult to measure experimentally, as it is not usually possible to directly measure the mass of gas in the cylinder at inlet valve close. As discussed in section 7.4.1, the flow rate of air entering the engine was measured. Since the device used to measure the mass flow rate can be located away from the engine, specialised precision air flow rate measuring devices can be used. In this case the specified accuracy of the instrument was $\pm 2\%$.

However, the mass flow rate recorded entering the engine manifold is not necessarily the same as the mass of air trapped in the cylinder per unit time. During the scavenging section of the engine cycle, gas can travel directly from the inlet valve across the cylinder and out the exhaust valve. This small amount of air flow is included in the gas flow through the inlet manifold, but is not included in a volumetric efficiency calculation.

Therefore, as the term "volumetric efficiency" can be confusing, the air mass flowing into the engine through the intake manifold will now be referred to as "air consumption", and the air mass in the cylinder when the inlet valve shuts will be referred to as "trapped air mass".

Obviously an engine designer wishes to minimise this "short-circuit" gas as it wastes fresh air and fuel. However, high performance engines generally run with large valve overlaps and a degree of gas short-circuiting to improve the quality of the scavenging. Therefore the air consumption is slightly higher than the trapped air mass as only the former includes the short-circuit gas. Consequently, the air consumption of the engine is expected to be slightly higher than the trapped air mass as the experimental results also include the small contribution of the short-circuit gas.

The comparison between the trapped air mass predicted from the simulations and the air consumption measured on the dynamometer is shown in tables 8.3 and 8.4. For the 63 mm valve shown in table 8.3, it can be seen that the simulation has predicted an air mass flow rate 6.2 kg/h too high, or a 3% variation. For the 68 mm valve shown in table 8.4, it can be seen that the simulation has predicted an air

mass flow rate 11.5 kg/h too high, about a 6% variation.

This would seem to contradict the expected result of the experimental outcome being slightly larger than the CFD result. This problem can be addressed by normalising the flow rates against inlet conditions. As discussed in section 7.4.5, the temperature of the gas entering the inlet manifold of the CFD simulation was adjusted to match the experimental results. This effect is due to vapourisation of the fuel causing the gas in the inlet manifold to cool, and this effect is not taken into account in the CFD model.

For the CFD results, the gas state of the normalising air mass is calculated based on the conditions of the inlet boundary. For the experimental model the measured temperature and pressure of the gas entering the engine are used. The actual temperatures and pressures used for the reference state are listed in table 8.5 and 8.6. The normalised air mass flow rate is expressed as a ratio of the actual and reference gas flow rates, that is

$$m_n = \frac{m_{raw}}{m_{ref}} \tag{8.1}$$

where m_n is the normalised mass flow rate, m_{raw} is the air mass per cycle from the CFD or experimental, and m_{ref} is the reference air mass.

When the comparison is performed based on these normalised values, the CFD underpredicts the 63 mm value by 4%, and the 68 mm valve by 1%. These values are in good agreement with the experimental results, the result for the 68 mm valve is within the experimental error of the instrument. Additionally, the simulated flow rate is now slightly lower than that measured entering the engine. This is in agreement with the trapped air mass measured by the CFD being slightly lower than the air consumption measured entering the inlet manifold.

The reference temperature assumed in the CFD simulation is around 20 °C colder than the dynamometer conditions. This temperature variation has been justified in section 7.4.5 on the basis that fuel evaporation is not included in the simulations, and 5 °C boundary conditions were found to best reproduce the experimental inlet manifold wave. This highlights the importance of the reference conditions in a volumetric efficiency calculation, and that selection of a reference condition is not simple. However, overall the simulation appears to be modelling the air consumption of the engine accurately.

Run	CFD	Dynamometer					
	844	247	302	403	404	411	mean
kg/h	191.0	181.8	186.5	183.8	185.3	186.6	184.8
normalised (%)	111.4	114.9	114.8	114.8	115.2	116.6	115.2

Table 8.3: Comparison of CFD simulated trapped air mass and experimentally measured air consumption for 63 mm valve BRV engine at 15000 rpm.

Run	CFD	Dynamometer		
	851	399	401	mean
kg/h	194.0	183.0	182.1	182.6
normalised (%)	113.2	114.4	113.7	114.1

Table 8.4: Comparison of CFD simulated trapped air mass and experimentally measured air consumption for 68 mm valve BRV engine at 15000 rpm.

CFD Run	844	851
Temperature (°C)	5.0	5.0
Pressure (kPa)	101.3	101.3

Table 8.5: Reference conditions for the CFD trapped air mass calculations of tables 8.3 and 8.4.

Dynamometer Run	247	302	399	401	403	404	411
Temperature (°C)	27.5	21.4	25.0	24.8	25.3	23.4	25.3
Pressure (kPa)	101.5	101.7	101.4	101.4	101.6	101.4	101.6

Table 8.6: Reference conditions for the experimental volumetric efficiency calculations of tables 8.3 and 8.4.

8.2 Effect of the Inlet Manifold Wave

It is widely known that the pressure wave present in the inlet manifold can have dramatic effects on the volumetric efficiency of an engine, as discussed in section 4.3. It is less well known that the inlet manifold wave can also have significant effects on many other engine parameters, such as swirl, tumble or in-cylinder turbulence.

Two examples of the effects of the inlet manifold wave on engine performance are shown in figure 8.1 and figure 8.3.

Run 851, shown in figure 8.1, is simulating an engine speed of 15000 rpm. Shown are the results from the first and second revolution of the simulation for a variety of parameters. The engine configuration is obviously the same between the two cycles, so that the only difference between the two cycles is caused by the inlet manifold wave.

The inlet manifold wave has a major effect on when during the intake stroke the gas enters the cylinder. The mass flow rate of gas into the cylinder is shown in figure 8.1a, and it demonstrates that the peak flow occurs around 40 °CA earlier on the second cycle than in the first cycle. The flow rate in the second cycle is less than than the flow in the first cycle after 90 °CA, and the second cycle has significantly more back flow at the end of the intake stroke than the first cycle. This shows that more gas enters the cylinder early in the intake stroke of the second cycle than in the first.

This earlier flow is seen in the cylinder gas mass shown in figure 8.1b, where the gas mass is higher early in the intake stroke, but slows as the stroke progresses, and results in a lower final mass at IVC. The final reduction is around 8%.

The in-cylinder turbulence also significantly reduces from the first cycle to the second, as shown in figure 8.1c. The peak of turbulence occurs at 300 °CA for both cycles, but the magnitude of the peak in the second cycle is reduced by about 30% from that seen in the first cycle. Similarly, figure 8.1d shows that there is significantly more kinetic energy in the flow (as mass averaged velocity squared) in the first cycle than in the second cycle in the latter stages of the intake stroke. For instance, at 240 °CA, the mass averaged velocity squared in the first cycle is $4247\,\mathrm{m^2\,s^{-2}}$ and $2833\,\mathrm{m^2\,s^{-2}}$ in the second cycle, a reduction of 33%.

This major reduction in turbulence and kinetic energy appears to be caused by the peak of valve mass flow rate occurring earlier. In the first cycle there appears to be a much greater mass entering the cylinder late in the intake stroke, and a reduced amount of back flow. This increased flow entering the cylinder late in the stroke gives the in-cylinder flow field a final "kick" just before the inlet valve shuts,

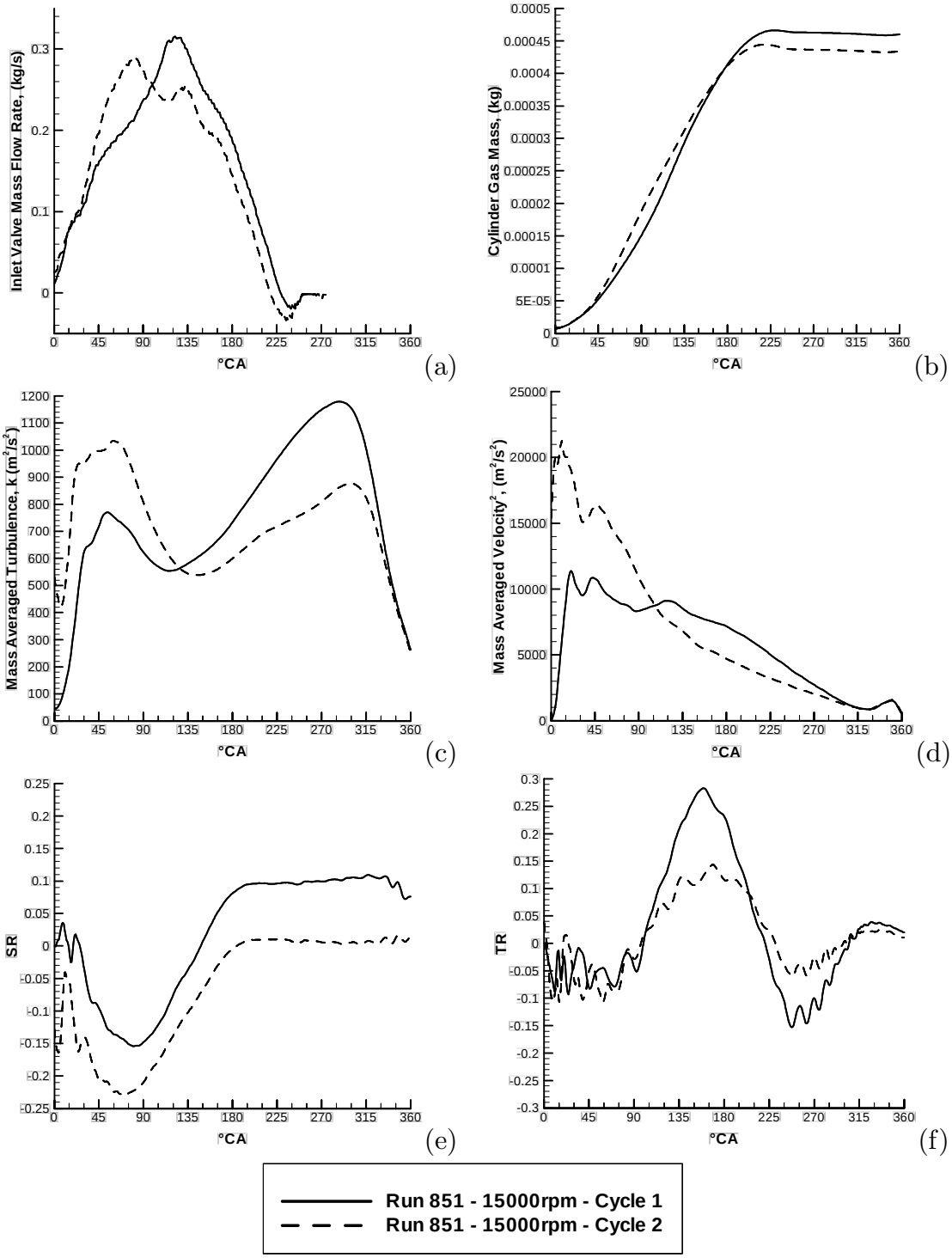

Figure 8.1: Comparison of first and second cycle results for run 851, at 15000 rpm. (a) – Valve mass flow rate; (b) – Cylinder gas mass; (c) – Mass averaged turbulent energy (k); (d) – Mass averaged velocity squared; (e) – Swirl ratio; and (f) – Tumble ratio.

and can significantly increase in-cylinder energy levels.

Back flow at the end of the inlet stroke appears to drain significant amounts of energy from the flow field. Back flow usually exists as a small high velocity jet, driven by a significantly higher pressure in the cylinder than in the inlet manifold. As this jet has a high velocity, there is a significant amount of energy required to accelerate the fluid, so back flow can reduce in-cylinder energy levels significantly. This reduction in in-cylinder energy levels leads to reduced turbulence levels, and reduced engine performance. Thus, back flow at the end of the intake stroke reduces engine performance in two separate ways—firstly by reducing volumetric efficiency, and secondly by reducing in-cylinder turbulence levels.

This effect can be seen in figure 8.2, where the flow field is shown at 222 °CA, just before the inlet valve shuts. The valve mass flow rate graph in figure 8.1a shows there to be a strong back flow occurring during the second cycle at this position. There is clearly a significantly lower level of fluid velocity and turbulence in the second cycle, particularly in the centre of the cylinder.

This reduction of the in-cylinder flow field energy is seen as a reduction of the swirl ratio in figure 8.1e, and the tumble ratio in figure 8.1f. Both the swirl ratio and tumble ratio are seen to be smaller in the second cycle than in the first. This is a sign of the general reduction in the in-cylinder energy levels shown in figure 8.1d.

When the same configuration is run at 18000 rpm, the results are very different. Figure 8.3a shows the first cycle mass flow rate to follow a similar trend as seen in first cycle at 15000 rpm. The second cycle is very different, and shows the flow rate to dramatically decrease in the range 45–135 °CA, before returning to similar levels as predicted for the first stroke. The remainder of the intake stroke after 135 °CA has quite similar flow rates in the first and second cycles, with the second cycle being fractionally higher than the first cycle. At this high speed there is no back flow in either cycle.

The region of reduced flow rate is seen in the air mass in the cylinder, figure 8.3b, as a region of significantly reduced gradient. This small region of reduced flow is caused by the inlet manifold wave. The manifold length used here was designed to be tuned at 15000 rpm, so at 18000 rpm it is substantially out of tune. Thus the inlet manifold wave arrives at the inlet valve at an inappropriate time and causes a significant reduction in volumetric efficiency compared with that possible with an in-tune manifold.

The small increase in flow in the second cycle after 135 °CA appears to be the reason for the slightly increased turbulence seen in figure 8.3c and the increased

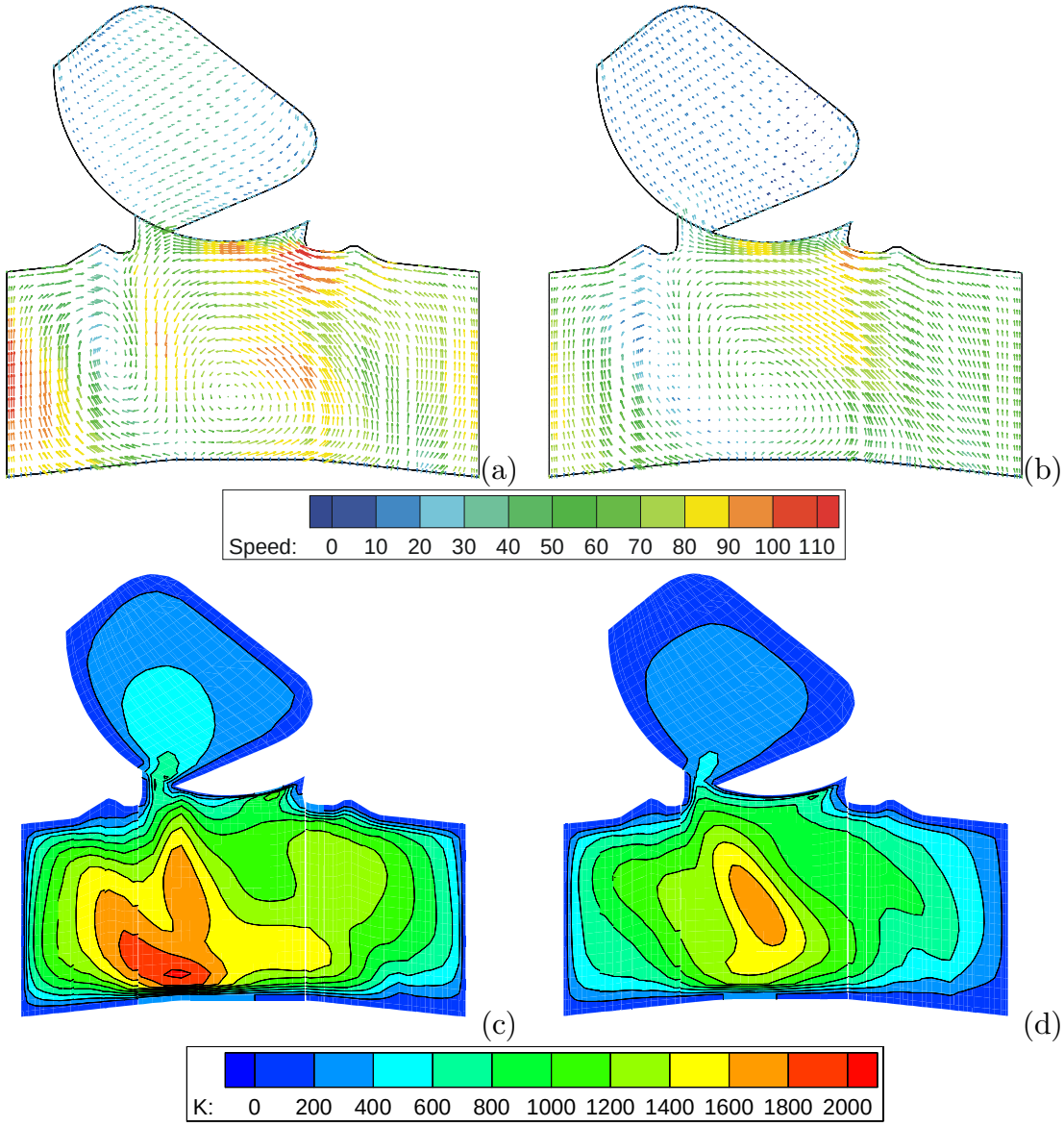

Figure 8.2: Comparison of first and second cycle simulation flow fields for run 851 at 222 °CA. (a) – First cycle, gas velocity; (b) – Second cycle, gas velocity; (c) – First cycle, turbulent energy (k); and (d) – Second cycle, turbulent energy (k).

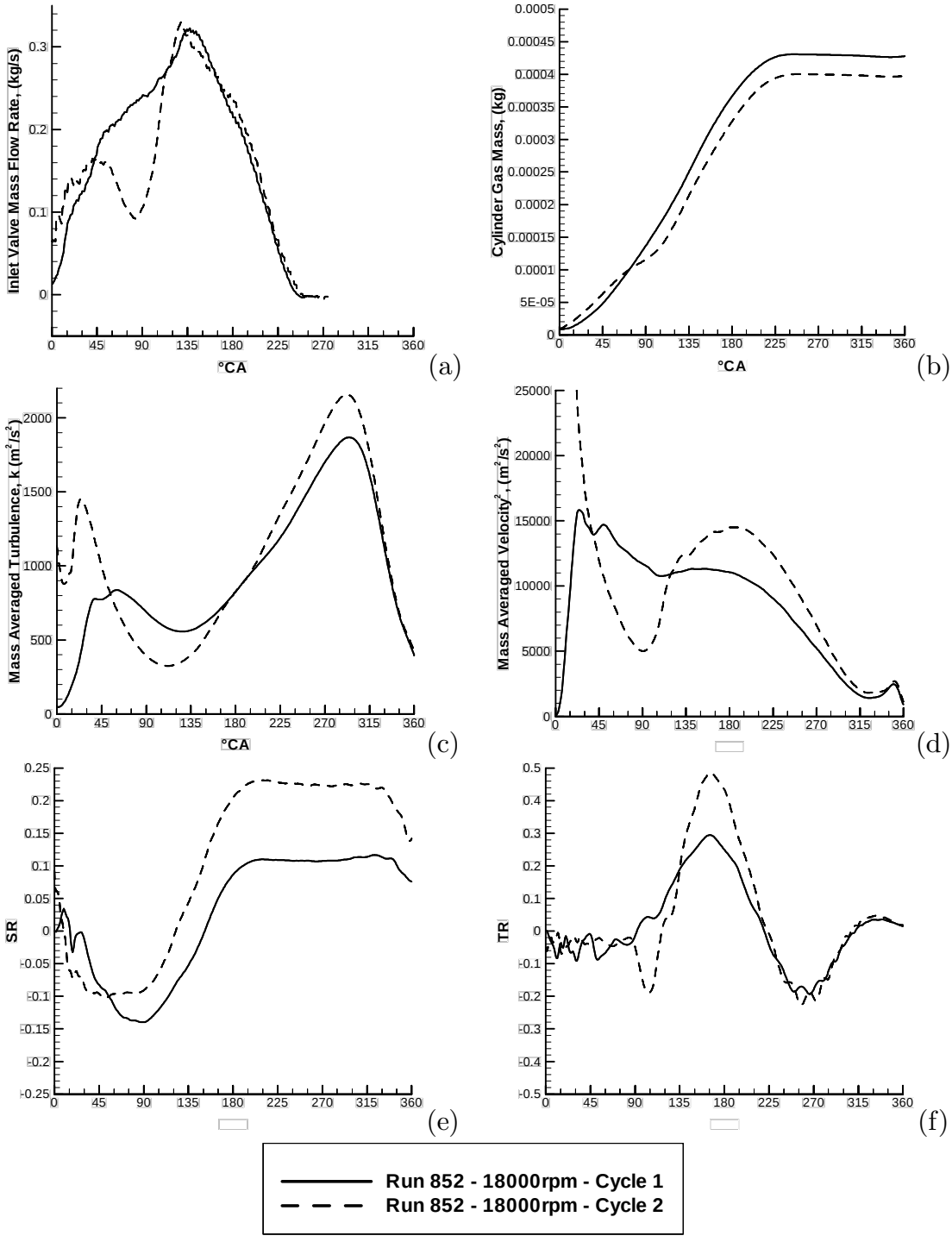

Figure 8.3: Comparison of first and second cycle results for run 852, at 18000 rpm. (a) – Valve mass flow rate; (b) – Cylinder gas mass; (c) – Mass averaged turbulent energy (k); (d) – Mass averaged velocity squared; (e) – Swirl ratio; and (f) – Tumble ratio.

kinetic energy seen in figure 8.3d after 180 °CA. This increased energy is also seen as higher levels of swirl and tumble in the second cycle, as seen in figures 8.3e and 8.3f.

There is no back flow at the end of the intake stroke, so there is no drain on the in-cylinder flow energy at the end of the intake stroke.

This demonstrates the important effects that the inlet manifold wave has, not only on the volumetric efficiency, but also on the in-cylinder turbulence. Obviously, the important factor for high volumetric efficiency is to maximise the area under the air mass flow rate against crank angle curve. However, in-cylinder turbulence is maximised by making the flow occur late in the intake stroke, and avoiding back flow at the end of the intake stroke.

8.3 Effect of Constrictions in the Valve

As the engine design progressed, it was thought that the valve was too large in cross section area, and that reducing the valve's cross section area (that is, constricting it) would increase performance. The increased performance was believed to originate from the issues discussed in section 4.2.3, that is, it would increase the velocity of the gas entering the cylinder, which in turn increases the in-cylinder gas kinetic energy and turbulence.

The effect of constricting the valve cross section was assessed by comparing runs 844 and 845. The only difference between these two simulations is that the valve in run 845 has its cross sectional area significantly reduced. The cross section profile through the valve is shown in figure 8.4 for the unconstricted valve (or "open" valve), and the constricted valve profiles are shown in figure 8.5. The constriction is most noticeable as a narrowing of the cross section around the central three cross sections, at $X = 30$, 40 and 50 mm.

The constriction was designed to smoothly blend into the original valve, and to use the same window and inlet manifold shape. This means that the difference between the two geometries is greatest in the centre of the valve, and reduces to become the same towards either end. Both simulations used the same head and trumpet geometries, valve timing and inlet manifolds.

The flow fields predicted for the two configurations are shown in figures 8.6 and 8.7 for the tumble plane, and figures 8.8 and 8.9 for the cross tumble plane. The tumble plane, the fluid speed shown in figure 8.6, shows the flow fields in the cylinder to be very similar in the two configurations. There are slight differences in the details of the in-cylinder flow vectors seen in figure 8.9, however the overall

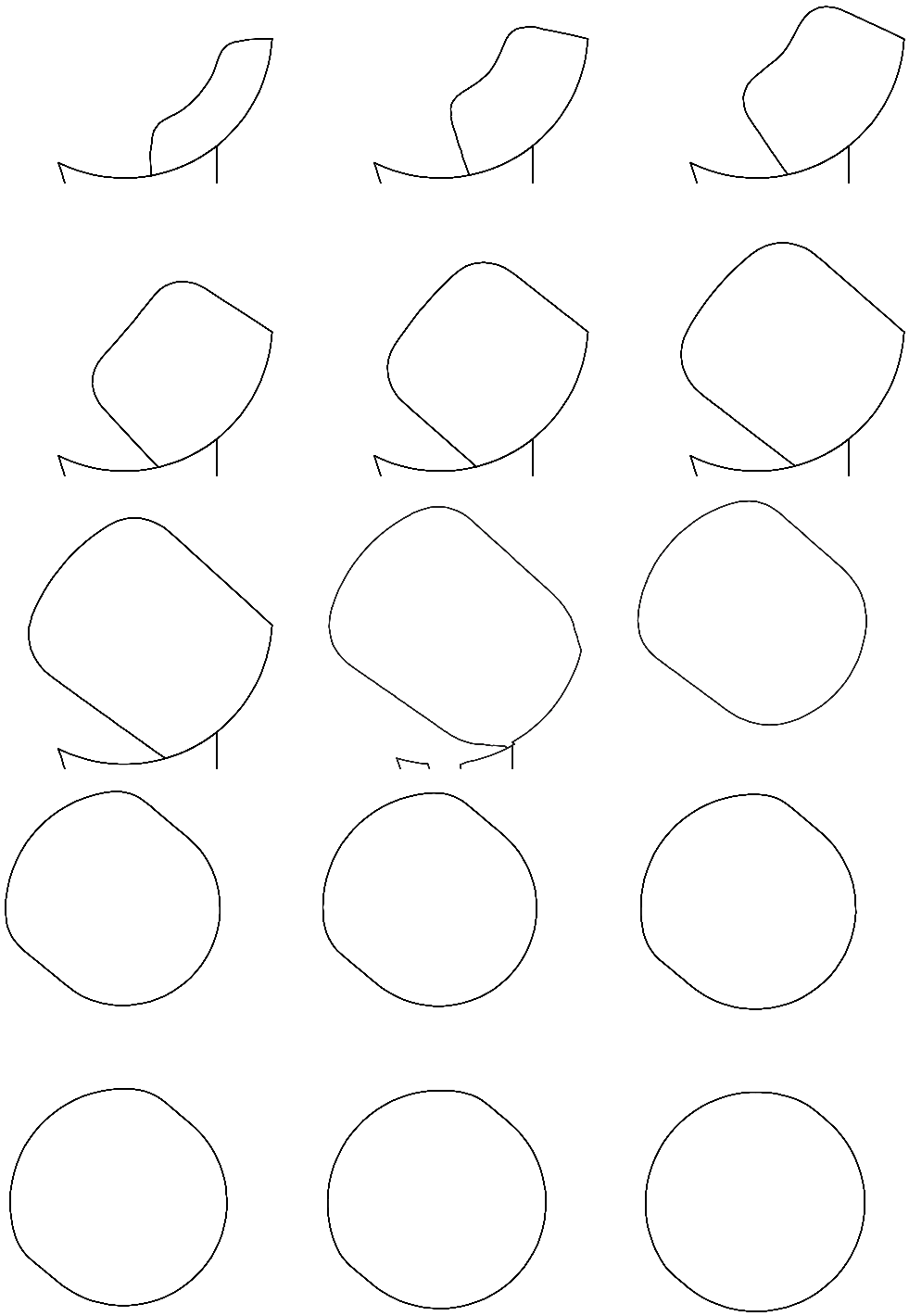

Figure 8.4: Valve cross sections for the open valve used in run 844. Top left is $X = -40\,\text{mm}$, incrementing in 10 mm steps to the bottom right at $X = 110\,\text{mm}$.

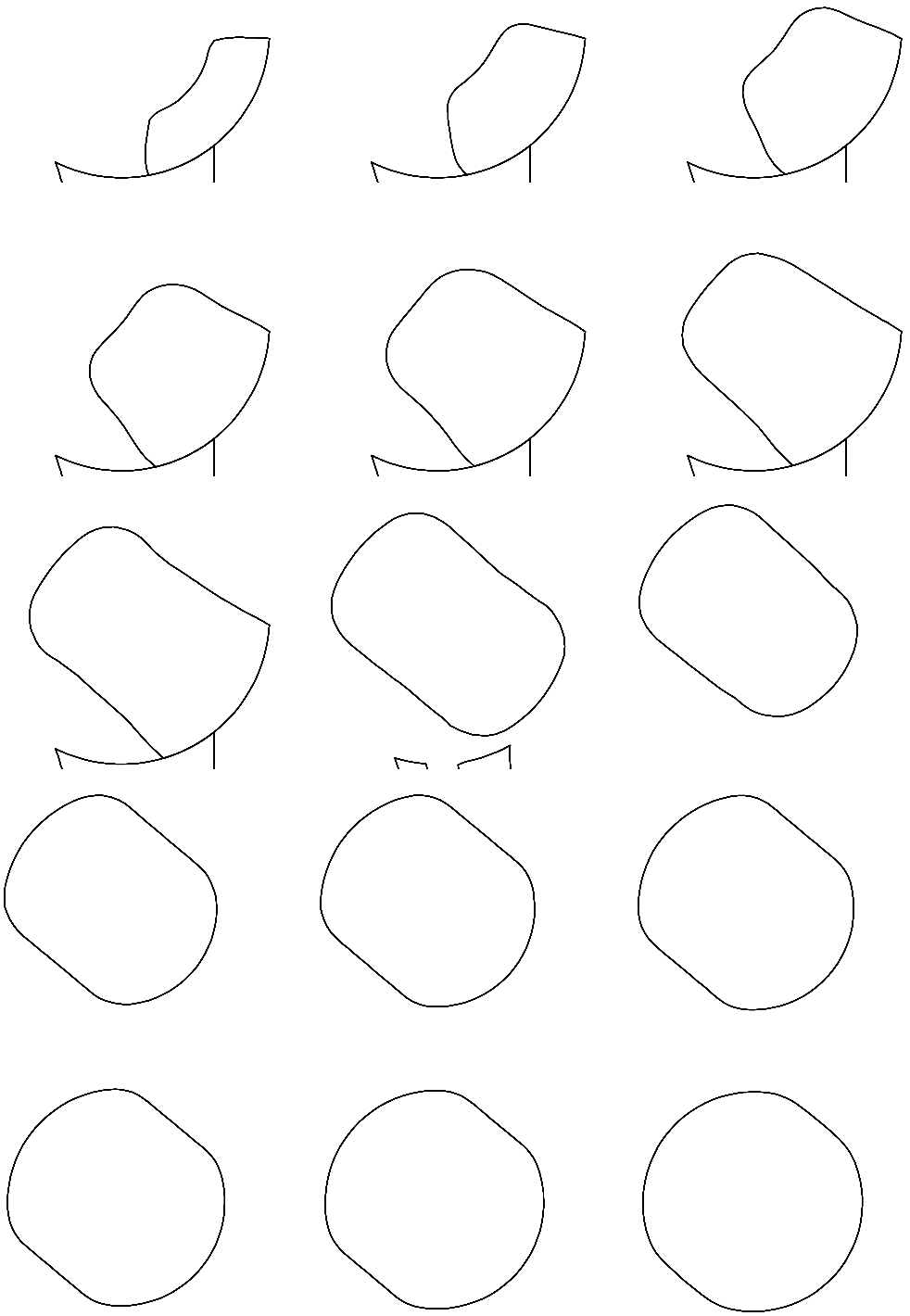

Figure 8.5: Valve cross sections for the constricted valve used in run 845. Top left is $X = -40\,\text{mm}$, incrementing in $10\,\text{mm}$ steps to the bottom right at $X = 110\,\text{mm}$.

flow is similar. The only significant difference between the two flows is seen in the inlet manifold, where the constricted valve is shown to exhibit significantly higher velocities in the middle section of the manifold.

In the cross tumble plane shown in figures 8.8 and 8.9, the velocity fields are also very similar. The gas scalar speed cross section shows that the magnitude of the fluid velocity has increased slightly in the constricted valve configuration. There is a significant increase in fluid velocities in the jet of gas entering the cylinder in the constricted valve engine, with the maximum value increasing from around $120\,\mathrm{m\,s^{-1}}$ to about $140\,\mathrm{m\,s^{-1}}$. The vectors, shown in figure 8.8, show the fields have essentially the same shape, the only difference being a shift in the location of the vortex centres. The shift is only small.

The differences in the averaged parameters between the open and constricted valves is shown in figure 8.10. The mass of air trapped in the cylinder is shown in figure 8.10a, and at IVC is seen to be effectively the same between the two configurations. More air flows into the cylinder for the open configuration between approximately 90 °CA and 135 °CA than is the case with the constricted arrangement.

A small amount of back flow is seen to occur in the open configuration just before the valve shuts. This back flow in the open valve is clearly shown in the mass flow rate in figure 8.10b. Here the open configuration has a significantly higher mass flow rate through most of the intake stroke up until around 160 °CA, where the situation reverses and the constricted valve allows a higher flow rate. The reason for the constricted valve having a higher flow rate after 160 °CA is due to the reduced flow rate earlier in the inlet stroke, resulting in a lower cylinder pressure. This reduced cylinder pressure is seen at 160 °CA in figure 8.10e. Due to the higher pressure difference in the constricted valve engine, the flow rate increases and the effect of back flow (caused by a pressure in the inlet manifold being lower than that in the cylinder) is reduced. Figure 8.10a shows that, by the end of the intake stroke, both cycles have a similar quantity of air trapped in the cylinder.

This suggests that the open valve engine can be redesigned to increase performance from the design modelled here, by modifications to inlet valve closing point, manifold length or other factors. These modifications can reduce the back flow at the end of the intake stroke and increase volumetric efficiency.

As expected, the higher velocities seen in the constricted valve manifest themselves as an increased level of turbulence (figure 8.10c) and flow bulk kinetic energy (mass average velocity square, figure 8.10d) after 135 °CA. This increase is also partly due to the constricted valve shifting the flow towards the end of the intake

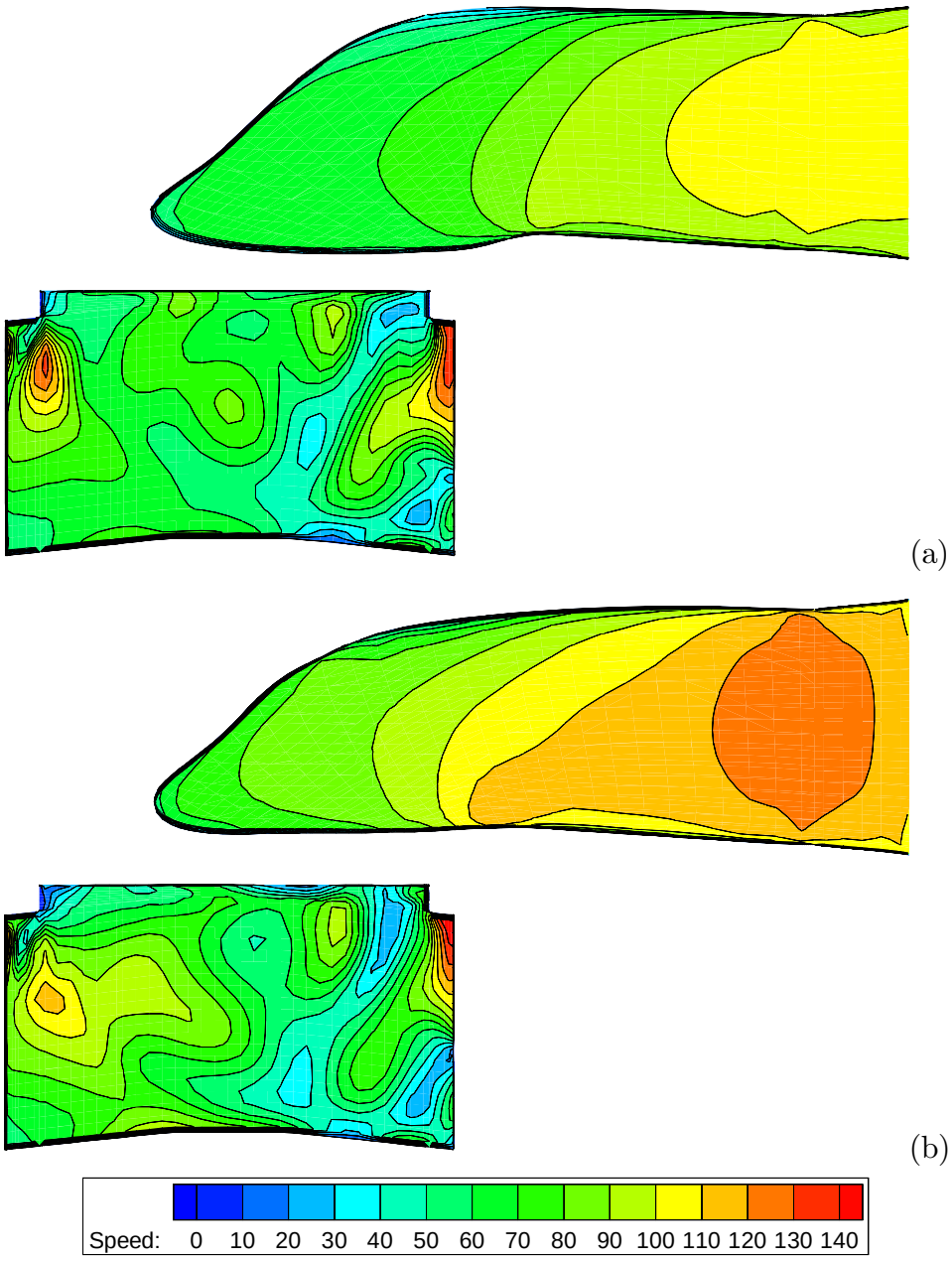

Figure 8.6: Comparison of tumble plane fluid speed for constricted and open valves at 218°CA. (a) – Open valve, fluid speed; and (b) – Constricted valve, fluid speed.

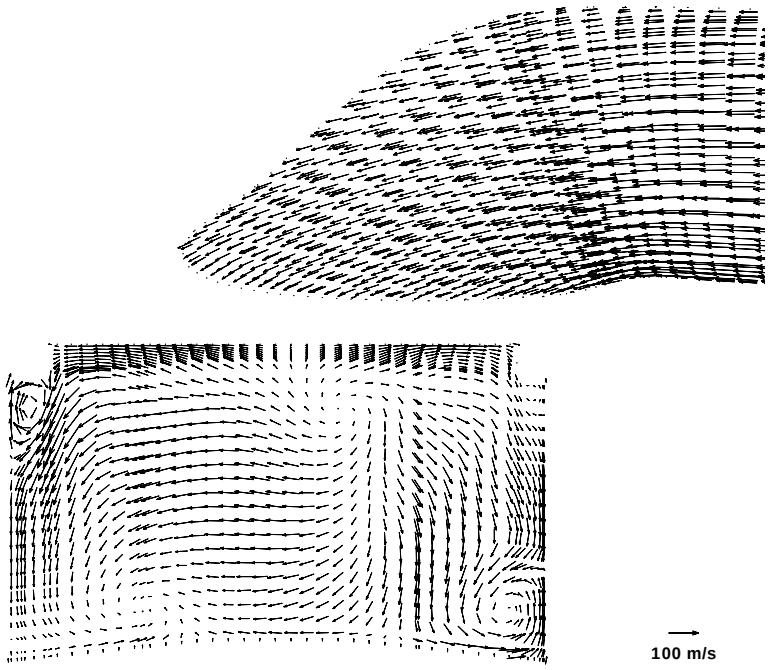

(a)

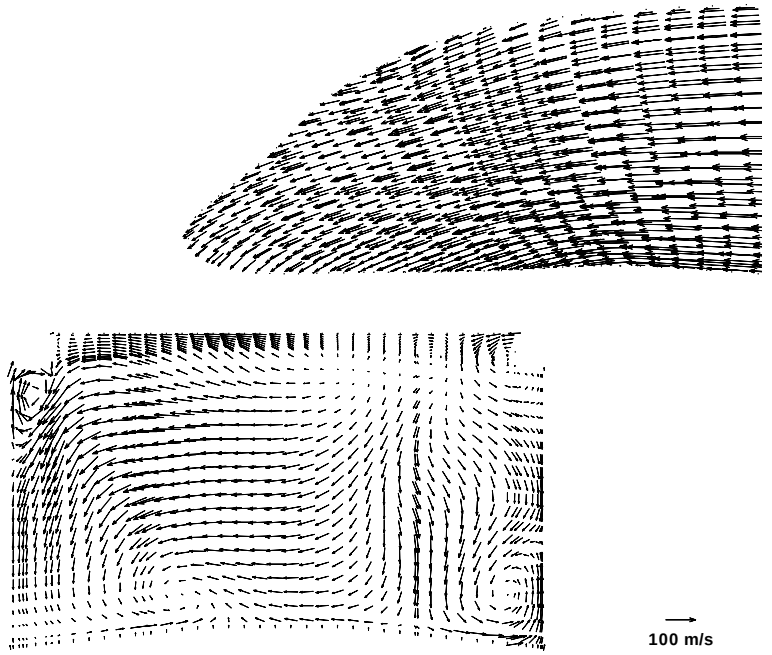

(b)

Figure 8.7: Comparison of tumble plane flow field for constricted and open valves at 218 °CA. (a) – Open valve, fluid velocity vectors; and (b) – Constricted valve, fluid velocity vectors.

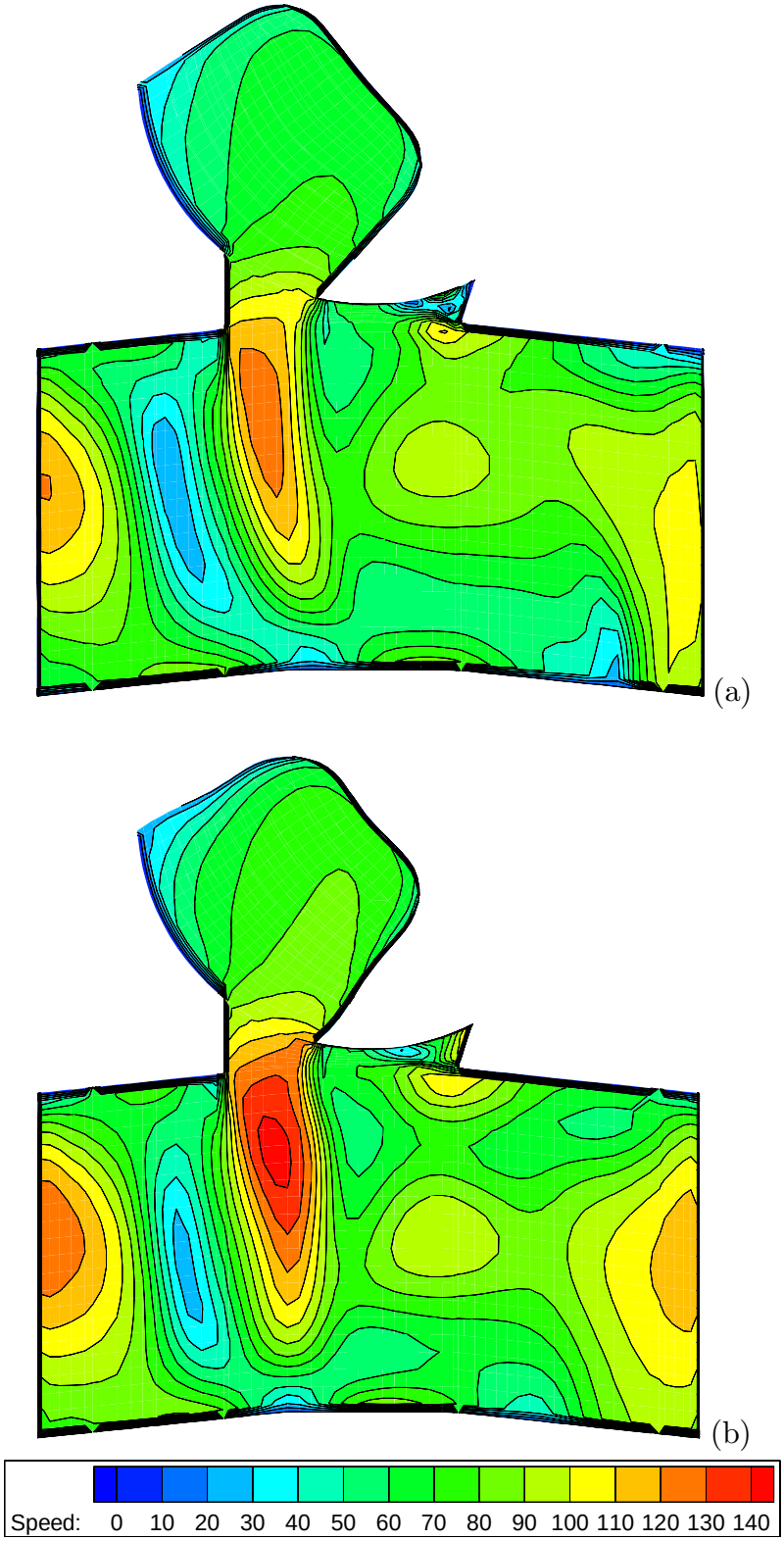

Figure 8.8: Comparison of cross tumble plane fluid speed for constricted and open valves at 218 °CA. (a) – Open valve, fluid speed; and (b) – Constricted valve, fluid speed.

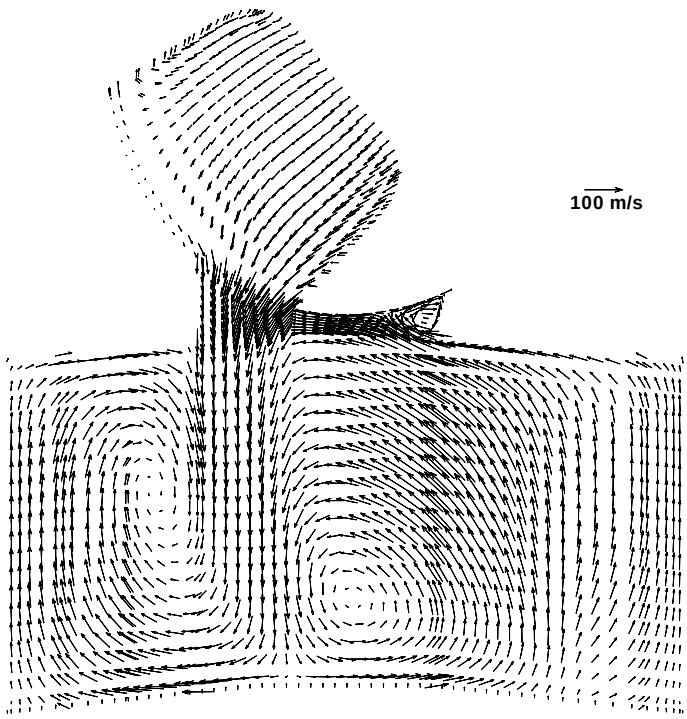

(a)

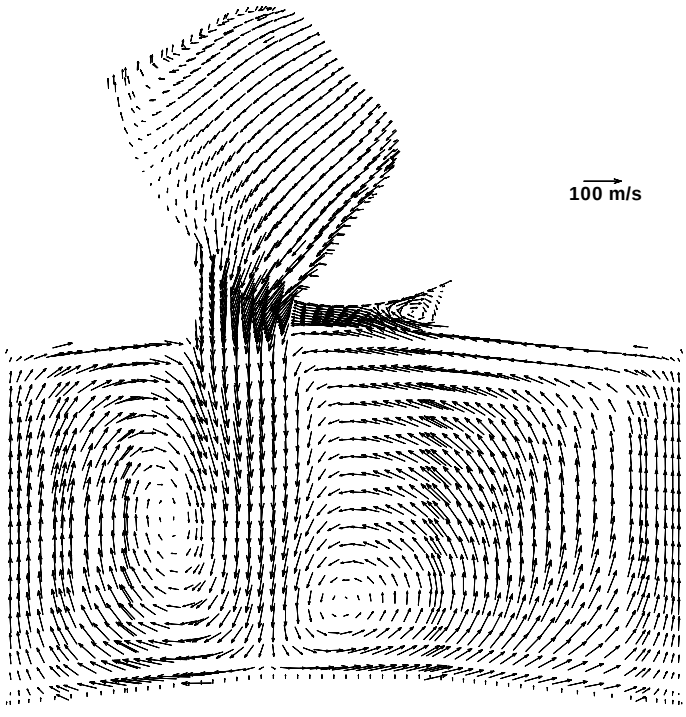

(b)

Figure 8.9: Comparison of cross tumble plane flow field for constricted and open valves at 218 °CA. (a) – Open valve, fluid velocity vectors; and (b) – Constricted valve, fluid velocity vectors.

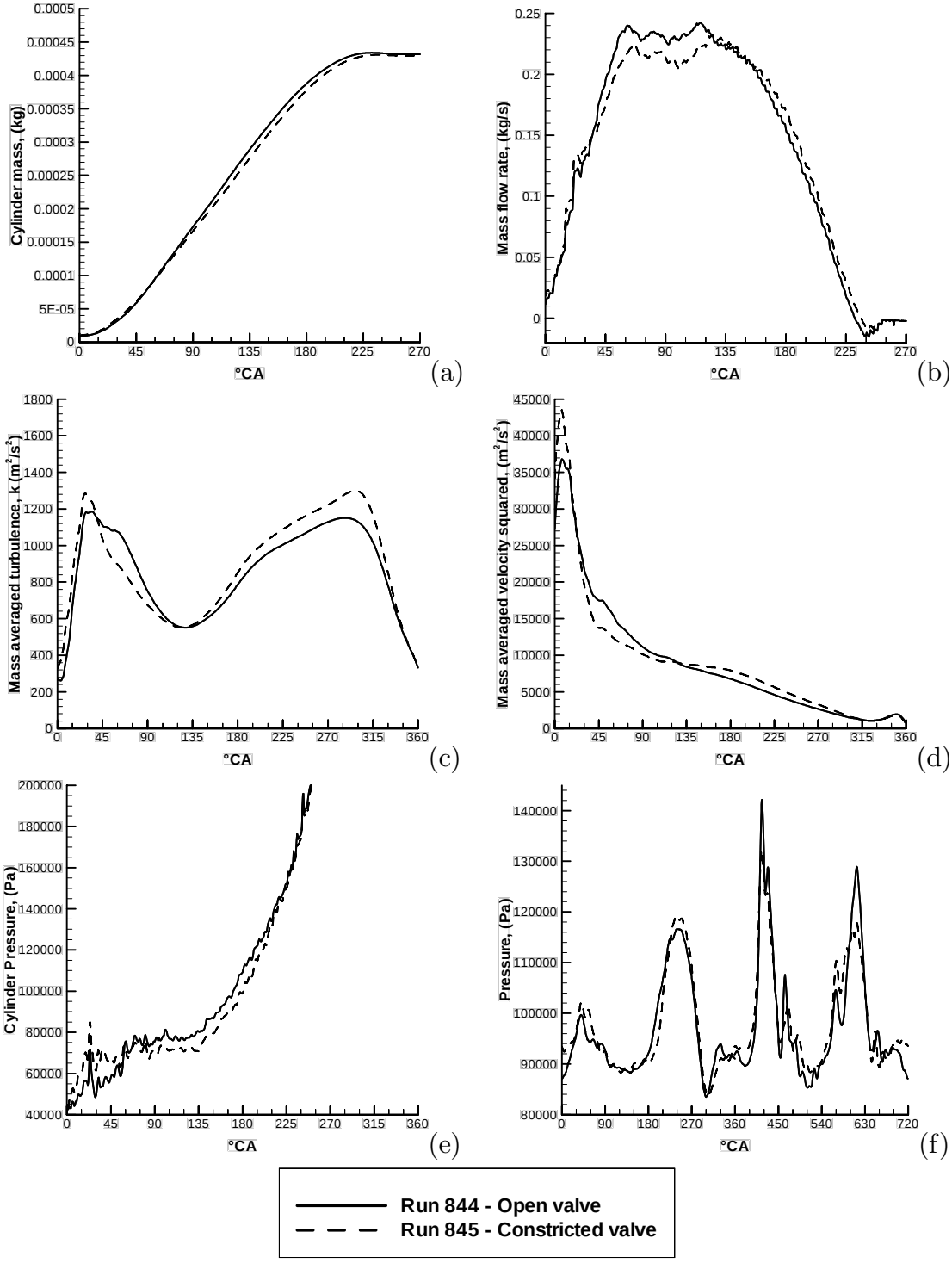

Figure 8.10: Comparison of in-cylinder parameters, open valve versus constricted valve. (a) – Cylinder mass; (b) – Mass flow rate; (c) – Mass averaged turbulent energy (k); (d) – Mass averaged velocity squared; (e) – Cylinder pressure; and (f) – Inlet manifold pressure.

stroke. The effect of flow during the final sections of the intake stroke on in-cylinder turbulence levels has been discussed in section 8.2.

The results presented here agree with the generally accepted design philosophy described in section 4.2.3, that a compromise must be reached between small cross sectional diameter ports to give high gas velocities to impart a strong in-cylinder flow, and the need for large diameter ports to reduce losses in the manifold. However, further work is required to optimise the engine manifold design and valve timing to make full use of the potential benefits of the inlet manifold wave in the current BRV engine.

8.4 Effect of Different Valve Sizes

It was found experimentally that the size of the valve was limiting performance at high engine speeds. To counter this and increase performance at high speeds, the outside diameter of the valve was increased from 63 mm to 68 mm. This resulted in an increase of the inlet manifold cross section area of around 30%.

It is very difficult to perform a completely objective test to assess the effect of increasing the valve diameter from 63 mm to 68 mm. This is due to the larger valve requiring a new cylinder head design, inlet manifold, and numerous other small changes. Many engine components must be changed in order to use the larger valve, so that a comparison between the two engines is the sum of the effects of all the changes, not just the valve diameter increase. Additionally, the valve timing being used on the 63 mm valve was thought not to be optimal, so that a slightly different timing was designed into the 68 mm valve. Thus, the comparison presented here is not a true "back to back" comparison. It is, however, the best comparison possible under the circumstances.

Figure 8.11 shows the mass flow rate into the cylinder during the intake stroke for three different engine configurations. Two different configurations of the 68 mm valve engine and one 63 mm valve engine configuration are presented. Details of these configurations is shown in tables 8.1 and 8.2. None of the configurations are directly comparable to each other, and each will have a slightly different inlet manifold wave pattern. This different inlet manifold wave is seen by the location of the peaks and troughs in the mass flow rate against crank angle curve appearing in different locations.

Despite the peaks and troughs occurring at different locations, the maximum flow which the valve can deliver will be primarily determined by the ability of the valve to allow air to flow into the engine. It will be largely independent of the valve

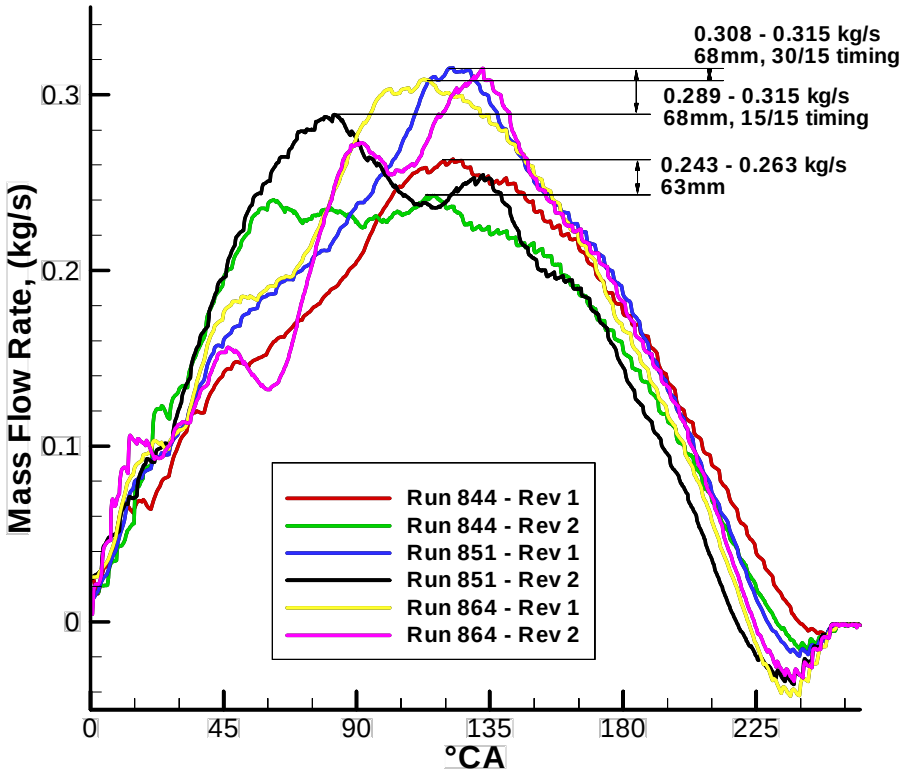

Figure 8.11: Comparison of maximum flow rates simulated during the inlet stroke in the 63 mm and 68 mm valve engines at 15000 rpm. Range of maximum flow rates predicted for each configuration is shown.

timing and inlet manifold length, as the inlet manifold wave pattern primarily affects the timing of the maximum flow point during the inlet stroke, not its magnitude.

Figure 8.11 shows the mass flow rate through the inlet valve for the three different configurations, showing results from both the first and second cycles. The 63 mm valve has a maximum flow range of 0.243–0.263 kg/s, and the 68 mm valve has a maximum flow range of 0.289–0.315 kg/s. Assuming that the higher value of the range indicates the maximum flow of which the valve is capable, it follows that the 68 mm valve engine has increased peak mass flow by 0.052 kg/s, an increase of 20%.

Note that this increase in possible peak flow will not necessarily result in an increase in volumetric efficiency. Figure 8.11 also shows that the 68 mm valve configurations simulated had significant back flow at the end of the intake stroke. This is may also be seen in the cylinder mass, figure 8.12. The mass of gas trapped at the end of the inlet stroke is tabulated in table 8.7. The 68 mm valve configurations has an increased mass of gas trapped; of up to 3.1×10^{-5} kg, an increase of 7%. This does not always occur, for instance the second revolution of run 851 shows a

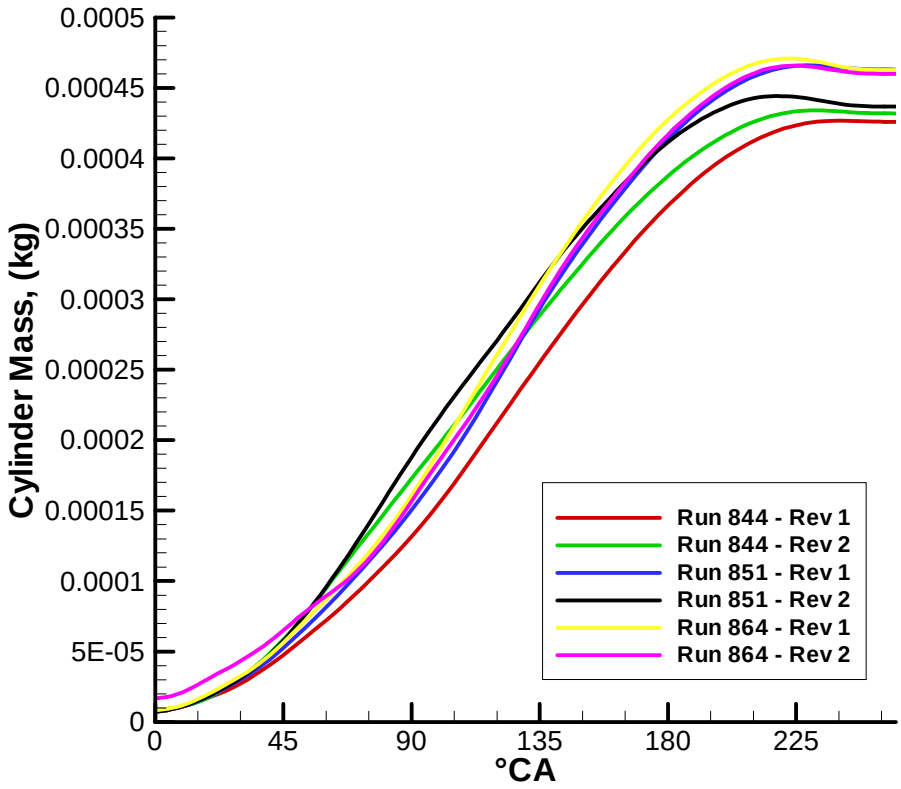

Figure 8.12: Comparison of mass of gas trapped in the cylinder during the intake stroke of 63 mm and 68 mm valve BRV engines.

trapped mass essentially the same as the 63 mm valve engine results. This occurred because of the large back flow, as mentioned earlier.

As a result of the 68 mm valve engine increasing the instantaneous flow capacity by around 20%, the trapped gas mass increases by up to 7%. However, this advantage can only be fully utilised when the valve timing and inlet manifold length has been optimised to the new geometry to take advantage of the increase in cross section area.

A further effect of increasing the valve diameter is that it decreases the air velocity in the valve during the inlet stroke. Since the velocity of the air entering the cylinder is the "energy source" for generating the in-cylinder flow field, this would indicate that the 68 mm valve configuration would have reduced levels of in-cylinder velocities, possibly leading to reduced levels of turbulence during the final stages of the compression stroke. This is the same reasoning as that used in section

Run 844 − 63 mm		**Run 851** − 68 mm		**Run 864** − 68 mm	
Cycle 1	**Cycle 2**	**Cycle 1**	**Cycle 2**	**Cycle 1**	**Cycle 2**
4.26×10^{-4}	4.32×10^{-4}	4.63×10^{-4}	4.37×10^{-4}	4.63×10^{-4}	4.60×10^{-4}

Table 8.7: Mass of air trapped (kg), at IVC for various configurations.

8.3, in which the effect of reducing the valve cross section area is assessed.

The turbulent energy and in-cylinder flow kinetic energy is shown in figure 8.13. The results of the first cycle of the simulation, shown in figure 8.13a and 8.13c clearly show that the 63 mm valve configuration imparts a higher level of in-cylinder kinetic energy during the end of the intake stroke, which leads to significantly increased levels of turbulence during the compression stroke.

The 63 mm valve engine does not have significantly higher levels of in-cylinder flow energy or turbulent energy in the second cycle of the simulations. In figure 8.13b and 8.13d it can be seen that the energy imparted to the flow at the end of the intake stroke is roughly the same between run 844 (63 mm) and run 864 (68 mm), leading to roughly similar levels of turbulence in the compression stroke.

The results from the first cycle confirm that, as expected, the increase in valve size has reduced in-cylinder kinetic energy and compression stroke turbulence. The first cycle of the simulation is a more objective comparison to use than the second as it is less affected by the inlet manifold wave. For a fully optimised engine of any valve size, the intake manifold wave would be fairly similar so this comparison can be justified. The simulations presented here have not had the valve timing or manifold lengths optimised, so the inlet manifold wave could be considerably different. A degree of similarity in the inlet manifold wave pattern between the two simulations is retained in the first revolution results as they all start from the same initial conditions, and so allows a better comparison between these simulations.

The dependence of the in-cylinder energy and turbulence on the inlet manifold wave is caused by the fact that flow entering the cylinder late in the intake stroke has a more significant effect on in-cylinder energy and turbulence than flow entering early in the stroke. This effect has been discussed in section 8.2.

The velocity and turbulence fields predicted by the simulations confirm that the 63 mm valve engine has higher in-cylinder velocity and turbulence levels. Figure 8.14 shows the velocity field in the cross tumble and tumble planes for the three simulations, at 252 °CA on the first intake stroke of the simulation. All three simulations display the dual tumble flow field, with the 63 mm in-cylinder velocity being considerably higher than the 68 mm valve simulations.

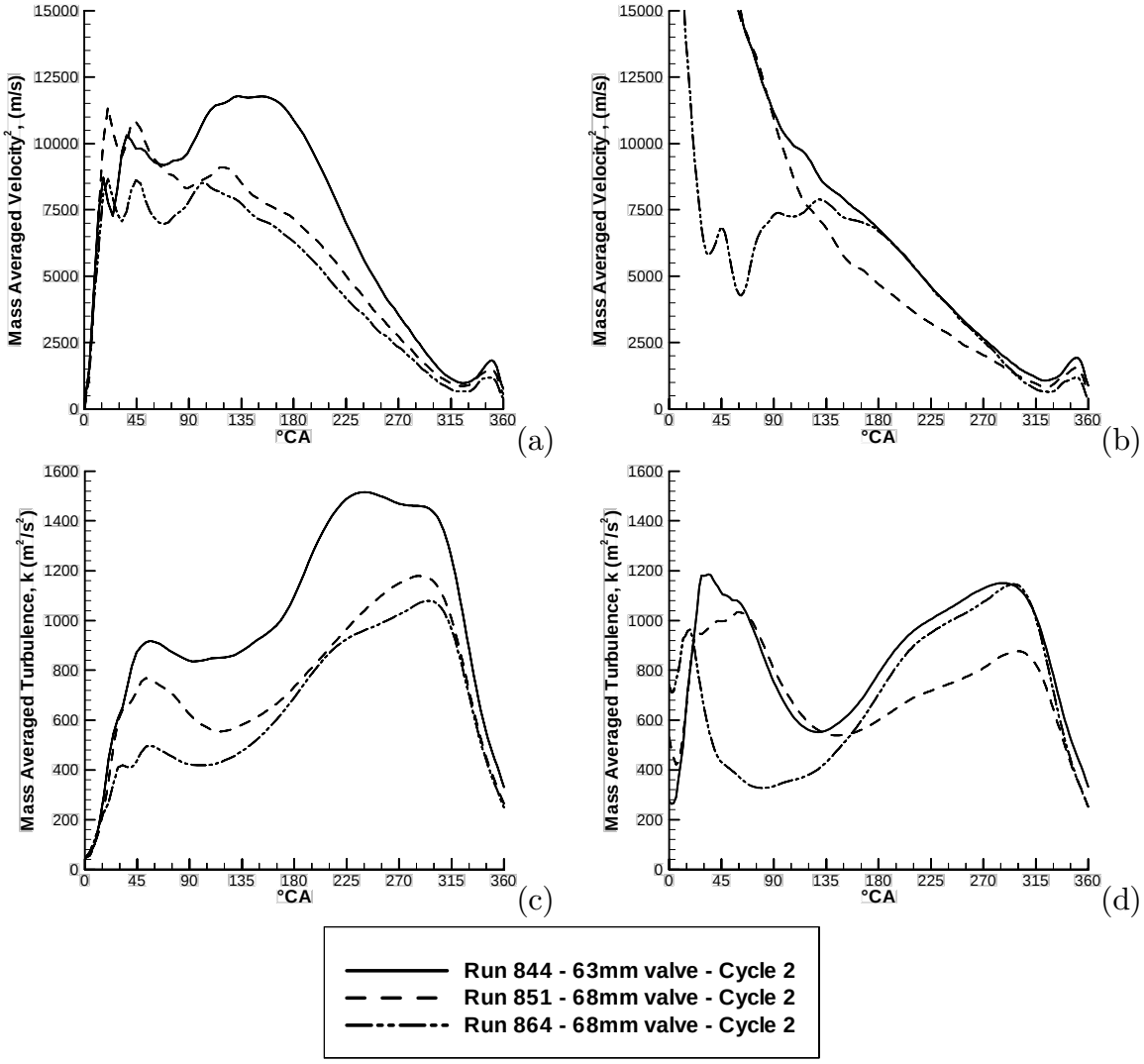

Figure 8.13: Comparison of the mass averaged velocity squared and turbulent energy for the 63 mm and 68 mm valve BRV engines. (a) – Mass averaged velocity squared for the first cycle of the simulation; (b) – Mass averaged velocity squared for the second cycle of the simulation; (c) – Mass averaged turbulent energy for the first cycle of the simulation; and (d) – Mass averaged turbulent energy for the second cycle of the simulation.

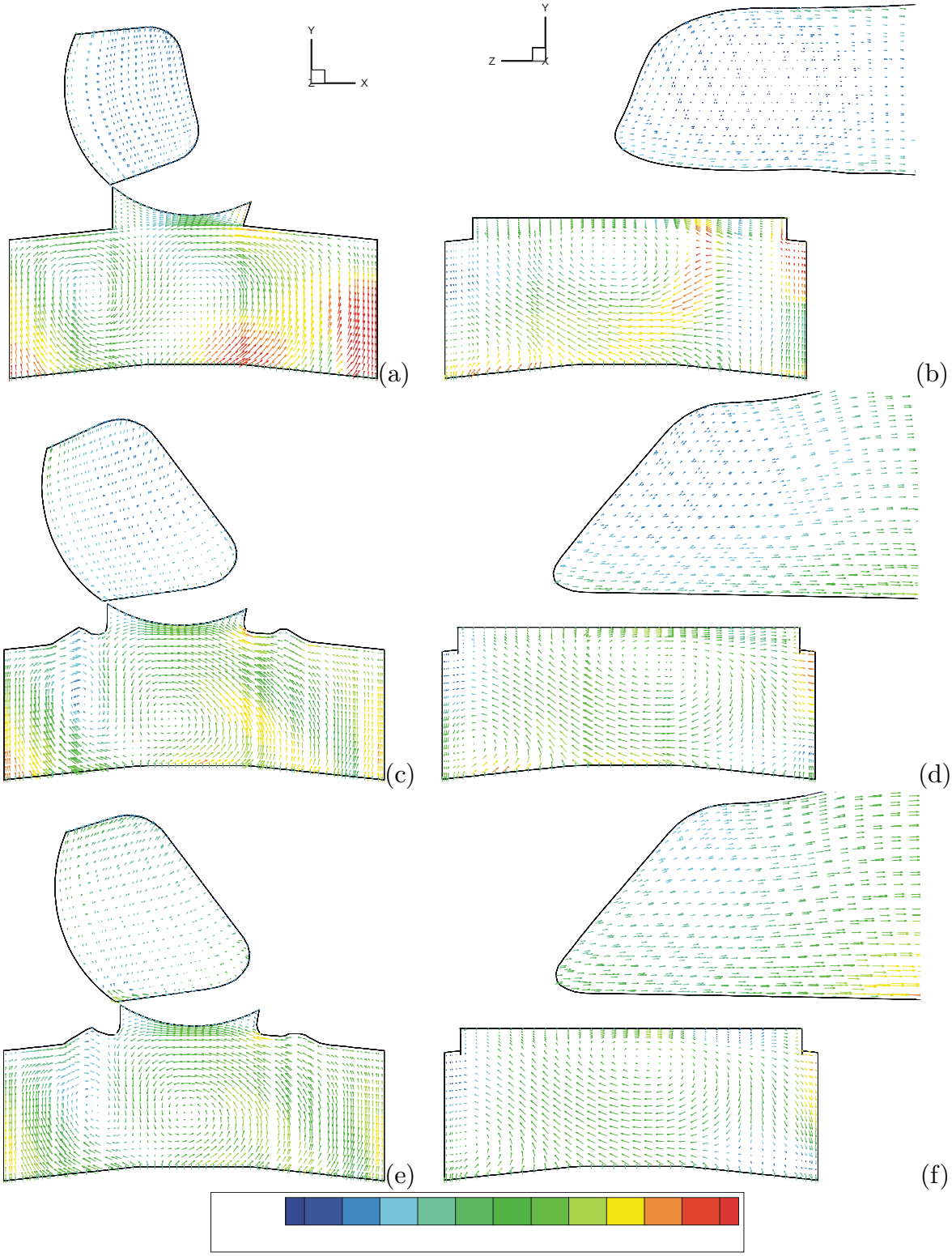

Figure 8.14: Comparison of velocity field of 63 mm and 68 mm valve simulations at 252 °CA on the first cycle of the simulation. (a) – Run 844 (63 mm valve), cross tumble plane; (b) – Run 844 (63 mm valve), tumble plane; (c) – Run 851 (68 mm valve), cross tumble plane; (d) – Run 851 (68 mm valve), tumble plane; (e) – Run 864 (68 mm valve), cross tumble plane; and (f) – Run 864 (68 mm valve), tumble plane.

Figure 8.15 shows the turbulent energy field for the three simulations at 252 °CA on the first intake stroke. Again, the 63 mm valve has considerably higher levels of turbulence in the cylinder than the 68 mm valve. This is particularly apparent in the tumble plane, where a region of very high turbulence exists in the lower right section of the cylinder which does not occur in either of the 68 mm valve simulations.

Note that in the first cycle results from the simulations shown in figures 8.14 and 8.15 that the two 68 mm valve simulations predict quite similar velocity and turbulence fields.

If the flow is visualised near the end of the intake stroke of the second cycle of the engine, the effect of the inlet manifold wave on the in-cylinder fluid can be seen. Figure 8.16 shows a visualisation at 200 °CA during the second cycle of the engine. The 63 mm valve (figure 8.16a) has a fractionally higher velocity in the intake jet at the valve than the second 68 mm valve engine (figure 8.16c). The other 68 mm valve engine, figure 8.16b, a greatly reduced velocity in the intake jet is seen, which is the cause of the significantly lower in-cylinder kinetic energy and turbulence levels shown in figure 8.13b and 8.13d. Thus, the large variation between the two 68 mm valve engine results for the second engine cycle is due to the effect of the inlet manifold wave, because during the first cycle of the engine they predicted very similar results. This confirms the first cycle results as a more direct comparison between the engines than the second cycle results.

This trend of turbulence levels decreasing with the increase in valve diameter has been captured experimentally. Turbulence is difficult to measure directly, so the effect of the turbulence is seen indirectly by its effect on the engine *BMEP* results. Figure 8.17 shows the result of a series of dynamometer experiments at a number of engine speeds. Run 411 is the 63 mm valve engine and run 523/524 is the 68 mm valve engine. It can be seen that the volumetric efficiency of the engines was effectively the same at 8000 rpm, 8500 rpm, 9500 rpm, 10000 rpm, 12500 rpm, 13000 rpm and 14500 rpm. The *BMEP* at each of these points was around 50 kPa higher in the 63 mm valve engine than the 68 mm engine. Since the volumetric efficiency at each of these points is unchanged, it follows that the 63 mm valve engine burns the charge better, which is probably due to an increased level of in-cylinder turbulence.

Figure 8.17 shows the volumetric efficiency at 15000 rpm to also be approximately the same between the 63 mm and 68 mm valve engines. This point is the only exception not showing a higher *BMEP* in the 63 mm valve engine.

Unfortunately the CFD simulations presented in this section were performed at an engine speed of 15000 rpm—the only speed measured where the 63 mm valve

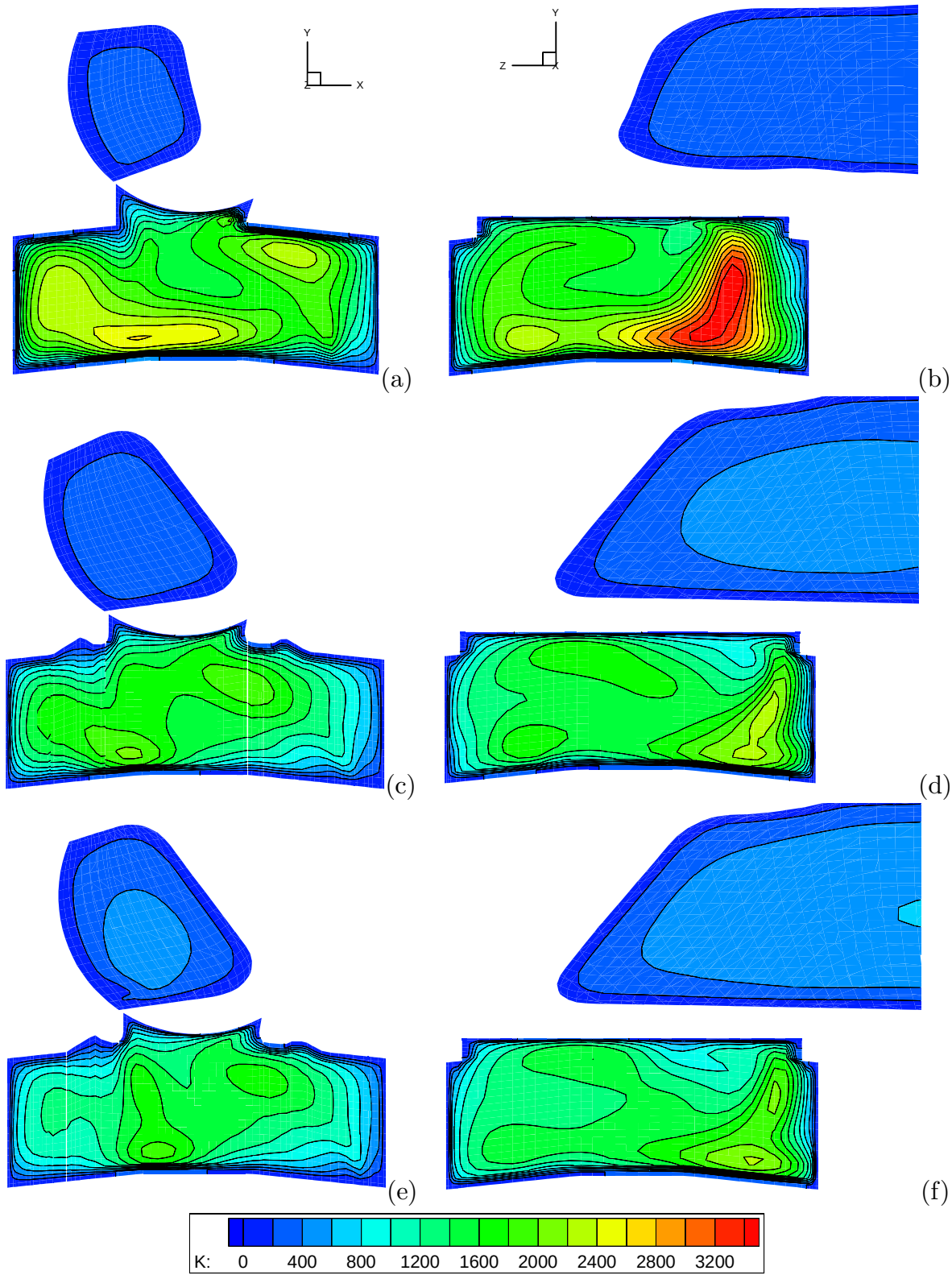

Figure 8.15: Comparison of turbulence field of 63 mm and 68 mm valve simulations at 252 °CA on the first cycle of the simulation. (a) – Run 844 (63 mm valve), cross tumble plane; (b) – Run 844 (63 mm valve), tumble plane; (c) – Run 851 (68 mm valve), cross tumble plane; (d) – Run 851 (68 mm valve), tumble plane; (e) – Run 864 (68 mm valve), cross tumble plane; (f) – Run 864 (68 mm valve), tumble plane;

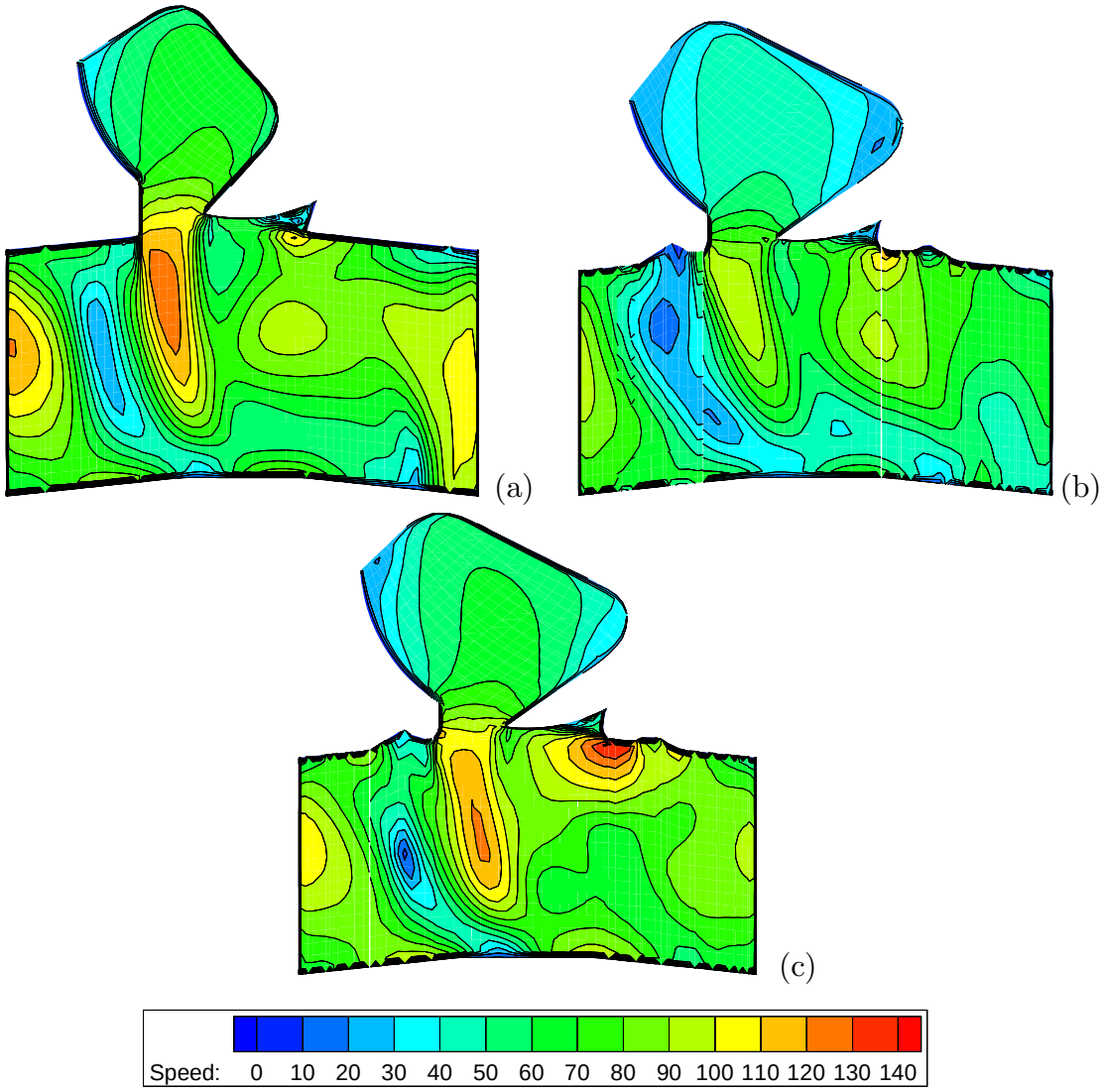

Figure 8.16: Speed simulated at 200 °CA in the $Z = 0$ cross tumble plane. Second cycle results. (a) – Run 844, 63 mm valve; (b) – Run 851, 68 mm valve; and (c) – Run 864, 68 mm valve.

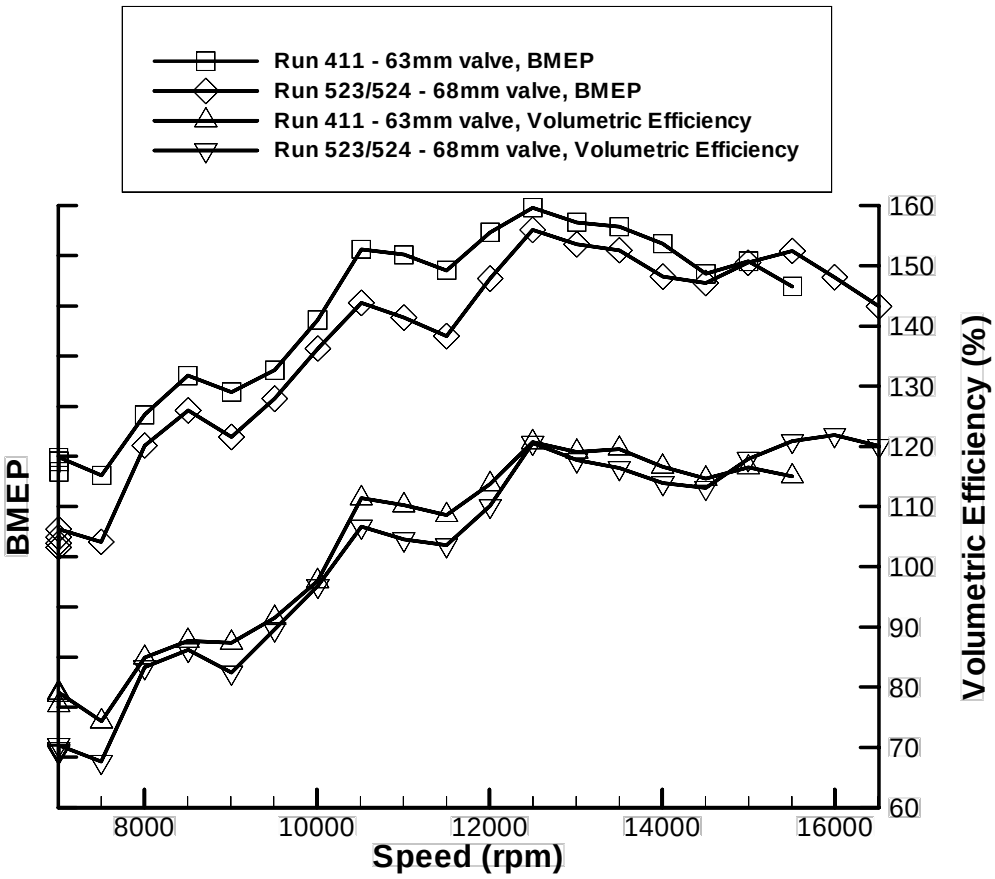

Figure 8.17: Comparison of dynamometer results for 63 mm and 68 mm valve BRV engines. Only relative *BMEP* data is shown as the absolute *BMEP* data is confidential. Each tick on the *BMEP* scale is 50 kPa.

engine had a similar performance to the 68 mm valve engine. This makes the experimental confirmation of the numerical results inconclusive. The conclusion that the 68 mm valve reduces in-cylinder energy and turbulence levels could be strengthened by performing the simulation at another speed where the experimental results predict there to be a clear benefit for the 63 mm valve (such as at 12500 rpm).

8.5 Effect of Manifold Wall Heat Transfer

It was inferred from results on the dynamometer that heat transfer from the inlet manifold and cylinder walls were significantly heating the gas. A number of methods are available to reduce the wall heat transfer, such as using an insulating coating on the inside surfaces of the valve. A series of numerical simulations were therefore performed to assess the possible effects of reducing wall heat transfer, using the wall temperatures listed in table 7.1. This was compared to a simulation where all walls (both in the inlet manifold and cylinder), were adiabatic. The simulations were otherwise identical, thus allowing the effect of wall heat transfer to be isolated.

The results of this comparison on the averaged in-cylinder parameters are shown in figure 8.18, and cross sections of the inlet manifold temperature field are shown in figure 8.19. The inlet manifold pressure wave is essentially unchanged between the two simulations (figure 8.18a). If the section of the inlet manifold wave just before the opening of the inlet valve is magnified, figure 8.18b, we see a small phase difference of around 4 °CA between the two simulations caused by the slightly cooler gas in the adiabatic wall simulation possessing a slightly lower acoustic velocity. This difference is slight and will not significantly affect results.

Figure 8.18c shows that the adiabatic wall model to have slightly higher levels of turbulence from around 180 °CA to 300 °CA. The increase is about 80 $m^2 s^{-2}$, or 5–7%. The reason for this slight increase in turbulence is seen in figure 8.18d, where a slightly larger air mass flow rate is predicted through the valve at around 120 °CA. This increase in mass flow rate results in higher turbulence levels due to the increased kinetic energy of the incoming air.

The mass of air trapped in the cylinder is shown in figure 8.18e, and a slightly reduced mass of air is found after inlet valve close in the simulation which included wall heat transfer. The reduction in volumetric efficiency is small, of the order of 5%, however this amount can be quite significant in high performance applications.

The reduction in volumetric efficiency occurs because the increase in air temperature of gas near the wall causes a reduction in air density of the incoming charge. However, as shown earlier, the inlet manifold wave is not significantly modified. The

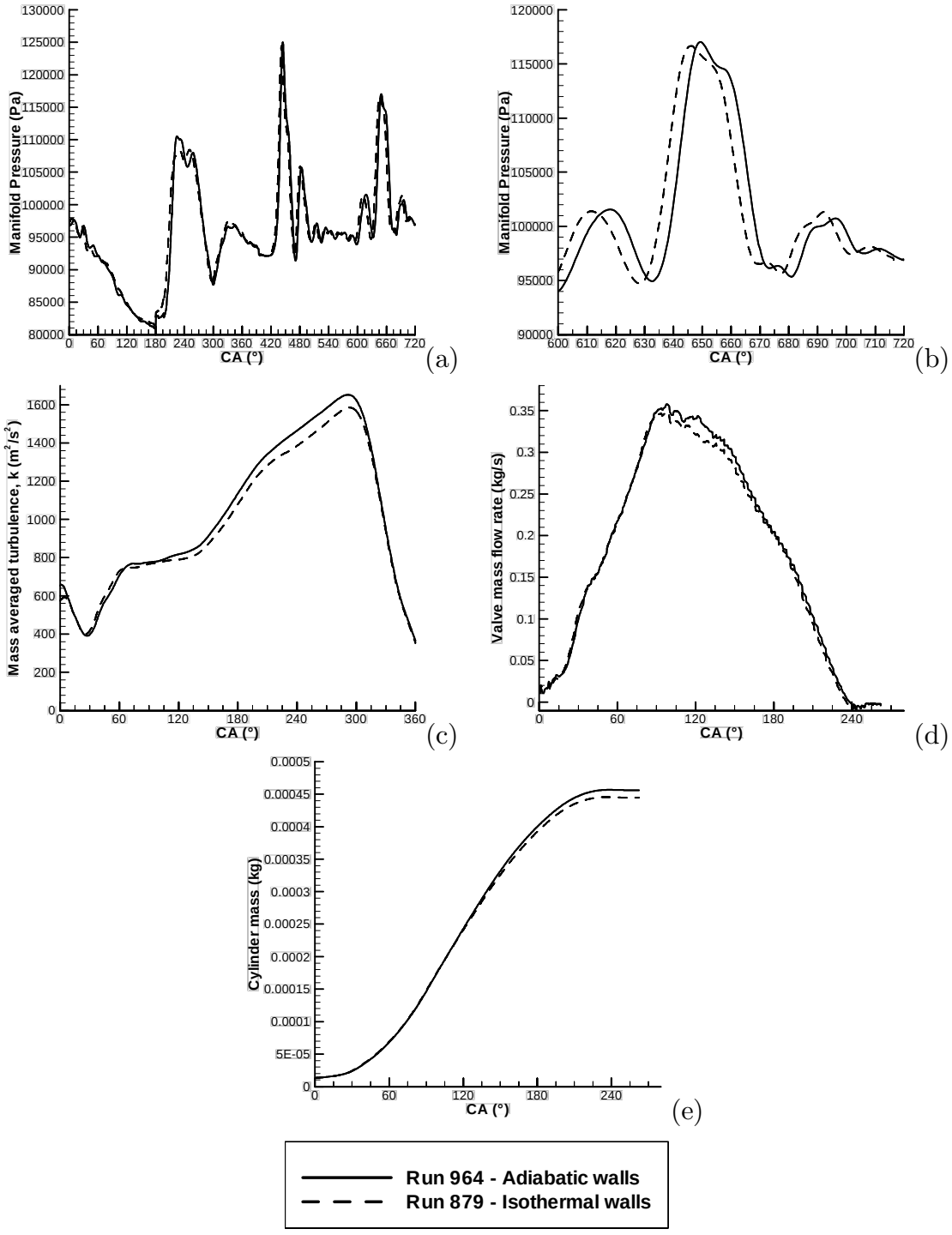

Figure 8.18: Comparison of isothermal and adiabatic wall heat transfer boundary conditions on the BRV engine simulation. (a) – Inlet manifold pressure; (b) – Magnification of the inlet manifold pressure; (c) – Mass averaged turbulence (k); (d) – Valve mass flow rate; and (e) – Cylinder mass.

increase in temperature is shown in figure 8.19. The temperatures in a cross-section of the inlet manifold early in the intake stroke at 1 °CA are shown in figures 8.19a and 8.19b. Here the inlet manifold gases have been almost stationary in the hot inlet manifold during the compression, expansion and exhaust strokes, so a significant time has elapsed for heat transfer from the walls to warm the gas in the manifold. It may be seen that the temperatures at the simulation with heat transfer (figure 8.19a) are several degrees higher than the simulation with adiabatic walls (figure 8.19b).

The temperature profile predicted after the inlet valve has shut is shown in figures 8.19c and 8.19d. The two temperature profiles are similar in the manifold, however the temperatures in the cylinder are between 10 °C and 20 °C higher for the case with wall heat transfer. Some of this temperature rise occurs in the cylinder rather than the manifold. The walls are hotter in the cylinder (modelled as 423 K) than in the manifold (modelled as 353 K), so the driving temperature gradient is larger in the cylinder than in the manifold.

This increased temperature in the cylinder at inlet valve close is the cause of the reduction of density, which consequently causes a reduction in the mass of gas trapped in the cylinder, seen in figure 8.18e.

This demonstrates that there may be up to a 5% trapped gas mass increase possible due to a reduction in wall heat transfer. This is a significant increase in volumetric efficiency, indicating that techniques to reduce wall heat transfer should be investigated. However, reducing the heat transfer will also affect factors not considered here, such as fuel evaporation on the walls. Whether the net effect of reducing the wall heat transfer will be beneficial is not certain.

8.6 Effect of Bore to Stroke Ratio

8.6.1 Introduction

High performance engines use high bore to stroke ratios (BSR) to allow high maximum engine speeds. The limiting factor on maximum engine speed is the forces required to create the reciprocating piston motion. A high BSR engine will have lower inertial forces from piston motion for a given displacement than a low BSR engine. The increase in maximum engine speed will then provide an increase in engine power, providing engine torque does not decrease excessively. Additionally, the reduced piston velocities in high BSR engines can lead to reduced friction losses.

The fundamental flow structure to be considered here is the forced vortex. A

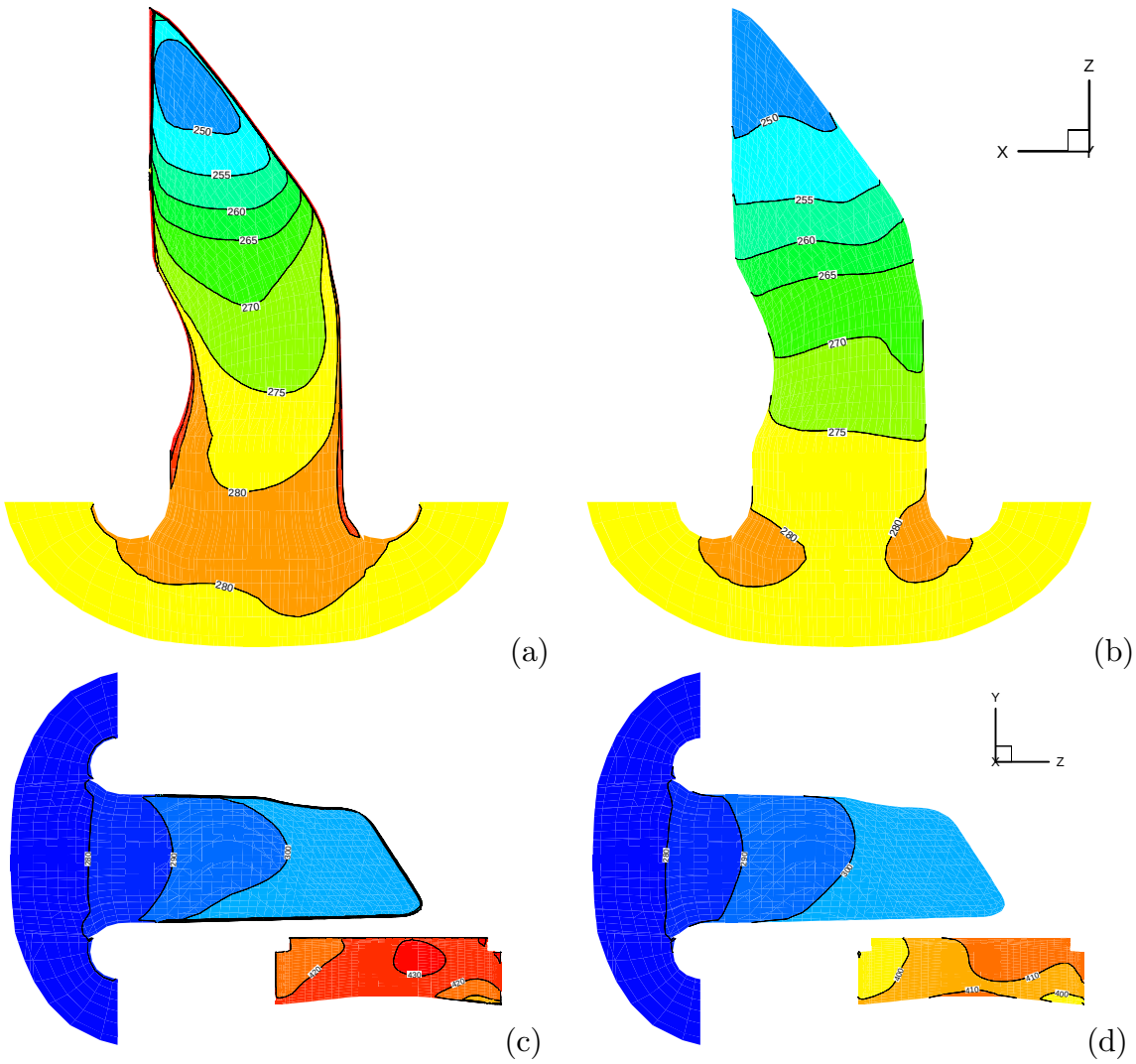

Figure 8.19: Visualisations of the temperature field in the inlet manifold of the BRV engine. (a) – With wall heat transfer at 1 °CA; (b) – Adiabatic walls at 1 °CA; (c) – With wall heat transfer at 271 °CA; and (d) – Adiabatic walls at 271 °CA.

forced vortex is defined as fluid undergoing solid body rotation, where the tangential velocity is proportional to the distance from the vortex centre [283]. It has been shown that for in-cylinder flows, swirl closely approximates forced vortex flow near TDC [137], and that tumble also approximates forced vortex flow, however it does exhibit significant variations from the ideal, as discussed in section 6.7.2.

If a tumble vortex in an engine cylinder is to approximate a forced vortex, the minimum departure from the ideal flow occurs when the vortex is circular. Alternatively, the ideal circular forced vortex shows no strain rate in the fluid, so a vortex in an engine rotates with minimum strain rate in a circular domain. The strain rate in the vortex represent energy losses, so a vortex with minimum strain conserves maximum energy. For a tumble vortex rotating in a engine cylinder, where the domain is non-circular, the minimum strain geometry exists when the aspect ratio of the region is one.

This suggests that the tumble combustion chamber design should have an aspect ratio of around one at BDC during the section of the intake stroke where the incoming gases "spin up" the tumble vortex, and decreases to a large number to compress the tumble vortex and cause it to break down into turbulence.

The limitation for existing pentroof poppet valve engines using the traditional "tumble" flow fields in the compression stroke is that as the BSR increases significantly above one, the aspect ratio of the tumble vortex moves away from this ideal figure. This causes the tumble vortex to suffer significant losses before the compression stroke. The breakdown aspect ratio is also reached earlier in the compression stroke, possibly leading to the breakdown process occurring too early and the turbulence generated to dissipate before it can be utilised to enhance combustion.

Thus with the conventional tumble engine design as the BSR increases, the combustion efficiency decreases. This results in an optimum operating point with a compromise between high BSR to allow high maximum engine speed, balanced against combustion effectiveness decreasing as the BSR increases.

As discussed in section 7.7, it is believed that dual cross tumble would be less sensitive to high BSR than poppet valve engines. If the BRV engine could still burn the charge effectively at higher BSR than is possible with traditional poppet valve engines, this would make it able to run at higher engine speeds, and a power increase would result.

As has been mentioned in section 4.4.3, a study of the effect of bore to stroke ratio in high performance engines is presented by Bianchi et al [41]. Since only the combustion chamber was simulated the computational model presented was considerably simplified. Initial velocity conditions were interpolated from an intake stroke

simulation and other fluid parameters such as pressure, density and turbulence were assumed uniform across the cylinder, and equal to the mass averaged values in the cylinder from the intake stroke simulation. However, despite these simplifications, the study indicated a number of important trends due to changes in bore to stroke ratio. In summary, they report that increasing bore to stroke ratio by 14% was found to:

1. Reduce compression ratio by 3.2% as the TDC clearance was kept constant;
2. Increase engine speed for maximum power by 3%;
3. Reduce turbulence (u') levels by 5% at 120 °CA before TDC, 3% at 60 °CA before TDC and 8% at 30 °CA before TDC;
4. Significantly increase flame frontal area;
5. Significantly increase wall area in contact with burnt gas;
6. Slightly decrease in-cylinder mean temperatures during combustion;
7. Reduce *IMEP* by 3%;
8. Reduce maximum cylinder pressure by 14%;
9. Increase time for 0–10% mass fraction burnt by 3 °CA and 0–90% mass fraction burnt by 6 °CA;
10. Reduce heat lost to cylinder walls by 9%; and
11. Reduce thermal efficiency by 2.8%.

The apparent contradiction of the increased BSR causing increased wall area in contact with burnt gas, yet heat lost to cylinder walls decreased was explained by the reduction in cylinder temperature.

This study of Bianchi et al [41] will be used as the baseline for the effect of BSR on high performance poppet valve engines.

The effect of BSR on the BRV engine performance was tested with the CFD model. No experimental verification was performed. An engine geometry was developed using the 68 mm valve, valve timing of IVO of 30 °CA before TDC and EVC of 15 °CA after TDC. The engine speed was 18000 rpm, and the inlet manifold length was 128 mm.

Engine Bore	Stroke	BSR	Compression Ratio
93 mm	44.2	2.11	15.8
95 mm	42.3	2.24	15.7
97 mm	40.6	2.39	15.5
99 mm	39.0	2.54	15.3

Table 8.8: Range of BSR simulations tested.

The inlet tract was chosen as an approximation of the correct tuned length for this speed. The various cylinder bores were implemented by adding a ring of nodes 1 mm thick to the outer edge of the combustion chamber, increasing the bore by 2 mm per ring. The piston stroke was then decreased to maintain a swept volume of 300 cc per cylinder. Other factors kept constant included the conrod length and the piston to head clearance at TDC.

Four BSRs were tested, as shown in table 8.8. Also shown are the stroke used for the configurations, the BSR and the compression ratio. The compression ratio varied slightly (3% over the full range tested) between simulations.

Only a small BSR range was simulated, as the primary purpose was to determine if the BRV engine could out-perform the current state-of-the-art poppet valve engines, which are limited to a BSR of about 2.3 [227]. The range of geometries tested vary by about 6% in bore size. However, this small increase would allow a similar small increase in maximum engine speed, and if the engine torque were to remain the same would then result in a 6% increase in peak power.

8.6.2 Results

In figure 8.20, the first three diagrams (cylinder pressure, inlet manifold pressure and instantaneous valve mass flow rate) show the four different BSR simulations predicting essentially identical results. This indicates that the flow predicted in the inlet manifold is essentially the same for all four BSR cases.

Figure 8.20d shows the swirl ratio in the cylinder, figure 8.20e shows the tumble ratio and figure 8.20f shows cross tumble ratio. As has been discussed in section 7.7, these parameters are not important to dual cross tumble flows, so the magnitudes of normal swirl, tumble and cross tumble predicted are quite low. However, they can still be calculated, and as expected, they show a general trend of decreasing swirl, tumble and cross tumble as BSR increases. This shows that increasing the BSR is reducing the magnitude of the velocities of the in-cylinder flow field.

The cross tumble calculation in figure 8.20f shows a fairly rapid decrease of cross tumble with increasing BSR during the compression stroke from 180 °CA to

360 °CA. The tumble ratio calculation in figure 8.20e, also shows a trend of tumble ratio decreasing with increasing BSR between 90 °CA and 225 °CA, however the tumble ratio changes sign after 225 °CA so the trend does not continue through the entire compression stroke. The swirl ratio also appears to show decreasing strength with increasing BSR in the mid sections of the intake stroke, however the magnitude of the swirl is very small (peaking at an absolute value of about 0.14), so the effect is small.

Figure 8.21 shows the comparison of mass averaged turbulence and velocity squared across the cylinder. As previously discussed, these two parameters are the most important global parameters for estimating the performance of the BRV in-cylinder flow. The turbulence levels (figure 8.21a) of the four simulations start with similar values, but diverge slightly from 60 °CA. At 135 °CA they converge again, and then diverge from 200 °CA. From 315 °CA to the end of the compression stroke they converge again and remain at similar values as they approach TDC.

During the first brief period of divergence between 60 °CA and 135 °CA, the higher BSR engines have higher turbulence levels, possibly due to the high velocities required by the flow to reach the extremities of the cylinder. A higher velocity is required as there is a greater proportion of the cylinder volume away from the valve window.

The second, and far more significant divergence shown in figure 8.21a is from 200 °CA to 315 °CA. Here the mass averaged turbulence (k) varies over a range of about 1500–1700 $\mathrm{m^2\,s^{-2}}$, with, as expected the lower BSR engines having the highest turbulence levels. When read in conjunction with the mass averaged velocity squared chart, figure 8.21b, it can be seen that the mass averaged velocity squared is essentially the same through the early intake stroke, but diverges slightly at around 165 °CA. This small divergence continues throughout the end of the intake stroke and the majority of the compression stroke, finally converging again when there is very little energy left in the flow at 315 °CA. Throughout the compression stroke there is slightly more mean flow energy in the lower BSR simulations, and this slight gain leads to the turbulence enhancement seen between 225 °CA and 315 °CA in the turbulence, figure 8.21a.

Beyond 315 °CA, the difference in the turbulence levels between the low and high BSR simulations remains near 200 $\mathrm{m^2\,s^{-2}}$. The curves appear to converge as the turbulence level is rapidly decreasing.

The flow fields are presented in figures 8.22 to 8.29. These figures show various cross sections of the flow fields during the second stroke of the simulation, at various

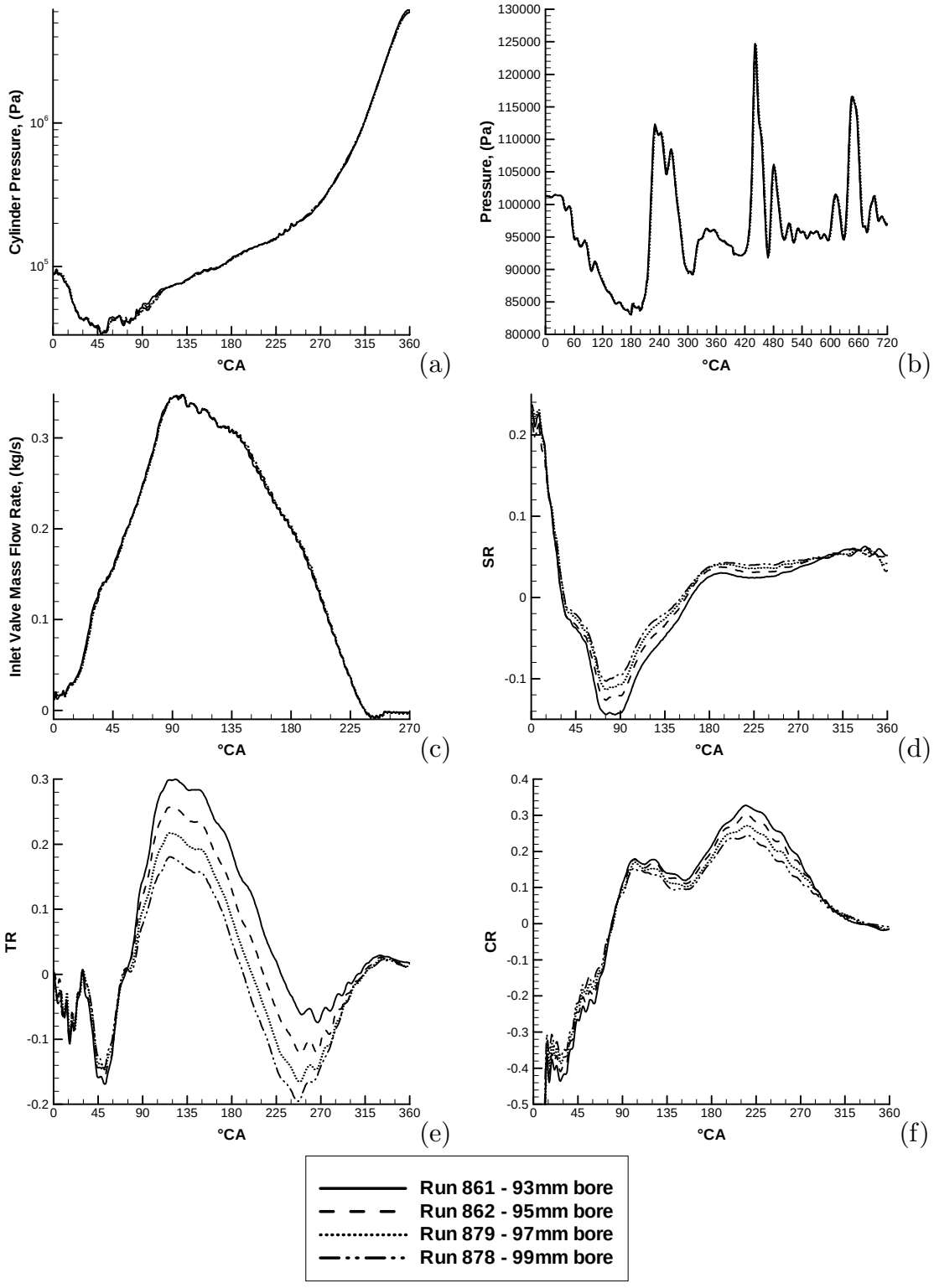

Figure 8.20: Comparison of various BSR BRV engines, based on 18000 rpm, 68 mm valve, 128 mm inlet manifold length. (a) – Cylinder pressure; (b) – Inlet manifold pressure; (c) – Mass flow rate through the inlet valve; (d) – SR; (e) – TR; and (f) – CR.

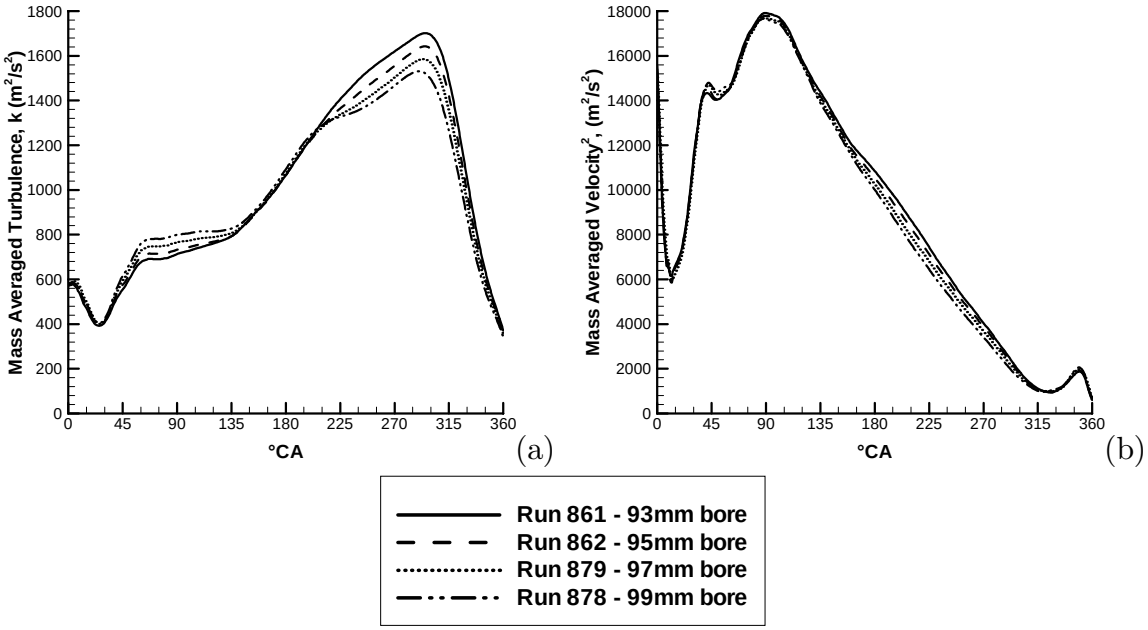

Figure 8.21: Comparison of various BSR BRV engines, based on 18000 rpm, 68 mm valve, 128 mm inlet manifold length. (a) – Mass averaged turbulence and (b) – Mass averaged velocity squared.

times during the intake and compression stroke.

The cross tumble plane flow at 181 °CA is presented in figure 8.22, in which there is very few differences between the simulations. The main difference, and it is only minor, appears to be the right vortex becoming more circular as the BSR decreases. At this stage of the intake stroke the mass averaged velocity squared and mass averaged turbulence (figure 8.21) are similar, which is in agreement with vector fields also being similar.

Again, few differences are visible in the tumble plane in figure 8.23. The only important difference appears to be the small recirculation shown in blue in the bottom right side of the 93 mm simulation, which becomes larger as the BSR increases.

In the swirl plane there are some variations between the engines with different BSR. Figure 8.24 shows that the central jet, shown in red in all simulations, and that the two vortices on either side of the jet are essentially unchanged. The main difference is the periphery of the cylinder, where significantly higher velocities occur near the cylinder wall in the 93 mm bore simulation, and different structures at the top of the slice are seen in the 99 mm simulation. This shows the lower BSR engine has higher flow velocities which will lead to higher turbulence later in the compression stroke. The structures seen in the top of the slice in the 99 mm simulation are not very significant as they are small, short lived structures under the main central

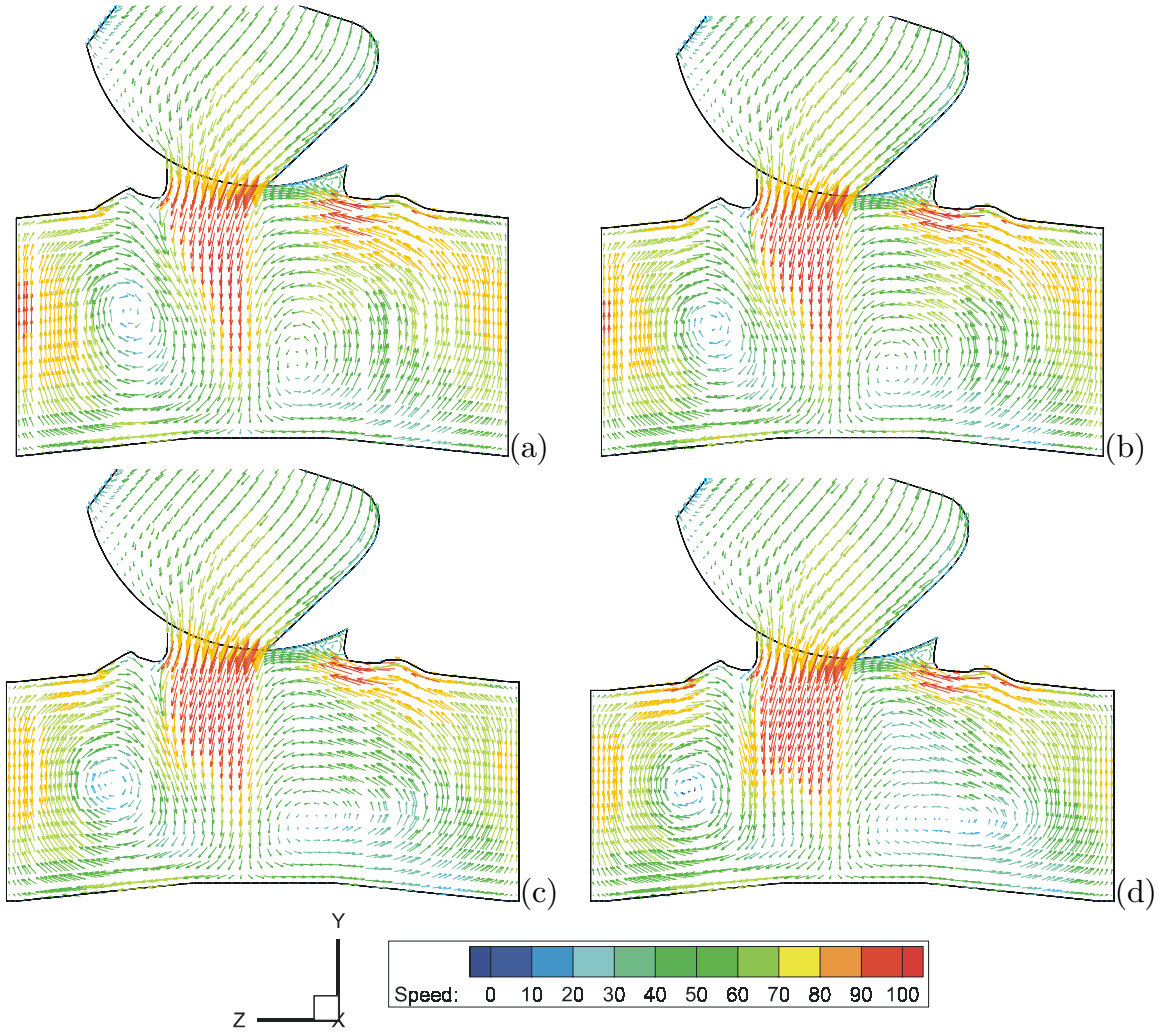

Figure 8.22: Visualisations of flow in the $Z = 0$ cross tumble plane at 181 °CA. (a) – 93 mm bore; (b) – 95 mm bore; (c) – 97 mm bore; and (d) – 99 mm bore.

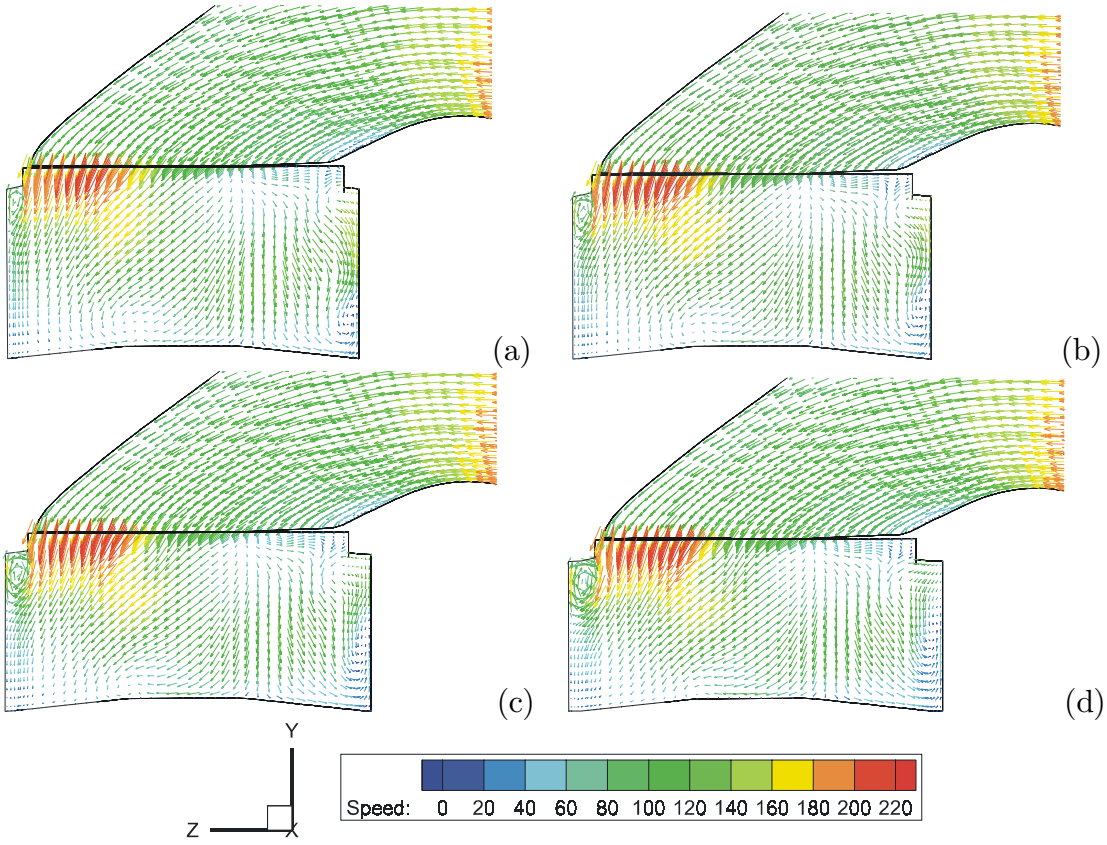

Figure 8.23: Visualisations of flow in the $X = 0$ tumble plane at 181 °CA. (a) – 93 mm bore; (b) – 95 mm bore; (c) – 97 mm bore; and (d) – 99 mm bore.

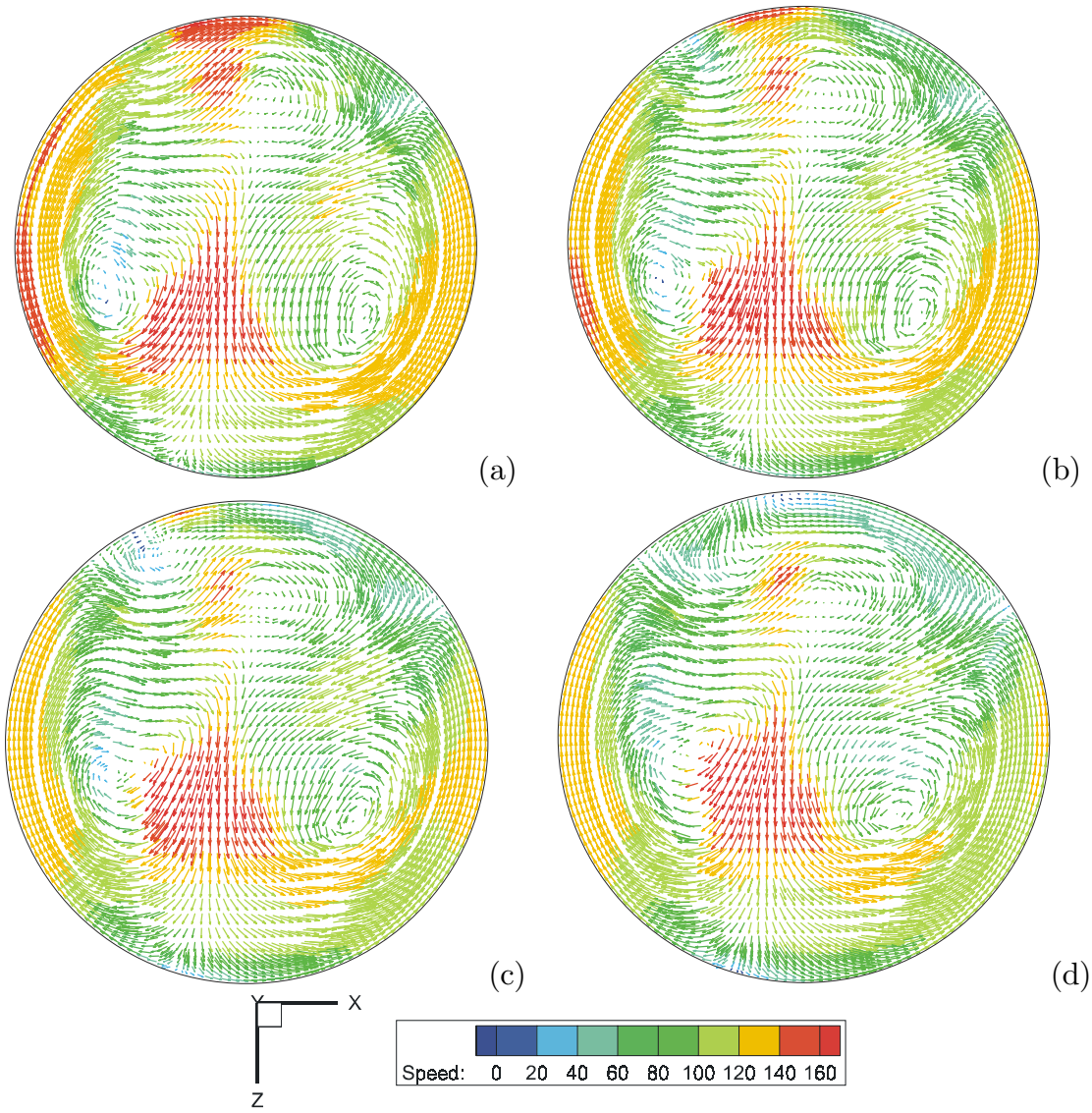

Figure 8.24: Visualisations of flow in the $Y = -55\,\text{mm}$ swirl plane at 181 °CA. (a) – 93 mm bore; (b) – 95 mm bore; (c) – 97 mm bore; and (d) – 99 mm bore.

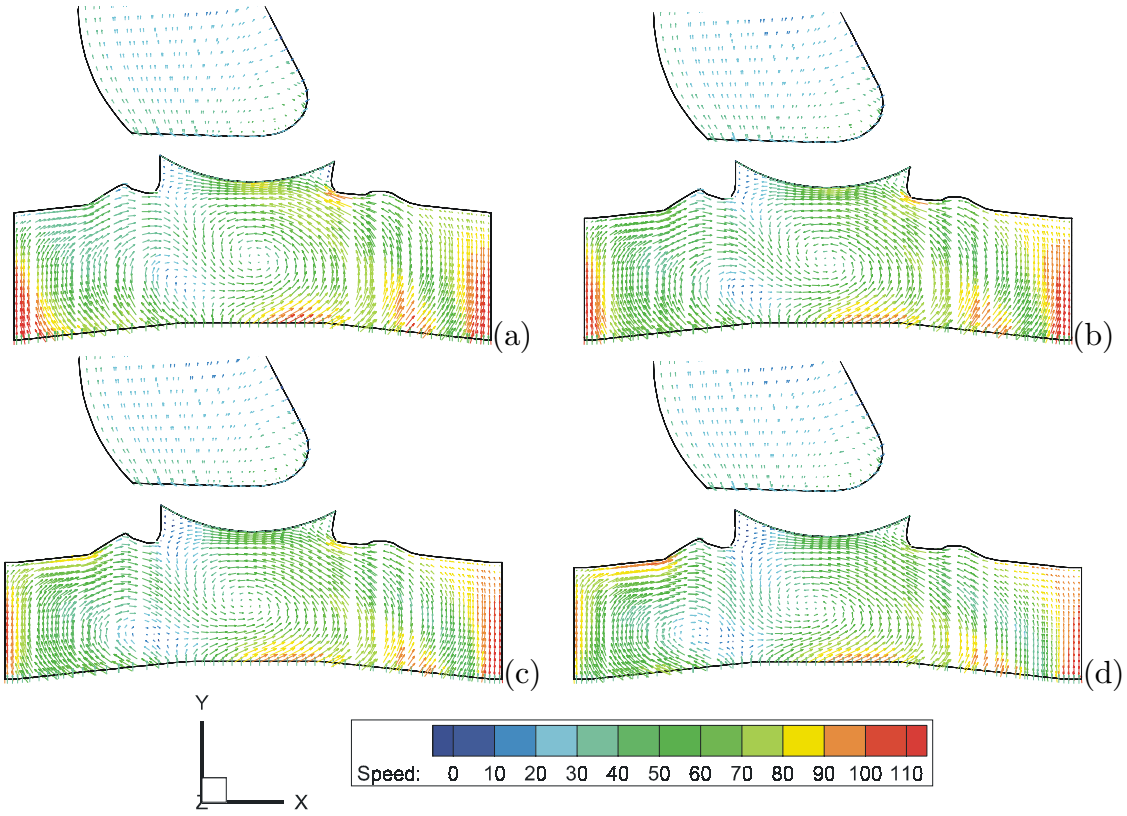

Figure 8.25: Visualisations of flow in the $Z = 0$ cross tumble plane at 271 °CA. (a) – 93 mm bore; (b) – 95 mm bore; (c) – 97 mm bore; and (d) – 99 mm bore.

air jet.

The simulations advance to 271 °CA, shortly after the intake valve has shut, and the compression stroke has begun. The mass averaged velocity squared and mass averaged turbulence (figure 8.21) considerable differences between the simulations. Figure 8.25 shows the cross tumble plane, with the more dominant vortex of the two moving to the centre of the domain and the weaker vortex now dying. There are few obvious differences between these simulations, however the 93 mm bore simulation has the main central vortex significantly less "squashed" than the 99 mm bore simulation, and the weaker vortex has a slightly different shape.

The tumble plane is shown in figure 8.26. There are small differences between the simulations, but again they are fundamentally similar. The flows in the tumble plane are of low magnitudes, and are not of great significance in comparison with the flows seen in the cross tumble plane (figure 8.25). An interesting feature of this simulation is that the tumble vortex appears to be rotating in the opposite direction to a traditional tumble vortex. This reversal can be clearly seen in all simulations, and is the reason for the tumble ratio calculation changing sign during

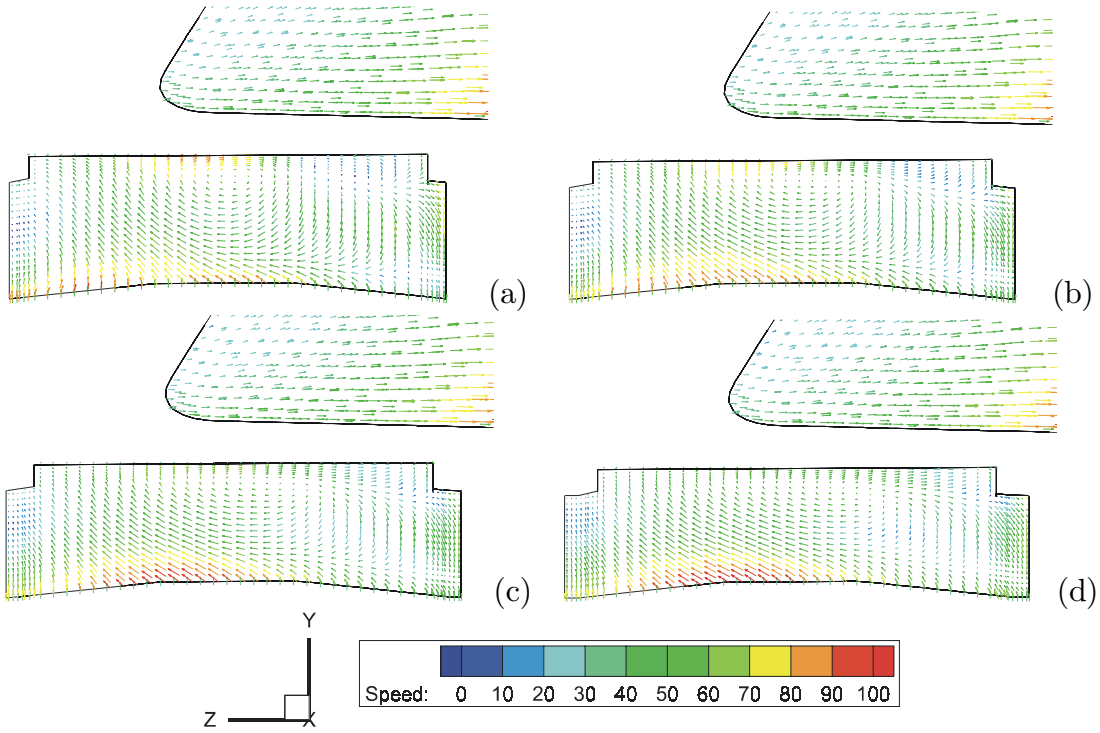

Figure 8.26: Visualisations of flow in the $X = 0$ tumble plane 271 °CA. (a) – 93 mm bore; (b) – 95 mm bore; (c) – 97 mm bore; and (d) – 99 mm bore.

the compression stroke, shown in figure 8.20e.

The swirl plane is shown in figure 8.27. One major vortex appears on the right hand side of all simulations. Numerous smaller structures are seen throughout the remainder of the slice. Again, all simulations are fundamentally the same in the central region. Near the periphery the velocities in the 93 mm bore simulation are significantly higher than those in the 99 mm simulation.

The turbulence levels at 271 °CA in the cross tumble and tumble planes are shown in figures 8.28 and 8.29 respectively. These figures, especially figure 8.29, indicate a clear trend of the turbulence intensity decreasing with each increase in bore size. This can be directly correlated with the trend in figure 8.21a.

Figures 8.30 and 8.31 illustrate the turbulence after the compression stroke has progressed to 331 °CA. This is the approximate time of ignition of the spark. The general trend of turbulence decreasing with increasing BSR seen in figure 8.21a is still apparent. It may be seen that the turbulence intensity is concentrated in the centre section of the combustion chamber, and the outer squish regions have relatively little turbulence. The intensity of turbulence in this central region reduces significantly as the BSR is increased, in both the cross tumble and tumble planes.

The turbulence in the outer periphery of the squish regions, especially in the

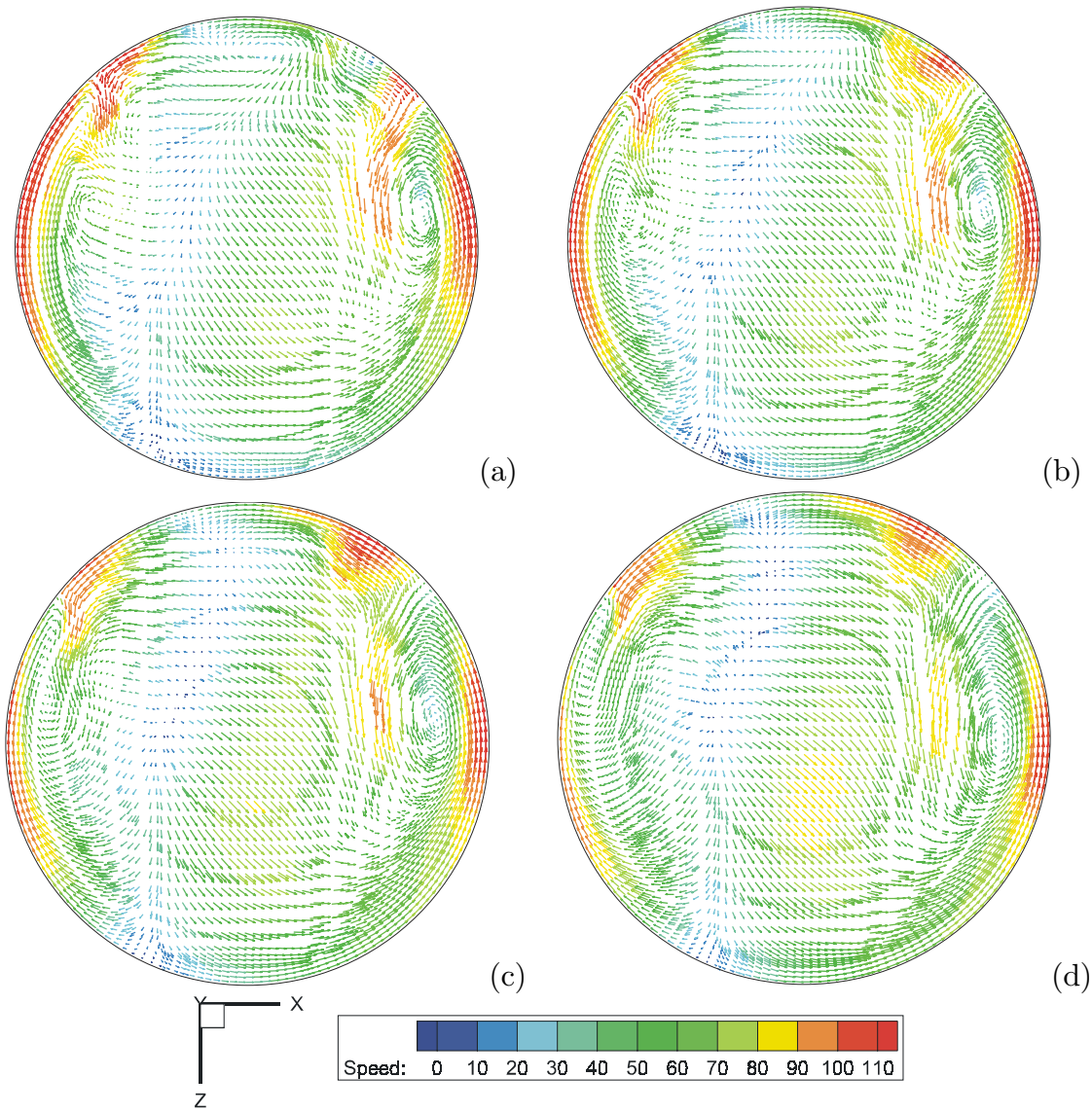

Figure 8.27: Visualisations of flow in the $Y = -55\,\text{mm}$ swirl plane 271 °CA. (a) – 93 mm bore; (b) – 95 mm bore; (c) – 97 mm bore; and (d) – 99 mm bore.

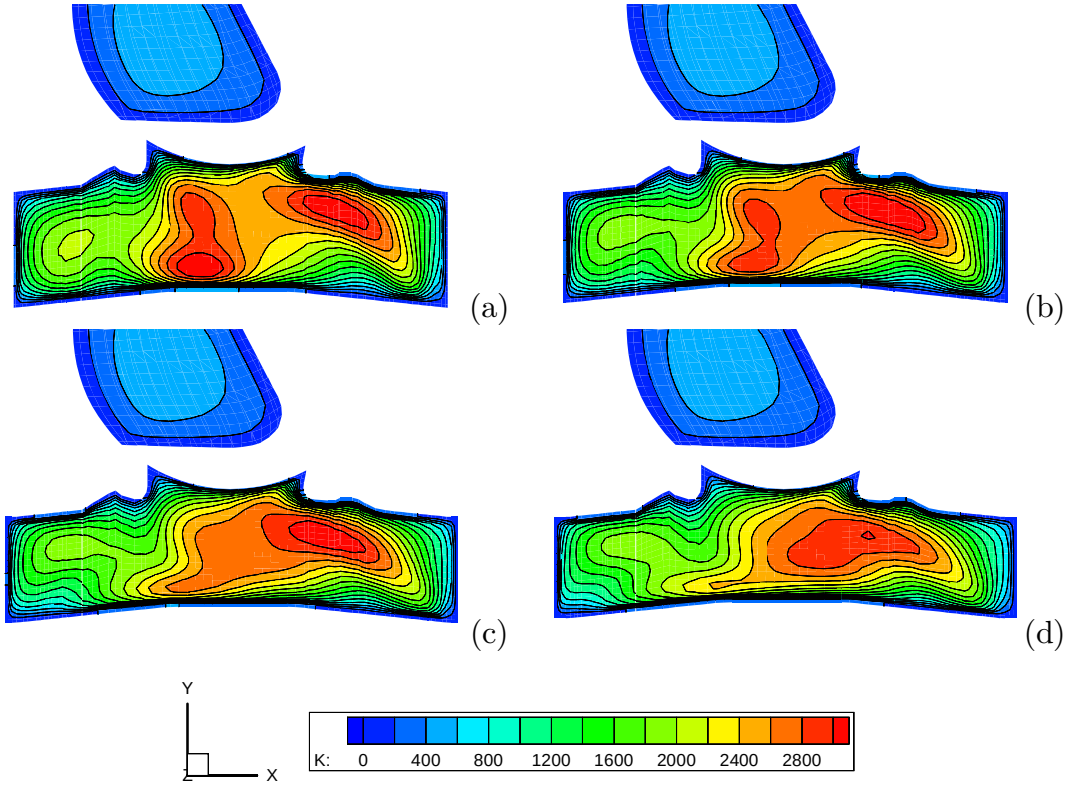

Figure 8.28: Visualisations of turbulence, k (m^2/s^2) in the $Z = 0$ cross tumble plane at 271 °CA. (a) – 93 mm bore; (b) – 95 mm bore; (c) – 97 mm bore; and (d) – 99 mm bore.

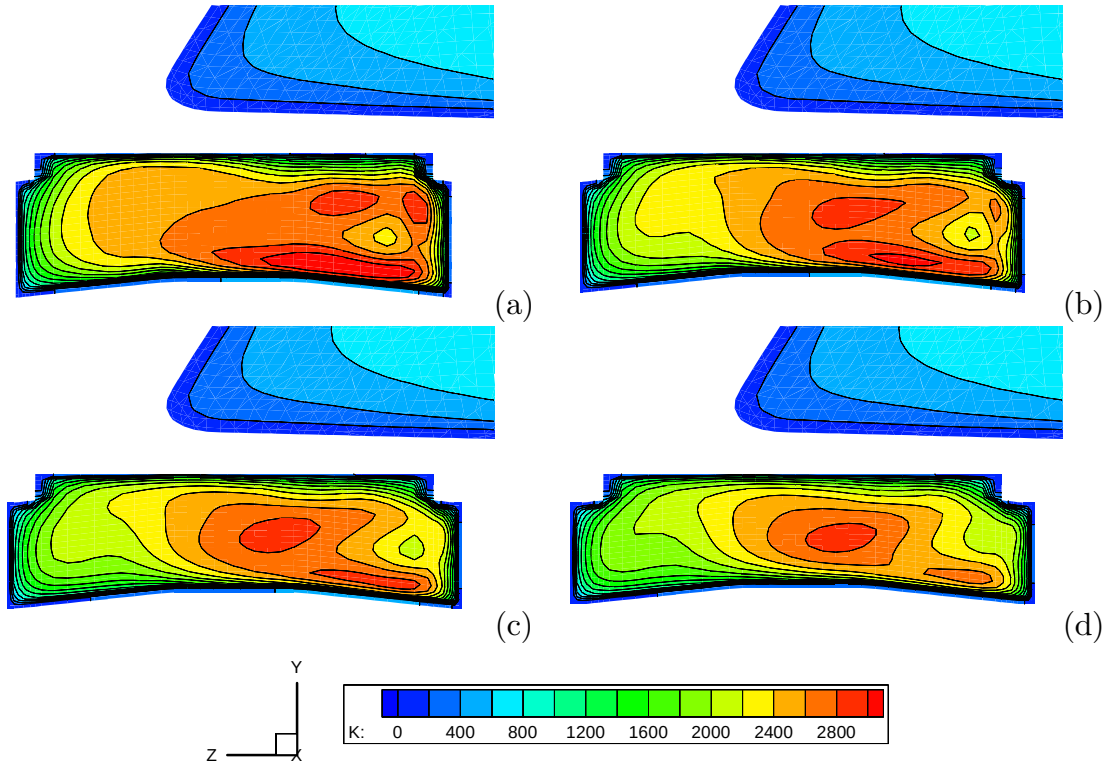

Figure 8.29: Visualisations of turbulence, k (m^2/s^2) in the $X = 0$ tumble plane at 271 °CA. (a) – 93 mm bore; (b) – 95 mm bore; (c) – 97 mm bore; and (d) – 99 mm bore.

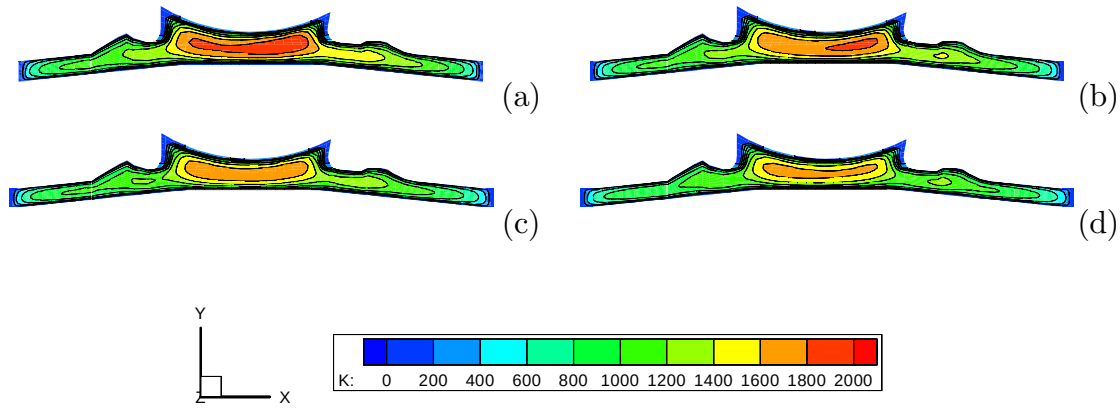

Figure 8.30: Visualisations of turbulence, k (m^2/s^2) in the $Z = 0$ cross tumble plane at 331 °CA. (a) – 93 mm bore, (b) – 95 mm bore, (c) – 97 mm bore and (d) – 99 mm bore.

cross tumble planes, does not change significantly with BSR. This is to be expected as the dominant flow in the periphery regions late in the compression stroke is a squish flow.

8.6.3 Discussion

The results presented confirm that an increase in bore size from 93 mm to 99 mm will result in a decrease in turbulence levels by the end of the compression stroke. To estimate the amount of turbulence reduction, two measures of turbulence will be used—firstly, the turbulence levels at the centre of the upper section combustion chamber will be extracted, and secondly by calculating the mass averaged turbulence across the entire cylinder. The data was extracted from the simulation at 331 °CA (figures 8.30 and 8.31).

The result is summarised in figure 8.32. The turbulence energy (k, figure 8.32a) in the central region of the domain decreases linearly, with the line having a gradient of $-41\,m^2\,s^{-2}$ per mm bore. The averaged turbulence energy also decreases linearly, but more slowly as its gradient is $-28\,m^2\,s^{-2}$ per mm bore. This more rapid decrease in the central section as compared to the averaged figure is a result of the turbulence in the periphery of the domain being largely independent of bore size, as was shown in figure 8.30.

An alternate way of expressing turbulence intensity is as a velocity fluctuation, u'. As discussed in section 4.1, this is a useful method of expressing turbulence intensity in an engine as the combustion speed is roughly proportional to the turbulent velocity fluctuations. Turbulent kinetic energy (k) can be converted to turbulent

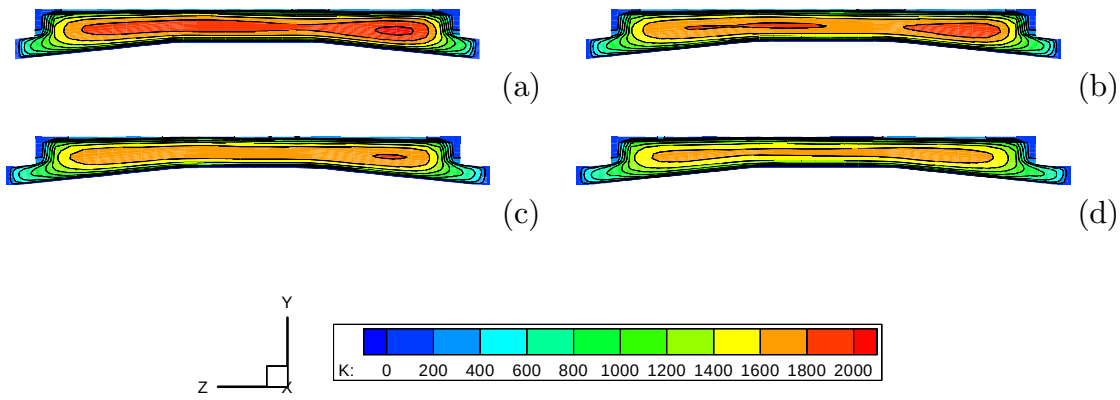

Figure 8.31: Visualisations of turbulence, k ($\mathrm{m}^2/\mathrm{s}^2$) in the $X = 0$ tumble plane at 331 °CA. (a) – 93 mm bore, (b) – 95 mm bore, (c) – 97 mm bore and (d) – 99 mm bore.

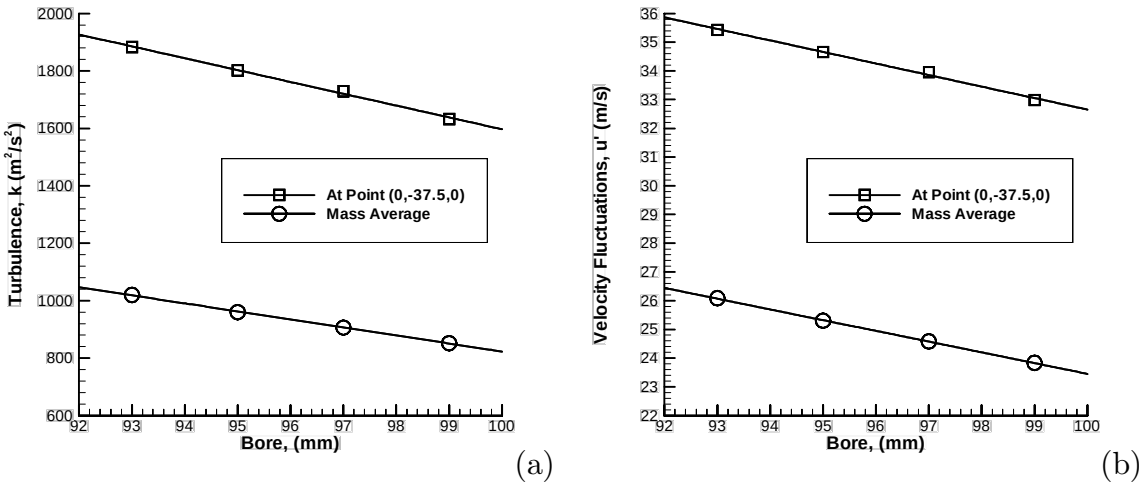

Figure 8.32: Turbulence at 331 °CA versus bore size. Shown is data extracted from figure 8.30 at the centre of the combustion chamber at point $(0, -37.5\,\mathrm{mm}, 0)$, and mass averaged turbulence across the entire combustion chamber from figure 8.21a. (a) – Turbulent kinetic energy (k); and (b) – Turbulent velocity fluctuations (u').

velocity fluctuations (u') using

$$u' = \sqrt{\frac{2}{3}k}. \tag{8.2}$$

The turbulent velocity fluctuations (u', figure 8.32b) are also shown to decrease linearly, this time with a gradient of $-0.40\,\mathrm{m\,s^{-1}}$ per mm bore for the central point, and $-0.37\,\mathrm{m\,s^{-1}}$ per mm bore for the averaged figure. When normalised against the 93 mm bore results, this represents a reduction of 1.1% per mm bore and 1.4% per mm bore respectively. As already mentioned in section 4.1, there is roughly a linear relation between the turbulent combustion speed and the turbulent velocity fluctuations, so a reduction in combustion speed in the engine of around 1.1% to 1.4% per mm bore increase above 93 mm is to be expected.

When a high performance poppet valve engine was simulated by Bianchi et al [41], they found a 8% decrease in in-cylinder turbulence (u') at 330 °CA when the BSR was increased by 14%. If the results from the BRV engine were also scaled to a 14% increase in BSR (equivalent to increasing the bore from 93 mm to 97 mm), a decrease in turbulence (u') of between 4.5% to 5.6% is predicted, with the lower figure being the turbulence reduction in the centre of the cylinder, and the higher figure being the in-cylinder averaged turbulence. This suggests that the reduction in turbulence caused by increasing BSR may be smaller in the BRV engine than in poppet valve engines. This reduced sensitivity of the BRV engine using a dual tumble flow field to increasing BSR means that it may be able to operate at higher BSR than poppet valve engines using a tumble flow field. The increased BSR allows higher engine speeds and greater engine power.

This is an encouraging result, and suggests the BRV engine does indeed posses advantages over the poppet valve engine for high performance applications. However, it must be kept in mind that flame speed does not have a simple relationship with engine performance. For example, the significant increase in squish areas will cause greater flame quenching in the periphery of the cylinder, and this effect is not taken into account in the above analysis.

8.7 Turbulence Scaling

The turbulence levels (as velocity fluctuations, u', from equation 8.2) in an engine is thought to scale with engine speed; this has been discussed in section 4.1. A series of simulations were performed to determine whether this occurs on the BRV engine.

Two configurations were tested. "Configuration 1" consists of runs 851 and

	15000 rpm	18000 rpm	% increase
300 °CA	1.26	1.33	6
330 °CA	0.99	1.03	4
360 °CA	0.60	0.59	2

Table 8.9: Comparison of normalised turbulence during the compression stroke of the first engine cycle for engine configuration 1 at 15000 rpm and 18000 rpm (runs 851 and 852).

	15000 rpm	18000 rpm	% increase
300 °CA	1.21	1.30	7
330 °CA	0.98	1.02	4
360 °CA	0.59	0.60	2

Table 8.10: Comparison of normalised turbulence during the compression stroke of the first engine cycle for engine configuration 2 at 15000 rpm and 18000 rpm (runs 864 and 861).

852, modelled with identical engine configurations but were simulated at 15000 rpm and 18000 rpm respectively. "Configuration 2" consists of runs 864 and 861, again with identical engine configurations but were simulated at 15000 rpm and 18000 rpm respectively. Further details of these two runs are shown in table 8.1.

The mean piston velocity is commonly used as a velocity scale [137], and is calculated from

$$MPV = \frac{2Ns}{60}, \tag{8.3}$$

where N is the engine speed in rpm, and s is the stroke length. For the 93 mm bore engine, the MPV is 22.1 m s^{-1} at 15000 rpm and 26.5 m s^{-1} at 18000 rpm.

Turbulent velocity fluctuations normalised against MPV may be seen in figure 8.33 for the first cycle of the simulation for the two configurations. The first cycle results, figure 8.33, show that the normalised turbulence is slightly higher at 18000 rpm than at 15000 rpm for both configurations. The normalised turbulence for configuration 1 is tabulated in table 8.9 for three locations near the end of the compression stroke. Similarly the normalised turbulence for configuration 2 is shown in table 8.10. The increase in turbulence from the 15000 rpm simulation to the 18000 rpm is 6–7% at 300 °CA, is 4% at 330 °CA, and is 2% at TDC. This shows that the turbulence is increasing faster than it would if it were directly proportional to engine speed.

The results from the second cycle of the simulations are shown in figure 8.34, and are tabulated in table 8.11 for configuration 1 and table 8.12 for configuration 2. Configuration 1 has a dramatic increase in turbulence with speed, being 29%

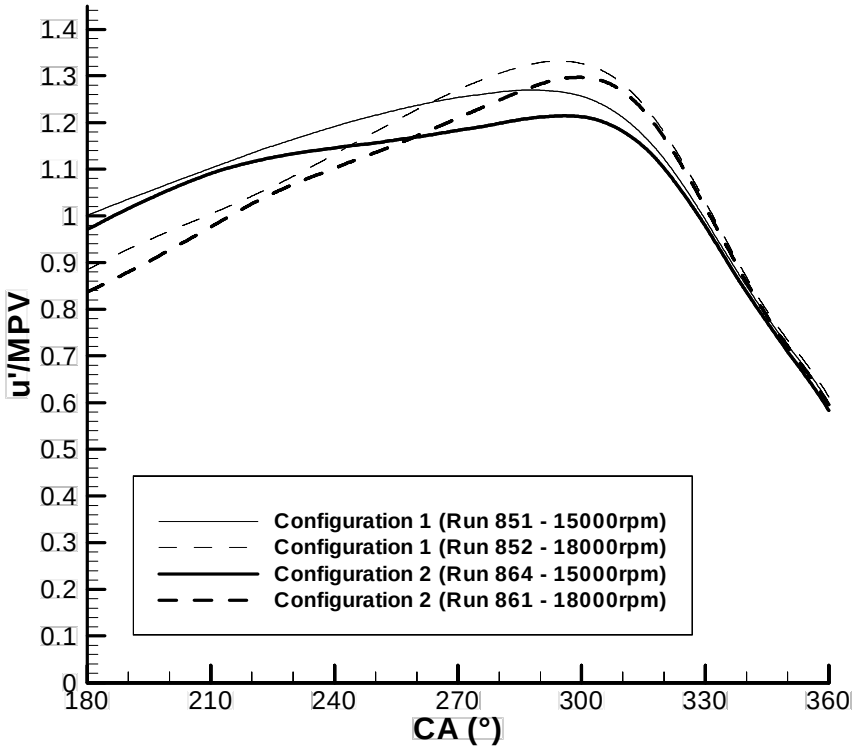

Figure 8.33: Normalised turbulence (u'/MPV) during the compression stroke of the BRV engine, showing data from the first cycle of the simulation.

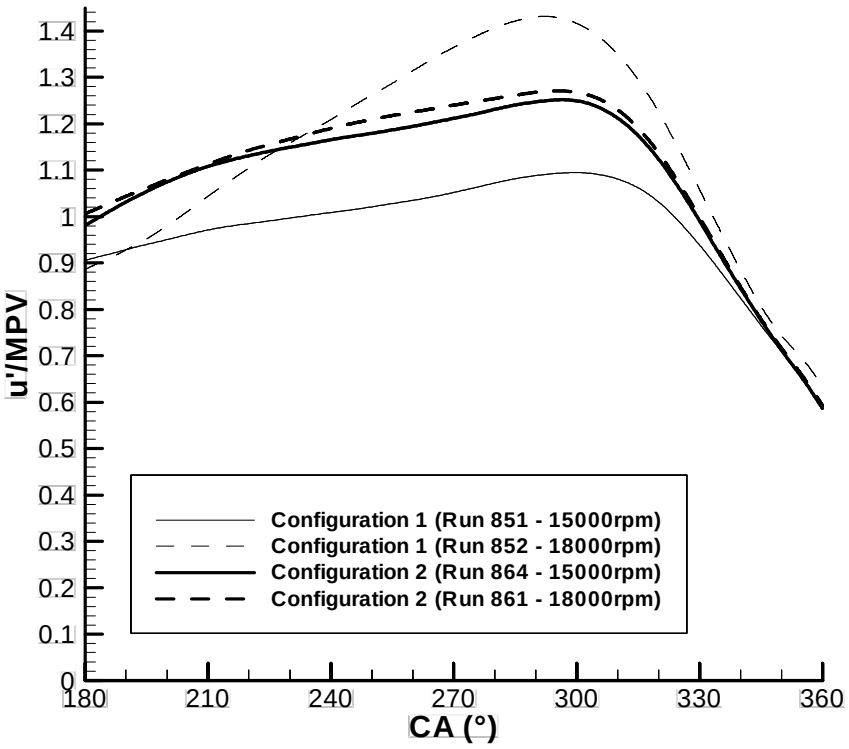

Figure 8.34: Normalised turbulence (u'/MPV) during the compression stroke of the BRV engine, showing data from the second cycle of the simulation.

at 300 °CA, 13% at 330 °CA and 8% at TDC. Configuration 2 shows only a slight increase of 1–2%.

The increase in turbulence predicted for the first cycle of the simulations is small, but significant. The results from the second revolution exhibit great variation, varying from small to very large increases. As discussed in section 8.2, the first cycle results are a better guide to performance when the engine is operating out of tune, as the second revolution results are significantly affected by the inlet manifold wave.

When the comparison is made using the first revolution data, the increases between configurations are quite similar. As has been previously mentioned, the range of increases predicted at 300 °CA is 6–7%, at 330 °CA is 4%, and 2% at TDC. This suggests the first revolution results provide a more reliable basis for comparison as both sets of simulations give similar results. For the second cycle results the range is 2–29% at 300 °CA, 1–13% at 330 °CA and 1–8% at TDC, indicating a large

	15000 rpm	18000 rpm	% increase
300 °CA	1.09	1.41	29
330 °CA	0.94	1.06	13
360 °CA	0.59	0.64	8

Table 8.11: Comparison of normalised turbulence during the compression stroke of the second engine cycle for engine configuration 1 at 15000 rpm and 18000 rpm (runs 851 and 852).

	15000 rpm	18000 rpm	% increase
300 °CA	1.25	1.27	2
330 °CA	0.99	1.00	1
360 °CA	0.59	0.59	1

Table 8.12: Comparison of normalised turbulence during the compression stroke of the second engine cycle for engine configuration 2 at 15000 rpm and 18000 rpm (runs 864 and 861).

amount of fluctuation caused by the inlet manifold wave.

As mentioned in section 4.1, the turbulent flame velocity is roughly proportional to the turbulent fluctuation velocity, u'. If the normalised turbulence (u'/MPV) is constant for an engine against speed, the spark advance required for the engine should remain constant with varying engine speed[1]. If the normalised turbulence increases at a faster rate than the engine speed, as predicted in the BRV engine, the spark advance requirement should decrease with increasing speed.

Figure 8.35 shows the experimentally determined spark advance used for five BRV engines, as run in the dynamometer. All five engines have quite different configurations, some have 63 mm valves, some 68 mm valves, different port geometries and so on, but the trend for all configurations is clear. All five engines show a linear trend with spark advance reducing with increasing engine speed, all at roughly 0.4 °CA per 1000 rpm. The average spark advance at 15000 rpm was 37 °CA, and extrapolating the trend to 18000 °CA gives an expected spark advance of around 36 °CA. This represents a reduction of spark advance of 3%, and assuming the mass fraction burnt at TDC remains constant this means the combustion is occurring 3% faster. The range of turbulence increase predicted using the CFD simulation here is 4% at 330 °CA or 2% at TDC. This experimentally measured spark advance

[1] This assumes that the initial and final burn periods of the combustion also scale linearly with turbulent fluctuation velocity. This is not quite true [137]. However, as the initial and final burn periods of combustion represent only a small part of the total combustion duration in a high speed engine, it can be approximated that the flame velocity is a linear function of the turbulent velocity fluctuation magnitude.

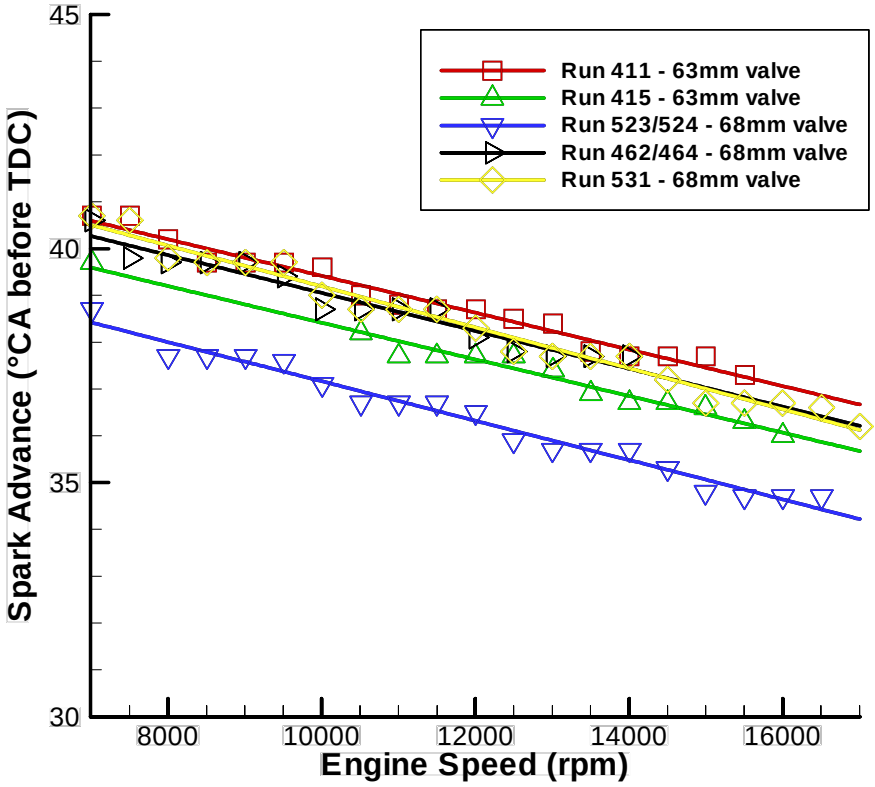

Figure 8.35: Spark advance of the experimental engine for various configurations.

requirement agrees with the trend predicted by the simulations.

The cause for this decrease in spark advance requirements with increasing engine speed is thought to be caused by the gasses entering the cylinder later in the intake stroke as the engine speed increases. The gas enters later as the time lag caused by gas compressibility leads to a longer relative delay as the engine speed increases. As the gas enters later, the in-cylinder flow field and turbulence decays less before combustion, in a similar manner to the effect of the inlet manifold wave on in-cylinder flow and turbulence, discussed in section 8.2.

There are many other factors bearing on the optimum spark advance for an engine at any given speed that have not been considered here, however the trend shown by the BRV engine on the dynamometer is clear. This is a very crude form of analysis, due partly to the small number of engine configurations and speeds simulated, and partly to the fact that many effects besides turbulence levels affect spark advance. However, the magnitude of the decrease in spark advance can be

explained as a direct consequence of the turbulence level increasing at a rate faster than if directly proportional to engine speed. This is a further encouragement that the simulation is predicting the in-cylinder turbulence levels consistently.

8.8 Discussion

The analysis performed in this chapter indicates that the CFD model presented here appears to accurately predict many engine parameters. The model is shown in section 8.1 to accurately predict the mass of gas in the cylinder at the end of the intake stroke. The importance of the inlet manifold wave on the volumetric efficiency, as well as the in-cylinder flow velocities and turbulence fields was demonstrated in section 8.2. Section 8.7 shows the model successfully predicted the experimentally measured trend of spark advance decreasing with increasing engine speed.

Changes in design were evaluated using the simulation model, without requiring the engines to be physically made and experimentally tested. This makes computational modelling an ideal way of testing design ideas at greatly reduced expense compared with traditional experimental modelling. The effect of reducing the valve cross-section area (section 8.3) and the effect of increasing the valve size (section 8.4) was tested. It was found that constrictions in the valve reduced the peak mass flow rates and decreased in-cylinder velocities and turbulence, and that increasing the valve size increased peak mass flow rates and reduced in-cylinder velocities and turbulence. This result is in agreement with the traditional engine design philosophy.

Changing the heat transfer properties of the walls of the model to adiabatic was found to increase the mass of gas in the cylinder at the end of the intake stroke by around 5%, which is a significant increase. This was analysed in section 8.5, and indicates wall heat transfer has a significant affect on engine output, and indicates that the use of insulating materials in the valve may improve engine performance.

The effect of bore to stroke ratio on the BRV engine was determined in section 8.6. When compared to poppet valve engines it was found that the BRV engine appears to have a reduced sensitivity to increases in bore to stroke ratio. For instance, Bianchi et al [41] found that increasing the bore to stroke ratio by 14% decreased turbulence (u') at 330 °CA by 8%. The same 14% increase in bore to stroke ratio in the BRV engine was found to decrease turbulent levels by between 4.5%–5.6%. This increased turbulence means that the BRV engine, using the dual cross tumble flow field, is likely to be able to maintain better performance at higher bore to stroke ratios than traditional poppet valve engines using tumble flow fields.

This is turn means that the BRV engine can be run at higher engine speeds, resulting in greater power.

Finally an analysis of how the in-cylinder turbulence scales with engine speed was performed in section 8.7. It was found that the turbulence (u') in the BRV engine appears to increase slightly more than in proportion to engine speed. This suggests that the BRV engine combustion performance will improve with increasing engine speed. This characteristic, together with the ability to perform using higher bore to stroke ratio engines means that the BRV engine is likely to continue to perform well at higher engine speeds than is possible with poppet valve engines. This has the potential to make the BRV engine perform significantly better than existing poppet valve engines.

Chapter 9

Conclusion

A numerical Computational Fluid Dynamics (CFD) simulation of the Bishop Rotary Valve (BRV) engine has been developed. The simulation used an existing commercial CFD code, CFX 4.3, with a number of new routines to allow it to simulate the conditions and motions present in a rotary valve internal combustion (IC) engine. This included a sliding interface model to allow simulation of the opening and closing of the rotating valve window.

The code has been extensively validated for a wide variety of flows, and additional validations have been performed by the current author to justify the application of the code to internal combustion engines. The first validation study was to assess the code's ability to model transient compressible wave motion, similar to that which occurs in the manifolds of an internal combustion engine. The one-dimensional shock tube problem was used as the benchmark problem. The predicted post-shock gas state was compared to analytical results, and was found to be in excellent agreement, better than 0.02%. The position of the shock wave, rarefaction wave and contact surface was calculated with an accuracy better than 2% when the coarse mesh (100 nodes) was used, and better than 0.4% when the fine mesh simulation (800 nodes) was used. The discontinuities at the shock, and to a lesser extent the contact surface, were smeared over four to six mesh points for all meshes. This means the gradient of resolution of the shock is proportional to mesh density.

A second validation study was performed simulating tumble vortex breakdown during the compression stroke of a square piston model engine. The results of these simulations were compared to high quality experimental particle image velocimetry (PIV), laser Doppler anemometry (LDA) and laser Doppler velocimetry (LDV) data performed by other researchers. Both two- and three-dimensional models were

tested, using both the k-ϵ and Reynolds stress turbulence models.

All models yielded good agreement during the intake stroke. However, significant variations between the models occurred during the compression stroke. The two- and three-dimensional k-ϵ turbulence model failed to predict the fundamental tumble vortex breakdown process. The k-ϵ model also failed to predict the departure from solid body rotation that was seen in the experimental results at bottom dead centre (BDC). However, the turbulence intensities at various points and the tumble ratio were predicted with reasonable accuracy.

The two-dimensional Reynolds stress turbulence model was found to accurately predict the structures that form during the tumble vortex breakdown process, and was in close agreement with the experimental PIV measurements of the process. However, the predicted turbulence intensities at various points and tumble ratio over the cylinder were significantly different from the experimental results. The three-dimensional Reynolds stress model also predicted a breakdown process, however it was significantly different to the process predicted by the two-dimensional model and PIV measurements. The turbulence intensities at various points and tumble ratio in the cylinder were predicted with good accuracy. Both the two- and three-dimensional Reynolds stress models successfully predicted the departure from solid body rotation at BDC.

To the current author's knowledge, this is the first time that the tumble vortex breakdown process during the compression stroke has been successfully simulated and close agreement with experimental data obtained. The process modelled and seen in the experimental results is that the tumble vortex at BDC becomes smaller during the early compression stroke, breaking up into three vortices, and then breaking up again into approximately nine vortices close to top dead centre (TDC).

Overall, the three-dimensional Reynolds stress model proved to be the most accurate, and the two- and three-dimensional k-ϵ models proved to be the least accurate. However, despite the k-ϵ models failing to predict the tumble breakdown process at all, it did predict the turbulence intensity during the compression stroke with reasonable accuracy, for example the agreement with the three-dimensional RSM model at TDC was within 15%.

A simple three-dimensional LES model was also developed for the square cylinder model engine. It used no explicit sub-grid model, instead using a second order upwinding differencing scheme to dissipate the sub-grid energy. Despite its simplicity, this model provided reasonably accurate results—indeed the results proved more accurate by many measures than the k-ϵ model simulations. It did predict a tumble vortex breakdown process, but the process significantly varied from the

experimentally measured mechanism. It correctly predicted a departure from solid body rotation at BDC, and the turbulence intensities at various points and tumble ratio over the cylinder were reasonably accurately predicted. The most significant shortcoming of the LES model presented here is that it is based on only one cycle of the engine, so results can be significantly affected by cycle to cycle variations. A number of cycles of the engine would need to be modelled to obtain a statistically significant measure of the true flow, similar to that performed for the experimental results. The model proved sufficiently accurate that further work in the area is warranted.

The Reynolds Stress turbulence model requires an additional seven equations to be solved, and the model equations are numerically stiff leading to convergence difficulties. As simulations of real engine geometries are already large and computationally intensive, this makes the Reynolds Stress model impractical on modern computers. Simulations using the k-ϵ model are of a size appropriate to modern computers, so the k-ϵ model is the most suitable turbulence model for general engine modelling. The k-ϵ model failed to predict the tumble breakdown process during the compression stroke, however it did predict the turbulence existing at the end of the compression stroke with reasonable accuracy. The turbulence existing at the end of the compression stroke is the critical parameter for determining the effectiveness of the combustion, so the k-ϵ model is cautiously justified for IC engine simulations, as long as its shortcomings are acknowledged.

The validated numerical model was applied to the BRV engine. The unique combustion chamber shape of the BRV engine means that the simulations predict a flow in the cylinder of the engine which is not adequately described by the traditional engine flows of squish, swirl and tumble. The new flow structure is named "dual cross tumble", and is characterised by two counter-rotating vortices in the cross tumble plane on either side of the inlet air jet. The generation of this flow structure was discovered to be the cause of a significant performance increase measured on the dynamometer when a modification to the BRV cylinder head geometry was made.

The dual cross tumble structure is found to be most useful in high bore to stroke ratio engines. Normal tumble structures are inefficient in high bore to stroke ratio chambers as the vortex must be considerably distorted to rotate in a high aspect ratio volume. Dual cross tumble reduces this distortion as it reduces the effective aspect ratio of the vortices in the combustion chamber by a factor of around two.

The dual cross tumble flow structure has been predicted or visualised by a small number of previous researchers, and a small number of researchers have recognised

that vortex based turbulence enhancement processes (for instance traditional swirl and tumble flows) need not be limited to only one major vortex. However, no previous researchers have appeared to recognise the significance or potential benefits of dual cross tumble. This appears to be due to the traditional four valve pentroof being unable to generate significant dual cross tumble flow.

The simulation model was applied to a number of BRV engine geometries to further understand the engine. As part of the verification of this model it was found to predict the inlet manifold wave and volumetric efficiencies with very good agreement with experimental results.

The effect of reducing the valve cross sectional area was assessed, and found to lower volumetric efficiency and increase in-cylinder flow field velocities and turbulence, in accordance with traditional thinking for engine design. Likewise, the effect of increasing the valve dimensions was simulated, and found that it potentially increased volumetric efficiency by increasing maximum possible flow rates, but reduced the in-cylinder velocities and turbulence. The inlet manifold wave was found not only to effect the volumetric efficiency of the engine, but also the in-cylinder turbulence. It was found that for high levels of in-cylinder turbulence in the compression stroke, the velocities in the final section of the intake stroke must be high and reverse flow needs to be avoided.

The effect of heat transfer from the inlet manifold and cylinder walls was assessed, and found to influence volumetric efficiency by up to 5%, in comparison to an equivalent model with all walls being adiabatic. This suggests reducing wall heat transfer may significantly increase volumetric efficiency, leading to improved engine performance.

The effect of increasing the bore to stroke ratio of the engine was simulated. Increasing bore to stroke ratio was found to reduce turbulence levels, in agreement with traditional engine design philosophy. However, the reduction in the BRV engine appears to be less than for equivalent poppet valve engines. This is asserted to be due to the dual cross tumble flow structure being less affected by high aspect ratio combustion chambers. Finally, the effect of engine speed is assessed. Traditional thinking is that in-cylinder turbulence levels increase in proportion with the engine speed. However, the BRV engine is found to have an increase slightly higher than directly proportional, and the amount of increase agreed well with experimentally measured spark advance requirements. This effect is thought to be primarily due to the intake stroke gas entering the cylinder later in the stroke due to the time lag effect caused by gas compressibility.

This work has presented a well validated numerical simulation, and applied it to a new engine technology. This opens up a whole new area of engine aerodynamics research as no detailed examination of the flows in a rotary valve engine have been presented previously. In the process, it discovers a new compression stroke turbulence generation mechanism, "dual cross tumble", which offers the potential of performance levels not possible using poppet valve engines.

Bibliography

[1] Coates rotary valve. http://www.coatesengine.com/, 1999.

[2] AVL BOOST. http://www.avl.com/, January 2000.

[3] CFX for in cylinder flows. http://www.software.aeat.com/cfx/industry/automotive/cylinder.htm, August 2000.

[4] Ferrari - vetture formula. http://www.ferrari.it/comsport/formula1/vettf1.html, 2000.

[5] The Mitsubishi GDI engine. http://www.mitsubishi-motors.co.jp/GDI2000/, 2000.

[6] PC Dyno2000. http://www.motionsoftware.com/dyno2000prodpage.htm, 2000.

[7] SEC info - coates international Ltd/DE - 10KSB - for 12/31/99. http://www.secinfo.com/dSu65.5c.htm, April 2000.

[8] WAVE V3.5. http://www.ricardo.com/index.htm?pages/wave35.htm, December 2000.

[9] Cross manufacturing company (1938) limited. http://www.crossmanufacturing.com/, 2001.

[10] Formula 1 homepage of GP results & history. http://www.fortunecity.com/olympia/grange/54/index1.htm, March 2001.

[11] O Aaen. Design and development of an 850 cc single crankshaft V-4 two-stroke engine for SCCA D-Sports racing. *Society of Automotive Engineers*, (983071), 1998.

[12] S Adachi, K Horio, Y Nakamura, K Nakano, and A Tanke. Development of Toyota 1ZZ-FE engine. *Society of Automotive Engineers*, (981087), 1998.

[13] AEA Technologies, Harwell. *CFX 4.3 User Manual*, 2000.

[14] H Affes, N Trigui, D Smith, and V Griaznov. Shape optimization of IC engine ports and chambers. *Society of Automotive Engineers*, (980127), 1998.

[15] B Ahmadi-Befrui and A D Gosman. Assessment of variants of the k-ϵ turbulence model for engine flow applications. *International Journal for Numerical Methods in Fluids*, 9:1073–1086, 1989.

[16] S Aïta, A Tabbal, G Munck, K Fujiwara, H Hongoh, E Tamura, and S Obana. Numerical simulation of port-valve-cylinder flow in reciprocating engines. *Society of Automotive Engineers*, (900820), 1990.

[17] J H Alderton and N S Wilkes. Some applications of new finite difference schemes for fluid flow problems. Technical Report AERE-R 13234, Harwell Laboratory, August 1988.

[18] A A Amsden, T D Butler, P J O'Rourke, and J D Ramshaw. KIVA—a comprehensive model for 2-D and 3-D engine simulations. *Society of Automotive Engineers*, (850554), 1985.

[19] C Angelberger, T Poinsot, and B Delhay. Improving near-wall combustion and wall heat transfer modeling in SI engine computations. *Society of Automotive Engineers*, (972881), 1997.

[20] C Arcoumanis, editor. *Internal Combustion Engines*. St Edmundsbury Press, Suffolk, 1988.

[21] C Arcoumanis, P Begleris, A D Gosman, and J H Whitelaw. Measurements and calculations of the flow in a research diesel engine. *Society of Automotive Engineers*, (861563), 1986.

[22] C Arcoumanis, S N Godwin, and J W Kim. Effect of tumble strength on combustion and exhaust emissions in a single-cylinder, four valve, spark-ignition engine. *Society of Automotive Engineers*, (981044), 1998.

[23] C Arcoumanis and J H Whitelaw. Fluid mechanics of internal combustion engines—a review. *Proceedings of the Institution of Mechanical Engineers*, 201(C1):57–74, 1987.

[24] B F Armaly, F Durst, J C F Pereira, and B Schönung. Experimental and theoretical investigation of backward-facing step flow. *Journal of Fluid Mechanics*, 127:473–496, 1983.

[25] U Asaka, N Kurata, and M Masumura. Rotary valve in an internal combustion engine. US Patent 4,404,934, September 1983.

[26] F M Aspin. Driving means for rotary valves of internal-combustion engines, compressors and the like. US Patent 2,407,127, September 1946.

[27] F M Aspin. Internal combustion engines. US Patent 4,033,317, July 1977.

[28] M Auriemma, F E Corcione, R Macchioni, and G Valentino. Assessment of the k-ϵ turbulence model in KIVA-II by in-cylinder LDV measurements. *Society of Automotive Engineers*, (952385), 1995.

[29] M Auriemma, F E Corcione, R Macchioni, and G Valentino. Interpretation of air motion in reentrant bowl in-piston engine by estimating Reynolds stresses. *Society of Automotive Engineers*, (980482), 1998.

[30] O Bailly, C Buchou, A Floch, and L Sainsaulieu. Simulation of the intake and compression strokes of a motored 4-valve SI engine with a finite element code. *Oil and Gas Science and Technology—Review IFP*, 54(2):161–168, 1999.

[31] A J S Baker and M E Cross. Four-cylinder, four cycle engine with two reciprocating components. *Proceedings of the Institution of Mechanical Engineers*, 188(38):505–511, 1974.

[32] C J Bates, M L Yeoman, and N S Wilkes. Non-intrusive measurements and numerical comparison of the axial velocity components in a two-dimensional flow channel for a backward facing step and a rib roughened surface. Technical Report AERE-R 10787, Harwell Laboratories, 1983.

[33] W Bauer, J B Heywood, O Avanessian, and D Chu. Flow characteristics in intake port of spark ignition engine investigated by CFD and transient gas temperature measurement. *Society of Automotive Engineers*, (961997), 1996.

[34] M R Belmont, J Hacohen, and P W Carpenter. Tumble and swirl: Are they a mixed blessing? *Proceedings of the Institution of Mechanical Engineers, Part D (Journal of Automotive Engineering)*, 208(3):223–226, 1994.

[35] S F Benjamin, J H Weaving, D R Glynn, N C Markatos, and D B Spalding. Development of a mathematical model of flow, heat transfer and combustion in a stratified charge engine. *Proceedings of the Institution of Mechanical Engineers*, (C403/80), 1980.

[36] H Bensler, C Freek, B Beesten, A Ritter, and W Hentschel. An experimental and numerical study of the steady-state flow of a SI-engine intake port. *Society of Automotive Engineers*, (982470), 1998.

[37] R S Benson. Disharge from an engine cylinder to atmosphere. *The Engineer*, 203:946–949, 1957.

[38] R S Benson. A comprehensive digital computer program to simulate a compression ignition engine including intake and exhaust systems. *SAE*, (710173), 1971.

[39] R S Benson. *The Thermodynamics and Gas Dynamics of Internal Combustion Engines*, volume one. Clarendon Press, Oxford, 1982.

[40] R S Benson, R D Garg, and D Wollatt. A numerical solution of unsteady flow problems. *International Journal of Mechanical Science*, 6:117–144, 1964.

[41] G M Bianchi, G Cantore, E Mattarelli, G Guerrini, and F Papetti. The influence of stroke-to-bore ratio and combustion chamber design on Formula-One engines performance. *Society of Automotive Engineers*, (980126), 1998.

[42] A E Bishop. Rotary valve for internal combustion engines. US Patent 4,852,532, August 1989.

[43] A J Blair and G P Blair. Gas flow modelling of valves and manifolds in car engines. *Proceedings of the Institution of Mechanical Engineers*, (C11/87), 1987.

[44] G P Blair and F M M Drouin. Relationship between discharge coefficients and accuracy of engine simulation. *Society of Automotive Engineers*, (962527), 1996.

[45] H Blaxill, J Downing, J Seabrook, and M Fry. A parametric approach to spark-ignition engine inlet-port design. *Society of Automotive Engineers*, (1999-01-0555), 1999.

[46] J Borée, D Marc, R Bazile, and B Lecordier. On the behavior of a large scale tumbling vortex flow submitted to compression. In *ESAIM Proceedings, 3rd International Workshop on Vortex Flows and Related Numerical Methods*, number 7, pages 56–65, 1999.

[47] A A Boretti, M Borghi, and G Cantore. Numerical study of volumetric efficiencies in a high speed, four valve, four cylinder, spark ignition engine. *Society of Automotive Engineers*, (942533), 1994.

[48] A A Boretti, M Borghi, G Cantore, and E Mattarelli. Numerical optimization of a racing engine with variable intake and exhaust geometry and valve actuation. *Society of Automotive Engineers*, (962542), 1996.

[49] A A Boretti, G Cantore, and E Mattarelli. Numerical correlation of combustion evolution and port and combustion shape in a high speed, four valve, spark ignition engine. *Society of Automotive Engineers*, (942534), 1994.

[50] A A Boretti, G Cantore, E Mattarelli, and F Preziosi. Experimental and computatinal analysis of a high performance motorcycle engine. *Society of Automotive Engineers*, (962526), 1996.

[51] J Boris, F Grinstein, E Oran, and R Kolbe. New insights into large-eddy simulation. *Fluid Dynamics Research*, 10:199–228, 1992.

[52] D Bortoluzzi, V Cossalter, and A Doria. The effect of tunable resonators on the volumetric efficiency of an engine. *Society of Automotive Engineers*, (983045), 1998.

[53] P Bradshaw. Turbulence: The chief outstanding difficulty of our subject. *Experiments in Fluids*, 16:203–216, 1994.

[54] P Camus. La dernière ligne droite du W12 MGN. *Auto Hebdo*, pages 60–65.

[55] P Camus. Le MGN/W12 sur l'AGS. *Auto Hebdo*, (596):60–62, 1987.

[56] P Camus. Sans tambour ni soupape. *Auto Hebdo*, pages 43–47, February 1988.

[57] A Carapanayotis and M Salcudean. Mathematical modeling of the scavenging process in a two-stroke Diesel engine. In *Basic Processes in Internal Combustion Engines*, pages 97–106, New Orleans, Lousiana, 1988. American Society of Mechanical Engineers.

[58] S Caulfield, B Rubenstein, J K Martin, P Ruppel, M Meyer, S Lewis, A Tang, and B Tillock. A comparison between CFD predictions and measurements of inlet port discharge coefficient and flow characteristics. *Society of Automotive Engineers*, (1999-01-3339), 1999.

[59] M Chapman. Two dimensional numerical simulation of inlet manifold flow in a four cylinder internal combustion engine. *Society of Automotive Engineers*, (790244), 1979.

[60] C Charoenphonphanich, M Otaka, H Ennoji, T Iijima, and M Hukumoto. In-cylinder fluid motion and mixing of a dual intake valve spark ignition engine. *Society of Automotive Engineers*, (960266), 1996.

[61] A Chen, A Veshagh, and S Wallace. Intake flow predictions of a transparent DI diesel engine. *Society of Automotive Engineers*, (981020), 1998.

[62] G Chen, T W Asmus, and G T Weber. Fuel mixture temperature variations in the intake port. *Society of Automotive Engineers*, (961194), 1996.

[63] W-C Choi. Effects of operating speed on 3-D mean flows measured at the end of intake stroke in an IC engine. *Japanese Society of Mechanical Engineers, Series B*, 41(2):338–343, 1998.

[64] W Church and P V Farrell. Effects of intake port geometry on large scale in-cylinder flows. *Society of Automotive Engineers*, (980484), 1998.

[65] M Ciofalo and M W Collins. k-ϵ predictions of heat transfer in turbulent recirculating flows using an improved wall treatment. *Numerical Heat Transfer, Part B*, 15(1):21–47, 1989.

[66] G Cipolla and G Cugnetto. Three-dimensional flow field calculation of combustion chamber geometries for production direct injection diesel engine. *Proceedings of the Institution of Mechanical Engineers*, (C47/88), 1988.

[67] D S Clarke, J R Moore, and N S Wilkes. Predictions of the three dimensional boundary layer flow in an S-shaped channel using Harwell-FLOW3D. Technical Report AEA-InTec-0073, Harwell Laboratories, July 1990.

[68] D S Clarke and N S Wilkes. The calculation of turbulent flows in complex geometries using a differential stress model. Technical Report AERE-R 13428, Harwell Laboratories, April 1989.

[69] C Clutton, C Posthumus, and D Jenkinson. *The Racing Car—Development and Design*. B T Batsford Ltd, London, 1962.

[70] G J Coates. Spherical rotary valve assembly for use in a rotary valve internal combustion engine. US Patent 5,361,739, November 1994.

[71] R J Craver, R S Podiak, and R D Miller. Spark plug design factors and their effect on engine performance. *Society of Automotive Engineers*, (700081), 1970.

[72] M E Cross. Means of valving small four-stroke IC engines. *Institution of Mechanical Engineers*, (C128/78):145–157, 1978.

[73] M E Cross. The rotary valve as an alternative. *Society of Automotive Engineers*, (800888), 1980.

[74] M E Cross. Some more experiments with internal combustion engines. *Proceedings of the Institution of Mechanical Engineers*, 194:123–130, 1980.

[75] M E Cross and A E Coles. Rotary valves. US Patent 3,990,423, November 1976.

[76] R C Cross. Valve for internal combustion engines and pumps. US Patent 1,887,997, November 1932.

[77] R C Cross. Valve for internal combustion engines. US Patent 1,997,133, April 1935.

[78] R C Cross. Rotary valve controlled internal combustion engine. US Patent 2,354,305, July 1944.

[79] Y Cui, W Pan, J H Leylek, R G Sommer, and S K Jain. Cylinder-to-cylinder variation of losses in intake regions of IC engines. *Society of Automotive Engineers*, (981025), 1998.

[80] S Das and Dent J C. Simulation of the mean flow in the cylinder of a motored 4-valved spark ignition engine. *Society of Automotive Engineers*, (952384), 1995.

[81] J C Date and S R Turnock. Computational evaluation of the periodic performance of a NACA 0012 fitted with a Gurney flap. *Journal of Fluids Engineering*, 2000. Submitted for publication.

[82] J C Date and S R Turnock. Computational fluid dynamics estimation of skin friction experienced by a plane moving through water. *Transactions of the Royal Institution of Naval Architects*, 2000.

[83] P O A L Davies. Piston engine intake and exhaust system design. *Journal of Sound and Vibration*, 190(4):677–712, 1996.

[84] R De Haller. The application of a graphic method to some dynamic problems in gases. *Sulzer Technical Review*, 1(6), 1945.

[85] M Dekena and N Peters. Combustion modeling with the G-equation. *Oil and Gas Science and Technology—Review IFP*, 54(2):265–270, 1999.

[86] B Delhaye and B Cousyn. Computation of flow and combustion in spark ignition engine and comparison with experiment. *Society of Automotive Engineers*, (961960), 1996.

[87] A R Denlinger, Y G Guezennec, and W Choi. Dynamic evolution of the 3-D flow field during the latter part of the intake stroke in an IC engine. *Society of Automotive Engineers*, (980485), 1998.

[88] S Diana, V Giglio, G Police, G Bella, and S Cordiner. Heat transfer evaluation in 3D computations of premixed SI engines. *Society of Automotive Engineers*, (972876), 1997.

[89] C Dimitriadis and M A Leschziner. Computations of three-dimensional flow in duct junctions by a zonal approach.

[90] P Dimopolous and K Boulouchos. Turbulent flow field characteristics in a motored reciprocating engine. *Society of Automotive Engineers*, (972833), 1997.

[91] R Douglas, F A McGinnity, and G P Blair. A study of gas temperature effects on the prediction of unsteady flow. *Proceedings of the Institution of Mechanical Engineers*, (C433/036), 1991.

[92] S El Tahry. Application of a Reynolds stress model to engine-like flow calculations. *Transactions of the American Society of Mechanical Engineers*, 107:444–450, 1985.

[93] S H El Tahry and D C Haworth. Directions in turbulence modeling for in-cylinder flows on reciprocating engines. *Journal of Propulsion and Power*, 8(5):1040–1048, 1992.

[94] L Fan, R D Reitz, and N Trigui. Intake flow simulation and comparison with PTV measurements. *Society of Automotive Engineers*, (1999-01-0176), 1999.

[95] M A Faure, M Sadler, K K Oversby, J Stokes, S M Begg, L S Pommier, and M R Heikal. Application of LDA and PIV techniques to the validation

of a CFD model of a direct injection gasoline engine. *Society of Automotive Engineers*, (982705), 1998.

[96] J H Ferziger and M Perić. *Computational Methods for Fluid Dynamics*. Springer-Verlag, Heidelberg, second edition, 1999.

[97] R Fleck and A Cartwright. Coefficients of discharge in high performance two-stroke engines. *Society of Automotive Engineers*, (962534), 1996.

[98] C A J Fletcher. *Computational Techniques for Fluid Dynamics*, volume I. Springer-Verlag, Heidelberg, second edition, 1991.

[99] C A J Fletcher. *Computational Techniques for Fluid Dynamics*, volume II. Springer-Verlag, Heidelberg, second edition, 1991.

[100] A Foster. Transient flow in IC engines. *CFX Update*, (16):8, Autumn 1998.

[101] D L Franz. Rotary valve. US Patent 3,892,220, July 1975.

[102] C J Freitas. Perspective: Selected benchmarks from commercial CFD codes. *Transactions of the American Society of Mechanical Engineers*, 117:208–218, 1995.

[103] I Fukutani and E Watanabe. Air flow through poppet inlet valves—analysis of static and dynamic flow coefficients. *Society of Automotive Engineers*, (820154), 1982.

[104] C Fureby and F F Grinstein. Monotonically integrated large eddy simulation of free shear flows. *AIAA Journal*, 37(5):544, 1999.

[105] P W Gabelish, A R Vial, and P E Irving. Rotary valves for small four-cycle IC engines. *Society of Automotive Engineers*, (891793), 1989.

[106] T H Gau and Y Y Peng. A high performance and low emissions motorcycle engine with the VIP system. *Society of Automotive Engineers*, (972103), 1997.

[107] C F Gerald and P O Wheatley. *Applied Numerical Analysis*. Addison-Wesley, California, fifth edition, 1994.

[108] A Gharakhani and A F Ghoniem. 3D vortex simulation of intake flow in a port-cylinder with a valve seat and a moving piston. *Society of Automotive Engineers*, (961195), 1996.

[109] A Gharakhani and A F Ghoniem. Simulation of the piston driven flow inside a cylinder with an eccentric port. *Journal of Fluids Engineering*, 120:319–326, 1998.

[110] A Gharakhani and A F Ghoniem. 3D vortex simulation of flow in an opposed-piston engine. In *ESAIM Proceedings, 3rd International Workshop on Vortex Flows and Related Numerical Methods*, volume 7, pages 161–172, 1999.

[111] E Giffen. Rapid discharge of a gas from a vessel into atmosphere. *Engineering*, 150(139), 1940.

[112] Y Gong and X Bai. Shallow water modeling method for simulating squish movement in diesel engines. *Society of Automotive Engineers*, (961128), 1996.

[113] M A Gorokhovshii and V P Khlynin. Calculation of the gas dynamics of compression in a cylinder of an internal combustion engine with combustion chambers of different shape. *Inzhenerno-Fizicheskii Zhurnal*, 57(2):285–291, 1989.

[114] A D Gosman. Multidimensional modelling of cold flows and turbulence in reciprocating engines. *Society of Automotive Engineers*, (850344), 1985.

[115] A D Gosman. State of the art of multi-dimensional modeling of engine reacting flows. *Oil and Gas Science and Technology—Review IFP*, 54(2):149–159, 1999.

[116] A D Gosman, A Melling, J H Whitelaw, and P Watkins. Axisymetric flow in a motored reciprocating engine. *Proceedings of the Institution of Mechanical Engineers*, 192(11):213–223, 1978.

[117] A D Gosman, Y Y Tsui, and C Vafidis. Flow in a model engine with a shrouded valve—a combined experimental and computational study. *Society of Automotive Engineers*, (850498), 1985.

[118] H Grotjans and F R Menter. Wall functions for general application CFD codes. In *ECCOMAS*. John Wiley and Sons, 1998.

[119] O L Guelder. Turbulent premixed combustion modelling using fractal geometry. In *Proceedings of the 23rd International Syposium on Combustion*. The Combustion Institute, 1990.

[120] W D Guenther. Rotary valve seal assembly. US Patent 4,019,487, April 1977.

[121] W D Guenther. Stratified charge engine. US Patent 4,036,184, July 1977.

[122] O Hadded and I Denbratt. Turbulence characteristics of tumbling air motion in four-valve S.I. engines and their correlation with combustion parameters. *Society of Automotive Engineers*, (910478), 1991.

[123] T Hagen. Inside Honda's rotary valve four-stroke!

[124] J Halliday, C Teixeira, and C Alexander. Simulation of engine internal flows using Digital Physics. *Oil and Gas Science and Technology—Review IFP*, 54(2):187–191, 1999.

[125] Z Han, L Fan, and R D Reitz. Multidimensional modeling of spray atomization and air-fuel mixing in a direct-injection spark-ignition engine. *Society of Automotive Engineers*, (970884), 1997.

[126] Z Han, R D Reitz, F E Corcione, and G Valentino. Interpretation of k-ε computed turbulence length-scale predictions for engine flows. In *The 26th International Symposium on Combustion*, pages 2717–2723, 1996.

[127] I R Hawkins and N S Wilkes. Moving grids in Harwell-FLOW3D. Technical Report AEA-InTec-0608, Harwell Laboratory, August 1991.

[128] D C Haworth. Large-eddy simulation of in-cylinder flows. *Oil and Gas Science and Technology—Review IFP*, 54(2):175–185, 1999.

[129] D C Haworth and S H El Tahry. Probability density function approach for multidimensional turbulent flow calculations with application to in-cylinder flows in reciprocating engines. *American Institute of Aeronautics and Astronautics*, 29:208–218, 1991.

[130] D C Haworth and K Jansen. Large-eddy simulation on unstructured deforming meshes: Towards reciprocating IC engines. *Computers and Fluids*, 29:493–524, 2000.

[131] Y He and C Rutland. Application of artificial neural network for integration of advanced engine simulation methods. In S R Bell, editor, *Proceedings of the 2000 Fall Technical Conference of the ASME Internal Combustion Engine Division*, pages 53–64, Peoria, Illinois, September 2000.

[132] H Heisler. *Advanced Engine Technology.* Arnold, Great Britain, 1995.

[133] S Henriot, A Chaouche, E Cheve, and J M Duclos. CFD aided development of a SI-DI engine. *Oil and Gas Science and Technology—Review IFP*, 54(2):279–286, 1999.

[134] S Henriot, A Chaouche, E Chevé, J M Duclos, P Leduc, P Ménégazzi, G Monnier, and A Ranini. NSDI-3: A small bore GDI engine. *Society of Automotive Engineers*, (1999-01-0172), 1999.

[135] W Hentschel, A Grote, and O Langer. Measurement of wall film thickness in the intake manifold of a standard production SI engine by spectroscopic technique. *Society of Automotive Engineers*, (972832), 1997.

[136] R P Hessel and C J Rutland. Intake flow modeling in a four-stroke diesel using KIVA-3. *Journal of Propulsion and Power*, 11(2):378–384, 1995.

[137] P G Hill and D Zhang. The effects of swirl and tumble on combustion in spark-ignition engines. *Progress in Energy and Combustion Science*, 20:373–429, 1994.

[138] J O Hinze. *Turbulence*. McGraw-Hill, New York, second edition, 1975.

[139] C Hollnagel, L Borges, and W Muraro. Combustion development of the Mercedes-Benz MY1999 CNG-engine M366LAG. *Society of Automotive Engineers*, (1999-01-3519), 1999.

[140] H Hori, T Ogawa, and T Kuriyama. CFD in-cylinder flow simulation of an engine and flow visualization. *Society of Automotive Engineers*, (950288), 1995.

[141] G D Horrocks. CFD modelling of gas flows in an IC engine. Bachelors Degree Thesis, Faculty of Engineering, The University of Technology, Sydney, 1997.

[142] G D Horrocks, J A Reizes, and G Hong. Tumble vortex breakdown during the compression stroke of a model internal combustion engine. In S R Bell, editor, *Proceedings of the ASME Internal Combustion Engine Division Fall Technical Conference*, volume 1, pages 39–52, Peoria, Illinios, September 2000.

[143] G D Horrocks, J A Reizes, and S G Mallinson. Numerical study of flow in a rotating shock tube. In M C Thompson and K Hourigan, editors, *Proceedings of the 13th Australiasian Fluid Mechanics Conference*, volume 1, pages 563–566, Monash University, Melbourne, Australia, December 1998.

[144] G D Horrocks, J A Reizes, and S G Mallinson. Contact surface instabilities in rotating shock tube flow. In *Proceedings of the 22nd International Symposium on Shock Waves*, number 1291, July 1999.

[145] R Houston and G Cathcart. Combustion and emissions characteristics of Orbital's combustion process applied to multi-cylinder automotive direct injected 4-stroke engines. *Society of Automotive Engineers*, (980153), 1998.

[146] K Y Huh, I-P Chang, and J K Martin. A comparison of boundary layer treatments for heat transfer in IC engines. *Society of Automotive Engineers*, (900252), 1990.

[147] M C I Hunter. *Rotary Valve Engines*. Wiley, New York, 1946.

[148] F P Incropera and P DeWitt. *Fundamentals of Heat and Mass Transfer*. Wiley, Singapore, third edition, 1990.

[149] N Ishikawa and J W Daily. Flame wall quenching in a single compression flame. In *Proceedings of the Western States Section of The Combustion Institute Meeting*, Seattle, Washington, April 1977.

[150] N Ishikawa and J W Daily. Observation of flow characteristics in a model I.C. engine and cylinder. *Society of Automotive Engineers*, (780230), 1978.

[151] H Jasak, J Y Luo, B Kaluderčić, A D Gosman, H Echtle, Z Liang, F Wirbeleit, M Wierse, S Rips, A Werner, G Fernström, and A Karlsson. Rapid CFD simulation of internal combustion engines. *Society of Automotive Engineers*, (1999-01-1185), 1999.

[152] Jayatilleke. The influence of Prandtl number and surface roughness on the resistance of the laminar sublayer to momentum and heat transfer. *Progress in Heat and Mass Transfer*, 1:193, 1969.

[153] D R M Jeffrey. *An Investigation Into the Aerodynamics of Gurney Flaps*. PhD thesis, Department of Aeronautics and Astronautics, Faculty of Engineering, University of Southampton, Highfield, Southampton, March 1998.

[154] J D Anderson Jr. *Computational Fluid Dynamics: The Basics with Applications*. McGraw-Hill, 1995.

[155] K Y Kang and J H Baek. LDV measurement and analysis of tumble formation and decay in a four-valve engine. *Experimental Thermal and Fluid Science*, 11:181–189, 1995.

[156] K Y Kang and J H Baek. Turbulence characteristics of tumble flow in a four-valve engine. *Experimental Thermal and Fluid Science*, 18:231–243, 1998.

[157] S M H Karimian and G E Schneider. Application of a control-volume-based finite-element formulation to the shock tube problem. *American Institute of Aeronautics and Astronautics*, 33(1):165–167, 1994.

[158] B Khalighi. Intake swirl process generated by an engine head: A flow visualization study. *Journal of Engineering for Gas Turbines and Power*, 113:433–439, 1991.

[159] B Khalighi. Multidimensional in-cylinder flow calculations and flow visualization in a motored engine. *Transactions of the American Society of Mechanical Engineers*, 117:282–288, 1995.

[160] B Khalighi, S H El Tahry, D C Haworth, and M S Huebler. Computation and measurement of flow and combustion in a four-valve engine with intake variations. *Society of Automotive Engineers*, (950287), 1995.

[161] J Kim, P Moin, and R Moser. Turbulence statistics in fully developed channel flow at low Reynolds number. *Journal of Fluid Mechanics*, 177:133–166, 1987.

[162] Y J Kim, S H Lee, and N H Cho. Effect of air motion on fuel spray characteristics in a gasoline direct injection engine. *Society of Automotive Engineers*, (1999-01-0177), 1999.

[163] C S Kong, C J Rutland, and R D Reitz. Implementation of a spray and combustion model library in engine CFD codes. In *10th Multidimensional Engine Modelling Users Group Meeting*, Detroit, March 2000.

[164] S C Kong and C W Hong. Multidimensional intake flow modeling of a four-stroke engine with comparisons to flow valocity measurements. *Society of Automotive Engineers*, (970883), 1997.

[165] S-C Kong and R D Reitz. Use of detailed chemical kinetics to study HCCI engine combustion with consideration of turbulent mixing effects. In S R Bell, editor, *Proceedings of the 2000 Fall Technical Conference of the ASME Internal Combustion Engine Division*, pages 73–80, Peoria, Illinois, September 2000.

[166] D M Krishna, K Rajagopal, P S Rao, and V Ganesan. Three-dimensional modelling of fluid flow in a four-stroke compression ignition engine. *Indian Journal of Engineering and Materials Sciences*, 1:135–148, June 1994.

[167] T W Kuo and S Chang. Three-dimensional computations of flow and fuel injection in an engine intake port. *Journal of Engineering for Gas Turbines and Power*, 113:427–432, 1991.

[168] K Kuwahara and H Ando. TDC flow field structures of two-intake-valve engines with pentroof combustion chamber. *Japanese Society of Mechanical Engineers, Series B*, 36(4):688–696, 1993.

[169] S J Lacher, L Fan, B Backer, J K Martin, R Reitz, J Yang, and R Anderson. In-cylinder mixing rate measurements and CFD analyses. *Society of Automotive Engineers*, (1999-01-1110), 1999.

[170] F J Laimböck, H Klasnic, S Grilc, G F Meister, and M J Dorfstätter. AVL SDIS Mk.II—low cost automotive FI applied to 2-stroke engines for future CARB—regulations. *Society of Automotive Engineers*, (1999-01-3285), 1999.

[171] L M Larosiliere. Wave rotor charging process: Effects of gradual opening and rotation. *Journal of Propulsion and Power*, 11(1):178–184, 1995.

[172] L M Larosiliere and M Mawid. Analysis of unsteady wave processes in a rotating channel. *International Journal of Numerical Methods in Fluids*, 21:467–488, 1995.

[173] B E Launder, G J Reece, and W Rodi. Progress in the development of a Reynolds-stress turbulence closure. *Journal of Fluid Mechanics*, 68(3):537–566, 1975.

[174] J-F Le Coz, S Henriot, and P Pinchon. An experiemental and computational analysis of the flow field in a four-valve spark ignition engine—focus on cycle-resolved turbulence. *Society of Automotive Engineers*, (900056), 1990.

[175] L Lebrère, M Buffat, L Le Penven, and B Dillies. Application of Reynolds stress modeling to engine flow calculations. *Transactions of the American Society of Mechanical Engineers*, 118:710–721, 1996.

[176] L Lebrère and B Dillies. Engine flow calculations using a Reynolds stress model in the Kiva-II code. *Society of Automotive Engineers*, (960636), 1996.

[177] M A Leschziner and K P Dimitriadis. Numerical simulation of three-dimensional turbulent flows in exhaust-manifold junctions. *Proceedings of the Institution of Mechanical Engineers*, (C09/87):183–190, 1987.

[178] H W Liepmann. The rise and fall of ideas in turbulence. *American Scientist*, 67:221–228, 1979.

[179] H W Liepmann and A Roshko. *Elements of Gas Dynamics*. Wiley, 1957.

[180] J M Lipman. Internal combustion engine. European Patent 0 342 893 A1, November 1989.

[181] M G Lisbona. CFD engine applications at FIAT research centre. *Oil and Gas Science and Technology—Review IFP*, 54(2):287–291, 1999.

[182] Y Liu and R D Reitz. Multidimensional modeling of engine combustion chamber surface temperature. *Society of Automotive Engineers*, (971593), 1997.

[183] R D Lonsdale. An algebraic multi-grid solver for the Navier Stokes equations on unstructured meshes. *International Journal of Numerical Methods in Heat and Fluid Flow*, 3, 1993.

[184] K H Luo and K N C Bray. 3D simulation of induction port flow of a four-valve engine configuration. *Society of Automotive Engineers*, (920586), 1995.

[185] Z Mahmood, A Chen, M Yianneskis, and G Ganti. On the structure of steady flow through dual-intake engine ports. *International Journal for Numerical Methods in Fluids*, 23:1085–1109, 1996.

[186] R R Mankbadi. *Transition, Turbulence and Noise: Theory and Applications for Scientists and Engineers*. Kluwer Academic Publishers, 1994.

[187] D Marc. *Etude Expérimentale de la Compression D'un Écoulement de Rouleau. Situation Modéle de L'aérodynamique Interne Des Moteurs Á Pistons.* PhD thesis, l'Institut National Polytechnique de Toulouse, 1998.

[188] D Marc, J Boree, R Bazile, and G Charnay. Tumbling vortex flow in a model square piston compression machine: PIV and LDV measurements. *Society of Automotive Engineers*, (972834), 1997.

[189] S Maurel, L Ben, J Moreau, J Boree, R Bazile, and G Charnay. On the interpretation of PIV results in a compressed flow. In *EUROMECH 411*, Rouen, May 2000.

[190] A McLandress, R Emerson, P McDowell, and C Rutland. Intake and in-cylinder flow modeling characterization of mixing and comparison with flow bench results. *Society of Automotive Engineers*, (960635), 1996.

[191] C W Miller. Packing for valves. US Patent 985,618, February 1911.

[192] R Miller, C Newman, W Dai, N Trigui, G Davis, D Trumpy, and J Glidewell. Up-front design prediction of the effects of cylinder head design on combustion rates in SI engines. *Society of Automotive Engineers*, (981049), 1998.

[193] R Mittal and P Moin. Suitability of upwind-biased finite difference schemes for large-eddy simulation of turbulent flows. *American Institute of Aeronautics and Astronautics Journal*, 35:1415–1417, 1997.

[194] A Miyauchi, M Nakachi, and K Kobayashi. Development of high performance combustion chamber for four-stroke cycle small utility engines. *Society of Automotive Engineers*, (1999-01-3336), 1999.

[195] J R Moore and N S Wilkes. The prediction of a laminar flow over a backstep at a moderately high Reynolds number. Technical Report AEA-InTec-0054, Harwell Laboratories, July 1990.

[196] Y Moriyoshi, T Kamimoto, and M Yagita. Definition of turbulence in in-cylinder flow fields. *Japanese Society of Mechanical Engineers, Series B*, 36(1):172–177, 1993.

[197] T Muroki, Y Moriyoshi, and S Sekizuka. A study of rotary valve for a single cylinder engine. *Society of Automotive Engineers*, (1999-01-3322), 1999.

[198] K Naitoh, H Fujii, T Urushihara, Y Takagi, and K Kuwahara. Numerical simulation of the detailed flow in engine ports and cylinders. *Society of Automotive Engineers*, (900256), 1990.

[199] K Naitoh, T Itoh, Y Takagi, and K Kuwahara. Large eddy simulation of premixed-flame in engine based on the multi-level formulation and the renormalization group theory. *Society of Automotive Engineers*, (920590), 1992.

[200] K Naitoh and K Kuwahara. Large eddy simulation and direct simulation of compressible turbulence and combusting flows in engines based on the BI-SCALES method. *Fluid Dynamics Research*, 10:299–325, 1992.

[201] K Naitoh, Y Takagi, and K Kuwahara. Cycle-resolved computation of compressible turbulence and premixed flame in an engine. *Computers Fluids*, 22(4/5):623–648, 1993.

[202] K Naitoh, Y Takagi, K Kuwahara, E Krause, and K Ishii. Computation of transition to turbulence in the compression stage of a reciprocating engine. *Fluid Dynamics Research*, 6:277–294, 1990.

[203] P M Najt and T W Kuo. An experimental and computational evaulation of two dual-intake-valve combustion chambers. *Society of Automotive EngineersEngineers*, (902140), 1990.

[204] J A Naser and A D Gosman. Flow prediction in an axisymmetric inlet Valve/Port assembly using variants of k-ϵ. *Journal of Automobile Engineering*, 209:57–69, 1995.

[205] J A Naser and A D Gosman. Prediction of compressible subsonic flow through an axisymmetric exhaust valve-port assembly. *Journal of Automobile Engineering*, 209:289–295, 1995.

[206] G Negre. Process and apparatus for controlling a gas evacuation circuit of a rotational distribution motor. US Patent 4,788,945, December 1988.

[207] H J Neußer, L Spiegel, and J Ganser. Particle tracking velocimetry – a powerful tool to shape the in-cylinder flow of modern multi-valve engine concpets. *Society of Automotive Engineers*, (950102), 1995.

[208] B Nkonga and H Guillard. Godunov type method on non-structured meshes for three-dimensional moving boundary problems. *Computer Methods in Applied Mechanics and Engineering*, 113:183–204, 1994.

[209] N Nonaka and T Nakayama. A unified method for the numerical analysis of compressible and incompressible viscous flows. *Computational Mechanics*, 18:369–376, 1996.

[210] G B Northam and H K Rivers. Evaluation of piston bowl geometry. `http://smc.larc.nasa.gov/mtsb/personnel/rivers/CCEC/aemart.html`, June 2000.

[211] J M Novak and R A Kach. Computer optimization of camshaft lift profiles for a NASCAR V-8 engine with restrictor plate. *Society of Automotive Engineers*, (962514), 1996.

[212] L O'Conner. A new turn for rotary-valve engines. *Mechanical Engineering*, pages 54–58, January 1993.

[213] J F O'Connor and N R McKinley. CFD simulations of intake port flow using automatic mesh generation: Comparison with laser sheet, swirl and LDA measurements for steady flow conditions. *Society of Automotive Engineers*, (980129), 1998.

[214] A Onorati and G Ferrari. Modeling of 1-D unsteady flows in I.C. engine pipe systems: Numerical methods and transport of chemical species. *Society of Automotive Engineers*, (980782), 1998.

[215] E S Oran and J P Boris. Computing turbulent shear flows—a convenient conspiracy. *Computers in Physics*, 7(5):523–533, 1993.

[216] P J O'Rourke and A A Amsden. A spray/wall interaction submodel for the KIVA-3 wall film model. *Society of Automotive Engineers*, (2000-01-0271), 2000.

[217] P J O'Rourke and M S Sahota. A variable explicit/implicit numerical method for calculating advection on unstructured meshes. *Journal of Computational Physics*, 143:312–345, 1998.

[218] P J O'Rourke, S Zhang, and M S Sahota. A parallel, unstructured-mesh methodology for device-scale combustion calculations. *Oil and Gas Science and Technology—Review IFP*, 54(2):169–173, 1999.

[219] W Pan, Y Cui, J H Leylek, R G Sommer, and S K Jain. A CFD study of losses in a straight-six Diesel engine. *Society of Automotive Engineers*, (1999-01-0230), 1999.

[220] F Papetti, S Golini, M Maggiore, S Succi, P Gaillard, and J M Perez. Internal combustion engine design on IBM platforms. *IBM Systems Journal*, 31(4):774–787, 1992.

[221] B N V Parsons. Rotary valves. US Patent 4,838,220, June 1989.

[222] B N V Parsons. Rotary drives. US Patent 4,898,042, February 1990.

[223] S V Patankar. A calculation procedure for two-dimensional elliptic situations. *Numerical Heat Transfer*, 2, 1979.

[224] S V Patankar. *Numerical Heat Transfer and Fluid Flow*. Hemisphere, USA, 1980.

[225] S V Patankar and D B Spalding. A calculation procedure for heat, mass and momentum transfer in three-dimensional parabolic flows. *International Journal of Heat and Mass Transfer*, 15:1787–1806, 1972.

[226] S Pierson and S Richardson. A port in the storm. *Mechanical Engineering*, pages 78–79, November 1999.

[227] G Piola. *Formula1 '99 Technical Analysis*. Giorgio Nada Editore, Milan, 2000.

[228] M Poloni, D E Winterbone, and J R Nichols. The calculation of pressure and temperature discontinuity in a pipe by the method characteristics and the two-step differential Lax-Wendroff method. In *Fluid Flow and Heat Transfer in Reciprocating Machinery*, Boston, Massachusetts, December 1987.

[229] E Pomraning and C J Rutland. Testing and development of LES models for use in multidimensional modeling. In *10th Multidimensional Engine Modelling Users Group Meeting*, Detroit, March 2000.

[230] P Ponticel. High-pressure fuel injection by PSA. *Automotive Engineering International*, pages 71–72, November 2000.

[231] B D Raghunathan and R G Kenny. CFD simulation and validation of the flow within a motored two-stroke engine. *Society of Automotive Engineers*, (970359), 1997.

[232] J I Ramos. *Internal Combustion Engine Modeling*. Hemisphere Publishing Co., New York, 1989.

[233] M Reeves, C P Garner, J C Dent, and N A Halliwell. Particle image velocimetry analysis of IC engine in-cylinder flows. *Optics and Lasers in Engineering*, 25:415–432, 1996.

[234] M Reeves, M J Haste, C P Garner, and N A Halliwell. Barrel swirl breakdown in spark-ignition engines: Insights from particles image velocimetry measurements. *Proceedings of the Institution Mechanical Engineers, Part D*, 213:595–609, 1999.

[235] O Reynolds. On the dynamical theory of incompressible viscous fluids and the determination of the criterion. *Philosophical Transactions of the Royal Society of London*, 186:123, 1895.

[236] H R Ricardo. *The High-Speed Internal-Combustion Engine*. Blackie and Son, Ltd., Glasgow, fourth edition, 1953.

[237] P J Roache. *Fundamentals of Computational Fluid Dynamics*. Hermosa Publishers, Albuquerque, New Mexico, 1998.

[238] M Roberts, O Backland, and P Keen. Volvo-Cosworth 4.3 Litre V-10 concept engine. *Society of Automotive Engineers*, (1999-01-0326), 1999.

[239] W Rodi. *Turbulence Models and Their Application in Hydraulics—A State of the Art Review*. University of Karlsruhe, Karlsruhe, second edition, 1984.

[240] E Rouland, A Floch, A Ahmed, D Dionnet, and M Trinité. Characterisation of intake generated tumble flow in 4-valve engine using cross-correlation particle image velocimetry. In *8th International Symposium of Flow Visualisation*, pages 195.1–195.15, 1998.

[241] E Rouland, M Trinité, F Dionnet, A Floch, and A Ahmed. Particle image velocimetry measurements in a high tumble engine for in-cylinder flow structure analysis. *Society of Automotive Engineers*, (972831), 1997.

[242] D L Ruess, T Kuo, B Khalighi, D Haworth, and M Rosalik. Particle image velocimetry measurements in a high-swirl engine used for evaluation of computational fluid dynamics calculations. *Society of Automotive Engineers*, (952381), 1995.

[243] C J Rutland, N Ayoub, Z Han, G Hampson, S Kong, D Mather, D Montgomery, M Musculus, M Patterson, D Pierpont, L Ricart, P Stephenson, and R D Reitz. Diesel engine model development and experiments. *Society of Automotive Engineers*, (951200), 1995.

[244] C Sches, S Guilain, and F Maroteaux. Modeling of the fuel behavior in the intake manifold of a port-injected spark-ignition engine. *Society of Automotive Engineers*, (972992), 1997.

[245] D Scott. Rotary valve engine uses eccentric crank and radial layout. *Automotive Engineering*, 84(3):20–23, March 1975.

[246] M Y E Selim, Dent J C, and S Das. Application of CFD to the matching of in-cylinder fuel injection and air motion in a four stroke gasoline engine. *Society of Automotive Engineers*, (971601), 1997.

[247] J Senda, M Ohnishi, T Takahashi, H Fujimoto, A Utsunomiya, and M Wakatabe. Measurement and modeling on wall wetted fuel film profile and mixture preparation in intake port of SI engine. *Society of Automotive Engineers*, (1999-01-0798), 1999.

[248] P K Senecal, D T Montgomery, and R D Reitz. Diesel engine optimization using multi-dimensional modeling and genetic algorithms applied to a medium speed, high load operating condition. In S R Bell, editor, *Proceedings of the 2000 Fall Technical Conference of the ASME Internal Combustion Engine Division*, pages 19–26, Peoria, Illinois, September 2000.

[249] P W Sephenson, P J Claybaker, and C J Rutland. Modeling the effects of intake generated turbulence and resolved flow structures on combustion in DI Diesel engines. *Society of Automotive Engineers*, (960634), 1996.

[250] A H Shapiro. *The Dynamics and Thermodynamics of Compressible Fluid Flow*. The Ronald Press Co., New York, 1954.

[251] C T Shaw and S Simcox. The numerical predicition of the flow around a simplified vehicle geometry. Technical report, Harwell Laboratories, 1988.

[252] Y Shimamoto, M Oka, and Y Tanaka. A research of inertia charging effect of intake system in multi-cylinder engines. *Japanese Society of Mechanical Engineers*, 21(153):502–510, 1978.

[253] P H Simth and J C Morrison. *The Scientific Design of Exhaust and Intake Systems*. Robert Bentley, Inc., Massachusetts, third edition, 1971.

[254] R Sinclair, T Straus, and P Schindler. Code coupling, a new approach to enhance CFD analysis of engines. *Society of Automotive Engineers*, (2000-01-0660), 2000.

[255] D K Sinha and M K Gajendra Babu. Performance studies of a dual spark plug ignition engine. In *Proceedings of the 23rd IEEE Intersociety Energy Conversion Engineering Conference*, pages 139–144, 1988.

[256] N Sinha, P A Cavallo, A Hosangadi, R A Lee, H Affes, and D Chu. Efficient CFD simulations for in-cylinder flows using hybrid grids. *Society of Automotive Engineers*, (1999-01-1184), 1999.

[257] N Sinha, P A Cavallo, R A Lee, A Hosangadi, D C Kenzakowski, S M Dash, H Affes, and D Chu. Novel CFD techniques for in-cylinder flows on tetrahedral grids. *Society of Automotive Engineers*, (980138), 1998.

[258] S Soltani and A Veshagh. Effect of intake port configuration on in-cylinder flow of a four-valve spark ignition engine. In *ASME Internal Combustion Engine Division 1998 Fall Technical Conference*, number 98-ICE-142 31-2, pages 123–134, 1998.

[259] P R Spalart. Strategies for turbulence modelling and simulations. *International Journal of Heat and Fluid Flow*, 21:252–263, 2000.

[260] R H Stanglmaier, M J Hall, and R D Matthews. Fuel-Spray/Charge-motion interaction within the cylinder of a direct-injected, 4-valve, SI engine. *Society of Automotive Engineers*, (980155), 1998.

[261] P W Stephenson and C J Rutland. Modeling the effects of valve lift profile on intake flow and emissions behavior in a DI diesel engine. *Society of Automotive Engineers*, (952430), 1995.

[262] H L Stone. Iterative solution of implicit approximations of multidimensional partial differential equations. *SIAM Journal of Numerical Analysis*, 5(3):530–558, September 1968.

[263] R Stone. *Introduction to Internal Combustion Engines*. Macmillan Press, London, third edition, 1999.

[264] P Stopford. Particulate matter from Diesel engines. *CFX Update*, page 5, Spring 1998.

[265] N Storer and T Nelson. Rotary valve system for a four cycle G-Kart racing engine. *Society of Automotive Engineers*, (942500), 1994.

[266] S Sugiura, T Yamada, T Inoue, K Morinishi, and N Satofuka. Numerical analysis of flow in the induction systems of an internal combustion engine—multi-dimensional calculations using a new method of lines. *Society of Automotive Engineers*, (900255), 1990.

[267] R J Tabaczynski, C R Ferguson, and K Radhakrishnan. A turbulent entrainment model for spark-ignition engine combustion. *SAE*, (740191), 1974.

[268] S Takeyama, S Ishizawa, Y Yoshikawa, and Y Takagi. Gas exchange simulation model for improving charging efficiency of four-valve internal combustion engine. *Proceedings of the Institution of Mechanical Engineers*, (C28/87):123–129, 1987.

[269] I Taki and T Ohira. Fuel economy improvement by optimized intake-port configuration and comphrensive specifications. *Society of Automotive Engineers*, (972102), 1997.

[270] J C Tannhill, D A Anderson, and R H Pletcher. *Computational Fluid Mechanics and Heat Transfer*. Taylor and Francis Publishers, Washington, second edition, 1997.

[271] C F Taylor. *The Internal-Combustion Engine in Theory and Practice*, volume I. Massachusetts Institute of Technology Press, Massachusetts, second edition, 1966.

[272] C F Taylor. *The Internal-Combustion Engine in Theory and Practice*, volume II. Massachusetts Institute of Technology Press, Massachusetts, 1968.

[273] W Taylor III, J H Leylek, R G Sommer, and S K Jain. IC engine intake region design modifications for loss reduction based on CFD methods. *Society of Automotive Engineers*, (981026), 1998.

[274] W Taylor III, J H Leylek, L T Tran, R D Shinogle, and S K Jain. Advanced computational methods for predicting flow losses in intake regions of Diesel engines. *Society of Automotive Engineers*, (970639), 1997.

[275] J M Towers and R L Hoekstra. Engine knock, a renewed concern in motorsports—a literature review. *Society of Automotive Engineers*, (983026), 1998.

[276] N Trigui, V Griaznov, H Affes, and D Smith. CFD based shape optimization of IC engine. *Oil and Gas Science and Technology—Review IFP*, 54(2):297–307, 1999.

[277] N Trigui, J C Kent, Y Guezennec, and W C Choi. Characterisation of intake generated fluid flow fields in IC engines using 3-D particle tracking velocimetry (3-D PTV). *Society of Automotive Engineers*, (940279), 1994.

[278] K Tsuboi, T Tamura, and K Kuwahara. Numerical study of vortex induced vibration of circular cylinder in high Reynolds number flow. *AIAA Paper*, (89-0294), 1979.

[279] Y-Y Tsui and H-P Cheng. Characterization of tumbling motion in IC engines by vorticity. *Journal of the Chinese Society of Mechnical Engineers*, 18(5):485–490, 1997.

[280] J Y Tu and L Fuchs. Overlapping grids and multigrid methods for three-dimensional unsteady flow calculations in IC engines. *International Journal for Numerical Methods in Fluids*, 15:693–714, 1992.

[281] T Uzkan. The effects of engine speed on the scavenging characteristics of a two-cycle engine. In *Basic Processes in Internal Combustion Engines*, pages 79–86, New Orleans, Louisiana, 1988. American Society of Mechanical Engineers.

[282] C Vafidis, G Vorropoulos, and J H Whitelaw. Effects of intake port and combustion chamber geometry on in-cylinder turbulence in a motored reciprocating engine. In *Fluid Flow and Heat Transfer in Reciprocating Machinery*, Boston, Massachusetts, December 1987.

[283] J K Vennard and R L Street. *Elementary Fluid Mechanics*. Wiley, Singapore, sixth edition, 1982.

[284] H K Versteeg and W Malalasekera. *An Introduction to Computational Fluid Dynamics*. Longman, 1995.

[285] R Verzicco, J Mohd-Yusof, P Orlandi, and D Haworth. Large eddy simulation in complex geometry configurations using boundary body forces. *American Institute of Aeronautics and Astronautics Journal*, 38(3):427–433, March 2000.

[286] R M Wagner, J A Drallmeier, and C S Daw. Prior-cycle effects in lean spark ignition combustion— fuel/air charge considerations. *Society of Automotive Engineers*, (981047), 1998.

[287] T Wakisaka, Y Isshiki, Y Shimamoto, and N Magarida. Numerical analysis of the diffusion process of intake mixture in dual-intake valve engines. *Japanese Society of Mechanical Engineers, Series B*, 2(38):213–221, 1995.

[288] T Wakisaka, Y Shimamoto, and Y Isshiki. Induction swirl in a multiple intake valve engine— three-dimensional numerical analysis. *Proceedings of the Institution of Mechanical Engineers*, (C40/88), 1988.

[289] T Wakisaka, Y Shimamoto, Y Isshiki, and T Shibata. Numerical simulation of gas flows in the cylinders of four-stroke cycle engines. *Bulletin of the Japanese Society of Mechanical Engineers*, 29(258):4276–4284, December 1986.

[290] F J Wallace and G Boxer. Wave action in diffusers for exhaust-pipe systems, with special reference to the scavenging of two-stroke engines. *Proceedings of the Institution of Mechnical Engineers*, 170(39):1131–1156, 1956.

[291] J Wallesten, A N Lipatnikov, and J Nisbet. Turbulent flame speed closure model: Further development and implementation for 3-D simulation of combustion in SI engine. *Society of Automotive Engineers*, (982613), 1998.

[292] A B Wallis. Gas sealing system for rotary valves. US Patent 5,526,780, June 1996.

[293] A B Wallis. Lubrication system for rotary valve. US Patent 5,529,037, June 1996.

[294] A B Wallis. Rotary valve with seal supporting tongue. US Patent 5,503,124, April 1996.

[295] A B Wallis and A D Thomas. Sealing means for rotary valves. US Patent 5,509,386, April 1996.

[296] Z U A Warsi. *Fluid Dynamics : Theoretical and Computational Approaches.* CRC Press, Boca Raton, Florida, second edition, 1999.

[297] A P Watkins, S Dessipris, and H Khaleghi. The combined effects on fluid flow during compression of piston bowl shape and offset, and swirl ratio. *Society of Automotive Engineers*, (870595), 1987.

[298] D C Wilcox. *Turbulence Modeling for CFD.* DCW Industries, California, second edition, 1998.

[299] D E Winterbone and R J Pearson. *Design Techniques for Engine Manifolds: Wave Action Methods for IC Engines.* Arrowsmith, London, 1999.

[300] P O Witze, J K Martin, and C Borgnakke. Measurements and predictions of the precombustion fluid motion and combustion rates in a spark ignition engine. *Society of Automotive Engineers*, (831697), 1983.

[301] O Yaşar, I Sauers, P G Datskos, R J Toedte, J Thomas, J Armfield, and R L Graves. A new approach to spark ignition end engine combustion modeling. Draft paper.

[302] S L Yang, Y K Siow, B D Peschke, and R R Tacina. Simulation of engine flow with swirl using Re-stress turbulence model in KIVA code. In *10th Multidimensional Engine Modelling Users Group Meeting*, Detroit, March 2000.

[303] I Yavuz and I Celik. A new approach in Smagorinsky based eddy viscosity modeling for IC engine applications. In S R Bell, editor, *Proceedings of the 2000 Fall Technical Conference of the ASME Internal Combustion Engine Division*, volume 1, pages 81–88, Peoria, Illinois, September 2000.

[304] Y Zeng and C-F Lee. Computations of air/fuel preparation process in a port-injected spark-ignition engine during cold-starting phase. In S R Bell, editor, *Proceedings of the 2000 Fall Technical Conference of the ASME Internal Combustion Engine Division*, pages 27–37, Peoria, Illinois, September 2000.

[305] Y Zeng and C-F Lee. Modeling of multicomponent fuel effects in internal combustion engines. In *10th Multidimensional Engine Modelling Users Group Meeting*, Detroit, March 2000.

[306] M A Zimmerman. Rotary valve internal combustion engine. US Patent 3,871,340, March 1975.

[307] M Zolver, C Griad, and S Henriot. 3D modeling applied to the development of a DI Diesel engine: Effect of piston bowl shape. *Society of Automotive Engineers*, (971599), 1997.

Appendix A

Fortran Subroutines

A.1 pointinquad

This subroutine is the code used for the description of section 7.2.2. It returns `.true.` if the location specified by `xp`, `yp` is located inside the quadrilateral specified by arrays `x` and `y`. The arrays `x` and `y` are four element arrays, with the points listed in the order specified in figure 7.14.

```
      logical function pointinquad(x,y,xp,yp)

C**********************************************************************
C
C Function to determine whether point (xp,yp) is inside
C 2-dimensional quadrilateral defined by x(1-4),y(1-4).
C
C**********************************************************************

      double precision x(4),y(4)
      double precision xp,yp
      double precision p1x,p2x,p3x,p4x,p1y,p2y,p3y,p4y
      double precision p2p1,p4p3,p1p3,p2p4

      p1x=x(1)-xp
      p1y=y(1)-yp
      p2x=x(2)-xp
      p2y=y(2)-yp
```

```
      p3x=x(3)-xp
      p3y=y(3)-yp
      p4x=x(4)-xp
      p4y=y(4)-yp
      p2p1=p2x*p1y-p1x*p2y
      p4p3=p4x*p3y-p3x*p4y
      p1p3=p1x*p3y-p3x*p1y
      p2p4=p2x*p4y-p4x*p2y
      pointinquad = ((p2p1*p4p3).le.0.0d0)
     +                        .and. ((p1p3*p2p4).le.0.0d0)
      return
      end
```

A.2 manreblock

This subroutine is the reblocking code used for section 7.2.2. The variables `ni` and `nj` define the size of the block in the i and j directions respectively. The logical array `rbdone` defines whether the node has been reblocked successfully or not, and is also used to specify nodes which are not to be reblocked in this operation. The integer variable `bits` is the number of blocks the routine has used to reblock the region. The four arrays `ibst`, `jbst`, `ibfn` and `jbfn` are the i and j locations of the start and finish node of each block.

```
      subroutine manreblock(rbdone,ni,nj,bits,ibst,jbst,ibfn,jbfn)

C*****************************************************************
C
C Reblocks a region
C
C*****************************************************************

      integer bits,ni,nj,ibst,jbst,ibfn,jbfn
      logical ok,rbdone
      dimension rbdone(35,35),ibst(100),jbst(100)
      dimension ibfn(100),jbfn(100)
```

```
      bits=0
      do i=1,ni
        do j=1,nj
          if (.not.rbdone(i,j)) then
            ifn=i
            jfn=j
30          continue
            if (.not.rbdone(ifn+1,j) .and. (ifn.lt.ni)) then
              ifn=ifn+1
              goto 30
            endif
31          continue
            ok=.true.
            do ii=i,ifn
              if (rbdone(ii,jfn+1)) ok=.false.
            enddo
            if (ok .and. (jfn.lt.nj)) then
              jfn=jfn+1
              goto 31
            endif
            bits=bits+1
            ibst(bits)=i
            jbst(bits)=j
            ibfn(bits)=ifn
            jbfn(bits)=jfn
            do ii=i,ifn
              do jj=j,jfn
                rbdone(ii,jj)=.true.
              enddo
            enddo
          endif
        enddo
      enddo
      return
      end
```

Appendix B

Publications

This appendix contains a copy of a paper published on the work presented in this thesis.

Other related publications produced during this work include:

- G D Horrocks, J A Reizes and S G Mallinson. Numerical study of flow in a rotating shock tube. In *Proceedings of the 13th Australasian Fluid Mechanics Conference*, Monash University, Melbourne, 1998. Editors M C Thompson and K Hourigan.
- G D Horrocks, J A Reizes and S G Mallinson. Numerical study of flow in a rotating shock tube. In *Proceedings of the 22nd International Symposium on Shock Waves*, Imperial College, London, 1999.

B.1 "Tumble Vortex Breakdown During the Compression Stroke of a Model Internal Combustion Engine", 2000

This paper was presented at the 2000 Fall Technical Conference of the American Society of Mechanical Engineers (ASME), Internal Combustion Engine Division. The conference was held at Peoria, Illinois, from 23-26 September 2000. The editor was Stuart Bell, from the University of Alabama.